Photophysics and Spin Chemistry of Donor-Acceptor substituted Dipyrrinato-Metal-Complexes

Dissertation zur Erlangung

des naturwissenschaftlichen Doktorgrades der

Julius-Maximilians-Universität Würzburg

vorgelegt von

Stefan Riese

aus Würzburg

Würzburg, 2019

Eingereicht bei der Fakultät für Chemie und Pharmazie am

28.01.2019

Gutachter der schriftlichen Arbeit

1. Gutachter: Prof. Dr. Christoph Lambert

2. Gutachter: Prof. Dr. Ulrich Steiner

Prüfer des öffentlichen Promotionskolloquiums

1. Prüfer: Prof. Dr. Christoph Lambert

2. Prüfer: Prof. Dr. Ulrich Steiner

3. Prüfer: Prof. Dr. Todd Marder

Datum des öffentlichen Promotionskolloquiums

26.03.2019

Doktorurkunde ausgehändigt am

Die vorliegende Arbeit wurde in der Zeit von Oktober 2013 bis Januar 2019 am Institut für Organische Chemie der Universität Würzburg angefertigt.

Mein besonderer Dank gilt

Herrn Prof. Dr. Christoph Lambert

für die Vergabe des interessanten und vielseitigen Themas, sowie das stets offene Ohr wenn die Arbeit daran einmal nicht so lief wie geplant. Vielen Dank für viele Diskussionen über Magnetfeldeffekte und Molekülgeometrien. Danke außerdem für die Möglichkeit an diversen, bereichernden Tagungen teilzunehmen sowie Ihre schier unerschöpfliche Geduld vor und während der Heimreise vom SCM 2017 in Schluchsee.

COPYRIGHT

CONTENTS

ABBREVIATIONS

ahfc	anisotropic hyperfine coupling
CC	central chromophore
CMC	central metal complex
CR	charge recombination
CS	charge separation
CSS	charge separated state
CT	charge transfer
DDQ	2,3,-dichloro-5,6-dicyano-1,4-benzoquinone
ET	electron transfer
esdi	electron-spin-spin-dipolar interaction
gta	g-tensor anisotropy
GPC	gel permeation chromatography
HOMO	highest occupied molecular orbital
ihfc	isotropic hyperfine coupling
LC	ligand centered
LUMO	lowest unoccupied molecular orbital
MFE	magnetic field effect
MLCT	metal-to-ligand charge transfer
NDI	1,4,5,8-naphthalene diimide
ppz	1-phenylpyrazole
PS	photosensitizer
rmsd	rout mean square deviation
SEC	spectroelectrochemistry
sri	spin rotational interaction
TAA	triarylamine
TEA	triethylamine
TFA	trifluoroacetic acid
TBAHFP	tetrabutylammonium hexafluorophospate
(TD)DFT	(time dependent) density functional theory

1 Introduction

In 1966, *Wiltschko et al.* demonstrated that the behavior of the European robin (*Erithacus rubecula*) can be influenced by the application of a magnetic field, and thus could prove the suspected ability of birds to sense the inclination of the geomagnetic field.[1-3] Since then, the magnetoreceptive sense was found for a variety of other birds,[4] and other vertebrates and invertebrates.[5-10] Furthermore, this finding inspired a thorough search for the biophysical mechanism of the magnetoreception. Based on various experiments two principle hypotheses have been developed. While one is based on the direct physical reception of the geomagnetic field by forces on magnetic single domain crystals of iron minerals,[7, 11-12] the other proposes the modulation of photochemical reactions by the earth's magnetic field due to the radical pair mechanism as described by *Schulten et al.*[13-15] The latter is based on results which suggest that many magnetoreceptive birds cannot sense the magnetic field in the total absence of light. The mechanism is assumed to be connected to cryptochromes, a light absorbing flavoprotein class which was found in the retinas of a variety of magnetoreceptive species. Cryptochromes are known to influence various biological processes and have been shown to form radical pairs under light excitation, which in turn are sensitive towards low magnetic fields of about 1 mT. Further investigations of artificial model systems perforemed by *Timmel et al.* and other groups revealed that magnetic fields as low as the earth magnetic field of about 60 µT can influence the photophysical and photochemical properties of radical pairs.[13, 16-20]

The radical pair mechanism was initially developed to explain the chemically induced dynamic nuclear and electron polarization observed during the investigation of certain chemical reactions by NMR and EPR spectroscopy[21-22] and thus also has a significant impact on photophysical and photochemical[23-41] processes in general. Accordingly, magnetic fields can influence the device performance of important modern applications such as organic light emitting diodes (OLEDs)[42-43] or photovoltaics[44-45], which include radical pairs as important reaction intermediates.

The question arises how conventionally achievable magnetic fields can influence chemical reactions which usually are governed by driving forces many orders of magnitudes stronger. Which characteristics are required of chemical system to be sensitive to magnetic fields?[16, 20, 46]

To answer these questions, a detailed understanding of the involved processes is needed. As can be seen from the example of the magnetoreception, artificial model systems often provide a more suitable basis for the investigation of fundamental processes since they reduce the complexity of the underlying problems. Thus, the following chapters will first establish a general understanding of the spin chemical principles behind the radical pair mechanism, and will then focus on possible model systems for a further investigation of central spin chemical and photophysical issues such as photoinduced charge separation, spin interconversion and charge recombination.

1.1 Spin Chemistry of Radical Pairs

1.1.1 Spin States of Radical Pairs

The *Pauli* exclusion principle states that two electrons can occupy the same orbital only if their spins are oriented in opposite directions (antiparallel). Since the magnetic environment of two electrons occupying the same orbitals is identical, the two spins have a constant phase relation resulting in an overall spin momentum of zero for paired electrons. In contrast, radicals are species which comprise an unpaired electron and thus have an overall spin of either +1/2 (α) or -1/2 (β). Accordingly, for a spin correlated radical pair, that is a pair of radicals whose spins form specific linear combinations, four spin substates are possible which can be visualized as vectorial sums of the spin vectors s_1 and s_2 as depicted in **Figure 1** (A).[20, 24, 27, 46-48]

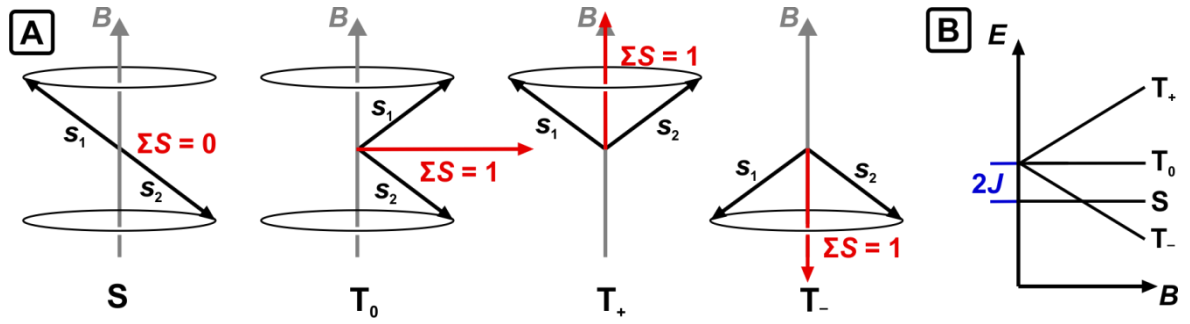

Figure 1: The spin substates S, T_0, T_+ and T_- of a correlated radical pair visualized as a linear combination of two electron spins s_1 and s_2 which precess around a strong external magnetic field *B* resulting in an overall spin angular momentum ΣS (A) as well as the associated state energies in dependence of the exchange interaction *J* and the magnetic field strenght (B).

While the antiparallel alignment of s_1 and s_2 results in a singlet state (S) with an overall spin of zero, a parallel alignment of the spins results in three triplet substates (T) which are characterized by an overall spin angular momentum of 1. The difference between the three sub-states T_+, T_0 and T_- can only be understood in relation to a magnetic field *B* around which the spins precess. While the spin angular momentum is perpendicular to *B* in T_0, it is oriented parallel or antiparallel in T_+ and T_-, respectively. Thus, the energy of T_+ and T_- is dependent on the external field, while S and T_0 are not influenced by magnetic fields. This results in the *Zeeman* splitting of the three triplet sublevels as shown in **Figure 1** (B). The energy difference between T_0 and S is dependent on the electron exchange interaction *J*, which decreases with lower electronic couplings and larger distances between the radical centers. This work will focus on systems in which the radical centers are only coupled weakly and have distances around 15 – 30 Å. For such systems, the exchange interaction *J* is expected to be between 0.1 mT and a few tens of mT, and thus will only be considered at weak magnetic fields where it is expected to influence the spin evolution.[27, 40, 46-53]

1.1.2 Mechanisms of Spin Evolution

In general, the initial spin state of radical pairs is not stationary and there may be transitions between the singlet and the triplet states over time. This spin evolution is caused by a variety of mechanisms most of which are influenced by an external magnetic field B_0.

Coherent Spin Evolution

The coherent spin evolution is mainly due to the hyperfine coupling (hfc) interaction of the electron spins with the nuclear spins of the nuclei involved in the respective radical center. In a semi classical approximation introduced by *Schulten et al.*, the combined isotropic hyperfine coupling (ihfc) interactions with all nuclei present in the respective radical center can be described as an effective nuclear hyperfine field B_{hfc}. For individual radical centers *i,* the hyperfine field $B_{hfc}(i)$ can be estimated from the ihfc constants a_k and the nuclear spin quantum numbers I_k of the respective involved nuclei *k* using equation (1).[27, 46, 50, 54-57]

$$B_{hfc}(i) = \sqrt{\sum_k a_k^2 I_k (I_k - 1)} \tag{1}$$

If an external magnetic field B_0 is applied, the resulting active magnetic field $B(i)$ on the electron spins can be described as the vector sum of B_0 and $B_{hfc}(i)$ of the radical center.[27, 46, 54-55, 57]

$$B(i) = B_0 + B_{hfc}(i) \tag{2}$$

The electron spins in the radical centers precess around the respective field $B(i)$ with the *Larmor* frequency ω_0 which is given by equation (3).[27, 46, 48, 57]

$$\omega_0(i) = \frac{g\mu_B}{\hbar} B(i) \tag{3}$$

Here, *g* is the isotropic g-value of the respective radical and μ_B is the *Bohr* magneton.

At low external magnetic fields, B_{hfc} significantly contributes to both the orientation as well as the strength of $B(i)$. Accordingly, the respective electron spins s_1 and s_2 precess with different frequencies around different axes and relative orientation of the two spins to each other, and thus the spin state of the radical pair changes over time (**Figure 2** (A)). With increasing external magnetic field strength, the active field $B(i)$ becomes more and more determined by B_0, and the precession axis of s_1 and s_2 converge. This decreases the possibility for the spin flip transitions between S or T_0 and T_+ or T_-, which are completely shut down at high external magnetic fields. However, even at very high fields the component of $B_{hfc}(i)$ along the axis of the external magnetic field acts as an additional local

magnetic field on the electron spins, thus retaining the difference between the precession frequencies of both electron spins. Therefore, the rephasing transition between S and T_0 is not influenced by the external magnetic field and occurs even at high external magnetic field strengths (**Figure 2** (B)). **Figure 2** illustrates both the of spin transitions for a theoretical radical pair in which only one of the spins (s_2) couples to a nuclear magnetic field $B_{hfc}(2)$.[24, 27, 46, 48-49, 58]

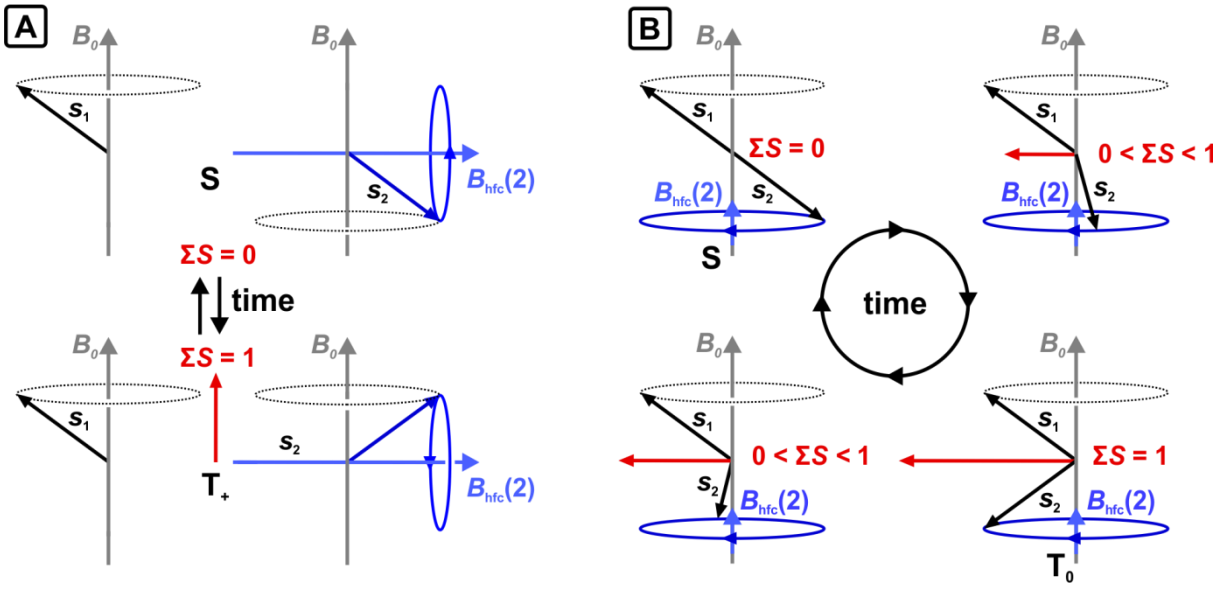

Figure 2: Coherent electron spin evolution for a theoretical radical pair in which only s_2 experiences hyperfine coupling to a nuclear magnetic field $B_{hfc}(2)$. The figures are drawn in a reference frame rotating in phase with the precession of s_1 around the external magnetic field B_0 so that s_1 seems to be stationary. Spin flip transitions between S or T_0 and T_+ or T_- only occur in weak external magnetic fields since the spins rotate around different effective axes (A). The rephasing transition between S and T_0 is also effective in strong external magnetic fields since the difference between the two Larmor frequencies due to $B_{hfc}(2)$ is retained even at high fields (B).

From equation (3) a second coherent mechanism for the rephrasing transition between S and T_0 can be derived. Differences in the precession frequency of the electron spins are not necessarily exclusively due to different active magnetic fields, but may also arise from a difference Δg of the g-values of the respective radicals. Hence, this second mechanism is called Δg-mechanism. In contrast to the isotropic hyperfine coupling, the spin evolution due to the Δg-mechanism is directly proportional to the external magnetic field strength. Hence, the Δg-mechanism is negligible at low magnetic fields. This is especially true for organic radicals which typically exhibit a Δg of about 0.001. At fields lower than a few Tesla this results in spin interconversion rates several orders of magnitude slower than the contribution of the isotropic hyperfine coupling. Thus, the Δg-mechanism usually is negligible when discussing coherent spin interconversion, except if the radical pair involves heavier atoms which influence the *g-value* significantly.[24, 26-27, 48, 50, 57-59]

The magnetic field dependence of the coherent spin evolution can be addressed comfortably when looking at the dependence of the *Zeeman* splitting of the spin states on the external magnetic field strength depicted in **Figure 1** (B). The energies of the spin substates are modified by the isotropic hyperfine coupling and thus increase or decrease slightly in energy. A transition between the states is only possible if the energy difference between the states is within the average ihfc coupling strength. Assuming an electron exchange interaction of $J = 0$, all four spin substates are degenerate at zero field, and the spin evolution proceeds unhindered. With increasing magnetic field, T_+ and T_- will gradually leave the energy range which can be overcome by ihfc. Thus, after a threshold magnetic field strength, the transition between S and T_0 is the only effective pathway and the coherent spin evolution reaches its lower limit. The magnetic field $B_{1/2,\,\mathrm{hfc}}$, at which the coherent spin evolution due to isotropic hyperfine coupling reaches half its limiting value, can be estimated from the nuclear hyperfine fields $B_{\mathrm{hfc}}(i)$ of the respective radicals using equation (4).[32-33, 37, 46, 54, 56, 60]

$$B_{1/2,\,\mathrm{hfc}} = \sqrt{3\,(B_{\mathrm{hfc}}(1)^2 + B_{\mathrm{hfc}}(2)^2)} \tag{4}$$

At fields higher than $B_{1/2,\,\mathrm{hfc}}$, the coherent spin interconversion between the outer Zeeman levels T_+ and T_- and the inner Zeeman levels T_0 and S is increasingly suppressed until at a certain magnetic field strength the coherent spin interconversion is slower than the otherwise much slower incoherent spin relaxation. Although the coherent transition between S and T_0 is still as fast as at zero field, the overall spin evolution is governed by incoherent mechanisms at higher field strengths since they pose the only effective transition to or from T_+ and T_-.[24-25, 27, 41, 46, 57-59]

Furthermore, if the exchange interaction $2J$ is larger than the average ihfc strength, no coherent transition between the singlet state and the degenerate triplet states is possible at zero field. However, at a certain magnetic field $B = 2J$, either T_+ or T_- will be degenerate with S, enabling a coherent spin flip. This *J*-resonance gets suppressed at higher fields, and the spin evolution is dominated by the slower incoherent spin relaxation, as described for $J = 0$.[27, 37, 48, 57, 61-62]

Incoherent Spin Evolution

The incoherent spin evolution is mainly due to spin-lattice relaxation and spin-spin relaxation of the individual radicals. These two mechanisms are commonly known in the field of electron paramagnetic resonance (EPR)[63-64] and nuclear magnetic resonance (NMR)[21, 65-66] spectroscopy, where they are described by the spin-lattice relaxation time T_1 and the spin-spin relaxation time T_2. The spin-spin relaxation only changes the phase relation between the two electron spins and thus can only interconvert between S and T_0. Since, as explained above, the coherent contribution to this transition is very large even at high fields, T_2 can usually be neglected.[27, 32, 35, 46, 58, 67]

In contrast, the spin-lattice relaxation changes the orientation of the spins, interconverting between the outer and inner Zeeman levels and thus is expected to contribute significantly to the overall spin evolution at high fields. Spin-lattice relaxation occurs through essentially four mechanisms, all of which are due to stochastic modulations of the electron spin *Hamiltonian* caused by the translational and rotational *Brownian* motion of the radicals. These mechanisms are the spin rotational interaction (sri), the g-tensor anisotropy (gta), the anisotropic hyperfine coupling (ahfc) and the electron spin dipolar interaction (esdi). The spin-lattice relaxation rate T_1^{-1} caused by the respective mechanism can be estimated using equations (5) – (8). [26, 32, 35, 59, 68-73]

$$\frac{1}{T_1(\text{sri})} \sim \left[\sum_{i\,=\,\text{x,y,z}} (g_{ii} - g_\text{e})^2\right] \frac{1}{\tau_\text{c}} \tag{5}$$

$$\frac{1}{T_1(\text{gta})} \sim \left[\sum_{i\,=\,\text{x,y,z}} (g_{ii} - g_\text{iso})^2\right] \mu_\text{B}^2 B^2 \frac{\tau_\text{c}}{1+\omega_0^2\tau_\text{c}^2} \tag{6}$$

$$\frac{1}{T_1(\text{ahfc})} \sim \left[\sum_{i\,=\,\text{x,y,z}} (A_{ii} - A_\text{iso})^2\right] I(I+1) \frac{\tau_\text{c}}{1+\omega_0^2\tau_\text{c}^2} \tag{7}$$

$$\frac{1}{T_1(\text{esdi})} \sim \frac{g_\text{e}^2\mu_\text{B}^2}{d_\text{min}^3 d_\text{max}^3} \frac{\tau_\text{c}}{1+\omega_0^2\tau_\text{c}^2} \tag{8}$$

In these equations, g_e is the *g*-factor of the free electron while g_{ii} and g_iso denote the anisotropic and the isotropic component of the *g*-tensor associated with the radical center. Similarly, A_{ii} and A_iso denote the anisotropic and the isotropic component of the hyperfine coupling. Furthermore, μ_B is the *Bohr* magneton, *B* the active magnetic field which, in a high field approximation, is equal to the external magnetic field, *I* is the total nuclear angular momentum quantum number and d_min and d_max are the closest and farthest possible distances between the two radical centers. Finally, the last term in all equations describes the dependence of the relative mechanism on the tumbling motion of the radical centers which is characterized by the rotational correlation time τ_c. For gta, ahfc and esdi the last term also includes ω_0, the *Larmor* frequency of the electron spin as given by equation (3), and indicates the *Lorentzian* type behavior of the spectral density of the corresponding stochastic motion of rotational or translational diffusion at varying active magnetic fields. An additional interference term describing the combined effect of gta and ahfc, which are not simply additive, is omitted in this discussion. [26, 32, 35, 59, 68-75] From a comparison of equations (5) – (8), a number of conclusions regarding the physical principles behind the four mechanisms and their contribution to the overall spin lattice relaxation rate can be drawn.

While sri, gta and ahfc describe the influence of the rotation of a single radical center on the electron spin and could in principle also be applied to unpaired free radicals, the esdi describes the spin relaxation due to the interaction of two separate electron spins. Hence, the esdi also describes the influence of translational diffusion of two radical centers in relation to each other, and is very dependent on the distance between the two radical centers. Furthermore, the contribution of esdi to the overall spin relaxation decreases with rising magnetic field strength.[26, 32, 35, 71-72, 76]

The sri and the gta describe the modulation of the electron spin due to a stochastic change of the anisotropic component of *g*-tensor associated with the radical. Both mechanisms are only effective if the g-factors of the radical centers are different from that of the free electron. While the contribution of sri to the overall spin relaxation is independent of the external magnetic field, the relaxation rate due to gta increases with rising magnetic field strength and approaches a saturation limit at high magnetic fields.[26, 32, 35, 68, 74]

Finally, the ahfc describes the effect of the anisotropic component of the hyperfine coupling interaction between the electron spin and the nuclear spins. For radicals which comprise atoms with a non-zero nuclear spin the relaxation due to ahfc usually is very fast at low to moderate magnetic fields, but slows down at higher fields. The field dependence of the ahfc and the esdi is identical since it is determined solely by the last term in equations (7) and (8), which describes the Lorentzian behavior of the rotational or translational diffusion.[32, 35, 59, 68]

Although the relative contributions of the four different mechanism to the incoherent spin relaxation have to be estimated individually for every radical pair, solvent environment and external magnetic field, a few general tendencies can be summarized as follows. For typical organic radicals without significant contributions of heavy atoms, which will be the focus of this work, the sri and the gta can usually be neglected at commonly achievable magnetic fields since the *g*-factors of the radicals differ by less than 0.001 from the *g*-factor of the free electron of $g_e \approx 2.0023$. Furthermore, a spin evolution by esdi is only effective if the average spatial separation between the radical centers is very small. Thus, the esdi is usually only significant if the radical centers are somehow confined into a defined, small space (limiting d_{max}), but still have a degree of translational freedom so that the molecular motion can produce very close contacts between the radicals (decreasing d_{min}). This is usually only achieved in micellar cages or for radical pairs with flexible linkers. For rigidly linked radical pairs with a fixed distance d_{DA} between the radical centers, which will be the focus of this work, the esdi is dependent on d_{DA}^{-6} and is significantly hindered for distances longer than about 10 Å. That leaves the ahfc as the main contributor to the overall incoherent spin relaxation, since most organic radicals comprise atoms with a non-zero nuclear spin such as ^{1}H, ^{14}N, ^{19}F or ^{11}B and thus show effective relaxation due to ahfc especially at low magnetic fields.[26, 32, 35, 59, 65, 68-74]

1.1.3 The Radical Pair Mechanism

As a direct consequence of the general tendency of chemical reactions to occur under conservation of the overall spin angular momentum, the spin state of a radical pair can have a significant influence on the products and kinetics of any follow-up reactions associated with a given radical pair. Furthermore, as was discussed in the previous section, even relatively small external magnetic fields have an influence on the interconversion rate between the different spin-substates of a given radical pair. This answers the question how weak external magnetic fields can influence chemical reactions - not through thermodynamic reaction control but through kinetic control of the radical pair.

This was first proposed as the radical pair mechanism by *Closs*[77] and *Kaptein et al.*[21] and later extended by *Hayashi* and *Nagakura*[25, 78] to include incoherent spin relaxation as depicted in **Figure 3**. [24, 32, 35, 59, 76] Finally, *Steiner et al.* could show that both the coherent and the incoherent contributions to the spin evolution, as well as the influence of the exchange interaction *J* can quantitatively be accounted for by the classical model, when incorporating a generalized energy dependence of the rate constants of all spin conversion processes.[59, 61-62, 79]

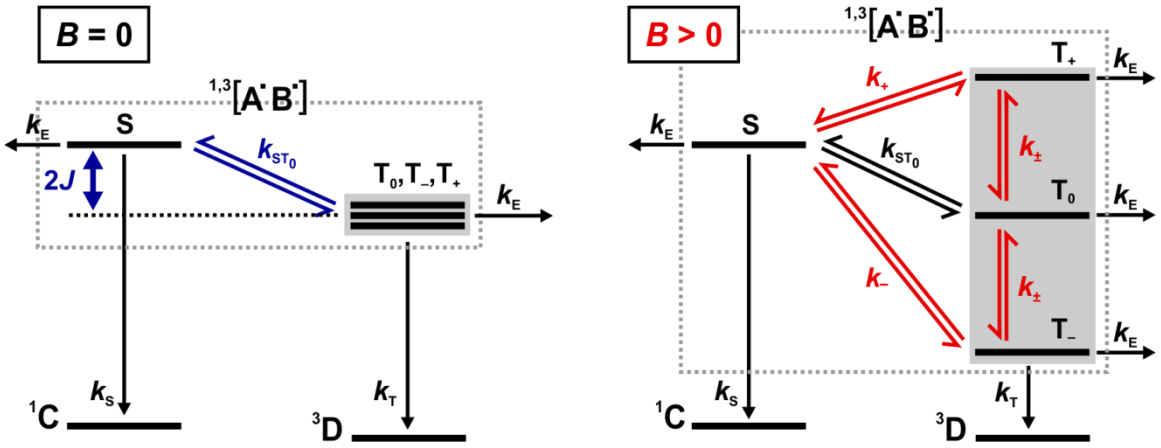

Figure 3: Reaction dynamics of a radical pair [A·B·] with non-zero exchange interaction *J* at zero magnetic field and at high magnetic field.

The reaction of a spin correlated radical pair A·B· results in different products depending on the spin state at the time of reaction due to the spin conservation rule. Accordingly, the associated rate constants k_S and k_T usually are different. Furthermore, the radical pair can escape the range in which a reaction is possible with the rate k_E, resulting in free radicals which deactivate slowly by interaction with the surrounding medium. Additionally, the distance between the two radical centers strongly affects the magnitude of the exchange interaction *J*. Since *J* influences the coherent spin evolution summarized by the rate k_{ST0} and causes differences between the rates k_+, k_- and $k_\pm$ describing the incoherent spin relaxation, the spin dynamics are also dependent on the distance between the

radical centers. An exact mathematical description of the manifold dependencies is often not possible since too many variables are unknown. Furthermore, k_{ST0}, as well as k_+, k_- and $k_\pm$ themselves are average rate constants caused by all the described possible spin interconversion mechanisms, further increasing the complexity of the problem.[24-25, 27, 37-38, 41, 49, 51, 58, 76]

Model systems in which some of the variables can be neglected can reduce the complexity of this problem and facilitate an interpretation of observed magnetic field effects (MFE). Depending on the variable which is desired to be omitted, a variety of suitable model systems can be imagined. The formation of free radicals with the rate k_E can be reduced effectively by confining the radical centers into a small space with micellar cages or prevented altogether by covalent linking of the radical pair. If the radical centers are connected in a defined distance with a rigid bridge, the exchange interaction becomes approximately constant, and can even be neglected if the electronic coupling between the radical centers is very weak. For those cases, the incoherent rates become identical ($k_+ = k_- = k_\pm$) and only one magnetic field dependent rate $k_\pm$ has to be considered. Finally, for radical pairs which cannot form triplet products, the singlet state is the only effective reaction pathway and k_T becomes more or less negligible.[19, 25, 32, 35, 37, 39, 41, 51, 59, 62, 71, 80]

In principle, the MFE is not dependent on the way the radical pair is formed, however in most published studies, the radical pair is formed by photoinduced charge separation (CS) between an electron donor and an electron acceptor. For neutral donor-acceptor pairs the transfer of one electron results in a charge separated state (CSS) which comprises two unpaired electrons and thus represents a radical ion pair. Charge recombination (CR) from the singlet generally regenerates the ground state with k_S, while CR from the triplet state with k_T usually results in an intermediate triplet state which subsequently deactivates to the singlet ground state. Depending on the rates k_S and k_T, as well as the initial spin multiplicity of the CSS, an external magnetic field influences the decay kinetics of the CSS in various ways and thus can be observed for example by means of time resolved transient spectroscopy. To facilitate the investigation of the MFE, the CSSs should be populated with a high quantum efficiency and exhibit suitable lifetimes.[17-19, 27, 34-37, 59, 62, 81]

Since both the initial spin multiplicity as well as k_S and k_T are governed by the CS and CR mechanism associated with the CSS, a good understanding of the photophysics of the investigated compounds is often helpful for a correct interpretation of the observed spin-chemistry. Therefore, the following chapters will summarize the basic concepts of charge transfer in donor-acceptor compounds and give a few basic examples of structure-property relationships.

1.2 Electron Transfer in Donor-Acceptor Substituted Triads

The desire to thoroughly investigate electron transfer reactions was mostly inspired by the photosynthetic reaction center and the wish to generate chemical and electric energy from solar energy by mimicking the process of photosynthesis. Analogous to the investigation of spin chemistry, suitable model systems had to be developed to reduce the complexity of the occurring photo induced electron transfer processes. Many successful studies were performed on molecules comprising designated electron donor (D) and electron acceptor (A) moieties which are connected covalently by a bridging unit. Chromophores are often used for the bridging unit to increase the efficiency of light absorption. In these cases they are usually labeled as photosensitizer (PS). In this thesis, D-PS-A structures comprising three individual chromophores will be referred to as a donor-acceptor substituted triads or simply triads. **Figure 4** depicts a schematic design of such triads, as well as several possible electron transfer reactions induced by photoexcitation of the central photosensitizer from the ground state PS to an excited state PS*.[19, 37, 51, 53, 59, 76, 81-88]

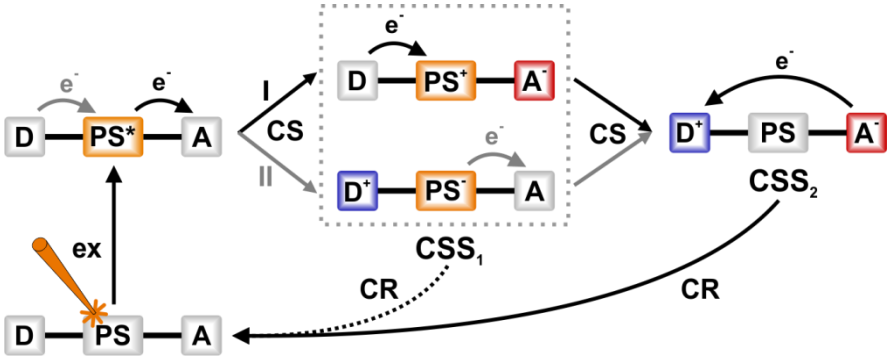

Figure 4: Possible stepwise mechanisms of photoinduced charge separation (CS) to CSS_1 and CSS_2 and subsequent charge recombination (CR) of CSS_2 to the ground state.

The initial electron transfer can either occur from the PS to the acceptor (I), as well as from the donor to the PS (II), resulting in two possible initial charge separated states (CSS_1). The reverse process to this charge separation (CS) is the charge recombination (CR), which deactivates CSS_1 to the ground state. The CR competes with a second CS which forms the final charge separated state (CSS_2). In CSS_2, the charge is separated between the donor and the acceptor, that is over a longer distance. CSS_2 deactivates by CR to the ground state. Which electron transfer processes actually take place, as well as the quantum yield and lifetime of the CSSs, is determined by the redox potentials and state energies associated with the donor, photosensitizer and acceptor moieties, as well as the electronic interaction between the individual subunits.[19, 37, 51, 53, 59, 76, 81-90]

1.2.1 *Marcus* Theory

The *Marcus* theory relates the kinetics of a given electron transfer with compound- and solvent-specific thermodynamic parameters. As shown in **Figure 5**, the electron transfer (ET) along a dimensionless ET-coordinate is described as a transition between two diabatic, parabolic free energy surfaces representing the compound before (reactant state) and after (product state) ET.[91-92]

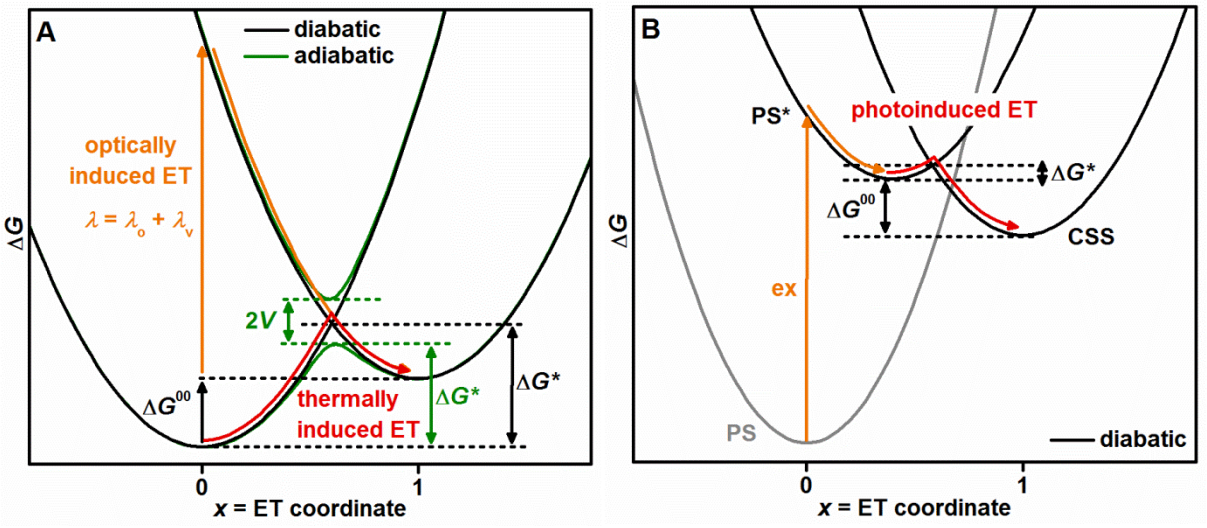

Figure 5: Schematic representation of the diabatic and adiabatic free energy surfaces of the reactant and product states of an exemplary optically or thermally induced electron transfer reaction (A) and a photoinduced charge separation (B).

A typical optically induced ET as depicted in **Figure 5** (A) starts with a vertical excitation according to the *Franck-Condon* principle, from the minimum of the reactant state directly to the product state which subsequently relaxes to its energetic minimum. The excitation energy needed for the ET is the sum of the free energy difference ΔG^{00} between the reactant and product states and the reorganization energy λ, which itself consists of the solvent reorganization energy λ_0 and the inner reorganization energy λ_v. While λ_o describes the reorientation of the solvent molecules which is induced by a charge redistribution due to the ET, λ_v describes the structural rearrangement of the compound itself due to the change of the oxidation state of the electron donor and acceptor moieties.[90, 93-97]

This is in contrast to the photoinduced charge separation described in **Figure 4** and **Figure 5** (B), where initially an excited state formed by photoexcitation (ex) acts as the reactant state for the ET. The product state after ET is a charge separated excited state.[90, 93-94, 97-99]

However, the electron transfer rate of the photoinduced charge separation is dependent on the same parameters as the rate of the thermally induced ET depicted in **Figure 5** (A) According to *Marcus* theory, k_{ET} can be expressed as a function of the activation energy ΔG^* using equation (9)

$$k_{ET} = A e^{-\frac{\Delta G^*}{k_B T}} \quad (9)$$

where k_B is the Boltzmann constant, T is the temperature in Kelvin and A is a pre-exponential factor describing the nuclear motion along the ET-coordinate and the probability that ET can occur at a given nuclear arrangement.[93-94, 96-97, 100]

In the diabatic limit, where the electronic coupling V between the involved redox centers is small compared to the thermal energy $k_B T$, the activation energy can be calculated by equation (10).

$$\Delta G^* = \frac{\left(\lambda + \Delta G^{00}\right)^2}{4\lambda} \quad (10)$$

From this expression, some basic predictions regarding the relationship between the free energy difference ΔG^{00}, the reorganization energy λ and the electron transfer rate k_{ET} can be made. For $\Delta G^{00} = -\lambda$, ΔG^* becomes zero and the ET proceeds unhindered. If $0 > \Delta G^{00} > -\lambda$, the system is in the *Marcus* normal region and k_{ET} increases with increasing ΔG^{00}. If $\Delta G^{00} < -\lambda$, the system is in the *Marcus* inverted region and k_{ET} decreases with increasing ΔG^{00}.[88, 93-95, 101] However, if the electronic interaction between the two redox centers increases and V becomes non-negligible compared to $k_B T$, the energy surfaces can no longer be described diabatically. According to the *Marcus-Hush* theory, the diabatic energy surfaces instead couple to form two adiabatic free energy surfaces which represent the adiabatic ground state and the adiabatic excited state. As can be seen from **Figure 5** (A), the minimal free energy difference between the two adiabatic states corresponds to two times the electronic coupling V. Furthermore, the activation energy ΔG^* for a thermally induced ET is clearly decreased due to the electronic coupling V. For a non-degenerate case a quantification of this effect is complex, however for a degenerate ET, that is $\Delta G^{00} = 0$, ΔG^* can be expressed purely in terms of reorganization energy λ and electronic coupling V according to equation (11).[93-94, 100-101]

$$\Delta G^* = \frac{\lambda}{4} - V + \frac{V^2}{\lambda} \quad (11)$$

Hence, for systems were $V << \lambda$, the activation energy in a first approximation decreases with rising electronic coupling between the two redox centers, resulting in a faster electron transfer. For this reason, the observed ET rates decrease with an increasing distance between the two redox centers since V is dependent on the an overlap of the wave functions of donor and acceptor and the amplitude of the wave functions decreases exponentially at long distances. However, the bridges between the two redox centers can influence V by mixing of their state energies with those of the donor and acceptor moiety. This superexchange mechanism often is responsible for a non-zero electronic interaction even at long distances .[37, 102]

1.2.2 Design Principles of Donor-Acceptor Substituted Triads

To efficiently store the energy provided by the excitation light, it is of interest to design systems in which the CSSs are formed with high quantum yields, have a high energy relative to the ground state and a long lifetime. This can be achieved by tuning the structure in a way that the photoinduced charge separation proceeds more or less unhindered, that is fast, while the thermally activated charge recombination lies deep in the *Marcus* normal or *Marcus* inverted region and thus is slowed down. For this, the *Marcus* inverted region is favorable since higher energies of the CSSs can be achieved without decrease of the lifetime. Additionally, the electronic coupling between the donor and acceptor subunits should be as low as possible to prevent an effective charge recombination due to the decrease of the activation barrier. These conditions can be achieved by a careful design of the model compound since the free energy difference ΔG^{00}, the reorganization energy λ and the electronic coupling V are dependent on the redox-potentials and size of the involved electron donor and acceptor, as well as the center to center distance d_{DA} between them and the structure of the bridges linking the redox centers.[37, 83, 90, 102-103]

Furthermore, some additional requirements can be imposed on a compound to be an efficient model system for the investigation of photoinduced charge separation, charge recombination and the spin chemistry of the intermediate radical pair.

The electron donor and acceptor need to be stable under light excitation and should exhibit a reversible redox behavior to allow for multiple cycles of charge separation and recombination without decomposition of the compound. To avoid unwanted side reactions of the CSSs, the radical ions of the donor and acceptor moieties should be chemically stable and exhibit a characteristic absorption spectra to allow for an easy detection of the CSS. Some of the more commonly used electron acceptors include quinones, fullerenes and aromatic imides and diimides, while carotenoids, tetrathiafulvalenes and aromatic amines are often used as electron donors.[37, 83-84, 104]

The photosensitizer of course has to absorb light in the visible spectrum where the spectrum of the sunlight reaches its maximum. The redox potentials of the resulting excited state have to be high enough that they can induce a charge transfer to the donor or acceptor. Furthermore, the excited state should have a long lifetime, since the deactivation to the ground state competes with the charge transfer. Additionally it can be useful if the unsubstituted photosensitizer exhibits a strong emission, since the CS can then be observed by a quenching of the emission. Commonly used photosensitizers include perylene and naphthalene mono and diimides, stilbenes, anthracene and especially transition metal complexes with various central metal ions and ligands.[39, 51, 83, 85-86, 90, 105-106]

Porphyrins and their metal complexes present a special case, since, depending on the central metal ion, they are commonly used as donors, acceptors and photosensitizers, and often even fulfill multiple roles in donor acceptor substituted triads.[37, 96, 102, 107]

Some exemplary triads which have successfully been investigated in terms of their photophysics and spin chemistry are shown in **Scheme 1**. A brief discussion of the obtained results will give insights into the interplay of the different structural motifs and reveal some basic relations between compound structure, photophysics and spin chemistry.

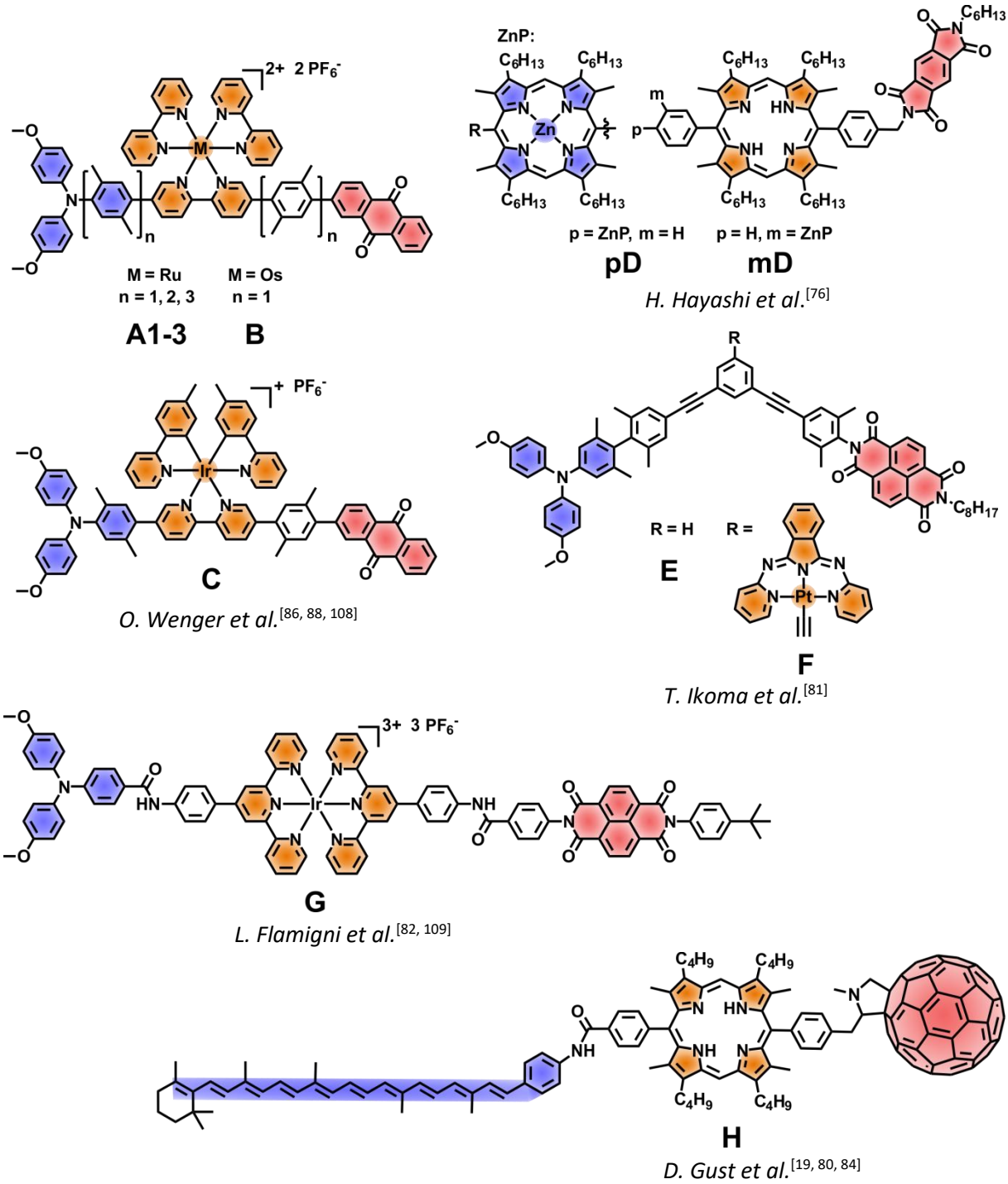

Scheme 1: Some examples of well understood donor-acceptor substituted triads. The colors indicate the role of the respective subunit as an electron donor (blue), electron acceptor (red) or photosensitizer (orange).

While **A1-3** differ only in the distance between the redox centers, **A**, **B** and **C** involve different photosensitizers. While the donor-acceptor distance d_{DA} increases steadily from **A1** to **A2** to **A3**, the CR in **A2** is significantly faster than in **A1** and **A3**. This unexpected observation could be rationalized with the distance dependence of λ, which results in an unhindered CR for **A2**, while **A1** recombines in the *Marcus* inverted region and **A3** in the deep *Marcus* normal region.[88, 108] While the CS occurs stepwise in **A1**, **B** and **C**, the order and the quantum efficiency of the two subsequent ETs is different. Furthermore, the CSS lifetime of **B** is significantly lower than that of **A1** and **C** due to energetically similar states associated with the central Os(II)-complex. This proves that although the final CSS is expected to be independent from the central PS in well decoupled systems, the PS has a significant influence on the formation of the CSS and sometimes even on the CR.[86]

Triads **pD** and **mD** exhibit a biexponential decay of the CSS which was explained by a competition between the CR from the initially formed singlet ^{1}CSS and an intersystem crossing to the triplet ^{3}CSS due to the spin evolution processes discussed in chapter 1.1.2. Although the compounds differ only in the *meta*- or *para*-connection between the donor and the PS, **pD** shows a steady behavior with rising magnetic field, while **mD** exhibits a small but distinct *J*-resonance.[76]

After excitation of **E** at the TAA, ^{1}CSS is formed virtually instantaneously in the singlet state while excitation of **F** at the PS leads to a slow population of the triplet ^{3}CSS with a lifetime of about 760 ns. At zero magnetic field, both **E** and **F** exhibit CSS-lifetimes of about 4 µs. However, the initial spin state has major consequences for the magnetic field dependence of the decay kinetics. Since CR is only possible from ^{1}CSS, the exclusive population of ^{3}CSS in **F** results in a monoexponential decay with a lifetime of 9.6 µs at high magnetic fields since the spin interconversion becomes the rate limiting step. In contrast, population of ^{1}CSS in **E** results in a biexponential decay since, due to spin evolution of CSS^1 to ^{3}CSS in the $T_\pm$ states, both the direct CR of ^{1}CSS to the ground state with a lifetime of 1.5 µs and the slow CR of ^{3}CSS with a lifetime of 8.8 µs can be observed.[81]

Triad **G** exhibits very long CSS lifetimes of 120 µs, which is about 2 orders of magnitude larger than for all other depicted triads. The massive lifetime was attributed to the long donor-acceptor distance of d_{DA} = 37 Å, and an effective electronic decoupling of the subunits provided by the saturated benzamide linkers between donor, PS and acceptor. On the other hand, the quantum yield of CSS is only 0.1 since the second CS step is in concurrence to a fast recombination of the initial CSS between the donor and the photosensitizer. [82, 109]

This is in contrast to compound **H,** which shows a high quantum yield of 0.88 for the formation of CSS but a CSS-lifetime of only 0.88 µs despite a similarly large donor-acceptor distance (d_{DA} > 20 Å) and the use of saturated linkers between the redox centers. The lower lifetime is caused among other reasons by the ability of the CSS to recombine both to the singlet ground state and to a low lying triplet excited state centered on the carotenoid donor which is not present in triad **G**. [19, 80, 84]

1.3 Transition Metal Complexes

As can be seen from the examples shown in **Scheme 1**, a wide variety of transition metal complexes are commonly used as photosensitizers in donor-acceptor substituted triads due to their suitable photophysical properties. The photophysics of transition metal compounds can be tuned to suit special requirements by variation of the central metal ion or the ligands.

1.3.1 Photophysics

According to ligand field theory, the degenerate d-orbitals of metal ions are destabilized and split in the electric field of the coordinating ligands. This split is centered around an energetic barycenter which is equal to the degenerate d-orbitals in a spherical field and is dependent on the complex geometry. **Figure 6** (A) depicts the d-orbitals of a central ion with d^6- and d^8-electron configuration. While d^6-ions generally adopt an octahedral complex geometry, d^8-ions usually exhibit a square planar geometry, especially for high ligand field splitting energies *Δ*. *Δ* increases with rising strength of the ligand field, with the spatial extension of the d-orbitals and the oxidation state of the central ion. Absorption of a photon of suitable energy can promote an electron from a lower to a higher orbital. A transition between the d-orbitals is localized on the metal and thus labeled metal centered (MC), while transitions between the π- and π*-orbitals of the ligands are labeled ligand centered (LC). Additionally, an electron can be transferred in a charge transfer transition from the metal center to the ligand (MLCT) or from the ligand to the metal center (LMCT). For complexes with a singlet ground state, the absorption is dominated by singlet-singlet transitions, although a small contribution of the respective singlet-triplet- transitions can be observed for complexes of heavy transition metals.[110-111]

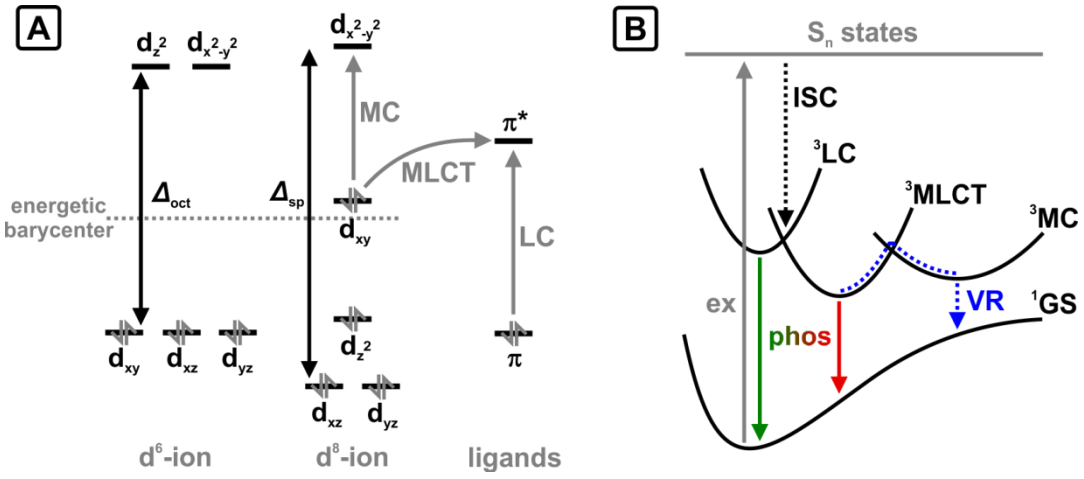

Figure 6: (A) Ligand field splitting *Δ* for a d^6-metal ion in an octahedral ligand field and a d^8-metal ion in a square planar ligand field, as well as an orbital representation of MC, MLCT and LC transitions. (B) Electronic transitions associated with the corresponding triplet excited states. Dotted arrows indicate non-emissive processes.

This is due to the high spin orbit coupling (SOC) constants associated with heavy transition metal ions, which also lead to an effective inter system crossing (ISC) between the singlet and triplet excited states. To differentiate between the magnetic field independent spin evolution due to SOC and the magnetic field dependent spin evolution due to the processes associated with a radical pair discussed in chapter 1.1, only the former will be described as ISC, while the latter will always be labeled otherwise throughout this thesis.[26-27, 110-112]

Figure 6 (B), shows the electronic transitions involving the triplet excited states of typical transition metal complexes. After excitation of any singlet excited state (S_n), the lowest excited triplet state is populated by efficient ISC which usually occurs with a rate of about 10^{12} s^{-1}, and thus is significantly faster than a deactivation of the excited singlet states to the ground state (GS). The populated triplet state decays to the singlet ground state either non-emissive or by phosphorescence. Although the strong SOC increases the rate of the formally spin forbidden phosphorescence significantly, resulting in rates of about 10^4 – 10^6 s^{-1}, it is still much slower than the typical fluorescence of excited singlet states with rates between 10^7 – 10^8 s^{-1}. Hence, disregarding non-emissive deactivation mechanisms, excited triplet states usually exhibit longer lifetimes than excited singlet states, and thus are promising lowest excited states for an efficient charge separation.[59, 110-118]

However, the emissive triplet states ^{3}LC and ^{3}MLCT can often be quenched by thermally activated population of the ^{3}MC state which rapidly deactivates to the ground state due to its metal centered character, but is *Laporte*-forbidden and thus non-emissive. Furthermore, this generally undesired deactivation pathway can be prevented efficiently by increasing the energy difference between the ^{3}LC and the ^{3}MLCT states and the ^{3}MC state. [110-111, 117-119]

A higher ligand field splitting Δ increases the energy difference between the occupied and the unoccupied d-orbitals, and therefore destabilizes the MC-states. Hence, a combination of ligands with a strong ligand field and central ions with large d-orbitals and a high oxidation state can make the ^{3}MC-states thermally inaccessible. A prominent example of this strategy are cyclometalated Ir(III) complexes, which usually show high excited state lifetimes and large emission quantum yields. The high quantum yields can be achieved in a broad spectral range since it is possible to tune the ligand centered LUMO independently from the metal-centered HOMO, thus varying the MLCT-transition energy without significantly stabilizing the ^{3}MC-states. This is mostly achieved by modification of the cyclometalating ligands with electron donating and withdrawing groups or by incorporation of ancillary ligands with low lying LUMOs, resulting in a reduction of the MLCT transition energy. If the ancillary ligand exhibits a low band gap, the HOMO often is also located at the ligand and the ^{3}LC-state becomes the lowest excited state. In these cases the photophysics are mostly governed by the ligand, as is the case for the dipyrrinato complexes discussed in the next chapter.[97, 110-111, 120-123]

1.3.2 Dipyrrinato Complexes

Dipyrrins (dipy) are bidentate ligands with an extended π-system which is delocalized over two pyrrole rings and a methine bridge. This results in a low band gap due to a stable LUMO and a relatively high energy HOMO. Accordingly, complexes incorporating dipyrrin and its derivatives usually exhibit photophysics which are governed by LC transitions. **Scheme 2** shows the synthesis of the unsubstituted parent dipyrrin by formal oxidation of its dipyrromethane precursor as well as the common numbering system for dipyrrins. Since the unsubstituted dipyrrin is unstable above 40 °C due to the electron rich nature of the heterocycles, most studies are focused on dipyrrins which are substituted in positions 1 and 9 (also called α-positions) or in position 5 (*meso*-position).[124-126]

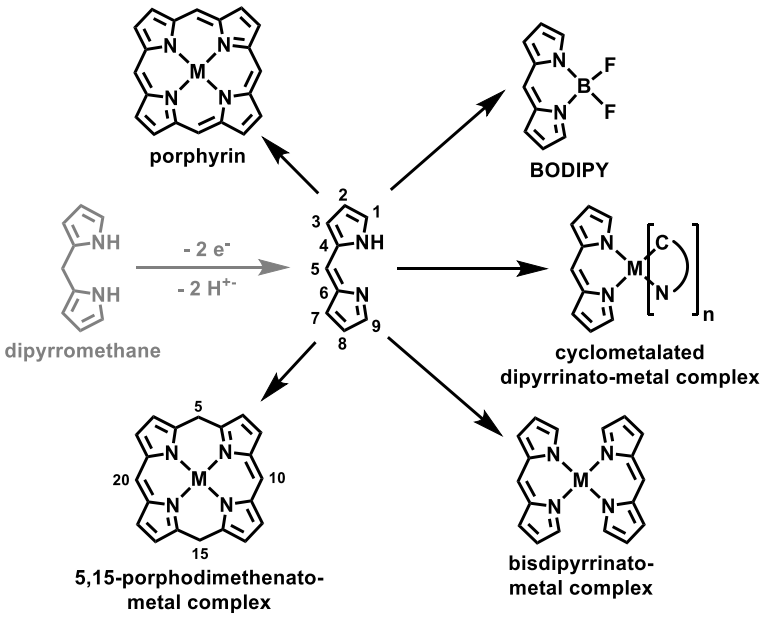

Scheme 2: Formal oxidation (grey) of a dipyrromethane precursor to the dipyrrin chromophore with numbering system and some complexes of dipyrrin and its derivatives.

Scheme 2 also shows some complexes which include dipyrrin as a mutual structural motif. Porphyrins, which formally contain two fully conjugated dipyrrin units, and BODIPYs are certainly the two most prominent dipyrrin derivatives. They have been thoroughly investigated and used in a manifold of applications due to their photophysical properties.[127-131] However, dipyrrins and its derivatives are also known as ligands for transition metals, forming a variety of homo- and heteroleptic complexes. Among these, cyclometalated dipyrrinato complexes can be seen as the closest relatives to BODIPYs since they only comprise one dipyrrin ligand. Complexes comprising two dipyrrin ligands include homo- and heteroleptic bis-dipyrrinato-metal complexes. Bridging of the two dipyrrin ligands results in 5,15-porphodimethenato complexes which can be seen as structural intermediates between dipyrrin-complexes and porphyrins. [124-125, 132-135]

Cyclometalated dipyrrinato-metal complexes

Cyclometalated dipyrrinato-complexes are only known for heavy transition metals. With d^6-ions such as Ir(III)[117, 136] or Rh(III)[137], an octahedral complex comprising two cyclometalating ligands an one dipyrrin is formed while d^8-ions such as Pt(II) or Pd(II)[138] adopt a square planar geometry with only one cyclometalating ligand.[133] Some of the investigated complexes are depicted in **Scheme 3**.[133]

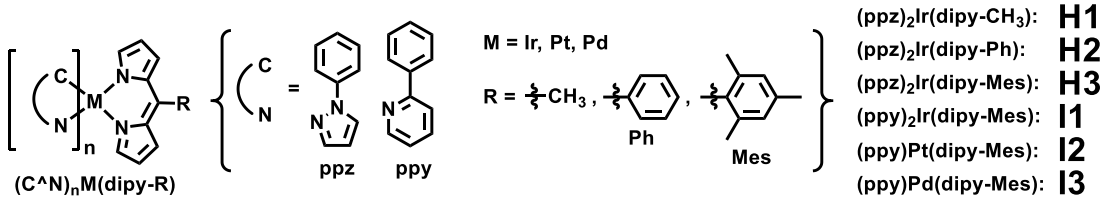

Scheme 3: General structure and examples of cyclometalated dipyrrinato metal complexes.

The absorption and emission spectra of complexes **H1-3** are nearly identical, and are dominated by an absorptive transition into the ^{1}LC-state with an energy of around 20000 cm^{-1} and phosphorescence from the ^{3}LC-state at around 15000 cm^{-1}, respectively. The maxima of these transitions differ only by about 600 cm^{-1} between compounds **H1-3**, indicating that the additional π-system of the phenyl- and mesityl-substituent in 5-position does not influence the dipyrrin ligand significantly compared to the simple methyl-substituent. This can be explained by a nearly orthogonal geometry between the dipyrrin and the aromatic ring in 5-position which electronically decouples the two π-systems.[128, 136] While the emission spectra of complexes **H3** as well as **I1-3** also seem to be more or less independent of the central metal ion and the cyclometalating ligand, a comparison of the absorption spectra reveals a dependence of the extinction coefficient on the central metal ion. While the Ir(III) complexes **H3** and **I1**, as well as the Pd(II) complex **I3**, show relatively sharp and intense absorption spectra, the absorption of the Pt(II)-complex **I2** is broad and reaches only about half of the intensity.[136, 138]

In contrast to the emission energies, the emission lifetime and quantum yields are influenced by the central ion and the substituents in 5-position. For the series **H1-3**, the emission lifetime τ_{phos} and quantum yield Φ_{phos} decrease from 10 µs and 0.09 for **H1** to 5 µs and 0.06 for **H2** and then rise again to 13 µs and 0.11 for **H3**. This is due to an increased non-radiative rate in **H2** caused by rotational motions of the phenyl ring, which is prevented in case of the sterically more demanding mesityl substituent in **H3**.[136, 139-141] An even more pronounced trend can be observed for compounds **I1-3**. While **I1** is relatively strong triplet emitter with τ_{phos} = 6 µs and Φ_{phos} =0.10, **I2** emits only weakly with τ_{phos} = 18 µs and Φ_{phos} =0.01 and **I3** is virtually non-emissive at room temperature. This can be attributed to increased non-emissive rates and decreased emissive rates due to stronger distortions of the dipyrrin in the Pt(II) and Pd(II) complexes caused by the square planar geometry.[133, 136, 138]

Bisdipyrrinato-metal complexes

Bisdipyrrinato metal complexes are known for a variety of first row transition metal ions and a few heavier ions such as Pd(II) and Hg(II). They are readily accessible by treatment of a solution of the ligand with a base and an appropriate metal source, which makes them interesting molecules for self-assembly studies.[139, 142-148] Since bisdipyrrinato complexes comprise two dipy-chromophores in close proximity, the effects of exciton coupling have to be considered when discussing their photophysics. As can be seen in **Figure 7**, the transition moment $\vec{\mu}$ of the main transition into the ^{1}LC-state is oriented along the long axis of the dipyrrin backbone. Due to the close proximity of the two chromophores, the transition dipole moments are perturbed by dipolar coupling, resulting in two excitonic states. In a perfect square planar complex geometry, the dihedral angle between the two dipyrrin-planes is α = 0° and the chromophores are coplanar. This H-type arrangement results in a coulombic stabilization of the excitonic state with antiparallel phase of the transition moments and a equivalently strong destabilization of the excitonic state with parallel phase of the transition moments. The energy difference between the two is called exciton splitting ΔE_{ec}. Since an excitation of a state with $\vec{\mu}$ = 0 is not allowed, only transitions into the higher electronic state are allowed for H-aggregates. With increasing α, the exciton coupling becomes less effective, until at α = 90° the transition dipole moments are arranged orthogonally and no coupling is possible. This results in two degenerate, allowed transitions of the two individual dipyrrins.[149-153]

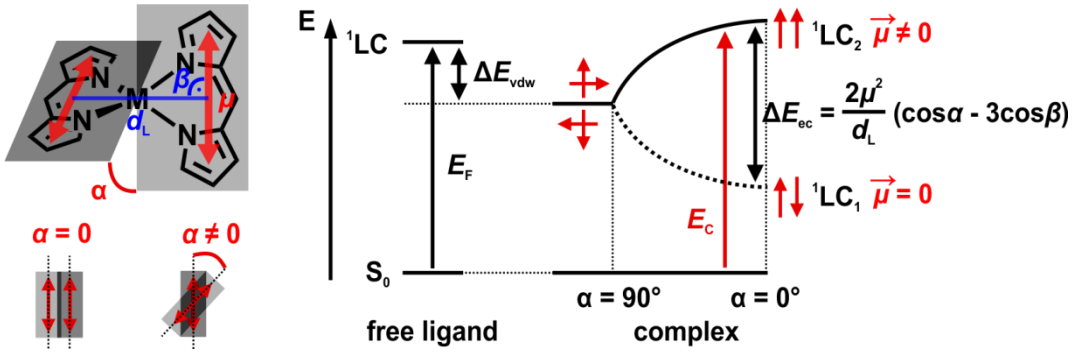

Figure 7: Exciton coupling in bisdipyrrinato-metal complexes, in dependence of the angle α between the transition dipole moments along the long axis of the individual dipyrrin chromophores.

In bisdipyrrinato-metal complexes, α can be controlled to some extent. For Zn(II) centered derivatives, a tetrahedral structure, that is $\alpha \approx 90°$, is preferred exclusively. In contrast, other central ions tend to adopt square planar geometries, which can be distorted towards a tetrahedral structure by the incorporation of bulky substituents in 1- and 9-position. Studies by *Dolphin et al.* revealed a bathochromic shift for increasing angles α, which was accompanied by higher extinction coefficients. This is in line with the expectations derived from exciton coupling theory.[124, 139, 144, 146-148, 154]

Since the lowest excited singlet state in bisdipyrrinato-metal complexes is the lower excitonic state which is non-emissive due to its zero overall transition dipole moment and internal conversion (IC) between the excitonic states usually is very fast, all square planar and distorted tetrahedral bisdipyrrinato complexes show virtually no fluorescence.[153, 155-156] For the strictly tetrahedral Zn(II)-complexes, a homoleptic derivative with bulky mesityl substituents in the 5-position was shown by *Lindsey et al.* to have a fluorescence quantum yield of 0.36 in non-polar solvents.[139] *Thompson et al.* could rationalize the rapid decrease of the quantum yield in polar solvents with a deactivation pathway involving an intermediate CSS between the two equivalent dipyrrin ligands.[157] Based on this interpretation, *Nishihara et al.* could consistently design Zn(II)-complexes with good fluorescence quantum yields by employing two different dipyrrin ligands in one complex. In these heteroleptic bisdipyrrinato complexes the quenching of the fluorescence by CS between the two dipyrrin chromophores is prevented due to the different HOMO and LUMO energies associated with the dipyrrins.[158-160]

However, almost no studies concerning the photophysics of bisdipyrrinato complexes of other, especially heavier transition metal ions are available, although they could be potentially interesting phosphorescence emitters since their photophysics are governed by triplet excited states due to higher spin-orbit coupling constants.

5,15-Porphodimethenato- metal complexes

5,15-Porphodimethene (PDM) comprises two dipyrrin subunits which are covalently linked by saturated bridges, and can be transformed to the fully conjugated porphyrin by formal oxidation at the bridging C-Atoms. Therefore, only PDMs which bear no hydrogen-atoms at the 5- and 15-position are stable under air. Although their synthesis is complicated and limited to small scales, PDM-metal complexes are known for many first row transition metals, as well as Pd(II).[132, 161-163]

Since PDM and its metal complexes comprise two individual, non-conjugated dipyrrin chromophores, the excited states of PDM and its metal-complexes could be described by exciton coupling theory. Compared to bisdipyrrinato-metal complexes, the dihedral angle α can cover a significantly smaller range due to the more rigid structure of the ligand which forces a more or less distorted square planar complex geometry even for the Zn(II)-complex.[161, 164]

However, due to their close structural relationship with the well understood porphyrins, the photophysics of PDMs often get interpreted in relation to the respective porphyrin. Hence, the few available studies on the excited state properties of PDM-metal complexes usually are based on density functional theory (DFT) calculations and describe PDMs as a single chromophore with multiple absorptive transitions similar to the way porphyrins are treated.[132, 165-166]

Both approaches can help to rationalize the complicated absorption spectra observed for most PDMs which are dominated by multiple intense and broad absorptions between 18200 – 28600 cm^{-1}, usually associated with LC-transitions. Similar to porphyrins, only the free base PDM and metal complexes of ions with completely filled d-orbitals, that is Zn(II), have been found to be fluorescence emitters. However, studies on the emissive behavior of PDMs are vanishingly rare.[132, 161, 163, 167]

In contrast, significantly more studies are available concerning the structure of PDM-metal complexes and their synthesis. These can be summarized as follows: Due to the saturated bridges, PDMs are structurally more flexible than porphyrins resulting in a wider range for the size of the complexation cavity formed by the 4 N-atoms. The greater structural flexibility also results in a rooftop- or butterfly arrangement of the ligand backbone in most cases, which can be characterized by the cant-angle β between the two dipyrrin subchromophores as shown in **Figure 8**. Typical values for β range from 180° to 120°. This makes the central metal ion relatively easily accessible for secondary ligands which often leads to complexation of solvent molecules.[132, 163-166, 168]

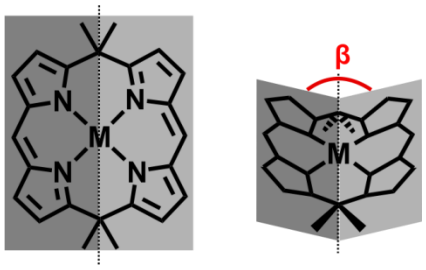

Figure 8: Butterfly-geometry of the PDM-backbone and the characterizing angle β.

1.4 State of the Art

In the past years, the spin chemistry and photophysics of the triads shown in **Scheme 4** were investigated intensively by *Lambert et al*. They are based on the cyclometalated Ir(III)-dipyrrinato complex **H2** as a photosensitizer (PS), two triarylamines (TAA) as electron donors and a napthalenediimide (NDI) as an electron acceptor. The triads are designed according to the principles outlined in chapter 1.2.2. The TAA is attached to the cyclometalating ligand at two points using saturated ethylene and methylene bridges to ensure a defined geometry and a weak electronic interaction between the two moieties. The electronic coupling between PS and acceptor is small due to the nearly orthogonal arrangement of the dipyrrin-π-system and the bridging phenylene ring in 5-position. Furthermore, the LUMO of the NDI exhibits a nodal plane along the axis connecting the nitrogen atoms, further reducing the electronic coupling. Finally, the donor and acceptors have a center to center distance of d_{DA} = 20 Å for the short triad **D_2IrA** and of 24 Å for the elongated triad **$D_2Ir_{Ph}A$** with a biphenyl bridge between PS and acceptor.[59, 70, 79, 115]

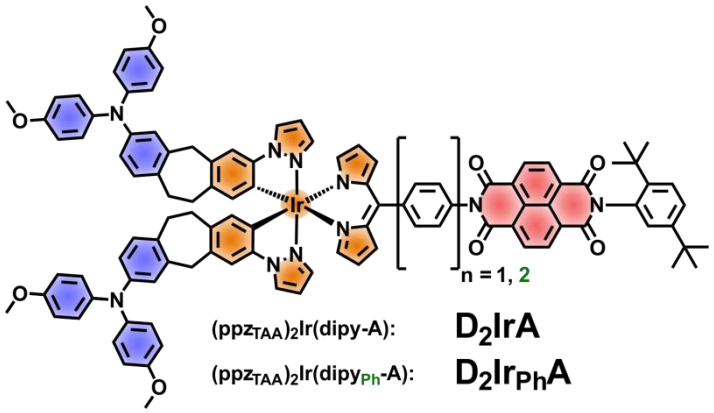

Scheme 4: Donor-acceptor substituted cyclometalated dipyrrinato-Ir(III) complexes studied by *Lambert et al*.[59, 70, 79, 115]

Excitation of **D$_2$IrA** into the ^{1}LC-state of the central complex results in ultrafast ISC to the ^{3}LC state, which, in contrast to **H2**, shows no long lived phosphorescence, because it is quenched by a fast charge transfer. Initially, CSS_1 gets formed by electron transfer from the PS to the NDI with a time constant of about 1 ns. The subsequent reoxidation of the PS by the TAA is even faster, and results in CSS_2, which comprises the PS in the ground state, a TAA radical cation and a NDI radical anion. CSS_2 recombines to the ground state with a lifetime of 580 ns in MeCN and 140 ns in the less polar THF where CSS_2 is stabilized to a lesser extent. Hence, the CR occurs in the *Marcus* normal region since it gets faster with decreasing free energy difference (see chapter 1.2.1). In contrast, for the elongated triad **D$_2$Ir$_{Ph}$A**, the charge separation occurs with a time constant of about 30 ns while CSS_2 is extremely long lived and shows a biexponential decay with a short component of about 15 µs and a long component of about 80 µs. The quantum yield of CSS_2 after excitation of the PS was determined to be close to unity for both complexes but is reduced to about 0.5 after excitation of the NDI. This was attributed to the partial formation of a CT state between the NDI core and the terminal phenyl ring which deactivates to the ground state.[59, 70, 115]

The high quantum yields of charge separation, and the resulting good signal to noise ratio of the decay traces recorded by ns-transient absorption spectroscopy facilitated the magnetic field dependent investigation of the CR-kinetics. While no significant magnetic field effect (MFE) was observed for the deactivation of CSS_2 in **D$_2$Ir$_{Ph}$A**, the CSS-lifetime of **D$_2$IrA** was increased by a factor of about 4 with increasing magnetic field strength, and became biexponential at fields higher than 10 mT. This behavior could be rationalized using the relaxation mechanism introduced in chapter 1.1.3. With a detailed mathematical analysis of the collected data, a transition of the spin evolution from a field range dominated by coherent mechanisms (see chapter 1.1.1) to a regime dominated by incoherent mechanisms (see chapter 1.1.2) could be observed for the first time reported in literature. This interpretation was later confirmed by a complete quantum dynamical description of the system by *Steiner et al*.[59, 79]

2 Scope of the Work

The aim of this work is to gain a deeper understanding of the relationship between the chemical structure of donor-acceptor substituted triads and the resulting photophysics and spin chemistry. Special attention will be paid to the central photosensitizer (PS), which is expected to influence the process of charge separation directly, but could also indirectly influence the charge recombination as well as the spin chemistry of the excited state radical pair.

The first part of this work (chapter 3) deals with donor-acceptor substituted cyclometalated dipyrrinato complexes similar to the triads introduced in chapter 1.4. The influence of the complex geometry and the central metal ion of the PS on the properties of the triads will be investigated by a comparison of **DPtA** and **DPdA** with their literature-known Ir(III) analogue **DIrA**.[59, 70, 79, 115] Furthermore, the quantum yield of CSS_2 in **D_2IrA'**, a triad with a modified NDI-acceptor comprising only one adjacent phenyl ring will be determined to further investigate the mechanism of the charge separation (CS) after excitation at the NDI.

The synthesis of the triads depicted in **Scheme 5**, as well as the respective reference dyads and the central PS will be described briefly (3.1). The optical and electrochemical steady state properties will be determined to gain first insights on the influence of the central metal complex (3.2). Afterwards, the photoinduced CS and subsequent CR of the charge separated state will be investigated by transient absorption (TA) spectroscopy in the ns- and fs- time range (3.3). Finally, the spin chemistry of the CSS will be investigated by magnetic field dependent ns-TA spectroscopic measurements. The resulting data will be interpreted on a spin-chemical basis according to the principles introduced in chapter 1.1.(3.4)

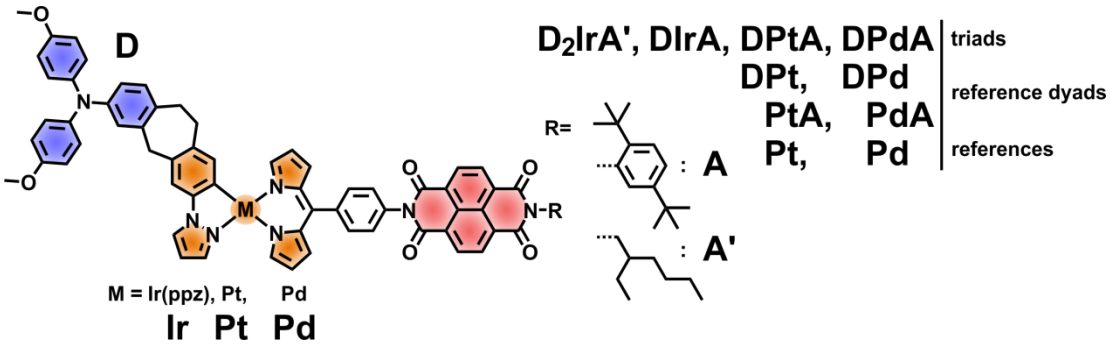

Scheme 5: Structure of all cyclometalated dipyrrinato-metal complexes investigated in this thesis. The unsubstituted reference compounds are marked in orange, while addition of the TAA (D) or/and the different NDIs (A, A') results in the reference dyads and the donor-acceptor substituted triads, respectively.

The second part of this work (chapter 4), deals with the donor-acceptor substituted bisdipyrrinato-metal complexes and porphodimethenato-compounds depicted in **Scheme 6** and **Scheme 7**. First, the synthesis of the compounds is described (4.1). Afterwards, the steady state properties and excited state dynamics of the chromophores depicted in **Scheme 6** will be investigated systematically to test them for their suitability as photosensitizers in donor-acceptor substituted triads (4.2).

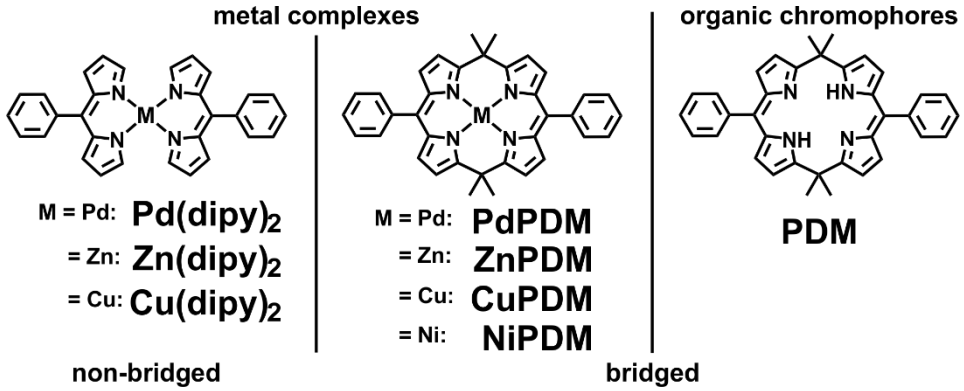

Scheme 6: Structure of the bisdipyrrinato-metal complexes and porphodimethenato (PDM) compounds of potential use as photosensitizers in donor-acceptor substituted triads.

Finally, of the compounds depicted in **Scheme 7**, the triads and dyads based on **Pd(dipy)$_2$**, **PdPDM** and **PDM** will be investigated with the methods already described in chapter 3 to gain insight on their photophysics and spin chemistry. A comparison of **D-Pd(dipy)$_2$-A**, **D-PdPDM-A** and **D-PDM-A** will focus on the influence of the central chromophore, while a comparison of the short triad **D-PdPDM-A** and the elongated triad **D$_{Ph}$-PdPDM-A** will reveal the influence of the electronic coupling and distance between the respective redox centers (4.3).

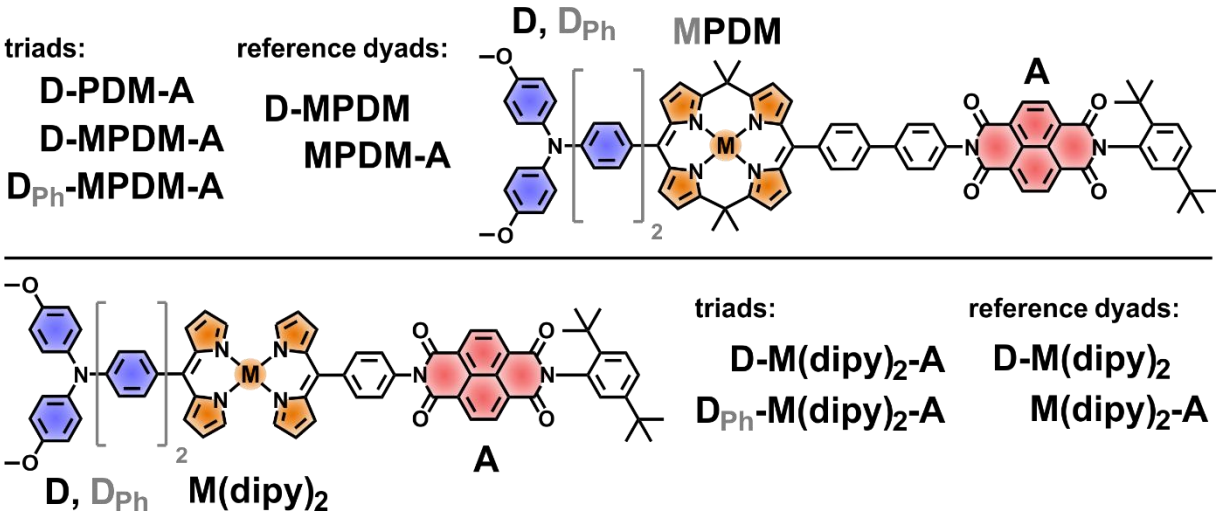

Scheme 7: Target triads based on the central metal complexes depicted in **Scheme 6**. Substitution of the respective central chromophore with the different TAAs (D, D$_{Ph}$) or/and the NDI (A) results in the reference dyads and the donor-acceptor substituted triads, respectively.

3 Cyclometalated Dipyrrinato-Complexes[a]

3.1 Synthesis

The synthesis of the cyclometalated dipyrrinato-metal complexes generally followed a procedure first introduced by *Nonoyama et al.* for Iridium complexes, which has been utilized successfully for a variety of different ligands and central metal ions. [115, 136, 138, 169-172] The procedure consists of a two-step synthesis of the target compound. First, the cyclometalating ligand and the central metal ion form a binuclear complex, which then readily reacts with an ancillary ligand to form the final complex. Since in this route the complex-formation occurs under relatively mild conditions, most functional groups are tolerated. Therefore, the electron donor and electron acceptor functionalities could be formed separately and prior to complexation, resulting in a minimized material consumption and reduced synthetic difficulties. In this work phenylpyrazole (ppz) was used as the cyclometalating ligand, while dipyrrin (dipy) was used as the ancillary ligand and was prepared directly prior to complexation from the respective dipyrromethane precursor. The triarylamine (TAA) donor- and the naphthalene diimide (NDI) acceptor functions are attached to the phenylpyrazole (ppz) and the dipyrrin ligand, respectively. The following sections describe the synthesis of the donor ligand and the precursors of the ancillary ligands, as well as the complex-formation and the structural analysis of some of the obtained compounds.

Ligand-synthesis

The synthesis of the TAA-functionalized phenylpyrazole ligand **4** followed the literature known route depicted in **Scheme 8**. Direct bromination of commercially available dibenzosuberone gave 3,7-dibromobezosuberone **1** in 32 % yield and subsequent reduction using an excess of sodium borohydride resulted in the formation of **2** with 88 % yield.[173-174] In the next step the coordination site was formed by a copper(I) catalyzed *Ullmann* coupling of **2** with one equivalent of pyrazole, yielding **3** in 51 %.[116, 175] Lastly, the TAA-function was introduced by a palladium(0) catalyzed *Buchwald-Hartwig* coupling using a slight excess of *bis*(4-methoxyphenyl)amine to yield the donor substituted cyclometalating ligand **4** in 70 % yield.[115, 176]

[a] Reprinted or adapted in part with permission from:
Nanoviscosity effect on the spin chemistry of an electron donor/Pt-Complex/Electron acceptor triad - classical and quantum kinetics interpretation, S. Riese, L. Mungenast, A. Schmiedel, M. Holzapfel, N. N. Lukzen, U. E. Steiner, C. Lambert, *Mol. Phys.*, **2018**, DOI: 10.1080/00268976.2018.1511867; Copyright 2018 Taylor & Francis
Parts of this chapter have been investigated in a bachelor thesis under the supervision of S. Riese:
Synthese und Charakterisierung von Donor-Akzeptor-substituierten Platinkomplexen, L. Mungenast, bachelor thesis, Julius-Maximilians-Universität Würzburg, **2015**.

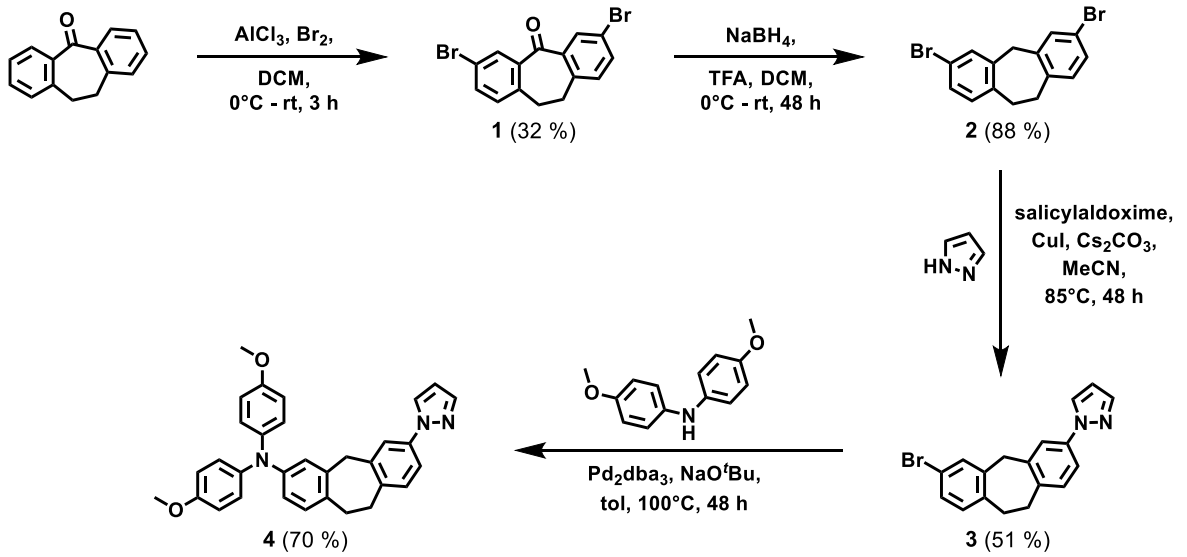

Scheme 8: Synthesis of the donor-substituted cyclometalating ligand **4**.

As shown in **Scheme 9,** the first step in the synthesis of the non-functionalized ligand precursor 5-phenyldypyrromethane **5** and its NDI-functionalized derivatives **8** and **9** was the acid catalyzed condensation of two equivalents of pyrrole with one equivalent of the appropriate aldehyde. In this reaction introduced by *Lindsey et al.*, pyrrole is used not only as a reactant but also as the solvent. A high degree of dilution is needed to prevent the formation of longer oligomers due to a further condensation of the formed products with additional equivalents of aldehyde. A ratio of 1 equivalent aldehyde to 25 – 30 equivalents pyrrole was found to be the optimal compromise for the prevention of side products using the smallest possible amount of pyrrole. Using trifluoroacetic acid (TFA) as a catalyst and commercially available pyrrole, **5** could easily be prepared in large amounts of high purity with a yield of 70 %.[177]

The same conditions resulted with 56 % yield in 5-(4-nitrophenyl)dipyrromethane **6**, which was reduced to 5-(4-aminophenyl)dipyrromethane **7** in 97 % yield with hydrogen gas using palladium on activated charcoal as a catalyst[178]. Compound **7** colorless, but becomes tan and later brick red when stored on air due to oxidation. Nonetheless no decrease in the effectivity of the following reactions could be observed when comparing freshly prepared and older **7** as a starting material. Both acceptor-functionalized precursors **8** and **9** can be classified as asymmetrical napthalenediimides. The dipyrromethane serves as a precursor for the coordination site. The other substituent is introduced to improve solubility and prevent intermolecular aggregation due to π-stacking. In general, asymmetric NDIs can be synthesized stepwise[104] or in a one-pot-reaction. In this work, a microwave-assisted one-pot-route was chosen and resulted in yields of 31 % for **8** and 24 % for the novel compound **9**.[115, 179] Taking into account the statistics of the one-pot-approach, these yields were satisfying and both compounds could easily be prepared on the gram scale.

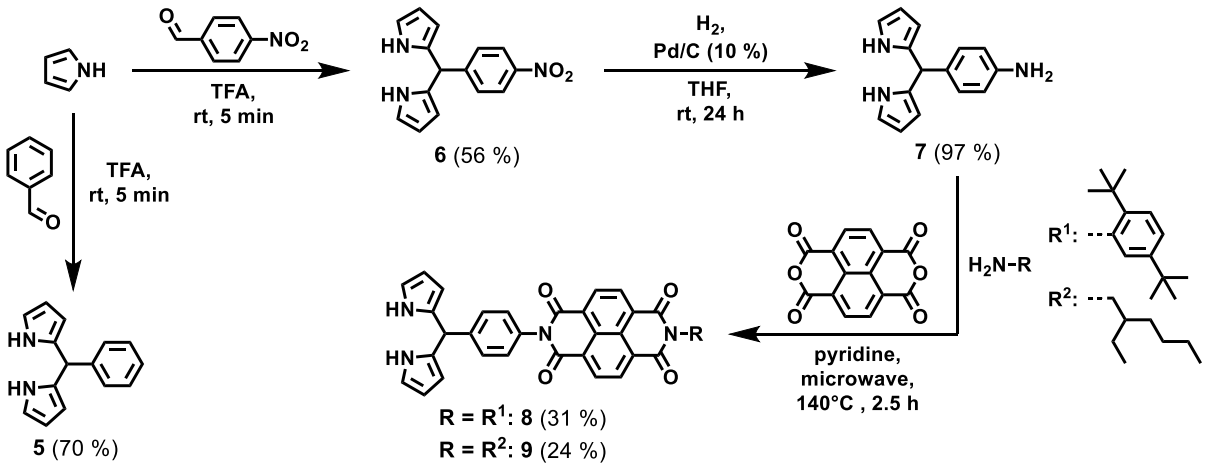

Scheme 9: Synthesis of the ancillary ligand precursors **5**, **8** and **9**.

Complex-Synthesis

In the first step of the complex-synthesis commercially available ppz or compound **4** was treated with the respective transition metal source to form binuclear complexes as shown in **Scheme 10**.

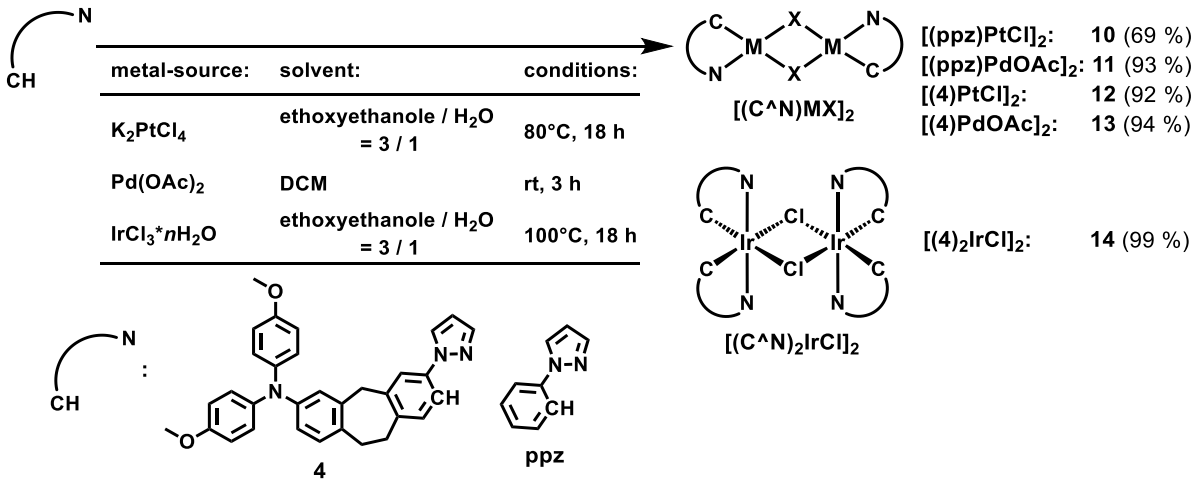

Scheme 10: Synthesis of cyclometalated μ-bridged binuclear transition metal complexes of ppz (**10**-**11**) and **4** (**12**-**14**).

In the binuclear complexes, the two metal ions are bridged in the μ-position by two of the counter ions from the metal source, e.g. chloride for Pt(II) and Ir(III) and acetate for Pd(II). The remaining coordination sites of the respective metal ion are occupied by one bidentate cyclometalating ligand for the d^8-ions Pt(II) and Pd(II), and by two bidentate cyclometalating ligands for the d^6-ion Ir(III). The difficulty in this reaction was to find conditions in which both the organic ligands as well as the metal sources are soluble and the complexation is still the most desirable reaction of the system. For $Pd(OAc)_2$, which is soluble in organic solvents, this was easily achieved in dichloromethane (DCM) at room temperature (rt).[170] For the inorganic salts potassium tetrachloroplatinate(II) and

iridium(III)chloride hydrate a mixture of ethoxyethanole and water had to be used at higher temperatures.[115, 171-172] For the Platinum case it turned out to be crucial to keep the temperature below 90°C because otherwise an insoluble black side product was formed. In general, successful reactions resulted in grey to yellow precipitates upon dilution of the reaction mixture with water (for Pt(II) and Ir(III)) or diethyl ether (for Pd(II)). These were used without further purification, thus making the determination of the yield inaccurate. Under the assumption of purity, the yields were above 90 % in all cases, except for compound **10**, which was only isolated in 69 % yield.

For the synthesis of Iridium complexes with only one donor-substituent the mixed-ligand binuclear complex mixture **15** had to be prepared using a one-pot-synthesis as shown in **Scheme 11**. The resulting product is composed of a statistical mixture of 6 different complexes and their diastereomers. Ignoring the diastereomers, these complexes vary only in the degree and pattern of substitution. This method was previously introduced by *Lambert et al.* and is explained in greater detail in the literature.[59, 70]

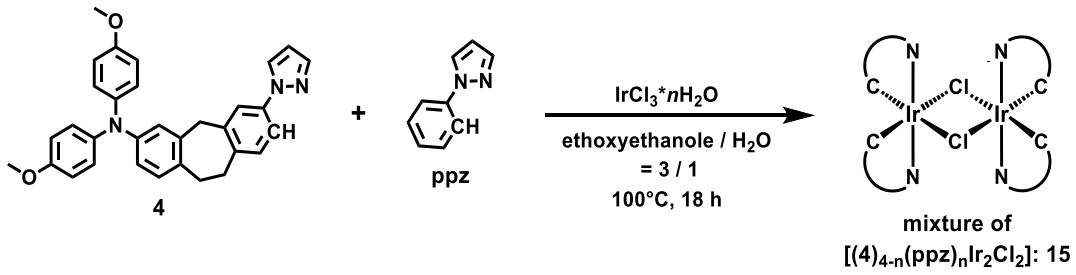

Scheme 11: Preparation of the complex-mixture **15**.

The second step of the complex-synthesis is shown in **Scheme 12**. First, dipyrromethanes **5**, **8** and **9** were oxidized to the respective ancillary ligands with 2,3,-dichloro-5,6-dicyano-1,4-benzoquinone (DDQ). After complete consumption of the starting material, potassium carbonate was added in order to deactivate any remaining DDQ and to increase the pH of the mixture. Without any work up, the binuclear complex was added and the reaction was stirred over night at rt for the Pt(II) and Pd(II) complexes and 80°C for the Ir(III) complexes.[136, 138] All complexes were purified by flash column chromatography on silica. For the Pd(II)-compounds the silica gel had to be deactivated with 10 % TEA prior to use. For the NDI-containing dyads and triads an additional purification by GPC in THF was necessary. All complexes were then precipitated first from DCM into MeOH and secondly from DCM into n-pentane, and were isolated as red to brown solids in yields between 10 – 70 %. Since the dinuclear starting complexes were of unknown purity, it is unclear if the main reason for the moderate to low yields was the starting material, the reaction conditions or the work-up. However, a considerable amount of product was lost due to slow decomposition of the donor-substituted compounds even on deactivated silica, and of the acceptor-substituted compounds during the GPC.

Nevertheless, all novel target complexes shown in **Scheme 13** could be prepared in amounts sufficient for all desired measurements. The purity of the compounds was high enough to meet the criteria for publication as was proved by ^{1}H- and ^{13}C-NMR spectroscopy, as well as CHN-microanalysis (see chapter 6.2.3.2).

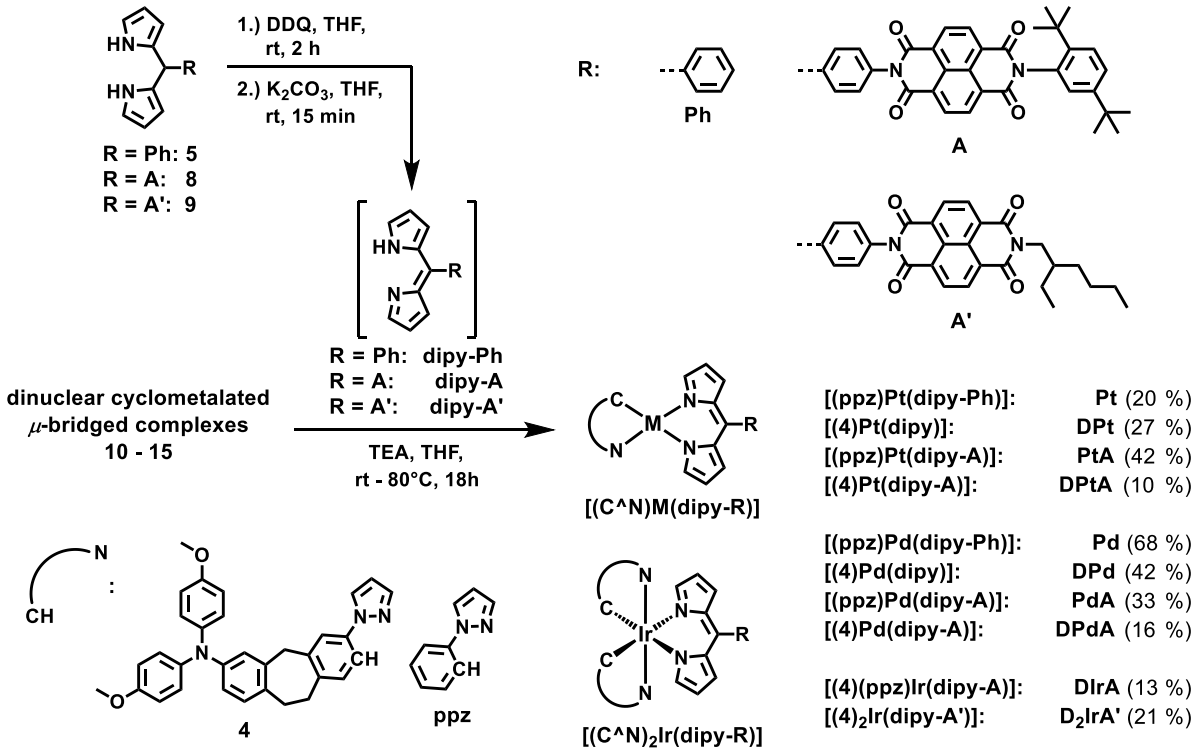

Scheme 12: Synthesis of the target reference complexes **Pt** and **Pd**, the donor- and acceptor-substituted dyads **DPt**, **PtA** and **DPd**, **PdA** and the triads **DPtA**, **DPdA** and **DIrA**, **D2IrA'** from the precursors of the ancillary ligands **5**, **8** ,**9** and the binuclear complexes **10**-**15**.

Structural Analysis

For **Pt** and **Pd**, crystals suitable for single crystal X-ray diffraction were obtained by slow diffusion of hexane into a saturated DCM-solution. The determined structures are shown in **Figure 9**, and dihedral angles between planes characteristic for the molecule geometry as well as selected bond lengths are summarized in **Table 1**. For **Pt** an asymmetric unit cell comprised of two molecules with slightly different geometries was found. Since the differences between the geometries are only on the order of 3° for dihedral angles and 0.02 Å for distances and likely due to crystal packing forces this is neglected in the following discussion.[142, 157] In both complexes the central metal ion has a distorted square planar coordination sphere with bond lengths between 2.02 – 2.07 Å in **Pt** and 2.00 – 2.10 Å in **Pd**. Furthermore, the dipyrrin ligands are highly bent (dihedral angles between planes 1 and 2 of $\Theta_{1/2}$ = 148.1° and 144.1°, respectively) and tilted away from the plane defined by the central metal ion and its four surrounding atoms ($\Theta_{3/4}$ = 153.6° and 146.4°, respectively).

This results in a "canted" structure of the complexes which is most likely assumed as to avoid steric repulsion between the hydrogen atoms at the C1- and C9-position of the dipyrrin with those at the ppz. For the same reasons, the ppz-ligand is also tilted slightly away from the central plane ($\Theta_{6/7}$ = 167.2° and 171.2°) and is distorted from its usual planar structure ($\Theta_{8/9}$ = 162.4° and 167.2°). While the tilt of the dipyrrin is stronger in **Pd**, the tilt of the ppz is stronger in **Pt**. Lastly, the bond lengths of the dipyrrin-backbone (N1-C4-C5-C6-N2) indicate a stronger delocalization of the π-electrons for **Pt** than for **Pd** since they alternate less between long and short bonds. The observed structural features will most likely result in differences between the photophysical properties of the Pt-complexes and those of the Pd-complexes, which will be discussed in the following chapters.

Table 1: Dihedral angles Θ between characteristic planes as indicated in **Figure 9** and selected bond lengths of **Pt** and **Pd** as obtained from single crystal X-ray diffraction.

dihedral angles Θ between planes /°	Pt	Pd	distances /Å	Pt	Pd
1,2	148.1	144.1	**M-N1**[a]	2.073	2.005
1,4	162.6	157.9	**M-N2**[a]	2.030	2.099
3,4	153.6	146.4	**M-N3**[a]	2.020	2.029
3,6	177.2	173.9	**M-C18**[a]	2.027	2.001
4,5	176.6	171.4	**N1-C4**	1.387	1.384
6,7	167.2	171.2	**C4-C5**	1.392	1.415
7,8	169.5	174.6	**C5-C6**	1.394	1.388
8,9	162.4	167.2	**C6-N2**	1.404	1.404

[a] M = Pt(II) for **Pt** and Pd(II) for **Pd**

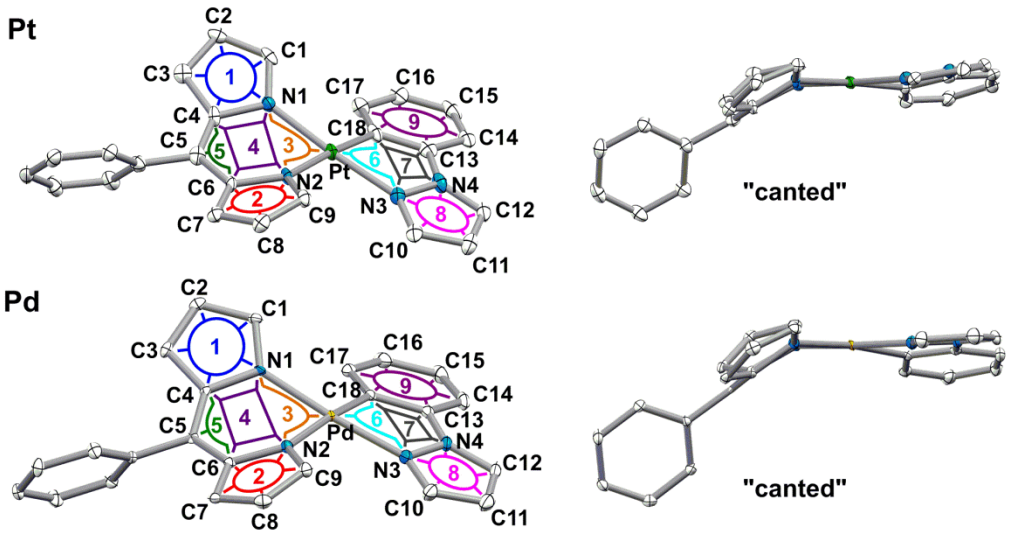

Figure 9: X-ray crystal structure of **Pt** and **Pd**. Hydrogen atoms are removed for clarity. Thermal ellipsoids are at 50% probability level. For **Pt** only one half of the observed bimolecular, asymmetric cell is shown.

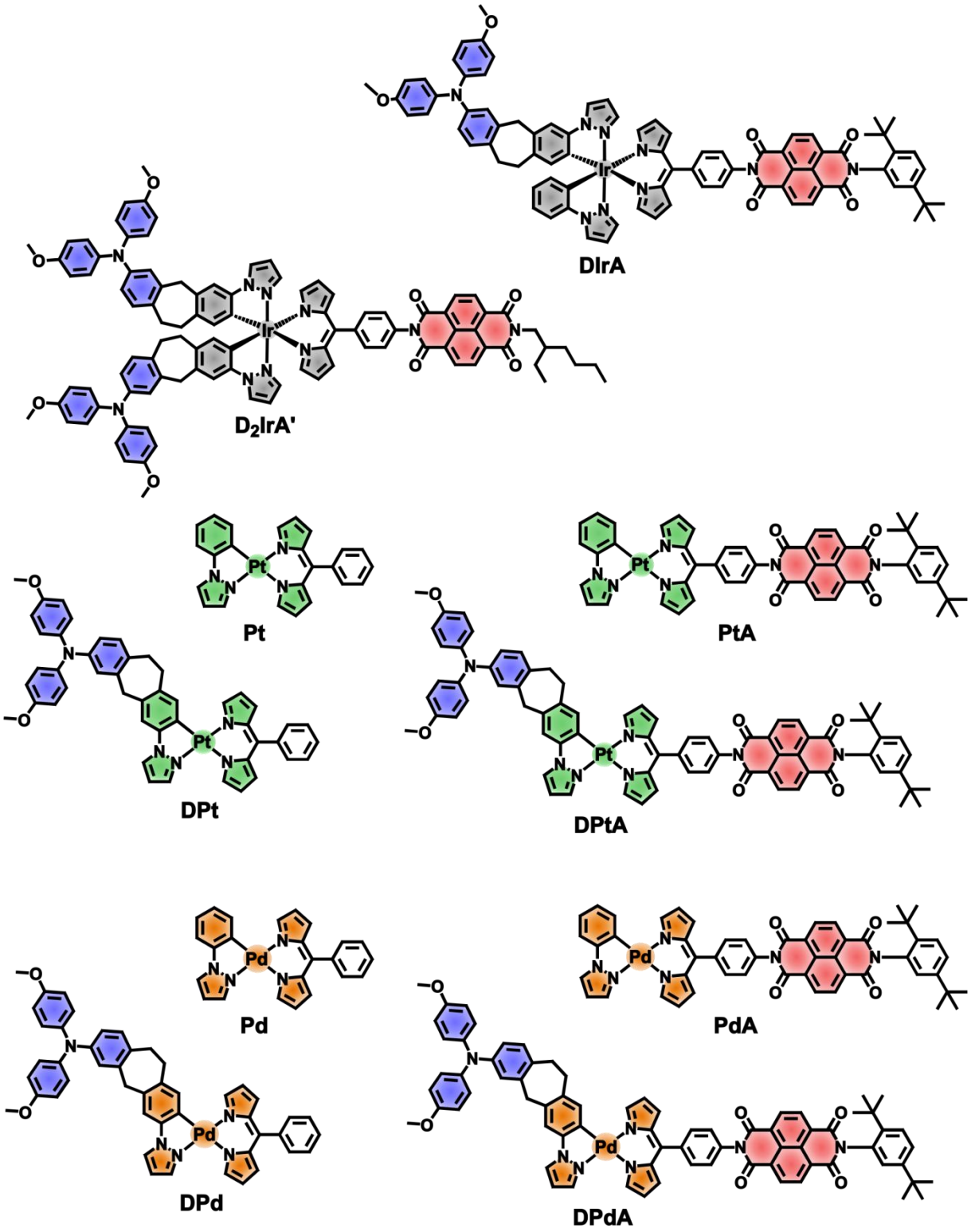

Scheme 13: The novel Ir(III) complex **D_2IrA'** as well as the literature known[59, 115] target complex **DIrA** and the novel target Pt(II) complexes **Pt**, **DPt**, **PtA**, **DPtA** and Pd(II) complexes **Pd**, **DPd**, **PdA**, **DPdA**. The presented color code will be kept during the discussion of the measurements. Molecules containing only donor or acceptor groups will be depicted in blue and red respectively, while all other compounds will be given in the color of the respective CMC (central metal complex).

3.2 Steady State Properties

To gain first insights into the optical and electrochemical properties of the donor-complex-acceptor-triads and their behavior after photoexcitation, a number of steady state experiments were performed. The results of the different methods will be presented in the following chapters. The reference dyads containing solely a donor- or an acceptor-group will only be compared to the triads and metal-complexes with the same central metal ion and will always be depicted in blue and red respectively, with the unsubstituted metal-complex being depicted in black and the triad in the color of the respective central metal complex (CMC) as shown in **Scheme 13**, i.e. black for Ir(III), green for Pt(II) and orange for Pd(II). **D_2IrA'** was only synthesized as a proof of principle concerning the quantum yield of charge separation and will only be discussed in terms of steady state absorption, cyclic voltammetry and ns-transient absorption characteristics. The literature-known triad **DIrA** was solely synthesized as a reference-compound for the magnetic field dependent measurements discussed in chapter 3.4 and will only be mentioned there.[59, 70, 79] When suitable, the unsubstituted central Iridium complex **Ir** shown in **Figure 10** will also be used as a reference. All data on **Ir** was taken from the PhD thesis of Dr. Johannes Klein.[70]

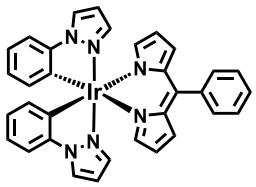

Ir

Figure 10: The unsubstituted central Ir(III) complex **Ir**, which will be used as a reference throughout this chapter. Data will be taken from the PhD-thesis of Dr. Johannes Klein.[70]

3.2.1 UV/Vis-Absorption Spectroscopy

The steady state absorption of the complexes was measured in solvents of different polarity (MeCN, THF, DCM and toluene). The absorption maxima and extinction coefficients of characteristic bands are listed in **Table 2** for all compounds and solvents. Since the principal results do not differ between solvents, only the measurements in THF will be discussed in detail. Afterwards, the solvent dependence of the spectral features will be addressed briefly. Spectra of the triads **D_2IrA'**, **DPtA** and **DPdA**, as well as the respective unsubstituted central metal complexes **Ir**, **Pt** and **Pd** are shown in **Figure 11**.

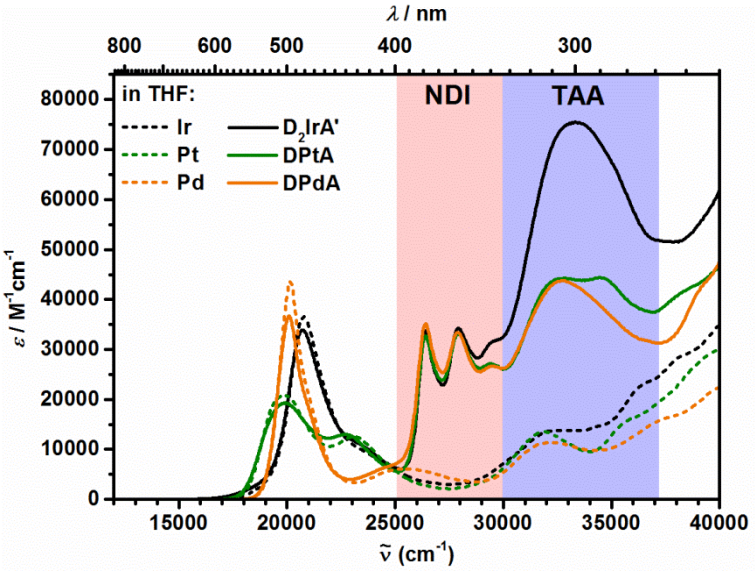

Figure 11: Absorption spectra of the triads (solid lines) **D_2IrA'** (black), **DPtA** (green) and **DPdA** (orange) as well as the respective unsubstituted references (dashed lines) **Ir** (black), **Pt** (green) and **Pd** (orange) in THF at rt. Shaded areas are strongly influenced by the NDI (red) and TAA (blue) moieties respectively.

The absorption spectra of the triads can roughly be divided into three areas.

The lowest energy absorptions between 15000 – 25000 cm^{-1} are solely related to transitions of the CMC. The main absorption peak in this region occurs at 20700 cm^{-1} for the Ir-complexes, around 19900 cm^{-1} for the Pt-complexes and around 20100 cm^{-1} for the Pd-complexes and can be assigned to a dipyrrin-ligand centered (LC) π-π*-transition in all cases. Although the central metal ion does not take part directly, it still has an influence on the transition by its electron withdrawing character and influence on the complex geometry. Additionally, all central complexes show a metal-to-ligand charge transfer (MLCT) transition onto the dipyrrin at higher energies. In the Ir-complexes this transition manifests as a shoulder at ca. 23500 cm^{-1}, while it forms a distinct band at around 23000 cm^{-1} in the Pt(II)-complexes and around 25400 cm^{-1} in the Pd(II)-complexes. The MLCT-transition is shifted to significantly higher energies in the Pd(II) complexes, because Pd(II) has higher oxidation-potentials compared to Pt(II), thus increasing the band-gap between the electron donating Pd(II)-centered MO and the electron accepting ligand centered MO.[138] Furthermore, the Ir(III)-complexes display a very broad foot with small intensity towards the low energy-site of the spectrum, which due to the strong heavy atom effect of the Ir(III) ion, can possibly be assigned to spin-forbidden transitions to LC-triplets.[59]

Between 25000 – 30000 cm^{-1}, the absorption is mainly due to the typical π-π*-transition of the NDI with its vibronic fine-structure.[180-181] The first maximum lies at 26400 cm^{-1} and the second and third maxima are separated by 1500 cm^{-1} each, lying at 27900 cm^{-1} and 29400 cm^{-1}, respectively.

Between ca. 30000 – 37000 cm^{-1} the lowest π-π*-transitions of the TAA are superimposed on higher energy transitions of the CMC which mostly correspond to LC and MLCT transitions associated with the cyclometalating ligand. The TAA absorption shows a maximum at around 33000 cm^{-1}. The difference in extinction coefficients at 33000 cm^{-1} between **Ir** and **D_2IrA'** is twice as large as between **Pt** and **DPtA** as well as **Pd** and **DPdA**, which is expected since **D_2IrA'** contains two TAA-moieties instead of one.[122-123, 138, 176, 182-183]

The other differences between the three triads are negligible in the spectral range influenced by TAA and NDI. That points to an insignificant influence of the CMC on the donor- and acceptor- units. This assumption is further supported by a comparison of the complexes of the Pt- and Pd-series as shown in **Figure 12**.

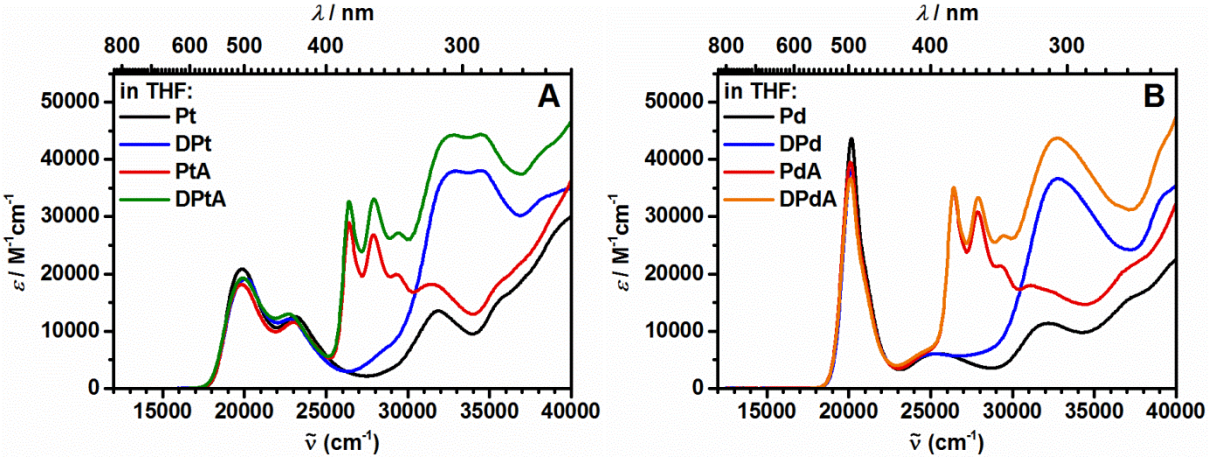

Figure 12: Absorption spectra of the complexes of the Pt-series (A) and the Pd-series (B) in THF at rt.

It can be seen that the absorption of the triads is the sum of the spectra of the respective donor- and acceptor-dyads minus the spectra of the respective CMC to account for the total number of chromophores. Furthermore, the maximum of the TAA and NDI absorption undergoes virtually no shift from the respective dyad to the triad as can be seen in **Table 2**. The same is essentially true for the absorption of the CMC, with the exception that variations of the extinction coefficients cannot be attributed to a superposition of different transitions. For the Pd-series, a substitution of the dipyrrin ligand with the acceptor-group results in a small but systematic bathochromic shift of 100 cm^{-1} in all solvents. These slight differences are likely caused by a variation of the electronic properties of the central chromophore due to the different molecular structure of the functionalized ligands compared to the non-functionalized ligands, such as the electron withdrawing character of the imido-goup at the 4-position of the phenyl-ring of the dipyrromethane and the electron donating character of the aliphatic linkers in the donor-substituted cyclometalating ligand **4**.

Table 2: Absorption maxima $\tilde{\nu}_{max}$ (λ_{max}) and extinction coefficients ε_{max} of the characteristic absorption bands of the sub-units (M-dipy = metal-complex, NDI and TAA) of the respective complexes of the Pt- and Pd-series as well as **D_2IrA'**.

	solvent	^{1}LC (M-dipy) $\tilde{\nu}_{max}$ (λ_{max}) [ε_{max}] /cm^{-1} (nm) [M^{-1}cm^{-1}]	NDI[a] $\tilde{\nu}_{max}$ (λ_{max}) [ε_{max}] /cm^{-1} (nm) [M^{-1}cm^{-1}]	TAA $\tilde{\nu}_{max}$ (λ_{max}) [ε_{max}] /cm^{-1} (nm) [M^{-1}cm^{-1}]
D_2IrA'	MeCN	20900 (478) [31500]	26500 (377) [37100]	33700 (297) [69300]
	THF	20700 (483) [33900]	26400 (379) [33700]	33300 (300) [75500]
	DCM	20700 (483) [34600]	26300 (380) [37000]	33200 (301) [71700]
	toluene	20600 (482) [33900]	26200 (382) [21700]	33000 (303) [70400]
Pt	MeCN	19900 (503) [20400]	-	-
	THF	19800 (505) [20900]	-	-
	DCM	19800 (505) [21400]	-	-
	toluene	19700 (507) [21200]	-	-
DPt	MeCN	20000 (500) [18400]	-	32800 (303) [35900]
	THF	20000 (500) [19100]	-	32800 (303) [37900]
	DCM	19900 (503) [19000]	-	32700 (306) [36000]
	toluene	19800 (505) [19800]	-	32600 (307) [37600]
PtA	MeCN	19900 (503) [17400]	26400 (379) [33400]	-
	THF	19800 (505) [18200]	26400 (379) [28900]	-
	DCM	19700 (507) [18500]	26200 (382) [32300]	-
	toluene	19700 (507) [18900]	26100 (383) [20400]	-
DPtA	MeCN	20000 (500) [18700]	26500 (377) [37600]	32800 (303) [42800]
	THF	19900 (503) [19300]	26400 (379) [32700]	32800 (303) [44300]
	DCM	19800 (505) [19400]	26200 (382) [35800]	32600 (307) [43400]
	toluene	19800 (505) [19000]	26200 (382) [21700]	32500 (308) [43500]
Pd	MeCN	20300 (493) [36800]	-	-
	THF	20200 (495) [43600]	-	-
	DCM	20200 (495) [41700]	-	-
	toluene	20100 (498) [42100]	-	-
DPd	MeCN	20300 (493) [31800]	-	33000 (303) [32500]
	THF	20200 (495) [38200]	-	32800 (305) [36700]
	DCM	20200 (495) [33500]	-	32700 (306) [34500]
	toluene	20100 (498) [41100]	-	32500 (308) [36600]
PdA	MeCN	20200 (495) [34100]	26400 (379) [35600]	-
	THF	20100 (498) [39500]	26400 (379) [34800]	-
	DCM	20000 (500) [34300]	26200 (382) [34900]	-
	toluene	20000 (500) [37900]	26100 (383) [23400]	-
DPdA	MeCN	20200 (495) [32800]	26400 (379) [38800]	32900 (304) [41100]
	THF	20100 (498) [36600]	26400 (379) [35000]	32800 (305) [43800]
	DCM	20100 (498) [36800]	26200 (382) [39600]	32600 (307) [46300]
	toluene	20000 (500) [36800]	26200 (382) [20400]	32500 (308) [41800]

[a] values are always listed for the lowest energy peak, regardless of extinction coefficients - the higher energy peaks are located at around 27900 cm^{-1} (358 nm) and 29500 cm^{-1} (339 nm) respectively, with absorption coefficients dependent on the compound and solvent.

All complexes exhibit only a weak solvatochromic behavior as shown in **Figure 13** for the representative compounds **Pt** and **DPtA**. The most striking difference can be seen for the NDI-associated bands in toluene, which are significantly broadened compared to the other solvents. This is related to the aromaticity of the solvent and not to the polarity since no broadening can be observed from MeCN to DCM. The most likely explanation is an exciplex-formation often observed for aromatic solvents, which could include the NDI-moiety.[184]

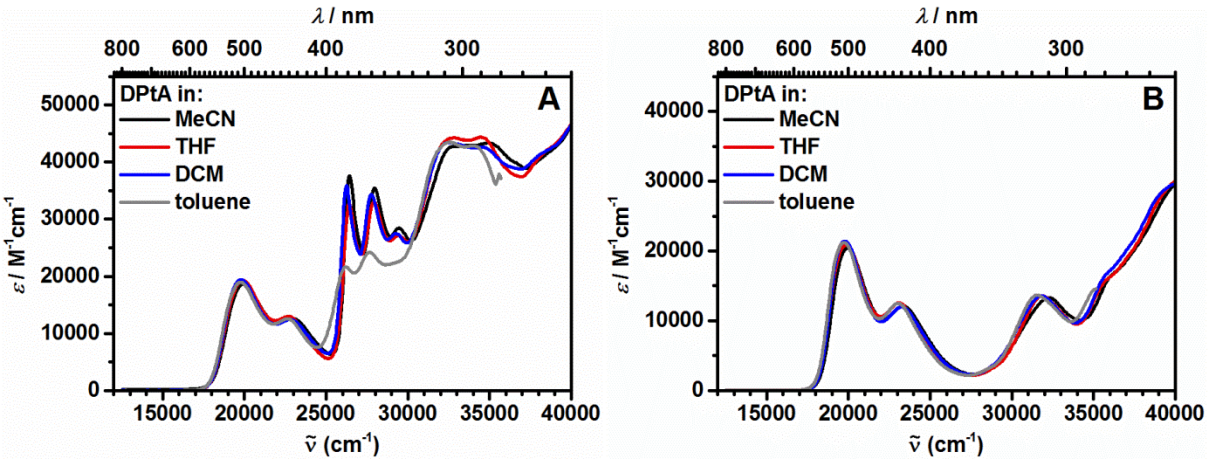

Figure 13: Absorption spectra of **DPtA** (A) and **Pt** (B) in MeCN (black), DCM (blue), THF (red) and toluene (grey) at rt. The solvatochromic behavior is representative of all other novel target complexes.

For a more detailed analysis of the differences between the solvents, the exact values taken from **Table 2** have to be considered. The strongest solvent dependence can be observed for the TAA absorption which shows a hypsochromic shift of 200 cm^{-1} to 700 cm^{-1} depending on the compound. This is likely due to a combination of a small shift of the TAA-absorption, which shows a weakly solvatochromic behavior due to participation of a CT-transition[182], and an analogous shift of the superimposed MLCT-transitions associated with the cyclometalating ligand and the metal ion of the respective central complex. These superimposed MLCT transitions around 32000 cm^{-1} show a small but significant negative solvatochromism as can be seen in **Figure 13** (B). This solvatochromic behavior of the MLCT transitions has been reported before and is expected, since the dipole moment of the compound is changed during this excitation due to its charge transfer character.[90, 110-111, 122-123] The absorption bands associated with the NDI and the M-dipy moiety show a weaker hypsochromic shift with increasing solvent polarity of about 300 cm^{-1} and 200 cm^{-1}, respectively, indicating only a small change of the dipole moment upon excitation. Lastly, it has to be mentioned that in MeCN, **D_2IrA'** was only sparingly soluble.

3.2.2 Cyclic Voltammetry

To gain insight into the electrochemical properties of the target molecules and to estimate the energy of possible CS states in the dyads and especially triads, cyclic voltammetry was performed. All measurements were carried out under argon atmosphere at rt in DCM, using TBAHFP at a concentration of about 0.2 M as the supporting electrolyte. All measurements were referenced against the ferrocene/ferrocenium (Fc/Fc^+) redox couple. Chemical reversibility of the different redox-processes was tested with multicycle thin layer experiments. The determined anodic peak potentials E_{pa}^{ox} of the first irreversible oxidation and half-wave potentials $E_{1/2}$ of all other observed redox-processes are listed for each compound in **Table 3**. The cyclic voltammograms of the target triads are shown in **Figure 14**.

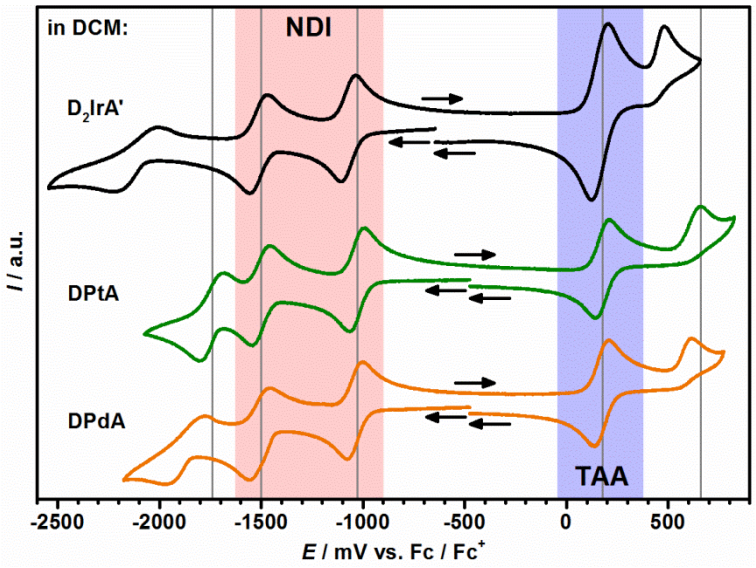

Figure 14: Cyclic voltammograms of **D_2IrA'** (black), **DPtA** (green) and **DPdA** (orange) in a 0.2 M solution of TBAHFP in DCM at a scan rate of 250 mV s^{-1}. All potentials are referenced against Fc/Fc^+. Black arrows indicate the start, end and direction of the measurement. For better comparison, potentials of –1740, –1500, –1030, 175 and 660 mV are highlighted by grey lines. Shaded areas mark processes associated with the NDI-(red) and TAA-(blue) moiety, respectively.

The first two reductive potentials at around –1050 and –1500 mV are completely reversible and can be assigned, in accordance with the literature, to the first and second reduction of the NDI core respectively.[115, 179, 181, 185-187] The first oxidative potential at around 170 mV on the other hand corresponds with the reversible first oxidation of the TAA moiety.[115, 179, 182, 186] The potentials of the redox-processes of both the NDI and the TAA stay virtually constant when changing the CMC. Again, this indicates a weak coupling between the different subunits. Since the intensity of the observed signals is related to the number of electrons involved in the process, the higher intensity of the TAA signal in **D_2IrA'** can be attributed to the presence of two donor-moieties.

The remaining redox potentials can be assigned to the first reduction and oxidation of the respective central metal complexes as can be derived from literature, but also from **Figure 15** and **Table 3**. The oxidative process is clearly irreversible and shows only the oxidative wave. Although for the reductive signal both the reduction and the back-oxidation could be observed, it is also irreversible as proved by multicycle thin layer experiments. Both processes are located at the dipyrrinato part of the respective CMC since the reduction- and oxidation-processes associated with the cyclometalating ligands usually occur at higher and lower potentials, respectively.[123, 136, 171]

Table 3: Halfway potentials[a] ($E_{1/2}$), anodic peak potentials[a] (E_{pa}) and potential difference (ΔE_{redox}) of the observed redox processes of the target molecules in a 0.2 M solution of TBAHFP in DCM.

	M-dipy $E_{1/2}^{red}$ /mV	**NDI** $E_{1/2}^{red1}$ **(**$E_{1/2}^{red2}$**)** /mV	**TAA** $E_{1/2}^{ox}$ /mV	**M-dipy** E_{pa}^{ox} /mV	ΔE_{redox} $E^{ox} - E^{red}$ /mV
D_2IrA'	–2110[i]	–1070[r] (–1520[r])	160[r]	480[i]	1230
Pt	–1720[i]	-	-	610[i]	-
DPt	–1720[i]	-	170[r]	620[i]	1890
PtA	–1740[i]	–1040[r] (–1510[r])	-	650[i]	1690
DPtA	–1740[i]	–1030[r] (–1500[r])	170[r]	660[i]	1200
Pd	–1790[i]	-	-	550[i]	-
DPd	–1800[i]	-	170[r]	570[i]	1970
PdA	–1850[i]	–1060[r] (–1550[r])	-	610[i]	1670
DPdA	–1870[i]	–1040[r] (–1510[r])	170[r]	610[i]	1210

[a] referenced against Fc/Fc^+ at a scan rate of 250 mV s^{-1}, [i] irreversible process, [r] reversible process

Concerning differences between the three central metal complexes, a clear influence of the central ion is observable. While the reduction occurs at –2110 mV for **D_2IrA'**, it is shifted to –1740 mV for **DPtA** and –1870 mV for **DPdA**. This trend can be explained by the electronic situation of the respective central metal ion. In contrast to the d^8-ions Pt(II) and Pd(II), the Ir(III) ion has d^6-configuration and is cyclometalated twice instead of only once. Since the cyclometalating ligand ppz is a very strong σ-donor and, due to the relative high electron density of the pyrazole, only a moderate π-acceptor, the electron density on the central metal ion gets increased significantly by the cyclometalation. This effect is strong enough that it overcompensate the formally higher positive charge of the Ir(III) ion, resulting in a higher electron density on the ancillary dipyrrinato ligand in the Ir(III)-complexes. This leads to a destabilization of the LUMO and therefore the reduction is shifted to lower potentials. The same principle can be applied to explain the trend of the oxidation potentials, which increase from 480 mV for **D_2IrA'** to 660 mV for **DPtA** and 610 mV for **DPdA**,.[111, 121, 171]

The small but noticeable differences between the Pt(II)- and the Pd(II)-complexes are more difficult to explain. Since palladium is located in a lower row of the periodic table, it should in theory have a higher effective nuclear charge and therefore stronger electron withdrawing properties. This would lead to a decrease in reduction potential and an increase in oxidation potential.[138] That the opposite trend is observed is probably due to a slight distortion of the CMC from the quadratic planar geometry for the Pd(II)-series as observed in the crystal structure of **Pd** and the literature.[138] This could result in a smaller influence of the ppz-ligand on the Pd(II)-dipy-fragment when compared to the Pt-complexes, which could compensate the stronger electron affinity.

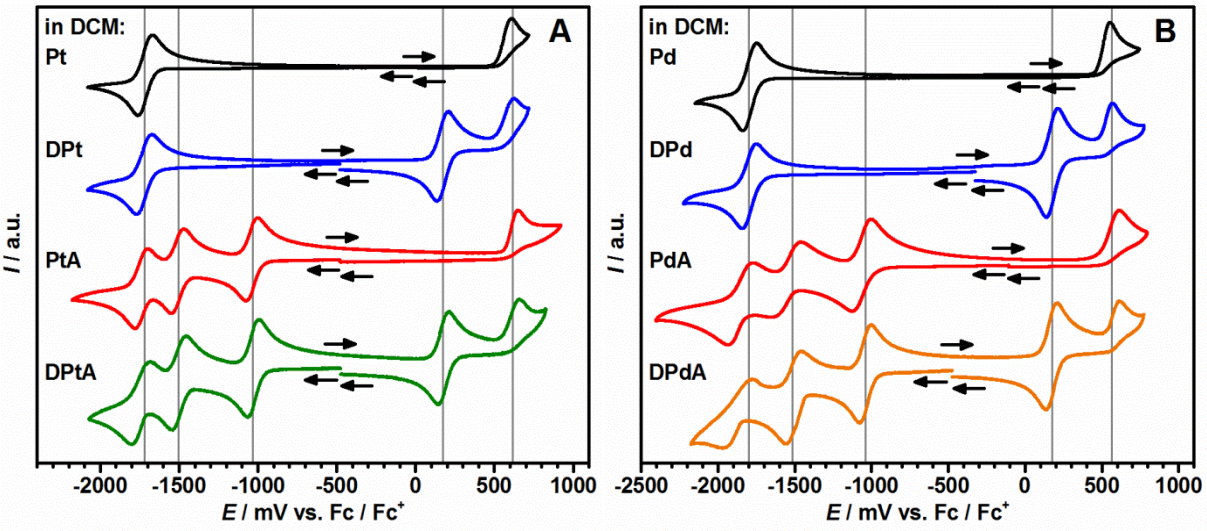

Figure 15: Cyclic voltammograms of the complexes of the Pt-series (A) and the Pd-series (B) in a 0.2M solution of TBAHFP in DCM at a scan rate of 250 mV s^{-1}. All potentials are referenced against Fc/Fc^{+}. Black arrows indicate the start, end and direction of the measurement. For better comparison, potentials of –1500, –1030 and 175 mV as well as (A) –1720 and 610 mV and (B) –1790 and 650 mV are highlighted by grey lines.

Figure 15 depicts the cyclic voltammograms of the complete Pt- (A) and Pd-series (B). Together with the values taken from **Table 3** the following conclusions can be drawn:

1) The potentials associated with the TAA and NDI moieties stay virtually constant throughout the series. This is yet another sign for a strong decoupling of the different subunits in the target complexes. The small differences in **PdA** are most likely due to irregularities in the measurement, since the reduction signals of the NDI seem rather asymmetric in comparison with the other NDI-signals. This is probably caused by solubility-issues, which were regularly observed for **PdA** and could lead to a stacking of the NDI-parts of different molecules, thus altering the redox-behavior. Since the deviations are quite small, this phenomenon was not investigated in more detail.[97, 115, 181, 188]

2) A substitution with NDI has a greater impact on the potentials associated with the M-dipy part of the CMC, than a substitution with TAA. This is observation can be attributed mainly to the fact that the NDI is attached directly to the dipyrrin and therefore influences the electronic properties of the dipyrrin because of the strong electron withdrawing character of the imido-group. This stabilizes the HOMO and LUMO of the dipyrrin and therefore increases the oxidation potential and decreases the reduction potential respectively.[136, 138, 189]

3) The effect described above is more pronounced in the Pd-series, which probably relates to the aforementioned distortion of the CMC from the quadratic planar geometry and the resulting lowered influence of the ppz-ligand on the Pd-dipy fragment. This would probably result in a relatively increased influence of the dipyrrin-substituents on the redox-properties of the M-dipy fragment when compared with the Pt-series.

4) Most importantly, the potential difference between the first oxidation- and reduction waves (ΔE_{redox}) obviously decreases dramatically with the addition of the donor and acceptor moieties. This theoretically enables the formation of a charge separated state for the triads and acceptor substituted dyads, but not for the donor-substituted dyads.[70, 115]

3.2.3 Emission-Spectroscopy

The emissive properties of the compounds of the Pt- and the Pd-series have been investigated in a variety of solvents of different polarity (MeCN, THF, DCM and toluene) at rt and in MeTHF at 77 K. Since not all compound-solvent combinations are necessary to draw reliable conclusions, some compounds were only measured in a few solvents. All samples were degassed by purging with dry argon for at least 20 minutes to remove oxygen from the solution which could quench possible phosphorescence.[111, 136, 138, 183] All measurements at rt were performed using standard photomultiplier detection which only works well down to 12500 cm^{-1} although the complexes show emission bands which extend significantly below that energy. This was done because the emission is very weak in all cases and the standard photomultiplier has a higher sensitivity in the range down to 12500 cm^{-1}. In fact the emission was so weak that all emission spectra had to be corrected for the pure solvent background, because the intensity of the emissive signals was on the order of magnitude of the *Raman* scattered excitation light. For that reason no lifetimes were determined and the quantum yields are assumed to be significantly below $\Phi = 0.01$.[144, 157] To keep the data at least somewhat comparable nonetheless, most measurements were performed using samples of similar optical densities at the excitation energy, similar excitation intensities and the same step-size, integration time and repetitions. All obtained data is summarized in **Table 4**.

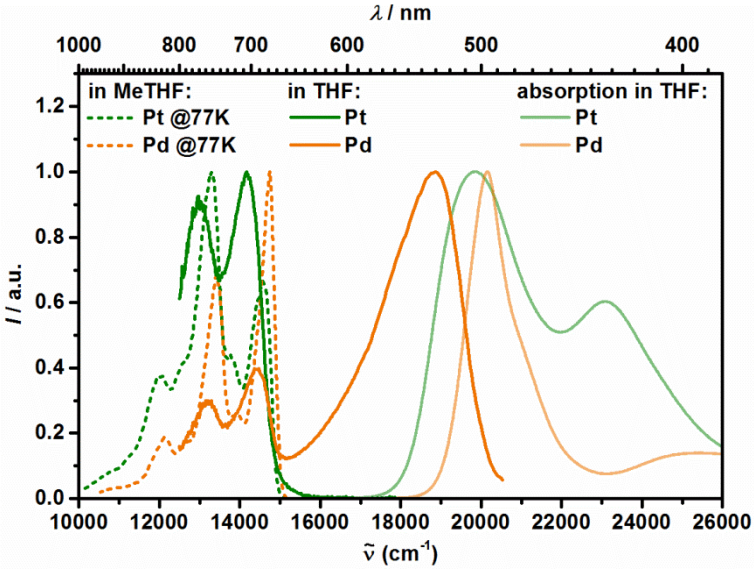

Figure 16: Normalized emission spectra at 77 K in MeTHF (dotted lines) and at rt in THF (solid lines) of **Pt** (green) and **Pd** (orange) in comparison with the respective normalized steady state absorption spectra at rt in THF (pale lines).

Figure 16 shows the emission spectra of **Pt** (green) and **Pd** (orange) at rt in THF and at 77 K in MeTHF in comparison with the respective absorption spectra in THF. At rt, **Pt** shows a emission at around 14200 cm^{-1} with vibronic fine structure which extends below 12500 cm^{-1} in which the first peak has a higher intensity than the second one at 13000 cm^{-1}. When measuring in a glassy matrix in MeTHF at 77 K the emission intensity increases significantly so that the whole spectra down to 10000 cm^{-1} can be recorded. Furthermore, additional peaks and shoulders can be observed since the vibronic fine structure gets sharper. Lastly, the emission intensity ratio of the first and second peak inverts and the emission energy gets shifted only slightly (400 cm^{-1}) to higher energies. The weak rigidochromic behavior indicates that there is little change in dipole moment between the ground and excited state. The same reasoning applies for the weak solvatochromic effect observable in **Figure 17** A and **Table 4**. This and the vibronic fine structure point towards a ligand centered emissive state since MLCT transitions should show broad and featureless solvent dependent emission. The large energy difference between the absorptive and emissive 0-0-transitions and the relative consistent emission energy when changing to 77 K are indicators for phosphorescence. In accordance with the literature the emission can be classified as dipyrrin-centered phosphorescence from a ^{3}LC-state.[111, 136, 138, 189-190] On the other hand, **Pd** shows dual luminescence at rt. The more intense emission at 18900 cm^{-1} behaves roughly like a mirror of the absorption with a *Stokes* shift of 1300 cm^{-1}, but extends at least down to 15000 cm^{-1}. There the first emission band gets superimposed by the second band, which is very similar in shape to the emission of **Pt**. The second band has a maximum at 14400 cm^{-1} and a second peak at 13200 cm^{-1}. When measuring at 77 K in MeTHF, the high energy band is no longer observable since the intensity of the lower energy band is greatly increased. Again, additional peaks

and shoulders can be observed due to the sharpening of the vibronic fine structure, but in contrast to **Pt**, the intensity of the first and second peak does not invert from rt to 77K. Similar to **Pt**, the low energy emission can be assigned to dipyrrin centered phosphorescence. On the other hand, the high energy emission is assigned fluorescence from a ^{1}LC-state located at the dipyrrin ligand due to the small *Stokes*-shift and the weak solvatochromic behavior of the emission which is shown in **Figure 17** (B) and **Table 4**. The dual luminescence of Pd is most likely caused by a reduced ISC rate from the ^{1}LC to the ^{3}LC state in **Pd** due to the decreased heavy atom effect compared to the much heavier Pt(II) centered **Pt.** A dual luminescence was also observed in the literature for the lighter Rh(II)-centered dipyrrinato complexes, but not for the heavier Ir(III)-centered analogues.[117, 138, 190]

As can be seen from **Figure 17** and **Table 4** the solvatochromic behavior of **Pt** and **Pd** is virtually negligible. The small deviation of the fluorescence spectra of **Pd** at around 17000 cm^{-1} are due to an incomplete correction of the signal for the influence of Raman-scattered excitation light. Concerning the relative intensities *I* of the different peaks no real trend can be observed. The small differences between the maximum and the vibrational progression of the phosphorescence can probably be explained by the bad signal to noise ratio and small overall intensity. The much more prominent differences in intensity between the fluorescence and the phosphorescence in **Pd**, show no clear trend with solvent polarity as well. The intensity ratio is not concentration dependent as was proved by concentration dependent measurements. At the moment no explanation of this behavior can be given. The same holds true for the unexpected inverted intensity ratio between rt and 77 K in **Pt**, which was not observed in a publication by *Bronner et al.* on complexes very similar to **Pt** [138] Nonetheless, first computational results obtained in the group of Prf. Dr. Marian at the University of Düsseldorf indicate that the phosphorescence originates from more than one triplet geometry, which could explain the observed behavior of Pt at 77 K and both complexes at rt.[191-192]

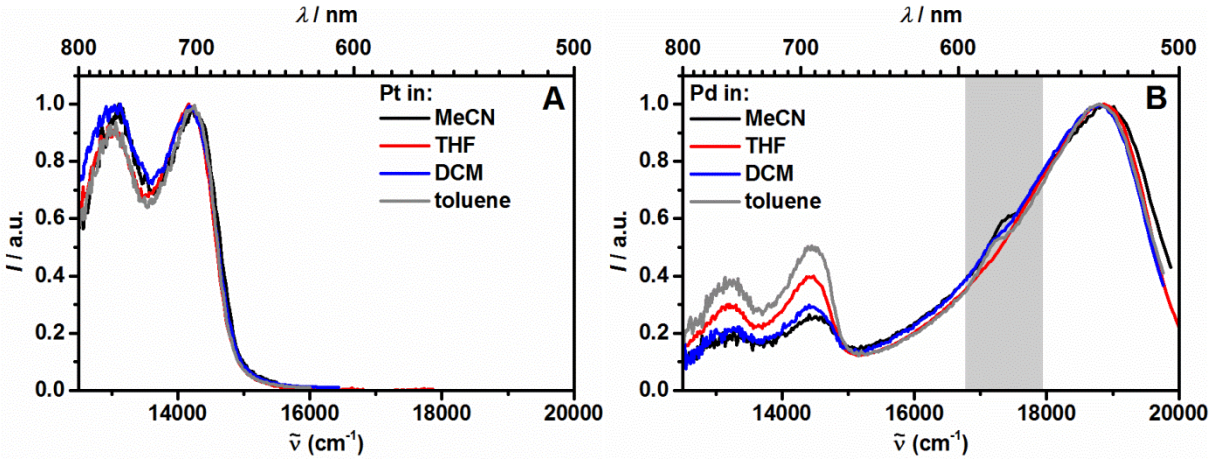

Figure 17: Emission spectra of **Pt** (A) after excitation at 20000 cm^{-1} (500 nm) and **Pd** (B) after excitation at 21300 cm^{-1} (470 nm) in MeCN (black), DCM (blue) THF (red) and toluene (grey) at rt. The grey shaded area in (B) is influenced by *Raman* scattered excitation light.

Table 4: Emission maxima $\tilde{\nu}_{max}$ (λ_{max}) and relative intensities *I* of the characteristic emission bands of the respective complexes of the Pt- and Pd-series in different solvents at rt and MeTHF at 77K after excitation at or near the maximum absorption of the CMC (see **Table 2**).

	solvent	fls. $\tilde{\nu}_{max}$ (λ_{max}) [*I*] /cm^{-1} (nm) [a.u.]	phos. $\tilde{\nu}_{max}$ (λ_{max}) [*I*] /cm^{-1} (nm) [a.u.]	phos. vibration $\tilde{\nu}_{max}$ (λ_{max}) [*I*] /cm^{-1} (nm) [a.u.]
Pt	MeTHF (@ 77 K)	-	14600 (685) [0.7]	13300 (752) [1]
	MeCN	-	14200 (704) [1]	13100 (763) [1]
	THF	-	14200 (704) [1]	13000 (769) [0.9]
	DCM	-	14200 (704) [1]	13000 (769) [1]
	toluene	-	14200 (704) [1]	13000 (769) [0.9]
DPt	MeCN	-	14200 (704) [1]	13000 (769) [1]
	DCM	-	14200 (704) [1]	13100 (763) [0.8]
	toluene	-	14200 (704) [1]	13000 (769) [0.9]
PtA	MeCN	-	-[b]	-[b]
	DCM	-	14000 (714) [0.8]	13000 (769) [0.8]
	toluene	-	14100 (709) [1]	12900 (775) [0.9]
DPtA	MeCN	-	14100 (383) [0.9]	13000 (769) [0.8]
	DCM	-	14000 (714) [1]	12800 (781) [0.9]
	toluene	-	14000 (714) [1]	12800 (781) [0.9]
Pd	MeTHF (@ 77 K)	-	14700 (680) [1]	13400 (746) [0.7]
	MeCN[a]	18900 (529) [1]	14500 (690) [0.3]	13200 (758) [0.2]
	THF[a]	18900 (529) [1]	14400 (694) [0.4]	13200 (758) [0.3]
	DCM[a]	18800 (532) [1]	14400 (694) [0.3]	13200 (758) [0.2]
	toluene	18800 (532) [1]	14400 (694) [0.5]	13200 (758) [0.4]
DPd	MeCN[a]	18900 (529) [1]	14400 (694) [0.5]	13200 (758) [0.4]
	THF[a]	18900 (529) [1]	14400 (694) [0.8]	13200 (758) [0.6]
	DCM[a]	18800 (532) [1]	14400 (694) [0.5]	13200 (758) [0.4]
	toluene[a]	18900 (529) [1]	14400 (694) [0.8]	13200 (758) [0.6]
PdA	MeCN	19000 (526) [1]	-	-
	DCM	18900 (529) [1]	-	-
	toluene	18900 (529) [1]	14200 (704) [0.3]	13000 (769) [0.3]
DPdA	MeCN	19000 (526) [1]	-	-
	DCM	19000 (526) [1]	-	-
	toluene	19000 (526) [1]	14300 (699) [0.5]	13000 (769) [0.4]

[a] after excitation at 21300 cm^{-1} (470 nm), [b] no distinct emissive signal was observed

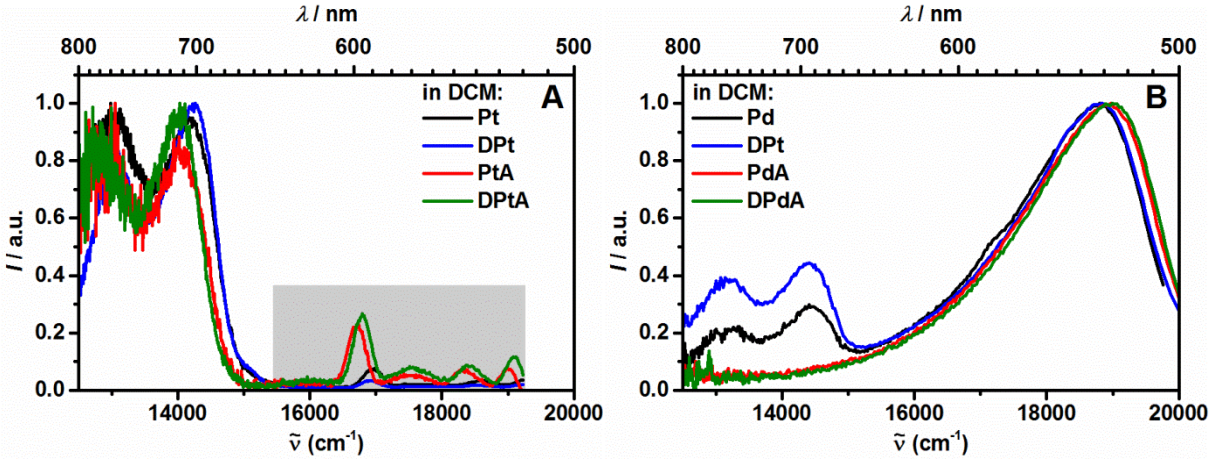

Figure 18: Emission spectra of the complexes of the Pt-series (A) and the Pd-series (B) in DCM at rt. The grey shaded area in (A) is influenced by *Raman* scattered excitation light and can serve as a reference for the comparison of the emission intensities.

When comparing the emission spectra of the different complexes of the Pt- and Pd-series with the help of **Table 4** and **Figure 18** one can see that substitution with TAA and NDI has virtually no effect on the emission energies. Merely a small hypsochromic shift of the fluorescence is observable for the NDI-substituted Pd-complexes **PdA** and **DPdA**. Way more striking and important are the differences in emission intensity. While **Pt** and **DPt** have comparable emission intensities, as can be seen from the signal to noise ratio and the ratio of the *Raman* scattered excitation light to the emission in **Figure 18** (A), the phosphorescence intensity drops significantly for the NDI-substituted complexes **PtA** and **DPtA** in DCM. The effect is even more pronounced for the complexes of the Pd-series. While **Pd** and **DPd** show the dual luminescence described above, **PdA** and **DPdA** show only fluorescence and no phosphorescence at all in DCM.

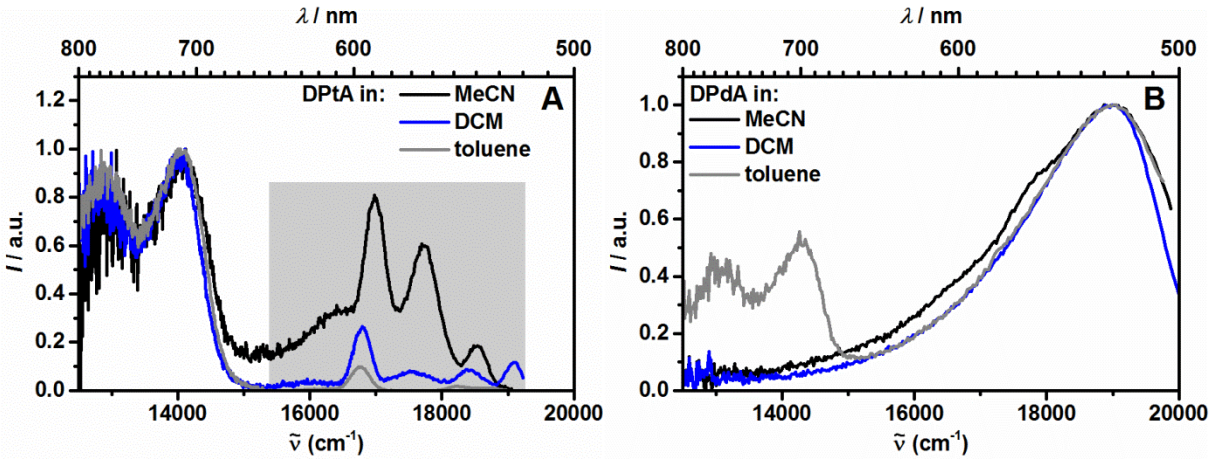

Figure 19: Emission spectra of **DPtA** (A) and **Pt** (B) in MeCN (black), DCM (blue) and toluene (grey) at rt. The grey shaded area in A is influenced by *Raman* scattered excitation light and can serve as a reference for the comparison of the emission intensities in addition to the signal to noise ratio.

The process responsible for the quenching of the phosphorescence is clearly solvent dependent as can be seen from **Table 4** and is illustrated in **Figure 19**. While the phosphorescence intensities of **DPtA** and **DPdA** are comparable to the unsubstituted reference complexes in non-polar solvents such as toluene, they get reduced drastically in more polar solvents such as DCM and MeCN. As will be proven in the following chapters, the process responsible for the quenching of the phosphorescence is the formation of a charge separated state.[59, 115-116, 179, 186, 188-189]

3.2.4 Conclusions

The process responsible for the phosphorescence quenching in the acceptor-substituted complexes was attributed to charge separation (CS). During this process an electron is transferred from the donor to the acceptor. In the triads, the role of donor and acceptor are obviously occupied by the TAA and NDI respectively. In the dyads, the CMC takes the role of the missing subunit. Charge separation only occurs if the energy of the charge separated state (CSS) is lower than the energy of the state from which it gets occupied. The free energy (ΔG_{CSS}) of potential CSSs can be estimated by the *Weller* approach using equation 12 and the potential difference ΔE_{redox} between the first reduction of the acceptor and oxidation of the donor as determined by cyclic voltammetry.[193]

$$\Delta G_{CS} = \frac{N_A}{1000} ze[\Delta E_{redox}] - \frac{N_A e^2}{4000\pi e_0}\left[\left(\frac{1}{2r_D} + \frac{1}{2r_A}\right)\left(\frac{1}{\varepsilon_r} + \frac{1}{\varepsilon_s}\right) + \frac{1}{\varepsilon_s d_{DA}}\right] \quad (12)$$

where N_A is the *Avogadro* constant, z is the number of transferred charges, e is the elementary charge, ε_0 is the vacuum permittivity, r_D, r_A and d_{DA} are the radii of the donor and acceptor moiety as well as the center to center distance between them, respectively, ε_r is the permittivity of the solvent used for CV and ε_S is the permittivity of the solvent in which the free energy is to calculated.

The radii r_D and r_A were calculated assuming an ideal spherical shape from the *Connolly* Molecular Surfaces of the subunits, which were estimated using ChemBio 3D Ultra on a molecular model obtained from DFT calculations at a PBE1PBE level of theory using *Gaussian09*[194]. The distance d_{DA} was taken from the same model. The calculations were only performed for the acceptor-substituted complexes of the Pt- and the Pd-series because the donor-substituted dyads and the unsubstituted central complexes did not show any sign of charge separation.

Furthermore, the 0-0 transition energies of the dipyrrin centered transitions can be estimated from the intersection of the x-axis and a tangent fitted on the inflexion point of the low energy rise of the absorption and the high energy rise of the phosphorescence respectively. The obtained values correspond to the energy of the ligand centered (LC) triplet ($\Delta E(^3M)$) and singlet ($\Delta E(^1M)$) excited states of the central metal complexes in relation to the ground state.

Table 5: Energy of the singlet ($\Delta E(^1M)$) and triplet ($\Delta E(^3M)$) excited state as well as the charge separated state (ΔG_{CSS}) in different solvents determined as described in the main text using the potential-difference ΔE_{redox} from **Table 3** and the given values for the donor-acceptor distance (d_{DA}) and the radii of the involved redox centers (r_D and r_A).

	d_{DA} /Å	r_D /Å	r_A /Å	solvent	ΔE (^{1}M) /cm^{-1}	ΔE (^{3}M) /cm^{-1}	ΔG_{CSS} /cm^{-1}
Pt	-	-	-	MeCN	18400	14900	-
				THF	18200	14800	-
				toluene	18100	14800	-
PtA	12.7	4.72	3.97	MeCN	18200	-	11100
				THF	18100	-	13000
				toluene	18100	14700	18100
DPtA	22.1	4.81	3.97	MeCN	18100	14700	7400
				THF	18100	-	9600
				toluene	18000	14700	15800
Pd	-	-	-	MeCN	19200	15200	-
				THF	19100	15100	-
				toluene	19000	15000	-
PdA	12.7	5.20	3.97	MeCN	19000	-	11000
				THF	19000	-	12800
				toluene	18900	15100	17700
DPdA	22.0	4.81	3.97	MeCN	19000	-	7400
				THF	19000	-	9600
				toluene	18900	14900	15800

From the determined state energies summarized in **Table 5** it can be seen that the ^{1}Pt- and ^{3}Pt- state energies stay relatively constant when changing solvent or substitution pattern. The same is true for the ^{1}Pd- and ^{3}Pd- state energies in the analogue Pd-complexes. For that reason, the ^{3}M-state energies of the respective unsubstituted CMC can act as a reasonably good approximation for the gaps present in **Table 5** for the acceptor-functionalized complexes. The energy of the CSSs on the other hand is influenced significantly by the solvent polarity and the subunit which acts as an electron donor. Since intersystem crossing (ISC) is usually pretty fast for transition metal complexes, and no sign of fluorescence quenching was observed in the emission experiments, it is a safe assumption that the CSSs are occupied from the ^{3}Pt- and ^{3}Pd-state respectively. Even assuming the lowest triplet-state energies for the acceptor substituted compounds the CSSs are lower in energy, enabling the possibility of CS, in each tested solvent except toluene. This is in good agreement with the findings from the emission spectroscopy, where no phosphorescence quenching could be observed in toluene. The energetic situation for the triads is also visualized in the state diagrams in **Figure 20**.

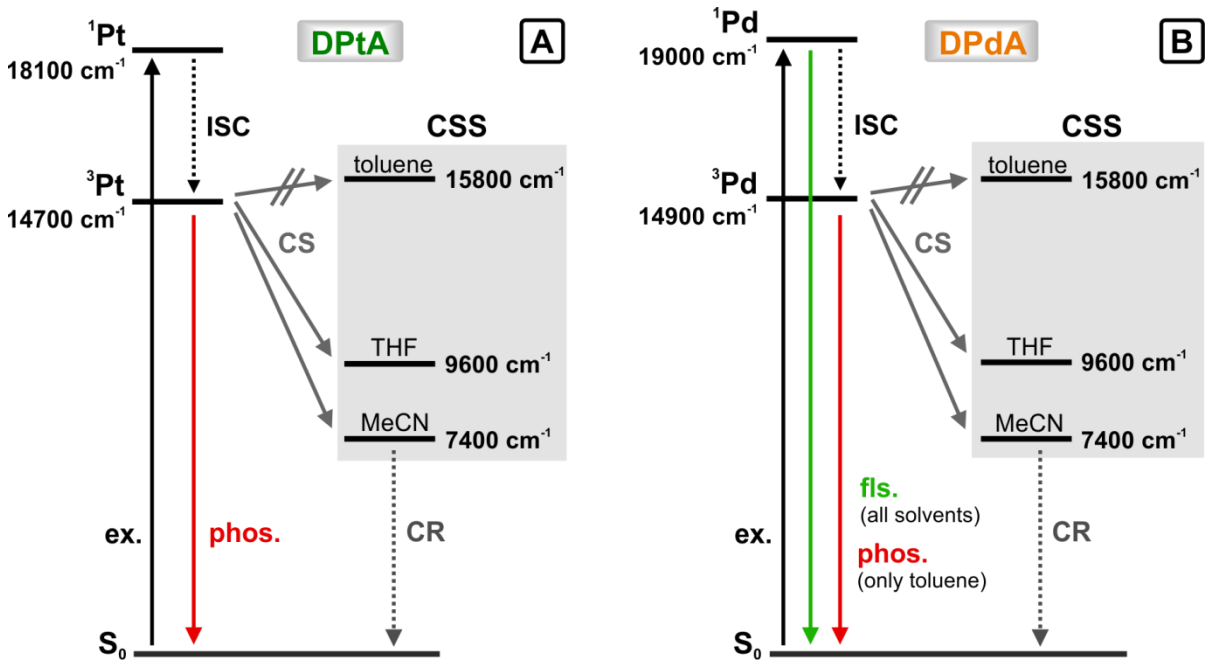

Figure 20: State diagrams of **DPtA** (A) and **DPdA** (B). For the respective ^{3}M-energies, the lowest possible values determined were used. Transitions depicted in grey are assumed to take place, but cannot be proved by the steady state measurements.

Of the processes depicted in **Figure 20** only excitation, fluorescence and phosphorescence have been observed directly in the steady state experiments. Since phosphorescence was observed, the ISC is indirectly proved to take place although no kinetics could be determined. Although CS is very strongly supported by the findings of the steady state measurements, it can only be proved by transient absorption measurements. To prove CS, the transient absorption spectra of the complexes have to be similar to a superposition of the spectra of the $NDI^{\bullet-}$ monoradical anion and the $TAA^{\bullet+}$ monoradical cation, which can be determined by spectroelectrochemistry (SEC).

Since the steady state measurements of the target compounds confirmed that the electronic coupling between the subunits is very weak, a potential charge separated state (CSS) should only be dependent on the donor- and acceptor units, and the distance between the donor and acceptor. This assumption is supported by the exact agreement of the CSS-energies determined above. Hence, it was concluded that the spectroelectrochemical measurements performed previously by Dr. Johannes Klein on similar Ir(III)-complexes[59, 70, 115] are a reasonable reference and no SEC was performed on the target complexes. The results of the previous SEC-measurements are illustrated in **Figure 21**. The sum of the spectra of the monoradical cation of TAA and the monoradical anion of NDI should be a good estimation of the absorption spectra of CSSs proposed above.[82, 115, 173, 180, 182, 186-187] To finally prove the formation of CSSs transient absorption spectroscopy can be performed as described in the following chapters.

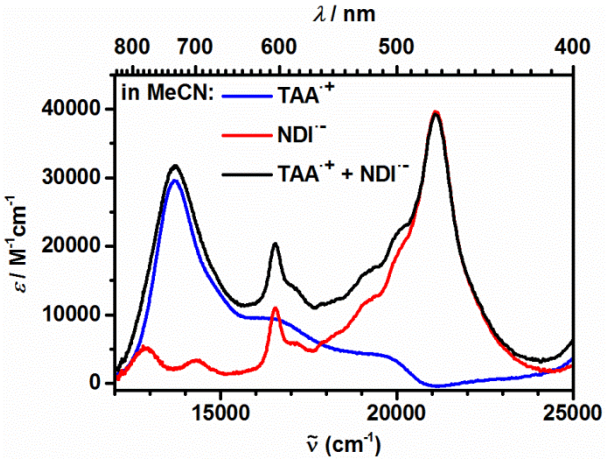

Figure 21: Spectra of the monoradical cation of TAA (blue), the monoradical anion of NDI (red) and the sum of both (black) in a 0.1 M TBAHFP in MeCN as measured for **D₂IrA** by Dr. Johannes Klein.[70]

3.3 Charge-Separation and Recombination

The previous chapters gave valuable information on the steady state photophysics of the complexes. For the acceptor-substituted dyads **PtA** and **PdA** and the full triads **DPtA** and **DPdA** charge separation was proposed as a preliminary interpretation. To validate this hypothesis, transient absorption (TA) spectroscopy was performed on the compounds mentioned above and **D₂IrA'**. If charge separation occurs, the transient absorption spectra should match the spectra derived from the SEC-measurements shown in **Figure 21**. Furthermore, the kinetics of the charge-separation and recombination can be derived from the fs- and ns-measurements respectively. For reference, the unsubstituted compounds **Pt** and **Pd** were also investigated. During the following chapters several global deconvolution fits are shown that were performed[b] using the GLOTARAN software (v. 1.2).[195]

3.3.1 ns-Transient Absorption Spectroscopy

ns-Laser-flash spectroscopy was performed on the complexes of the Pt-series and the Pd-series in solvents of different polarity, that is in MeCN, THF and toluene, while **D₂IrA'** was examined only in MeCN. All solvents were of spectroscopic grade and used without further purification. Only THF was freshly distilled prior to use and stored under argon to prevent the formation of peroxides. Since the absorption bands of the NDI-moiety and the CMC are relatively well separated, an excitation wavelength dependent analysis is possible. As can be seen from the stationary absorption depicted in **Figure 11**, excitation energies from 18000 – 25000 cm^{-1} exclusively excite the CMC, while excitation

[b] All global analysis were performed by Dr. Marco Holzapfel

between 25000 – 30000 cm^{-1} corresponds to a mixed excitation of the NDI and the CMC in a ratio strongly favoring the NDI. Two different excitation sources were used. Excitation at 28200 cm^{-1} and 24000 cm^{-1} was achieved with a Continuum Minilite II Nd:YAG laser and a Raman-Shifter charged with hydrogen (50 bar). Excitation at around 20000 cm^{-1} and at 26400 cm^{-1} was achieved with the output of an EKSPLA NT 342A Nd:YAG laser at 28200 cm^{-1} which was shifted to the desired wavelength with an optical parametric oscillator. In all cases the white light was provided by a Xe-flash lamp. For further experimental details also see chapter 6.1.5.

All samples were degassed with a stream of argon for at least 30 minutes prior to measurement to ensure an oxygen free environment which does not artificially decrease charge separated state lifetime.[28-29, 179] To exclude bimolecular reaction pathways, all compounds were measured at different concentrations and excitation intensities. Only monomolecular processes were found for samples of an optical density between 0.2 and 0.3 at the excitation wavelength and excitation pulse intensities of 8 mW for NDI-excitation and 12 mW for excitation of the CMC. All determined excited state lifetimes as well as quantum yields of charge separation are collected in **Table 6**. However, since in most cases the principal results do not change drastically between solvents, only the measurements in THF are depicted in the following figures. Throughout the whole work, early spectra will be depicted in blue to green color, while later spectra are shown in yellow to red colors.

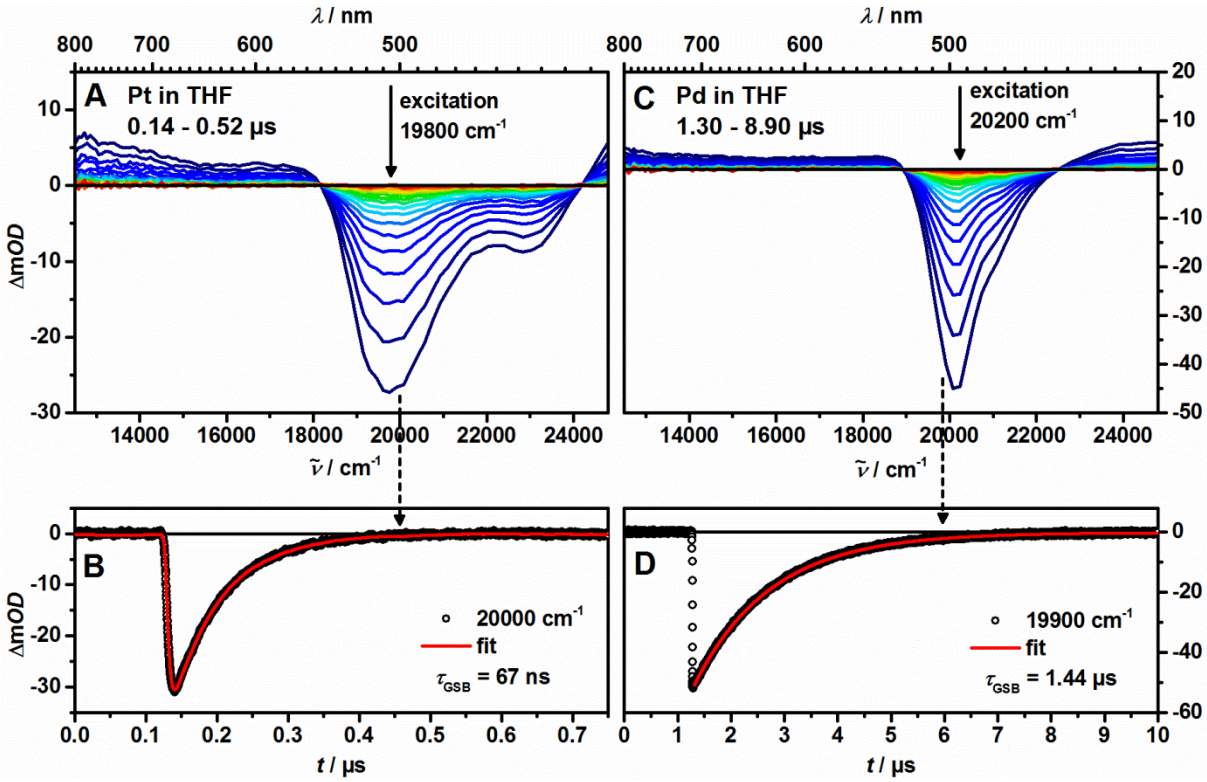

Figure 22: ns-Transient absorption spectra of **Pt** and **Pd** in THF at rt after excitation at 19800 cm^{-1} and 20200 cm^{-1}, respectively (A and C), and kinetic traces with fit at selected wavenumbers (B and D). Early spectra are depicted in blue to green and later spectra in orange to red color.

Figure 22 shows the resulting transient absorption (TA) spectra of **Pt** (A) and **Pd** (C) in THF and the decay-kinetics at characteristic wavenumbers (B and D). TA spectra can in general consist of three superimposed components: 1) negative signals due to a relatively reduced concentration of molecules in the ground state, called ground state bleaching (GSB), 2) negative signals due to stimulated or spontaneous emission (SE) and 3) positive signals due to absorptive transitions from the excited state, called excited state absorption (ESA). Stimulated emission can be excluded in the ns-laser flash spectroscopic measurements since the measurements are run with a fluorescence correction which subtracts possible emissive signals. Therefore, the negative signals in the transient spectra of **Pt** and **Pd** can easily be assigned to ground state bleaching. As expected, the GSB matches very well with a negative of the UV/Vis-absorption of the respective complex and has a maximum at around 19800 cm^{-1} for **Pt** and 20100 cm^{-1} for **Pd**. Furthermore, in the recorded spectral range both complexes show only minimal ESA which consists of a very broad and featureless band towards lower energies and a slightly more intense band at higher energies than the GSB. As explained in chapter 3.2.4, both complexes show phosphorescence, hence the excited state is assigned to a ligand centered triplet state ^{3}M of the respective CMC (^{3}Pt and ^{3}Pd).

From the decay traces, the lifetime of the ^{3}M-state (τ_{GSB}) can be derived. For lifetimes below 100 ns this was done by a reconvolution fit which includes the instrument response function (IRF). Longer lifetimes were simply determined by exponential fitting of the tail. The excited state lifetimes of **Pt** and **Pd** in THF are 67 ns and 1.44 µs respectively. Since both **Pt** and **Pd** show similarly low phosphorescence intensities the huge difference in lifetime is most likely due to a combination of higher radiative rates and higher non-radiative rates in **Pt**. Higher radiative rates in **Pt** seem reasonable since Pt(II) is the heavier central metal ion and should therefore facilitate the spin-forbidden phosphorescence by its higher SOC-constant.[117, 119, 196-197] Non-radiative rates usually are enhanced by low lying metal-centered triplet states (^{3}MC-states), and intramolecular movements such as rotations, vibrations and geometrical distortions and rearrangements. The differences between **Pt** and **Pd** regarding these parameters are less clear. While the ^{3}MC-states should be more destabilized for the *5d*-ion Pt(II),[111, 136] the intramolecular distortions have been found to be greater for the Pd(II)-complexes in a series of similar Pt(II) and Pd(II) complexes, which also exhibit a reversed trend of excited state lifetime at 77 K.[138] The influence of the solvent-polarity on the excited state lifetimes is the same for **Pt** and **Pd** as can be seen from **Table 6**. The lifetimes increase from 40 ns in MeCN to 90 ns in toluene for **Pt** and from 0.88 µs in MeCN to 1.88 µs in toluene for **Pd**. A more detailed explanation of the lifetime differences cannot be given at the moment. The basic results which are important for the following interpretation of the more complex compounds is that the unsubstituted metal complexes show virtually only GSB as a transient signal and the decay to the ground state can be fitted with a single exponential.

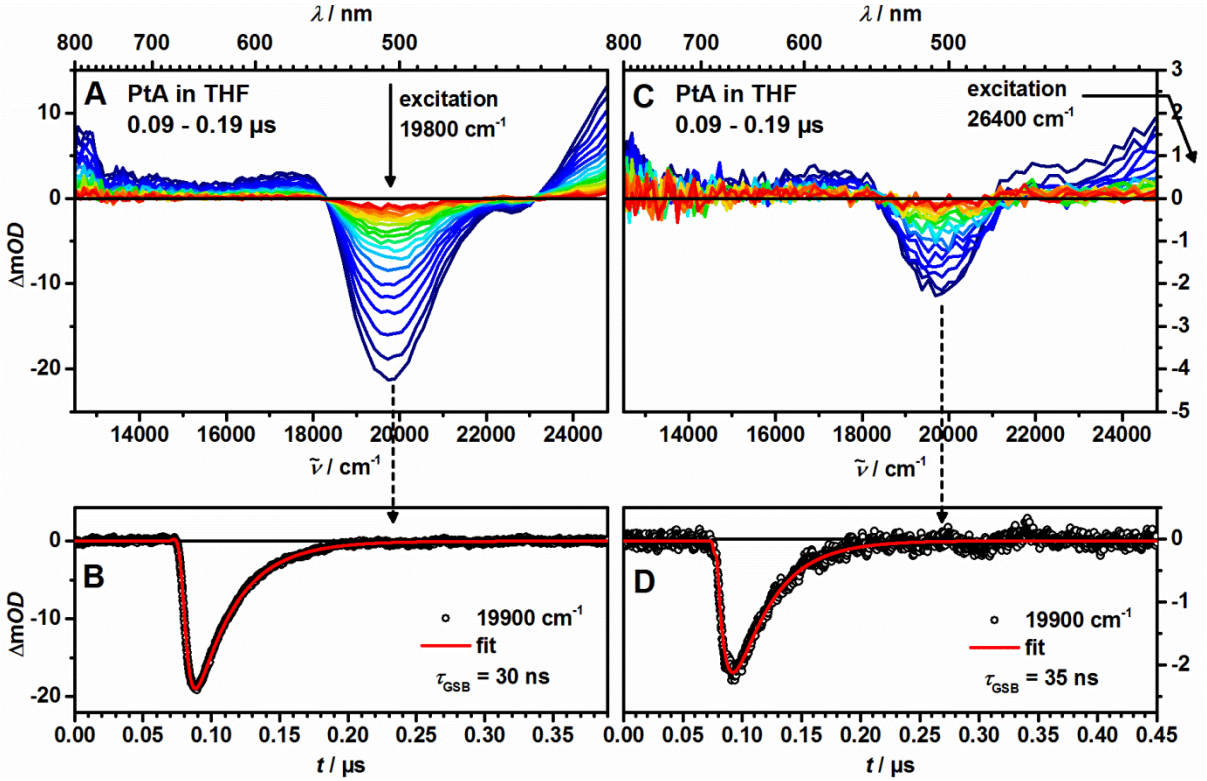

Figure 23: ns-Transient absorption spectra of **PtA** in THF at rt after excitation at 19800 cm^{-1} (A) and 26400 cm^{-1} (C), respectively and kinetic traces with fit at selected wavenumbers (B and D).

Figure 23 shows the TA spectra of **PtA** in THF after excitation at 19800 cm^{-1} (A) and 26400 cm^{-1} (C) and the respective decay kinetics at the wavenumber of the GSB-maximum (B and D). At the first glance, the spectra after excitation at the CMC (19800 cm^{-1}) seem very similar to the transient spectra of **Pt** with a dominating GSB around 20000 cm^{-1}. However, the shoulder of the bleaching signal at around 22500 cm^{-1} is less intense in **PtA** and is shifted to lower energies, while the ESA at higher energies is significantly more pronounced in **PtA**. Furthermore, the GSB decays with 30 ns more quickly to the ground state than in **Pt**. Excitation at 26400 cm^{-1} gives considerably lower signal intensities of the GSB although the amount of absorbed quanta was kept similar throughout both experiments. This was achieved by compensating the slightly higher extinction coefficient of **PtA** at 26400 cm^{-1} with an adequately lower excitation intensity. As can be determined from the extinction coefficients of **Pt** and **PtA**, at 26400 cm^{-1} ca 91% of the quanta are absorbed by the NDI and only 9% by the CMC. If one assumes that all excited NDI deactivates to the ground state faster than the IRF of the setup, then only excited CMC is registered in the measurement and the decrease in signal intensity and the missing of signals associated with the $NDI^{\bullet-}$ monoradical ion become reasonable. At the same time, the shoulder of the GSB at 22500 cm^{-1} is replaced by a small ESA which decays basically with the IRF, supporting the thesis of fast NDI-deactivation. The kinetics at 19900 cm^{-1} on the other hand stay practically the same as after excitation at 19800 cm^{-1}, indicating that the excited CMC deactivates in a similar manner after excitation at either energy.

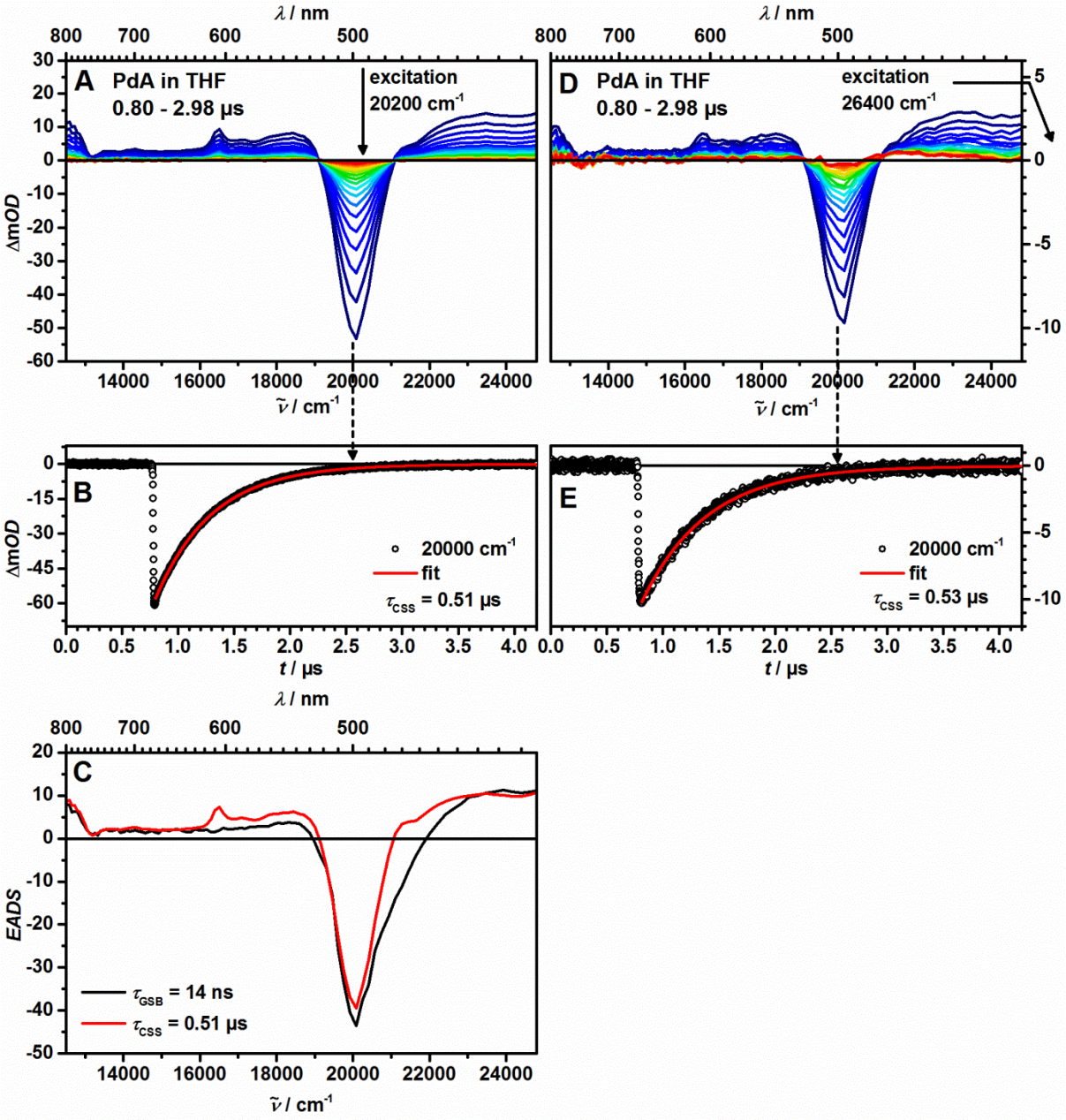

Figure 24: ns-Transient absorption spectra of **PdA** in THF at rt after excitation at 20200 cm^{-1} (A) and 26400 cm^{-1} (D), kinetic traces with fit at selected wavenumbers (B and E) and evolution associated difference spectra (EADS) from a global fit.

Figure 24 shows the TA spectra of **PdA** after excitation at 20200 cm^{-1} (A) and 26400 cm^{-1} (C) and the respective decay kinetics at the wavenumber of the signal maximum (B and D). The results vary significantly from those for **PtA**. Both TA spectra show a strong GSB at 20000 cm^{-1} and a less intense but significant ESA at 16500 cm^{-1}. This ESA is characteristic for the $NDI^{\bullet-}$ monoradical anion as can be seen in **Figure 21** and the literature.[179-180, 186-187, 198] The second peak of this moiety at 21100 cm^{-1} is not present since it is superimposed by the GSB of the CMC. This also explains the differences in the shape of the GSB between **Pd** and **PdA**. Since all signals decay monoexponentially with very similar

lifetimes of about 0.51 µs, the whole TA spectrum results from one excited state. This state is characterized by a CMC in an excited state and a reduced NDI-moiety and is therefore assigned to a CSS between the central Pd-complex, which acts as an electron donor and the NDI-acceptor. Additionally, a global analysis using a sequential model was performed for the experiment after excitation at 20200 cm^{-1}. The resulting evolution associated difference spectra (EADS) and their respective lifetimes are shown in **Figure 24** (E). As can be seen, the global fit results in two individual spectral components (transients). The first transient shows GSB associated with ^{3}Pd including the shoulder at higher energies also observed for **Pd** but no ESA at 16500 cm^{-1} associated with the reduced NDI. ^{3}Pd evolves with a lifetime of 14 ns to the second transient which shows the characteristic NDI radical ion band, and a diminished shoulder of the GSB, indicating a CSS which decays with a lifetime τ_{CSS} of 0.51 µs to the ground state.

Moving on to the donor-functionalized triads, **Figure 25** shows the TA spectra of **DPtA** after excitation of the CMC at 24000 cm^{-1} at early times (A) and later times (C), as well as the kinetics at wavenumbers characteristic for the respective time-range (B and D). As can be seen, the first transient signal is the GSB of the CMC at around 20000 cm^{-1}. The GSB has a lifetime of 26 ns and transforms to an ESA which shows the characteristic bands for the $NDI^{\bullet-}$ monoradical anion at 21100 cm^{-1} and 16500 cm^{-1} as well as for the $TAA^{\bullet+}$ monoradical cation at 13600 cm^{-1} and decays monoexponentially to the ground state with a lifetime of 0.39 µs. [115, 179-180, 182, 186-187, 198] Additionally, a global fit was performed using a sequential model. The resulting evolution associated difference spectra (EADS) and their respective lifetimes are shown in **Figure 25** (E). As can be seen, the results agree with the traditional analysis. The first transient is the GSB and evolves with a lifetime of 25 ns to the second transient which shows the characteristic radical ion bands and decays with a lifetime of 0.39 µs. Both the second transient from the global fit and the later spectra of the traditional analysis match very well with the simulation of the CSS-transient absorption depicted in **Figure 21** thus proving the formation of a charge separated state with a negative charge on the NDI-moiety and a positive charge on the TAA-moiety.

To distinguish this charge separated state from the one between CMC and NDI-acceptor previously observed in **PdA**, the states will be labeled CSS_1 and CSS_2, corresponding to the charge separation between NDI and CMC and the charge separation between TAA and NDI, respectively.

Figure 26 shows the TA spectra of **DPtA** after excitation at 28200 cm^{-1} at early times (A) and later times (C) as well as the kinetics at wavenumbers characteristic for the GSB of the CMC and the formed CSS (B and D). Furthermore, species associated difference spectra (SADS) obtained from a global target analysis are depicted in **Figure 26**(E).[195] The fitting with a target model was chosen to account for the parallel excitation of the NDI moiety and the central complex at 28200 cm^{-1} which was necessary for **DPtA** to achieve a clear separation of the transients associated with ^{3}LC and CSS_2.

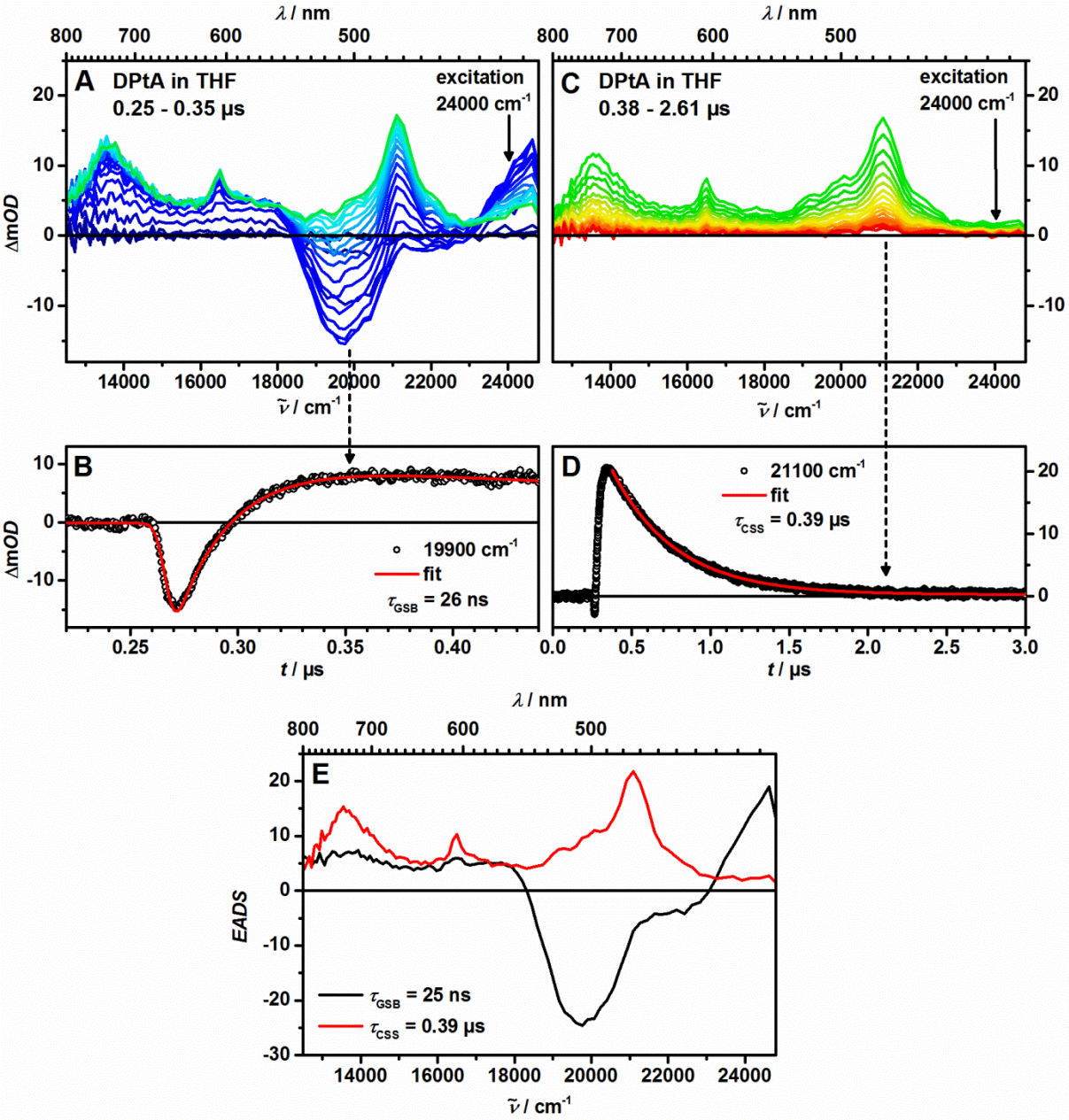

Figure 25: ns-Transient absorption spectra of **DPtA** in THF at rt after excitation at 24000 cm^{-1} at early times (A) and later times (C), kinetic traces with fit at selected wavenumbers (B and D) and evolution associated difference spectra (EADS) obtained from a global fit (E).

The TA spectra at early times show no distinct GSB but already the signals associated with CSS_2. Nevertheless, at around 20000 cm^{-1} the rise of a shoulder can be seen, which actually refers to a decay of the superimposed GSB in this spectral region. Again, the lifetime of the GSB is 26 ns. After the CSS is fully developed it looks virtually identical to the spectra after excitation at 24000 cm^{-1}, except for a small dip in absorption intensity at around 18400 cm^{-1}, which is an artefact of the measurement. The biphasic increase of the signal intensity in **Figure 26** (B) indicates that CSS_2 is occupied by two individual processes. The faster process seems to occur during the response function of the instrument, since the peaks associated with CSS_2 arise simultaneously during the first

10 ns. The slower process is connected to the decay of the GSB with a lifetime of 26 ns. The occurrence of two simultaneous CS-processes is due to the parallel excitation of the CMC and the NDI. Here, excitation of the CMC is associated with the slow CS, while excitation of the NDI results in a very fast charge separation. These findings are confirmed by the result of the global target analysis, which gives a transient with a lifetime of 22 ns that shows the characteristic GSB of the CMC, and a second transient with a lifetime of 0.39 µs, showing all signals characteristic for CSS_2.

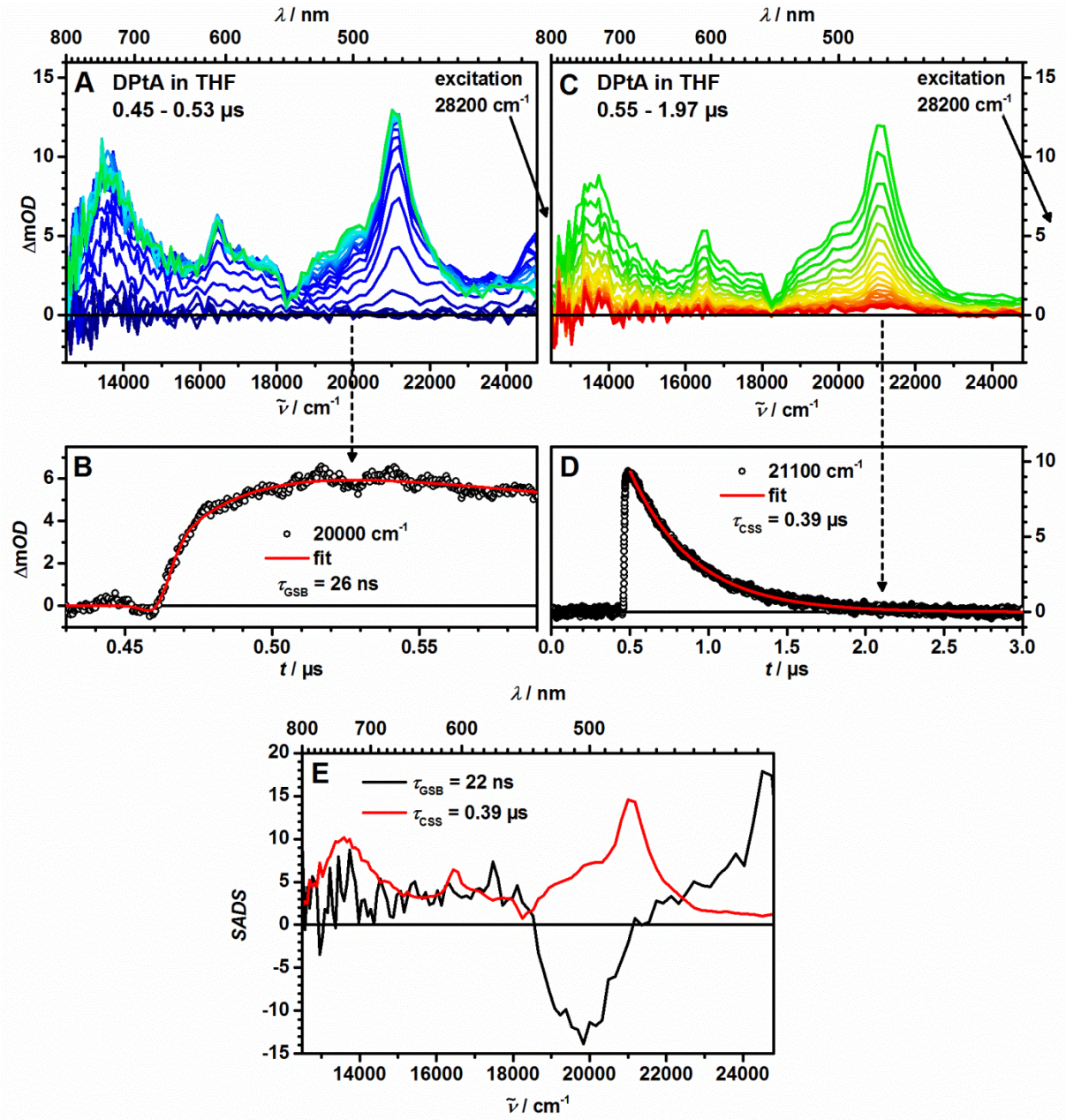

Figure 26: ns-Transient absorption spectra of **DPtA** in THF at rt after excitation at 28200 cm^{-1} at early times (A) and later times (C), kinetic traces with fit at selected wavenumbers (B and D) and species associated difference spectra (SADS) obtained from a global fit (E).

Figure 27 and **Figure 28** show the TA spectra of **DPdA** after excitation of the CMC at 20100 cm^{-1} and after excitation at the NDI moiety and the CMC at 26400 cm^{-1} respectively at early times (A) and later times (C) as well as the kinetics at wavenumbers characteristic for the GSB of the CMC and the formed CSS (B and D). Furthermore, EADS obtained from a global fit using a sequential model are depicted in **Figure 27** (E) and **Figure 28** (E).

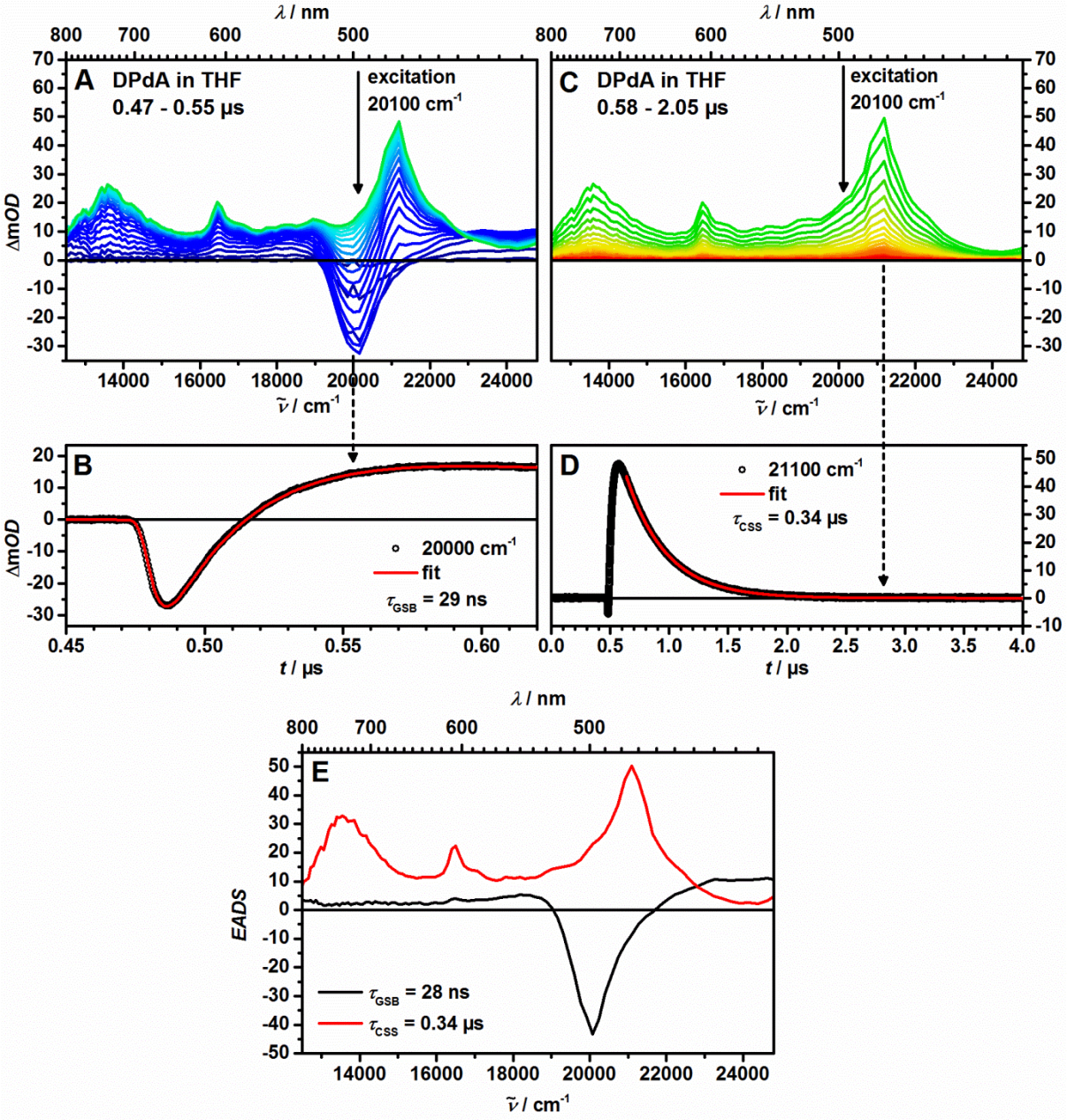

Figure 27: ns-Transient absorption spectra of **DPdA** in THF at rt after excitation at 20100 cm^{-1} at early times (A) and later times (C), kinetic traces with fit at selected wavenumbers (B and D) and evolution associated difference spectra (EADS) obtained from a global fit (E).

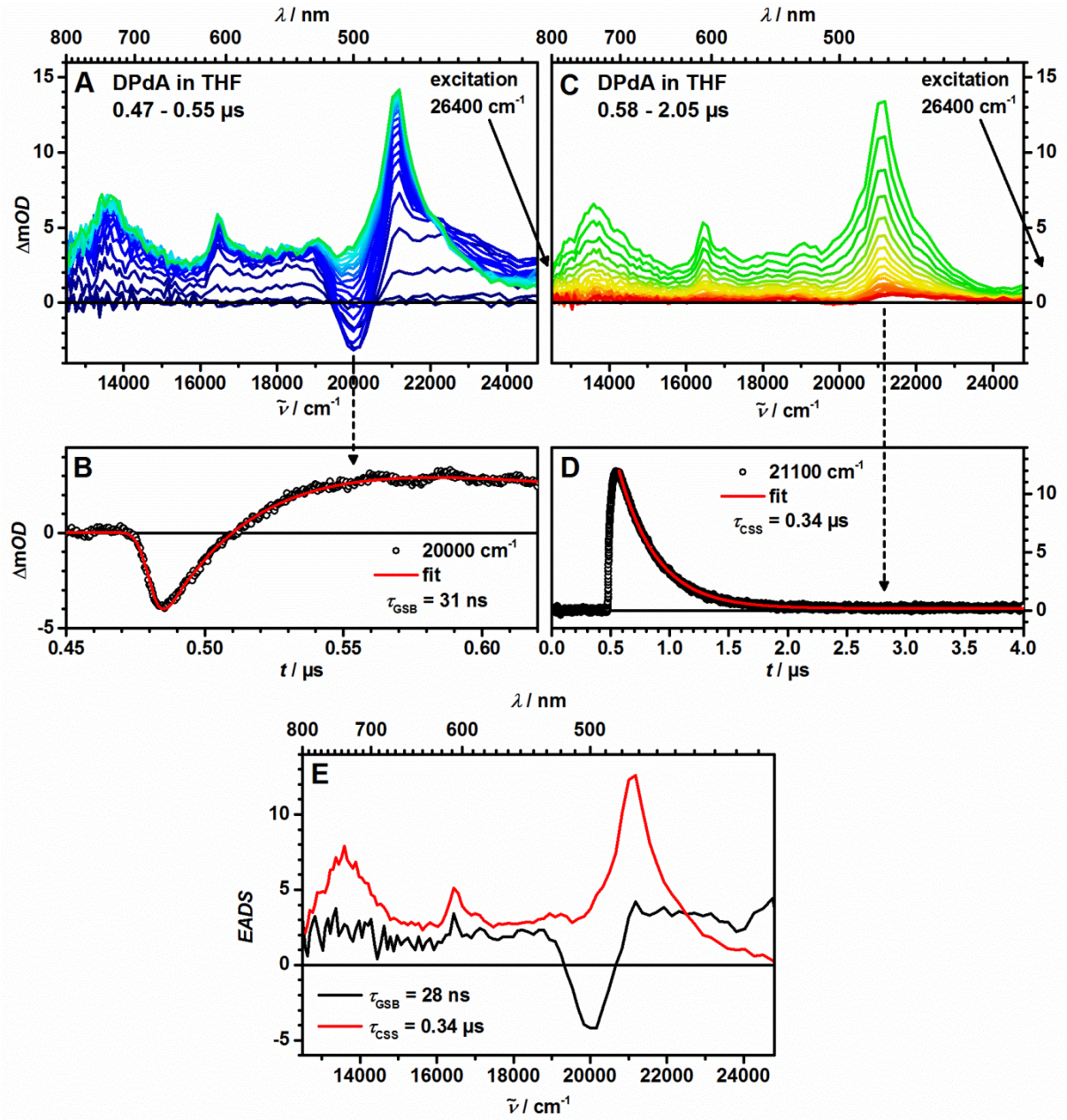

Figure 28: ns-Transient absorption spectra of **DPdA** in THF at rt after excitation at 26400 cm^{-1} at early times (A) and later times (C), kinetic traces with fit at selected wavenumbers (B and D) and evolution associated difference spectra (EADS) from a global fit (E).

The results are very similar to those obtained for **DPtA**. At early times a GSB of the CMC evolves with a lifetime of about 30 ns to an ESA which shows the peaks characteristic for the $NDI^{\bullet-}$ monoradical anion and the $TAA^{\bullet+}$ monoradical cation, and agrees well with the simulation of the CSS-transient absorption depicted in **Figure 21**. Again, this traditional analysis is confirmed by the global analysis thus proofing the formation of CSS_2. The lifetime of CSS_2 was determined to be 0.34 µs.

The TA-data and the excited state lifetimes of **DPt**, **DPtA**, **DPd** and **DPdA** in different solvents are summarized in **Table 6**.

Table 6: Excited state (^{3}M and CSS) lifetimes (τ_{GSB} and τ_{CSS} respectively) and quantum yields of charge separation (Φ_{CSS}) in solvents of different polarity at rt after excitation at the given wavelengths.

	excitation[a] $\tilde{\nu}_{ex}$ /cm^{-1}	**solvent**	**^{3}M lifetime** τ_{GSB}	**CSS**[b] **lifetime** τ_{CSS}	**CSS**[b] **quantum yield** Φ_{CSS}
D_2IrA[c]	24000	MeCN	-	0.58 µs	1.00
	28200	MeCN	-	0.58 µs	0.47
D_2IrA'	24000	MeCN	-	0.57 µs	0.99
	28200	MeCN	-	0.56 µs	0.59
Pt	19800	MeCN	40 ns	-	-
		THF	67 ns	-	-
		toluene	90 ns	-	-
PtA	19800	MeCN	19 ns	-	-
		THF	30 ns	-	-
		toluene	41 ns	-	-
DPtA	24000	MeCN	17 ns	1.68 µs	0.26
		THF	26 ns	0.39 µs	0.25
		pTHF	20 ns	0.61 µs	-
		toluene	39 ns	-	-
	28200	MeCN	18ns	1.68 µs	0.13
		THF	26 ns	0.39 µs	0.12
		toluene	40 ns	28 ns	-
Pd	20200	MeCN	0.88 µs	-	-
		THF	1.44 µs	-	-
		toluene	1.82 µs	-	-
PdA	20200	MeCN	23 ns	0.28 µs	-
		THF	14 ns	0.51 µs	-
		toluene	0.73 µs	-	-
	26400	MeCN	-	0.27 µs	-
		THF	-	0.53 µs	-
		toluene	0.74 µs	15 ns	-
DPdA	20100	MeCN	20 ns	1.76 µs	0.32
		THF	29 ns	0.34 µs	0.30
		pTHF	17 ns	0.81 µs	-
		toluene	0.72 µs	-	-
	26400	MeCN	21 ns	1.76 µs	0.15
		THF	31 ns	0.34 µs	0.16
		toluene	0.74 µs	18 ns	-

[a] excitation at higher wavenumbers correspond to a parallel excitation of the NDI and the CMC while at lower wavenumbers only the CMC is excited; [b] CSS equals CSS_1 for **PtA** and **PdA**, and CSS_2 for **D_2IrA**, **D_2IrA'**, **DPtA** and **DPdA**; [c] values taken from the PhD thesis of Dr. Johannes Klein.[70]

As expected, the most striking solvent dependence is observed for the lifetimes of the charge separated states CSS_1 and CSS_2, since the highly polarized CSSs are significantly stabilized in more polar solvents (also see **Table 5**).[96, 193, 199] Interestingly, the relation between the energy and lifetime of the CSS is opposite for CSS_1 and CSS_2. For CSS_1 the lifetime increases with rising CSS-energy from 0.28 µs in MeCN to 0.51 µs in THF. This indicates that charge-recombination from CSS_1 in **PdA** occurs in the *Marcus* inverted region. For CSS_2 on the other hand the lifetimes decrease with rising CSS-energy from 1.68 µs in MeCN to 0.39 µs in THF for **DPtA** and 1.76 µs in MeCN to 0.34 µs in THF for **DPdA**, indicating a charge recombination in the *Marcus* normal region.[91-92, 103] Since the polarity of poly-THF (average molar mass 650 g/mol, corresponding to a degree of polymerization of 9, pTHF) is lower than that of THF, the lifetimes obtained for CSS_2 in pTHF seemingly contradict this interpretation.[200] This is most likely due to the high viscosity of pTHF in comparison to THF. A decrease of intramolecular electron transfer rates with rising solvent viscosity is consistent with the *Marcus* theory since the viscosity influences the solvent reorganization, and has been observed in the literature before, especially for strongly coupled systems.[96, 201-203]

All observed CSSs have very short lifetimes in toluene and are only occupied after excitation of the NDI-moiety. This is because both CSS_1 as well as CSS_2 are higher in energy than the excited triplet state of the CMC (^{3}M) and the CSSs can thus only be populated from the singlet excited state of the NDI which has an energy of about 25800 26200 cm^{-1} and is thus less stable than the CSSs even in toluene.[70, 115, 186, 204]. Furthermore, the ^{3}M-state can serve as an additional deactivation pathway for the CSSs which decreases the lifetimes. In the case of CSS_1, even ^{3}NDI with an energy of around 16500 cm^{-1} can serve as an additional deactivation pathway.[89, 186, 198, 205]

A clear dependence of the ^{3}MC lifetime of the CMC from a functionalization with TAA and NDI can only be observed in toluene since where no charge separation can take place and the ^{3}MC state can only deactivate directly to the ground state. While the ^{3}MC lifetimes are reduced significantly by a functionalization with the NDI-acceptor, they are not susceptible to a functionalization with the TAA-donor. This is expected, since the ^{3}M-state is localized at the dipyrrin ligand which is much more strongly influenced by the direct substitution with NDI than by the indirect influence of a modification at the cyclometalating ligand with the TAA.[111, 115, 122, 136, 138, 206]

Finally, the difference between **PtA** and all other acceptor-substituted compounds has to be addressed. In **PtA** no CSS was observed. On the other hand, the decay kinetics of the GSB match very well with those determined for **DPtA**, suggesting that the deactivation mechanisms are similar for both compounds. Hence, it is proposed that in **PtA** a charge separation to CSS_1 occurs, but that CSS_1 deactivates much faster than it is occupied thus preventing an observation of the state with the ns-setup. This interpretation will further be addressed during the discussion of the fs-transient absorption spectroscopy.

Lastly, **Figure 29** shows the TA of **D_2IrA'** in MeCN after excitation at 28200 cm^{-1}. The ESA again confirms the formation of CSS_2. In contrast to **DPtA** and **DPdA**, no GSB and no rise time for the ESA can be observed, indicating a charge separation which occurs faster than the time resolution of the ns-setup. This is in line with results obtained before for the very similar complex **D_2IrA**, for which a time constant of about 1 ns was found for the charge separation.[70, 115] CSS_2 in both complexes decays to the ground state with a lifetime of about 0.57 µs.[59, 70, 115] This lifetime is significantly shorter than the lifetime of the Pt- and Pd-triads in MeCN of 1.68 µs and 1.76 µs, respectively. The same trend is found in THF where a lifetime of 0.16 µs was found for CSS_2 in **D_2IrA** compared to lifetimes of 0.39 µs and 0.34 µs for **DPtA** and **DPdA**.[70] This indicates an even stronger electronic decoupling of donor and acceptor in the Pt- and Pd- triads when compared to the Ir-triads. The strong electronic decoupling has previously been attributed to the large spatial separation, the aliphatic bridge connecting TAA and CMC, the twist angle of around 90° between the M-dipyrrin plane and the phenyl ring which acts as a bridge to the NDI and the nodal plane in the LUMO of the NDI-acceptor moiety.[59, 70, 115] Obviously the CMC has to be included in this list. The decoupling effect of the CMC is most likely caused by the electronic configuration of the CMC or by the different complex geometries which result in an increase of the donor-acceptor distance from 20.1 Å in the Ir(III)-triads to about 22.0 Å in the Pt(II) and Pd(II)-triads.

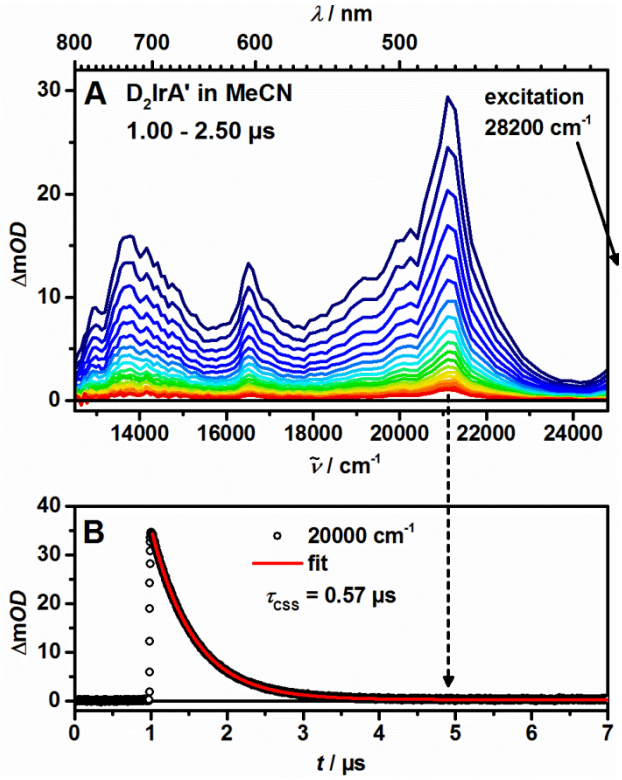

Figure 29: ns-Transient absorption spectra of **D_2IrA'** in MeCN at rt after excitation at 28200 cm^{-1} (A) and kinetic traces with fit at 21100 cm^{-1} (B).

The quantum yield of charge separation for all triads was determined by actinometry vs $Ru(bpy)_3Cl_2$ in water at 24000 cm^{-1} and vs benzophenone in benzene at 28200 cm^{-1} as described in the experimental section using extinction coefficients and quantum yields taken from the literature.[70, 115, 207-208] The determined quantum yields are collected in **Table 6**. In MeCN, **D_2IrA'** has a quantum yield of 0.99 after excitation at 24000 cm^{-1} but only of 0.61 after excitation at 28200 cm^{-1}. This trend is even more pronounced in **DPtA** and **DPdA** which show quantum yields of 0.26 and 0.32 after excitation of the CMC and 0.13 and 0.15 after excitation at higher energies, respectively. The lower quantum yield after excitation at 28200 cm^{-1} was also observed in the literature known Iridium complex **D_2IrA** where the quantum yield drops from unity to 0.47 and was attributed to the partial recombination of a NDI-associated charge-transfer (CT) state associated with the process of charge separation as determined by fs-TA spectroscopy. This will further be addressed after the discussion of the fs-Pump-Probe-Spectroscopy in the next chapter. In general, the quantum yields of charge separation are significantly lower in the Pt- and Pd-complexes. This is most likely due to the slow charge separation observed for **DPtA** and **DPdA** in comparison to **D_2IrA** and will be discussed after the detailed investigation of the charge-separation process in the following chapter. On the other hand, the solvent polarity seems to have no significant effect on the quantum yield, other than that in toluene no CSS could be observed after excitation at the CMC and only negligible charge separation occurs after excitation of the NDI.

The most important results of the ns-transient absorption spectroscopy can be summarized as follows. The occurrence of charge separation between TAA and NDI (CSS_2) was proved for all investigated triads. For the dyad **PdA** a charge separation between CMC and NDI (CSS_1) was confirmed, while for **PtA** strong indicators for charge separation were found but no definitive conclusion could be drawn. Charge recombination occurs in the *Marcus* inverted region for CSS_1 (in **PdA**) and in the *Marcus* normal region for CSS_2 (in the triads). The process of charge separation is much slower and the quantum yield of charge separation is decreased significantly for the Pt- and Pd-compounds when compared to **D_2IrA'** and the Ir-triads described in the literature, while still leading to equivalent CSSs.[59, 70, 115] At the same time the lifetimes of CSS_2 are longer for the Pt-and Pd-triads indicating a stronger electronic decoupling of donor and acceptor by the central metal complex.[59, 115] Excitation of the complexes at the NDI leads to the same CSSs as excitation at the CMC, but with quantum yields reduced by about half. Additionally at least in **DPtA**, the process of charge separation seems to consist of two parts after the combined excitation of the NDI and the CMC at 26400 cm^{-1}: an initial part which occurs very fast and an additional slow process with time constants comparable to those after excitation at the CMC.

3.3.2 fs-Transient Absorption Spectroscopy

The ultrafast photoinduced dynamics of the compounds were investigated by fs-Pump-Probe spectroscopy.[c] All compounds were excited at the absorption maximum of the respective CMC (19800 cm^{-1} for the Pt-series and 20200 cm^{-1} for the Pd-series). Additionally, all compounds containing the NDI-acceptor moiety were also excited at the absorption maximum of the NDI (26400 cm^{-1}). This excitation energy corresponds to a mixed excitation of the CMC and the NDI-subunit in a ratio strongly favoring the excitation of the NDI (0.09 / 0.91 for the Pt-series and 0.16 / 0.84 for the Pd-series). The resulting transient maps were corrected for chirp and scattered pump light and analyzed by a global exponential fit to yield the minimum number of individual spectral components (transients) in form of evolution associated difference spectra (EADS, corresponding to a model of sequential decay) or decay associated difference spectra (DADS, corresponding to a model of parallel decay), needed for a satisfying fit. For further experimental details see chapter 6.1.4. All original results of the global fits are depicted in **Figures A1-A10** on page 283*ff*. in the appendix

All measurements are depicted showing the transient maps in blue to green colors at early times and yellow to red colors at later times. Furthermore the figures show the resulting EADS together with the associated lifetimes (and if needed for the discussion normalized DADS) as well as time traces at characteristic wavenumbers together with the corresponding fit curves. Each measurement is connected to a state diagram which proposes an explanation of the observed spectra and lifetimes. The colors of the states in the diagrams always correspond to the colors of the obtained transients in the associated measurement. In the state diagrams solid lines indicate states and transitions directly observed in the measurements, while dotted lines indicate transitions which are expected to occur but are not directly observable in the measurement. In the case of the dyads and triads, black values and lines correspond to the excitation at the CMC while grey values and lines correspond to the mixed excitation of the NDI and the CMC at 26400 cm^{-1}.

Figure 30 shows the fs-TA results for **Pt** (A, B, C). Three independent spectral components were obtained. The first EADS is superimposed by the coherent artefact but was necessary for a satisfying fit. The first transient has a lifetime of τ_1 = 82 fs and evolves to a second transient which transforms with a time constant of τ_2 = 23 ps to the third and final transient for which a lifetime of τ_3 = 72 ns was determined. All three EADS basically consist only of GSB of the CMC, with a weak ESA around 25000 cm^{-1} for the final EADS. The last transient matches well with the ns-TA shown in **Figure 22** (A) and the associated ^{3}M-lifeteime of 67 ns. Since no distinct spectral features besides the GSB are observed, all transients are associated with states localized at the Pt-dipyrrin moiety. As depicted in **Figure 31** (A), the first time constant τ_1 = 82 fs is attributed to ISC from ^{1}Pt to ^{3}Pt.[112, 117, 206, 209]

[c] All measurements were performed by Alexander Schmiedel.

The second lifetime τ_2 = 23 ps is probably due to a conformational change of the molecule since vibrational relaxation and solvent reorganization usually occur on shorter timescales.[210] Such a conformational change could include a distortion of the dipyrrin-chromophore or a rotation of the phenyl-ring at the 5-position of the dipyrrin ligand.[136, 139, 143, 145, 157, 211] States which differ only in their molecular conformation will be labeled consistently throughout this chapter. The initial geometry will be labeled with a small "I" as subscript, while the final geometry has no subscript at all. All intermediate geometries are labeled with a small "j" as a subscript.

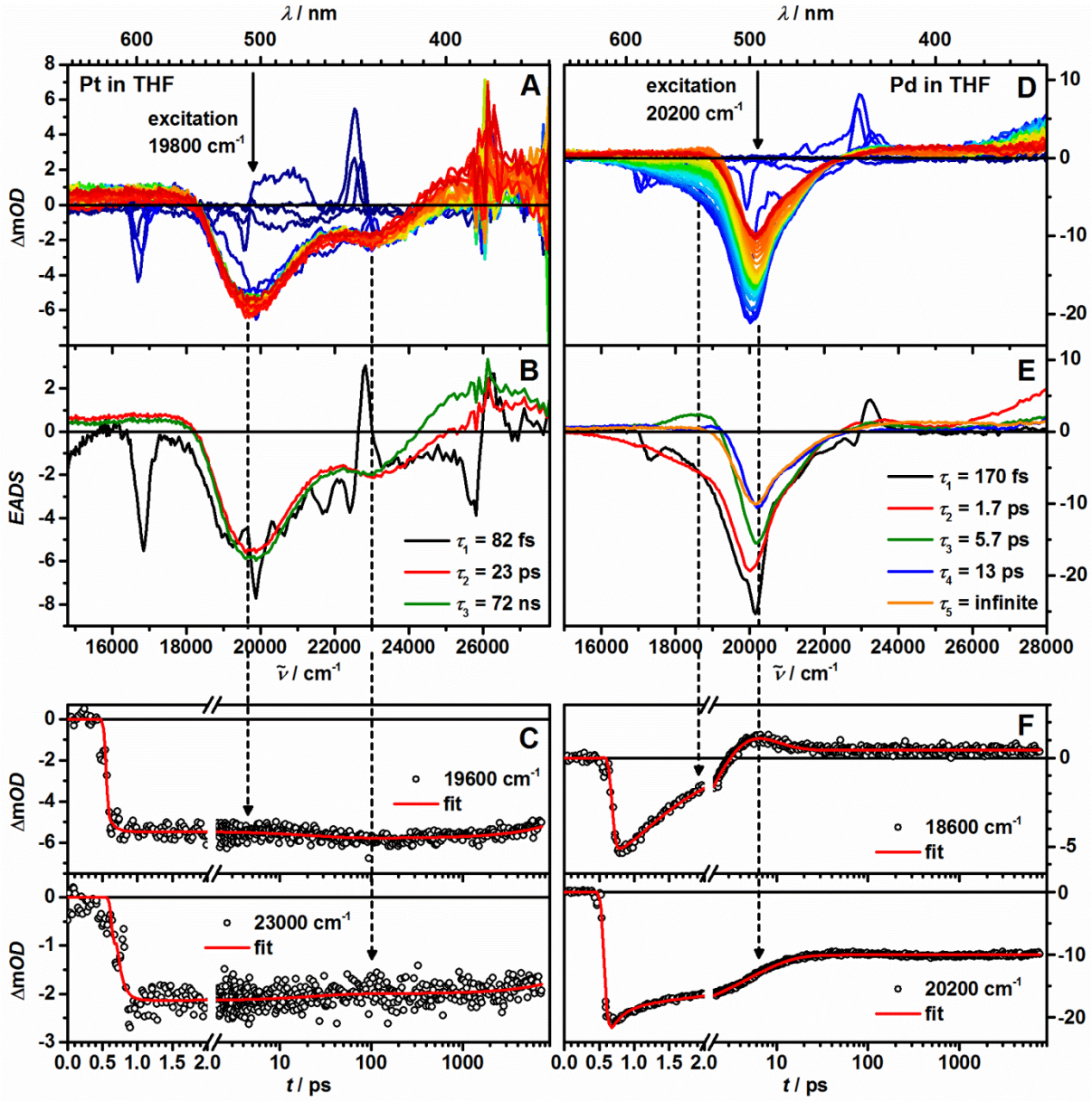

Figure 30: Chirp corrected transient absorption spectra of **Pt** and **Pd** in THF at rt after excitation at 19800 cm^{-1} and 20200 cm^{-1}, respectively (A and D), evolution associated difference spectra (EADS) from a global fit (B and E), and time traces at selected wavenumbers with fit (C and F).

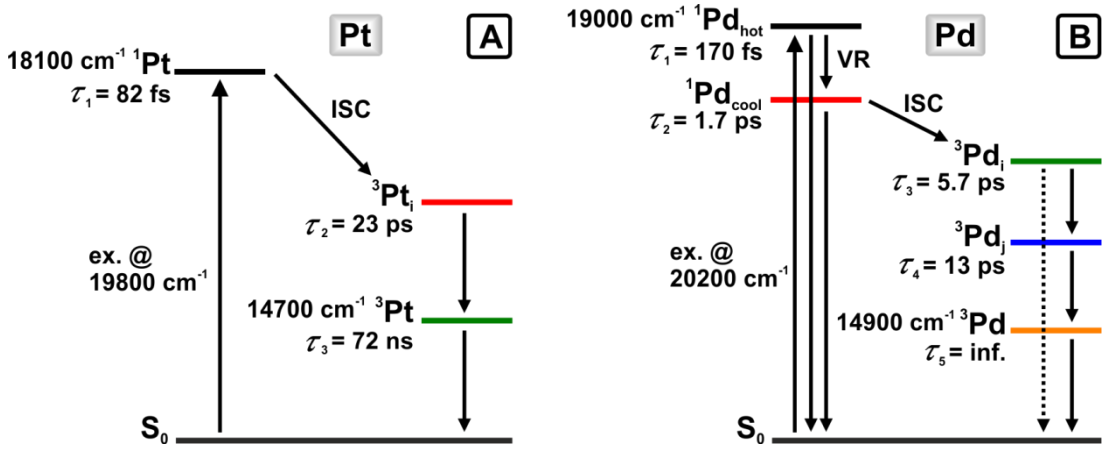

Figure 31: Photophysical processes in **Pt** (A) and **Pd** (B) after excitation at 19800 cm^{-1} and 20200 cm^{-1}, respectively. The colors of the states correspond to the EADS in **Figure** 30 (B) and (E). Energies are estimated as described in chapter 3.2.4.

As can be seen from **Figure 30** (D, E, F) and **Figure 31** (B) the ultrafast dynamics of **Pd** is more complicated than that of **Pt**. The global fit results in five transients which differ in their spectral shape and intensity. Since the Pd-dipyrrin-chromophore is constantly in an excited state throughout the measurement, the intensity of the GSB should be more or less constant throughout all transients. Differences in its intensity are therefore related to a deactivation into the ground state, while changes in the spectral shape usually are due to a superposition with ESA or stimulated emission (SE) in a varying ratio. To omit the contribution of the GSB to the transients, the negative UV/Vis-absorption of **Pd** in THF (scaled to the match the intensity of the respective EADS) was subtracted from the EADS to yield the reduced spectra shown in **Figure 32** (A) which only show the contribution of the ESA as positive amplitudes and the contribution of SE as negative amplitudes.

The first two EADS with lifetimes of τ_1 = 170 fs and τ_2 = 1.7 ps show strong SE around 19000 cm^{-1} which matches very well with the steady state fluorescence. The first lifetime is assigned to vibrational relaxation (VR) of the excited singlet LC-state and solvent reorganization while the second lifetime is assigned to ISC to the triplet state. To further investigate the SE, fluorescence upconversion (FUC) was measured at 19000 cm^{-1}. The resulting time trace and fit are shown in **Figure 32** (B) and gave two lifetimes of 0.95 ps and 2.8 ps which are in reasonable agreement with the 1.7 ps observed in the fs-TA spectroscopy. The shortest lifetime was not observed in the fs-FUC because here, the IRF of 310 fs was longer than the time constant τ_1 = 170 fs observed for the VR in the fs-TA. Furthermore, since the FUC was only measured at one wavenumber, a slight shift of the fluorescence maximum due to VR may not even be noticeable. Overall, the fs-FUC confirm the ISC-time constant of about 1-2 ps, and thus the proposed assignment of the states and transitions. Furthermore, the SE from $^1Pd_{cool}$ further explains the drop in intensity of the GSB for the first two transients, since fluorescence depopulates the excited state by deactivation to the ground state.

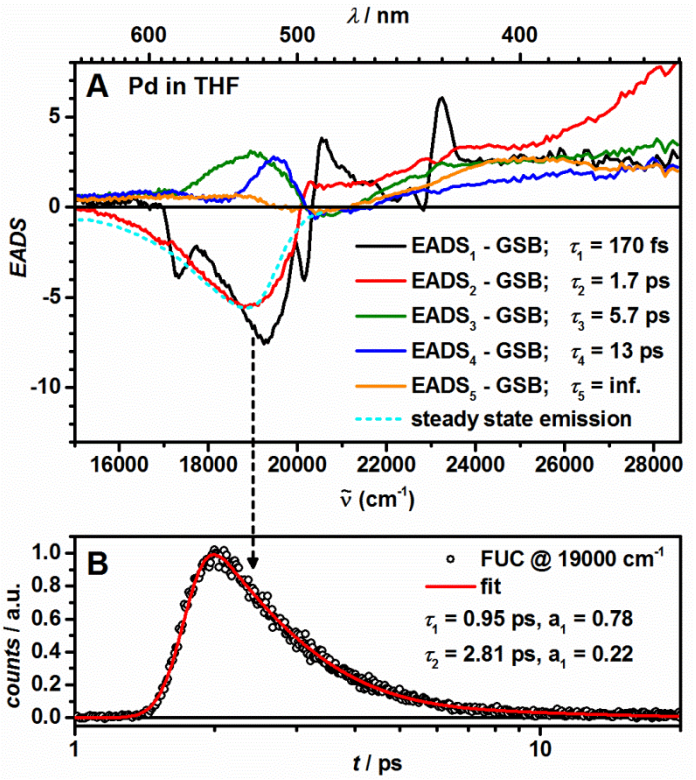

Figure 32: Reduced fs-transient absorption spectra (A) and fluorescence upconversion (B) gated at 19000 cm^{1} (IRF 340 fs) of **Pd** in THF at rt after excitation at 20200 cm^{-1}.

The third transient shows an ESA around 19000 cm^{-1} which is narrower in the fourth transient. The final EADS only shows a broad and featureless ESA at higher energies, which is present in all other transients as well and has a lifetime τ_5 = infinite, which is too high to be registered by the fs-setup. Since it matches very well with the ns-TA spectra, it is assigned to the ^{3}M-state which has a lifetime of 1.44 µs. The third and fourth EADS may therefore be associated with two consecutive conformational changes of the triplet excited ^{3}Pd-state with lifetimes of τ_3 = 5.7 ps and τ_4 = 13 ps, respectively.

In conclusion, the investigation of the ultra-fast photoinduced processes revealed a few characteristic differences between **Pt** and **Pd**. **Pt** undergoes a very fast ISC to the triplet-LC-state ^{3}Pt, which shows only one conformational rearrangement. **Pt** is therefore comparable in its photophysics to the analogue Ir(III)-complex **Ir**[70, 117] in which the final ^{3}M-state is occupied with a quantum efficiency near unity. On the other hand, in **Pd** the final triplet excited state ^{3}Pd is proposed to be reached with a lower quantum efficiency due to a slower ISC which enables a significant deactivation to the ground state by fluorescence. Furthermore, **Pd** undergoes two consecutive conformational rearrangements in the triplet LC-state ^{3}Pd before assuming its final geometry. The complex photophysics of the CMC will also be apparent in the discussion of the dyads and triads, which will thus be even more complicated for the complexes of the Pd-series. For that reason, the compounds of the Pt-series will be discussed first.

In the following discussion EADS obtained from a sequential model will be interpreted using branched models. This usually is no valid method, but can give first insights on the observed processes. A proper global fit using a target model could not be achieved.

Figure 33 shows the fs-TA results for **PtA** after excitation at 19800 cm^{-1} (A, B, C) and 26400 cm^{-1} (D, E, F) which are interpreted in the state diagram depicted in **Figure 34**. After excitation at the CMC only two transients with lifetimes of τ_1 = 77 ps and τ_2 = 32 ns were observed which, comparable to **Pt**, show mainly GSB except for an ESA at 25500 cm^{-1} in the last transient. The very fast ISC is not observed in **PtA**, probably due to negligible spectral changes and a lifetime shorter than the IRF of about 130 fs. The lifetime of τ_1 = 77 ps is assigned to a conformational change from ^3Pt_i to ^3Pt analogous to that in **Pt**, which is slower in **PtA** due to the substitution of the large NDI-acceptor moiety. Beside non-radiative deactivation and phosphorescence directly to the ground state, ^3Pt is assumed to deactivate by slow charge separation to CSS_1. CSS_1 in turn might decay quickly to the ground state, preventing an observation due to low intermediate concentrations.[59, 70, 115]

This assumption is further strengthened by measurements with excitation at 26400 cm^{-1} which yields 6 components. In accordance with the literature, the first three transients are all associated solely with the NDI-moiety.[70, 115, 198] The first EADS has a lifetime of τ_1 = 130 fs and shows a peak at 16900 cm^{-1} and can therefore be assigned to the singlet excited state of the NDI (^{1}NDI). The second EADS displays ESA absorption signals at 16500 cm^{-1} and 21100 cm^{-1} which are characteristic for the $NDI^{\bullet-}$ monoradical anion. The additional electron is proposed to originate from one of the phenyl rings adjacent to the NDI as was previously described in the literature for similarly substituted NDIs.[70, 115, 198] The second EADS is therefore assigned to a NDI-localized CT-state and transforms with a lifetime of τ_2 = 930 fs to the third EADS which shows the same signals but with a sharper band shape. The sharpening of an otherwise similar spectrum often is a sign for VR and/or solvent reorganization.[212-214] Thus, the transition from the second to the third EADS is associated with a VR from an energetically higher state labeled $^1CT_{hot}$ to a more stable state labeled $^1CT_{cool}$ which is probably accompanied by solvent reorganization.[210] $^1CT_{cool}$ has a lifetime of τ_3 = 5.8 ps and is followed by two consecutive EADS which both show the $NDI^{\bullet-}$ monoradical-signals. Additionally, an increase of the GSB of the CMC at 20200 cm^{-1} can be observed. Since the transfer of the positive charge localized at the phenyl-ring bridging dipyrrin-ligand and NDI-core onto the CMC would lead to an increase in GSB-intensity the transients are assigned to a charge separated state between the CMC and the NDI, previously labeled CSS_1. The difference between the two EADS is a relative increase of ESA around 23000 cm^{-1} which occurs with a lifetime of τ_4 = 45 ps. The increased ESA probably is an indicator for a conformational change of the CMC since a similar rise of the ESA at higher energies can be observed with a similar lifetime in **Pt** and in **PtA** after excitation at 19800 cm^{-1}.

This interpretation is reasonable since the initially formed charge separated state, labeled CSS_{1i}, is formed with the CMC in the ground state geometry. After an electron is removed from the CMC a change in conformation is expected to occur, forming the charge separated state in its final geometry, labeled CSS_1. CSS_1 decays with a lifetime of $\tau_5 = 2.8$ ns.

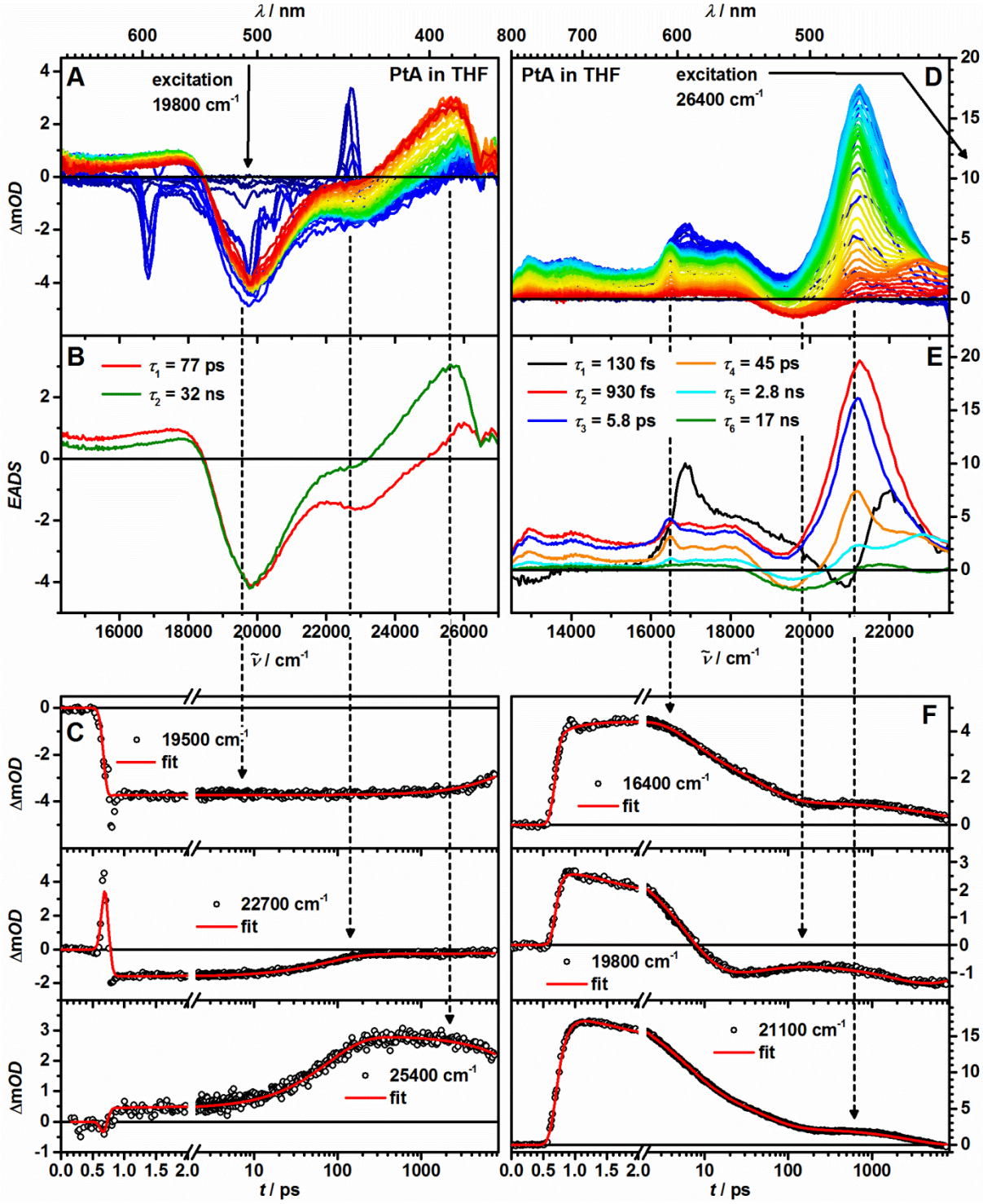

Figure 33: Chirp corrected transient absorption spectra of **PtA** in THF at rt after excitation at 19800 cm^{-1} and 26400 cm^{-1} (A and D), EADS (B and E) from a global fit, and time traces at selected wavenumbers with fit (C and F).

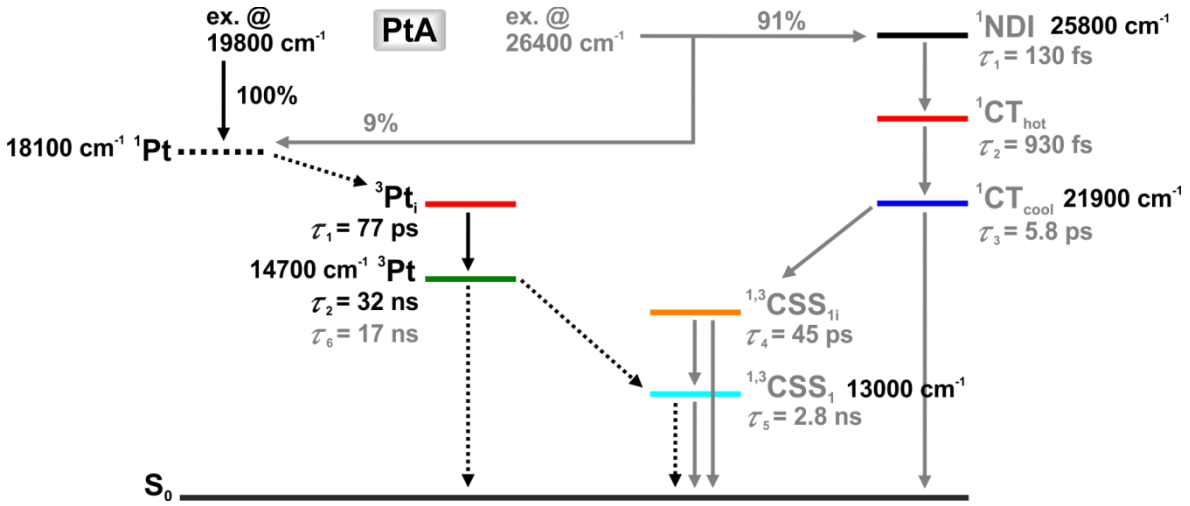

Figure 34: Photophysical processes in **PtA** after excitation of at 19800 cm^{-1} (black) and 26400 cm^{-1} (grey). The colors of the states correspond to the EADS in **Figure 33** (B and E). Dotted arrows and lines indicate processes and states which are expected to participate but cannot be observed directly in the performed measurements. The ratio of absorption at 26400 cm^{-1} was estimated from the extinction coefficients of the compounds described in chapter 3.2.1.

Finally, the last EADS after excitation at 26400 cm^{-1} shows only GSB of the CMC with a lifetime of τ_6 = 17 ns and is therefore attributed to ^{3}Pt, which is formed to a small amount due to the parallel excitation of the CMC and the NDI-moiety. ^{3}Pt deactivates to the ground state in the same way assumed above for **PtA** after excitation at 19800 cm^{-1}, that is both by radiative and non-radiative deactivation to the ground state and by charge separation to CSS_1 and subsequent charge recombination to the ground state. This hypothesis is supported by the lifetimes of 2.8 ns found for CSS_1 and 17 – 32 ns found for ^{3}Pt in **PtA**. Since ^{3}Pt deactivates both by relaxation to the ground state and charge-separation to CSS_1, the time-constant associated with the charge separation should be even larger than 32 ns.[215] Therefore the occupation of CSS_1 from ^{3}Pt is by at least an order of magnitude slower than its deactivation to the ground state by charge recombination, thus keeping the intermediate concentration of CSS_1 too low to be detected. [59, 70, 115] The big difference between the two determined lifetimes for CSS_1 is acceptable since the delay line of the fs-TA spectrometer limited to 8 ns. For this reason, lifetimes in the multi-ns time regime are relatively unreliable.

Lastly, in **Figure 33** (E) a decrease in signal intensity can be observed from the second EADS to the fourth EADS. Although the sequential model underlying the EADS assumes a quantum yield of unity for each transition, the decrease in signal intensity indicates a partial deactivation of the associated states to the ground state. In theory, the extinction coefficient of the $NDI^{\bullet-}$ monoradical-signals (and the GSB of the central metal complex) should be more or less constant throughout the different states, leaving only a decrease in relative concentration as an explanation of the decreased signal intensity. This is similar to the results obtained for **Pd**, where the deactivation to the ground state could also be proved directly by the observed fluorescence.

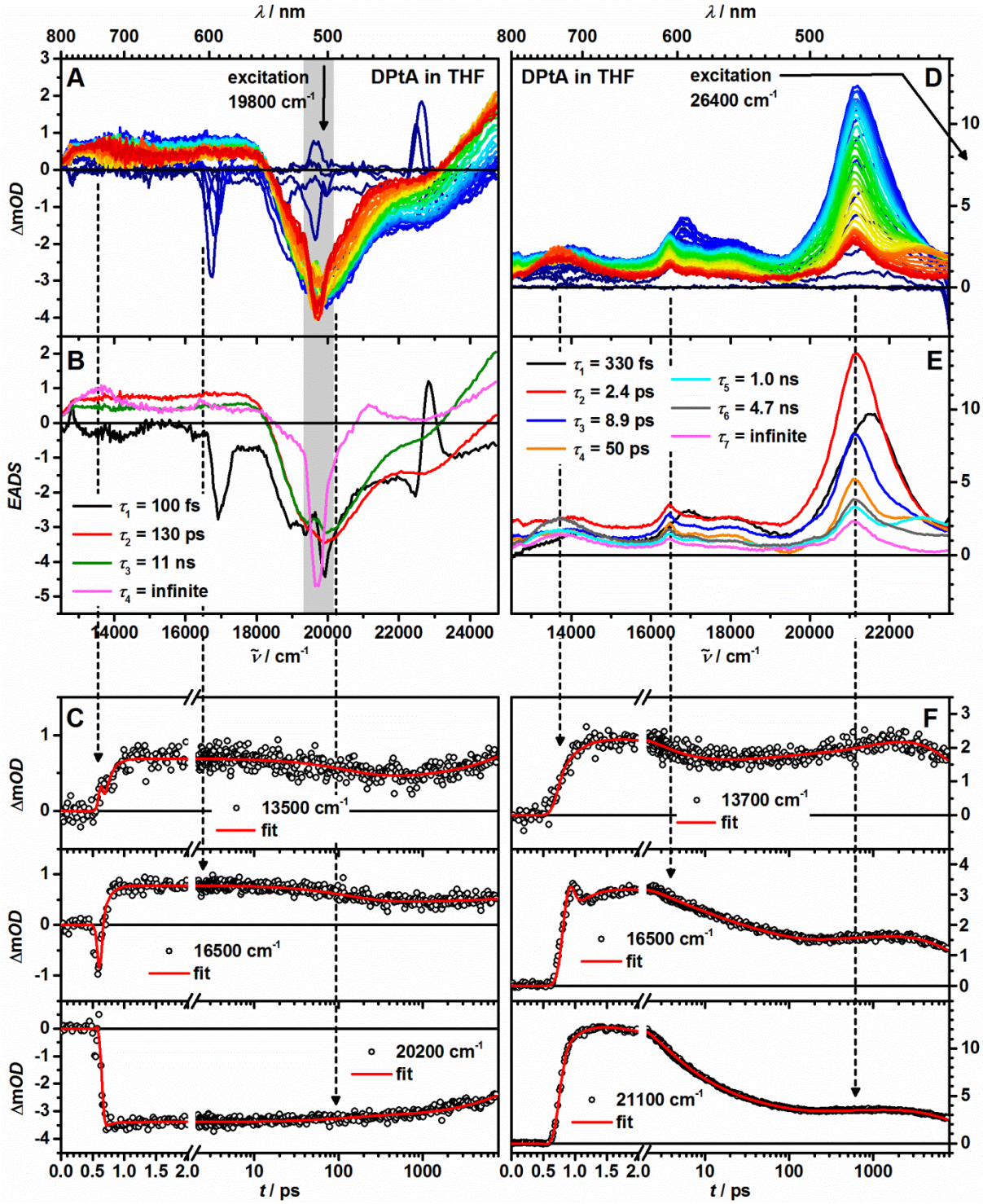

Figure 35: Chirp corrected transient absorption spectra of **DPtA** in THF at rt after excitation at 19800 cm^{-1} and 26400 cm^{-1} (A and D) and EADS (B and E) from a global fit (the grey box marks the spectral range strongly influenced by scattered light), and time traces at selected wavenumbers with fit (C and F).

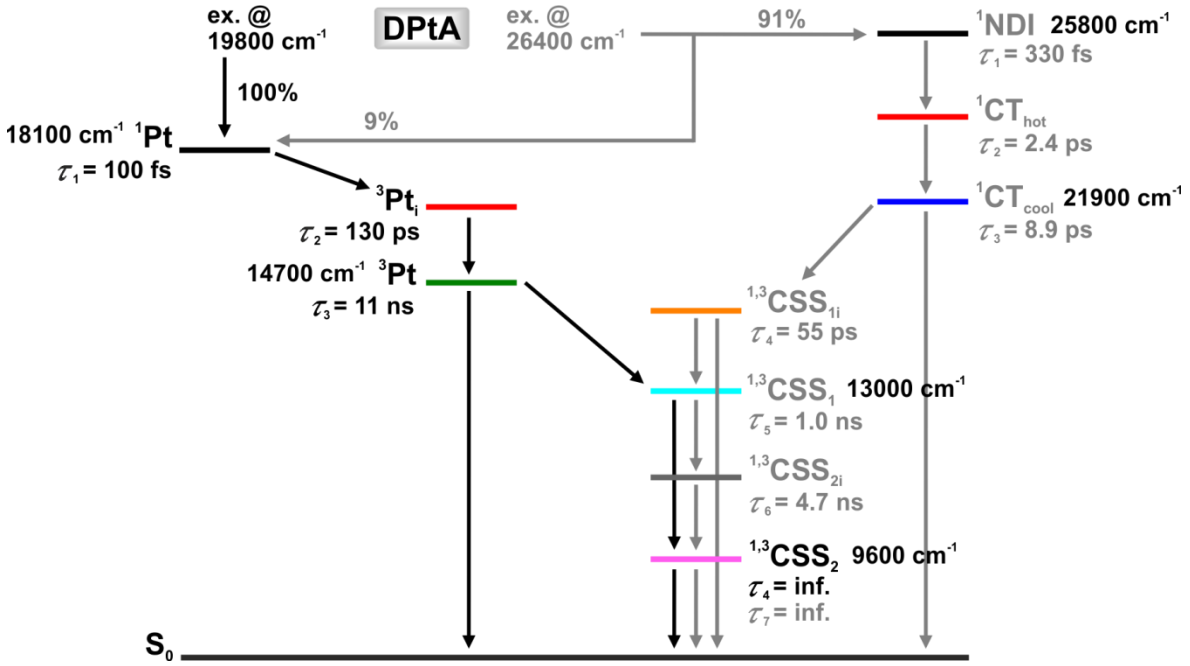

Figure 36: Photophysical processes in **DPtA** after excitation at 19800 cm^{-1} (black) and 26400 cm^{-1} (grey). The colors of the states correspond to the EADS in **Figure 35** (B and E). Dotted arrows and lines indicate processes and states which are expected to participate but cannot be observed directly in the performed measurements.

Figure 35 shows the fs-TA results for **DPtA** after excitation at 19800 cm^{-1} (A, B, C) and 26400 cm^{-1} (D, E, F) which are interpreted in the state diagram depicted in **Figure 36**. Excitation of the CMC leads to 4 independent spectral components. The first three consist mostly of GSB of the CMC and can be described similar to the transients observed in **Pt**. The first transition with a lifetime of τ_1 = 110 fs is associated with ISC from the singlet excited state to the triplet excited state. The subsequent conformational rearrangement of ^3Pt_i occurs with a lifetime of τ_2 = 130 ps which is slower than in **PtA** (τ_2 = 77 ps) and in **Pt** (τ_2 = 23 ps). The inverse relationship between the lifetime of the conformational change and the size of the molecule is reasonable since larger substituents could slow down rearrangements in the central part of the superstructure. The third EADS has a lifetime of τ_3 = 11 ns and decays to the final transient, in which the signals characteristic for the $NDI^{\bullet-}$ monoradical anion at 21100 cm^{-1} and 16500 cm^{-1} and the $TAA^{\bullet+}$ monoradical cation at 13500 cm^{-1} are very weakly developed. Therefore the final EADS is attributed to the charge separated state between TAA and NDI, previously labeled CSS_2. In comparison with the results of the ns-TA, the time-constant for the charge separation is estimated shorter in the fs-experiment. Furthermore, in the fs-TA the GSB of the CMC is still present in the final transient. These deviations are most likely due to the limited delay time of 8 ns in the fs-setup, which is much shorter than the estimated time constants for the charge separation. This leads to inaccuracy in the determination of long lifetimes and may lead to corruption of the final EADS with residual signals from earlier transients. Lastly, the final EADS is also superimposed by scattered light from the excitation pulse between 19300-20100 cm^{-1}. Due to that,

the influence of this spectral range on the global analysis was set to zero to prevent a corruption of the results by artefacts of the measurement. The lifetime of the CSS_2 was set to infinity since it was too long to be measured by the fs-setup.

Excitation of **DPtA** at 26400 cm^{-1} leads to seven EADS, of which the first five can be treated equivalently to those observed for **PtA**. The NDI-moiety is excited to the singlet state ^{1}NDI, which has a lifetime of τ_1 = 330 fs and undergoes charge transfer to form $^1CT_{hot}$ which relaxes with a lifetime of τ_2 = 2.4 ps to $^1CT_{cool}$. From here, charge separation to the initial CSS_{1i} occurs with a time constant of τ_3 = 8.9 ps and the conformational rearrangement of the CMC results in the final CSS_1 with a time constant of τ_4 = 55 ps. For CSS_1 a lifetime of τ_5 = 1.0 ns was determined, further supporting the theory of charge-separation by a two-step process after excitation at 19800 cm^{-1}. Again, the decrease of the signal intensity at 21100 cm^{-1} indicates a deactivation to the ground state during these processes. The main difference to the measurements in **PtA** are the unusual shape and lifetime of the EADS associated with ^{1}NDI which differ from all other measurements and the literature.[70, 115, 198] This deviation is most likely due to a corruption of the transients with contributions of the following CT_{cool} state and cannot be explained at the moment. since the following transients show the expected behavior this deviation will not be discussed further in the following. The first new transient observed in **DPtA** after excitation at 26400 cm^{-1} is the sixth EADS. It shows all signals characteristic for CSS_2, but has a lifetime of only τ_6 = 4.7 ns, which is obviously too short compared to the lifetime observed for CSS_2 in the ns-TA measurement. The seventh EADS has essentially the same spectral shape as the sixth EADS, but shows a lifetime too long to be determined with the fs-setup which is thus set to τ_7 = infinite. Although the spectral features of the sixth and the final EADS are virtually identical, both species are needed for a satisfying fit. Similar to the observations made for CSS_1, a possible explanation could be a conformational change of the CMC from the oxidized state geometry assumed in CSS_1 to the ground state geometry assumed in CSS_2 The proposed rearrangement seems to be accompanied by deactivation to the ground state by charge recombination as can be seen from the signal intensities in the EADS. Since the formation of CSS_1 was observed after excitation at 26400 cm^{-1} it is expected that the charge separation after excitation at 19800 cm^{-1} also proceeds stepwise as was described for similar Ir-complexes in the literature. First an electron is transferred slowly from the CMC to the NDI-acceptor, forming CSS_1. A subsequent charge transfer from the TAA-donor to the oxidized CMC forms the final CSS_2. Since the second charge transfer is much faster in relation to the first, no intermediate CSS_1 (and thus no CSS_{2i}) is observed due to low concentrations.

In conclusion, the results obtained for the Pt-compounds can be explained with a similar model as was used for the equivalent Ir-complexes which in turn was based on target-fits.[59, 70, 115, 117] The interpretation of the fs-TA spectroscopy for **PtA** and **DPtA** is therefore deemed relatively trustworthy although no target analysis was performed.

The ultrafast photophysics of the Pd-series are even more complex than those of the Pt-series. **Figure 37** shows the fs-TA results for **PdA** after excitation at 20100 cm^{-1} (A, B, C, D) and 26400 cm^{-1} (E, F, G, H) which are interpreted in the state diagram depicted in **Figure 38**. In contrast the observations made in **PtA,** excitation of **PdA** at the CMC yields six transients with partially very small differences to each other. At this point it has to be mentioned that a global analysis with that many lifetimes practically gives satisfying fits in any case, thus making the assignment of the EADS to distinct states relatively vague. Another possible explanation for the complex photophysics could be a distribution of rates for a single process due to slightly different orientations of the different subunits of the molecule to each other. However, since the differences between the lifetimes are relatively large, this possibility was neglected in the following discussion. The first two EADS are similar to those observed for **Pd** and thus the first transition can be associated with a VR in the singlet state from the energetically high $^1Pd_{hot}$ to the energetically lower $^1Pd_{cool}$ with a lifetime of τ_1 = 230 fs. $^1Pd_{cool}$ has a lifetime of τ_2 = 1.9 ps, which refers to ISC and which is similar to the lifetime observed for **Pd**, but the third transient shows a weak ESA at 16500 cm^{-1} and the GSB has a somewhat steeper flank towards high energies which is attributed to a superposition with an ESA around 21300 cm^{-1}. Both absorptive signals are characteristic for the $NDI^{\bullet-}$ monoradical anion, and thus the third EADS is associated with CSS_{1i}. CSS_{1i} has a lifetime of τ_3 = 4.8 ps and transitions to the fourth EADS which has a similar shape except for a decrease in ESA around 19000 cm^{-1}. From the normalized DADS it can be seen that the transition affects the spectrum only in the range of the CMC, since the DADS represent the spectral differences between two consecutive transients and the third DADS only shows signals between 17000 – 22000 cm^{-1}. Furthermore, the shape and lifetime of the third DADS in **PdA** are similar to those observed for the third reduced spectra of **Pd**, shown in **Figure 32** (A). The transition is therefore associated with a conformational change of the CMC to CSS_{1j}. As can be seen from the normalized DADS, CSS_{1j} decays with a lifetime of τ_4 = 76 ps by charge recombination since all signals associated with CSS_1 are decreasing during the process. The fifth EADS shows only GSB, similar to the final EADS in **Pd** and is therefore associated with the final triplet excited LC-state ^3Pd. The population of ^3Pd is proposed to occur parallel to the population of CSS_{1j}. The missing EADS associated with the precursors of ^3Pd can most likely be explained by lifetimes and spectral features similar to those of the observed CSS_1-states. The parallel deactivation of ^1Pd to ^3Pd_i and CSS_{1i} could also explain the weak signal intensity of the peaks characteristic for the reduced NDI-moiety. The EADS associated with ^3Pd decays with a lifetime of τ_5 = 4.5 ns to the final EADS. From the normalized DADS it can be seen that during this transition, all peaks characteristic for CSS_1 are developed. The last EADS is therefore associated with the CSS_1 in its final conformation which has a lifetime registered as infinite by the short time range of the fs-setup. The shorter time range also explains the different lifetime of the formation of CSS_1 compared to the 14 ns determined by ns-TA measurements.

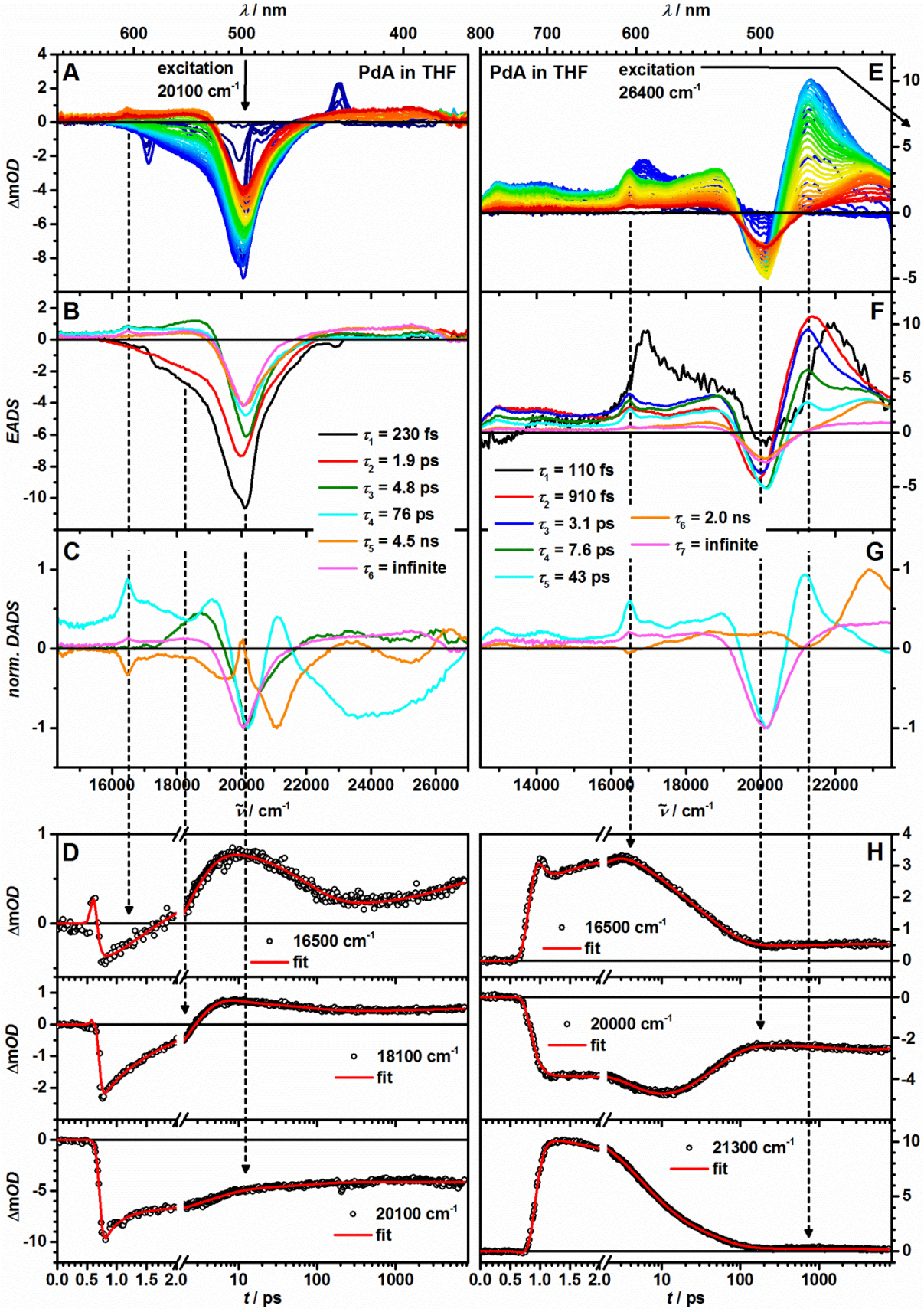

Figure 37: Chirp corrected transient absorption spectra of **PdA** in THF at rt after excitation at 20100 cm^{-1} and 26400 cm^{-1} (A and E), EADS (B and F) and selected normalized DADS (C and G) from a global fit, and time traces at selected wavenumbers with fit (D and H).

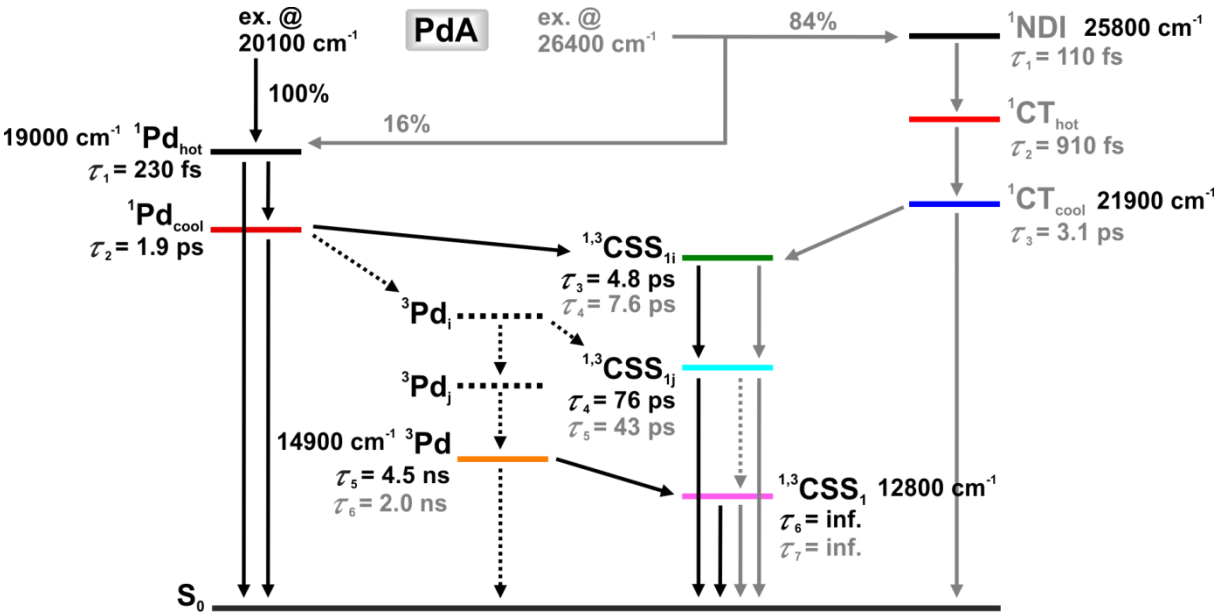

Figure 38: Photophysical processes in **PdA** after excitation at 20100 cm^{-1} (black) and 26400 cm^{-1} (grey). The colors of the states correspond to the EADS and normalized DADS in **Figure 37** (B,C and F,G). Dotted arrows and lines indicate processes and states which are expected to participate but cannot be observed directly in the performed measurements.

Excitation at 26400 cm^{-1} yields seven transients of which the first three are associated with the previously discussed transitions of the NDI-moiety. ^{1}NDI transforms with a lifetime of τ_1 = 110 fs to $^1CT_{hot}$ which relaxes with a lifetime of τ_2 = 910 fs to $^1CT_{cool}$. In all three transients, a significant dip in the ESA signal can be observed around 20000 cm^{-1} which is caused by a superposition of the spectra with the GSB of the CMC. This is probably a result of the parallel excitation of NDI and CMC at 26400 cm^{-1}. Most likely, similar lifetimes of the states associated with the excited CMC and the excited NDI prevent a separation of the two states by the global analysis. $^1CT_{cool}$ has a lifetime of τ_3 = 3.1 ps and transforms to a state which is connected to an EADS with an increased bleaching signal at 20000 cm^{-1} and the ESA-bands characteristic for the reduced NDI at 16500 cm^{-1} and 21300 cm^{-1}. The Fourth EADS is therefore associated with CSS_{1i}. From here on the results are similar to those observed after excitation of **PdA** at 20100 cm^{-1}. CSS_{1i} has a lifetime of τ_4 = 7.6 ps and forms CSS_{1j} by conformational rearrangement. CSS_{1j} decays mainly to the ground state with a lifetime of τ_5 = 43 ps as can also be seen from the normalized DADS. A small ratio of direct formation of CSS_1 from CSS_{1j} cannot be excluded. The sixth EADS is associated with ^{3}Pd which is populated due to the simultaneous excitation of NDI and CMC at 26400 cm^{-1}. From ^{3}Pd, CSS_1 is formed by charge separation with a time constant of τ_6 = 2.0 ns which is faster than after excitation at 201000 cm^{-1}. The difference in the lifetimes determined for ^{3}Pd is negligible since the lifetimes again approach the maximal time window of the fs-setup. The lifetime of the final EADS is again too long to be determined with the fs-setup and is therefore set to τ_7 = infinite.

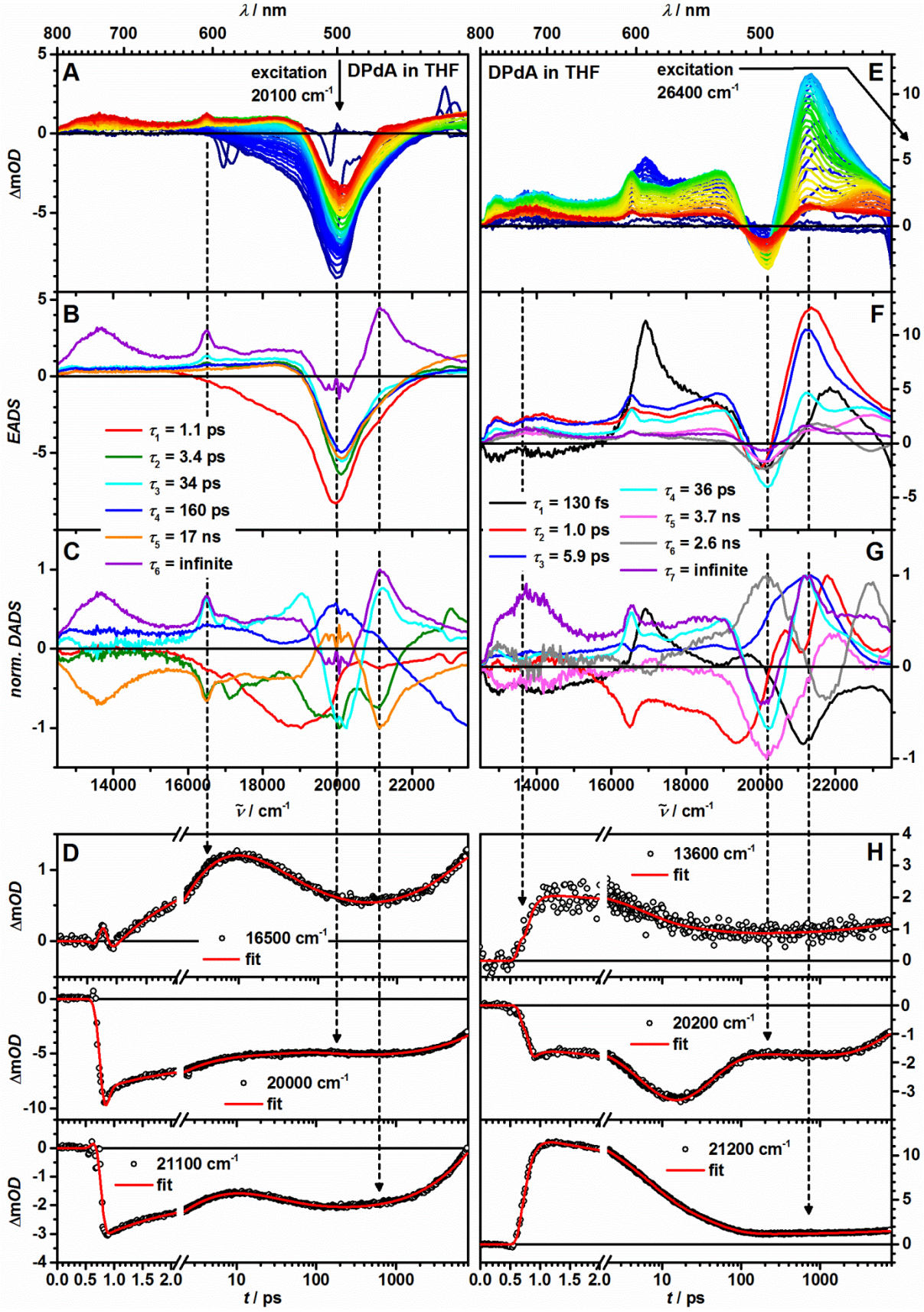

Figure 39: Chirp corrected transient absorption spectra of **DPdA** in THF at rt after excitation at 20100 cm^{-1} and 26400 cm^{-1} (A and E), EADS (B and F) and selected normalized DADS (C and G) from a global fit, and time traces at selected wavenumbers with fit (D and H).

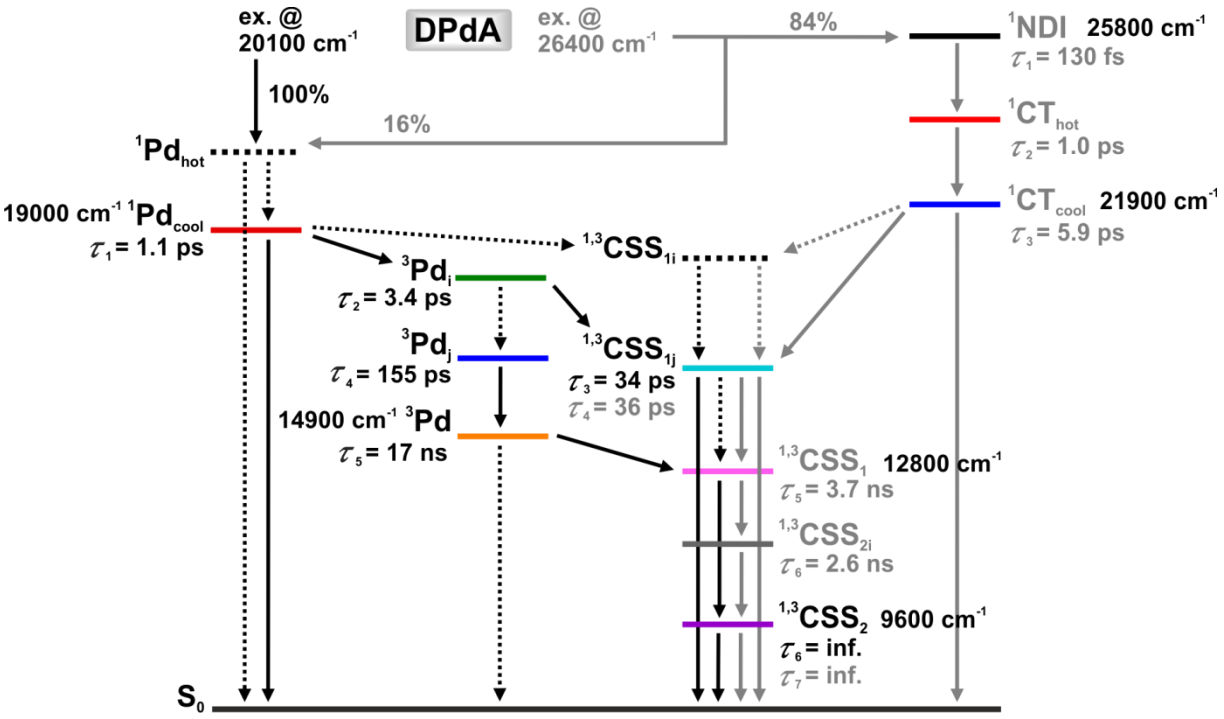

Figure 40: Photophysical processes in **DPdA** after excitation at 20100 cm^{-1} (black) and 26400 cm^{-1} (grey). The colors of the states correspond to the EADS and normalized DADS in **Figure 39** (B,C and F,G). Dotted arrows and lines indicate processes and states which are expected to participate but cannot be observed directly in the performed measurements.

Figure 39 shows the fs-TA results for **DPdA** after excitation at 20100 cm^{-1} (A, B, C, D) and 26400 cm^{-1} (E, F, G, H) which are interpreted in the state diagram depicted in **Figure 40**. Excitation at the CMC yields six transients. The first EADS has a lifetime of τ_1 = 1.1 ps and has a similar shape as the second EADS observed in **PdA** and is therefore associated with the energetically lower singlet excited LC state $^1Pd_{cool}$. The unrelaxed $^1Pd_{hot}$ is not observed in **DPdA**, probably due to its low lifetime and small spectral differences to the following state. The second EADS has a lifetime of τ_2 = 3.4 ps and shows no spectral features indicating the formation of a charge separated state but rather looks equivalent to the third EADS observed in **Pd** and is therefore associated with the triplet excited LC state in its initial conformation ^3Pd_i. The third EADS finally shows the spectral features associated with a charge separated state between the CMC and the NDI and is, due to its lifetime of τ_3 = 34 ps, associated with the excited state conformation CSS_{1j}. The different reaction pathways of the occupation of CSS_{1j} observed in **PdA** and **DPdA** after excitation of the CMC are proposed to occur simultaneously in both complexes. Due to a varying ratio of both mechanisms, this appears as charge separation from $^1Pd_{cool}$ in **PdA** and as charge separation from ^3Pd_i in **DPdA**. Just as in **PdA**, CSS_{1i} deactivates to the ground state as can be seen from the related DADS. Accordingly, the subsequent fourth EADS shows no signals associated with a charge separated state but shows only GSB with a lifetime of τ_4 = 160 ps and looks similar to the fourth EADS observed in **Pd** and is therefore associated with ^3Pd_j. The difference in lifetime of ^3Pd_j (160 ps in **DPdA** and 13 ps in **Pd**) can be rationalized with the trend observed

throughout this chapter for both the Pt-series and the Pd-series, that larger substituents slow down conformational changes associated with the CMC. The fifth EADS observed for **DPdA** can be associated with the triplet excited LC-state in its final conformation ^{3}Pd due to its spectral shape. ^{3}Pd evolves with a lifetime of τ_5 = 17 ns to the final transient which shows all spectral features associated with a charge separated state between the TAA-donor and the NDI-acceptor, CSS_2. Again, the related DADS prove the occurrence of charge separation from ^{3}Pd, since all signals associated with CSS_2 rise simultaneously. Nevertheless it is proposed that charge separation occurs in two steps as was proposed before for **DPtA** and in the literature.[70, 115] Again, this assumption is supported by the results of the experiments after excitation of **DPdA** at the NDI-moiety.

Excitation at 26400 cm^{-1} yields 7 independent spectral components and exhibits the most complex photophysics of all the conducted experiments. Nevertheless, the first three EADS can be described equivalent to those in **PdA**, with lifetimes of τ_1 = 130 fs for ^{1}NDI, τ_2 = 1.0 ps for $^1CT_{hot}$ and τ_3 = 5.9 ps for $^1CT_{cool}$. The fourth EADS has a lifetime of τ_4 = 36 ps and shows all signals characteristic for a charge separation between the CMC and the NDI-acceptor and thus is assigned to CSS_{1j}. CSS_{1j} decays mainly to the ground state as can be seen from the associated DADS and the huge drop in signal intensity to the fifth EADS. Due to their low signal intensity a clear interpretation of the later EADS is very difficult and the following assumptions have to be taken as speculative. From the respective normalized DADS, it can be seen that the fifth and sixth transient with lifetimes of τ_5 = 3.7 ns and τ_6 = 2.6 ns mainly compensate each other. The only differences are a decrease of ESA at 18500 cm^{-1} and at 23000 cm^{-1} as well as a small increase in ESA at 13600 cm^{-1} which is characteristic for the oxidized TAA-donor moiety. Since the fifth EADS still shows the ESA-signals characteristic for the reduced NDI and a bleaching signal around 20000 cm^{-1} it is associated with CSS_1 in its final conformation. CSS_1 is proposed to be occupied by a conformational rearrangement of CSS_{1j} which occurs in concurrence to the charge recombination to the ground state. Although the rise in ESA at 13600 cm^{-1} is only very weak, the sixth EADS is associated with CSS_{2i} in an initial conformation, similar to the results obtained for **DPtA**. Since the subsequent final EADS matches well with the final EADS after excitation at 20100 cm^{-1} it is associated with the fully charge separated CSS_2 in its final conformation which has a lifetime of τ_7 = infinite. The disproportionally intense GSB is proposed to be due to the parallel excitation of the CMC and the NDI at 26400 cm^{-1} which causes an occupation of ^{3}Pd. Since the lifetime of ^{3}Pd is on the ns-time range and therefore similar to the fifth and sixth transient it is most likely not recognized as an independent spectral component by the global analysis. Since a large part of the excited NDI deactivates to the ground state from CT_{cool} and CSS_{1i}, charge separation from ^{3}Pd is most likely a big contribution to the formation of CSS_2.

Lastly, it has to be stressed again that the interpretation of the results for **PdA** and **DPdA** is deemed speculative and is only done this way since it fits the same model as used for the Pt-compounds.

3.3.3 Conclusions

The ns-TA and fs-TA measurements confirm charge separation in THF for all dyads and triads after excitation both at the CMC and the NDI. In **PtA** and **PdA** a charge separated state between the CMC and the NDI-acceptor (CSS_1) is formed which recombines to the ground state with lifetimes of 2.8 ns and 0.58 µs, respectively. The huge difference in the lifetimes of CSS_1 is most likely due to a conformational rearrangement which could decouple the positive charge located at the CMC from the negative charge at the NDI. Although a conformational rearrangement was observed for **PtA** as well as **PdA,** the decoupling effect could be unique to **PdA** due to a more significant rearrangement since Pd-complexes have shown large rearrangements in the excited state (also see chapter 4.2.7) and are generally known for a very diverse coordination geometry.[149, 216-218] At the moment this assumption is speculative at best, and no further conclusions can be made from the measurements alone.

For the triads **DPtA** and **DPdA** a charge separated state between the TAA-donor and the NDI-acceptor moiety (CSS_2) has been observed. **Figure 41** shows a comparison of the theoretical spectrum of CSS_2 as predicted by SEC for **D_2IrA** with the spectra determined for **DPtA** (A) and **DPdA** (B) by the fs-TA- and ns-TA-spectroscopy.

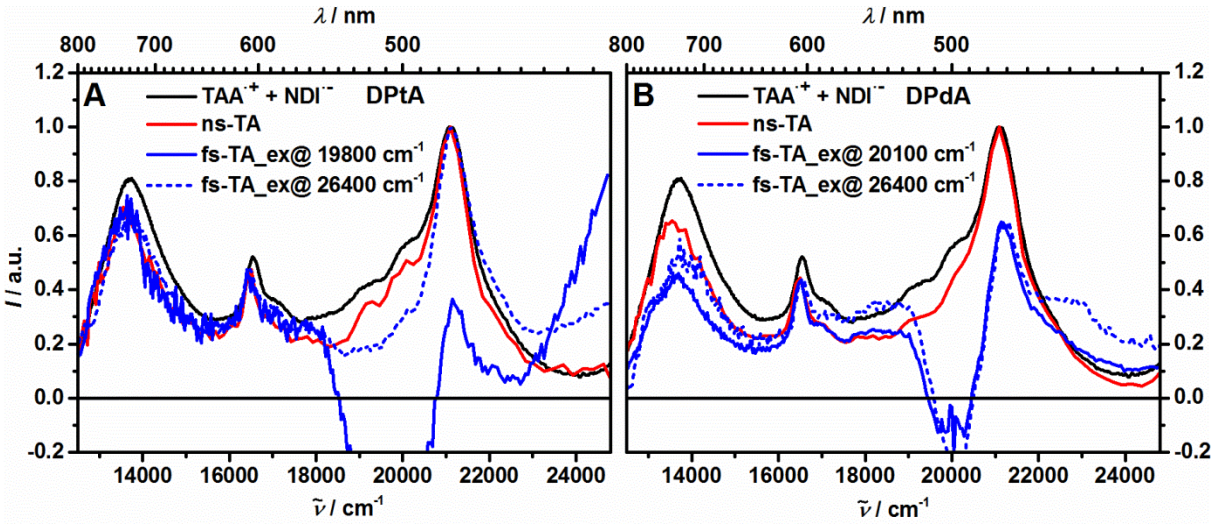

Figure 41: Spectra of CSS_2 in **DPtA** (A) and **DPdA** (B) as obtained from ns-TA spectroscopy in THF (final EADS; red) and fs-TA spectroscopy in THF (final EADS after excitation at the CMC; solid blue and after excitation at 26400 cm^{-1}; dotted blue) in comparison to an overlay of the TAA-cation and NDI-anion spectra determined by SEC for **D_2IrA** as taken from literature[70, 115]; black.

For the ns-TA measurement the observed and simulated spectra match quite well. Small differences can be explained by the different solvent polarities since the TA-spectroscopy was performed in THF and the SEC was performed in MeCN and its polarity was further increased by the addition of TBAHFP as a conducting salt. Furthermore, the SEC experiments were performed with a different compound

(**D_2IrA**). Although this should in theory have no influence since the donor- and acceptor moieties are not influenced by the CMC a small contribution to the differences in the spectra cannot be excluded. On the other hand, the fs-TA spectra show greater deviations from the theoretical spectrum. For the excitation of **DPtA** at 19800 cm^{-1} this is mostly due to the huge contribution of stray light to the final EADS. Nevertheless, the intensity-ratio of the peaks at 16500 cm^{-1} and 13500 cm^{-1} is equivalent to the ratio observed in the ns-TA spectroscopy. For the excitation at 26400 cm^{-1} the spectra match much better. The small deviation around 20000 cm^{-1} can be explained by a small contribution of the GSB of the CMC to the final EADS due to the simultaneous excitation of CMC (0.09) and NDI (0.91) at 26400 cm^{-1}. The same is true for the fs-TA of **DPdA** after excitation at 20100 cm^{-1} and 26400 cm^{-1} except that here the contribution of the GSB of the CMC to the final EADS is even stronger since in the Pd-complexes the ratio of excitation at the CMC is higher (0.16) and the ^{1}LC-transition associated with the GSB has a higher excitation coefficient. The corruption of the final EADS by the GSB signal is caused by the very slow charge separation from the ^{3}M states with lifetimes of 26 ns for **DPtA** and 30 ns for **DPdA** which are much longer than the maximal time-range of the fs-setup. For the same reason lifetimes longer than about 8 ns are very likely determined incorrectly by fs-TA spectroscopy and the different time-constants for the charge separation can be explained.

All aspects considered, the whole photophysical reaction sequence starting with the excitation of the compound to the complete formation of CSS_2 is too slow to be described accurately by the fs-TA-experiments. Therefore the time constants and spectra determined with the ns-set-up will be taken as the correct values, even for the process of charge separation which therefore occurs with time constants of 26 ns for **DPtA** and 30 ns for **DPdA** in THF. The reason for the slower charge separation compared to the Ir-complexes may be associated with the decoupling effect of the CMC already described in chapter 3.3.1 to explain the longer lifetimes of CSS_2 observed for **DPtA** (1.68 µs) and **DPdA** (1.76 µs) in MeCN compared to the Ir-triads (0.58 µs in MeCN).

Nevertheless, the fs-TA measurements give valuable information on the mechanism of the charge separation which can help to explain the differences in the quantum yield determined for CSS_2 after excitation at the NDI and at the CMC and the different quantum yields in **DPtA** and **DPdA** compared to the Ir(III) complexes.

As described in **Table 6** in chapter 3.3.1 and the literature, the quantum yield of CSS_2 after excitation at the NDI is much lower than the quantum yield after excitation at the CMC, both for the Ir(III) complexes as well as the Pt(II) and Pd(II) complexes. This was previously attributed to the presence of two phenyl rings adjacent to the NDI core. The fs-TA measurements show that after excitation of the NDI, a charge-transfer state (CT_{cool}) is formed in which an electron is transferred from an adjacent phenyl-ring onto the NDI-core. As shown in **Figure 42**, for NDI **A**, CT_{cool} can in theory be formed both with the phenyl ring bridging the NDI to the CMC and the terminal phenyl ring.[70, 115]

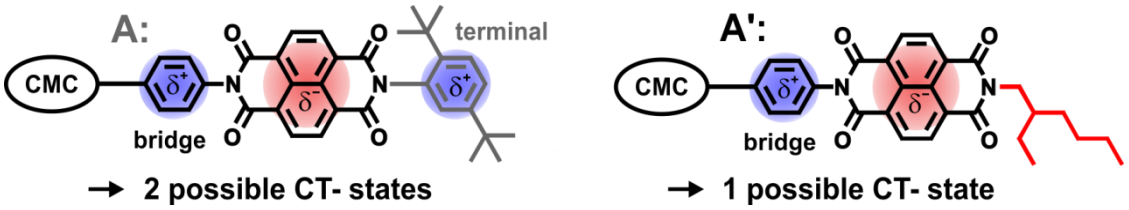

Figure 42: The usual acceptor **A** with two adjacent phenyl rings and the modified acceptor **A'** in which the terminal phenyl ring was substituted with an aliphatic tail. For **A**, electron transfer from a phenyl ring onto the NDI-core results in two possible CT-states. For **A'**, only the CT-state between the phenylene bridge and the NDI core is possible.

It could be argued that a further charge transfer from the CMC to the oxidized phenyl ring is only possible if CT_{cool} is formed between the bridging phenyl ring and the NDI core and that instead, CT_{cool} can only react by charge recombination to the ground state if the electron is transferred from the terminal phenyl ring. Accordingly, the quantum yield of charge separation would be decreased by a factor of 0.5 if CT_{cool} is formed to equal parts by CT from the phenylene bridge and CT from the terminal phenyl ring. If a quantum yield of unity is assumed for the charge separation from CT_{cool} at the phenylene bridge, this would result in an overall quantum yield for CSS_2 of around 0.5, which is close to the value of 0.47 found for **D_2IrA**.[70, 115] However, this hypothesis is in conflict with the results obtained for **D_2IrA'**, comprising the modified acceptor moiety **A'**, for which a quantum yield of only 0.59 was found after excitation at the NDI. Since no terminal phenyl ring is present in **A'**, CT_{cool} can only be formed with the phenylene bridge and thus the quantum yield of CSS_2 should instead be close to unity according to the first hypothesis. Instead, CT_{cool} is apparently formed primarily with the phenylene bridge even in **A** where a terminal phenyl ring is present, but the subsequent charge separation proceeds with a similar lifetime as the charge recombination of CT_{cool} to the ground state, resulting in the reduced quantum yield determined in $CSS_2$for both **D_2IrA** and **D_2IrA'**. The preferred formation of CT_{cool} with the phenylene bridge can most likely be explained by the electron donating character of the dipyrrin-π-system which increases the electron density of the phenylene bridge, and thus the stability of CT_{cool}, compared to the terminal phenyl ring. The same explanation also holds true for **DPtA** and **DPdA**, except that the quantum yields after excitation at the NDI are decreased even further to 0.13 and 0.15 in MeCN, respectively. The lower quantum yields are most likely caused by additional decay paths in the reaction sequence from CT_{cool} to CSS_2 or a slower initial charge separation, further favoring the recombination of CT_{cool} to the ground state.

Of greater interest is the difference between **DPtA** and **DPdA** and the equivalent literature known Ir(III)-complexes **DIrA** and **D_2IrA** after excitation of the CMC. After excitation of the CMC the quantum yield of CSS_2 in MeCN was described to be close to unity for the Ir(III) complexes, while for **DPtA** and **DPdA** values of only 0.26 and 0.32 respectively were determined in this thesis. The decreased quantum yield observed for **DPtA** and **DPdA** compared to the Ir-complexes can be explained by the

excited state lifetimes determined by ns- and fs-TA spectroscopy and the emission properties discussed before.

In **Pt** the lifetime of ^{3}Pt is 67 ns in THF, while the time constant of the charge separation observed for **DPtA** is 26 ns in THF. Therefore, the process of charge separation from ^{3}Pt occurs on a similar timescale as the deactivation of ^{3}Pt to the ground state and both processes contribute significantly, decreasing the yield of charge separation.[85, 219-220] This hypothesis is supported by the observation of residual phosphorescence in **PtA** and **DPtA** even in MeCN and THF were the phosphorescence should be quenched by charge separation. In contrast, the equivalent Ir(III)-compounds show ^{3}Ir-lifetimes of 1.86 µs which is about three orders of magnitude higher than the time constant of 1 ns determined for the charge separation, rendering the direct deactivation of ^{3}Ir to the ground state virtually ineffective.

In the Pd-compounds on the other hand, the ^{3}Pd lifetimes in THF are 1.44 µs in **Pd** and 29 ns in **DPdA**, indicating an effective occupation of CSS_1 from ^{3}Pd since similarly to the Ir-complexes the charge separation seems to be several orders of magnitude faster than the deactivation of ^{3}Pd to the ground state. This is in line with the complete quenching of the phosphorescence from ^{3}Pd in MeCN and THF. Instead the lowered quantum yield of charge separation is due to a less effective formation of ^{3}Pd from its singlet precursors. As observed in the steady state emission and fs-TA measurements all Pd(II)-complexes show fluorescence even in solvents for which a charge separation is confirmed. This is due to a slow ISC to the triplet state which takes about 1.5 ps in **Pd** compared to the 100 fs found for **Pt** and **Ir**. The slow ISC is most likely caused by the decreased heavy atom effect of Pd(II), which results in lower SOC-constants and thus causes a slower ISC. Hence while the Pt(II)- and Ir(III)-complexes show no fluorescence, the fluorescence of the analogous Pd(II)-complexes is quenched only partially, resulting in the observed dual luminescence described in chapter 3.2.3, and the less effective formation of ^{3}Pd. Additionally, during the conformational rearrangement of the CMC in the triplet state, a part of the molecules deactivates to the ground state. Furthermore, the multiple pathways of charge separation from higher excited states than ^{3}Pd most likely leads to CSSs in different conformational arrangements which decay to the ground state faster than they form CSS_2, thus further reducing the quantum yield of CSS_2.

Lastly, it has to be noted that although a description of the spin-state was performed for the states localized at the respective metal-dipyrrin-moiety and the NDI, no further description was done for all charge separated states. Instead, both spin-multiplicities were given in the state diagrams. This is due to the possible occurrence of spin-equilibria in CSSs comprising highly decoupled donor- and acceptor moieties. The nature of these spin-equilibria will be the main focus of the next chapter.

3.4 Spin Chemistry

As mentioned in the introduction (chapter 1.1 and 1.2), charge separated states such as CSS_2 can be described as radical pairs and thus may form an equilibrium between the singlet and the triplet states. The kinetics of this equilibrium is sensitive to an external magnetic field which can therefore strongly influence the yield and kinetics of photochemical reactions associated with radical pairs. An example for a photochemical reaction which shows such a magnetic field effect (MFE) is the charge recombination (CR) of charge separated states to the ground state which can easily be monitored by ns-TA-spectroscopy as shown above (chapter 3.3.1). The present chapter describes the investigation of the MFE on the CR-kinetics of CSS_2 in the triads **DPtA** and **DPdA** as well as the reference compound **DIrA** starting from the magnetic field dependent measurements, to the data preparation and fitting procedure to the theoretical interpretation of the results using spin-chemical models.

The magnetic field dependent measurements were performed on the same set-up as the ns-TA spectroscopy. An electromagnet was used to apply magnetic fields up to 1800 mT. All samples were excited with 5 ns pulses from an EKSPLA NT 342A Nd:YAG laser with an intensity of 12 mW at the maximum of the respective absorption band associated with the CMC. The samples had an optical density between 0.2 and 0.3 at the energy of excitation except for **DPdA** in THF, which had to be measured at a reduced concentration to prevent bimolecular reactions at very high fields. Since MFEs are extremely sensitive to trace amounts of oxygen, all solvents were degassed by multiple freeze-pump-thaw cycles and stored in a glovebox with an oxygen-amount below 1 ppm in which the sample preparation was done. A special cuvette equipped with a *Young's* valve was used to ensure gas-tight conditions which were checked multiple times by repeated measurements of the decays at several different magnetic fields. For further experimental details also see chapter 6.1.5.

DIrA has only been examined in MeCN to validate the measurements by comparison with the literature. This was necessary since the excitation-source of the set-up was modified compared to the experiments previously performed by Lambert et. al. and an improved method of data preparation and fitting was applied.[79] Furthermore, the excitation energy of the new measurements was different to the literature. [59, 70] **DPtA** was measured in MeCN, THF and pTHF to investigate the influence of solvent specific parameters such as polarity and viscosity on the MFE. For **DPdA** the measurements could only be performed in THF and pTHF since in MeCN bimolecular side reactions occurred at higher magnetic field strengths even at very low concentrations.

3.4.1 Magnetic Field Dependent ns-TA Spectroscopy

To investigate the MFE, the lifetime of CSS_2 was determined at different magnetic fields. Therefore, kinetic traces at 21100 cm^{-1} (corresponding to the $NDI^{\bullet-}$ monoradical anion) were measured at roughly 90 different magnetic fields between 0 – 1800 mT. The width of the laser pulse, the finite response time of the instrument and especially the slow population of CSS_2 from the respective ^{3}M-precursor prevent the detection of the theoretical maximum concentration of CSS_2 at time zero. To account for this, all experimental decay traces were transformed into the theoretical decay prior to further analysis of the data. As illustrated exemplarily for **DPtA** in THF at B = 0 in **Figure 43**, this was achieved by deconvolution of the kinetics with the instrument response function (IRF), the rise-time of the signal (which is equal to τ_{GSB} from **Table 6**), and one to two decay-times. Subsequent back-extrapolation of only the decay-part of the fit to the time of the signal-onset results in the theoretical decay with an infinitely short excitation pulse and rise time. The signal onset was then defined as time zero (t = 0). During this procedure the time zero, the IRF and the rise-time were kept constant for all magnetic fields for the respective sample, while the lifetimes of the decay were variable. Lastly, the residuals of the fit were added to the respective theoretical decay trace to produce a realistic noise for the modified decay curves.

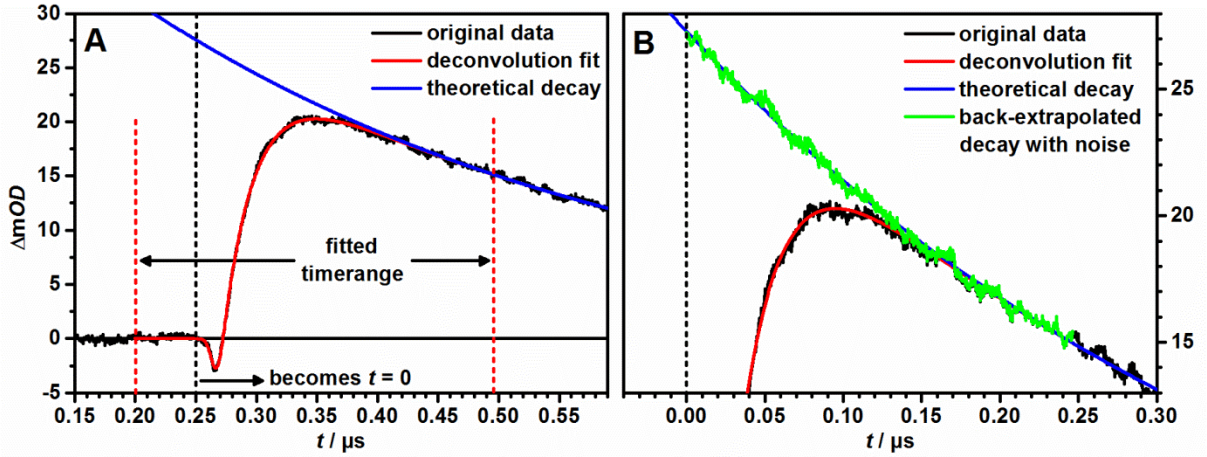

Figure 43: Back-extrapolation of the early part of the transient absorption signal for **DPdA** in THF at B = 0. (A): Roughly 0.3 µs of the early kinetics are deconvoluted with the IRF and the 26 ns rise time of CSS_2 (red). The theoretical decay without IRF and rise time is shown in blue. (B): To generate a proper noise for the back-extrapolated decay, the residual of the deconvolution fit is added to the theoretical decay between 0.25 µs and time zero (green).

Additionally, the transformed decays were individually corrected for a small offset at very late times which is intrinsic to the set-up. Lastly, all decay curves were normalized to 1 to compensate for laser intensity fluctuations. All resulting groups of decay traces at various specific magnetic fields are shown for each compound in all tested solvents in **Figure 44** (A – F).

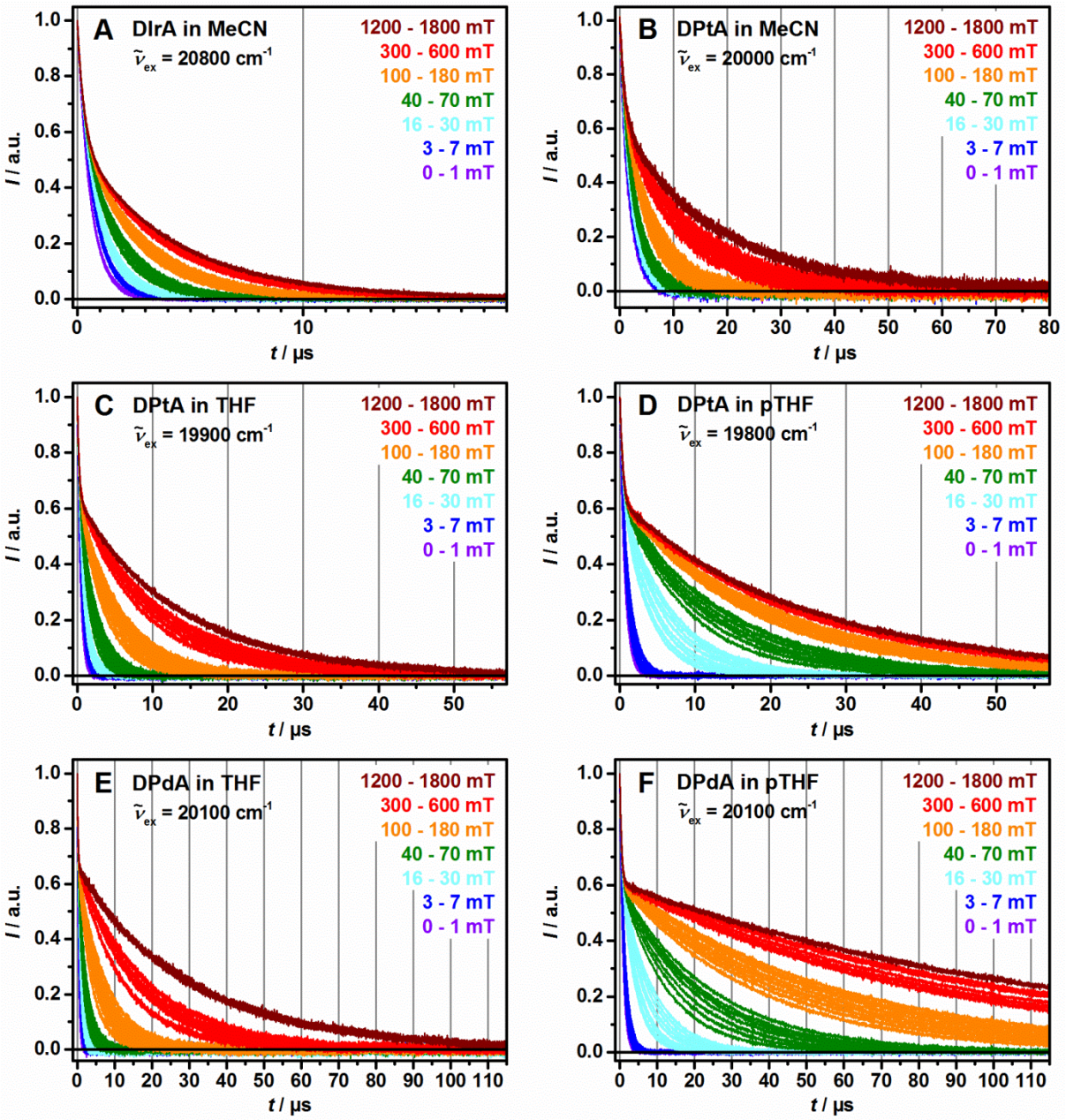

Figure 44: Magnetic field dependence of the decay traces recorded at 21100 cm^{-1} for **DIrA** in MeCN (A), **DPtA** in MeCN (B), THF (C) and pTHF (D) and **DPdA** in THF (E) and pTHF (F) at selected magnetic fields after excitation at the given wavelengths. The experimental data has been transformed as described in **Figure 43** and the main text. Magnetic field strengths are indicated by a uniform color code from purple to blue at low fields, cyan to orange at medium fields and red to brown at high fields. The vertical grey lines indicate time-steps of 10 µs to facilitate a comparison of the different groups of decay traces.

As can be seen, all samples show a significant sensitivity to an applied magnetic field. In all cases, the decay of the signal is slowed down with rising magnetic field strengths, whereby at each point in time the decay curves change in a monotonic way, that is without curve crossings. For each sample, the decay is best described as monoexponential at low fields and becomes biexponential towards higher fields. At very high fields, the MFE saturates, and a further increase of the magnetic field results in

only minor changes in the CSS-lifetimes. The samples differ mainly in the magnitude of the MFE and the magnetic field range in which the MFE is strongest as well as the magnetic field range where the MFE saturates.

A more detailed inspection of **Figure 44** with the help of **Table 7**, reveals several interesting trends. While **DIrA** and **DPtA** in MeCN have significantly different lifetimes at 0 mT, both samples display a relatively similar elongation of the lifetimes with rising magnetic field. When comparing the long lifetime of the biexponential decay at 1800 mT with the lifetime at 0 mT a 7.5-fold increase is found for **DIrA**, and a 10.5-fold increase is found for **DPtA**. On the other hand, the decay in **DPtA** can be described as monoexponential up to higher fields and the MFE saturates significantly later than in **DIrA**. This indicates a delayed influence of the magnetic field on the decay kinetics in **DPtA**, and therefore a reduced sensitivity of the sample to low magnetic fields.

Next, the MFE on **DIrA** in MeCN, **DPtA** in THF and **DPdA** (corresponding to relatively similar decay kinetics at 0 mT) will be compared. As can be seen from **Figure 44** (A,C,E), the time range of the measurements had to be increased significantly from **DIrA** to **DPtA** to **DPdA** to cover the complete decrease of the signals, which already implies a much stronger MFE in the latter triads. This is confirmed by the lifetimes given in **Table 7**. While **DIrA** in MeCN displays a 7.5-infold increase of the lifetimes, **DPtA** and **DPdA** in THF display a 39-fold and 90-fold increase respectively. This huge increase seems to be mostly due to a significantly later saturation of the MFE, since the increase in lifetimes seems to be comparable up to ca. 20 – 100 mT.

Table 7: Decay times (τ) and respective amplitudes (a) at different magnetic field strengths (B) for the decay traces shown in **Figure 44** for **DIrA**, **DPtA** and **DPdA** in various solvents.

sample[a]		τ_1 / τ_2 /µs (a_1 / a_2) at B =					
		0 mT	**5 mT**	**20 mT**	**100 mT**	**500 mT**	**1800 mT**
DIrA	**MeCN**	0.58 (1)	0.72 (1)	0.34 / 1.0 (0.21 / 0.79)	0.30 / 2.3 (0.38 / 0.62)	0.32 / 4.0 (0.44 / 0. 56)	0.33 / 4.4 (0.46 / 0.54)
DPtA	**MeCN**	1.77 (1)	1.92 (1)	2.10 (1)	0.81 / 4.2 (0.19 / 0.81)	1.1 / 13.8 (0.33 / 0.67)	1.1 / 18.8 (0.38 / 0.62)
	THF	0.40 (1)	0.53 (1)	0.28 / 0.86 (0.15 / 0.85)	0.25 / 3.3 (0.26 / 0.74)	0.29 / 11.3 (0.30 / 0.70)	0.31 / 14.3 (0.32 / 0.68)
	pTHF	0.65 (1)	0.95 (1)	0.36 / 4.2 (0.25 / 0.75)	0.41 / 17.1 (0.34 / 0.66)	0.42 / 24.9 (0.35 / 0.65)	0.41 / 25.9 (0.36 / 0.64)
DPdA	**THF**	0.34 (1)	0.47 (1)	0.28 / 0.82 (0.21 / 0.79)	0.24 / 3.8 (0.24 / 0.76)	0.23 / 19.0 (0.28 / 0.72)	0.27 / 30.6 (0.31 / 0.69)
	pTHF	0.81 (1)	1.1 (1)	0.42 / 4.8 (0.29 / 0.71)	0.45 / 36.4 (0.34 / 0.66)	0.46 / 103 (0.36 / 0.63)	0.46 / 118 (0.33 / 0.67)

[a] after excitation at the maximum absorption of the respective CMC (see **Figure 44**).

A comparison of **DPtA** in MeCN, THF and pTHF shows that the magnitude of the MFE increases with decreasing solvent polarity from a 10.5 fold increase in MeCN to a 35-fold increase in THF and a 40-fold increase in pTHF. Furthermore, the sensitivity of the sample to low magnetic fields is decreased in MeCN, most likely due to the long lifetime at zero magnetic field. The most striking difference between the solvents is demonstrated by the color code in **Figure 44** (C,D). While in MeCN and THF, the MFE is strongest at medium to high fields, in pTHF the MFE is strongest at low to medium fields and saturates much earlier. The observed shift of the main MFE towards lower field strengths seems to be caused by the viscosity of the solvent rather than the solvent-polarity, since the effect is only found in the very viscous pTHF.

As can be seen from Figure 44 (E,F), the same observation is made for **DPdA** in THF and pTHF. With increasing solvent viscosity the main MFE is shifted towards lower magnetic fields. Furthermore, the saturation of the MFE in pTHF occurs later for **DPdA** than for **DPtA**. This leads to the most pronounced MFE observed in all the samples, with a 145.5-fold increase in lifetimes from 0 - 1800 mT. At this point it should be noted that all decay traces were recorded on a time range that allowed the signal to decrease back to zero, but the decays in pTHF are depicted on a shorter timescale to facilitate a comparison with the measurements in THF.

3.4.2 Global Data Analysis

For a further discussion of the MFE, one has to take into account a spin chemical model for the charge recombination of radical pairs, since the observed decay traces are only the experimentally observable result of a more complicated kinetic scheme. In the investigated triads the spatial separation of the radical pairs is large, and the exchange interaction is assumed to be negligible due to the strong electronic decoupling of the radical centers. Hence, the singlet and triplet levels are assumed to be virtually degenerate. Therefore, one can resort to the reaction scheme derived by *Hayashi* and *Nagakura et al.* shown in **Figure 45**.[25, 33, 78] The reaction kinetics of excited state radical pairs are governed both by the charge recombination to the ground state and the spin interconversion between the associated singlet and triplet states. At very low magnetic fields, coherent spin mixing between the degenerate singlet and triplet states occurs. At higher magnetic fields the triplet sublevels spilt into T_+, T_0 and T_- due to the *Zeeman* effect. While the interconversion between the singlet and T_0 is still coherent, transitions between states of different *Zeeman* energy are now mainly governed by significantly slower incoherent spin relaxation processes of the radicals. Since CR to the singlet ground state should be much faster from the singlet radical pair state than from the triplet radical pair state due to the spin conservation rule a slower spin interconversion results in a slower decay of the CSS which results in the observed MFE effect.[24-25, 33, 36-37, 50, 221]

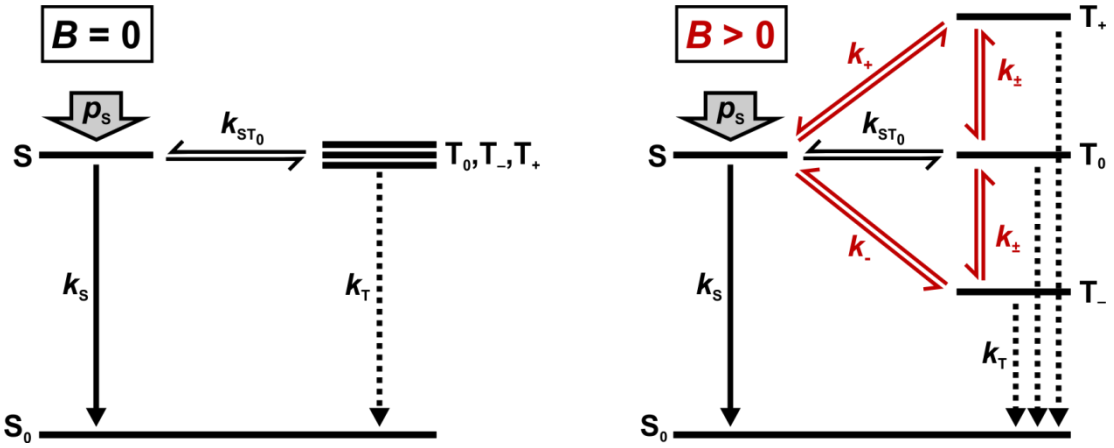

Figure 45: Spin chemical model for the charge-recombination of radical pairs with degenerate S and T_0 states at zero magnetic field (left) and non-zero field (right). Magnetic field dependent processes are depicted in red.

The time dependent concentrations of the four spin substates associated with the excited state radical pair are given by the following differential rate equations (13).[24-25, 33]

$$\begin{aligned}
\frac{d[S]}{dt} &= -\left(k_S+k_+ +k_- +k_{ST_0}\right)[S]+k_{ST_0}[T_0]+k_+([T_+]+k_-[T_-]) \\
\frac{d[T_0]}{dt} &= k_{ST_0}[S]-\left(k_T+k_+ +k_- +k_{ST_0}\right)[T_0]+k_+([T_+]+k_-[T_-]) \\
\frac{d[T_+]}{dt} &= k_+[S]+k_+[T_0]-(k_T+2k_+)[T_+] \\
\frac{d[T_-]}{dt} &= k_-[S]+k_-[T_0]-(k_T+2k_-)[T_-]
\end{aligned} \tag{13}$$

Since the signal intensity I of the experimental decay curves represents a superposition of the concentration of the spin substates at any given time ($I = [S] + [T_0] + [T_+] + [T_-]$) a fit of the data to the differential rate equations can give further insights on the associated rate constants. For the numerical solution of this problem, some simplifications were made:

1.) The rate constant k_T for the spin-forbidden CR from the triplet excited state to the singlet ground state was assumed to be negligible and was thus set to be zero.[59]

2.) The rate constant k_{ST0}, describing the coherent spin interconversion between S and T_0 is magnetic field independent and $k_{ST0} = 4 \cdot 10^7\ s^{-1}$. This value was derived from a classical approximation of the spin evolution as predicted by the semi classical model by Schulten et. al.[54-56, 59]

3.) The rate constant for the charge recombination k_S as well as the initial population of the excited singlet state p_S are assumed to be parameters specific for a single compound-solvent combination, but more importantly, magnetic field independent.[25, 32, 35]

4.) The rate constants k_-, k_+ and $k_\pm$ for processes between spin levels of different *Zeeman* energy are assumed to be identical functions of the magnetic field, since S and T_0 are degenerate and spin dipolar interactions can be neglected due to the large spatial separation in the present radical pairs. They can therefore be summarized in a single rate constant $k_\pm$, which is the only magnetic field dependent parameter.[25, 76]

In the following, the fitting procedure applied to determine the correct values for $k_\pm$ will be described. Prior to the numerical analysis of the data, the corrected decay traces were reduced in their amount of data-points by selecting around 250 points, with a high data point density at early times and continuously lower density towards later times. This was done to reduce the duration of the performed calculations. Since for one sample, k_S and p_S have to be constant over all magnetic field strengths, they have to be determined using a global fit comprising the decay curves at representative fields to ensure the validity of the determined parameters over the complete magnetic field range. The global fit was performed using MATLAB and script 1 given in the appendix. Since the MATLAB script only allows a modulation of the rate constants, the population of the singlet excited state at time zero p_S and the corresponding populations of the triplet sublevels at time zero (p_T, p_{T0}, p_{T+}) have to be determined manually by trial and error. Reasonable starting values for these parameters can be derived from the shape of the decay traces and the amplitudes given in **Table 7**. For a start, the lack of crossings between different decay traces indicates values of $p_S \leq 0.25$.[62] Furthermore, at high fields, the signals decay biexponentially with a short lifetime and a long lifetime. The long lifetimes should roughly correspond to the decay of the outer *Zeeman* levels T_- and T_+ since $k_\pm$ is the rate limiting constant at high fields. On the other hand, the short lifetimes are on the same order of magnitude as the lifetimes observed at low fields and thus should correspond to the deactivation of the inner *Zeeman* levels S and T_0, since here the rate limiting constant is k_S. For these reasons p_S can roughly be estimated from the ratio of the amplitudes associated with the respective short and long lifetimes. Hereby, the ratio of the long lifetimes a_2 corresponds to $p_T + p_{T+}$ (the sum of the population of T_- and T_+ at time zero), while the ratio of the short lifetimes a_1 corresponds to $p_S + p_{T0}$. Since the triplet substates are formed statistically, and therefore $p_{T-} = p_{T0} = p_{T+}$, p_S can roughly be estimated by equation (14)

$$p_S = a_1 - \frac{a_2}{2} \tag{14}$$

For example, this method estimates a value of p_S = 0.19 for **DIrA** in MeCN, which is close to the reported value of p_S = 0.25. In the same way, a value of p_S = 0.02 is estimated for **DPtA** in THF. Since negative values for the population at time zero are physically meaningless, a very low value for p_S was used as a starting value for the global fit instead. In the end, p_S = 0.07 was found for **DPtA** in THF.

Using the estimated starting values, p_S could be optimized with a relatively small number of global analyses. On the other hand, k_S was found to be variable to some degree while still giving satisfying fits. It turns out that in classical kinetic systems, as the one described by equations (13), identical decay curves can result from different combinations of rate constants.[35, 79] In the present case, higher values of k_S can be compensated with lower values of $k_\pm$ and *vice versa.* Therefore, $k_\pm$ was determined for multiple values of k_S at all magnetic field strengths using script 2 given in the appendix. The results are different sets of $k_\pm$-values and rout mean square deviations (rmsd) as shown exemplarily for **DPtA** in THF in **Figure 46**.

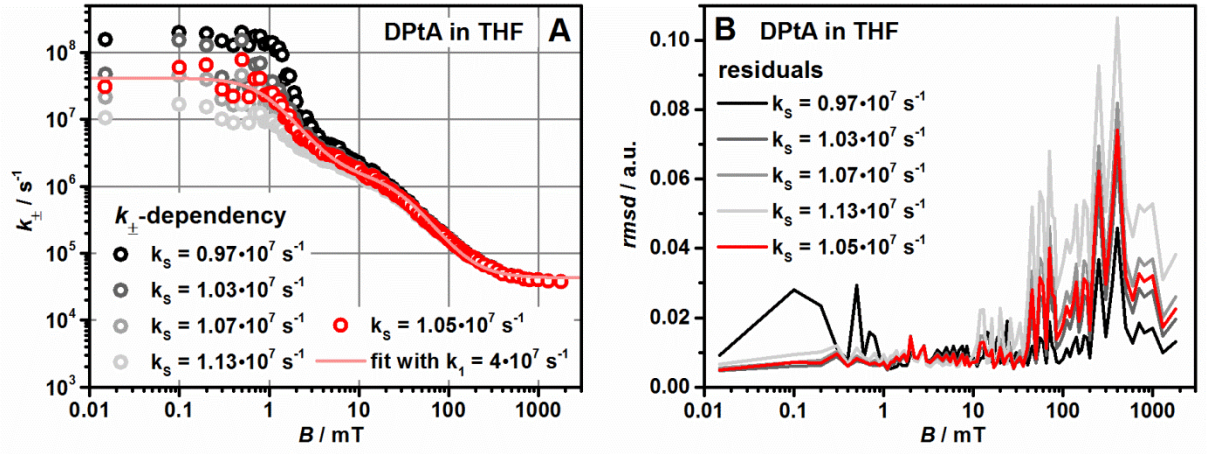

Figure 46: Influence of k_S on the behavior of $k_\pm$ (A) and the quality of the fit of equation (13) to the decay curves as indicated by the rmsd (B). Lower values of k_S (dark grey) lead to significantly higher values of $k_\pm$, and higher values of k_S (light grey) lead to higher values of $k_\pm$ while the rmsd is influenced only very slightly. The best match to an extrapolation using equation (15) with k_1 = $4 \cdot 10^7$ s^{-1} (light red curve) is achieved for values of k_S = $1.05 \cdot 10^7$ s^{-1} (red).

Especially at low magnetic fields $k_\pm$ differs significantly when varying k_S. This effect is reduced towards higher fields where $k_\pm$ becomes the rate limiting constant and is therefore less sensitive to variations of k_S. To arrive at a physically sensible, unique solution the determined magnetic field dependence of $k_\pm$ was extrapolated to B = 0 using the double *Lorentzian* equation (15).[79]

$$k_\pm(B) = \frac{k_1}{1 + (B/B_1)^2} + \frac{k_2}{1 + (B/B_2)^2} + k_0 \qquad (15)$$

Here, the first term represents the contribution of coherent spin mixing, whereas the second term describes the incoherent spin relaxation processes. Since the triplet sublevels are assumed to be degenerate at zero magnetic field, k_1 should be equal to k_{ST0}. Therefore, the value of k_S was adjusted in a way that the resulting $k_\pm$-values could be fitted using equation (15) under the condition of $k_1 = k_{ST0} = 4 \cdot 10^7$ s^{-1}. As shown in **Figure 46** (A), for **DPtA** in THF this was achieved with a k_s-value of $1.05 \cdot 10^7$ s^{-1}.

At this point it has to be noted that in a strict sense, this method is only viable if the two terms of the *Lorentzian* contribute with significantly different orders of magnitude, that is if the dependence of $k_{\pm}$ shows a distinct two step behavior as observed for **DPtA** in THF. Only in these cases the contribution of the second term at low fields can be neglected. This is not the case for the measurements in pTHF where the contributions of coherent and incoherent mechanism of spin mixing at low fields are less clearly separated in their orders of magnitude. Therefore, the second term contributes significantly at low fields which under the condition of $k_1 = k_{ST0} = 4{\cdot}10^7\ s^{-1}$ would result in values of $k_{\pm}$ which are higher than $4{\cdot}10^7\ s^{-1}$ at zero magnetic field. This would contradict the assumption that $k_{\pm} = k_{ST0}$ in the case of degenerate triplet sublevels. To counteract this problem, one would have to assume the condition of $k_1+k_2 = k_{ST0} = 4{\cdot}10^7\ s^{-1}$. This would introduce a new uncertainty to the problem, since the ratio of k_1 and k_2 cannot be determined without knowing $k_{\pm}$. Furthermore, the difference to the ideal case of **DPtA** in THF is assumed to be relatively small, since at zero magnetic field the coherent spin mixing should still be significantly faster than the incoherent relaxation processes with a maximal spin interconversion rate close to $4{\cdot}10^7\ s^{-1}$.[32, 35, 50, 59] Therefore, the described approach for the determination of k_S was applied even for the measurements in pTHF.

The optimum values determined for the global parameters p_S and k_S, as well as for the parameters for the double *Lorentzian* fit B_1, B_2, k_2 and k_0 obtained by fitting the respective $k_{\pm}$-dependence are summarized in **Table 8**. In the following, the MFE on $k_{\pm}$ will be described phenomenological for all samples, before the data will interpreted on a spin chemical basis.

Table 8: Global parameters according to equation (13) for $k_{ST0} = 4.0{\cdot}10^7\ s^{-1}$ and $k_T = 0$ and parameters for the double *Lorentzian* fit of the resulting $k_{\pm}$-dependence according to equation (15) with $k_1 = 4.0{\cdot}10^7\ s^{-1}$.

sample[a]		p_S	k_S /$10^7 s^{-1}$	B_1 /mT	k_2 /$10^6 s^{-1}$	B_2 /mT	k_0 /$10^4 s^{-1}$
DIrA	**MeCN**	0.25	0.71	0.68	1.3	29.1	14
DPtA	**MeCN**	0.10	0.24	1.25	0.9	38.6	3.6
	THF	0.07	1.05	0.93	1.4	28.7	4.3
	pTHF	0.07	0.66	0.95	6.5	0.95	2.5
DPdA	**THF**	0.00	1.27	0.93	1.2	33.3	2.0
	pTHF	0.00	0.49	0.94	3.0	0.94	0.52

[a] after excitation at the maximum absorption of the respective CMC (see **Figure 44**).

Figure 47 compares the results for **DIrA** in MeCN which were obtained during this work to the results obtained in the literature for the same compound and solvent.[59, 70, 79] It turns out that neither $k_{\pm}$ nor its behavior with rising magnetic field are dependent on the excitation energy, at least as long as the CMC is excited. Furthermore, the new data preparation and the improved fitting procedure give results comparable to the literature. The small differences which are noticeable nonetheless are most likely due to systematic variations during the measurements. The decrease of $k_{\pm}$ seems to start at slightly lower magnetic fields for the literature-data. This could be due to a decreased data point density at lower fields, or to a slightly varied calibration curve of the hall-sensor used to determine the magnetic field strengths. The slightly lower values of $k_{\pm}$ towards higher fields observed for the new data set could be due to a lower residual amount of oxygen in the sample. As described earlier, in this work the solvent was degassed by multiple freeze-pump-thaw cycles and a special cuvette equipped with a *Young's* valve was used. This was not the case for the literature data. Even though the difference in residual oxygen is most likely very low, it may not be negligible due to the very high sensitivity of the spin interconversion dynamics to traces of oxygen.[28, 32, 35] Another parameter which could in theory influence the CR-dynamics, and thus the behavior of $k_{\pm}$, is the concentration of the samples. Both measurements were performed with an optical density of about 0.25 at the excitation energy but since the extinction coefficient of **DIrA** is significantly higher at 20800 cm^{-1}, the concentration of the literature sample was about a factor of four times higher than the one investigated in this work. Nevertheless, for both measurements the occurrence of bimolecular processes was not observed. The conclusion of this comparison is that the validity of the new data preparation and fitting routine, as well as the independence of $k_{\pm}$ from the excitation energy was confirmed for **DIrA**. This is expected to be similar for all other compounds as well.

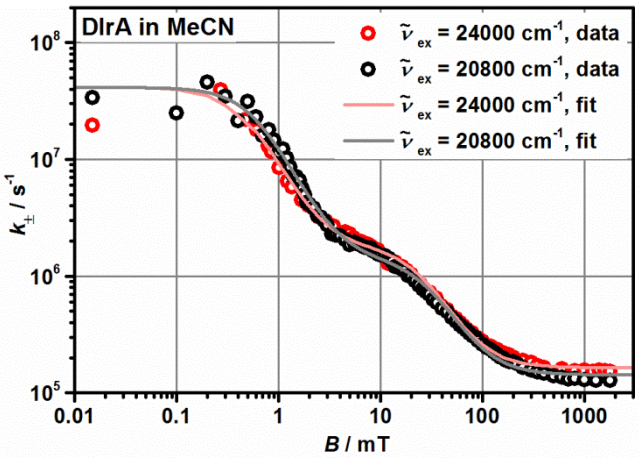

Figure 47: Magnetic field dependence of $k_{\pm}$ (circles) and double *Lorentzian* fit according to equation (15) (lines) for **DIrA** in MeCN after excitation at different energies associated with the CMC. Data for excitation at 24000 cm^{-1} was taken from the literature (red).[59, 79] Data for excitation at 20800 cm^{-1} was obtained in this work (black).

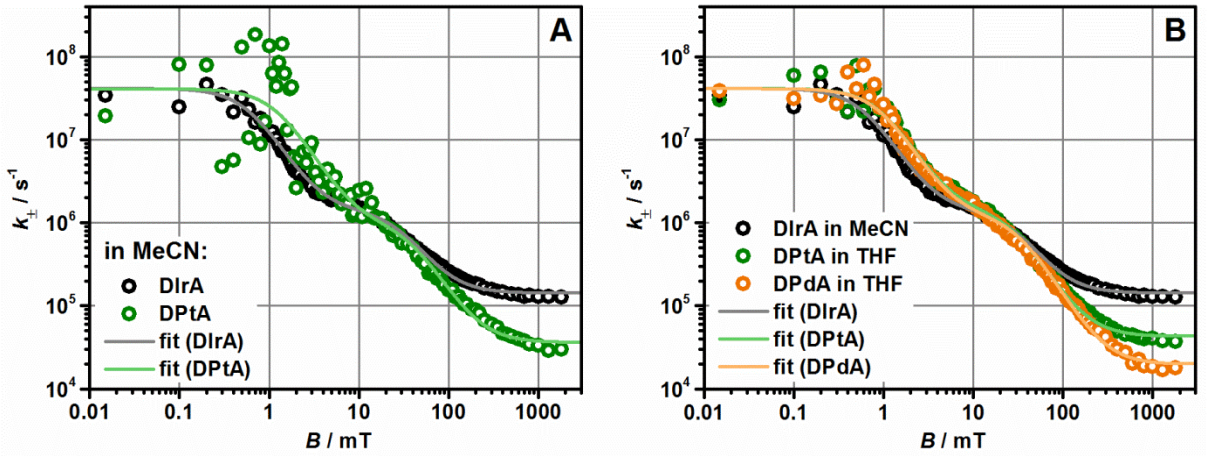

Figure 48: Magnetic field dependence of $k_\pm$ (circles) and double *Lorentzian* fit according to equation (15) with parameters taken from **Table 8** (lines) for **DIrA** (black) and **DPtA** (green) in MeCN (A) and for **DIrA** in MeCN (black) as well as **DPtA** (green) and **DPdA** (orange) in THF (B) after excitation at the maximum absorption of the respective CMC.

Figure 48 shows the magnetic field dependence of $k_\pm$ for **DPtA** and **DIrA** in MeCN (A) and for all investigated triads in different solvents (B).

The most striking difference in the behavior of $k_\pm$ between **DIrA** and **DPtA** in MeCN is the increased scattering of the data points at fields up to around 10 mT for **DPtA**. This is strongly related to the mutual dependence of $k_\pm$ and k_S at low magnetic fields as described in **Figure 46**. It was found that in equation (13) $k_\pm$ and k_S can compensate each other as long as their contribution to the experimentally observable decay kinetics is comparable or mostly due to k_S. As soon as $k_\pm$ becomes the rate limiting step this relation breaks down and $k_\pm$ becomes largely independent from k_S. Since at low magnetic fields **DPtA** has much higher lifetimes than **DIrA**, a significantly lower value for k_S was determined by the global analysis of the decay traces. The k_S-values are $0.71 \cdot 10^7$ s^{-1} for **DIrA** and $0.24 \cdot 10^7$ s^{-1} for **DPtA.** As can be seen from **Figure 48** (A) $k_\pm$ approaches the value of k_S at around 1 mT for **DIrA**, but only at around 10 mT for **DPtA**. Accordingly, the scattering of the data points of **DIrA** at fields slightly lower than 1 mT is comparable to the scattering found for **DPtA** at fields around 10 mT, especially if one takes into account the logarithmic nature of the ordinate. Furthermore, **DPtA** $k_\pm$ has nearly no influence on the decay kinetics at fields lower than about 1 mT since here, k_S is at least an order of magnitude lower and therefore the rate determining constant. This also explains the delayed influence of the magnetic field on the decay kinetics observed in **Table 7**. The second difference between **DIrA** and **DPtA** is the limiting value of $k_\pm$ towards very high fields as represented by k_0 in **Table 8**. k_0 is significantly lower for **DPtA**, which is in accordance to the observations made on the decay kinetics in **Figure 44** (A,B) which showed a stronger MFE for **DPtA** towards high fields.

Since the magnitude of k_S has a significant influence on the CR-kinetics, the solvents for the further comparison of the triads in **Figure 48** (B) were chosen such that the decay kinetics at zero magnetic field were as similar as possible. Therefore, any difference in MFE should more or less exclusively be related to a different behavior of $k_\pm$. Thus, the results for **DIrA** in MeCN will be compared to the results for **DPtA** and **DPdA** in THF where the compounds show lifetimes of 0.58 µs and 0.41 µs and 0.34 µs, respectively. The biggest difference between the samples is found for the limiting value of $k_\pm$ towards higher magnetic fields which becomes significantly lower from **DIrA** to **DPtA** to **DPdA**. The lower values for $k_\pm$ confirm the observations made on the decay curves in **Figure 44** (A, C, E) which indicated a stronger MFE for the Pt- and Pd-triads towards high fields. Furthermore, the behavior of $k_\pm$ is very similar at magnetic fields up to about 50 mT. Lastly, in **DIrA**, $k_\pm$ seems to decrease at slightly lower fields than in **DPtA** and **DPdA**. These observations are in agreement with the values determined by the double *Lorentzian* fit, which yields very similar values for k_2 and B_2, the parameters describing the second part of the two-stepped behavior of $k_\pm$. Additionally, the double *Lorentzian* fit reveals a slight difference between the three triads at very low fields. The first *Lorentzian* is almost exclusively described by the parameter B_1, since k_1 is fixed to $k_1 = 4 \cdot 10^7\ s^{-1}$. Not only does the lower value of B_1 for **DIrA** confirm a slightly increased sensitivity towards lower fields, but the deviation of the values and the fit is higher for **DPtA** and especially **DPdA**. Both complexes show slightly higher values than expected by the double *Lorentzian* fit at around 0.7 mT. While this could be an insignificant discrepancy due to the high error of the determined $k_\pm$-values at very low fields, the fact that values and fit match almost perfectly for **DIrA** hints at compound specific differences. As has been observed before by *Schäfer et. al.* for purely organic TAA-NDI dyads, one phenomenon which could result in an increase of $k_\pm$ is *J*-resonance. This is described in greater detail in chapter 1.1.2 and would require a non-zero value for the exchange interaction *J*. Although *J* was deemed negligible in the examined triads and was therefore defined to be zero for the global analysis of the decay kinetics an influence of a small "residual" exchange interaction on $k_\pm$ at low fields cannot be excluded completely.[59, 62, 79]

Lastly, **Figure 49** shows the solvent dependence of the MFE for **DPtA** (A) and **DPdA** (B). First off, a comparison of **DPtA** in MeCN and THF shows that the influence of the solvent polarity on the behavior of $k_\pm$ is negligible. The only significant difference is the decreased signal to noise ratio at low fields for MeCN. Equivalently to the comparison of **DIrA** and **DPtA** in MeCN, this can be attributed to the longer lifetimes and the resulting lower value of k_S for **DPtA** in MeCN compared to THF. Furthermore, the limiting value of $k_\pm$ towards high fields is a bit lower in MeCN. This agrees with the larger absolute lifetimes observed for **DPtA** in MeCN when compared to THF as can be seen from **Table 7** and **Figure 44**. Although $k_\pm$ spans the same orders of magnitude in both solvents, the relative effect on the decay kinetics is larger in THF due to the larger value for k_S.

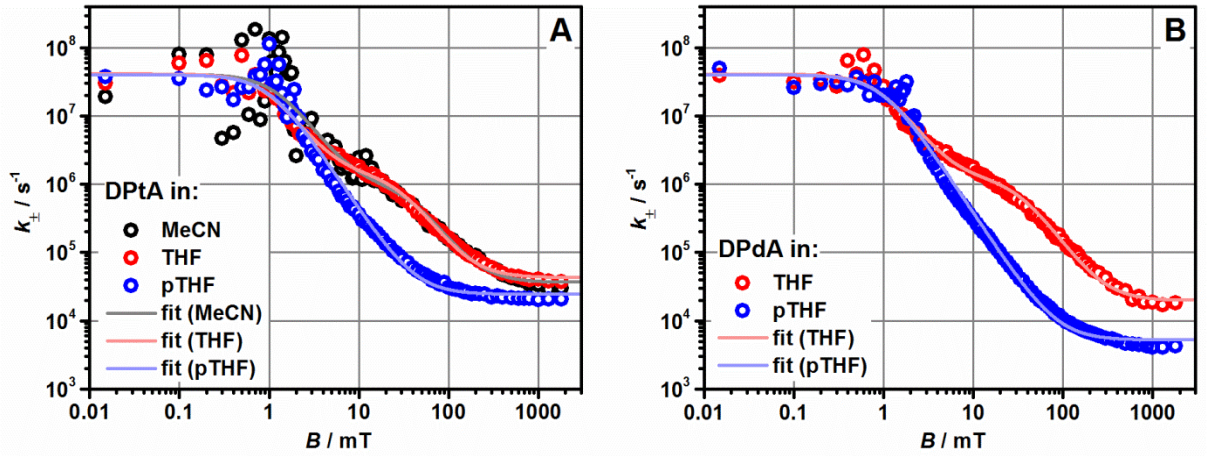

Figure 49: Magnetic field dependence of $k_\pm$ (circles) and double *Lorentzian* fit according to equation (15) with parameters taken from **Table 8** (lines) for **DPtA** (A) as well as **DPdA** (B) in MeCN (black), THF (red) and pTHF (blue) after excitation at the maximum absorption of the respective CMC.

The viscosity of the solvent on the other hand has a significant influence on the MFE on both **DPtA** and **DPdA**. While $k_\pm$ shows a clear two step behavior in solvents of low viscosity, the second step vanishes in the highly viscous pTHF. This effect is so pronounced that for both **DPtA** and **DPdA** in pTHF the behavior of $k_\pm$ can be fitted to equation (15) with multiple sets of parameters for B_1, k_2 and B_2, without changing the quality of the fit. Even a description without the second *Lorentzian* of equation (15) is possible, but is of a somewhat lesser quality. To compromise the quality of the fit with the apparently very small difference between the two *Lorentzian*s, the parameters were chosen such that B_1 and B_2 were kept equal, while k_2 was adjusted freely. The resulting values are summarized in **Table 8**.

When comparing the values in THF to those in pTHF, it turns out that B_1 is largely unaffected while k_2 increases significantly and simultaneously B_2 is decreased by about two orders of magnitude. Furthermore, the high field limit of $k_\pm$ as described by k_0 is decreased in pTHF. While this trend is pronounced only weakly for **DPtA**, it is significant in **DPdA** where k_0 is decreased by a factor of about 0.25. This behavior of $k_\pm$ agrees with the observations made on the related decay kinetics in **Figure 44** (C – F) and **Table 7** which proposed a shift of the strongest MFE towards lower fields and explains the strongly increased MFE observed for **DPdA** in pTHF. Lastly, the experiments in pTHF support the suggestion of an observable *J*-resonance at low magnetic fields. Especially in **DPtA**, a clear increase of $k_\pm$ is observable at around 1 mT. Although it is possible to include the exchange interaction *J* in the global analysis of the decay curves, as has been shown by *Schäfer et. al.*, this was not done in the course of this work since the exchange interaction has to be very low to produce a *J*-resonance at 1 mT and was only clearly observed in one case in pTHF.[62]

3.4.3 Spin Chemical Interpretation

So far, the MFE was described on the basis of experimental observables, and has further been investigated by fitting the results to a classical model of the spin chemistry to reduce the complex decay kinetics to one magnetic field dependent parameter $k_{\pm}$. The behavior of $k_{\pm}$ was described for all samples and gave trends which match well with the observations made for the experimental decays and in the literature. However no further interpretation of the parameters which describe the spin interconversion have been made. This will be done on the following pages for the investigated triads.

General remarks

As discussed in chapter 1.1, spin interconversion occurs due to fast, coherent processes and slower incoherent processes. As has been shown before, the two terms of equation (15) can be related to the contribution of the coherent and incoherent processes to the overall spin transition between the inner *Zeeman*-levels S and T_0 and the outer *Zeeman*-levels T_+ and T_-.[59, 79] In most cases investigated in this work, $k_{\pm}$ displays a clear twostep behavior. In those cases, the coherent processes dominate the spin interconversion up to fields of about 8.0 mT, while at higher fields the incoherent processes dominate.[59, 79] In pTHF, on the other hand, no clear two step behavior of $k_{\pm}$ could be observed. Here, the contributions of coherent and incoherent processes to the spin interconversion are not clearly separated. A detailed understanding of a superposition of coherent and incoherent spin-transitions in the same magnetic field range is beyond the classical kinetic model and its numerical solution. Nevertheless, even in pTHF an interpretation of the parameters describing the behavior of $k_{\pm}$ in a spin chemical sense should still be possible, as long it is put into relation to results for which the separation between coherent and incoherent processes is maintained.

Population of S at time zero (p_S)

Although the population of the singlet $^1CSS_2$ (p_S) is not a parameter which describes the behavior of $k_{\pm}$ it has to be addressed, since it shows a very clear dependence on the central metal ion. For **DIrA**, the value of $p_S = 0.25$ which has been assumed in the literature before was confirmed by the present results.[59, 79] For **DPtA** and **DPdA** on the other hand, values of p_S = ~0.1 and $p_S = 0.0$ have been determined respectively. For all triads, fs-TA spectroscopy suggested a population of CSS_2 from the partially charge separated state CSS_1 which in turn is occupied from the ligand centered triplet state ^3M (see chapter 3.3.2). Due to the spin conservation rule this would suggest an initial singlet population of $p_S = 0.0$ for CSS_1 and due to the relatively short lifetime of CSS_1 a value of $p_S = 0.0$ for CSS_2 as well. For **DIrA**, the deviation from this expectation has been attributed to a very fast spin interconversion in CSS_1 which leads to a fast equilibration of the spins and the statistical value of $p_S = 0.25$. The fast spin relaxation was reasoned to be fast in CSS_1 because one of the unpaired

electrons is situated at the CMC. In the oxidized CMC, the central iridium atom formally is in an Ir^{4+}-oxidation state, and thus has a d^5 electron configuration. Complexes of central metal ions in d^5 electron configuration show spin relaxation lifetimes on the order of few ps due to a thermal population of energetically similar doublet states and very high SOC-constants caused by efficient formal mixing of singlet and triplet sub states.[34, 59, 67, 222] The Pt- and Pd- central ions of **DPtA** and **DPdA** on the other hand assume a d^7 electron configuration in the formally oxidized M^{3+}-state of the CMC in CSS_1. No cases of enhanced spin-interconversion rates for complexes with d^7-central metal ions have been found in the literature. Hence, it is assumed that, in contrast to **DIrA**, the triplet-favored population of CSS_1 is preserved for significantly longer times in **DPtA** and **DPdA** and thus CSS_2 is mainly formed in the triplet state. This effect is more pronounced for the Pd-complex, which is in line with the explanation that the lower SOC-constant leads to a slower ISC for the lighter Pd-ion. Furthermore, some cases of singlet-triplet mixing have been reported for complexes of Pt(II), although only for MLCT-transition states. These showed spin relaxation lifetimes of several hundreds of ns at very low temperatures which decreased significantly with temperatures approaching rt.[112, 206, 222-223]

Coherent spin interconversion

As outlined in chapter 1.1.2, the coherent spin interconversion is nearly exclusively due to isotropic hyperfine coupling (ihfc). The connection between the ihfc and the first term in equation (15) was already used to estimate the values for k_{ST0} and k_S during the global fitting procedure. Thus, it seems reasonable that B_1, the only free parameter for the description of $k_\pm$ at low fields should be comparable to the magnetic half field $B_{1/2,hfc}$. $B_{1/2,hfc}$ can be estimated from the hyperfine coupling constants of the nuclei involved in the radical centers by equation (16) which can be derived from equations (1) and (4).[33, 54, 56, 60, 75]

$$B_{1/2,\,\mathrm{hfc}} = \sqrt{3\sum_i \left[\sum_k a_k^2 I_k\,(I_k+1)\right]_i} \qquad (16)$$

Here, the characteristic magnetic field strength $B_{1/2,\,hfc}$ is given by the sum of the hyperfine coupling constants a times the corresponding nuclear spin quantum number I for all nuclei k in all radicals i. With values for a_N and a_H as taken from the literature for $TAA^{\cdot+}$[224] and $NDI^{\cdot-}$[225], $B_{1/2,\,hfc}$ is estimated equally for all triads to 2.5 mT which is significantly higher than the values obtained for B_1 from the behavior of $k_\pm$. This discrepancy can be understood when keeping in mind that B_1 refers to $k_\pm$ which appears only indirectly as a parameter of an assumed reaction mechanism, whereas $B_{1/2}$ by definition refers to the phenomenology of directly observable reaction parameters.[24, 32-33, 50, 54, 56, 59, 79]

In the present case a direct observable would be the signal intensity at certain times which can mathematically be addressed by an observed effective decay constant which will be named k_{eff} in the following. Since CR of CSS_2 can only occur from the singlet state due to the spin-conservation rule, k_{eff} is closely related to the recombination rate of the singlet state k_S and the quasi-stationary population of the singlet state p_S which is ultimately dependent on $k_{\pm}$. At zero magnetic field, the decay is monoexponential since $k_{\pm}$ becomes very large, and the spin equilibrium is established so fast that p_S is 0.25, the statistical maximum of p_S in a chemical equilibrium according to the reaction scheme depicted in **Figure 45**. This leads to equation (17) for the low field limit of the effective decay rate $k_{eff,1}$.[79]

$$k_{eff,1}(B=0) = \frac{k_S}{4} \tag{17}$$

At high fields the observed decay becomes biexponential, with the two rate constants $k_{eff,1}$ and $k_{eff,2}$ for the long and short part of the decay, respectively. While $k_{eff,1}$ is still associated with the recombination from S, the smaller rate constant $k_{eff,2}$ is related to the transition between the outer *Zeeman* levels and the inner *Zeeman* levels as governed by $k_{\pm}$. In the high field limit, where $k_{\pm}$ becomes very small, the effective decay at late times is equal to the decay of T_+ and T_- by a slow relaxation to S and T_0 and subsequent fast charge recombination from S. This sets the high field limit for the effective decay rate $k_{eff,2}$ to equation (18).[79]

$$k_{eff,2}(B\rightarrow\infty) = 2k_{\pm} \tag{18}$$

Combining the relations for the low field limit (17) and the high field limit (18) with relation (19) one arrives at equation (20) which, since k_S is constant over all fields, describes k_{eff} as a function of $k_{\pm}$ and thus as a function of the magnetic field.

$$\frac{1}{k_{eff}} = \frac{1}{k_{eff,1}(B=0)} + \frac{1}{k_{eff,2}(B\rightarrow\infty)} \tag{19}$$

$$k_{eff} = \frac{2k_S k_{\pm}}{k_S + 8k_{\pm}} \tag{20}$$

It has to be noted that equation (20) has an approximate character since it only combines two limiting values for a rate constant into a full function and can by no means be treated as an exact numerical solution to the kinetic scheme depicted in **Figure 45**. Nevertheless, equation (20) describes the observed effective decay rate reasonably well over the investigated magnetic field range. Equation (20) also comprises the magnetic fields where the decay transitions from a monoexponential to a biexponential behavior.[79]

Figure 50 (A) shows a plot of $k_{\pm}$ and k_{eff} versus the magnetic field strength for the example of **DPtA** in THF. Especially at low fields where the spin interconversion is dominated by ihfc the MFE on k_{eff} is weaker than on $k_{\pm}$. The characteristic magnetic field $B_{eff,\,1/2}$ at which the spin interconversion by ihfc is reduced to half its maximum rate can be derived from k_{eff}. As can be seen from **Figure 50** (A), in the magnetic field range between 0-8 mT the spin interconversion is mostly dominated by coherent processes. In this region, the extremes of k_{eff} are $2.54 \cdot 10^6$ s^{-1} at 0 mT and $1.58 \cdot 10^6$ s^{-1} at 8.0 mT which gives an arithmetic mean of $2.06 \cdot 10^6$ s^{-1}. This value of k_{eff} is found at a magnetic field of $B_{eff,\,1/2}$ = 2.99 mT, which is much higher than the half field value of B_1 = 0.93 mT derived from the behavior of $k_{\pm}$. Furthermore, **Figure 50** (B) depicts a purely phenomenological way of determining the half field value of the coherent processes by assessing the middle of the decay signals between 0 and 8.0 mT, which results in the very similar value of $B_{eff,\,1/2}$ = 3.3 mT.[56, 60]

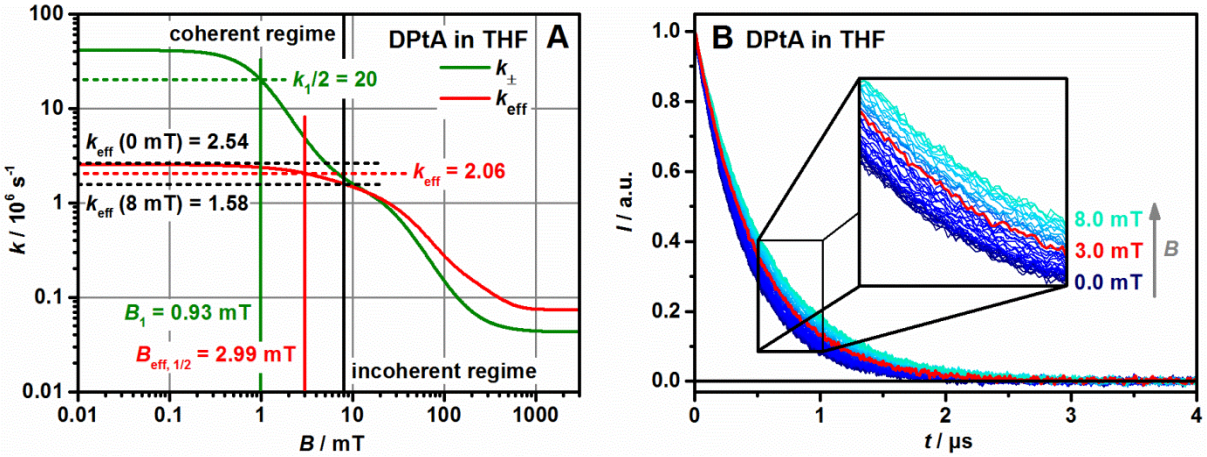

Figure 50: Magnetic field dependence of $k_{\pm}$ (green) and k_{eff} (red) for **DPtA** in THF. The mathematical methodology for the determination of B_1 and $B_{eff,\,1/2}$ is indicated graphically. The arithmetic mean of the extremes of k_{eff} in the coherent regime can be found at a magnetic field of $B_{eff,\,1/2}$ = 3.36 mT (A) By a pure phenomenological way, a very similar half field value can be determined from the signal intensity of the decay curves between 0 – 8.0 mT.

The methodologies for the determination of $B_{eff,\,1/2}$ described in **Figure 50** were applied to all investigated samples and lead to the values summarized in **Table 9**. It seems that the mathematically determined values of $B_{eff,\,1/2}$ vary over a greater field range than the values determined directly from the signal intensity. This is most likely due to the approximate character of equation (20) on which the mathematical method is based. Nevertheless, the mathematic determination has the advantage that its accuracy is not limited by the step size of the magnetic fields, as is the case for the phenomenological determination. A replacement of equation (20) with a numerically determined relation between k_{eff} and $k_{\pm}$ would lead to more consistent values of $B_{eff,\,1/2}$. Furthermore, the purely phenomenological approach is much more susceptible to systematic errors since the assessment of the middle of the signal intensities is bound to be somewhat subjective. Nevertheless, both

methodologies yield values for $B_{eff,½}$ which, in almost all cases, agree much better with the theoretical half field value of the ihfc as estimated from the hyperfine coupling constants of the radical centers by equation (16), than the values determined for B_1 from the behavior of $k_{\pm}$.

Only the measurements in pTHF are an exception to this rule. Here, $B_{eff,1/2}$ is much higher than for all other solvents and differs significantly from $B_{hfc,1/2}$. This is of course due to the superposition of coherent and incoherent spin interconversion, which makes the separation of the magnetic field range into a coherent and an incoherent regime obsolete. Furthermore, the higher values for $B_{eff,1/2}$ in pTHF, especially the ones determined directly from the signal intensity, indicate a stronger MFE on the decay at low fields. This is caused by a reduction not only of the ihfc but also the incoherent relaxation processes at low magnetic fields. In all other solvents the incoherent spin interconversion is influenced only at significantly higher magnetic fields as will be discussed in the next passage.

Table 9: Magnetic half field values characteristic for the isotropic hyperfine coupling as determined from the behavior of $k_{\pm}$ (B_1), from the hyperfine coupling constants of the radical centers ($B_{hfc,1/2}$) and from direct observables of the magnetic field dependent measurements ($B_{eff,1/2}$).

sample		B_1 /mT[a]	$B_{hfc,1/2}$ /mT[b]	$B_{eff,1/2}$ /mT[c]	$B_{eff,1/2}$ /mT[d]
DIrA	**MeCN**	0.68	2.50	2.23	2.6
DPtA	**MeCN**	1.25	2.50	3.87	3.0
	THF	0.93	2.50	2.99	3.0
	pTHF	0.95	2.50	4.49	5.0
DPdA	**THF**	0.93	2.50	2.56	3.0
	pTHF	0.94	2.50	4.38	5.0

[a] determined by equation (15); [b] determined by equation (16); [c] determined as shown in **Figure 50** (A); [d] determined as shown in **Figure 50** (B).

Incoherent spin interconversion

As outlined in chapter 1.1.2, the incoherent spin interconversion is due to a variety of mechanisms which enable a relaxation of the spins. The contribution of the g-tensor anisotropy is negligible in the present case since the g-values of the radical centers should not differ greatly from 2.0023, the typical value for aromatic radicals. For the same reason spin rotational interactions (sri) can also be neglected since they would require a significant deviation of the g-tensor components from the g-value of the free electron.[68] Lastly, the contribution of electron spin dipolar interactions (esdi) to the incoherent spin interconversion, has to be estimated. In contrast to the bimolecular radical pairs in micellar cages and intramolecular radical pairs with flexible linkers where electron spin dipolar interactions are of significant importance since stochastic motional dynamics often lead to very small distances between the radical pairs, the structure of the investigated triads is rather rigid.[25-26, 32, 35]

Due to the R^{-6}-dependence of the electron spin dipolar interactions and the fixed distance of about 20 Å (exact values can be found in **Table 5**) between the radical centers, the contribution of spin dipolar interactions is estimated to be of insignificant magnitude in the investigated triads.[26, 32, 35]
That leaves the anisotropic hyperfine coupling (ahfc) as the main contribution to incoherent spin interconversion. The second *Lorentzian* in equation (15) describes the influence of incoherent processes on $k_{\pm}$. Therefore, the characteristic parameters k_2 and B_2 can be related to the rate constant k_{rel} which describes the spin relaxation of the radical pair due to the rotational modulation of the ahfc. k_{rel} can be expressed as a function of the hyperfine coupling tensor of the radicals, the *Larmo*r frequency ω_0 of the electron and the rotational correlation time τ_c. Assuming axial orientation of the dominating hyperfine coupling interaction due to the ^{14}N-nucleus of the TAA$^{\cdot+}$-radical, the expression for the transversal relaxation time can be transformed to equation (21).[59, 226]

$$k_{rel} = \frac{2}{27}\Delta A^2 \frac{\tau_c}{1+\omega_0^2\tau_c^2} \tag{21}$$

Here, the hyperfine coupling anisotropy ΔA is given in angular frequency units, and the Larmor frequency ω_0 is defined as

$$\omega_0 = \gamma_e B_{rel} \tag{22}$$

and the rotational correlation time can be expressed as

$$\tau_c = \frac{1}{\gamma_e B_{rel}} \tag{23}$$

with the gyromagnetic ratio of the electron $\gamma_e = 1.76 \cdot 10^{11}$ rad·s^{-1}T^{-1}.
Substituting k_{rel} and B_{rel} with the values determined for k_2 and B_2 from the behavior of $k_{\pm}$ one can determine the rotational correlation time and the hyperfine coupling anisotropy of the triads in the respective solvent. The determined data are summarized in **Table 10**. Since these calculations are done under the assumption of a clear separation of coherent and incoherent contributions to the spin interconversion, ΔA cannot be determined for pTHF where this condition is not fulfilled. For the same reasons, the rotational correlation times determined for the molecules in pTHF would be corrupted and thus unreliable since B_2 cannot be determined exactly from the performed measurements. However, the kinetic change caused by the higher viscosity of pTHF should essentially be solely due to an increase of the rotational correlation time of the compounds. If we assume the elongation of τ_c to be described by an elongation factor x, a comparison of the second *Lorentzian* of equation (15) with equation (21) leads to the modified relaxation term (24).

$$k_{\pm,\,\mathrm{rel}}(B,x) = \frac{xk_2}{1 + (xB/B_2)^2} \tag{24}$$

Here, k_2 and B_2 are the values determined for the respective triad in THF, while x is adjusted such that the resulting behavior of $k_{\pm,\,\mathrm{rel}}$ matches the behavior of $k_\pm$ in pTHF. As can be seen from **Figure 51**, this is achieved with x = 26 for **DPtA** in pTHF (A) and with x = 31 for **DPdA** in pTHF (B). With the determined elongation factors, the rotational correlation time of the respective compound in pTHF can be calculated. The resulting values are summarized in **Table 10**.

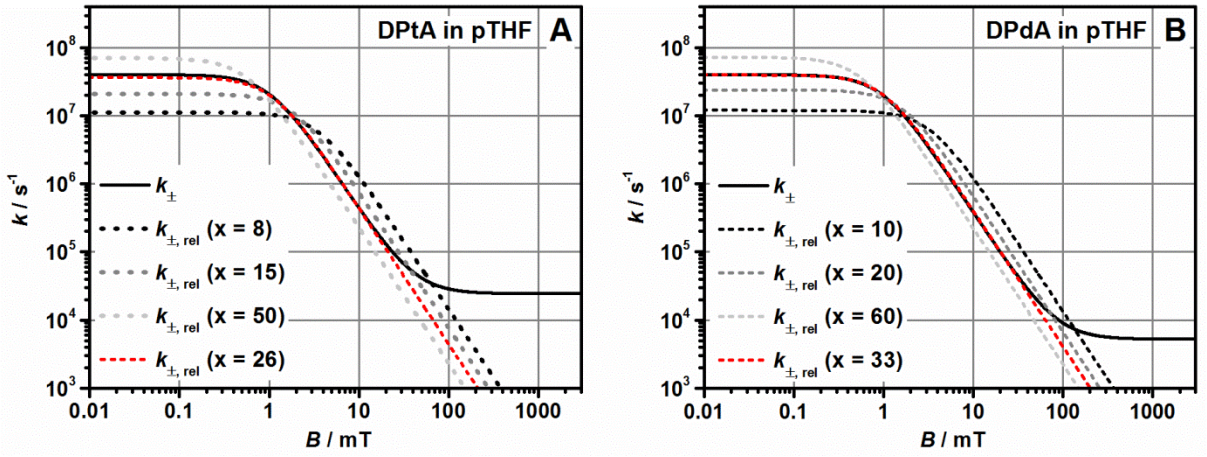

Figure 51: Estimation of the τ_c-elongation factor x for **DPtA** (A) and **DPdA** (B) in pTHF. The solid black curve indicates the behavior of $k_\pm$ as observed in pTHF, while the dotted lines show a transformation of the spin relaxation in THF according to equation (24). Black to light grey dotted curves show the behavior of $k_{\pm,\,\mathrm{rel}}$ for different inadequate factors x, while the red dotted line indicates the right factor x.

To evaluate the quality of the rotational correlation times determined from the spin chemical considerations, the values can be compared to a classical estimation of the molecular rotation based on the *Stokes-Einstein-Debye* (SED)-equation (25). With this equation, $\tau_{c,\,\mathrm{SED}}$ can be estimated from macroscopic values like the solvent viscosity η and the hydrodynamic radii[d] r_{hydro} of the compounds.[227-228]

$$\tau_{c,\,\mathrm{SED}} = \frac{4\pi r_{\mathrm{hydro}}^3}{3k_B T}\eta \tag{25}$$

[d] The hydrodynamic radii were determined by a back calculation of the molecular surface as estimated with the Connolly Molecular Area tool of the ChemBioDraw Ultra 12.0 software to the radius of an ideal sphere. The molecular structures were obtained from DFT-calculations performed by Dr. Marco Holzapfel using *Gaussian09* with the *PBE1PBE* functional, a 6-31G* basis set and pseudo potentials for the transition metal atoms.

Table 10: Hyperfine coupling anisotropy Δ*A* and rotational correlation times τ_c as determined from spin chemical calculations according to equations (21), (23) and (24) as well as rotational correlation times $\tau_{c,\,SED}$ as estimated from a hydrodynamic model according to equation (25).

sample		r_{hydro} /Å[a]	k_2 /$10^6 s^{-1}$	B_2 /mT	ΔA /mT[b]	τ_c /ns	$\tau_{c,\,SED}$ /ns[c]
DIrA	**MeCN**	9.54	1.3	29.1	1.68	0.20	0.30
DPtA	**MeCN**	8.98	0.9	38.6	1.62	0.15	0.25
	THF		1.4	28.7	1.76	0.20	0.34
	pTHF		6.5	0.95	-	5.20	326
DPdA	**THF**	9.00	1.2	33.3	1.75	0.17	0.34
	pTHF		3.0	0.94	-	5.44	329

[a] see footnote "d"; [b] equation (21) yields Δ*A* in rad/s. Division with γ_e gives Δ*A* in T; [c] calculated with viscosity-values of η(MeCN) = 0.343 mPa·s, η(THF) = 0.456 mPa·s, η(pTHF) = 443 mPa·s, at 298.15 K

All determined parameters characteristic for the rotational modulation of the ahfc are collected in **Table 10**. The obtained values for the hyperfine coupling anisotropy are very similar for all samples as was to be expected since the radical pair is comprised of the same radical centers in all compounds. Furthermore, the determined Δ*A* matches well with the, admittedly sparse, data on the hyperfine coupling isotropy for the ^{14}N-nucleus available in the literature. The available studies generally predict Δ*A* to be 2.3 – 2.7 times higher than the respective isotropic hyperfine coupling tensor. With the hyperfine coupling constant of 0.92 observed for the ^{14}N-nucleus in the TAA-moiety used in the investigated compounds this would lead to a value of 2.30·0.92 mT = 2.12 mT, which is very close to the values observed in this study.[59, 224, 229-231]

Concerning the rotational correlation times, a good agreement of the values obtained from the behavior of $k_\pm$ in this work and the values estimated by the *Stokes-Einstein-Debye* -model is found for THF, and MeCN. Furthermore, for compounds of similar size and geometry in solvents of comparable viscosity, the magnitude of the respective values for τ_c is similar as well.

As expected, the rotational correlation times in pTHF are significantly higher than in the solvents of lower viscosity. On the other hand, the correlation times evaluated from equation (23) (τ_c) and from the SED-equation (25) ($\tau_{c,\,SED}$) differ by roughly two orders of magnitude, which is a significantly bigger difference than between the different solvents and complexes. Generally, this could be mainly due to two reasons.

First, the determined rotational correlation time τ_c could be erroneous since equations (21) and subsequently (24) are based on the Redfield theory of relaxation, which (among other) is based on the condition that the spin relaxation is much slower than the rotational perturbation causing it. In other words this means that the observed spin-spin relaxation time, as expressed by the reciprocal of the spin relaxation rate k_{rel} from equation (21) has to be longer than the correlation time τ_c. This so called Redfield limit is known to be broken for spins in solid states but even for liquid solution at low temperatures or high viscosities.[232-233] Since pTHF could easily be of high enough viscosity to violate the Redfield limit, a closer inspection of the validity of the performed calculations is necessary. Applying the hyperfine coupling anisotropy values determined for THF with the rotational correlation times determined for pTHF to equation (21) and forming the reciprocal of the resulting rate constants k_{rel} gives spin relaxation lifetimes at zero magnetic field of 27.2 ns and 26.0 ns for **DPtA** and **DPdA**, respectively. The obtained relaxation lifetimes are obviously longer than the respective rotational correlation times of 5.20 ns and 5.44 ns. Hence, the Redfield conditions are approximately fulfilled even at low fields. With rising magnetic field strengths, the spin interconversion lifetime increases rapidly, leading to an even stricter compliance with the Redfield conditions. For example, at 2.5 mT, the characteristic half field of the coherent ihfc, the spin relaxation lifetime **DPtA** and **DPdA** in pTHF already are 170 ns and 175 ns, respectively, which is certainly on the safe side of the Redfield limit. Thus, the determined rotational correlation times τ_c are deemed valid.

More likely, the correlation times $\tau_{c,\,SED}$ as obtained from hydrodynamic considerations are erroneous. It has been shown that the SED-model works well if the solute is larger than the molecules comprising the solvent, but fails to explain the rotational and diffusional movement of small molecular solutes in polymeric solutions. This is due to a reduced friction between small solutes and solvent molecules of a long chain length. With increasing length of the solvent backbone, the probability for relaxation channels of an applied force, caused for example by the movement of a solute, increases significantly. The relaxation channels are mainly due to torsions of the solvent backbone and can thus accommodate the movement of a small object, but not of a large one. This results in lower solvent viscosities at the nanoscale compared to the macroscopic scale. Since viscosities are usually measured under conditions where the spatial scale of the flow velocity gradient is large compared to the size of the polymer coils, they correspond to the macroscopic viscosity. For the pTHF used in this study, the average degree of polymerization is around 7-8. This results in solvent molecules with an average chain of 38 bonds which is certainly long enough that the rotational correlation time of small molecules like the investigated triads is significantly shorter than predicted by the SED-equation (25).[234-237]

For a more correct description of the relation between the rotational correlation time of small solutes and the macroviscosity of polymeric solvents, a modified version of the SED-equation has been introduced.[235, 238]

$$\tau_c = \frac{\lambda}{6}\frac{4\pi r_{hydro}^3}{3k_B T}\eta + \tau_o \qquad (26)$$

Here, the additional term τ_0 represents the rotational correlation time of the solute in the case of unhindered rotation. Usually, τ_0 is on the order of a few ps and thus does not contribute significantly to the overall correlation time τ_C of the investigated triads in pTHF. The prefactor $\lambda/6$ describes the shape of the rotating particle and the friction between the surface of the particle and the surrounding solvent molecules. The friction can vary between the extremes of "stick-" and "slip-" conditions. Under stick-conditions, the surrounding solvent-molecules rotate with the surface of the solute, while under slip conditions, they are not influenced by the rotation of the solute. For a perfect sphere under perfect slip conditions, the rotational relaxation would be independent from the solvent viscosity and λ would be zero. For a perfect sphere under perfect stick-conditions λ equals 6, leading to the standard SED-equation if τ_0 is neglected. [228, 235] Applying the values for the rotational correlation time τ_C, the hydrodynamic radii r_{hydro} and the solvent viscosity η from **Table 10**, to equation (26) yields values for λ of 3.57 and 3.02 for **DPtA** and **DPdA** in THF, respectively and of 0.10 for both **DPtA** and **DPdA** in pTHF. The values in THF indicate close to stick conditions and deviate from 6 because of the non-spherical shape of the molecules. In pTHF, however, the situation is very close to slip conditions. This agrees very well with the observed diminished increase of the rotational correlation times relative to the huge increase in solvent viscosity from THF to pTHF and thus explains the difference between τ_c and $\tau_{c,\,SED}$ in pTHF.

These results are further supported by studies with epr spin-probes comparable in size to the investigated triads which were performed in THF and pTHF by the group of Prof. Dr. M. Drescher at the University of Konstanz. In these studies, rotational correlation times have been found leading to comparable values for λ and its change from THF to pTHF. Therefore, the presented methods enable the investigation of the nanoviscosity of polymers and oligomers by a spin chemical approach using magnetic field dependent ns-TA spectroscopy. The use of the investigated triads as a kind of nano-viscosimeter is in theory possible if the friction parameter λ is known. This would require a calibration and validation of the method on solvents of known nanoviscosity, that is small molecular solvents where the SED-model holds. Since this process would be very complicated for molecular shapes deviating from a perfect sphere like the investigated triads this was not pursued any further.

High-Field Saturation of $k_{\pm}$

While the influence of the central metal ion on the coherent spin interconversion and the incoherent spin interconversion at low to medium fields was found to be negligible, the high field limit of $k_{\pm}$ as represented by k_0 in **Table 8** is strongly dependent on the central metal ion and decreases from Ir(III) to Pt(II) to Pd(II). Furthermore, it seems to be also dependent on the solvent viscosity, especially for **DPdA**. Since the spin relaxation rate of the radical pair should in theory only be influenced by the radical centers and not by the CMC, this observation is quite unexpected and is not easily explainable. Furthermore, of the aforementioned incoherent relaxation mechanisms, only sri has a magnetic field independent influence on the spin interconversion and could produce a saturation limit of the MFE at high field.[26, 32] The mechanism of the sri is dependent on the difference of the *g*-factors of the radical center and the free electron. The *g*-factors of radicals are directly related to intramolecular SOC effects which generally require the presence of a heavy atom in the radical. For a heavy atom free, organic phenoxazine radical, the spin interconversion rate due to sri has been estimated to be on the order of 10^3 s^{-1}.[26, 35] Since both the TAA- and the NDI-radicals possess *g*-factors between 2.003 and 2.004, the resulting spin interconversion rates due to sri are expected to be on the same order of magnitude.[62, 187] Hence, sri could maybe be responsible for the high field spin relaxation rate of $k_0 = 0.52 \cdot 10^4$ s^{-1} observed for **DPdA** in pTHF, but fails to explain the significantly higher values of k_0 for all other compounds and solvents. Spin relaxation rates at high magnetic fields which are higher than expected have been observed before and where often attributed to be due to a modulation of the SOC by local vibrational motions of the compounds.[35, 59] The proposed SOC-modulation has been described before for trityl radicals bearing thioether-substituents at their aromatic rings, but no further systematic investigations concerning this spin relaxation mechanism seem to be available in the literature.[239-240] Since, for these sulfur substituted trityl radicals the spin-relaxation rates were found to be independent from the solvent viscosity, the SOC-modulation was assigned to be due to local modes with a significant C-S-stretching contribution. However, for **DPtA** and **DPdA** the determined spin relaxation rates at high fields are clearly influenced by the solvent viscosity and can thus not be exclusively due to vibrational modes.[239-241]

An intramolecular movement which could modulate the SOC and therefore cause a magnetic field independent spin relaxation could be a rotation of the NDI and the phenylene-bridge relative to the CMC around the NDI-phenyl-CMC-bond axis. As described before, the bridging phenyl ring is orientated at a torsion angle of nearly 90° to the π-system of both the NDI- and the M-dipyrrinato-moiety and thus acts as a decoupling element. A rotation of the phenylene ring in 5-position is known to occur for a variety of dipyrrinato-compounds.[125, 136, 138-139, 141] In the excited state radical pairs, such a rotation could modulate the electronic coupling between the NDI and the CMC, and therefore the influence of the central transition metal ion on the SOC in the NDI-radical. This

hypothesis would be in line with both the trends observed for k_0. The influence of the central metal atom could be explained with the difference in the SOC-constants of the central metal ion, which decrease from Pt (4481 cm^{-1}) to Ir (3909 cm^{-1}) and Pd 1504 cm^{-1}.[197] Combined with the difference in the complex geometry between the octahedral **Ir** and the distorted quadratic planar **Pt** and **Pd** which could influence the respective SOC as well as the rotation of the phenylene ring, this could be in agreement with the trend observed for k_0.[242] Furthermore, an intramolecular rotational mode should to some extent still be dependent on the solvent viscosity. A slower rotation of the bridging phenyl ring would lead to a decreased modulation of the electronic coupling between CMC and NDI and thus in a reduced modulation of the SOC in the radical. Although this mechanism is purely speculative and cannot be proved purely based on the performed measurements, it would be a decent compromise between the local mode mechanism and the obvious viscosity dependence of k_0.

3.4.4 Conclusions

By means of the classical kinetic model introduced by *Hayashi* and *Nagakura et al.*, the MFE on the charge recombination kinetics of **DIrA**, **DPtA** and **DPdA**, could be described quantitatively.[24-25, 59] The obtained results agree very well with literature known data on **DIrA** in MeCN, thus validating the new measurement-method, data preparation and fitting procedure.[59, 79] In low viscous solvents, all triads show a double *Lorentzian* behavior of the spin interconversion rate $k_{\pm}$ between the outer *Zeeman* levels T_+ and T_- and the inner *Zeeman* levels S and T_0. The first and second *Lorentzian* could clearly be assigned to coherent and incoherent contributions to the spin interconversion, respectively. The coherent spin interconversion was shown to be due to isotropic hyperfine coupling, since it agrees well with theoretical estimations of the magnetic half field value. With rising field strength, the energy difference between the outer *Zeeman* levels and the still degenerate inner *Zeeman* levels rises and the rate of the spin interconversion due to ihfc decreases rapidly. Thus, incoherent spin interconversion processes become the dominating factor at about 5 mT as shown in **Figure 52** (A). Applying 5 mT as the new high field limit of the coherent contribution, the $B_{eff,\,1/2}$-values obtained as described in **Figure 50**, become even closer to the theoretical $B_{hfc,\,½}$-value of 2.5 mT as they decrease from 3.0 mT to 2.2 mT for **DPtA** in THF.[54, 56] The incoherent spin interconversion was shown to be mainly due to rotational modulation of the anisotropic hyperfine coupling of the ^{14}N-nucleous in the $TAA^{\cdot+}$ radical, since the determined hyperfine coupling anisotropy ΔA and rotational correlation times τ_c match very well with literature values and hydrodynamic predictions of the rotational motion, respectively. The ahfc also decreases towards higher fields, and thus the MFE saturates as $k_{\pm}$ approaches its high field limit after around 300 mT. The nature of this saturation could not clearly be explained, although it is most likely due to local molecular vibrational and/or rotational motions which modulate the SOC in the radical pair.[59, 239-240]

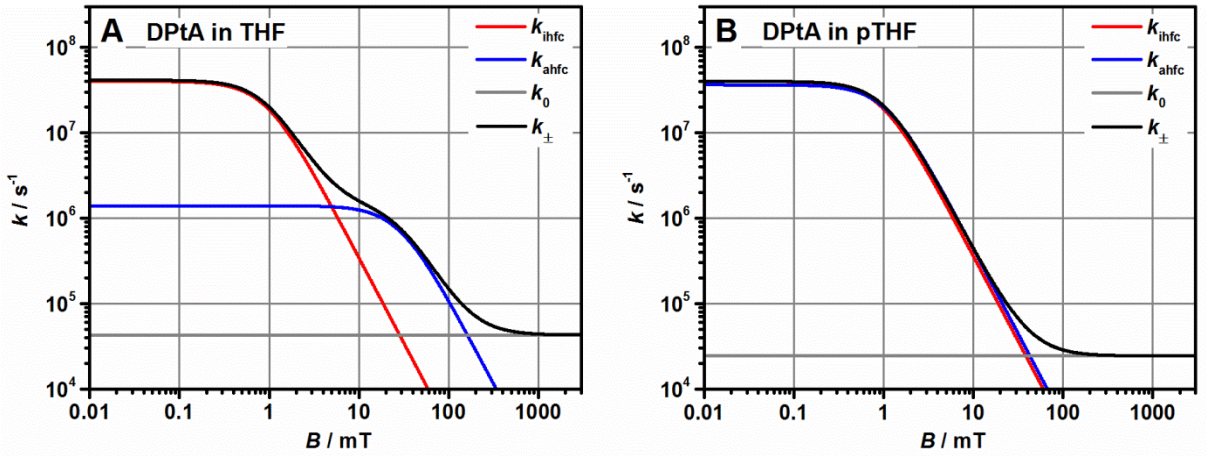

Figure 52: Magnetic field dependence of the relaxation rate $k_\pm$ (black) and magnetic field independent interconversion k_0 (grey), as obtained from a fit of the data to equation (15) as well as of the contribution of the spin interconversion due to coherent ihfc (red) and incoherent rotational modulation of the ahfc (blue) obtained from calculations using equations (15), (21) and(24) with parameters given in **Table 8**, **Table 10** and **Figure 51**, for **DPtA** in THF (A) and pTHF (B).

For the highly viscous solvent pTHF, the two *Lorentzian*s found for low viscous solvents merge into a single step indicating a strong overlap of the coherent and incoherent contribution to the overall spin interconversion. This is caused by a strong increase of the rate of relaxation due to a slowdown of molecular rotation. As can be seen from **Figure 52** (B), the classical kinetic scheme fails at a clear assignment of the contributions of coherent and incoherent spin motion to the overall spin interconversion rate $k_\pm$ since both the interconversion rate due to ihfc (k_{ihfc}) and to ahfc (k_{ahfc}) approach a value of around $4 \cdot 10^7$ s^{-1} at low fields. Since $k_\pm = k_{ihfc} + k_{ahfc} + k_0$ this would amount to a rate of roughly $8 \cdot 10^7$ s^{-1}. This contradicts strongly with an estimation of the spin interconversion between degenerate singlet and triplet sub-levels according to literature, which predicts a rate of about $4 \cdot 10^7$ s^{-1}, which is also supported by the results in low viscous solvents. Nevertheless, the classical kinetic scheme is still applicable for a phenomenological parametrization of the spin interconversion and yields rotational correlation times in pTHF which are only by a factor of 25 times longer than in THF, in contrast to an increase of the macroviscosity of about 3 orders of magnitude. This represents the first investigation of the nanoviscosity of oligomeric and polymeric systems by means of a spin chemical system. For **DPtA**, all results obtained from the classical treatment of the decay curves are supported by full quantum chemical simulations, kindly performed by Prof. Dr. U. E. Steiner at the University of Konstanz and Dr. N. Lukzen at the Novosibirsk State University, which gave essentially the same results.

Except for the saturation limit at high fields, the spin chemistry of the radical pairs is more or less independent of the CMC. Nevertheless, the population of S at time zero (p_S) and the recombination rate from the singlet state (k_S) are strongly influenced by the CMC, resulting in differences in the MFE on the experimentally observed charge recombination kinetics.

3.5 Conclusion and Future Outlook

In this chapter, the photophysics of a series of cyclometalated dipyrrinato-metal complexes was investigated by means of optical steady state and transient absorption methods. It turned out that the UV/Vis-absorption and emission of the metal-dipyrrinato-moiety can be modified by a variation of the central transition metal ion from Ir(III) to Pt(II) and Pd(II) without influencing the electronic or spectroscopic properties of donor- or acceptor- moieties attached to the complexes. While this indicates a strong decoupling of the different subunits, in polar solvents the emission of the complexes was quenched upon substitution with the NDI-acceptor.

As was confirmed by ns- and fs-transient absorption spectroscopy, this is due to an electron transfer from the excited central metal complex to the NDI, forming a charge separated state labeled as CSS_1. In the triads, a further electron transfer from the TAA-donor to the oxidized central complex forms a second, charge separated state labeled CSS_2. While these two successive charge separation processes occur very fast in the Iridium-complexes, they are significantly slower in **DPtA** and **DPdA** due to a much more complex reaction sequence in the central complexes, which complicated the interpretation of the fs-TA spectra considerably. A combination of an overall slower charge separation and the manifold deactivation pathways accessible in the Pt(II) and Pd(II)-complexes due to the complicated reaction sequence results in substantially lower quantum yields of CSS_2. Excitation at the NDI-core was shown to produce the same charge separated states, but with even lower quantum yields, even for **D_2IrA'** which comprised a modified acceptor moiety designed to prevent the partial deactivation of intermediate states after excitation of the NDI. This could be explained by a slight modification of the previously proposed charge separation reaction sequence. Additionally, the fs-fluorescence could clarify the occurrence of the observed dual luminescence of **Pd**, which is due to a fast fluorescence which occurs parallel to the ISC. The occupied LC-triplet state deactivates partially by phosphorescence.

The charge separation proceeds differently in all triads since it involves the central metal complexes (CMCs). On the other hand, the properties of the resulting charge separated states are only dependent on the donor and acceptor moieties since the CMCs are not involved directly. Nevertheless, the central metal complex significantly influences the charge recombination kinetics of CSS_2. While the Iridium complexes show lifetimes of around 0.6 µs in MeCN, **DPtA** and **DPdA** show lifetimes of up to 1.8 µs in MeCN. This 3-fold increase in the lifetimes indicates a further influence of the central metal complex on the decoupling of the donor and acceptor moiety. The electronic decoupling is stronger for the d^8-metal ions Pt(II) and Pd(II), either due to electronic reasons or an increased donor-acceptor distance caused by the square planar complex geometries. For all triads, the charge recombination occurs in the *Marcus* inverted region and becomes faster with decreasing

solvent polarity. In toluene, CSS_2 can only be populated from the excited NDI and is too short lived for detection with the ns-setup because it is of higher energy than the ligand centered triplet state of the CMC, which presents another possible deactivation pathway.

Last but not least, the spin chemistry of CSS_2 was investigated in various solvents by magnetic field dependent ns-TA spectroscopy. As can be seen in **Figure 53**, the observed MFE was rationalized using a classical kinetic analysis which gave results in good agreement with established theories for the spin interconversion. The coherent spin flip at low magnetic fields was found to be due to isotropic hyperfine coupling, while at higher fields, the rotational modulation of the anisotropic hyperfine coupling dominates the spin relaxation. Furthermore, various insights on the viscosity dependence of the incoherent spin interconversion as well as the nanoviscosity of polymeric solvents could be drawn. On the other hand, although the observed MFE on the decay kinetics was clearly enhanced for **DPtA** and especially **DPdA** when compared to **DIrA**, the influence of the different CMCs was found to be only indirect for the most part. Only the high field saturation limit of the rate constant $k_{\pm}$ was directly dependent of the central metal complex.

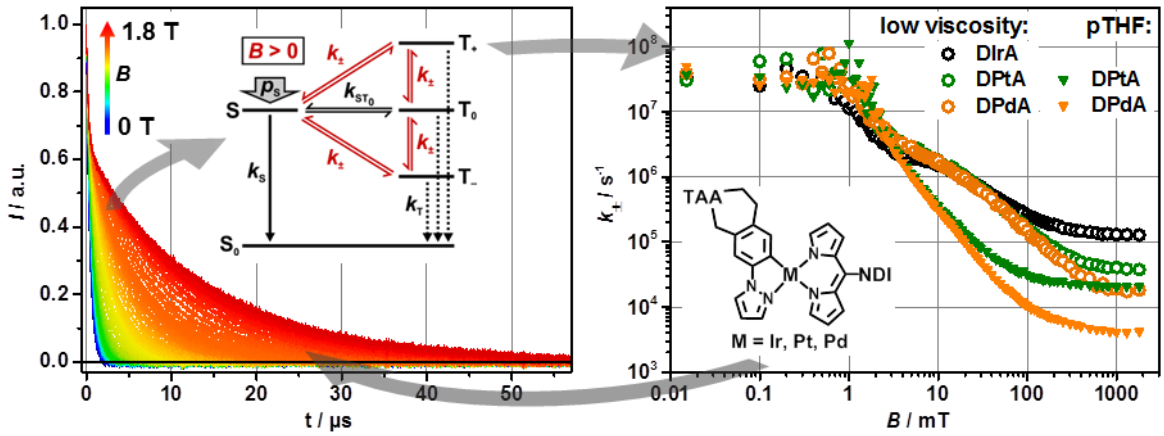

Figure 53: Following the arrows: cyclometalated triads examined in this work, MFE on the decay kinetics of CSS_2 exemplary for **DPtA** in THF, spin chemical model for the charge-recombination of radical pairs and values for of the rate constant $k_{\pm}$ obtained from a classical kinetic analysis of the decay curves in solvents of low viscosity (MeCN for **DIrA** and THF for **DPtA** and **DPdA**) and pTHF.

The saturation of the MFE at high fields is not well understood in the literature. Mechanisms which could result in a magnetic field independent spin interconversion at high fields include the spin rotational interaction and the g-tensor anisotropy, which are expected to be of very low significance in organic radical pairs as the investigated ones since they require a significant SOC in the radical centers.[26, 35] The only possible explanation was the scarcely mentioned local mode mechanism which has not yet been investigated systematically in the literature.[59] The investigated triads could present a valuable chance for such a systematic study. Measurements of the MFE in further

solvents (-mixtures) of steadily varying viscosity could give further insight on the solvent dependence of the high field limit. The local mode responsible for the modulation of the SOC in the radical centers could be identified by comparison of the IR-spectra of the compounds with temperature dependent cw- and pulsed ESR-measurements which were found to give insight on the energy of the responsible mode.[239-240] CIDNP-experiments performed by Prof. Dr. A. Yurkowskaya on the molecules of *Schäfer et al.*[62], gave insight on the influence of nuclei in the periphery of the radical centers on the radical pair. If such measurements revealed a participation of the bridging phenyl unit or even the dipyrrin in the radical pair, the influence of the central metal ion on the SOC of the radical pair could be significant. Lastly, the investigation of the decay kinetics at fields higher than 1800 mT could exclude, support or even spawn further theories on the saturation limit of the MFE, although it is debatable if the possible new insights are worth the huge investment into more powerful magnets.

4 Bisdipyrrinato- and Porphodimethenato-Compounds[e]

4.1 Synthesis

4.1.1 Bisdipyrrinato-Compounds

Retrosynthetic analysis

As shown in **Scheme 14** bisdipyrrinato complexes can readily be prepared from the respective dipyrromethane-precursors and a metal source. If two different dipyrromethanes are used in a one-pot synthesis, a mixture of the two possible symmetric and the one asymmetric complexes is obtained.[160, 243-244] In case of a statistical formation of the possible products, the ratio of symmetric compound A / symmetric compound B / asymmetric compound is 1 / 1 / 2, thus decreasing the maximum yield of the asymmetric complex. However, in this work, the symmetric side products substituted with two donor- or acceptor- moieties can function as reference dyads for the asymmetric donor-acceptor substituted triads. Hence, the statistical formation of the reaction products is acceptable.

Concerning the ligand-precursors, the synthesis of the unsubstituted dipyrromethane **5** and the acceptor-functionalized dipyrromethane **8** has already been described in chapter 3.1.1. Both the shorter and the elongated donor-substituted dipyrromethanes can be prepared by condensation of the respective literature known aldehydes with pyrrole.

[e] Reprinted or adapted in part with permission from:
Photoinduced Dynamics of Bis-dipyrrinato-palladium(II) and Porphodimethenato-palladium(II) Complexes: Governing Near Infrared Phosphorescence by Structural Restriction, S. Riese, M. Holzapfel, A. Schmiedel, I. Gert, D. Schmidt, F. Würthner, C. Lambert, *Inorg. Chem.*, **2018**, *57*, 12480-12488. Copyright 2018 American Chemical Society
Parts of this chapter have been investigated in bachelor theses under the supervision of S. Riese:
Synthese und Untersuchung von Donor-Akzeptor substituierten Metallo-Porphodimethenen, I. Gert, bachelor thesis, Julius-Maximilians-Universität Würzburg, **2016**
Synthesis and characterization of donor-acceptor substituted metal complexes, J. Selby, bachelor thesis, Julius-Maximilians-Universität Würzburg, **2014**

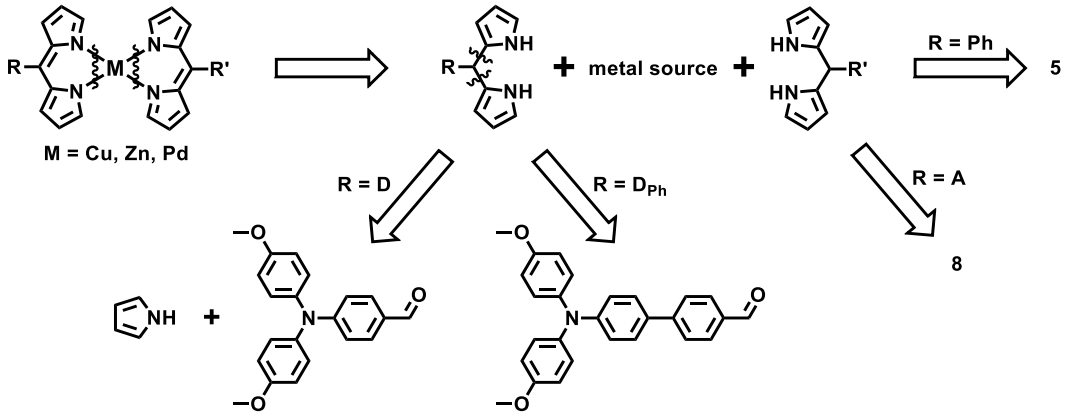

Scheme 14: Retrosynthesis of the target donor-acceptor substituted bisdipyrrinato-metal complexes and the respective references. One-pot synthesis with R = R' = Ph leads to the unsubstituted CMCs, R = R'= D, D_{Ph} and A leads to the reference dyads and R = D, D_{Ph} + R' = A leads to the asymmetric triads

Synthesis of the donor-substituted ligand precursors

The synthesis of the short donor-substituted dipyrromethane **18** is depicted in **Scheme 15**. Ligand-accelerated copper-catalyzed *Ullmann* condensation of commercially available aniline with two equivalents of 4-iodoanisole gave *N,N*-bis(4-methoxyphenyl)aniline **16** in 58 % yield.[245-246] Subsequent *Vilsmeier-Haack* formylation yields 4-formyl-*N,N*-bis(4-methoxyphenyl)aniline in 70 %, which was treated with a 30-fold excess of pyrrole in an acid catalyzed condensation reaction to form **18** in 51 % yield.[177, 246] **18** turned out to be quite unstable in solution and even the pure solid slowly oxidized at rt. Thus, for the purification by flash column chromatography, the silica had to be deactivated with TEA and the pure compound was stored at low temperatures under nitrogen atmosphere to prevent oxidation and decomposition. The instability of the compound was attributed to the strong electron donating effect of the TAA-moiety, making the 5-position of the dipyrromethane extremely electron rich and thus prone to oxidation. This effect has already been observed for 5-(4-aminophenyl)dipyrromethane **7**.[70]

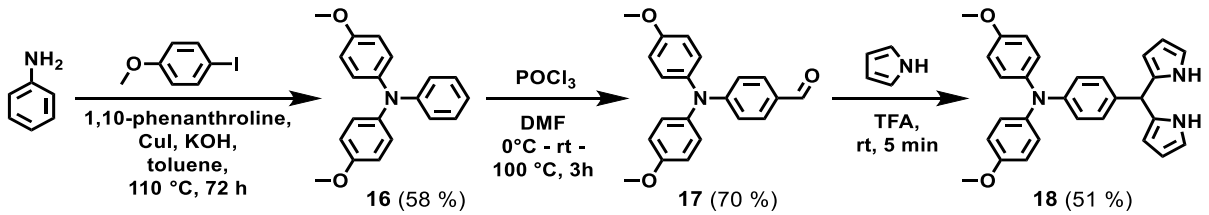

Scheme 15: Synthesis of the short donor-substituted dipyrromethane **18**.

Likewise, the synthesis of the elongated donor-substituted dipyrromethane started with a copper catalyzed *Ullmann* condensation of 4-bromoaniline with two equivalents of 4-iodoanisole to yield 4-bromo-*N,N*-bis(4-methoxyphenyl)aniline **20** in 52 %.[245, 247] As shown in **Scheme 16**, *Suzuki* coupling

of **20** with a slight excess of **19** gives the TAA-substituted benzaldehyde **21** in 86 % yield. The borylated benzaldehyde **19** was prepared beforehand in 97 % yield from 4-bromobenzaldehyde and bis-pinacolatodiboron using the *Miyaura* borylation.[248-250] Again, the last step was the acid catalyzed condensation of **21** with pyrrole, yielding **22** in 57 % yield.[177] Similar to **18**, **21** was found to be unstable in solution and as a solid. Although the instability of the compound was somewhat reduced by the extra phenylene-group between the dipyrromethane and the TAA-moiety, the compound was still purified on deactivated silica and stored at low temperatures under nitrogen.

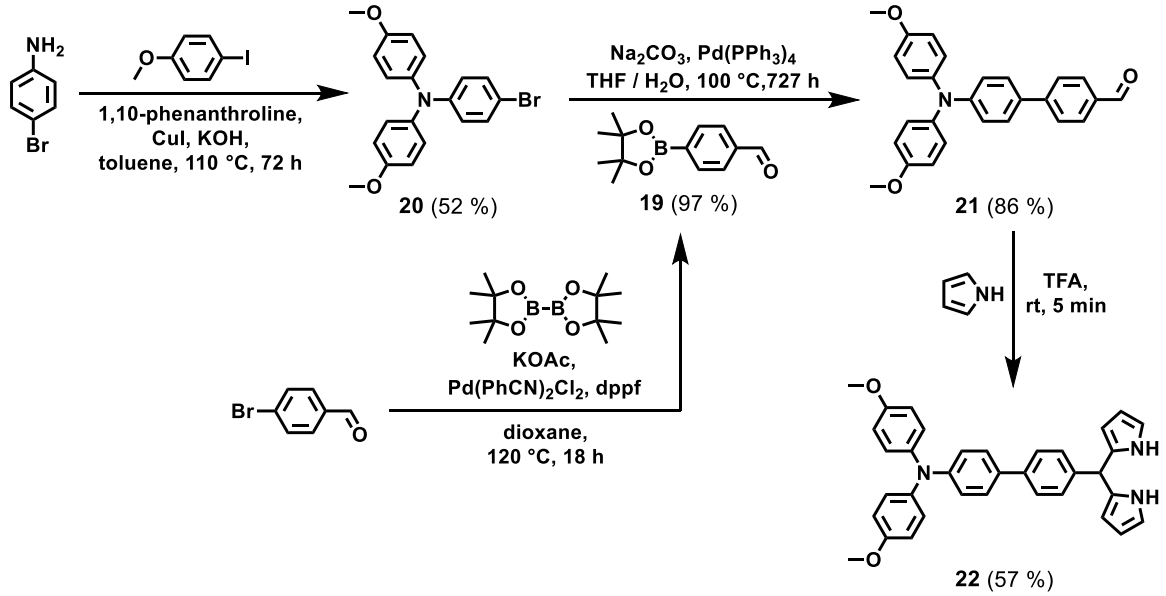

Scheme 16: Synthesis of the elongated donor-substituted dipyrromethane **22**.

Complex synthesis

To minimize the consumption of the more costly donor and acceptor substituted dipyrromethanes, the synthesis of the bisdipyrrinato metal complexes was first tested for the unsubstituted central complexes. As shown in **Scheme 17**, oxidation of the precursor **5** with DDQ, deactivation of excess DDQ with K_2CO_3 and treatment of the resulting mixture with the appropriate metal source and base gave the target complexes in moderate to good yields.[142, 145, 148, 154, 160, 251]

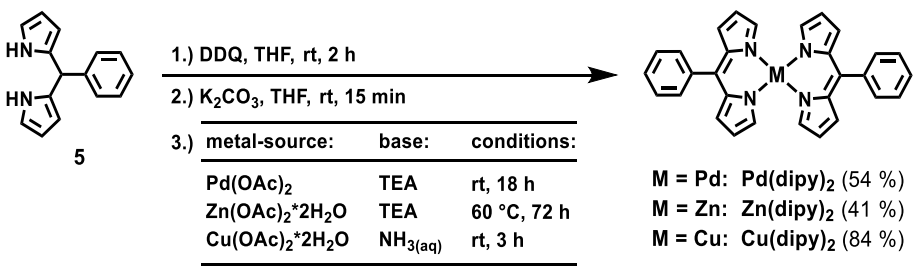

Scheme 17: Synthesis of the unsubstituted bisdipyrrinato-metal complexes **Pd(dipy)$_2$**, **Zn(dipy)$_2$** and **Cu(dipy)$_2$**.

The purification of **Pd(dipy)$_2$** and **Cu(dipy)$_2$** was achieved with flash column chromatography on silica. During the removal of the solvent, **Cu(dipy)$_2$** precipitated from the deep red solution as green metallic crystals which were analytically pure as confirmed by elemental analysis. A more detailed investigation of the compound by NMR-spectroscopy was not possible due to the paramagnetic character of the Cu(II)-central metal ion.

Pd(dipy)$_2$ was further purified by precipitation of a saturated DCM solution into hexanes to give the analytically pure compound as a red crystalline solid. Single crystals suitable for X-ray diffraction were obtained by slow diffusion of *n-hexane* into a concentrated solution in DCM.

The purification of **Zn(dipy)$_2$** was by far the most tedious. Even when using deactivated silica, the complex decomposed during flash column chromatography. NMR spectra indicated demetalation which lead to a contamination of the product fractions with free dipyrrin. After removal of the solvent, the resulting solid was sonicated in MeOH and filtered off to remove the biggest part of the free dipyrrin which, in contrast to the target complex, is soluble in MeOH. The relatively pure compound was then precipitated first from a saturated DCM-solution into MeOH and secondly from a saturated DCM-solution into hexanes to obtain the analytically pure complex as an orange solid.

Next, the same reaction conditions where applied to the synthesis of the short target donor- and acceptor-substituted dyads and triads as shown in **Scheme 18**. One equivalent of both the donor substituted dipyrromethane **18** and the acceptor-substituted dipyrromethane **8** were oxidized together using two equivalents of DDQ. After deactivation of remaining DDQ with K_2CO_3, one equivalent of the appropriate metal acetate and base was added to the crude one to one mixture of the donor- and acceptor-ligands.

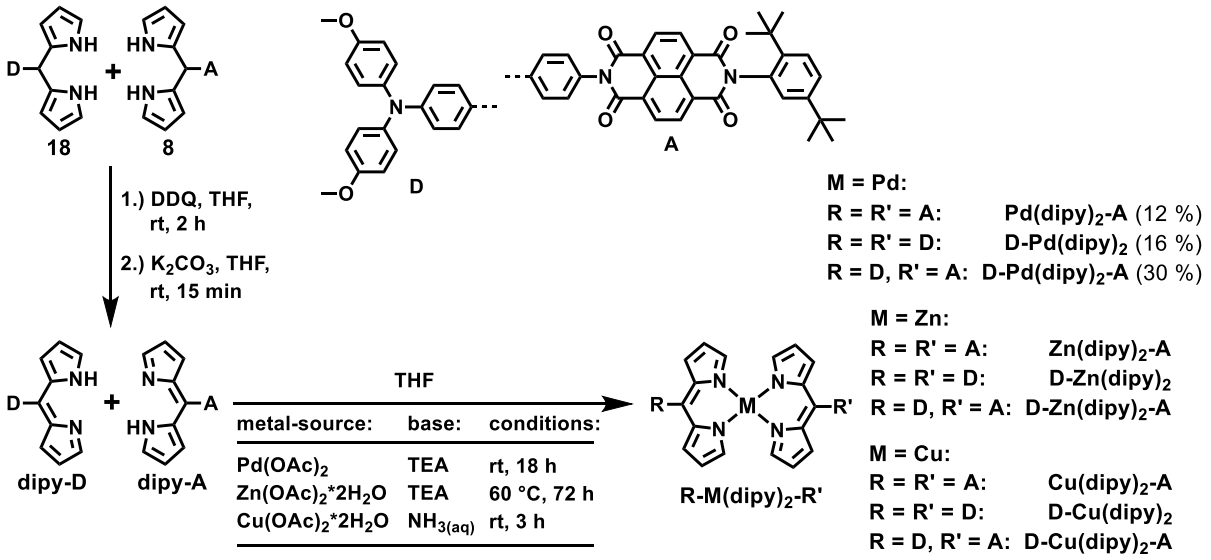

Scheme 18: Synthesis of the donor- acceptor substituted bisdipyrrinato metal triad **D-Pd(dipy)$_2$-A**, the respective reference dyads **D-Pd(dipy)$_2$** and **Pd(dipy)$_2$-A**, as well as the synthesis of their Zn- and Cu- centered derivatives.

After the first work up of the reaction mixtures, the synthesis of all target compounds was proved by mass spectrometry of the crude product mixture. The actual problem was the purification of the compounds. All product mixtures underwent a color change from orange-red to brown during column chromatography, indicating a decomposition of at least one of the involved compounds. The decomposition could have been caused either by a demetalation of the complexes as observed for **Zn(dipy)$_2$**, by oxidation of the TAA-dipyrrinato-moiety similar to the decomposition observed for the TAA-substituted dipyrromethane precursor **18** or a combination of both processes. Furthermore the compounds smeared out considerably during column chromatography, making a clear separation of the different products even more difficult.

Since the degradation of the compounds was the slowest for the Pd-complexes, it could be more or less stopped by the use of strongly deactivated silica and the addition of 2% TEA to the eluent mixture. Finally, the compounds could be separated with Et_2O / cyclohexane mixtures of increasing polarity. While the donor-substituted dyad **D-Pd(dipy)$_2$** was pure, the acceptor substituted dyad **Pd(dipy)$_2$-A** and the triad **D-Pd(dipy)$_2$-A** had to be further purified by GPC in THF. Since the complexes slowly decomposed during the GPC, a direct separation of the compound mixture by GPC was impossible. All target bisdipyrrinato-palladium(II)-complexes were analytically pure after precipitation of saturated DCM-solutions into hexanes. The final yields of 16 % for **D-Pd(dipy)$_2$**, 12 % for **Pd(dipy)$_2$-A** and 30 % for **D-Pd(dipy)$_2$-A** is in relatively good agreement to the statistical ratio of 1 / 1 / 2.

For the Cu-complexes the decomposition could be slowed down significantly by the use of deactivated silica and the addition of TEA to the eluent. Nevertheless, the compounds still smeared out on the column and no clear separation could be achieved. A purification of the compounds by GPC resulted in a relatively quick decomposition of the complexes and thus was not applicable. Since NMR-spectroscopic measurements were prevented by the paramagnetic Cu(II) central metal ion, the purity of all obtained fractions could only be analyzed by elemental analysis which can give no indication of the nature of the impurities and is no indisputable proof of the purity .[154]

Lastly, for the Zn-complexes, every attempt to prevent the decomposition of the compounds failed. While the color change, and therefore the oxidation of the TAA-dipyrrinato moiety, could be slowed significantly by the use of strongly deactivated silica and 2% TEA in the eluent, the complexes still decomposed due to the occurrence of effective demetalation. On the GPC the Zn-complexes decomposed even more quickly than the Pd- and Cu-complexes although the purification of asymmetric Zn-complexes by GPC was reported by *Nishihara et al.*[160, 243]

The quick decomposition of the target compounds was proposed to be mainly caused by the high electron density of the central metal complex due to the strong electronic coupling to the electron donating TAA-moiety. Therefore, the elongated donor-ligand **18** was prepared and the synthesis of the elongated Cu- and Zn-dyads and triads was attempted using the same conditions as shown in **Scheme 18** for the short analogues. Since the elongated TAA-substituted dipyrromethane **18** showed similar signs of decomposition as its short analogue **8**, it comes as no surprise that during the attempted purification of the elongated dyads and triads the same problems as described before for the short ones were encountered and could not be solved. For the described reasons, the synthesis of neither the Zn(II)- nor the Cu(II)-centered bisdipyrrinato triads could be achieved in this work.

4.1.2 Porphodimethenato-Compounds

Retrosynthetic analysis

The synthesis of the porphodimethenato compounds involves considerably more steps than the relatively straight forward synthesis of the bisdipyrrinato-complexes. First, the central 5,15-porphodimethenato-chromophores have to be prepared as shown in **Scheme 19**.

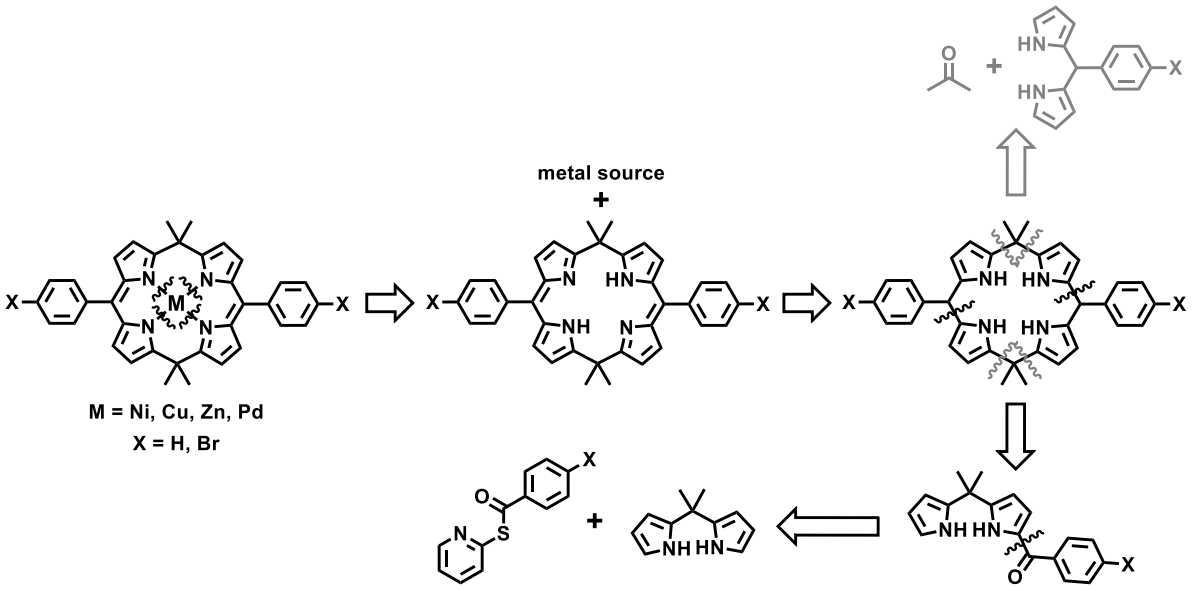

Scheme 19: Retrosynthesis of the target porphodimethenato chromophores (X=H) and the precursors for the synthesis of the donor-acceptor substituted triads (X=Br).

The metal ion can be inserted into the 5,15-porphodimethene (PDM) by reaction with an appropriate metal source. The porphodimethene is obtained by oxidation of the tetrapyrrolic precursor. The tetrapyrrole backbone can be formed using two different approaches.

C-C bond cleavage between two dipyrrin-subchromophores and the respective bridging groups results in a dipyrromethane and a carbonyl compound as precursors. In principle both the depicted

condensation of acetone with the respective 5-phenyldipyrromethane, as well as the condensation of 5,5-dimethyldipyrromethane with the respective aldehyde is possible. While the latter approach incorporates the minimal amount of synthetic steps and the precursors are either commercially available or easily prepared, the condensation is relatively unselective and is expected to result in many side products.[164, 168, 252-253]

Another approach was introduced by *Lindsey et al.*[162] C-C bond cleavage between the 5,5-dimethyldipyromethane subunit and only one of the adjacent benzyl-groups gives a mono-acyldipyrromethane precursor, which can self-condensate to form the tetrapyrrole backbone, thus avoiding some possible side products. The monoacyldipyrromethanes can be synthesized from the literature known 5,5-dipyrromethane and the respective *Mukaiyama* reagent.[254-255]

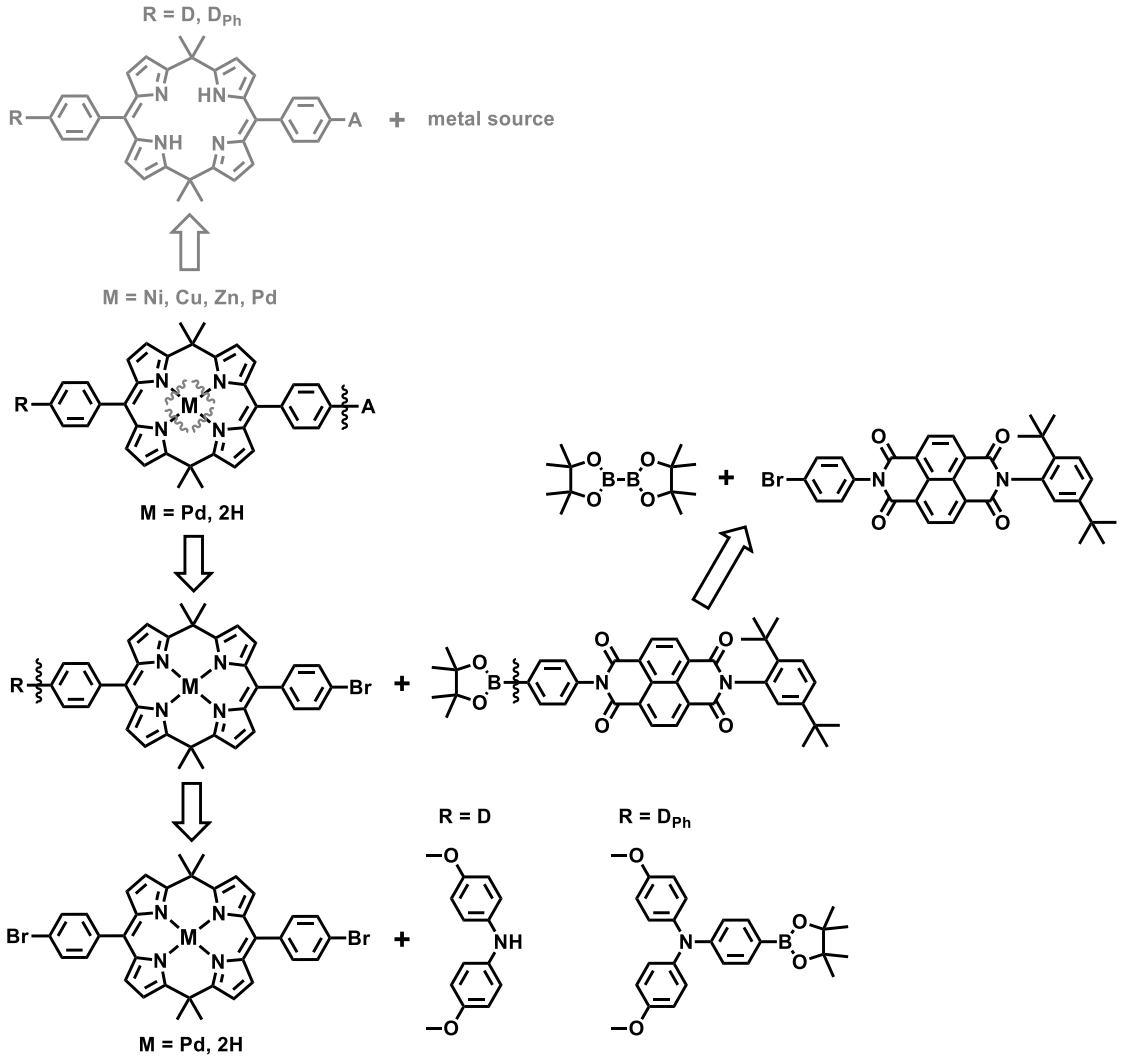

Scheme 20: Retrosynthesis of the target donor-acceptor substituted porphodimethenato triads. Substitution with two equivalents of the donor- and acceptor-moieties with the dibrominated precursor result in the respective reference dyads.

The donor-acceptor substituted triads can be build up by sequential cross coupling reactions as shown in **Scheme 20** by a *Suzuki* coupling from the donor substituted precursor and the borylated NDI acceptor which in turn can be prepared from a literature known brominated NDI by *Miyaura* borylation.[104, 179, 248-250] The donor substituted precursor can be formed by cross coupling of the brominated central porphodimethene to one equivalent of the respective donor moiety that is *Buchwald-Hartwig* coupling to bis(4-methoxyphenyl)amine for the short triads and *Suzuki* coupling to a borylated TAA for the elongated triads. The expected side products which are substituted twice by the respective donor moiety can be used as the donor-reference compounds and thus pose no significant problem.[173, 249-250, 256-257]

The most convenient method would be to first synthesize a purely organic donor acceptor functionalized PDM and then insert the central metal ion in the last step. By this, all target triads could be synthesized using the same synthetic route, only differing in the last step. However, the donor and acceptor substituents could interfere with the metalation reaction or worse, the substituted PDM could be unstable under the conditions applied for the metalation reaction. In those cases, the donor-acceptor-substituted porphodimethenato complexes would have to be obtained by stepwise coupling of the metalated PDM-metal complexes to the donor and acceptor moieties. Since *Lindsey et al.* have shown that bisdipyrrinato complexes of Ni(II), Cu(II) and Zn(II) can interfere with *Suzuki* cross-coupling reactions, the stepwise substitution of a metalated porphodimethene is most likely only available for the PDM-Pd(II) complexes.[145, 167]

Synthesis of the central chromophores

Scheme 21 shows the synthesis of the central porphodimethene chromophore **PDM**, as well as its dibrominated derivative **28**. First, 5,5-dimethyldipyrromethane **23** was prepared in 55 % yield by acid catalyzed condensation of acetone in a 25-fold excess of pyrrole.[177] Secondly, treatment of 2-pyridinethiol with a solution of either benzoyl chloride or 4-bromobenzyol chloride gave the thioesters **24** and **25** in yields of 89 % and 87 %, respectively.[254-255] **24** and **25** served as the *Mukaiyama* reagents for the mono-acylation of **23**. For that, a solution of **23** in THF was treated with 2.5 equivalents of freshly prepared ethyl magnesium bromide (EtMgBr) in THF. Then, a solution of one equivalent of **24** or **25** in THF was added slowly to the reaction mixture at -78° C. After a complete consumption of the starting materials, aqueous work up and purification of the raw product by flash column chromatography yielded the monoacylated 5,5-dimethyldipyrromethanes **26** and **27** in 54 % and 73 %, respectively.[162, 254-255] During this reaction the use of a stoichiometric amount of the *Mukaiyama* reagent and an excess of EtMgBr was applied to ensure a complete consumation of the thioesters, since they are very difficult to separate from the desired monoacylated dipyrromethanes.[254]

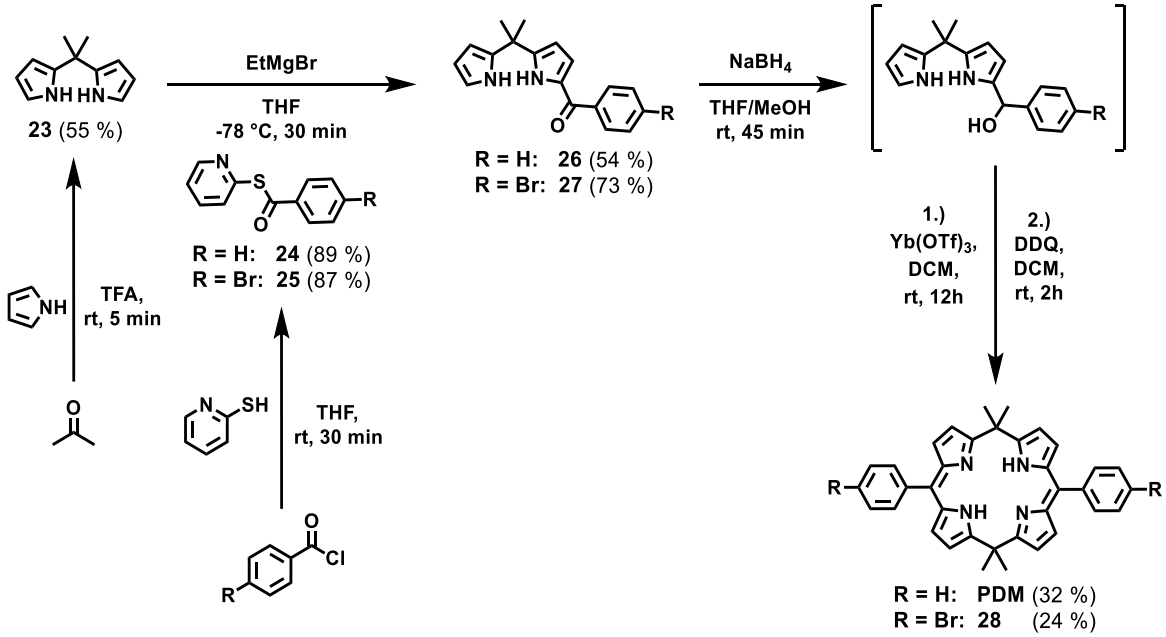

Scheme 21: Synthesis of the reference central porphodimethene chromophore **PDM**, and its dibrominated derivative **28**.

The obtained monoacylated dipyrromethanes **26** was then reduced with $NaBH_4$ in a mixture of THF and MeOH to give the respective monocarbinole which was used without further purification or characterization after a short aqueous work up, due to its instability.[162, 254] The self-condensation of the carbinol was catalyzed by the use of ytterbium(III)-trifluoromethanesulfonate as a mild Lewis acid. Furthermore the reaction was carried out under high dilution to favor intramolecular reactions over intermolecular reactions and thus minimize the yield of linear and higher order cyclic side products. DDQ was added to the reaction mixtures to oxidize the intermediates, the reaction was quenched with TEA and the mixture was concentrated to about 1/10 of its original volume and filtered through a plug of aluminum oxide. Purification of the resulting mixture by flash column chromatography on silica and subsequent recrystallization of the raw products gave the desired central porphodimethene chromophore **PDM** as a purple crystalline solid in 32 % yield and the related cyclic trimer as the main side product in 21 % yield.[162, 254-255]

Application of the same methods to the monoacylated dipyrromethane **27** gave the analogous dibrominated porphodimethene **28** in 24 % yield, which served as the starting material for the synthesis of the donor- and acceptor- substituted dyads and triads.

Although the applied synthetic route involved more steps, and still gave only moderate yields in the last step, this approach was by far more successful than the direct synthesis of the desired porphodimethenes by condensation of 5-phenyldipyrromethane **5** with acetone as well as 5,5-dimethyldipyrromethane **23** with benzaldehyde. In contrast to the literature, the latter reactions gave only trace amounts of the desired product for all performed attempts.[164, 168, 252]

The central porphodimethenato metal complexes were prepared by direct metalation of **PDM**. For this, a solution of **PDM** in a solvent of intermediate polarity were treated with a solution of the respective metal salt in MeOH and TEA as a base, for a varying time at different temperatures as shown in **Scheme 22**. These conditions applied to K_2PtCl_4 to obtain the analogous Pt(II)-complex **PtPDM**, but did not result in the desired compound. [132, 162-163, 167]

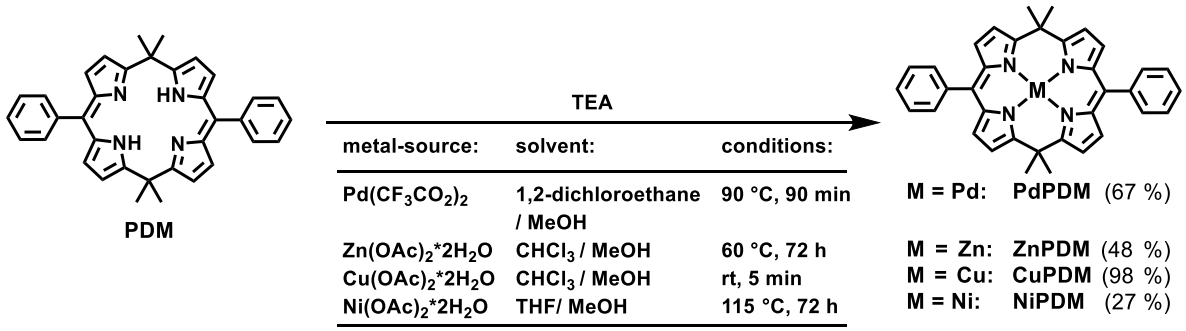

Scheme 22: Synthesis of the central porphodimethenato complexes **PdPDM**, **ZnPDM**, **CuPDM** and **NiPDM** by metalation of **PDM**.

After purification of the raw products by flash column chromatography on silica and subsequent recrystallization from DCM/MeOH, all desired compounds were obtained analytically pure.

A characterization of **CuPDM** by NMR-spectroscopy was not possible due to the paramagnetic nature, thus the purity was only confirmed by elemental analysis.

For **ZnPDM** and **NiPDM**, the purity was confirmed by ^{1}H- and ^{13}C-NMR spectroscopy, but the elemental analysis gave inconsistent results. During the weighing of the samples, an increase of the mass over time was observed, which was attributed to a hygroscopic behavior of the complexes.

For **PdPDM**, the purity was confirmed by ^{1}H- and ^{13}C-NMR spectroscopy as well as elemental analysis. Furthermore, single crystals suitable for X-ray diffraction analysis could be grown by slow diffusion of *n-hexane* into a concentrated solution in DCM.

Synthesis of the building blocks for the cross coupling reactions

Scheme 23 shows the two central chromophores **28** and **Pd-28** needed for the cross coupling reactions leading to the target donor- and acceptor-substituted triads and dyads

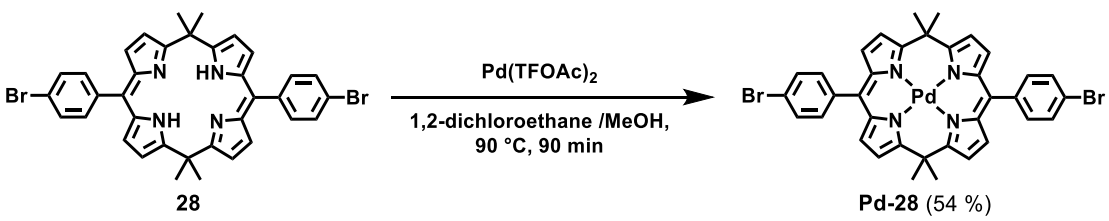

Scheme 23: Metalation of the central chromophore **28** to its Pd(II)-complex **Pd-28**.

Equivalently to the synthesis described in **Scheme 22**, treatment of porphodimethene **28** with palladium(II)-trifluoroacetate gave the porphodimethenato complex **Pd-28** in 54 % yield. The coupling partners for the central chromophores were the borylated donor and acceptor moieties **31** and **32**. Their synthesis is shown in **Scheme 24**. The microwave-assisted one-pot reaction of a stoichiometric mixture of commercially available starting materials gave the asymmetric bromo-functionalized NDI **30** in a satisfying yield of 30 %.[104, 115, 179] The Pd-catalyzed *Miyaura* borylation of **30** with a slight excess of bis(pinacolato)diboron gave the borylated NDI **31** in 71 % yield. Likewise, the borylated TAA **29** was prepared from the brominated TAA **20** in 87 % yield.[248, 250]

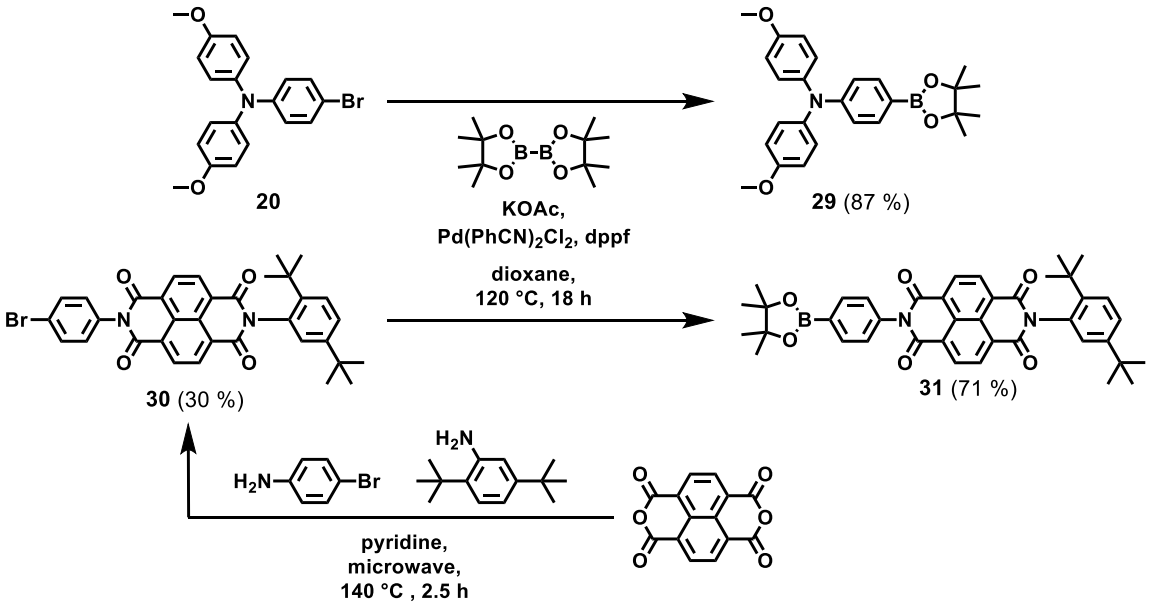

Scheme 24: Synthesis of the borylated building blocks **29** and **31**.

Synthesis of the donor- and acceptor-substituted dyads and triads

From the prepared or commercially available building blocks, the target dyads and triads could be prepared by sequential cross coupling reactions. **Scheme 25** shows the synthesis of the short porphodimethene-triad **D-PDM-A**. *Buchwald-Hartwig* coupling of one equivalent of bis(4-methoxyphenyl)amine to the central chromophore **28** gave a complex mixture of compounds. Beside the expected residual amount of starting material, doubly substituted side product and the desired donor-substituted porphodimethene **32**, a number of additional, unexpected side products were observed. By ^{1}H-NMR-spectroscopy these were later confirmed to be due to the occurrence of debromination during the cross coupling reaction.[173, 257] Unfortunately, the separation of **32** and its debrominated derivative was not possible by flash column chromatography, GPC or recrystallization due to the similar properties and slight instability of the two compounds. Therefore, the exact yield of the reaction could not be determined but was estimated to 30 % by ^{1}H-NMR-spectroscopy. Since the debrominated impurity could not act as a reactant in the following reaction, the contamination

was deemed inconsequential and no further optimization of the synthesis and purification was attempted. *Suzuki* coupling of **32** with the borylated NDI **31** gave the short donor-acceptor-functionalized porphodimethene **D-PDM-A** in 41 % yield.[249-250]

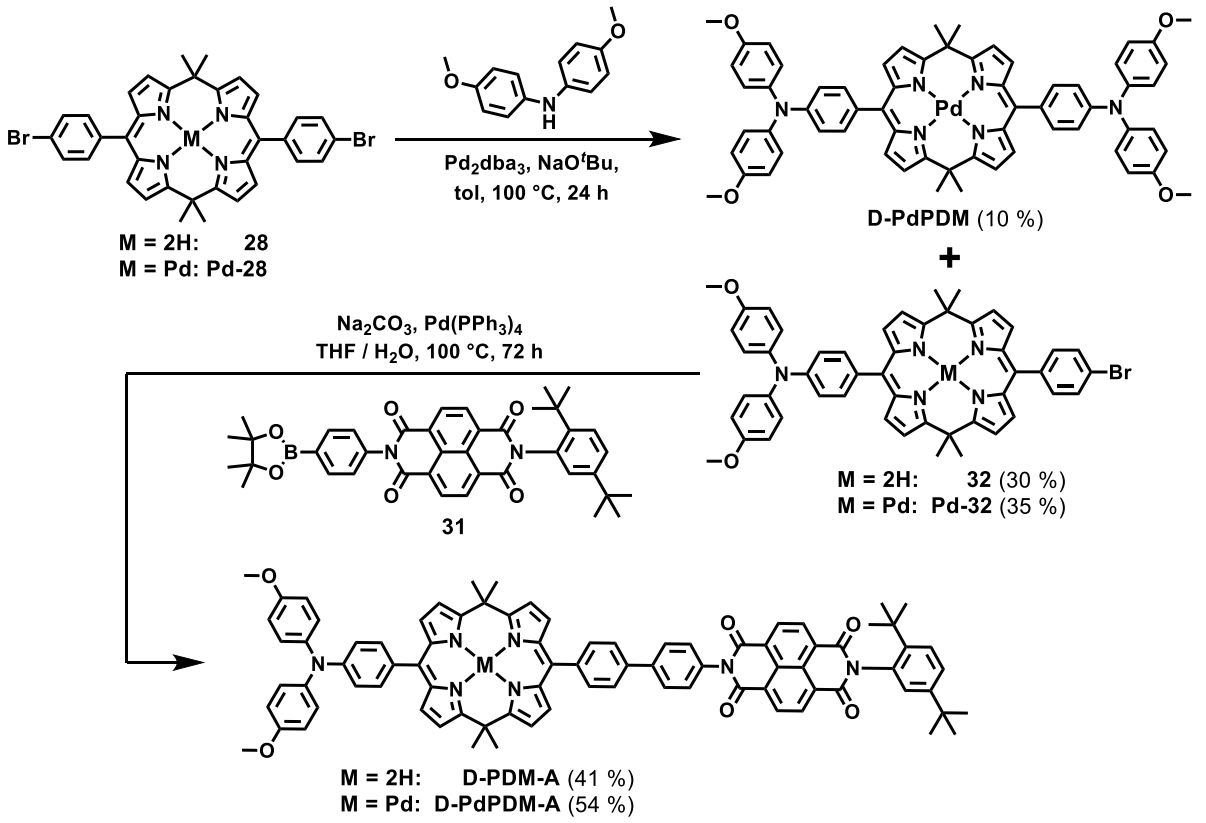

Scheme 25: Synthesis of the short porphodimethene-triad **D-PDM-A** and its Pd(II)-complex **D-PdPDM-A** by consecutive cross-coupling reactions.

The synthesis of the desired porphodimethenato-metal triads by direct metalation of **D-PDM-A** failed for all metals due to the instability of the ligand under all tested reaction conditions. Most likely, an irreversible oxidation of the TAA occurred, since a rapid color-change from red to brownish black was observed upon addition of the metal salts to a solution of the triad. The observed instability was attributed to a strong electronic coupling of the TAA to the electron-rich porphodimethene core. Therefore, only the Pd(II)-triad **D-PdPDM-A** could be prepared equivalently to **D-PDM-A** by consecutive cross coupling reactions starting from the dibrominated porphodimethenato-Pd(II)-complex **Pd-28** as shown in **Scheme 25**. *Buchwald-Hartwig* coupling of one equivalent of bis(4-methoxyphenyl)amine to **Pd-28** gave the donor-substituted porphodimethenato-Pd(II)-complex **Pd-32**. Again, a debromination was observed, although to a somewhat lesser extent. The yield of **Pd-32** was estimated to 35 %. Furthermore, the doubly donor-substituted dyad **D-PdPDM** could be isolated in 10 % yield. Finally, *Suzuki* coupling of **Pd-32** with the borylated NDI **31** gave the short donor-acceptor-functionalized porphodimethenato-Pd(II)-complex **D-PdPDM-A** in 54 % yield.[173, 249-250, 257]

The related elongated triads were prepared in a very similar way as shown in **Scheme 26**. *Suzuki* coupling of the brominated central chromophores **28** and **Pd-28** with one equivalent of the borylated TAA **29** gave the elongated donor-substituted porphodimethene **33** and its Pd(II)-complex **Pd-33** respectively. As for the *Buchwald-Hartwig* coupling for the short donor-substituted compounds, a debromination of the central chromophore occurred parallel to the cross coupling reaction. Again, the debrominated side products could not be separated from the desired compounds by conventional methods. The yields were thus estimated by ^{1}H-NMR-spectroscopy to be around 25 % for **33** and 30 % for **Pd-33**. The contaminated batches were used for the second following reaction without further purification. *Suzuki* coupling of **33** and **Pd-33** to the borylated NDI **31** gave the elongated triads **D_{Ph}-PDM-A** and **D_{Ph}-PdPDM-A** in yields of 38% and 33 %, respectively.[249-250] Although the electronic coupling between the TAA-donor moiety and the central porphodimethene should be weaker in the elongated triad, an irreversible oxidation of the TAA during the tested metalation reactions was observed nonetheless. Again, this prevented an easy synthesis of donor-acceptor substituted triads with central metal ions other than Pd(II) and no further attempts for the synthesis of the respective Zn(II), Cu(II) and Ni(II) complexes were made.[145]

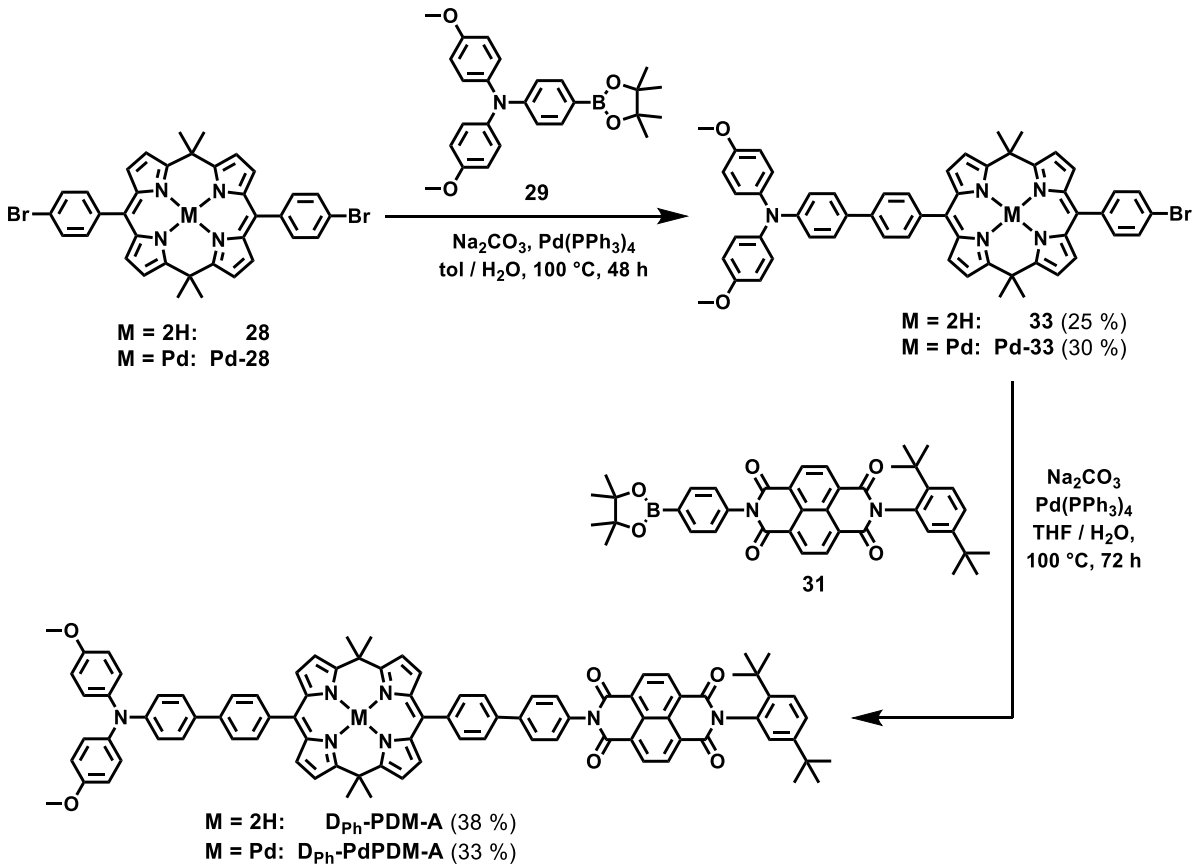

Scheme 26: Synthesis of the elongated triads **D_{Ph}-PDM-A** and **D_{Ph} -PdPDM-A** by two consecutive *Suzuki* coupling reactions.

Lastly, the acceptor-substituted porphodimethenato-palladium(II) dyad **PdPDM-A**, which served as a reference for both the short as well as the elongated Pd(II)-triads **D-PdPDM-A** and **D_{Ph}-PdPDM-A**, was prepared in 26 % yield by a *Suzuki* coupling of **Pd-28** with two equivalents of the borylated NDI **31** according to **Scheme 27**.[249-250]

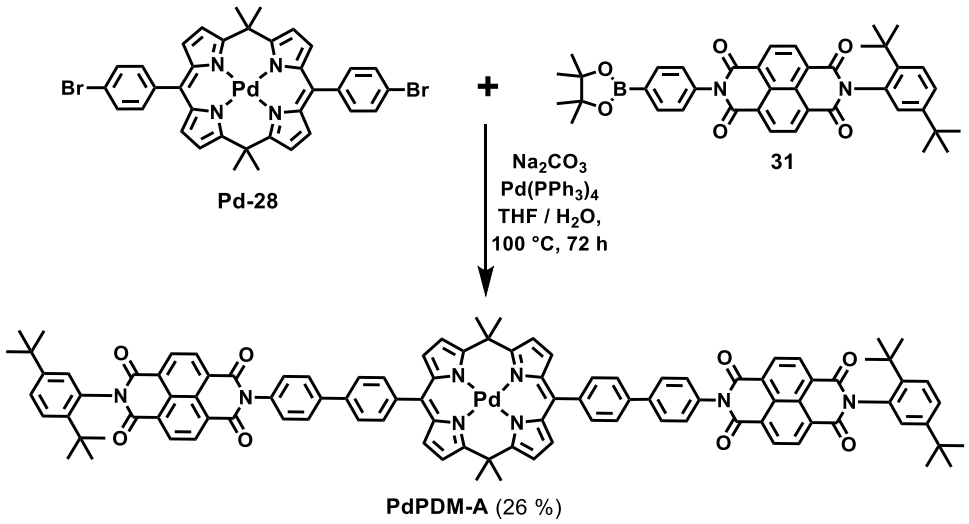

Scheme 27: Synthesis of the acceptor-substituted reference dyad **PdPDM-A**.

All described triads and dyads were obtained analytically pure after column-chromatography on silica, subsequent GPC in THF and further purification by precipitation from DCM into *n-hexane*. The purity was confirmed using ^{1}H- and ^{13}C-NMR-spectroscopy, as well as elemental analysis.

4.1.3 Short Conclusion

As was already mentioned throughout this chapter, not all reference compounds and possible triads were obtained. For the bisdipyrrinato-compounds this is mainly due to synthetic difficulties. A one-pot approach gives a statistical mixture of three compounds which was not separable for the Zn(II) and Cu(II) complexes due to the instability of the compounds. A stepwise cross coupling of the central bisdipyrrinato-metal complexes to the donor- and acceptor-moieties as performed for the porphodimethene-triad was not facile since it is known cross coupling reactions are not tolerant to Zn(II)- and Cu(II)-bisdipyrrinato complexes.[145] For the porphodimethenato compounds, only first attempts of the synthesis were performed in some cases. Therefore, no triads with central metal ions other than Pd(II) were obtained. Furthermore, not all donor- or acceptor-substituted reference dyads were synthesized. This is mainly due to first insights in the photophysical properties of the prepared complexes which will be discussed in next chapters. First, the properties of the central chromophores will be compared in chapter 4.2 , before the obtained dyads and triads will be discussed in chapter 4.3.

4.2 Properties of the Central Chromophores

The properties of the central chromophores were determined by a variety of steady state and time resolved experiments. The results of the different methods will be presented in the following chapters. Since the donor-acceptor substituted bisdipyrrinato complexes of Zn(II) and Cu(II) could not be obtained, a more detailed investigation of the literature known central complexes **Zn(dipy)$_2$**[139, 145] and **Cu(dipy)$_2$**[154] was deemed unnecessary and was not performed. Hence, of the synthesized central chromophores, only the ones depicted in **Scheme 28** will be discussed. They can either be divided into the categories metal complexes and the purely organic chromophores **PDM** and **PDMH$_2^{2+}$**, or into non-bridged bisdipyrrinato-Pd(II)-complex **Pd(dipy)$_2$** and bridged PDM-compounds.

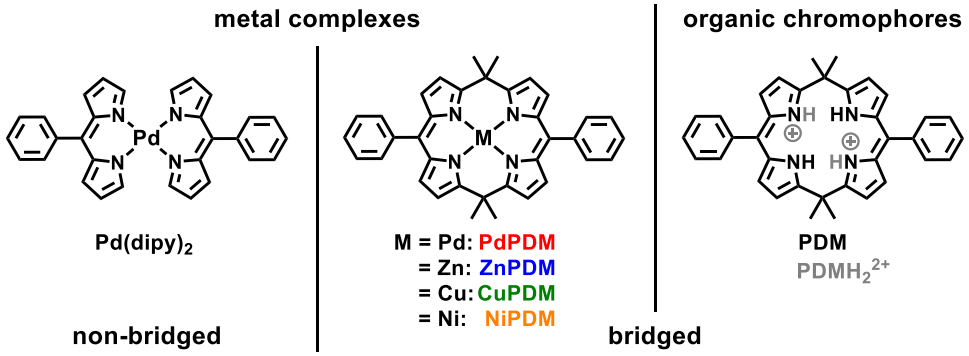

Scheme 28: The novel metal complexes **Pd(dipy)$_2$**, **CuPDM** and **NiPDM**, as well as the literature known but scarcely investigated chromophores **PDM**[253, 258], **PdPDM**[162] and **ZnPDM**.[167] The presented color code will be kept during this chapter.

In the following, the influence of the rigidity of the ligand-framework on the photophysics of the dipyrrin-derivatives will be investigated by comparison of the complexes **Pd(dipy)$_2$** and **PdPDM**. While the dimethylmethylene bridges in **PdPDM** could have a slight direct influence on the properties of the two dipyrrin subunits due to their electron-donating character, their rigidifying effect is expected to be more significant.

Furthermore, the influence of the central metal ion on the properties of the PDM-compounds will be addressed by comparison of **PDM**, its protonated form **PDMH$_2^{2+}$** and its metal-complexes **PdPDM**, **ZnPDM**, **CuPDM** and **NiPDM**. **PDMH$_2^{2+}$** was only formed *in situ* by addition of HCl in THF during the UV/Vis-absorption spectroscopy and will only be discussed there. Although **PDM**, **PdPDM** and **ZnPDM** are literature known compounds, no systematic study of their photophysics is available, making a new evaluation of their properties expedient.[162, 167, 253, 258] The photophysics of the bridged bisdipyrrinato framework of **PDM**, should be strongly dependent on the central metal ions, since they influence the coupling between the two dipyrrin-sub chromophores and enable additional electronic transitions, most prominently MLCT-transitions.

4.2.1 Single Crystal X-Ray Diffraction

The solid-state structures of **Pd(dipy)$_2$** and **PdPDM** were determined by single crystal X-ray diffraction and are depicted in **Figure 54**. Dihedral angles between planes characteristic for the molecule geometry as well as selected bond lengths are summarized in **Table 11**. For **Pd(dipy)$_2$**, an asymmetric unit cell comprised of two molecules with slightly different geometries was found. Since the differences between the geometries are only on the order of 0.5° for dihedral angles and 0.01 Å for distances, and likely due to crystal packing forces, only one molecule is considered in the following discussion.[142, 157]

Table 11: Dihedral angles *Θ* between characteristic planes as indicated in **Figure 54** and selected bond lengths of **Pd(dipy)$_2$** and **PdPDM** as obtained from single crystal X-ray diffraction.

dihedral angles *Θ* between planes /°	Pd(dipy)$_2$	PdPDM	distances /Å	Pd(dipy)$_2$	PdPDM
1,2	145.9	171.0	**Pd-N1**	2.008	2.013
1,4	160.2	176.8	**Pd-N2**	2.015	2.002
3,4	148.4	158.0	**Pd-N3**	-	2.004
3,6	-	177.1	**Pd-N4**	-	2.009
4,5	173.1	177.3	**N1-C4**	1.393	1.396
6,7		167.0	**C4-C5**	1.406	1.396
7,8		139.3	**C5-C6**	1.399	1.399
4,9 (=4,4')	180	134.4	**C6-N2**	1.399	1.390

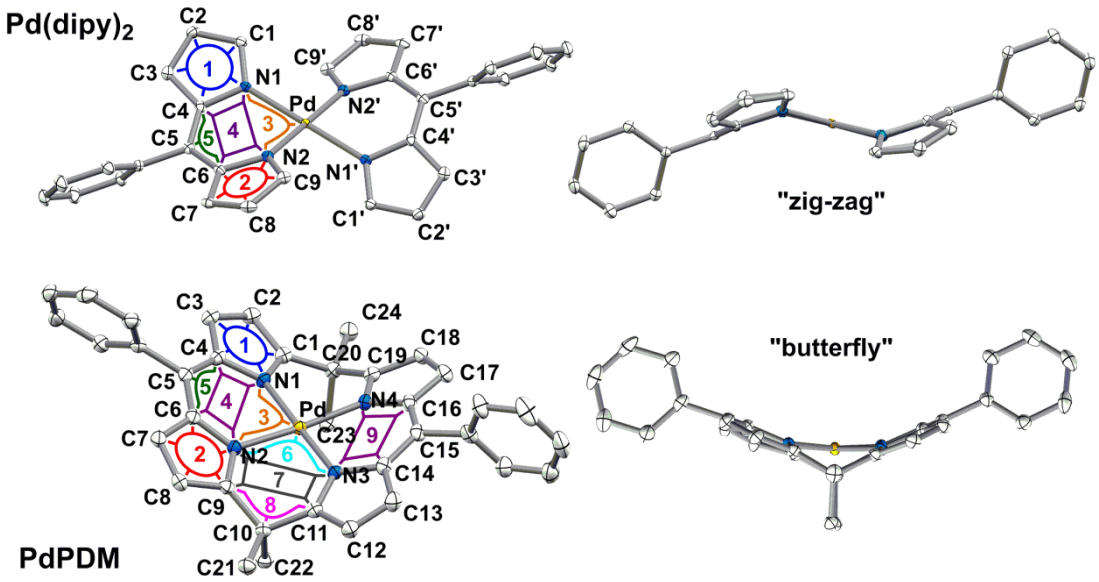

Figure 54: X-ray crystal structure of **Pd(dipy)$_2$** and **PdPDM**. Hydrogen atoms are removed for clarity. Thermal ellipsoids are at 50 % probability level. For **Pd(dipy)$_2$** only one half of the asymmetric cell is shown.

In contrast to its Zn(II)- and Cu(II)-analogues which show tetrahedral or highly distorted square planar structures with planar dipyrrin ligands, **Pd(dipy)$_2$** has a square planar coordination sphere with Pd-N distances of about 2.01 Å. .[145, 154] This results in a centrosymmetric (C_i) geometry, which results in considerable steric repulsion between the hydrogen atoms in C1/C9 position and those in C9'/C1' position. Accordingly, the two dipyrrin ligands are highly bent (dihedral angle between planes 1,2 $\Theta_{1/2}$ = 145.9°) and tilted in different directions relative to the central N_4Pd plane ($\Theta_{3/4}$ = 148.4°) forming a "zig-zag" geometry.

In **PdPDM**, the palladium has a slightly distorted square planar coordination sphere ($\Theta_{3/6}$ = 177.1°) with Pd-N distances of 2.00 – 2.01 Å. Furthermore, the short dimethylmethylene bridges between the two dipyrrin subunits enforce a butterfly geometry of the complex in which the two dipyrrin chromophores are almost planar ($\Theta_{1/2}$ = 171.0°) but tilted away from the central N_4Pd-plane in the same direction. This results in a tilt between the dipyrrin subunits ($\Theta_{4/9}$ = 134.4°), which is in strong contrast to the coplanar arrangement of the two dipyrrin ligands in the centrosymmetric non-bridged complex **Pd(dipy)$_2$** ($\Theta_{4/4'}$ = 180°).

Lastly, the conjugated π-system of the individual dipyrrins seems to be equally delocalized in both complexes as can be seen from the similarly alternating bond-lengths N1-C4-C5-C6-N2 in both complexes.

4.2.2 Steady State UV/Vis-Absorption Spectroscopy

The steady state absorption of the central chromophores was measured in solvents of different polarity (MeCN, DCM and toluene, and in some cases THF). The absorption maxima and extinction coefficients of characteristic bands are listed in **Table 12** for all compounds and solvents. Since the principal results do not differ between solvents, only the measurements in MeCN will be discussed in detail. Afterwards, the solvent dependence of the spectral features will be addressed briefly.

Figure 55 shows the UV/Vis-absorption spectra of **Pd(dipy)$_2$** and **PdPDM** in MeCN. The main absorption bands between 18000 – 23000 cm^{-1} can be assigned to ligand centered π-π*-transitions of the dipyrrin-metal chromophores in the molecules. To the lower energy side a weak but noticeable shoulder can be observed for both complexes. Furthermore, at higher energies between 24000 – 28000 cm^{-1} a pronounced MLCT band is visible.[138, 144-145, 149, 163]

The main spectral differences between the complexes can be explained by exciton coupling theory. The exciton coupling theory describes the interaction of two or more proximate chromophores. In the most simple case the degenerated excited states of two identical chromophores interact forming two non-degenerate excitonic states. One is energetically higher than the original states, while the other is energetically lower. The energy difference is called excitonic splitting and is dependent on the relative arrangement of the coupled transition dipole moments.[149-150, 152-153, 211]

In dipyrrin-chromophores, the π-π*-transition is polarized along the long axis of the chromophore. For the centrosymmetric geometry of **Pd(dipy)$_2$** this leads to a face to face arrangement of the two dipyrrin transitions resulting in an H-aggregate-like exciton splitting where the upper state (labelled $^1LC_2$) is strongly allowed but the lower state (labeled $^1LC_1$) is forbidden.[149-150]

The effect of the exciton splitting becomes particularly clear when comparing the bisdipyrrinato complex **Pd(dipy)$_2$** to its cyclometalated analogue **Pd** which only consists of one dipyrrin ligand and therefore is not affected by excitonic coupling. As can be seen in **Figure 55**, the main LC-transition of **Pd** is located around 20000 cm^{-1}, but no shoulder towards lower energies can be observed. On the other hand, the $^1LC_2$-transition in **Pd(dipy)$_2$** is shifted hypsochromically to around 20900 cm^{-1} and has a nearly two times higher extinction coefficient, while the $^1LC_1$-transition is shifted bathochromic and is only observed as a weak shoulder at around 18500 cm^{-1}.

In **PdPDM** on the other hand, the dimethylmethylene bridges influence the complex geometry and the electronic properties of the adjacent dipyrrin chromophores. Accordingly, both the absorption of the individual dipyrrins as well as the excitonic coupling between the two chromophores is different to the unbridged **Pd(dipy)$_2$**. For **PdPDM**, the influence of the dimethylmethylene bridges results in the observed broader spectrum with smaller extinction coefficients. The higher planarity of the dipyrrin-subchromophores probably cause an additional bathochromic shift of the $^1LC_2$-transition to around 20000 cm^{-1}. The $^1LC_1$-transition is still only observable as a shoulder towards lower energies, but with a smaller bathochromic shift compared to the $^1LC_2$-transition. The decreased energy difference between the $^1LC_1$- and $^1LC_2$-transitions most likely indicates a weaker excitonic coupling in **PdPDM**, which could be caused by the deviation of **PdPDM** from a strictly centrosymmetric geometry

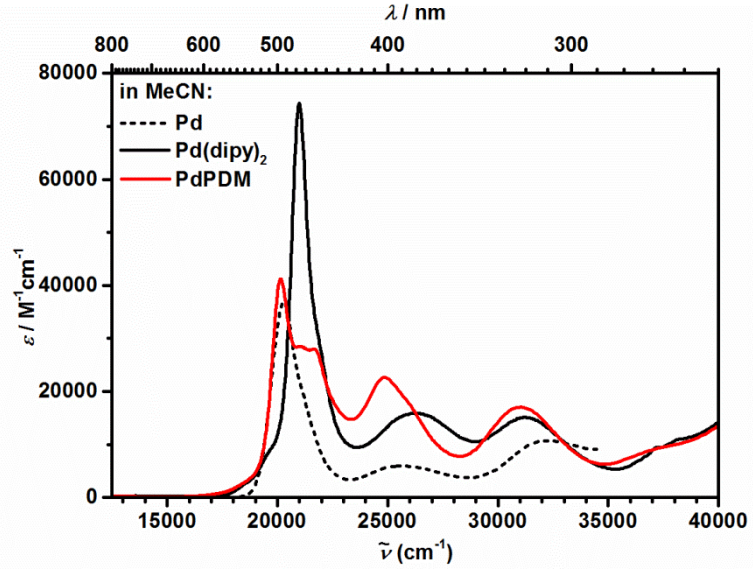

Figure 55: Absorption spectra of the target complexes **Pd(dipy)$_2$** (solid black) and **PdPDM** (red) as well as the cyclometalated monodipyrrinato-reference complex **Pd** (dotted black) in MeCN at rt

While the exciton coupling theory nicely describes the LC absorption, it cannot be applied to the MLCT-transitions since their oscillator strengths are too small to be coupled effectively.[150-151] The different MLCT-absorption characteristics of **Pd(dipy)$_2$** and **PdPDM** are therefore attributed to a stabilization of the dipyrrin-LUMO by the more planar form of the dipyrrin subunits and the electron donating effect of the dimethylmethylene bridges as well as a variation of the Pd(II)-orbital energies due to the slightly distorted square planar ligand field.

Figure 56 shows the stepwise formation of **PDMH$_2^{2+}$** by titration of **PDM** in THF with HCl in THF. Both for **PDM** and for **PDMH$_2^{2+}$** the main absorption bands between 22000 – 25000 cm^{-1} and 20000 – 23000 cm^{-1}, respectively, can be associated with dipyrrin centered transitions. Equivalently to free base dipyrrins, upon protonation the main absorption band becomes more narrow and intense and undergoes a significant bathochromic shift. This is due to the asymmetry of the chromophoric system in the free base dipyrrins. Upon protonation, the pyrrole-rings become equivalent, the delocalization of the electrons is increased and the energy of the main absorption is reduced.[135, 148-149, 154, 253, 259] Additionally, since both **PDM** as well as **PDMH$_2^{2+}$** consist of two dipyrrin subchromophores, exciton coupling occurs, leading to $^1LC_1$-transitions which cause the very broad shoulders towards lower energies. Upon protonation the shoulder becomes more intense since the stronger transition dipole moments in **PDMH$_2^{2+}$** lead to a more effective exciton coupling. Furthermore, it develops a fine structure which cannot be explained based on the performed measurements, but is likely due to a structural modification of the chromophores caused by the steric repulsion between the four central protons. A distortion of the dipyrrin structure is known to influence both the absorption spectra as well as the excitonic coupling between two chromophores.[149, 152-153, 260]

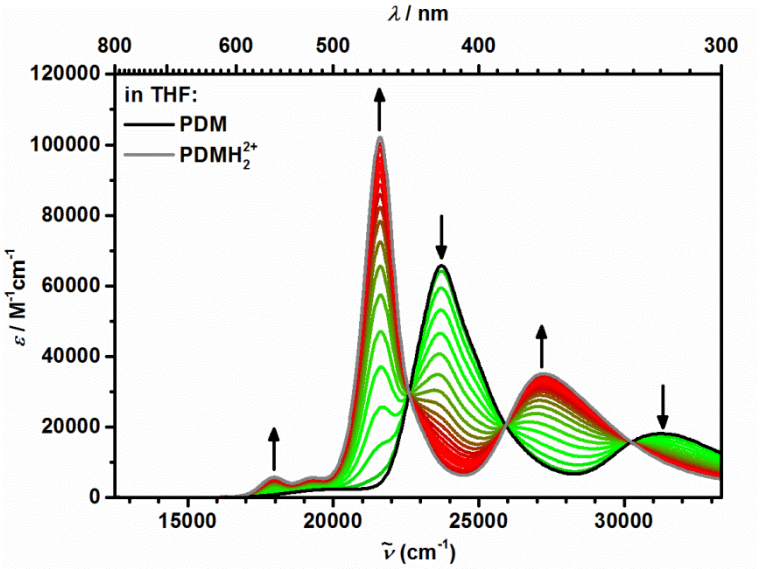

Figure 56: Titration of a solution of **PDM** in THF with HCl in THF (green to red colors) as well as the spectra of **PDM** (black) and **PDMH$_2^{2+}$** (grey) in THF at rt.

Lastly, protonation leads to the development of a new absorption band at higher energies between 25000 – 30000 cm^{-1}. Since this band is only observed for **PDMH$_2^{2+}$** but not for the **PDM**-metal complexes it is most likely due to a significant decrease of the LUMO+1-orbital due to the positive charge and not due to the removal of the asymmetry which is also achieved by deprotonation of **PDM** and complexation of a central metal ion.

Figure 57 compares the absorption spectra of all investigated PDM-compounds. The deprotonation and subsequent complexation of a metal ion during the complex formation also leads to an equalization of the pyrrole-rings, similar to the protonation. Thus, the **PDM**-metal complexes more closely resemble the protonated form **PDMH$_2^{2+}$** than to the free base **PDM**. The extent to which the pyrrole rings are equalized is dependent of the central metal ion as can be seen by comparison of the bond lengths of the dipyrrin backbone as determined from various published crystal structures.[132, 149, 163, 166, 259-260] As for the non-metalated references, the LC-absorption of the complexes can be described by exciton coupling theory. All lowest energy-transitions are due to only partially allowed $^1LC_1$-transitions, while the main absorption bands can be associated with strongly allowed $^1LC_2$-transitions. As mentioned above, the exciton coupling, and thus the observed UV/Vis-absorption, is strongly dependent on the arrangement of the transition dipole moments, which in turn are influenced by the molecular geometry, and thus the central metal ion. On the other hand, the transitions around 30000 – 32000 cm^{-1} are only influenced by the protonation and not by a complexation with a central metal ion. They can most likely be associated with secondary transitions of the porphodimethene chromophores.

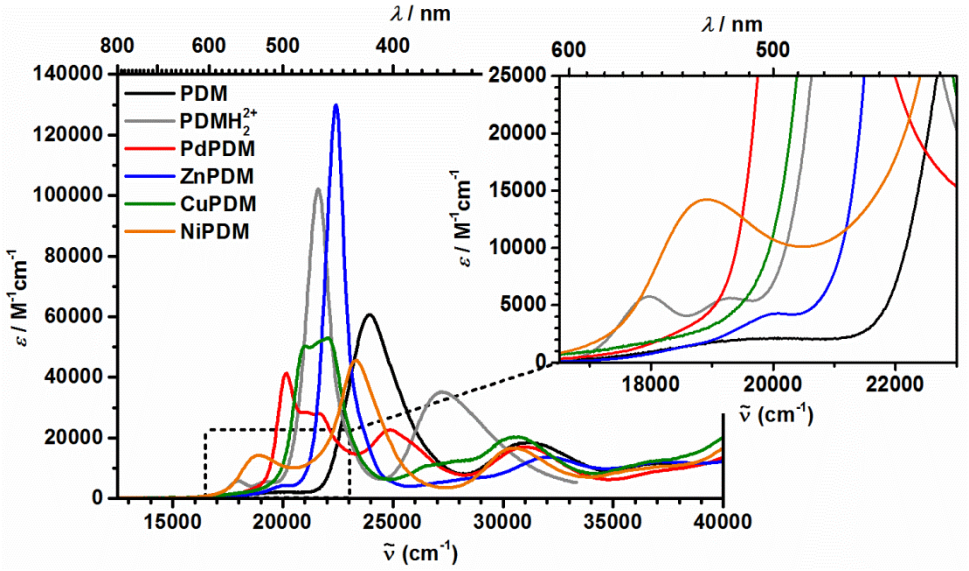

Figure 57: Absorption spectra of the porphodimethene **PDM** (black), its protonated form **PDMH$_2^{2+}$** (grey) as well as its metal-complexes **PdPDM** (red), **ZnPDM** (blue), **CuPDM** (green) and **NiPDM** (orange) at rt. All compounds were recorded in MeCN, except for **ZnPDM** which was recorded in 5 % MeOH in MeCN and **PDMH$_2^{2+}$** which was recorded in THF.

Since **PDM**, **$PDMH_2^{2+}$** and **PdPDM** have already been described in detail above, in the following only the LC-transitions of **ZnPDM**, **CuPDM** and **NiPDM** will be described in greater detail. For none of the PDM-compounds expect **PdPDM**, a MLCT-transition could be observed.

During the measurements on **ZnPDM**, a gradual small change of the UV/Vis-absorption was observed. Over time, the $^1LC_1$-transition at around 20000 cm^{-1} increased in intensity, while the $^1LC_2$-band was shifted slightly hypsochromic from 21800 cm^{-1} to about 22000 cm^{-1} and the full width at half maximum was narrowed by about 300 cm^{-1}. This change was attributed to the ability of **ZnPDM** to form a complex with the residual water present in the used solvents, which would be in accordance to the observations made during the elemental analysis of the compound. While this behavior is not reported in the only reference found on **ZnPDM**, a water-complex has been described for a similar porphodimethenato-Zn(II)-complex without aromatic groups in the 10- and 20-position of the porphodimethene.[163, 167] The change in absorption is due to a planarization of the dipyrrin-sub chromophores by the complexation of a water-molecule, which changes the ligand-field from a square planar one to a quadratic pyramidal one.[163] To ensure that all measurements are performed with a homogeneous sample, for the investigation of **ZnPDM** all solvents were mixed with 5 % MeOH, which also forms a complex with **ZnPDM** and thus saturates the binding site. For that reason, all reported data is actually for the **ZnPDM***MeOH-adduct. This adduct only slightly differs from the reported water-adduct in the intensity of the $^1LC_1$ transition. The huge difference in intensity and the large energetic separation between the two excitonic transitions indicates a nearly perfect H-type arrangement of the dipyrrin-sub-chromophores, which is in agreement with the observed planarization of the complex geometry by the complexation of a solvent molecule.

In **CuPDM**, the $^1LC_1$-transition at 21000 cm^{-1} and the $^1LC_2$-transition at 22000 cm^{-1} seem to have nearly identical intensities which would indicate a weak excitonic coupling. Another explanation would be that both peaks are associated with the $^1LC_2$ transition and that the $^1LC_1$ transition can be associated with the weak and broad shoulder towards lower energies. A reliable conclusion cannot be drawn from the experiments performed in this work.

In **NiPDM**, the $^1LC_1$-transition at 18900 cm^{-1} and the $^1LC_2$-transition at 23300 cm^{-1} are well separated, indicating a strong excitonic coupling. On the other hand, the $^1LC_1$-transition has a considerable intensity and is very broad, which usually is a sign of a weaker excitonic coupling.

The central metal ion not only influences the arrangement of the dipyrrin subunits, but also their planarity and the energy of their frontier orbitals and thus their absorption intensity and energy. Furthermore, the metal ions can directly influence the electronic coupling between the dipyrrin-subunits as will be shown in chapter 4.2.3. Hence, it is very hard to generalize the effect of the central ions and a detailed characterization of the excitonic coupling in the PDM-compounds is not possible from the UV/Vis-absorption alone.

Lastly, it has to be mentioned that in the literature, porphodimethenes are sometimes described not as two individual dipyrrins which are influenced by excitonic coupling, but as a single chromophore. Quantum-theoretical calculations based on this assumption also have to be performed for each porphodimethenato-complex individually, but can explain the absorption characteristics.[132, 165-166]

In conclusion, the main UV/Vis-absorption band of all central chromophores, can be assigned to a ligand centered transition into the first excited singlet-state. From **Table 12**, the solvent dependence of the compounds can be derived. All observed transitions show only negligible solvent dependence.

Table 12: Absorption maxima $\tilde{\nu}_{max}$ (λ_{max}) and extinction coefficients ε_{max} of the characteristic absorption bands of the respective complexes of the Pt- and Pd-series as well as **D_2IrA'**.

	solvent	$^1LC_1$ $\tilde{\nu}_{max}$ (λ_{max}) [ε_{max}] /cm^{-1} (nm) [$M^{-1}cm^{-1}$]	$^1LC_2$[a] $\tilde{\nu}_{max}$ (λ_{max}) [ε_{max}] /cm^{-1} (nm) [$M^{-1}cm^{-1}$]	MLCT $\tilde{\nu}_{max}$ (λ_{max}) [ε_{max}] /cm^{-1} (nm) [$M^{-1}cm^{-1}$]
Pd(dipy)$_2$	MeCN	only observed as low energy shoulders	21000 (476) [74300]	26110 (383) [15800]
	DCM		20800 (481) [77700]	26080 (383) [15200]
	toluene		20800 (481) [82400]	26010 (384) [14900]
PdPDM	MeCN	only observed as low energy shoulders	20200 (495) [35400]	24900 (402) [22600]
	DCM		20000 (500) [44300]	24700 (405) [22700]
	toluene		20000 (500) [49200]	24600 (405) [22600]
ZnPDM	MeCN[b]	20000 (500) [4300]	22400 (446) [129900]	-
	DCM[b]	19900 (503) [3900]	22100 (452) [138300]	-
	toluene[b]	20000 (500) [7700]	22000 (455) [127900]	-
CuPDM	MeCN	21000 (476) [50200]	22000 (455) [53000]	-
	DCM	20900 (478) [51500]	21900 (457) [55600]	-
	toluene	20700 (483) [56200]	21800 (459) [56500]	-
NiPDM	MeCN	18900 (529) [14200]	23300 (429) [45600]	-
	DCM	18800 (532) [15300]	23100 (433) [47500]	-
	toluene	18800 (532) [16100]	23000 (435) [47800]	-
PDMH$_2^{2+}$	THF	18000 (556) [5800]	21600 (463) [102900]	-
PDM	MeCN	20000 (500) [2100]	23900 (418) [61300]	-
	THF	20000 (500) [2400]	23700 (422) [65700]	-
	DCM	20000 (500) [2400]	23600 (424) [63700]	-
	toluene	20100 (498) [2300]	23600 (424) [67700]	-

[a] is the main absorption band in all cases; [b] mixture of the respective solvent with 5% MeOH

4.2.3 Cyclic Voltammetry

The electrochemistry of the central chromophores was investigated by cyclic voltammetry. All measurements were carried out under argon atmosphere at rt in DCM, using TBAHFP at a concentration of about 0.2 M as the supporting electrolyte. All measurements were referenced against the ferrocene/ferrocenium (Fc/Fc^+) redox couple. For each compound, the determined anodic peak potentials E_{pa}^{ox} of the first irreversible oxidation and the half-wave potentials $E_{1/2}$, as well as the potential differences between the first and second reduction are listed in **Table 13**. The respective cyclic voltammograms are shown in **Figure 58**.

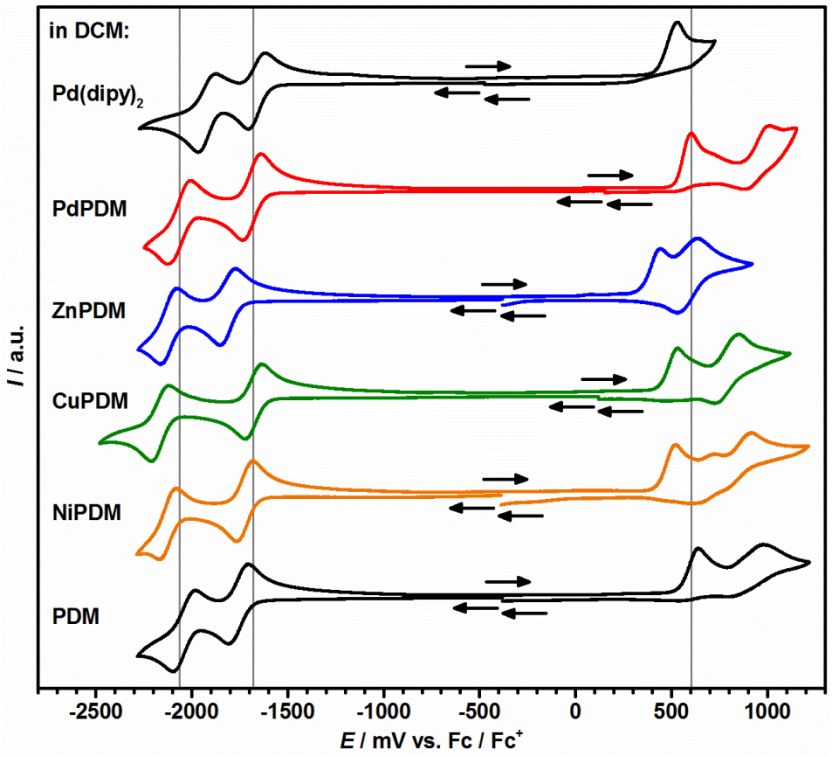

Figure 58: Cyclic voltammograms of the non-bridged and bridged central chromophores in a 0.2 M solution of TBAHFP in DCM at a scan rate of 250 mV s^{-1}. All potentials are referenced against Fc/Fc^+. Black arrows indicate the start, end and direction of the measurement. For better comparison the redox processes associated with **PdPDM** at potentials of –2060, –1680 and 600 mV are highlighted by grey lines.

All compounds show two reductive processes at potentials between –1600 mV and –2300 mV. The reductions are chemically irreversible as proved by multicycle thin layer experiments. Furthermore, a first irreversible oxidation can be observed for all compounds at potentials around 450 – 650 mV. Additional oxidative processes at higher potentials occur for all compounds but will not further be discussed. All observed redox-processes can be associated with the stepwise reduction or oxidation of the two dipyrrin- or dipyrrinato-metal-subunits.[136, 154]

Table 13: Halfwave potentials[a] ($E_{1/2}^{red}$) of the observed reductive processes and the potential difference[a] (ΔE_{red}) between the first and second reduction as well as the anodic peak potentials[a] (E_{pa}^{ox}) of the observed oxidative processes for the central chromophores.

	red 2 $E_{1/2}^{red}$ / mV	**red 1** $E_{1/2}^{red}$ / mV	ΔE_{red} $E^{red2} - E^{red1}$/mV	**ox 1** E_{pa}^{ox}/ mV
Pd(dipy)$_2$	–1920	–1650	270	530
PdPDM	–2060	–1680	380	600
ZnPDM	–2120	–1810	310	440
CuPDM	–2170	–1680	490	530
NiPDM	–2130	–1730	400	520
PDM	–2040	–1760	280	640

[a] referenced against Fc/Fc^+ at a scan rate of 250 mV s^{-1} in a 0.2 M solution of TBAHFP in DCM at rt

Since the dimethylmethylene bridges in **PdPDM** have an electron donating character compared to the protons located at the equivalent positions in **Pd(dipy)$_2$**, they should decrease the oxidation potentials and increase the reduction potentials. Instead, a bridging of the dipyrrin subunits shifts the first oxidation potential to higher potentials from 530 mV to 600 mV, indicating a slight stabilization of the HOMO for **PdPDM**. On the other hand the first reduction, stays nearly constant with potentials of –1650 mV and –1680 mV, respectively. This is due to the fact that the electron donating effect of the bridging units is compensated by the planarization of the dipyrrin subunits. Furthermore, the influence of the Pd(II)-ion on the frontier orbitals is different for both complexes due to the slightly modified coordination sphere, which is distorted more strongly and exhibits overall shorter Pd-N distances in **PdPDM** (see **Table 11**).

Comparing the porphodimethenato compounds, the free base **PDM** exhibits an oxidative potential of 640 mV. Upon complexation of a central metal ion, the oxidation is shifted to lower potentials. While this shift is very significant for **ZnPDM** which has an oxidation potential of only 440 mV, it is less pronounced for **CuPDM** and **NiPDM** (530 mV and 520 mV, respectively) and only weak for **PdPDM** (600 mV). The reduction potentials on the other hand show a less clear behavior upon complexation with a metal ion. Compared to the potential of –1760 mV in **PDM**, they are shifted to lower potentials for **ZnPDM** they are shifted to a lower potential of –1810 mV, while they are shifted to higher potentials for **NiPDM** (–1730 mV), **CuPDM** (–1680 mV) and **PdPDM** (-1680 mV). The effect of the central metal ion on the HOMOs and LUMOs can most likely be attributed mainly to the ability of the central metal to donate or withdraw electron density. The s^0d^{10}-ion Zn^{2+} has the most valence electrons, which is consistent with a reduction of the reductive and oxidative potentials. Cu^{2+} and Ni^{2+} on the other hand introduce less electron density into the complex and can stabilize more oxidation states than Zn^{2+}, thus increasing the reduction and oxidation potentials. Although Pd^{2+} and Ni^{2+} are

group 10 elements, Pd^{2+} is of a higher period and thus has an increased relative electron density. Furthermore, Pd^{2+} has a bigger radius than the first row transition metal ions and thus most likely interacts less with the dipyrrinato-ligand due to higher bond lengths to the ligand. The increased bond lengths can be confirmed by comparison of published crystal structures of various porphodimethenato-metal complexes which show average M-N bond lengths of 1.97 Å, 1.98 Å and 1.90 Å for Zn^{2+}, Cu^{2+} and Ni^{2+}, respectively but of 2.02 Å for Pd^{2+}.[132, 163] This is in agreement with the 2.01 Å average Pd-N distance found for **PdPDM**.

Finally, the potential difference between the first and second reduction ΔE_{red}, can give insights into the electronic coupling of the two dipyrrin subchromophores. Since the reduction of the first dipyrrin introduces a negative charge into the compound, it shifts the reduction potential of the second dipyrrin to lower potentials. With values of 270 mV and 280 mV respectively, this shift is the smallest for **Pd(dipy)$_2$** and **PDM**, which should also be the most strongly decoupled dipyrrins since they lack the coupling effect of either the dimethylmethylene bridges or a central metal ion. Consequently, the electronic coupling of the dipyrrin subchromophores should increase with the magnitude of the shift along the line **ZnPDM** (310 mV), **PdPDM** (380 mV), **NiPDM** (400 mV), **CuPDM** (490 mV).

4.2.4 Emission Spectroscopy

The emissive properties of the central chromophores have been investigated in MeCN at rt. Additionally, **Pd(dipy)$_2$** and **PDM** were characterized in THF and toluene at rt and in MeTHF at 77 K. All samples were excited at or near the absorption maximum of the respective chromophore, corresponding to an excitation of the $^1LC_2$-transition and were degassed by purging with dry argon for at least 20 minutes prior to the measurement.[111, 136, 138, 183]

Due to the low emission intensities of the chromophores, the measurements at rt were performed using standard photomultiplier detection which has a high sensitivity but is only usable down to 12500 cm^{-1}, although the emission bands extend significantly below that energy. For **CuPDM** and **NiPDM**, no emission could be observed at all. For most of the other compounds the emission spectra were corrected for the pure solvent background, no lifetimes were determined and the quantum yields are assumed to be significantly below $\Phi = 0.01$ because the intensity of the emissive signals was on the order of magnitude of the *Raman* scattered excitation light.[144, 157] Only for **PdPDM** it was viable to record the full emission spectrum at rt using a nitrogen cooled photodetector and thus determine the quantum yield. To keep the data somewhat comparable, the measurements were performed using samples of similar optical densities at the excitation energy, similar excitation intensities and the same step-size, integration time and repetitions. However, the signal to noise ratio of **PdPDM** is not comparable to all other compounds due to the use of a different detector. All obtained data is summarized in **Table 14**.

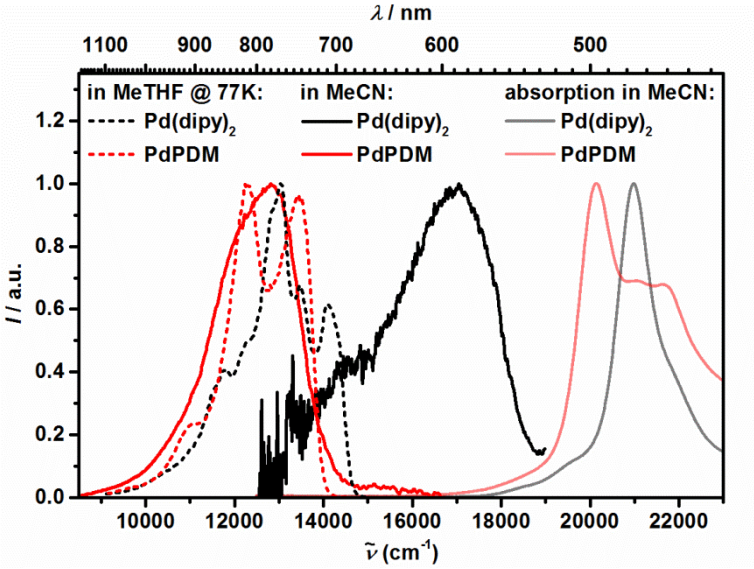

Figure 59: Normalized emission spectra at 77 K in MeTHF (dotted lines) and at rt in MeCN (solid lines) of **Pd(dipy)$_2$** (black) and **PdPDM** (red) in comparison with the respective normalized steady state absorption spectra at rt in THF (pale lines).

Figure 59 shows the emission spectra of the Pd(II)-complexes **Pd(dipy)$_2$** and **PdPDM** at rt in MeCN and at 77 K in MeTHF in comparison with the respective absorption spectra in MeCN. At 77 K in frozen MeTHF both complexes emit strong and structured phosphorescence between ca. 14500 – 9000 cm^{-1} which is distinctly redshifted compared to the emission of similar cyclometalated mono-dipyrrinato-Pd(II) complexes like **Pd** or its phenylpyridyl equivalent, but otherwise can be associated with a dipyrrin-centered triplet state (^{3}LC) due to its band shape and energy.[115, 117, 136, 138, 157] The emission behavior of the complexes changes dramatically at rt in fluid MeCN. Here, the non-bridged dipyrrin complex **Pd(dipy)$_2$** shows a weak and unstructured emission between 13000 – 19000 cm^{-1} which can be assigned to fluorescence from the ^{1}LC$_2$-state, but no phosphorescence. In contrast, the bridged complex **PdPDM** shows relatively strong but unresolved phosphorescence at the same spectral position as at 77 K, but no fluorescence. The quantum yield of the phosphorescence at rt is 0.01 in MeCN, increases to 0.02 in THF and toluene and is extremely oxygen sensitive. Other than that, the emission of both complexes is virtually solvent-independent.

The vastly different changes in emission-behavior for the two compounds when changing from rt to 77 K is due to a structural rearrangement quenching the phosphorescence of **Pd(dipy)$_2$** at rt, which will be discussed in more detail in chapter 4.2.7. The different possible molecular structures for **Pd(dipy)$_2$** could also explain the differences in the spectral shape of the emission at 77 K. If a stochastic mixture of two or more slightly different structures are present in the rt solution, which then is cooled rapidly to 77 K, forming a glassy matrix, the phosphorescence of the different structures would be superimposed and could lead to the unexpectedly complicated emission band shape observed for **Pd(dipy)$_2$**.

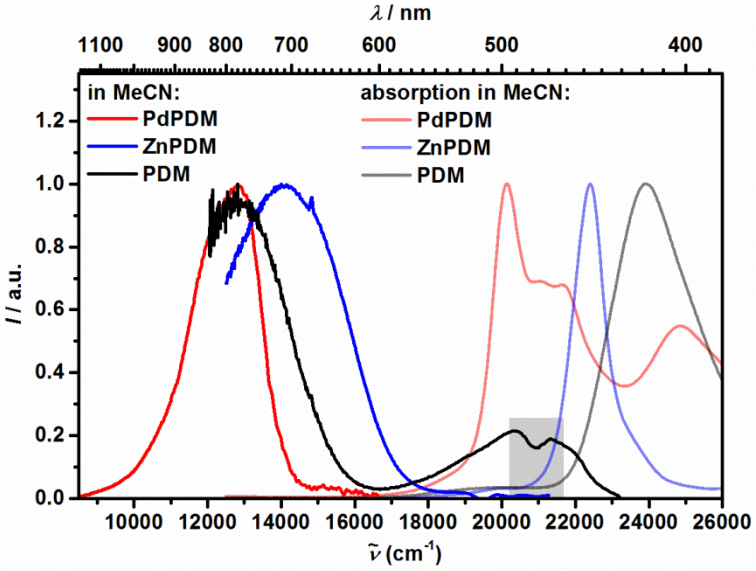

Figure 60: Normalized emission spectra of the **PDM**-based compounds in comparison with the respective normalized steady state absorption spectra at rt in MeCN (5% MeOH for ZnPDM). The fluorescence in the grey shaded area is influenced by *Raman*-scattered excitation light.

Figure 60 shows the emission spectra of the bridged chromophores **PdPDM**, **ZnPDM** and **PDM**. Compared to **PdPDM**, the emission of **ZnPDM** is blue shifted with a maximum at 14100 cm^{-1}. Furthermore, the emission is broadened and significantly less intense. These trends are even more pronounced for **PDM**, which has an emission maximum at around 12900 $cm^{-1}$and an even broader and less intense band shape. Furthermore, for **PDM** a second, weaker emission band can be observed at around 20500 cm^{-1}. The shape of the second band is influenced by *Raman*-scattered excitation light which could not be completely compensated by the background correction for pure solvent. Based on the difference between the *0-0*-transition energies of the absorptive and emissive transitions, and the unresolved band shapes, the lower energy emission bands are associated with phosphorescence, while the high energy emission of **PDM** should be due to fluorescence. Apparently an ISC from the exited singlet states to more stable triplet states is possible in porphodimethenato compounds. While this ISC is slow in the purely organic **PDM**, which thus shows a dual luminescence, the ISC rate is increased due to the heavy atom effect of the central transition metal ions in **ZnPDM** and **PdPDM**, which thus show only phosphorescence.

For a deeper insight on the origin of the emission, the emission lifetimes need to be determined. This was not possible directly for any of the compounds. For **PDM** this is due to the very low emission intensities, while the fluorescence lifetime of **$Pd(dipy)_2$** is too short for the used ns-set-up and the phosphorescence lifetimes of **PdPDM** and **ZnPDM** are so long that even the moderately intense emission of **PdPDM** is distributed over such a long lifetime that it becomes indistinguishable from the noise of the single photon counting detector. Instead, the excited state lifetimes were determined by ns-transient absorption spectroscopy and will be discussed in the next chapter.

Table 14: Emission maxima $\tilde{\nu}_{max}$ (λ_{max}) of characteristic emission bands and emission quantum yields Φ for the central chromophores in different solvents at rt and MeTHF at 77 K after excitation at or near the maximum absorption (see **Table 12**).

	solvent	fls. $\tilde{\nu}_{max}$ (λ_{max}) /cm^{-1} (nm)	phos. $\tilde{\nu}_{max}$ (λ_{max}) /cm^{-1} (nm)	quantum yield Φ
Pd(dipy)$_2$	MeTHF (@ 77 K)	-	13100 (763)	-
	MeCN	17100 (585)	-	<< 0.01[a]
	THF	17100 (585)	-	<< 0.01[a]
	toluene	17000 (588)	-	<< 0.01[a]
PdPDM	MeTHF (@ 77 K)	-	12300 (813)	-
	MeCN	-	12800 (781)	0.01
	THF	-	12800 (781)	0.02
	toluene	-	12800 (781)	0.02
ZnPDM	MeCN[c]	-	14100 (709)	<< 0.01[a]
PDM	MeCN	≈ 20500 (488)[b]	12900 (775)	<< 0.01[a]

[a] estimated by comparison with the *Raman* scattered excitation light and the literature[144, 157]; [b] a precise determination was prevented by *Raman* scattered excitation light, [s] mixture with 5% MeOH

4.2.5 ns-Transient Absorption Spectroscopy

ns-Laser-flash spectroscopy was performed in MeCN for all central chromophores and THF and toluene for the bridged and non-bridged Pd-complex. All compounds were excited at or near their absorption maximum, corresponding to an excitation of the $^1LC_2$-transition. All samples were degassed with a stream of argon for at least 30 minutes prior to measurement to ensure a correct determination of the excited state lifetimes in an oxygen free environment.[28-29, 179] To exclude bimolecular reaction pathways, all compounds were measured at different concentrations and excitation intensities. All acquired data is summarized in **Table 15**. **Pd(dipy)$_2$** exhibited monoexponential lifetimes at all concentrations, while **ZnPDM** gave biexponential lifetimes for all tested conditions. For **PdPDM** in MeCN a concentration dependence was observed, yielding biexponential lifetimes at high and monoexponential lifetimes at low concentrations. Thus the biexponential lifetimes were attributed to a bimolecular deactivation pathway due to stacking of the molecules. In the following only the monomolecular deactivation will be discussed. For **PDM** and its Cu(II)- and Ni(II)-complexes, no transient signals can be observed. While this is most likely due to a very fast deactivation of the excited state within the instrument response of about 7 ns for **CuPDM** and **NiPDM**, **PDM** exhibits phosphorescence and thus should be detectable with ns-TA spectroscopy. It is proposed that for **PDM**, the phosphorescent triplet state is formed only to such small amounts that the resulting transient signal is virtually indistinguishable from the noise of the set-up.

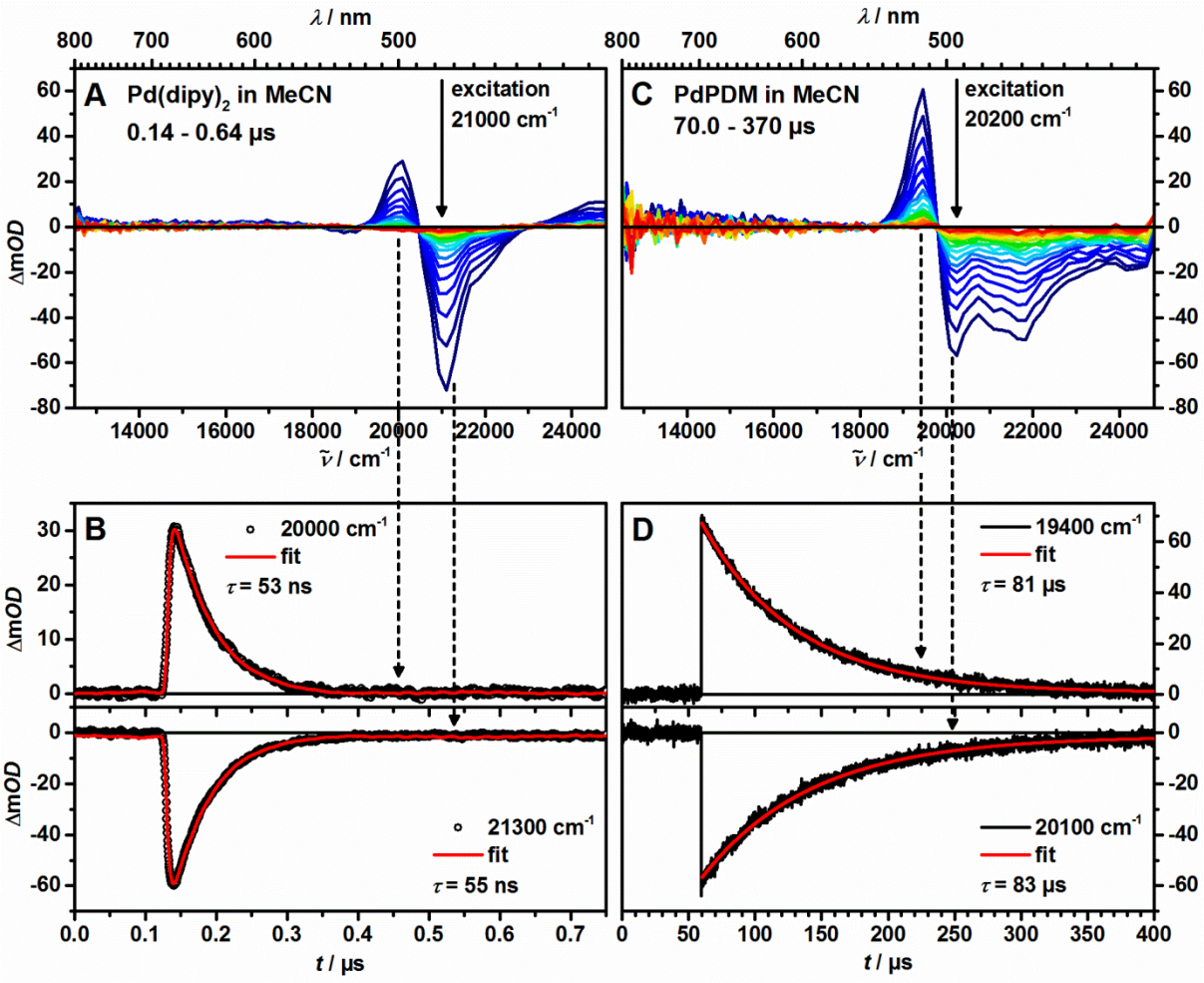

Figure 61: ns-Transient absorption spectra of **Pd(dipy)$_2$** and **PdPDM** in MeCN at rt after excitation at 21000 cm^{-1} and 20200 cm^{-1}, respectively (A and C) and kinetic traces with monoexponential fit at selected wavenumbers (B and D). Early spectra are depicted in blue to green and later spectra in orange to red color.

Figure 61 shows the ns-transient absorption spectra of **Pd(dipy)$_2$** (A) and **PdPDM** (C) after excitation of the $^1LC_2$ transition. Both complexes show ground state bleaching (GSB) at 21300 cm^{-1} for **Pd(dipy)$_2$** and 20100 cm^{-1} for **PdPDM** as well as a distinct excited state absorption (ESA) at lower wavenumbers of 20000 cm^{-1} and 19400 cm^{-1}, respectively. Equal monoexponential decay kinetics of the ESA and the GSB confirm the spectra to be due to a single excited state for both complexes. Furthermore, the rise of the transient signals is immediate on the ns-timescale. Most importantly, the kinetic traces gave excited state lifetimes of 53 ns for **Pd(dipy)$_2$** and 81 µs for **PdPDM**. This huge lifetime difference can be attributed to the structural confinement of **PdPDM** which is also the reason for the increased emission intensities and will be discussed separately in chapter 4.2.7. The transient absorption of both complexes is relatively solvent-independent. For **Pd(dipy)$_2$** a slight increase of the excited state lifetimes with increasing solvent polarity can be observed, while **PdPDM** shows considerably longer lifetimes of 363 µs in THF and 257 µs toluene, but no clear correlation with the solvent polarity.

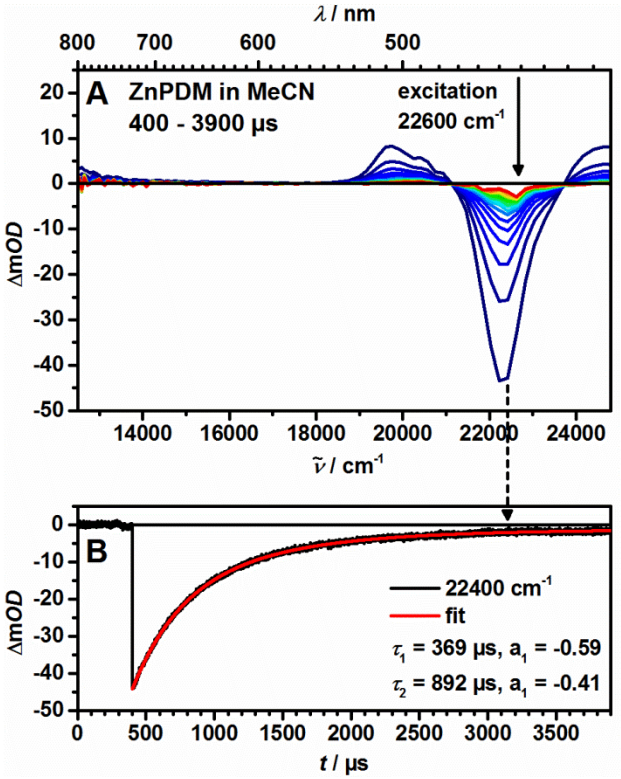

Figure 62: ns-Transient absorption spectra of **ZnPDM** in 5 % MeOH in MeCN at rt after excitation at 22600 cm^{-1} (A) and a selected kinetic trace with biexponential fit (B).

Figure 62 shows the ns-transient absorption spectrum of **ZnPDM** in MeCN. Similarly to the Pd-complexes, **ZnPDM** shows a GSB at 22400 cm^{-1} and a red shifted ESA at around 19800 cm^{-1}. The decay kinetics of the transient signal are biexponential and show huge lifetimes of 369 µs for the short and 892 µs for the long component. The contribution of the two components to the overall decay kinetics is on the same order of magnitude, slightly favoring the short component. At the moment, no explanation of the biexponential decay can be given, although an involvement of the MeOH attached to the Zn(II) central metal ion in the deactivation mechanism is probable.

Table 15: Excited state lifetimes (τ) of **Pd(dipy)$_2$** and **PdPDM** in solvents of different polarity and of **ZnPDM** in MeCN after excitation of the respective $^1LC_2$ absorption band.

	solvent	excited state lifetime τ
Pd(dipy)$_2$	MeCN	53 ns
	THF	68 ns
	toluene	76 ns
PdPDM	MeCN	81 µs
	THF	363 µs
	toluene	257 µs
ZnPDM	5% MeOH in MeCN	369 µs / 892 µs

4.2.6 Conclusions

Based on the discussed measurements, the photophysics of the central metal complexes can be summarized as shown in **Figure 63** and **Table 16**. After excitation of the allowed excitonic state $^1LC_2$, **PdPDM**, **ZnPDM** exhibit a relatively weak emission which is attributed to phosphorescence from a ligand centered triplet state ^3LC due to its big *Stokes* shift, spectral shape and very long corresponding excited state lifetimes. The ISC to the triplet state is assumed to take place from the forbidden $^1LC_1$ state although the internal conversion (IC) between the excitonic states cannot be proved by the performed methods, as it usually is a very fast process. [139, 156, 211, 261]

CuPDM and **NiPDM** are completely non emissive. Some publications report that for dipyrrinato-complexes of fourth row transition metals with only partially occupied d-orbitals, the emission is quenched by a fast non radiative deactivation to the ground state. It is suspected that the same holds true for the related investigated porphodimethenato complexes.[135, 161] This theory is further confirmed by the excited state lifetimes, which are estimated to be significantly shorter than 7 ns since the deactivation of the excited states is faster than the IRF of the ns-setup.

In **Pd(dipy)$_2$** and **PDM**, a very weak emission was observed which was associated with fluorescence due to the relatively small *Stokes* shifts. Since the emissive transition of the $^1LC_1$-state to the ground state is forbidden, the fluorescence has to originate from the allowed $^1LC_2$ state and can thus be quenched by the IC.

Table 16: 0-0-Transition energies of the allowed ($^1LC_2$) an dforbidden ($^1LC_2$) excitonic singlet states and the ligand centered triplet excited state (^3LC) and excited state lifetimes τ of the central chromophores in MeCN at rt.

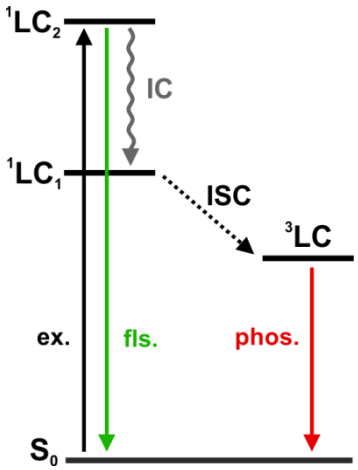

	ΔE ($^1LC_2$) /cm^{-1}	ΔE ($^1LC_1$) /cm^{-1}	ΔE (^3LC) /cm^{-1}	τ
Pd(dipy)$_2$	20000	≈18500	-	53 ns
PdPDM	19200	≈17600	14000	81 µs
ZnPDM	21300	17500	17200	369 µs
CuPDM	≈21000	19800	-	<< 7 ns
NiPDM	21400	17200	-	<< 7 ns
PDM	22000	15600	15400	<< 7 ns

Figure 63: Generalized state diagram of the central chromophores. The corresponding energies are listed in **Table 16**. Transitions which are assumed to take place, but cannot be proved by the performed measurements are depicted in grey. Fluorescence from $^1LC_2$ was only observed for **Pd(dipy)$_2$** and **PDM**, while phosphorescence from ^3LC was only observed for **PDM**, **PdPDM** and **ZnPDM**.

Furthermore, PDM shows a broad and unresolved emission band with a big *Stokes* shift, which is very similar to the phosphorescence observed for **PdPDM** and **ZnPDM**. On the other hand the excited state lifetime of **PDM** is also estimated to be shorter than 7 ns, which usually indicates a deactivation by fluorescence and is in stark contrast to the multi-µs lifetimes observed for the phosphorescent **PdPDM** and **ZnPDM**. The most likely explanation for this is a rapid non-radiative deactivation of the excited state reducing both the lifetime and the intensity of the phosphorescence.[85]

Comparing the suitability of the compounds for the use as a central photosensitizer in NDI-chromophore-TAA triads, all compounds have high absorption coefficients at wavenumbers lower than 25000 cm^{-1}, where they are not superimposed by the absorption of the TAA- or NDI-moieties. Especially **Pd(dipy)$_2$** and **ZnPDM** which show very high extinction coefficients, and **NiPDM** and **PdPDM** which have a broad range of absorption would be promising photosensitizers. Furthermore, all chromophores exhibit suitable first oxidation potentials which are higher than the ca. 100 – 300 mV typically observed for bismethoxy-TAAs, and thus should not interfere with the position of the positive charge in the charge separated states (CSSs). [93, 100, 115-116, 173, 179, 182, 186]

On the other side good photosensitizers usually have high emission quantum yields, since the quenching of the emission is a good indicator for the occurrence of charge separation. This is not the case for most of the investigated compounds. While very weak emission can be observed in **Pd(dipy)$_2$**, **PDM** and **ZnPDM**, only **PdPDM** exhibits emission intensities strong enough for the determination of the emission quantum yield. The most important characteristic of a good photosensitizer is the energy and lifetime of the lowest excited state. The ^{3}LC-states observed for **PdPDM**, **ZnPDM** and **PDM** should be of high enough energy to facilitate charge separation, no statement can be made for the other compound due to the lack of phosphorescence. Since charge separation usually takes place in the first 0.05 – 30 ns after photoexcitation (see also chapter 3.3), excited state lifetimes lower than 50 ns can easily result in poor quantum yields of charge separation.[89, 103, 107, 262]

For these reasons **CuPDM** and **NiPDM** are no suitable central chromophores for the investigation of charge separation in donor-acceptor triads, while the suitability of **PDM** and **Pd(dipy)$_2$** is questionable. **ZnPDM** and especially **PdPDM** on the other hand should be good central photosensitizers. Triads were realized for **Pd(dipy)$_2$**, **PDM** and **PdPDM**, but were not achieved for **ZnPDM** due to synthetic difficulties (see chapter 4.1). No further attempts of the synthesis of a **ZnPDM**-based triad were performed because the ability of the central complex to form a secondary complex with water and methanol would have complicated the intended investigations anyways. The differences between the seemingly similar central chromophores **Pd(dipy)$_2$** and **PdPDM** could easily influence the charge separation process in the triads and will be discussed in detail in the next chapter.

4.2.7 Conformational Rearrangement of $Pd(dipy)_2$

Among the discussed central chromophores, **$Pd(dipy)_2$** and **PdPDM** show unexpectedly huge differences in emission behavior and excited state lifetime. Since the complexes differ significantly in their ground state structures due to the dimethylmethylene bridges in **PdPDM** this is attributed to be due to the structural confinement of **PdPDM**. The proposed mechanism is that while **$Pd(dipy)_2$** undergoes a conformational rearrangement in the excited state which quenches the emission and shortens the lifetime significantly, **PdPDM** is restricted in its initial conformation and thus exhibits relatively strong and long lived phosphorescence. To further investigate this theory, fs-transient absorption (fs-TA) spectroscopy and fs-fluorescence upconversion (FUC) as well as density function theory (DFT) computations and time dependent DFT (TD-DFT) computations were performed.

fs-Transient Spectroscopy of $Pd(dipy)_2$ and PdPDM

In order to obtain information about the ultrafast dynamics of **$Pd(dipy)_2$** and **PdPDM**, fs-pump probe spectroscopy was performed in MeCN at rt.[f] All samples were excited at the maximum of their respective $^1LC_2$ absorption band and the excited states were probed by a delayed white light continuum. The resulting transient maps were corrected for chirp and scattered pump light and analyzed by a global deconvolution using the minimum number of exponentially decaying individual spectral components (transients) needed for a satisfying fit, to yield evolution associated difference spectra (EADS) in a sequential model with increasing lifetimes.[g] For further experimental details see chapter 6.1.4.

The TA spectra of **$Pd(dipy_2)$** and **PdPDM** are displayed in blue to green colors at early times and yellow to red colors at later times in **Figure 64** (A and D). Furthermore the EADS with the associated lifetimes (B and E) as well as time traces at characteristic wavenumbers together with the corresponding fit curves (C and F) are shown.

As can be seen, three EADS are found for both complexes. The final EADS of both complexes shows an infinite lifetime within the 8 ns time window accessible with the fs-set-up, matches very well with the TA spectra observed in the ns-TA spectroscopy (see chapter 4.2.5) and is therefore associated with the lowest excited state which decays monoexponentially to the ground state. The first and second EADS on the other hand possess lifetimes of 2.2 ps and 14.3 ps in **$Pd(dipy)_2$** and 15.6 ps and 47.5 ps in **PdPDM** and consist of varying amounts of ground state bleach (GSB), excited state absorption (ESA) and stimulated emission (SE)-contributions. While the second EADS in **$Pd(dipy)_2$** shows greater similarity to the first EADS, in **PdPDM** it matches almost exactly to the third EADS.

[f] All measurements were performed by Alexander Schmiedel.
[g] All global analysis were performed by Dr. Marco Holzapfel.

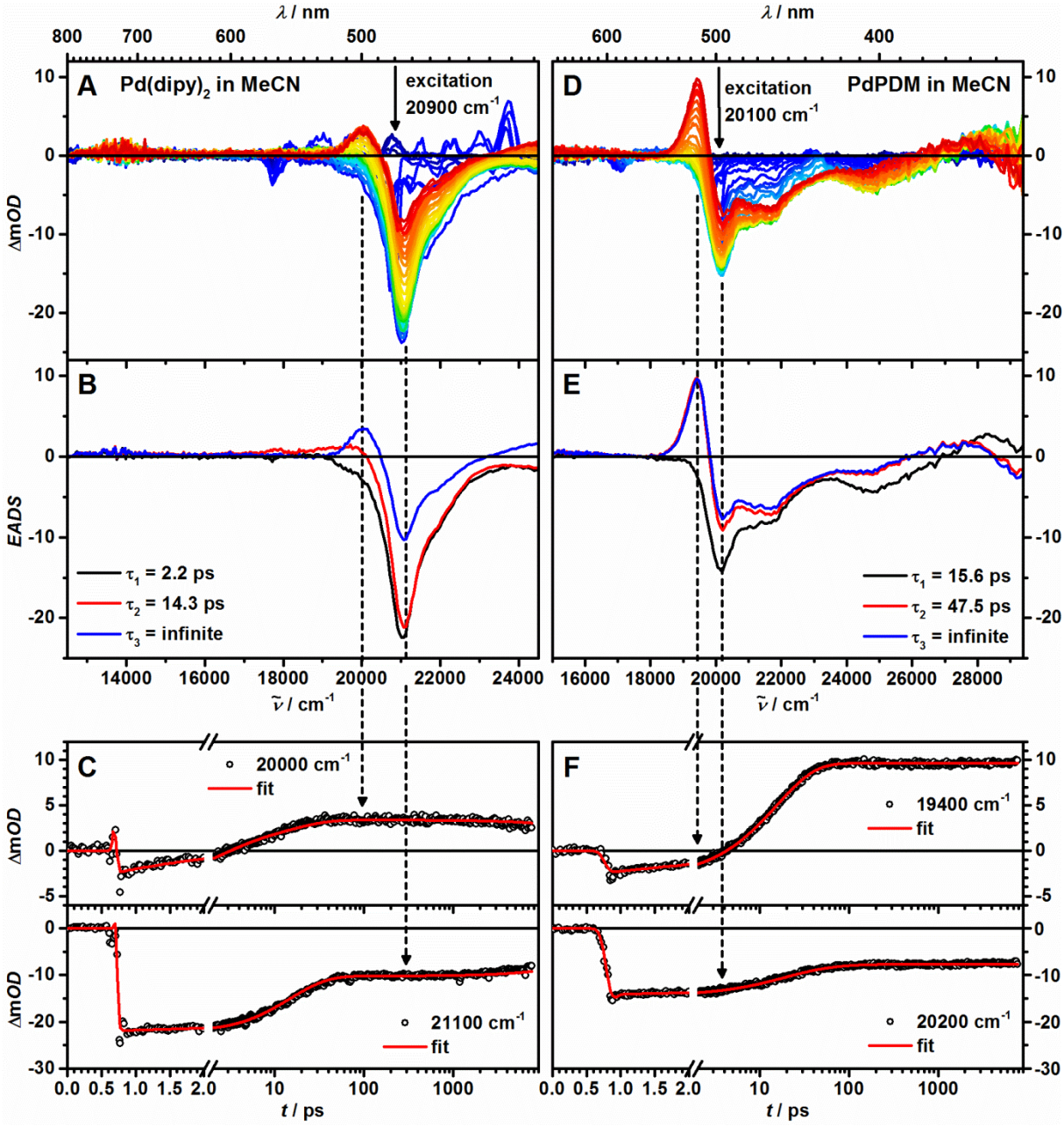

Figure 64: Chirp corrected transient absorption spectra of **Pd(dipy)$_2$** and **PdPDM** in MeCN at rt after excitation at 20900 cm^{-1} and 20100 cm^{-1}, respectively (A and D), evolution associated difference spectra (EADS) from a global fit (B and E), and time traces at selected wavenumbers for which the zero time delay was set arbitrarily with fit (C and F).

To further investigate the spectral shape of the EADS, the steady-state absorption spectrum was subtracted from the EADS giving reduced spectra which show only the contribution of ESA and SE to the EADS. As can be seen from **Figure 65** (A and C) for EADS1 of **Pd(dipy)$_2$** this subtraction gives an ESA with little structure because the EADS1 and the GSB (= steady state absorption spectrum) match very well. However, for the later components with longer lifetimes there is pronounced ESA visible at 21000 cm^{-1}. **PdPDM** behaves very similar, that is, the EADS1 matches very well with the steady-state

absorption spectrum, but here both EADS associated with longer lifetimes show a strong ESA contribution at ca. 19500 cm^{-1}.

Although the absence of negative amplitudes at the low energy site of the GSB in the reduced spectra implies that there is no contribution of SE to the EADS, fluorescence up-conversion measurements could be performed by excitation of the compounds with the frequency doubled output of the Ti:sapphire oscillator at 80 MHz. Thus, both complexes were excited at 25000 cm^{-1}, and the fluorescence was gated at 17200 cm^{-1} for **Pd(dipy)$_2$** and at 18700 cm^{-1} for **PdPDM**. The resulting fluorescence decays were convoluted with the instrument response using a minimal amount of exponential functions. The kinetic traces are superimposed with the respective fits in **Figure 65** (B and D). While **PdPDM** shows a decay with 110 fs as the dominating component, **Pd(dipy)$_2$** clearly displays multiexponential decay with three almost equally contributing components. The two longer time constants (3 ps and 13 ps) agree very well with those of the EADS of the TA measurements (2.2 and 14 ps). The fact that the transient associated with the shortest time constant of 290 fs was not observed in the TA spectra is probably caused by the fact that it is very short lived and most likely consists almost purely of GSB and therefore cannot be distinguished from the following transient associated with EADS1.

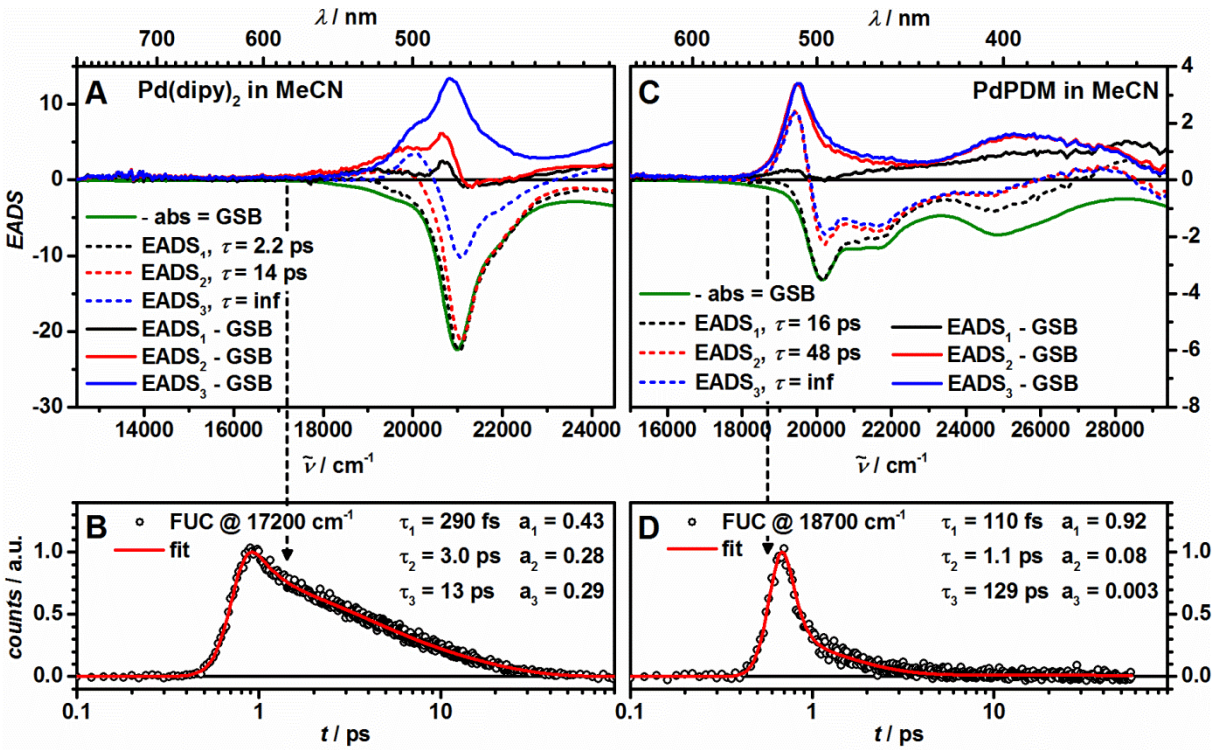

Figure 65: Reduced spectra after excitation of **Pd(dipy)$_2$** at 20900 cm^{-1} (A) and **PdPDM** at 20100 cm^{-1} (B) as well as fluorescence upconversion (B and D) after excitation at 25000 cm^{-1} in MeCN at rt. The FUC was gated at 17200 cm^{-1} (IRF 240 fs) for **Pd(dipy)$_2$** and 18700 cm^{-1} (IRF 170 ps) for **PdPDM**.

DFT-Calculations on Pd(dipy)$_2$ and PdPDM

In order to gain insight into structural and electronic aspects of the excited states involved in the ultrafast dynamics determined by fs-transient spectroscopy, DFT and TD-DFT computations were performed for both complexes. .[h] F Optimization of the ground states of **Pd(dipy)$_2$** and **PdPDM** shows the best agreement with the structure determined by single crystal X-ray diffractometry when using a PBE1PBE functional and SDD-6-31G* basis set combination. A comparison of the structural data is given in **Table A5** in the SI. While the computation gave only one ground state structure with C_S symmetry for **PdPDM**, an additional possible ground state structure with D_2 symmetry was found for **Pd(dipy)$_2$** in which the Pd(II) ion possesses a distorted tetrahedral coordination sphere. However, this structure is about 1600 cm^{-1} higher in energy than the C_i symmetric structure which corresponds to the experimental crystal structure. Based on the DFT optimized ground state structures with minimal energy the vertical excitations into the LC states were computed by the TD-DFT method. The determined excitation energies, oscillator strengths and the symmetry of the states are summarized in **Table 17**. As anticipated above, the lowest excited $^1LC_1$ state is forbidden (close to zero oscillator strengths)while the energetically higher $^1LC_2$ state is allowed. This is the consequence of a symmetric (A_g for **Pd(dipy)$_2$** and A'' for **PdPDM**) and antisymmetric (A_u for **Pd(dipy)$_2$** and A' for **PdPDM**) combination of dipyrrin-transition moments for the forbidden and allowed transition, respectively. While the absolute energies of the computed transitions into $^1LC_2$ are about 1500 cm^{-1} higher than the experimental energies (see **Table 16**), the energy difference between the two computed transitions of 1180 cm^{-1} for **Pd(dipy)$_2$** and 1632 cm^{-1} for **PdPDM** is reasonably good agreement with the difference of the experimental 0-0-transition energies of 1500 cm $^{-1}$ for **Pd(dipy)$_2$** and 1600 cm^{-1} for **PdPDM** as derived from **Table 16**. The lowest lying excited states of both complexes were optimized using two different strategies. The singlet $^1LC_1$ states were optimized by TD-DFT, and the resulting energies are summarized in **Table 17**. For **PdPDM**, this resulted in a nearly symmetric (~C_S) structure in which the fold-angle between the two dipyrrin subunits is even stronger than in the ground state ($\Theta_{4/9}$ ($^1LC_1$) = 120.3° vs. $\Theta_{4/9}$ (S_0) = 133.9°). For **Pd(dipy)$_2$** on the other hand, three different $^1LC_1$ structures were found. A structure with C_i symmetry very similar to the ground state structure, as well as a D_2 symmetric structure with a distorted tetrahedral coordination sphere of the Pd(II) ion turned out to be transition states by frequency analysis. However, a symmetry broken, distorted structure (C_1) turned out to be a minimum on the excited state hyper surface. In this structure, the Pd-N-distances vary slightly between the individual dipyrrinato ligands with 1.991 Å and 1.974 Å to one and 2.071 and 2.070 Å to the other, and the dipyrrin-chromophores are tilted even stronger away from the central plane ($\Theta_{3/4}$($^1LC_1$) = 157.2°) than in the DFT-optimized ground

[h]All DFT computations were performed by Dr. Marco Holzapfel.

state (($\Theta_{3/4}(S_0)$ = 149.0°) and the experimental crystal structure ($\Theta_{3/4}$ = 148.4°). For the corresponding triplet excited states unrestricted DFT (UDFT) was used since *Engels et al.* recently showed that using this strategy yields reasonable singlet-triplet energy differences. [263] The determined structures and spin densities are depicted in **Figure 66**, and the corresponding energies are summarized in **Table 17**. Again, only a single structure was found for **PdPDM** which has a similar symmetric (C_S) geometry as the $^1LC_1$ state and the spin density is delocalized over the two dipyrrin subunits. Thus the state is labeled ^{3}LC (C_s). A more complicated situation is found for **Pd(dipy)$_2$** for which three triplet structures were found, all of which represent an energetic minimum. In the first two, the spin density is delocalized over the two dipyrrin ligands. ^{3}LC (C_i) has a centrosymmetric geometry similar to the crystal structure with a square planar coordination sphere and bent dipyrrin ligands. ^{3}LC (D_2) has a strongly distorted tetrahedral coordination sphere and planar dipyrrin ligands. In the third and final structure, the molecule possesses a disphenoidal (seesaw) coordination sphere (~$C2$) and planar dipyrrin ligands. In this structure, the spin density is localized at the Pd(II) ion which leads to an elongation of the Pd-N bonds to 2.102 and 2.114 Å. Thus, the disphenoidal triplet state can be viewed as a metal centered ^{3}MC state.

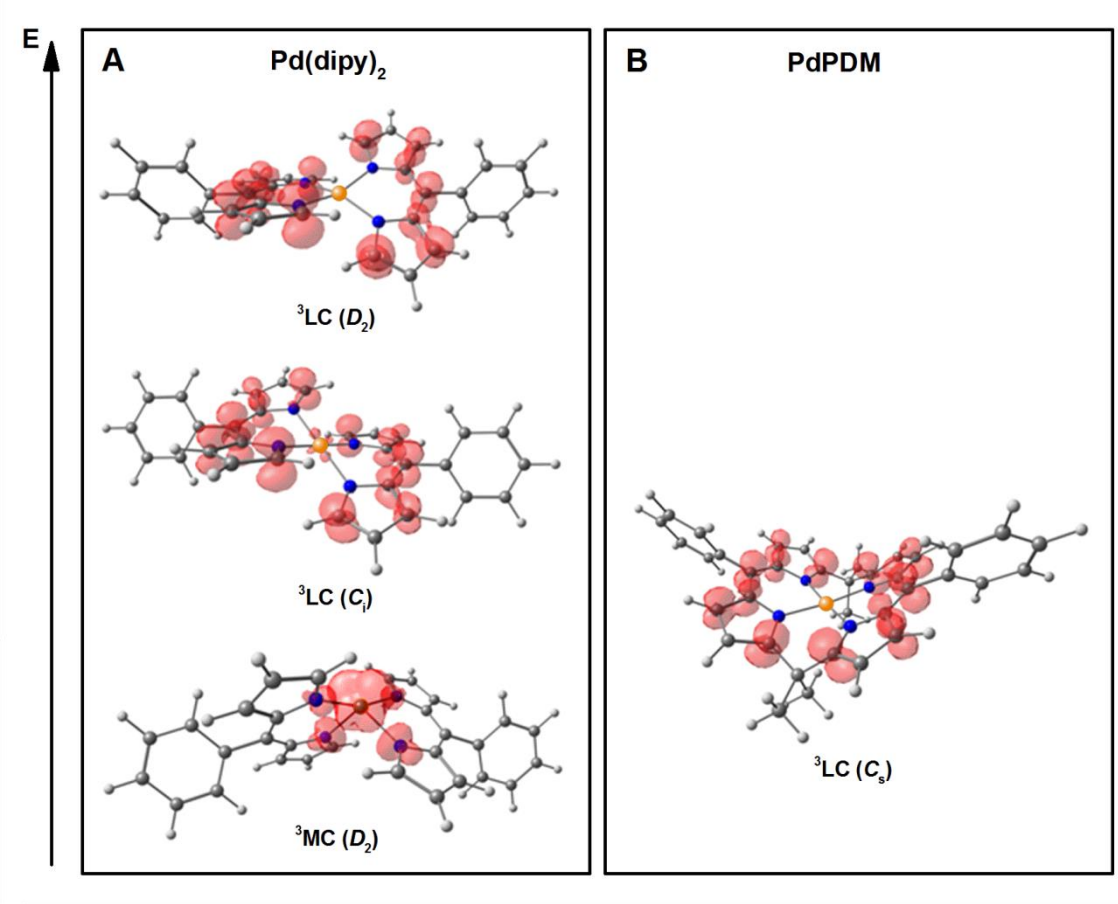

Figure 66: UDFT-calculated geometries and spin densities of the excited triplet states of **Pd(dipy)$_2$** (A) and **PdPDM** (B). The energy axis is not drawn to scale but represents the correct energetic order.

As can easily be seen from **Table 17**, the disphenoidal metal centered structure ^{3}MC (~*C*2) is the lowest energy triplet state for **Pd(dipy)$_2$**. While usually a square planar coordination sphere predominates for Pd(II) complexes in the ground state[138, 149], some exceptions are known which include tetrahedral[216], trigonal pyramidal[218] and disphenoidal[217] structures. For the tetrahedral structure a triplet ground state was rationalized based on magnetic measurements which show that deviations from square planar geometry can indeed be preferred for open-shell Pd(II) species as is the triplet MC state here.[216]

Table 17: DFT calculated energies (cm^{-1}), oscillator Strength (f) and symmetry of *Franck-Condon* (FC) and optimized excited States (TD-DFT for singlet and UDFT for triplet states)

	^{1}LC$_1$ /cm^{-1} **(FC) (f)**	**^{1}LC$_2$** /cm^{-1} **(FC) (f)**	**^{1}LC$_1$** /cm^{-1}	**^{1}LC$_1$** /cm^{-1}	**^{1}LC$_1$** /cm^{-1}	**^{3}LC** /cm^{-1}	**^{3}LC** /cm^{-1}	**^{3}MC** /cm^{-1}
Pd(dipy)$_2$	21737 (0.0000) (C_i)	22918 (0.0176) (C_i)	24037[a] (D_2)	20767[a] (C_i)	19272 (C_1)	19268 (D_2)	16692 (C_i)	12567 (~C_2)
PdPDM	20008 (0.0006) (C_S)	21640 (0.0270) (C_S)			18405 (~C_S)		14616 (~C_S)	

[a] transition state

Conclusion

Based on the information obtained by the fs-TA spectroscopy and the DFT-calculations the state diagrams of **Pd(dipy)$_2$** and **PdPDM** constructed in chapter 4.2.6 can be refined to yield the state diagrams shown in **Figure 67**. The state diagrams include the occurring ultrafast photophysical processes as well as the resulting emission characteristics at rt and 77 K and give an explanation for the vastly different behavior of the two complexes.

Although FUC was only performed for one wavenumber can give a first hint about the photoinduced dynamics involving both the ^{1}LC$_2$ and the ^{1}LC$_1$ state because emission from those states is to be broad and strongly overlapping which results in a significant contribution of both states to the obtained fluorescence decays. The fact that fluorescence can be observed at from the ^{1}LC$_1$ state which, according to exciton coupling theory should be a dark state for the ideal H-type arrangement of the dipyrrin chromophores in the centrosymmetric complex **Pd(dipy)$_2$**, is probably caused by the structural flexibility of the complex, which disturbs the C_i symmetry by an asymmetric vibration and makes fluorescence from the ^{1}LC$_1$ state partially allowed.

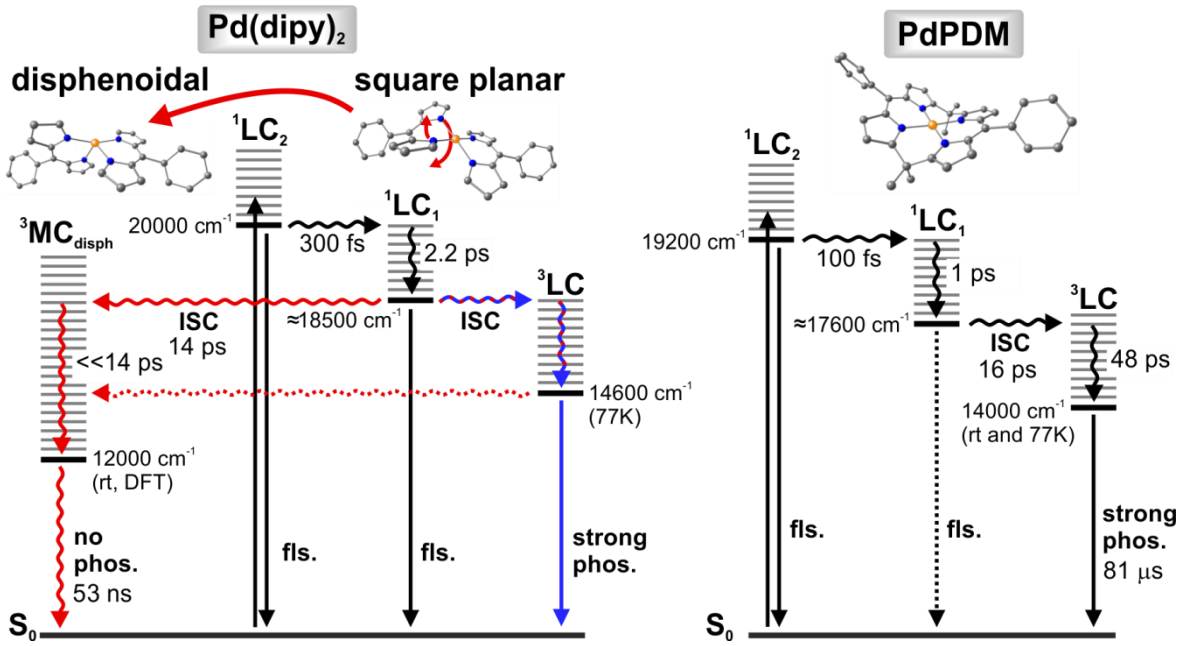

Figure 67: State diagram of **Pd(dipy)$_2$** and **PdPDM**. The excited state energies are taken from **Table 16** or the respective DFT calculations and emission measurements at 77 K when stated otherwise. The corresponding structures are calculated at DFT level. The given lifetimes are taken from the ns- and fs-TA spectroscopic measurements and refer to states but approximate inverted rates if one assumes that the assigned process dominates. Colored arrows indicate processes only occurring in fluid solution at rt (red) or glassy matrix at 77K (blue). Dotted arrows indicate processes which were not observed but cannot be excluded from the performed experiments.

Excitation of **Pd(dipy)$_2$** into the $^1LC_2$ band populates a very short lived singlet state as indicated by the 300 fs time constant of the fluorescence decay in the FUC measurement. This time constant refers to the internal conversion (IC) to the $^1LC_1$ state which is visible in the TA spectra as an EADS which consists of almost pure GSB. A component with τ = 3 ps in the FUC decay and 2.2 ps in the TA spectra can be associated with vibrational relaxation within the $^1LC_1$ state due to the very similar shape of the associated EADS in the deconvolution of the TA spectra. The slowest component of the fluorescence decay has a lifetime of 13 ps and is attributed to the quenching of the fluorescence by ISC to the triplet state. This process can also be observed in the TA by the rise of an ESA at lower energies with a lifetime of τ = 14 ps, resulting a final EADS which matches very well with the ns-TA spectra and thus can be associated with the lowest excited triplet state with a lifetime of 53 ns.

In fluid solution, the lowest energy triplet state of **Pd(dipy)$_2$** should adopt a disphenoidal geometry with pronounced ^{3}MC character as supported by the DFT calculations. The observed non-emissive and rather fast deactivation are in good agreement with typical results for other ^{3}MC-states.[90, 118, 206] However, in the glassy matrix of frozen MeTHF at 77 K, the conformational rearrangement from the square planar ground state geometry to the disphenoidal ^{3}MC geometry cannot take place. Accordingly, the complex shows strong and structured emission which can be associated with phosphorescence from a ^{3}LC state. The ^{3}LC-character of the lowest triplet state with a ground-state

geometry can again be confirmed by DFT-calculations. At this point it has to be mentioned that based on the performed experiments a slow population of ^{3}LC by ISC from the $^1LC_1$ state and a subsequent quick rearrangement to the ^{3}MC state at rt cannot be excluded, because if this scenario applies, the intermediate concentration of ^{3}LC would be too low to be detectable. Results obtained for the functionalized dyads and triads based on **Pd(dipy)$_2$** indicate that the stepwise ISC to ^{3}LC and subsequent rearrangement to ^{3}MC could indeed be the actual mechanism as will be discussed in chapter 4.3.2..

In contrast, **PdPDM** cannot undergo such structural reorganization even at rt, because the relative orientation of dipyrrin subunits and thereby the coordination sphere of the Pd(II) central ion is fixed by the two dimethylmethylene bridges. Excitation of **PdPDM** into the $^1LC_2$ state is followed by IC to the dark $^1LC_1$ state with a lifetime of τ = 100 fs as determined by FUC. A weak component with τ = 1 ps may indicate vibrational relaxation within the $^1LC_1$ state. However, this state is so weakly fluorescent that a direct observation of the ISC to the triplet state using FUC is not possible. Luckily, the ISC can be confirmed indirectly by the fs-TA results. The first detectable transient shows only GSB and is associated with the $^1LC_1$ state. It transitions with a lifetime of τ = 16 ps to the second EADS which shows an intense ESA absorption redshifted to the GSB. Both the lifetime and spectral changes caused by this transition are very similar to those observed for the transition from the second to the final EADS in **Pd(dipy)$_2$**, which was confirmed by FUC to be due to ISC. Thus, it is likely that the process from the first to the second EADS in **PdPDM** also refers to ISC to the ^{3}LC-state. A second transition with a lifetime of 48 ps has very little influence on the spectral shape and thus is assigned to be due a slow vibrational relaxation within the ^{3}LC state. As shown by ns-TA spectroscopy this state has a lifetime of 82 µs and is emissive both at rt in fluid MeCN and in frozen MeTHF because it cannot rearrange to a disphenoidal structure and thus has a negligible ^{3}MC-character.

In conclusion, the photophysics of **Pd(dipy)$_2$** and **PdPDM** is governed by a fast ISC process which occurs with a lifetime comparable to other Pd(II) complexes.[206, 264] While the non-bridged bis-dipyrrin complex **Pd(dipy)$_2$** can undergo structural reorganization towards a non-emissive ^{3}MC state, this is prevented by the structurally more rigid ligand backbone in the bridged complex **PdPDM**, which therefore shows significant NIR phosphorescence even in fluid solution at rt.[265-266] Since ns-TA measurements in fluid THF and toluene gave almost identical results and only slightly longer lifetimes the participation of any interligand CT states in the relaxation pathway of **Pd(dipy)$_2$** can be ruled out which is in contrast to observations made by *Thompson et al.* on bisdipyrrinato-Zn(II) complexes.[157]

Naturally, the described structural rearrangement can influence the formation and the lifetime of charge separated states in triads based on **Pd(dipy)$_2$** as a central metal complex, which could lead to significant difference to triads based on the electronically similar **PdPDM**. This will be one focus of the following chapter.

4.3 Donor- and Acceptor-Substituted Dyads and Triads

In the following, the properties of the novel donor-acceptor substituted triads shown in **Scheme 29** will be discussed. For **D-Pd(dipy)$_2$-A** and **D-PdPDM-A** the respective reference dyads can be used to discuss the influence of the donor and acceptor substituents. The reference dyads will always be depicted in blue and red respectively, with the unsubstituted metal-complex being depicted in black and the triad in the color of the respective central chromophore. The elongated triad **D$_{Ph}$-PdPDM-A** only differs from **D-PdPDM-A** in the additional phenyl ring between donor and central chromophore and thus is suitable to investigate the influence of the distance and the electronic decoupling between the donor and the central chromophore on the photophysical properties. **D$_{Ph}$-PdPDM-A** will be depicted in purple. Although the according elongated triad was also synthesized for the non-metalated triad, it will not be discussed since measurements on the short triad **D-PDM-A** already indicated a relatively unremarkable behavior of both compounds. Furthermore, the structure-property relationship can already be gaged from the metalated triads. Since the central chromophores have already been described in the previous chapter, differences between the triads based solely on the properties of the central metal complex will not be discussed in detail throughout this chapter. Instead, the focus will be on the behavior of the superchromophores as a whole.

4.3.1 Steady State Properties

To gain first insights into the optical and electrochemical properties of the compounds a number of steady state experiments were performed. The results of the different methods will be presented in the following chapters.

UV/Vis absorption

The steady state absorption of the central chromophores was measured in solvents of different polarity (MeCN, DCM and toluene). The absorption maxima and extinction coefficients of characteristic bands are listed in **Table 18** for all compounds and solvents. Since the principal results do not differ between solvents, only the measurements in MeCN will be discussed in detail. Afterwards, the solvent dependence will be addressed briefly.

Figure 68 shows the UV/Vis-absorption spectra of all investigated triads in comparison with the respective unsubstituted central chromophores. At higher energies, the absorptive transitions of the donor and acceptor moieties dominate the shape of the absorption spectra. The bands between 26000 – 30000 cm^{-1} can in all cases be associated with π-π-transitions of the NDI.[180-181] The TAA on the other hand absorbs between 31000 – 36000 cm^{-1} in **D-Pd(dipy)$_2$-A**, **D-PdPDM-A** and **D-PDM-A**, while its absorption is shifted about 3500 cm^{-1} towards lower energies in **D$_{Ph}$-PdPDM-A**.

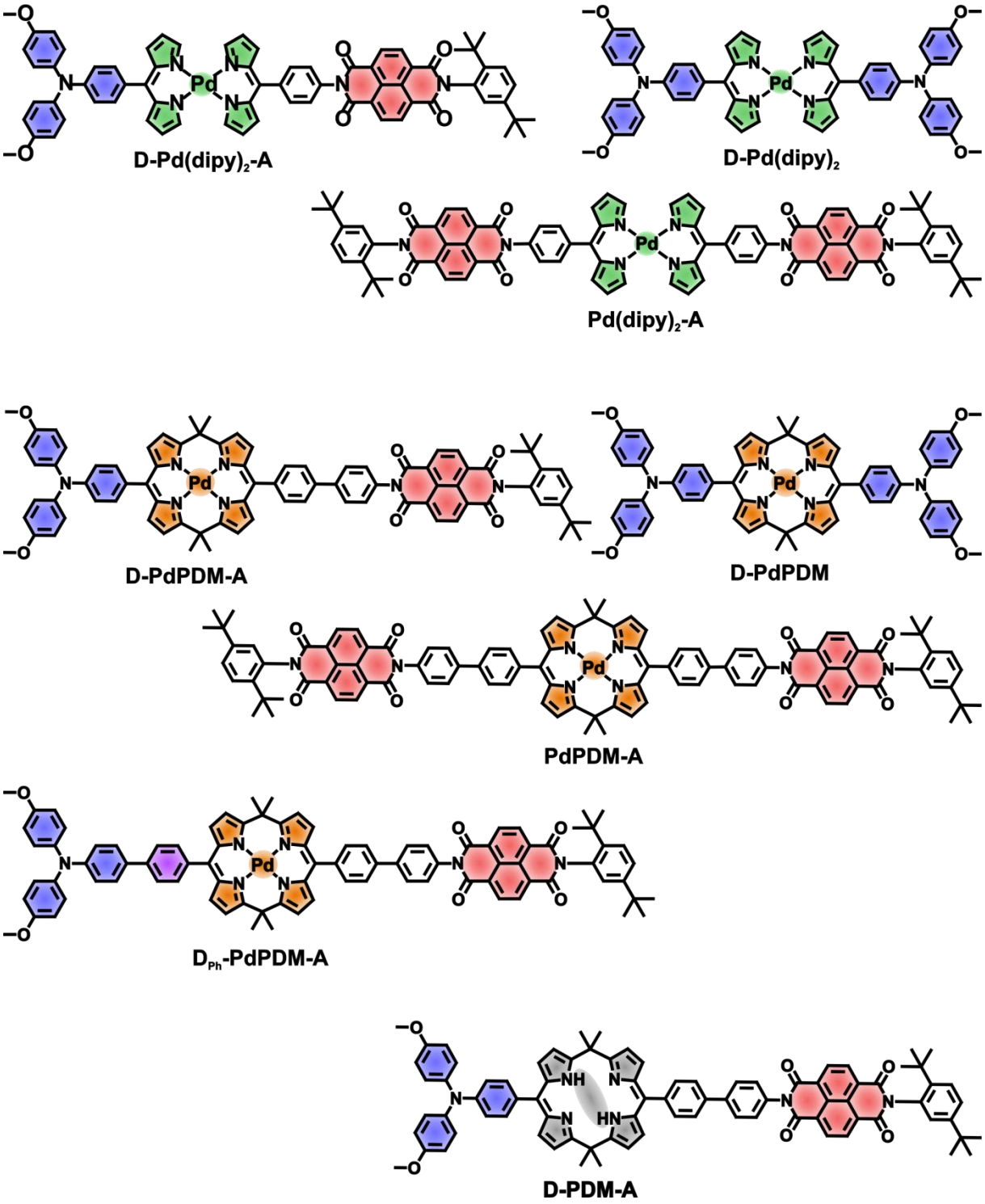

Scheme 29: The target triads **D-Pd(dipy)$_2$-A**, **D-PdPDM-A**, **D$_{Ph}$-PdPDM-A** and **D-PDM-A** as well as the reference dyads **D-Pd(dipy)$_2$**, **Pd(dipy)$_2$-A**, **D-PdPDM** and **PdPDM-A.** The presented color code will be kept during the discussion of the measurements. The elongated triad **D$_{Ph}$-PdPDM-A** will be depicted in purple, the donor and acceptor reference dyads will be given in blue and red respectively while all other compounds will be given in the color of the respective central chromophore.

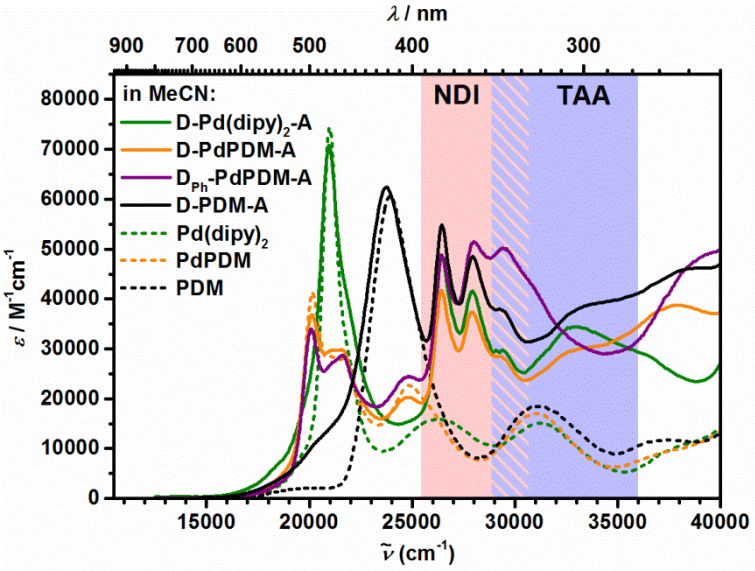

Figure 68: Absorption spectra of the triads (solid lines) **D-Pd(dipy)$_2$-A** (green), **D-PdPDM-A** (orange), **D$_{Ph}$-PdPDM-A** (purple) and **D-PDM-A** (black) as well as the respective unsubstituted central chromophores (dashed lines) **Pd(dipy)$_2$** (green), **PdPDM** (orange) and **PDM** (black) in MeCN at rt. Shaded areas are strongly influenced by the NDI (red) and TAA (blue) moieties respectively.

The bathochromic shift of the TAA-absorption in **D$_{Ph}$-PdPDM-A** is most likely due to the influence of the additional phenyl ring on the transition polarized along the long TAA-CMC axis. Furthermore, the additional phenyl ring can influence the electronic coupling between the donor and the central chromophore and thus the absorption characteristics of both moieties.[267]

This theory is further supported by the absorptive transitions at energies lower than 25000 cm^{-1}, which can be associated with the central chromophores. As can easily be seen, the $^1LC_1$ and $^1LC_2$ transitions of the triads are distinctly different from the unsubstituted central chromophores. Especially for **D-PDM-A** and **D-Pd(dipy)$_2$-A** a significant broadening of the absorption can be observed. This can partially be attributed to an increase of the difference between the two dipyrrin subchromophores, which results in more strongly allowed $^1LC_1$-transitions. [149-150, 152-153] However, a complete rationalization of the observed absorption behavior based solely on exciton coupling effects is not possible since the maximal extinction coefficients of the $^1LC_2$-transition only decrease marginally or are even increased as in the case of **D-PDM-A**. Thus, a direct electronic influence of the donor- and acceptor-substituents on the absorption of the central metal chromophore has to be assumed. The direct electronic influence of the donor and acceptor substituents on the central chromophore can be observed more clearly by a comparison of the UV/Vis-spectra of the full triads to the respective doubly donor- or acceptor-functionalized reference dyads and the central chromophores which is done in **Figure 69** (A and B) for the triads **D-Pd(dipy)$_2$-A** and **D-PdPDM-A** respectively. Substitution with the NDI acceptor moiety only leads to a small decrease of the absorption intensity of the central chromophores, without significantly changing the band shape.

Table 18: Absorption maxima $\tilde{\nu}_{max}$ and extinction coefficients ε_{max} of the characteristic absorption bands of the respective target triads and reference compounds.

	solvent	$^1LC_2$ $\tilde{\nu}_{max}$ [ε_{max}] /cm^{-1} [M^{-1}cm^{-1}]	NDI[a] $\tilde{\nu}_{max}$ [ε_{max}] /cm^{-1} [M^{-1}cm^{-1}]	TAA $\tilde{\nu}_{max}$ [ε_{max}] /cm^{-1} [M^{-1}cm^{-1}]
Pd(dipy)$_2$	MeCN	21000 [74300]	-	-
	DCM	20800 [77700]	-	-
	toluene	20800 [82400]	-	-
D-Pd(dipy)$_2$	MeCN	21000 [80100]	-	33400 [57800]
	DCM	20700 [92800]	-	33000 [54300]
	toluene	20700 [100100]	-	32800 [56000]
Pd(dipy)$_2$-A	MeCN	20900 [60900]	26400 [81700]	-
	DCM	20700 [65000]	26200 [77800]	-
	toluene	20700 [73700]	20600 [51600]	-
D-Pd(dipy)$_2$-A	MeCN	21000 [70800]	26400 [48600]	33000 [34400]
	DCM	20800 [79800]	26200 [47100]	32500 [36700]
	toluene	20700 [85900]	26200 [34800]	32400 [39100]
PdPDM	MeCN	20200 [35400]	-	-
	DCM	20000 [44300]	-	-
	toluene	20000 [49200]	-	-
D-PdPDM	MeCN	20200 [47600]	-	33000 [45500]
	DCM	20100 [50900]	-	32900 [48400]
	toluene	20000 [51200]	-	32800 [47900]
PdPDM-A	MeCN	20100 [32300]	26400 [74900]	-
	DCM	20000 [34600]	26200 [66100]	-
	toluene	19900 [33900]	26200 [40800]	-
D-PdPDM-A	MeCN	20100 [36800]	26400 [41800]	32900 [28300]
	DCM	20000 [37900]	26300 [39100]	32700 [28400]
	toluene	19900 [40600]	26000 [28600]	32700 [29500]
D$_{Ph}$-PdPDM-A	MeCN	20100 [33900]	26400 [48800]	29300 [50200]
	DCM	20000 [36600]	26300 [44800]	29400 [47900]
	toluene	19900 [41300]	26200 [32600]	29400 [47500]
PDM	MeCN	23900 [61300]	-	-
	DCM	23600 [63700]	-	-
	toluene	23600 [67700]	-	-
D-PDM-A	MeCN	23800 [62500]	26500 [55000]	33500 [38300]
	DCM	23600 [64600]	26200 [50100]	23400 [38700]
	toluene	23500 [66000]	26000 [36200]	33300 [33900]

[a] values are always listed for the lowest energy peak, regardless of extinction coefficients - the higher energy peaks are located at around 27900 cm^{-1} and 29500 cm^{-1} respectively, with absorption coefficients dependent on the compound and solvent.

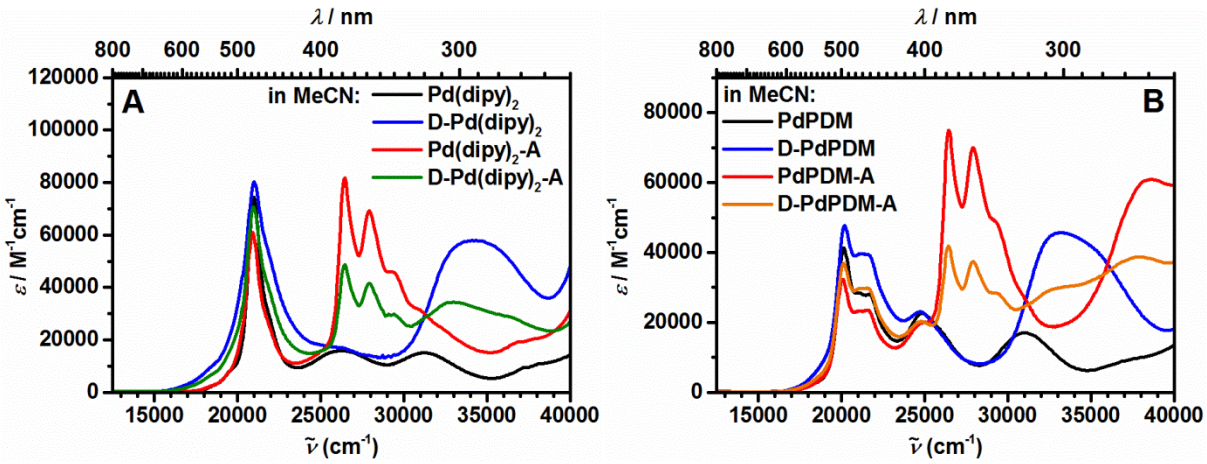

Figure 69: Absorption spectra of **D-Pd(dipy)$_2$-A** (A) and **D-PdPDM-A** (B) as well as the respective reference-compounds without donor and/or acceptor moieties in MeCN at rt.

On the other hand, a substitution of the central chromophore with two equivalents of TAA leads to an increased absorption intensity and broader band shape. In the donor-and acceptor-substituted triads, the positive effect of the donor and the negative effect of the acceptor on the extinction coefficients more or less compensate each other and only the broadening of the band shape due to the donor-function is observed. The fact that the broadening of the band shape is pronounced more strongly in the symmetric donor-functionalized dyads than in the asymmetric triads is not expected according to exciton coupling theory and thus has to be attributed to a direct electronic effect of the TAA on the central chromophore indicating a non-negligible electronic coupling between the subunits of the triad.[150-153]

On the other hand, the maximal absorption energies are influenced only slightly and apart from the transitions centered on the central chromophore, the absorption spectra of the triads can still be described as the sum of the absorption of the respective subunits. This strongly suggests that the electronic coupling between the different moieties is small enough that they can still be treated as individual chromophores.

All compounds show nearly no solvent dependent behavior. Beside the expected broadening of the NDI-associated transitions in toluene[184], only slight differences between the solvents can be observed with the help of **Table 18**. The strongest solvent dependence can be observed for the transitions associated with the central chromophores, which are shifted about 100 – 300 cm^{-1} towards lower energies and show considerably higher extinction coefficients in solvents of lower polarity. For the NDI-absorption the extinction coefficients show the reversed trend, while the absorption energies also undergo a bathochromic shift towards lower polarities. Lastly, The TAA-transitions show no clear trend, which is mainly due to difficulties in the determination of the absorption energies and extinction coefficients caused by the strong superposition of the TAA-transitions with other high energy-transitions of the compounds.

Emission

The main point of interest of the emission measurements is the identification of the emitting state and its energy, as well as the influence of the donor and acceptor moieties on the emission intensities. In donor-acceptor-substituted chromophores a reduced emission quantum yield usually indicates the formation of a charge separated state (CSS), as discussed in chapter 3.2.[115-116, 179, 186, 188-189] For the compounds investigated in this study, already the central chromophores themselves are only weak emitters, making a clear observation of an emission quenching difficult. The only exception to this is **PdPDM**, for which an emission quantum yield of 2 % could be determined. Furthermore, the emissive states are expected to be localized at the central chromophores in all cases and thus have been already described during the discussion of the central chromophores in chapter 4.2. For those reasons, the emission behavior of the dyads and triads will only be discussed briefly, and the description will focus on the few observable differences to the central chromophores. To ensure some degree of comparability, all measurements were performed with samples of comparable concentration and the same parameters. All samples were degassed with a stream of dry argon for at least 30 minutes prior to measurement.

The emission intensity of **Pd(dipy)$_2$** seems more or less unaffected by a substitution with the donor- or acceptor moieties. The emission maxima are slightly shifted from 17100 cm^{-1} for **Pd(dipy)$_2$** and 17000 cm^{-1} for **Pd(dipy)$_2$-A** to 16500 cm^{-1} for **D-Pd(dipy)$_2$** and **D-Pd(dipy)$_2$-A**. This shift can be associated with the influence of the donor-moiety on the central chromophore as already discussed for the steady state absorption.

For **PdPDM**, the absorption energies are unaffected by a substitution with TAA or NDI and stay at 12800 cm^{-1} for all compounds. On the other hand the intensity of the emission is decreased for both the short and elongated triads **D-PdPDM-A** and **D$_{Ph}$-PdPDM-A** as well as the acceptor functionalized reference dyad **PdPDM-A**. In MeCN and DCM this effect is so pronounced that the emission can only be recorded with the use of the standard photomultiplier detection, which is only sensitive down to 12500 cm^{-1} and thus cannot be used to determine the quantum yields for the compounds. In contrast, for the donor-functionalized reference dyad **D-PdPDM** the quantum yield was determined to be around 1 % in MeCN, which is on the same order of magnitude than for the central chromophore. The emission quenching upon substitution of the central chromophore with the NDI acceptor is a clear indication for the occurrence of charge separation (CS).

Lastly, for the purely organic central chromophore **PDM**, the situation is similar to **Pd(dipy)$_2$**. Substitution with both the NDI and the TAA does not seem to significantly affect the emission intensity of the central chromophore. Furthermore the emission maximum of the triad **D-PDM-A** is blue shifted only 200 cm^{-1} to 13400 cm^{-1}, indicating a very small influence of both the donor and the acceptor-moiety on the emissive state.

Electrochemistry

To estimate the energy of possible CSSs in the triads and the respective reference compounds, the redox-potentials of the compounds were determined by cyclic voltammetry. All cyclic voltammograms were recorded under argon atmosphere at rt in DCM, using TBAHFP at a concentration of about 0.2 M as the supporting electrolyte and a scan rate of 250 mV s^{-1}. All measurements were referenced against the ferrocene/ferrocenium (Fc/Fc^+) redox couple. Reversibility of the different redox-processes was tested with multicycle thin layer experiments. The determined anodic peak potentials E_{pa}^{ox} of the first irreversible oxidation and half-wave potentials $E_{1/2}$ of all other observed redox-processes are listed for each compound in **Table 19**. For **D-Pd(dipy)$_2$-A** and **D-Pd(dipy)$_2$** strongly overlapping oxidative signals were observed. Thus, differential pulse voltammetry (DPV) was performed on the compounds and results in comparable potentials for the oxidative processes as determined from the cyclic voltammetry.

The cyclic voltammograms of the target triads are shown in **Figure 70**. The first and second reversible reductions of the NDI are observed for all compounds at values around –1040 mV and –1510 mV as expected from comparison with published data on similar NDIs.[115, 179, 181, 185-187]

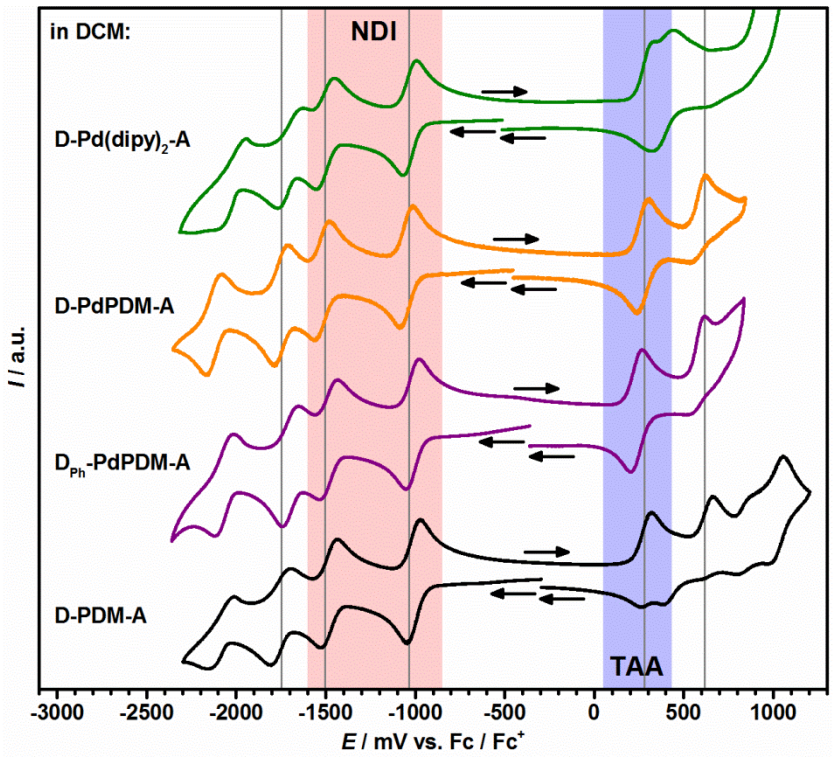

Figure 70: Cyclic voltammograms of **D-Pd(dipy)$_2$-A** (green), **D-PdPDM-A** (orange), **D$_{Ph}$-PdPDM-A** (purple) and **D-PDM-A** (black) in a 0.2 M solution of TBAHFP in DCM at a scan rate of 250 mV s^{-1}. All potentials are referenced against Fc/Fc^+. Black arrows indicate the start, end and direction of the measurement. For better comparison, potentials of –1750, –1500, –1040, 280 and 610 mV are highlighted by grey lines. Shaded areas mark processes associated with the NDI-(red) and TAA-(blue) moiety, respectively.

The first reversible oxidation occurs at potentials of 270 mV for **D-PdPDM-A**, 220 mV for **D_{Ph}-PdPDM-A** and 260 mV for **D-PDM-A**, which is in a typical range for double methoxy-substituted TAAs. The observed modification of the TAA-oxidation potential between the short and the elongated **PdPDM**-based triad is caused by the additional phenyl ring. This is either due to a direct electronic influence or the modification of the interaction between the donor and the central chromophore and thus possibly hints towards a non-negligible electronic coupling between the two subunits.[59, 100, 179, 182, 186]

For **D-Pd(dipy)$_2$-A** the first oxidative signal is due to a superposition of two different oxidative processes and is thus discussed more easily with the help of the differential pulse voltammograms shown in **Figure 71**. As can be seen, by the use of DPV the overlapping processes can almost be resolved. The signal at 390 mV can be assigned to the reversible oxidation of TAA since it is similar in shape and intensity to the first reductive signal, associated with the reversible reduction of NDI. The oxidation at 260 mV on the other hand is of lower intensity and thus is associated with the irreversible oxidation of the central chromophore. This interpretation is further supported by the DPV of the doubly donor substituted **D-Pd(dipy)$_2$**, which shows a splitting of the oxidative signal at higher potentials into two barely resolved signals at around 320 mV and 420 mV. This is due to the presence of two identical TAA-moieties in the molecule. Since the splitting between the two TAA-associated oxidations is somewhat larger than the statistical deviation of two non-interacting identical redox centers of 35 mV, the two TAA seem to interact weakly through the central metal chromophore which shifts the oxidation of the second TAA to slightly higher potentials. [256] Thus, an electronic coupling between the donor-moieties and the central chromophore is confirmed for the compounds based on **Pd(dipy)$_2$**.

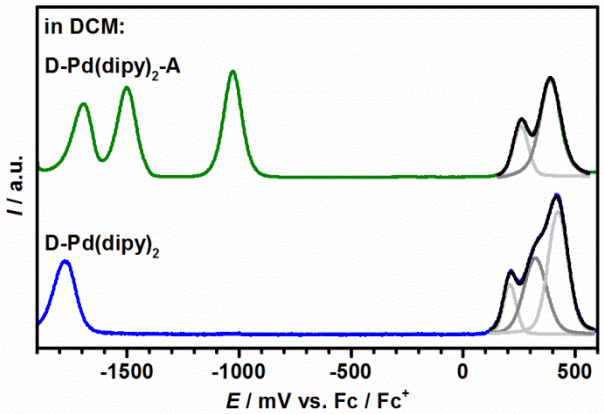

Figure 71: Differential pulse voltammograms of **D-Pd(dipy)$_2$-A** (green) and **D-Pd(dipy)$_2$** (blue) in a 0.2 M solution of TBAHFP in DCM at a scan rate of 2 mV s^{-1}. All potentials are referenced against Fc/Fc^+. The grey to black lines show the *Voigt* fits of the unresolved oxidative signals (grey) and the sum of both (black).

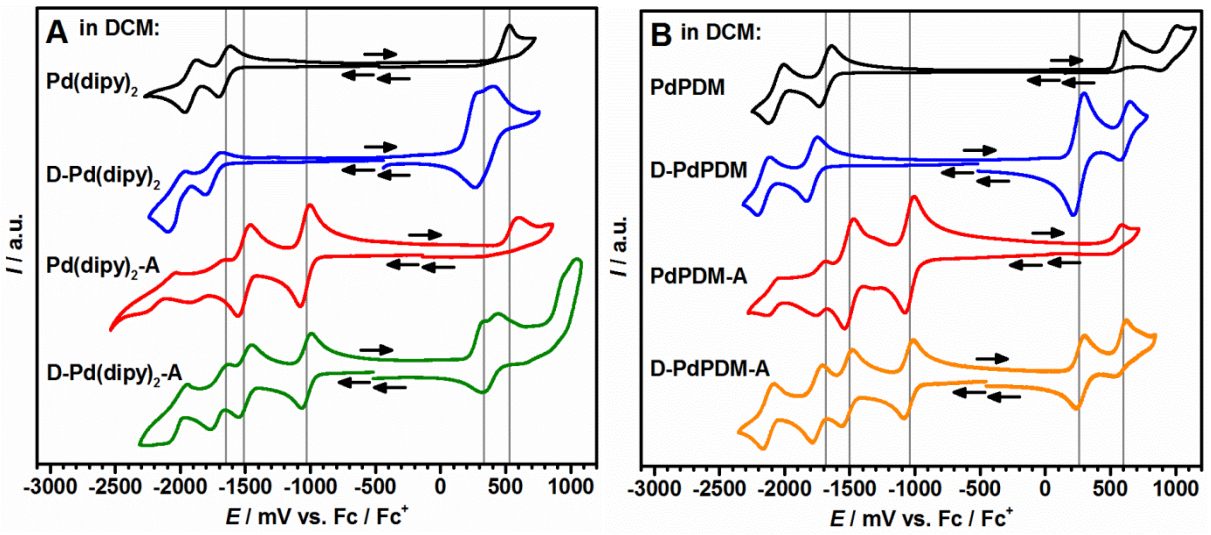

Figure 72: Cyclic voltammograms of **D-Pd(dipy)$_2$-A** (A) and **D-PdPDM-A** (B) as well as the respective reference-compounds without donor and/or acceptor moieties in a 0.2 M solution of TBAHFP in DCM at a scan rate of 250 mV s^{-1}. All potentials are referenced against Fc/Fc$^+$. Black arrows indicate the start, end and direction of the measurement. For better comparison, potentials of –1510 and –1030 mV as well as (A) –1650, 330 and 530 mV or (B) –1680, 260 and 600 mV are highlighted by grey lines.

A comparison of the triad with the respective reference-dyads and the central chromophore using **Table 19** and **Figure 72** (A and B) gives further insight on the influence of the donor- and acceptor-moieties on the electrochemical properties of the central chromophores.

Substitution of **Pd(dipy)$_2$** with TAA increases the electron density in the central chromophore and thus lowers the potential of the first oxidation by 320 mV for the doubly donor substituted **D-Pd(dipy)$_2$** and by 170 mV for the triad **D-Pd(dipy)$_2$-A**, indicating a roughly additive behavior of the electron donating effect. For the same reason, the first reduction is shifted by about 130 mV towards lower potentials. Simultaneously, the interaction with the central chromophore shifts the oxidation potential of TAA towards higher potentials compared to the dyads based on **PdPDM**. While this shift results in the already discussed superposition of the oxidative signals, the oxidation potential of TAA is higher in the triad, indicating an even stronger reduction of the electron density. This can be rationalized by the presence of the electron withdrawing NDI in the triad, if one takes into account the likely non-negligible electronic coupling between the acceptor and the central chromophore. Substitution of the central chromophore with two NDIs results in an increase of the oxidation potentials by 170 mV. Although the influence on the reduction potential may be corrupted due to the very shallow form of the reductive signal and the unusually large difference between its reductive and the oxidative halfway potential, this nonetheless points to this issue. Since the reduction potentials of the NDI are virtually unaffected, the electronic coupling seems to be weaker than between TAA and **Pd(dipy)$_2$**.

Table 19: Halfway potentials[a] ($E_{1/2}$) and anodic peak potentials[a] (E_{pa}) and potential difference (ΔE_{redox}) of the observed redox processes of the target compounds in a 0.2 M solution of TBAHFP in DCM.

	central chromophore $E_{1/2}^{red}$ /mV	**NDI** $E_{1/2}^{red1}$ ($E_{1/2}^{red2}$) /mV	**TAA** $E_{1/2}^{ox}$ /mV	**central chromophore** E_{pa}^{ox} /mV	ΔE_{redox} $E^{ox} - E^{red}$ /mV
Pd(dipy)$_2$	–1650[i]	-	-	530[i]	-
D-Pd(dipy)$_2$	–1770[i]	-	330[r, b]	210[i]	1990
Pd(dipy)$_2$-A	–1790[i]	–1040[r] (–1510[r])	-	600[i]	1640
D-Pd(dipy)$_2$-A	–1700[i]	–1030[r] (–1500[r])	390[r]	260[i]	1350
PdPDM	–1680[i]	-	-	600[i]	-
D-PdPDM	–1790[i]	-	260[r]	640[i]	2050
PdPDM-A	–1730[i]	–1040[r] (–1510[r])	-	590[i]	1630
D-PdPDM-A	–1750[i]	–1050[r] (–1520[r])	270[r]	620[i]	1320
D$_{Ph}$-PdPDM-A	–1720[i]	–1040[r] (–1510[r])	220[r]	600[i]	1260
PdPDM	–1760[i]	-	-	640[i]	-
D-PDM-A	–1780[i]	–1040[r] (–1510[r])	260[r]	630[i]	1300

[a] referenced against Fc/Fc^+ at a scan rate of 250 mV s^{-1}, [i] irreversible process, [r] reversible process; [b] a second oxidative signal at 420 mV can be observed with DPV.

For **PdPDM** on the other hand, substitution with TAA increases the oxidation potentials of the central chromophore by only 40 mV, while the reduction potentials are still lowered by 110 mV. Substitution of **PdPDM** with NDI has an even weaker influence since it only lowers the first reduction by 50 mV and does not affect the oxidation potentials at all. In the donor-acceptor substituted triad, the redox-potentials are more similar to the unsubstituted central chromophore since the contrary effects of the NDI and the TAA compensate each other.

These observations all point towards a more or less significant electronic coupling between the central chromophores and the attached donors and acceptors, and accordingly between the donor and acceptor moieties themselves. This coupling is strongest in **D-Pd(dipy)$_2$-A** where it even leads to a strong overlap and an inverse arrangement of the first oxidation-potentials of TAA and central chromophore, when compared to all other compounds investigated in this work. Hence, at this point it is unclear if a charge separated state (CSS) in **D-Pd(dipy)$_2$-A** would involve either both the TAA and the central chromophore or only one of the moieties as an electron donor. As explained in chapter 3.2.4, the energy of possible CSSs can be estimated from the potential difference between the first oxidation of the electron donor and the first reduction of the electron acceptor using the *Weller* approach. Only on the basis of the determined energies a prediction of the identity of the CSS in **D-Pd(dipy)$_2$-A** is possible. Since this approach also takes into account the solvent and the radii of, as

well as the distance between the respective donors and acceptors, the lowest charge separated state is not necessarily the one with the lowest potential difference. Nonetheless, for all other investigated compounds, the involved electron donors and acceptors should be clear, since no CS is expected to occur in the donor-reference dyads, and the lowest oxidation potential is clearly localized on the TAA for all compounds except **D-Pd(dipy)$_2$** and **D-Pd(dipy)$_2$-A**.

Spectroelectrochemistry (SEC)

Spectroelectrochemistry (SEC) was performed to investigate the spectral features of the cationic and anionic forms of the target triads. By a superposition of the determined spectra associated with the monoradical anion and the monoradical cation, the absorption spectrum of a possible CSSs can be simulated. Due to the strong overlap of the TAA-associated reversible oxidation and the irreversible oxidation of the central chromophore, SEC could not be performed for **D-Pd(dipy)$_2$-A**. For all other triads, the charge separated state (CSS) is expected to involve the $NDI^{\bullet-}$ and the $TAA^{\bullet+}$ monoradicals whose spectral features are expected to be very similar throughout all triads. Thus, SEC was only performed for **D-PdPDM-A**. For this purpose, a solution of the compound in DCM with 0.2 M TBAHFP as a conducting salt was reduced/oxidized stepwise by applying a steadily decreasing/increasing voltage to the solution. After each step, the UV/Vis absorption spectra was recorded for the respective voltage.

The determined voltage dependent spectra are shown in **Figure 73** (A) for the first reduction (red) and the first oxidation (blue). The the SEC of the triad is completely reversible as the back oxidation and reduction completely recovered the neutral species (black).

For the first reduction, the rise of five peaks can be observed. Three low energy signals have low intensities with maximal extinction coefficients of 5600 $M^{-1}cm^{-1}$ at 12900 cm^{-1}, 5600 $M^{-1}cm^{-1}$ at 14300 cm^{-1} and 11000 $M^{-1}cm^{-1}$ at 16500 cm^{-1}. The fourth signal at 20900 cm^{-1} is superimposed on the main absorption of the central chromophore and thus reaches extinction coefficients up to 58000 $M^{-1}cm^{-1}$. The final signal at around 36800 cm^{-1} is superimposed on the high energy transitions of the triad and reaches extinction coefficients up to 43900 $M^{-1}cm^{-1}$. Simultaneously, the characteristic, vibronically structured π-π*-transitions around 26200 cm^{-1} and 27900 cm^{-1} decrease, hinting at a reduction localized at the NDI as is to be expected from the cyclic voltammetry.

For the first oxidation, the rise of three peaks can be observed. The most intense signal at 13000 cm^{-1} shows a maximal extinction coefficient of 27900 $M^{-1}cm^{-1}$. A second low energy peak around 16700 cm^{-1} is very broad and of low intensity, while the third peak is superimposed on the main absorption of the NDI. Again, a simultaneous decrease of the TAA-associated absorption band at around 32700 cm^{-1} indicates a localization of the first oxidation on the TAA.

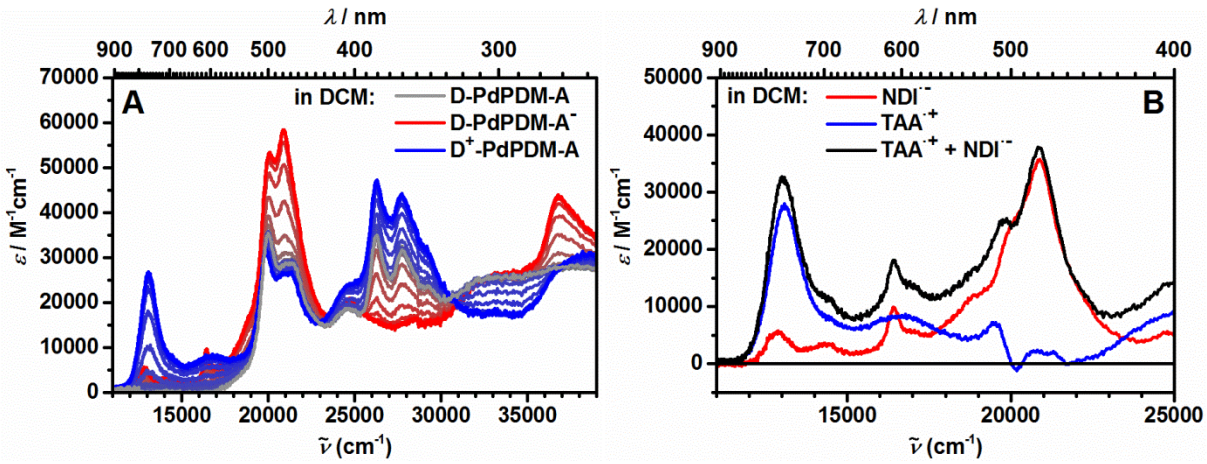

Figure 73: Stepwise first reduction (red) and first oxidation (blue) of **D-PdPDM-A** (black) in a 0.2 M solution of TBAHFP in DCM (A) and the resulting $NDI^{\bullet-}$ (red) and $TAA^{\bullet+}$ (blue) monoradical ion spectra and the superposition of both (black) corrected for the absorption of the central chromophore (B).

Since some of the signals associated with the first reduction and oxidation are superimposed on signals of the central chromophore, the spectra have to be corrected for the absorption of the neutral species to give the absolute absorption due to reduction and oxidation. The resulting spectra are shown in **Figure 73** (B) and exhibit the expected characteristic peaks of the $NDI^{\bullet-}$ and $TAA^{\bullet+}$ monoradical ions.[82, 181-182, 186-187, 204] The small deviations from the expected spectral shape between 19000 – 23000 cm^{-1} are due to the influence of the neutral TAA on the central chromophore. As discussed above, the substitution of **PdPDM** with TAA increases the absorption intensity of the main absorption band of the central chromophore between 17000 – 26000 cm^{-1}. Upon oxidation of the TAA, this effect seems to be diminished, reducing the extinction coefficients of the central chromophore and thus corrupting the correction of the $TAA^{\bullet+}$ monoradical ion spectra. The sum of the $NDI^{\bullet-}$ and $TAA^{\bullet+}$ monoradical spectra estimates the spectrum of the expected CSSs in which the NDI is reduced and the TAA is oxidized. The resulting spectra shows three signals. The high energy peak at 20900 cm^{-1}shows an extinction coefficient of 37700 $M^{-1}cm^{-1}$ is associated with the $NDI^{\bullet-}$ monoradical anion while the low energy peak at 13000 cm^{-1} shows an extinction coefficient of 32600 $M^{-1}cm^{-1}$ and is associated with the $TAA^{\bullet+}$ monoradical cation. The intermediate peak at 16400 cm^{-1} shows an extinction coefficient of 18100 $M^{-1}cm^{-1}$ and consists of contributions from both radical ions. While the spectral shape of the peak is dominated by $NDI^{\bullet-}$, a significant part of the signal intensity is due to the underlying broad absorption band of $TAA^{\bullet+}$. The estimated spectra of the CSS and the determined respective contributions of the NDI and the TAA significantly simplify the interpretation of the transient absorption spectra as will be seen in the next chapter.

Conclusions

Although the observed emission quenching clearly suggests the occurrence of charge separation only for the triad **D-PdPDM-A** and the acceptor-substituted reference dyad **PdPDM-A** this process is expected to occur in all compounds where the CSS is lower in energy than the state from which it is occupied. Since the ISC in **Pd(dipy)$_2$** and **PdPDM** was determined to be very fast, the CSSs are occupied from the lowest triplet state of the central chromophore. These are ligand centered (^{3}LC) for the compounds based on **PdPDM** and **PDM** and metal centered (^{3}MC) those based on **Pd(dipy)$_2$**. As explained in chapter 3.2.4, the energies of the involved states can be estimated from the steady state properties resulting in the values summarized in **Table 20**.[37, 82, 106, 115, 179, 189]

Table 20: Energy of the singlet ($\Delta E(^1LC_2)$) and triplet ($\Delta E(^3LC)$ / $\Delta E(^3MC)$) excited state as well as the charge separated state CSS_2 (ΔG_{CSS}) in different solvents determined as described in chapter 3.2.4 using the potential-differences ΔE_{redox} from **Table 19** and the given values for the donor-acceptor distance (d_{DA}) and the radii of the involved redox centers (r_D and r_A).

	d_{DA}[a] /Å	r_D[a] /Å	r_A[a] /Å	solvent	ΔE ($^1LC_2$) /cm^{-1}	ΔE (^{3}LC/^{3}MC) /cm^{-1}	ΔG_{CSS} /cm^{-1}
D-Pd(dipy)$_2$	9.1	4.81	5.11	MeCN	19500	12600[b]	14600
Pd(dipy)$_2$-A	12.7	5.11	3.97	MeCN	20000	12600[b]	10800
				THF	-	-	12500
				toluene	20000	-	17400
D-Pd(dipy)$_2$-A	21.9 (12.7)[c]	4.81 (5.11)[c]	3.97 (3.97)[c]	MeCN	19800	12600[b]	9000 (8000)[c]
				THF	-	-	11300 (9700)[c]
				toluene	19900	-	17500 (14600)[c]
D-PdPDM	9.1	4.81	5.20	MeCN	19100	14000	14000
PdPDM-A	16.9	5.20	3.97	MeCN	19200	14000	10800
				THF	-	-	12700
				toluene	19100	14000	19100
D-PdPDM-A	24.4	4.81	3.97	MeCN	19200	14000	8300
				THF	-	-	10600
				toluene	19100	14000	16900
D$_{Ph}$-PdPDM-A	28.6	4.81	3.97	MeCN	19200	14000	7800
				THF	-	-	10100
				toluene	19100	14000	16600
D-PDM-A	24.4	4.81	3.97	MeCN	22000	15900	8100
				THF	-	-	10400
				toluene	21800	15800	16800

[a] estimated from DFT-calculations; [b] estimated from DFT-calculations on **Pd(dipy)$_2$** as discussed in chapter 4.2.7; [c] values in brackets correspond to CSS_1 between the central chromophore and the NDI

Since the investigated compounds are not stable under strong laser-excitation in DCM, it is replaced by THF as another solvent of intermediate polarity in the following chapter. Although it was not proved by steady state measurements, the state energies of the central chromophores should be very similar to those in DCM and thus very similar to those in the solvents of vastly different polarities, MeCN and toluene.

As expected, no CS is possible in the donor substituted reference dyad **D-Pd(dipy)$_2$** since even in the highly polar solvent MeCN, which stabilizes the CSSs very effectively the energy of the CSS (ΔG_{CSS}) is higher than the energy of the lowest excited triplet state ($\Delta E(^3MC)$). For **D-PdPDM** on the other hand ΔG_{CSS} and $\Delta E(^3LC)$ have about the same magnitude. Nonetheless, no CS is expected since the compound exhibited phosphorescence of similar intensity as the unsubstituted central chromophore. For the acceptor functionalized reference compounds CS is possible in the highly polar solvent MeCN but not in the non-polar toluene due to the solvent dependence of ΔG_{CSS}. In THF, CS is expected for **PdPDM-A** due to the state energies and the observation of emission quenching in DCM which is of comparable polarity. For **Pd(dipy)$_2$-A**, the CSS and the ^{3}MC-state are of comparable energy. Since $\Delta E(^3MC)$ is only estimated by DFT calculations of the unsubstituted central complex, the actual energetic situation is unknown. Furthermore, the fluorescence of **Pd(dipy)$_2$** has a maximum lifetime of 13 ps as was shown in chapter 4.2.7, and thus is expected to occur significantly faster than the charge separation. This rationalizes the observed independence of the emission intensity from the substitution with the donor and acceptor groups and makes an observation of the CS via emission quenching impossible. For the triads, two CSS are possible. In CSS_1 the charge is transferred from the central chromophore to the NDI while in CSS_2 the charge is further separated between the TAA and the NDI. Usually, CSS_2 is by far the more stable state and CSS_1 is only observed as a short lived intermediate, if at all. While this is expected to be the case in **D-PdPDM-A**, **D$_{Ph}$-PdPDM-A** and **D-PDM-A**, the situation is different for **D-Pd(dipy)$_2$-A** where CSS_1 is even a bit more stable than CSS_2 and is thus expected to be observed in the TA spectroscopy.[59, 91-92, 103, 115, 193]

Furthermore, the steady state measurements indicated non-negligible electronic coupling between the central chromophore and the attached acceptor and especially donor moieties and also enables the interaction between the oxidized TAA and the reduced NDI in the charge separated states. This is in contrast to the cyclometalated dipyrrinato complexes discussed in chapter 3 and should affect the charge separation and charge recombination (CR) kinetics significantly. This will be one topic in the next chapter, where the occurrence of CS and the identity of the observed transient species will be investigated by comparison of the ns-TA spectra with the simulation of the CSS-absorption based on the SEC-measurements shown in **Figure 73**. Furthermore the kinetics of the CR will be investigated by ns-TA spectroscopy for all dyads and triads and the CS-kinetics will be discussed based on fs-TA measurements for **D-Pd(dipy)$_2$-A**.

4.3.2 Charge-Separation and Recombination

The steady state properties of the target molecules strongly indicates the occurrence of charge separation in the acceptor substituted compounds. To validate this assumption, transient absorption (TA) spectroscopy was performed on **D-PDM-A**, **D-PdPDM-A**, **D_{Ph}-PdPDM-A** and **D-Pd(dipy)$_2$-A** as well as the respective reference dyads. The transient absorption of the unsubstituted central chromophores has already been discussed in chapters 4.2.5 as well as 4.2.7 and will be used as a further reference throughout this chapter. If not stated otherwise, all discussed measurements were performed in degassed MeCN after excitation into the $^1LC_2$-band of the central chromophore.

ns-Transient absorption spectroscopy

Figure 74 shows the ns-TA spectra of **D-PDM-A**. At early times, the rapid decrease of a bleaching signal around 23900 cm^{-1} can be observed, which is associated with the excited state of the central chromophore. Simultaneously to the decay of the GSB, a weak excited state absorption (ESA) rises. Due to the signals around 21000 cm^{-1} and 16500 cm^{-1} characteristic for the NDI$^{\bullet-}$ monoradical anion and around 13600 cm^{-1} for the TAA$^{\bullet+}$ monoradical anion the ESA can be associated with a charge separated state between the donor and acceptor (CSS_2).[82, 115, 179, 182, 186-187, 198]

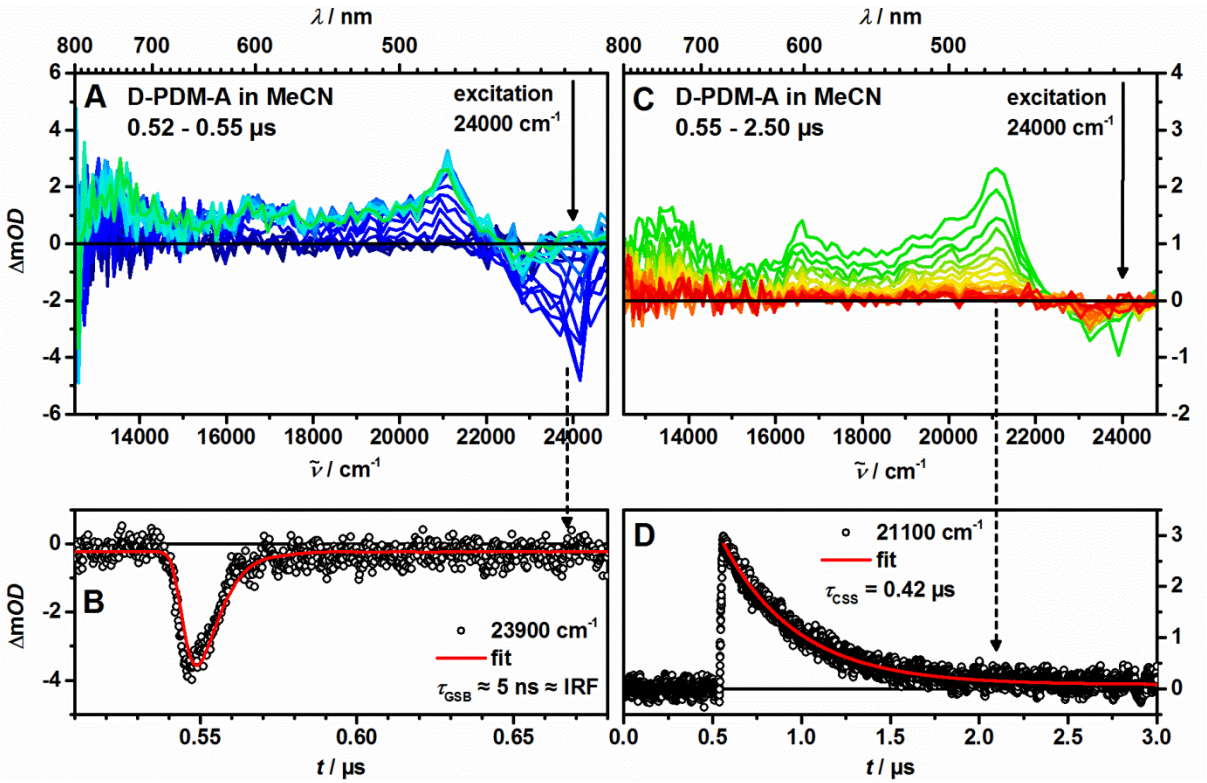

Figure 74: ns-Transient absorption spectra of **D-PDM-A** in MeCN at rt after excitation at 24000 cm^{-1} at early times (A) and later times (C) as well as kinetic traces with fit at selected wavenumbers (B and D). Early spectra are depicted in blue to green and later spectra in orange to red color.

The decay traces shown in **Figure 74** (B and D), give insight into the kinetics of the involved processes. The charge recombination from CSS_2 to the ground state occurs with a lifetime of τ_{CSS} = 0.42 µs. On the other hand, the decay of the GSB is so fast that It occurs within the response function of the instrument (IRF) of about 7 ns. Hence, the determined lifetime of τ_{GSB} = 5 ns is only a rough estimation. Since the unsubstituted porphodimethene **PDM** also shows a rapid deactivation of the excited state within the IRF, the decay of the GSB in **D-PDM-A** cannot only be associated with charge separation (CS) to CSS_2. Rather, the contribution of CS is smaller than the non-radiative and radiative deactivation of the central chromophore, explaining the overall very small signal intensities of the GSB and ESA since the competing processes deactivate the central chromophore during the IRF and reduce the quantum yield of charge separation significantly. For this reason, no further studies were performed on **D-PDM-A**.

Figure 75 shows the ns-TA spectra of the reference dyads **D-PdPDM** (A) and **PdPDM-A** (C) as well as kinetic traces at selected wavenumbers (B and D). Both complexes exhibit a GSB and an intense ESA towards lower energies which can be associated with the ^{3}LC-state of the central chromophore. The difference between the compounds is the decay kinetic of the signals. In **D-PdPDM** the GSB decays with a lifetime of τ_{GSB} = 47 µs which is on the same order of magnitude as for the unsubstituted **PdPDM** (τ_{GSB} = 83 µs), while the GSB decays much faster in **PdPDM-A** with a lifetime of τ_{GSB} = 4.0 µs.

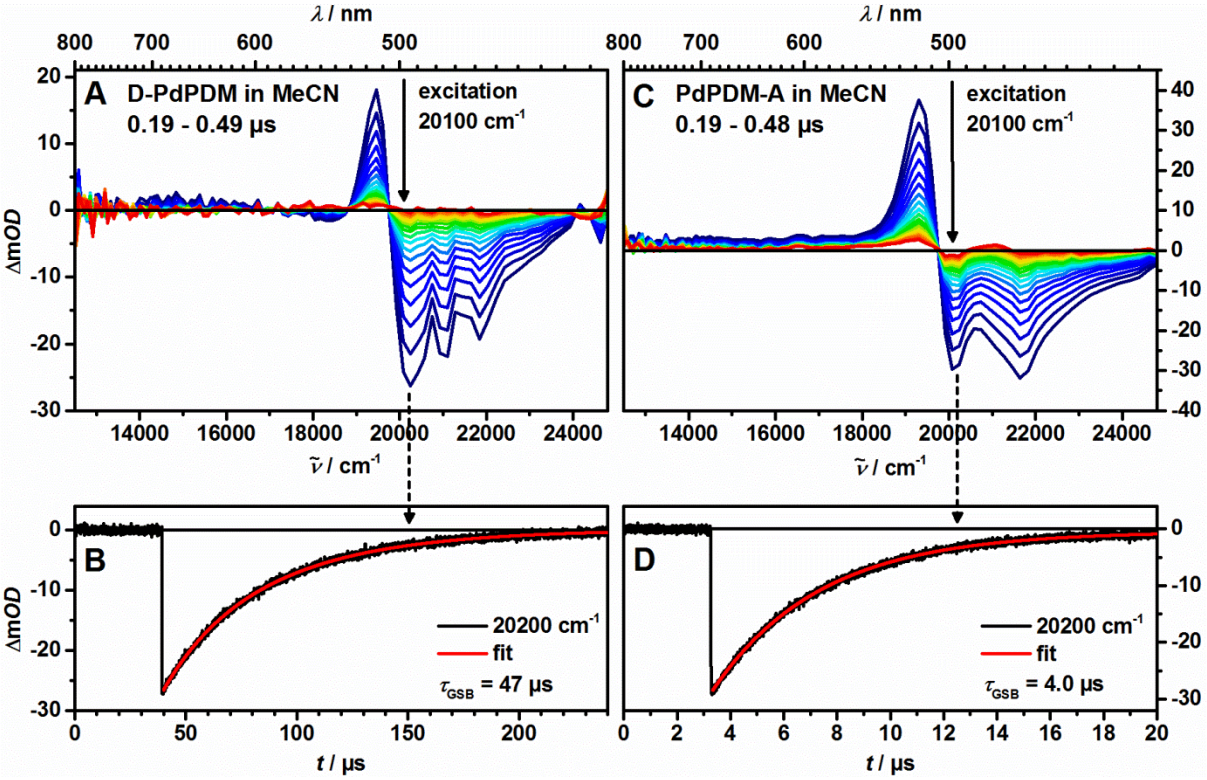

Figure 75: ns-TA spectra of **D-PdPDM** (A) and **PdPDM-A** (B) in MeCN at rt after excitation at 20100 cm^{-1} and kinetic traces with fit at selected wavenumbers (B and D).

Since similar observations were made for the cyclometalated dipyrrinato complexes in chapter 3.3, this significant decrease of the excited state lifetime can be attributed to the slow formation of a CSS between the central chromophore and the NDI (CSS_1) and a successive rapid charge recombination (CR) to the ground state. The assumed inverted lifetimes prevent the observation of CSS_1 due to very low intermediate concentrations. To confirm this suggestion, **PdPDM-A** was also excited at 28200 cm^{-1} which corresponds to a simultaneous excitation of the NDI and the central chromophore in a ratio of 0.85 / 0.15 favoring the NDI. The resulting data are shown in **Figure 76**. At early times (A) the signal at 16600 cm^{-1} proves the virtually instantaneous formation of a $NDI^{\bullet-}$ monoradical anion from the singlet excited state of the NDI as shown in chapter 3.3.2. The second signal of the reduced NDI around 21100 cm^{-1} is strongly superimposed by the GSB and ESA associated with **PdPDM**. Since this GSB is partially due to the oxidized state of the central chromophore in CSS_1 and partially due to residual **PdPDM** in its excited s ^{3}LC state, the depicted kinetic traces describe both CSS_1 and ^{3}LC. All traces indicate a biexponential behavior. The short component can be associated with the CR of CSS_1 with a lifetime of about τ_{CSS} = 0.39 µs, while the longer component indicates the lifetime of the GSB of τ_{GSB} = 3.8 µs. Accordingly, at longer times (C) the signals associated with CSS_1 are no longer observable. This is in excellent agreement with the observations after excitation at the central chromophore and the proposed deactivation mechanism.[62, 115, 179, 186, 198]

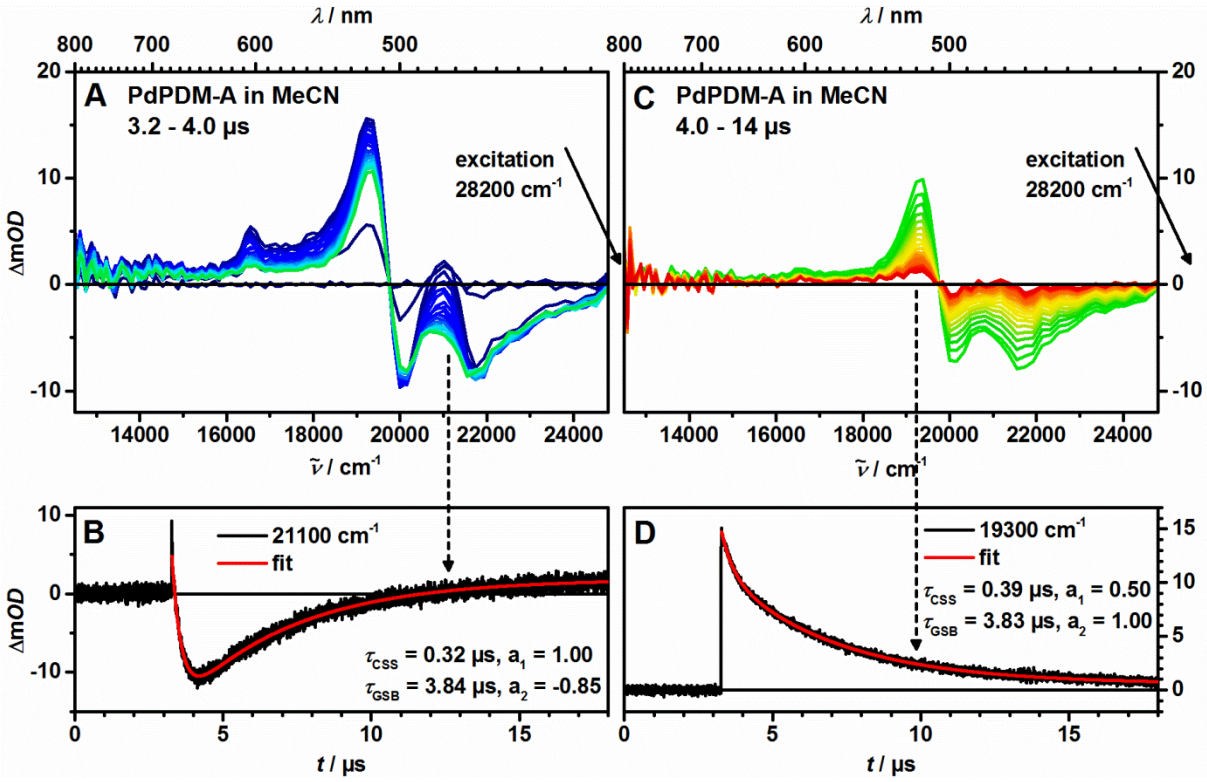

Figure 76: ns-TA spectra of **PdPDM-A** in MeCN at rt after excitation at 28200 cm^{-1} at early times (A) and later times (C) as well as kinetic traces with fit at selected wavenumbers (B and D).

Figure 77 shows the TA spectra of the short triad **D-PdPDM-A** at early times (A) and later times (C) as well as kinetic traces at selected wavenumbers (B and D). Furthermore, a global analysis was performed[i] on the data using a sequential model and the GLOTARAN software (v. 1.2).[195] The resulting evolution associated difference spectra (EADS) and their respective lifetimes are shown in **Figure 77** (E).

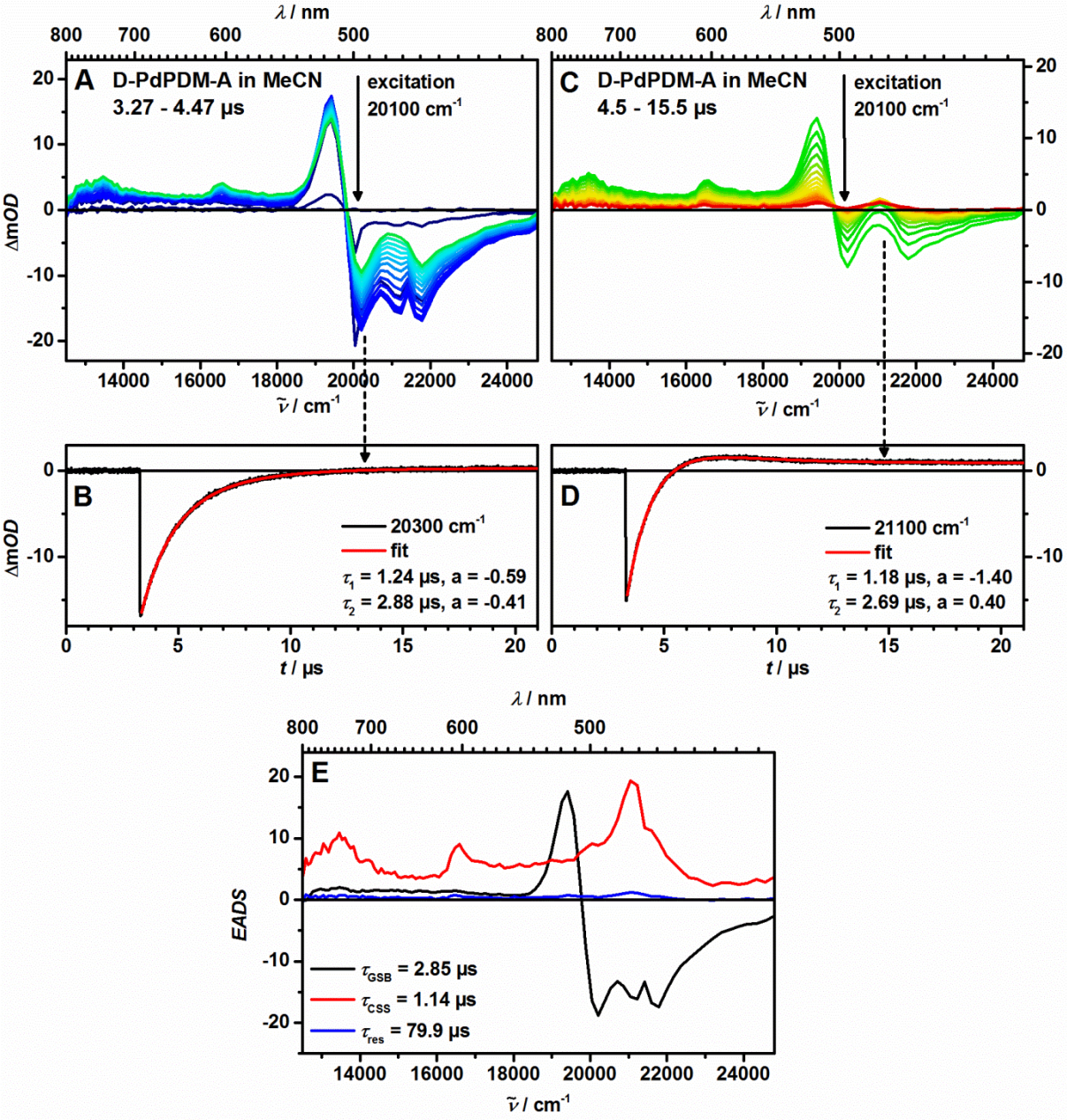

Figure 77: ns-TA spectra of **D-PdPDM-A** in MeCN at rt after excitation at 20100 cm^{-1} at early times (A) and later times (C) as well as kinetic traces with fit at selected wavenumbers (B and D) and evolution associated decay spectra (EADS) obtained from a global fit (E).

[i] All global analysis were performed by Dr. Marco Holzapfel

At early times, the GSB between 20000 – 22000 cm^{-1} and the ESA at 19500 cm^{-1} indicate a population of the ^{3}LC state of the central chromophore. The decay of those signals is accompanied by the rise of weak ESA at 16600 cm^{-1} and 13500 cm^{-1} which can be associated with the monoradical ions of the NDI and the TAA, respectively. As for **PdPDM-A**, the main absorption of the reduced NDI around 21100 cm^{-1} is superimposed by the signals associated with ^{3}LC and manifests as a reduction of the GSB. This proofs the formation of CSS_2 starting from the ^{3}LC-state of the central chromophore. At longer times all transient signals decay simultaneously. The kinetic traces reveal lifetimes of τ_1 = 1.2 µs and τ_2 = 2.8 µs. Since the small amplitudes of the signals associated with CSS_2 prevent a clear interpretation of the kinetics based solely on two kinetic traces the interpretation was backed up by a global deconvolution which reveals three EADS. The first two are clearly associated with ^{3}LC of the central chromophore and CSS_2 with lifetimes of τ_{GSB} = 2.9 µs and τ_{CSS} = 1.1 µs which agree very well with those from the fit of singular decay traces. Hence, the CS is assumed to be slower than the CR to the ground state which explains the low intensity of the signals associated with CSS_2. The third EADS has a lifetime of τ_3 = 80 µs, which can be considered virtually infinite on the investigated timescale of 40 µs. Furthermore it has a very low intensity and results from the small off-set observed at longer lifetimes also observable in **Figure 77** (C and D). The origin of this off-set is not completely clear at the moment although it is certainly compound-specific and not intrinsic to the set-up. Further observations regarding the amplitude at very long times were made during the magnetic field dependent measurements and will be described in the next chapter.

Figure 78 shows the TA data of the elongated triad **D_{Ph}-PdPDM-A**. The results are very similar to the short derivative **D-PdPDM-A**. At early times a relatively slow decay of the signals associated with ^{3}LC of the central chromophore is accompanied by a rise of the signals associated with CSS_2 indicating the occurrence of CS, while at longer times the signals for CSS_2 decay due to CR to the ground state. The main difference is found for the kinetics of the involved processes. While the lifetime of ^{3}LC of τ_{GSB} = 2.9 µs indicates that the CS is as fast as in the short triad, the CR becomes significantly slower with an associated CSS lifetime of τ_{CSS} = 7.7 µs. The longer lifetime of CSS_2 can be attributed to the increased distance between donor and acceptor and a reduced electronic coupling due to the additional phenyl ring, which slows down the charge recombination. The fact that the kinetic of the charge separation from ^{3}LC to CSS_2 remains unaffected indicates that the rate determining step does not involve the additional phenyl ring and the TAA. This is in line with a CS-mechanism comprised of two consecutive electron transfer reactions: At first an electron is transferred slowly from the excited central chromophore to the NDI, forming CSS_1 independently from the donor. The subsequent hole transfer from the central chromophore to the TAA is much faster forming CSS_2 almost instantly and preventing the observation of CSS_1.[32, 59, 82, 96, 105, 115-116, 186, 199]

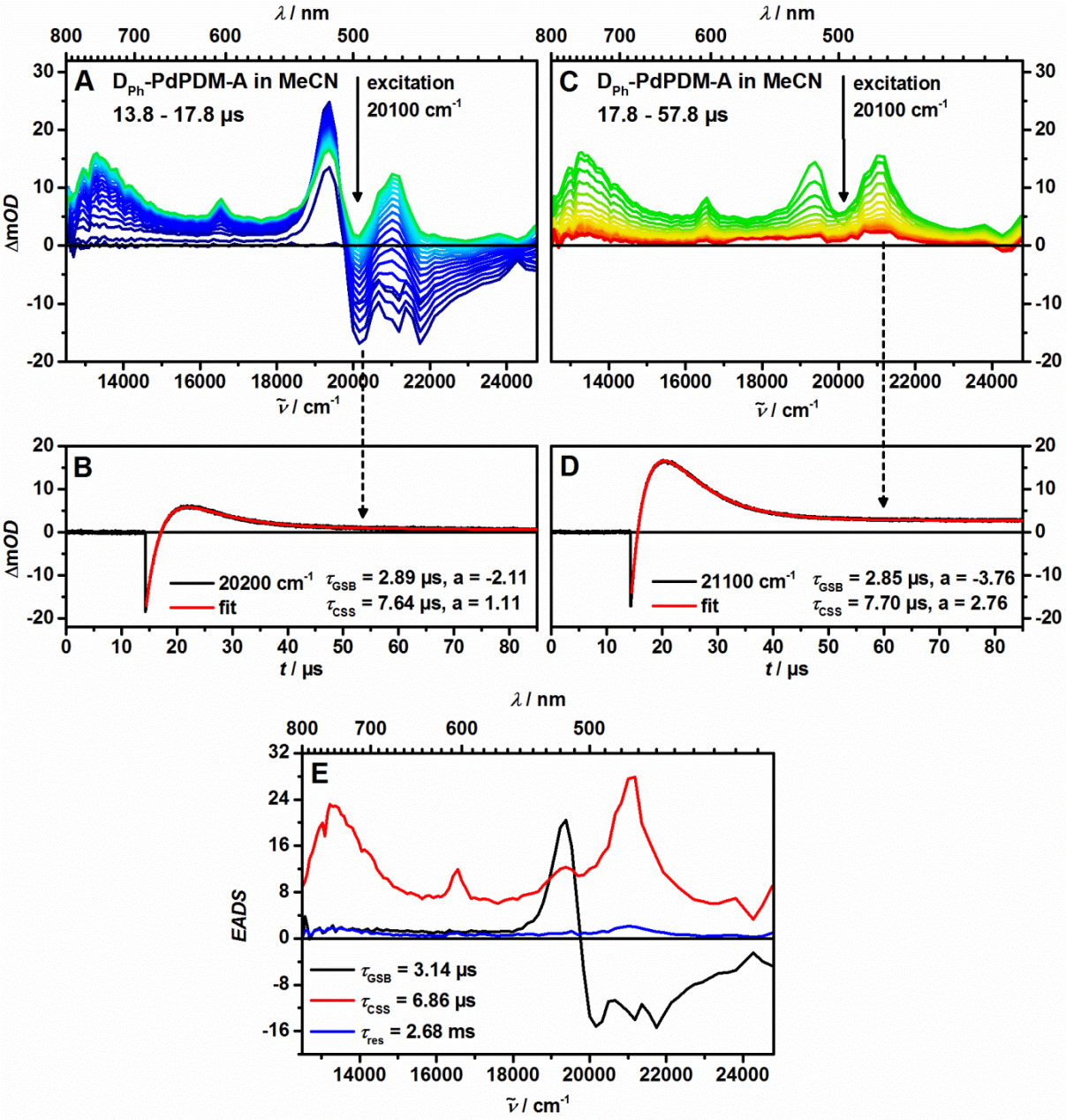

Figure 78: ns-TA spectra of **D$_{Ph}$-PdPDM-A** in MeCN at rt after excitation at 20100 cm^{-1} at early times (A) and later times (C) as well as kinetic traces with fit at selected wavenumbers (B and D) and evolution associated decay spectra (EADS) obtained from a global fit (E).

Moving on to the compounds based on the non-bridged bisdipyrrinato complex **Pd(dipy)$_2$**, **Figure 79** shows the ns-TA spectroscopy of the donor- and acceptor substituted reference dyads. **D-Pd(dipy)$_2$** and **Pd(dipy)$_2$-A** exhibit transient spectra similar to the unsubstituted central chromophore, with a strong GSB around 21000 cm^{-1} and an ESA around 20000 cm^{-1}, associated with the ^{3}MC excited state. The excited states decay with lifetime of τ_{GSB} = 70 ns and τ_{GSB} = 57 ns respectively, which also is comparable to the ^{3}MC lifetime of **Pd(dipy)$_2$** of 55 ns. Furthermore, a broad ESA of low intensity can be observed for **D-Pd(dipy)$_2$** between 15000 – 18000 cm^{-1} which may be due to the strong electronic coupling between the central chromophore and the donor-moieties.

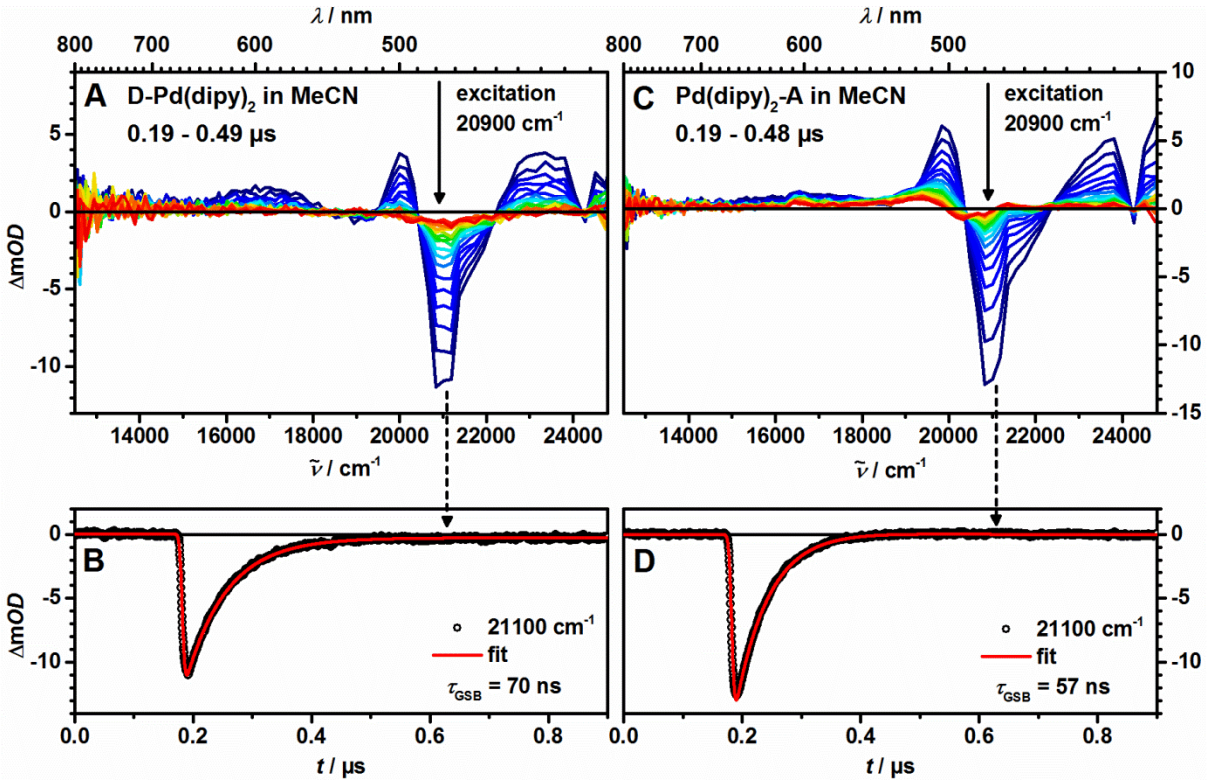

Figure 79: ns-TA spectra of **D-Pd(dipy)$_2$** (A) and **Pd(dipy)$_2$-A** (B) in MeCN at rt after excitation at 20900 cm^{-1} and kinetic traces with fit at selected wavenumbers (B and D).

In **Pd(dipy)$_2$-A** on the other hand, a signal with very low intensity can be observed at 16600 cm^{-1}. This signal is associated with the NDI$^{\bullet-}$ monoradical anion and usually indicates the formation of a charge separated state. The very low intensity could again be explained with a faster rate of the CR than of the CS resulting in low intermediate concentrations of CSS_1. However, control experiments after excitation at the NDI equivalently to those performed for **PdPDM-A**, result in the same spectra and kinetics as after excitation of the central chromophore and thus can give no additional insights.

Figure 80 shows the ns-TA of the full triad **D-Pd(dipy)$_2$-A**. Again, the GSB and ESA characteristic for the ^{3}MC-state of the central chromophore can be observed at early times (A). Simultaneously to the decay of the GSB, the rise of further absorptive signals at 16600 cm^{-1} and 13300 cm^{-1} can be observed which are related to the monoradical ions of the NDI and TAA indicating the formation of CSS_2. The missing second signal of the reduced NDI at 21100 cm^{-1} could again be explained by the superposition with the GSB signal and similar lifetimes of both. However, the lifetimes of the ^{3}MC-state of the central chromophore and the CSS state are τ_{GSB} = 47 ns and τ_{CSS} = 0.19 µs respectively, and thus different enough that a clear separation of the spectral features can be expected. Finally, the ESA at 20000 cm^{-1} associated with ^{3}MC is not observed at later times. To further investigate the obtained data, a global analysis according to a sequential model was performed and results in three EADS.

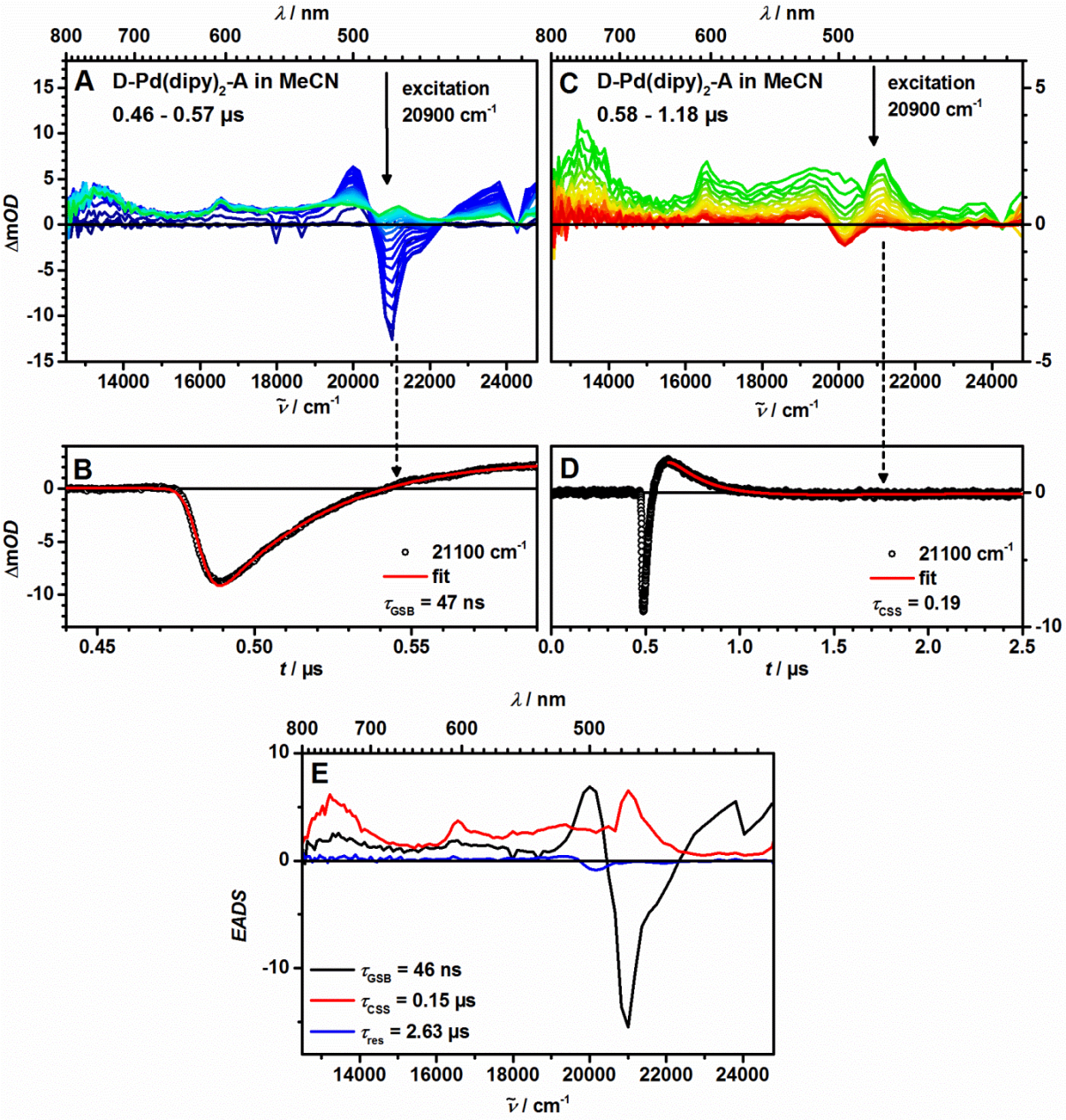

Figure 80: ns-TA spectra of **D-Pd(dipy)$_2$-A** in MeCN at rt after excitation at 20900 cm^{-1} at early times (A) and later times (C) as well as kinetic traces with fit at selected wavenumbers (B and D) and evolution associated decay spectra (EADS) obtained from a global fit (E).

The first and second EADS show the characteristic spectra of the ^{3}MC-state and CSS$_2$, with lifetimes of 46 ns and 0.15 µs respectively. Furthermore, a third EADS is obtained which has a lifetime of τ_{res} = 2.63 µs, a very low intensity and no distinct spectral features beside a small bleach around 20000 cm^{-1}. The third EADS will thus be treated as an offset at very long times and most likely is the cause for the unexpected spectral shape of the transient absorption data and the seemingly missing signal of the reduced NDI at 21100 cm^{-1}. At the moment, the cause for the offset at long times cannot be specified in greater detail. Possible reasons for the offset include a gradual decomposition of the compound, which is assumed to be reversible since no change in the UV/vis absorption could be

found when comparing spectra acquired before and after the ns-TA-spectroscopy. Nonetheless, the first two EADS confirm the formation of CSS_2 even though a lower energy was estimated for CSS_1. This is due to the uncertainty of the redox-potentials and donor-acceptor distances and especially the approximate nature of the Weller-calculation used in chapter 4.3.1 for the calculation of ΔG_{CSS}.

The overall low intensities of the signals associated with the CSS in **D-Pd(dipy)$_2$-A** are due to an inefficient charge separation. Since the ^{3}MC state has a lifetime of 47 ns in **D-Pd(dipy)$_2$-A,** the CS occurs on a similar lifetime as the non-radiative deactivation of the ^{3}MC state in **Pd(dipy)$_2$** with a lifetime of 55 ns. Hence, both processes contribute significantly to the decay of ^{3}MC, thus lowering the quantum yield of CSS.[85]

Finally, for the triads based on the bridged and non-bridged bisdipyrrinato metal complexes **PdPDM** and **Pd(dipy)$_2$** ns-TA spectroscopy was also performed in less polar solvents. All determined lifetimes are summarized in **Table 21** at the end of the chapter.

fs-Transient absorption spectroscopy

To further investigate the influence of the previously discussed structural rearrangement of **Pd(dipy)$_2$** on the process of charge separation, fs-TA maps were recorded[j] for **Pd(dipy)-A** and **D-Pd(dipy)-A** in MeCN at rt and analyzed by a global deconvolution using the minimum number of exponentially decaying individual spectral components (transients) needed for a satisfying fit to a sequential model.[k] The resulting evolution associated difference spectra (EADS) are depicted in **Figure 81**.

For **Pd(dipy)$_2$-A**, no signals associated with a CSS can be observed. Instead, the transient maps and the resulting EADS are very similar to those observed for the unsubstituted **Pd(dipy)$_2$**. The first three EADS show little to no ESA and consist only of GSB. They are thus associated with the fast internal conversion (IC) from the ^{1}LC$_2$-state to the ^{1}LC$_1$ state (τ_1 = 170 fs), the subsequent vibrational relaxation (VR) of the ^{1}LC$_1$ state (τ_2 = 2.9 ps) and the ISC (τ_3 = 13 ps) already discussed for **Pd(dipy)$_2$** and show very similar rates of the described transitions. Additionally, a further EADS with a lifetime of τ_4 = 72 ps is observed, which only differs slightly from the final fifth EADS which has a lifetime of τ_5 = 39 ns and is thus associated with the ^{3}MC-state. Both EADS exhibit a relatively sharp ESA at around 20000 cm^{-1} which was already observed for bisdipyrrinato compounds in the triplet state in chapter 4.2.7. The transition between the fourth and fifth EADS can essentially be due to two processes.

The first possibility is that the forth EADS is already associated with the ^{3}MC-state of the central chromophore and the transition is a VR within the ^{3}MC-state. This is similar to the slow vibrational relaxation of the ^{3}LC-staate observed in **PdPDM**. However, it is unclear why this VR is not observed in

[j] All measurements were performed by Alexander Schmiedel.
[k] All global analysis were performed by Dr. Marco Holzapfel.

Pd(dipy)$_2$ since the substitution with the acceptor moieties should not influence the VR of a state localized almost purely on the central metal ion.

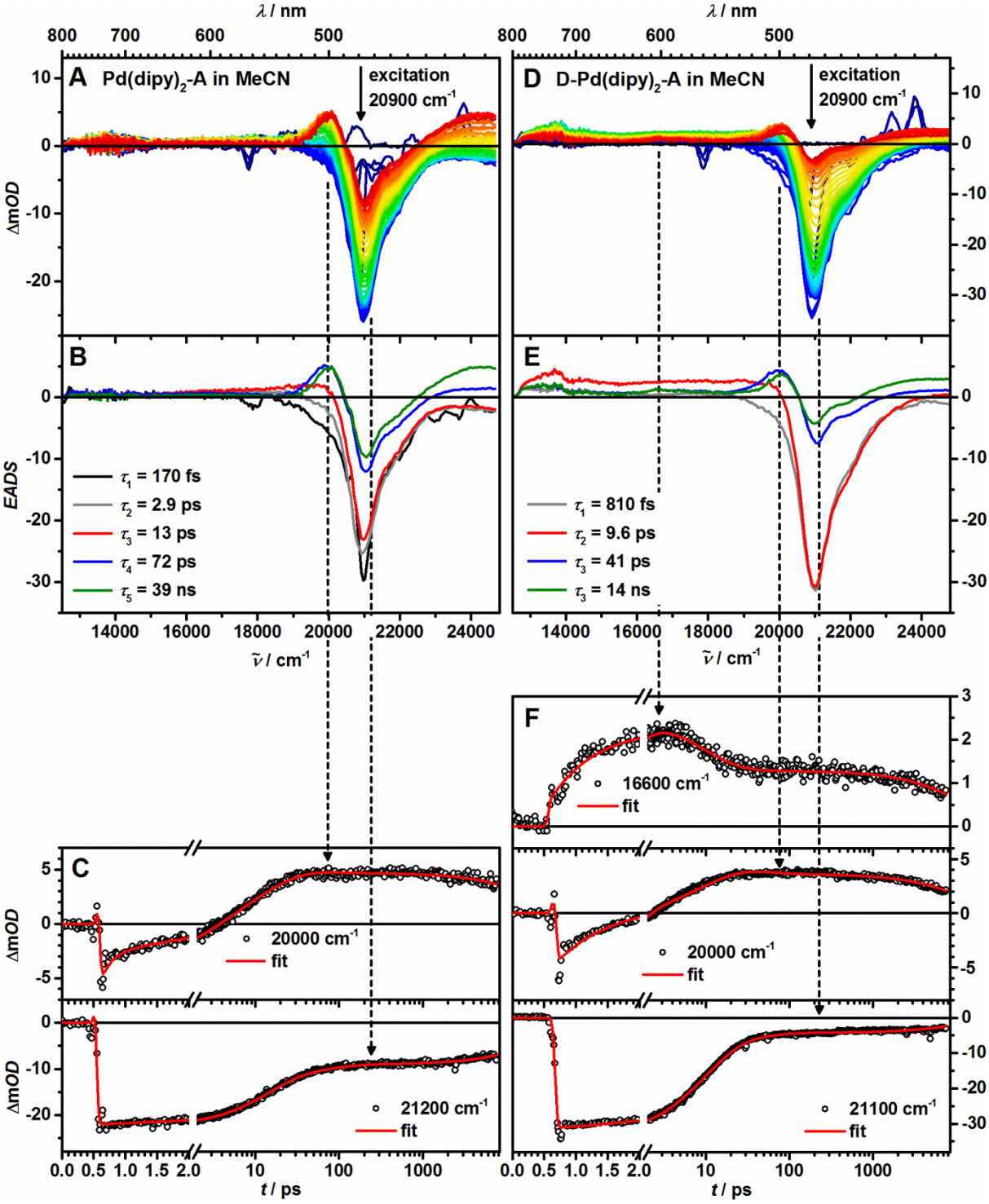

Figure 81: Chirp corrected transient absorption spectra of **Pd(dipy)$_2$-A** (A) and **D-PdPDM-A** (D) in MeCN at rt after excitation at 20900 cm^{-1}, evolution associated difference spectra (EADS) from a global fit (B and E), and time traces at selected wavenumbers for which the zero time delay was set arbitrarily with fit (C and F).

On the other hand, the interaction of the bulky NDI-substituents with the solvent shell of the compound could slow down the structural rearrangement of the central complex to a degree that it becomes observable. In this case, the fourth EADS would be associated with a triplet state in the geometry of the relaxed $^1LC_1$-state which would probably be ligand centered according to DFT-calculations on **Pd(dipy)$_2$** discussed in chapter 4.2.7. The subsequent transition to the fifth EADS would then be associated with the structural rearrangement of the central complex resulting in the ^{3}MC-state. This reaction pathway was already considered for **Pd(dipy)$_2$** but could not be observed since the structural rearrangement was assumed to be faster than the ISC resulting in low intermediate concentrations of the ^{3}LC state.

For **D-Pd(dipy)$_2$-A** the global analysis results in only four transients. The first and second EADS mainly consist of GSB and exhibit lifetimes of τ_1 = 810 fs and τ_2 = 9.6 ps. Due to its spectral features, the second EADS is associated with the relaxed $^1LC_1$ state of the central complex. Thus, the first EADS has to correspond to the excited $^1LC_2$ state, either before or after VR. The lifetimes associated with the IC and VR of the excitonic states may differ from those observed for the symmetric compounds **Pd(dipy)$_2$** and **Pd(dipy)$_2$-A** due to the asymmetric substitution of the central chromophore in **D-Pd(dipy)$_2$-A**. Furthermore, the electronic coupling between the TAA and the central chromophore could also lead to variations in the excited state lifetimes. The third EADS shows the combination of GSB and ESA characteristic for the triplet state of the central chromophore and a weak signal at 16000 cm^{-1} which can be associated with the reduced NDI. It is thus unclear if the EADS has to be associated with the excited central chromophore in the triplet state or CSS_1. The same holds true for the fourth EADS. The differences between the third and fourth EADS are similar to those observed between the fourth and fifth EADS in **Pd(dipy)$_2$-A** and thus are also associated with the two possible transitions in the triplet state of the central complex. In this case this transition occurs with a lifetime of τ_3 = 41 ps. The final EADS has a lifetime of 14 ns and agrees reasonably well with the early spectra observed in the ns-TA measurements depicted in **Figure 80** (A). Due to the low intensity of the signals associated with the reduced NDI, the similarity of the subsequent transitions to those observed in **Pd(dipy)$_2$-A**, and the lower lifetime of the EADS associated with $^1LC_1$ (τ_2 = 9.6 ps), it is proposed that in **D-Pd(dipy)$_2$-A**, $^1LC_1$ decays simultaneously by CS and ISC in a ratio strongly favoring the ISC. The resulting states cannot be separated in the global analysis due to the low concentration and presumably long lifetime of the formed CSS, and thus are only observed as additional features in the following third and fourth EADS which are associated with ^{3}LC and ^{3}MC, respectively.

Conclusions

The ns-TA measurements confirm charge separation for all investigated triads as well as **PdPDM-A** and strongly suggest CS for **Pd(dipy)$_2$-A**. Since no other redox active moieties are present in the dyads, the charge has to be separated between the oxidized central metal complex (CMC) and the reduced NDI electron acceptor forming CSS_1. For the triads based on bridged CMCs, the charge separation occurs between the donor and the acceptor moieties, forming CSS_2. As can be seen in **Figure 82** (A), the observed TA-spectra match well with a superposition of the signals associated with the $NDI^{\bullet-}$ and $TAA^{\bullet+}$ monoradical ions obtained from SEC confirming the proposed identity of the CSS.

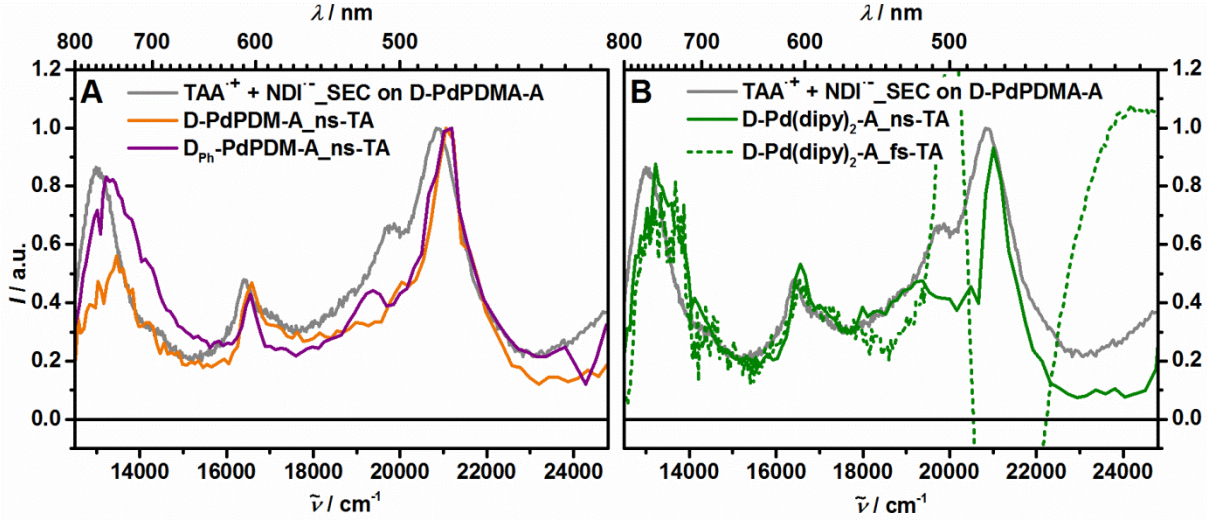

Figure 82: Spectra of CSS_2 of **D-PdPDM-A** and **D_{Ph}-PdPDM-A** (A) and **D-Pd(dipy)$_2$-A** (B) from a global deconvolution of the ns-TA spectroscopy (solid lines) and fs-TA spectroscopy (dotted lines) in MeCN in comparison to a superposition of the TAA-cation and NDI-anion spectra obtained from SEC of **D-PdPDM-A**.

For **D-Pd(dipy)$_2$-A** on the other hand, only the ns-TA spectrum of CSS_2 matches the simulation, while the spectrum obtained by fs-TA deviates significantly from the theoretical spectrum as can be seen from **Figure 82** (B). This is due to the incomplete CS during the time-window of the fs-setup and the resulting residual signal associated with the ^{3}MC-state of the CMC.

Furthermore, a state diagram of the photophysical processes can be constructed for the compounds based on the performed transient absorption experiments on the triads and reference compounds and additional data obtained by steady state experiments. This is done in **Figure 83** for **D-Pd(dipy)$_2$-A** and **D-PdPDM-A**. After excitation of **D-Pd(dipy)$_2$-A** into the $^1LC_2$ excitonic state, $^1LC_1$ is occupied by IC and VR. $^1LC_1$ simultaneously deactivates by radiative and non-radiative processes to the ground state and by ISC to a triplet state as well as CS to a charge separated state. The triplet state is expected to be initially formed in the C_i-symmetric geometry of the $^1LC_1$-state and thus is ligand centered based on DFT-calculations on **Pd(dipy)$_2$**.

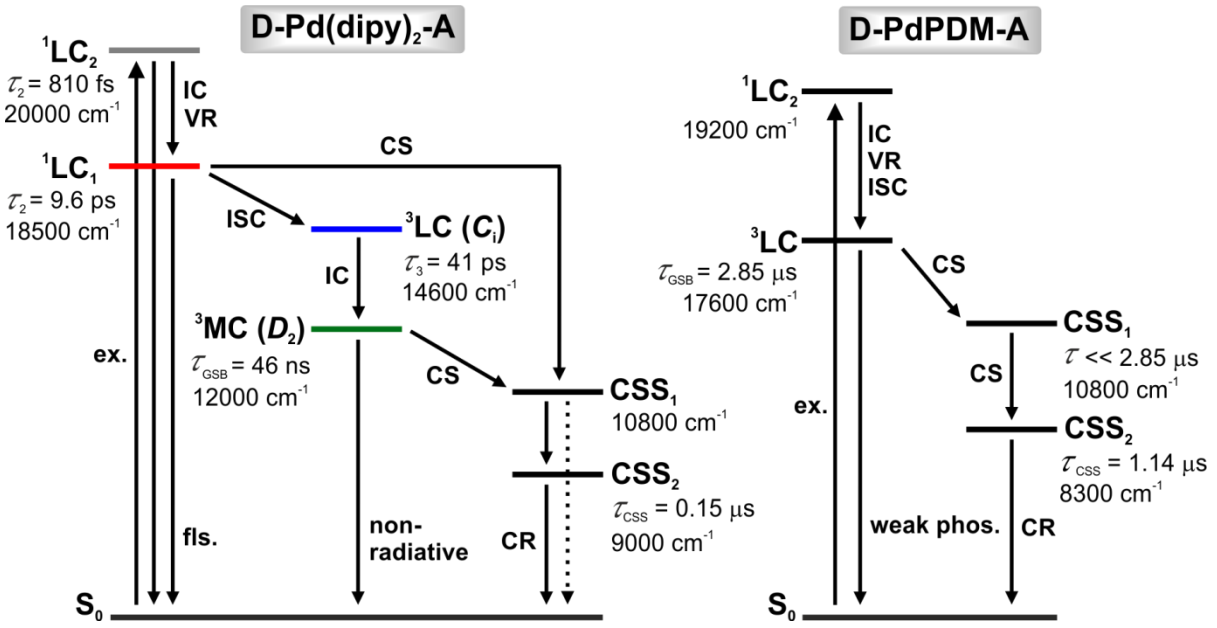

Figure 83: State diagram of **D-Pd(dipy)$_2$-A** and **D-PdPDM-A** in MeCN at rt after excitation at 20900 cm^{-1} and 20100 cm^{-1}, respectively. The colored states for **D-Pd(dipy)$_2$-A** refer to the EADS in **Figure 81**. The given lifetimes are taken from the ns- and fs-TA spectroscopic measurements.

The conformational rearrangement to the metal centered disphenoidal ^{3}MC-state is most likely slowed down in **D-Pd(dipy)$_2$-A** by the interaction of the bulky substituents with the solvent molecules and thus becomes observable. From the lowest excited ^{3}MC state the final charge separated state CSS_2 is formed most likely by an initial slow formation of CSS_1 and a subsequent fast formation of CSS_2 which prevents the detection of CSS_1 due to low intermediate concentrations. For **D-Pd(dipy)$_2$-A** a ^{3}MC-lifetime of 46 ns was determined by ns-TA spectroscopy which is not much shorter than the ^{3}MC-lifetime of the unsubstituted **Pd(dipy)$_2$**. Thus, the quantum efficiency of the CS is reduced considerably due to direct deactivation of ^{3}MC to the ground state.

For the dyads and triads based on **PdPDM**, the photophysics were only investigated by ns-TA spectroscopy since the charge separation only occurs on the microsecond timescale. Thus, only ^{3}LC and the respective CSS were observed for **PdPDM-A** and **D-PdPDM-A**. The determined lifetimes are collected in **Table 21**. After excitation into the $^1LC_2$ state of the central chromophore a ligand centered triplet state ^{3}LC is formed, virtually instantaneous on the ns-timescale. Presumably the involved transitions are equivalent to those observed for the unsubstituted central chromophore. While the decay of ^{3}LC in **D-PdPDM** is with a lifetime of 47 µs on a similar timescale as **PdPDM**, it decays much faster in the acceptor substituted compounds due to the occurrence of CS, forming CSS_1 for **PdPDM-A** and CSS_2 for the triads. From the similar ^{3}LC-lifetimes of τ_{GSB} = 3.8 µs in **PdPDM-A**, and τ_{GSB} = 2.9 µs in **D-PdPDM-A** and **D$_{Ph}$-PdPDM-A** It can be deduced that the initial CS is independent from the presence and properties of the donor-substituent and is thus associated with CS between the central chromophore and the NDI even for the donor-substituted triads. The subsequent hole

transfer from the oxidized central chromophore to the TAA-donor just occurs faster than the initial CSS and thus prevents the observation of CSS_1 due to low intermediate concentrations. This behavior is in line with observations made on similar cyclometalated dipyrrinato-complexes as shown in chapter 3 and reported in the literature.[59, 115-116] The massive reduction of the CS-rate towards CSS_1 when compared to the complexes using the standard acceptor functionalized dipyrrin **8** such as **D-Pd(dipy)$_2$-A** or **PdA** and **DPdA** can be attributed to the additional phenyl ring between the NDI and the central metal complex (CMC) present in the **PdPDM**-based complexes. The elongation of the NDI-CMC distance has been shown to significantly reduce the CT-rate from or to the NDI before, as expected from the general distance dependence of electron transfer reactions. For the same reasons, the lifetime of the respective CSSs increases from τ_{CSS} = 0.3 µs in **PdPDM-A** to τ_{CSS} = 1.1 µs in the short triad **D-PdPDM-A** and τ_{CSS} = 7.7 µs in the elongated triad **D$_{Ph}$-PdPDM-A**.[59, 96, 105, 199]

For the triads **D-Pd(dipy)$_2$-A**, **D-PdPDM-A** and **D$_{Ph}$-PdPDM-A**, the ns-TA spectra were also recorded in THF and toluene. As expected, no signs of charge separation could be observed in toluene, for any of the triads. In THF, no transient signals could be observed for **D-Pd(dipy)$_2$-A**, indicating that the excited states deactivate to the ground state significantly faster than the IRF.

Table 21: Lifetimes τ of the respective excited states of the investigated dyads and triads in MeCN and THF at rt after excitation of the $^1LC_2$ transition of the respective central chromophore and quantum yields Φ_{CSS} of the formed CSS.

	solvent	$^1LC_1$ [a]	^3LC [a]	^3LC / ^3MC[b,c]	CSS[b,d]	
		τ	τ	τ_{GSB}	τ_{CSS}[f]	Φ_{CSS}
D-Pd(dipy)$_2$	MeCN	-	-	70 ns	-	-
Pd(dipy)$_2$-A	MeCN	13 ps	72 ps	57 ns	-	-
D-Pd(dipy)$_2$-A	MeCN	9.6 ps	41 ps	47 ns	0.19 µs	0.07
	THF	-	-	< 5 ns	< 5 ns	-
D-PdPDM	MeCN	-	-	47 µs	-	-
PdPDM-A	MeCN[e]	-	-	3.83 µs	0.32 µs	-
D-PdPDM-A	MeCN	-	-	2.85 µs	1.14 / 80 µs	0.66[f]
	THF[e]	-	-	10.6 µs	0.57 / -	-
D$_{Ph}$-PdPDM-A	MeCN	-	-	2.85 µs	7.70 µs / 2.68 ms	0.74
D-PDM-A	MeCN	-	-	≈ 5ns	0.42 µs	-

[a] obtained by fs-TA spectroscopy; [b] obtained by ns-TA spectroscopy; [c] ^3MC for compounds based on **Pd(dipy)$_2$**, [d] CSS_{1+2} for **D-Pd(dipy)$_2$-A**, CSS_1 for **PdPDM-A**, otherwise CSS_2; [e] values determined after excitation at 28200 cm^{-1}, [f] determined at 1800 mT; [f] given as short component / long component for **D-PdPDM-A** and **D$_{Ph}$-PdPDM-A**

Since the ^{3}MC lifetime of the unsubstituted **Pd(dipy)$_2$** in THF is around 70 ns, the deactivation is assumed to be due to a very fast CS and subsequent CR. Combined with the involved state energies summarized in **Table 20** this indicates that both processes occur in the *Marcus*-normal region. On the other hand, CS was observed for both triads based on **PdPDM** in THF. Here the rate of CS decrease, while the CR from CSS_2 to the ground state becomes faster hinting towards a Marcus-inverted behavior of the initial CS to CSS_1 and a Marcus-normal behavior of the CR, which is further supported by the lifetimes observed for **PdPDM-A** in MeCN, where according to the electronic properties of the compounds CSS_1 is a bit more stable than in **D-PdPDM-A**, and the CS is slower. [91-92, 96]

One aim of the performed investigations presented in chapters 4.2 and 4.3 was to evaluate the suitability of the different central chromophores as photosensitizers for the photoinduced charge separation in donor-acceptor substituted triads. Naturally, the main criterion for a good photosensitizer is the achieved quantum yield of charge separation which can be determined by actinometry. This can be done most accurate if the formation of the investigated CSS is more or less instantaneously when compared to its lifetime and the timescale of the measurement. Since this is not the case for the examined triads, the transient signals of the CSSs have to be extrapolated back to their theoretical maximum after an instant formation. An accurate back extrapolation requires a more or less distinct separation of the signal in question from the other involved exponentials since otherwise the determined amplitude at times zero can be corrupted significantly. Although this problem could also be solved with a global fit, this method is not feasible since it requires the measurement of a whole set of kinetic traces at different wavenumbers instead of a single decay trace at one energy, thus elongating and complicating the measurement considerably.[79, 195, 207-208]

Unfortunately, this condition is not met for **D-PdPDM-A**. For the elongated triad **D$_{Ph}$-PdPDM-A** a quantum yield of Φ_{CSS} = 0.74 was determined for CSS_2. Since all photophysical processes except the CR are assumed to be more or less equivalent for **D-PdPDM-A** and **D$_{Ph}$-PdPDM-A** and the rate determining step of the charge separation is the formation of CSS_1, the quantum yields are expected to be similar for both compounds. This was further supported by the determination of the actual value of Φ_{CSS} = 0.66 in **D-PdPDM-A** which could be achieved utilizing the effect of an external magnetic field on the decay kinetics of CSS_2 as will be discussed in the next chapter.

Furthermore, the quantum yield of CSS_{1+2} in the non-bridged triad **D-Pd(dipy)$_2$-A** was determined to be around Φ_{CSS} = 0.07. This very low quantum yield is caused by a slow charge separation from ^{3}MC in combination with a relatively fast deactivation of ^{3}MC to the ground state. Under the assumption that the difference in the lifetime of ^{3}MC between the unsubstituted **Pd(dipy)$_2$** and the donor-acceptor substituted triad **D-Pd(dipy)$_2$-A** is only due to the occurrence of charge separation, the rate of the charge separation k_{CS} can be deduced from the observed ^{3}MC-lifetimes according to equation (27).[85, 97, 219-220]

$$k_{CS} = \frac{1}{\tau_{GSB}(triad)} - \frac{1}{\tau_{GSB}(CMC)} \quad (27)$$

This yields a rate of k_{CS} = 2.41·10^6 s^{-1} for values of τ_{GSB}(CMC) = 53 ns and τ_{GSB}(triad) = 47 ns. From those rates, the theoretical maximal quantum yield of the charge separation Φ_{CS} from ^{3}MC to CSS_{1+2} can be calculated using equation (28).[97, 219-220]

$$\Phi_{CS} = \frac{k_{CS}}{k_{CS}+[\tau_{GSB}(CMC)]^{-1}} \quad (28)$$

Which yields Φ_{CS} = 0.11 for the charge separation. Taking into account the uncertainty of the determined values τ_{GSB} and Φ_{CSS}, as well as the fact that, since fluorescence is observed from both $^1LC_2$ and $^1LC_1$, not 100 % of the absorbed photons result in the formation of ^{3}MC the theoretical quantum yield of charge separation Φ_{CS} = 0.11 and the actual quantum yield of CSS_{1+2} of Φ_{CSS} = 0.07 match quite well. Due to the low quantum yield of the charge separation, caused by the conformational rearrangement of the central metal complex and the resulting occupation of the relatively short lived metal centered ^{3}MC-state, the unbridged bisdipyrrinato-Pd(II)-complex **Pd(dipy)$_2$** is not suitable as a photosensitizer in triads which are supposed to exhibit an efficient formation of charge separated states.

In a similar way, the suitability of the purely organic, bridged porphodimethene **PDM** as a central chromophore can be judged independently from a direct determination of the quantum yield. Even with a fast CS on the timescale of about 5 ns the observed intensities of the signals associated with CSS_2 are extremely low. This is due to the fast deactivation of the central chromophore from the ^{3}LC-state to the ground state which occurs significantly faster than the IRF of the ns-setup of about 5 ns, decreasing the quantum efficiency of the charge separation significantly. Hence, **PDM** is no good central chromophore for the achievement of good quantum yields of charge separation, at least in triads based on the donor and acceptor moieties used in this work.

In contrast, the bridged Pd(II)-porphodimethenato complex **PdPDM** achieves high quantum yields in the elongated triad **D$_{Ph}$-PdPDM-A** and, as will be shown in the next chapter, also the short triad **D-PdPDM-A** and is thus a potentially good photosensitizer for the achievement of high quantum yields of photo-induced charge separation

4.3.3 Spin Chemistry

Magnetic field effect (MFE) on the excited state kinetics

To test the triads based on Pd(II) complexes for a sensitivity towards an external magnetic field, kinetic traces were measured for all compounds at various different magnetic fields between 0 - 1800 mT. The traces were recorded at 21100 cm^{-1} since at this energy both the GSB associated with the central metal complex (CMC) as well as the ESA associated with the reduced NDI acceptor contribute to the signal. Thus, from one kinetic trace, conclusions on the CS and the CR can be drawn. The recorded kinetic traces were normalized to the minimum of the GSB, since no influence of the magnetic field on the quantum yield of their formation is expected at the applied low to moderate field strengths, and their formation is virtually instantaneous on the ns-timescale. The resulting sets of magnetic field dependent kinetic traces are depicted in **Figure 84**. The parameters of a biexponential fit of the traces are summarized in **Table 22**.[18, 25-26, 32, 221]

Obviously, the decay kinetics of all complexes are sensitive towards an external magnetic field. As can be derived from the virtually constant lifetimes τ_{GSB} of the GSB associated with the central chromophores, the triplet excited state lifetimes of the respective metal complexes τ_{GSB} stay constant over the whole magnetic field range, indicating the expected independence of the charge separation from the magnetic field. On the other hand, the CSS-lifetimes τ_{CSS} increase significantly with higher magnetic field strengths. This effect is the strongest for **D-Pd(dipy)$_2$-A** with a roughly 30 fold increase, moderate for **D-PdPDM-A** with a 15 fold increase and very weak for **D$_{Ph}$-PdPDM-A** with only a 1.3 fold increase. In contrast to the results obtained for the MFE on the cyclometalated complexes, no additional exponentials were needed to describe the decay of the signal at higher magnetic fields.

Table 22: Lifetime of the lowest excited triplet state of the CMC (τ_{GSB}) and the respective CSSs (τ_{CSS}) as well as the associated amplitudes (a) at different magnetic field strengths (B) for the decay traces shown in **Figure 84** for **D-Pd(dipy)$_2$-A**, **D-PdPDM-A** and **D$_{Ph}$-Pd(dipy)$_2$-A** in MeCN.

sample[a]	τ_{GSB} / τ_{CSS} /µs (a / a) at B =				
	0 mT	**20 mT**	**100 mT**	**500 mT**	**1800 mT**
D-Pd(dipy)$_2$-A	0.05 / 0.19 (–1.63 / 0.63)	0.04 / 0.48 (–1.50 / 0.50)	0.04 / 1.81 (–1.41 / 0.41)	0.04 / 4.79 (–1.39 / 0.39)	0.04 / 6.34 (–1.40 / 0.40)
D-PdPDM-A	2.71 / 1.29 (0.73 / –1.73)	2.48 / 2.03 (4.71 / –5.71)	2.38 / 4.34 (–3.91 / 2.91)	2.36 / 13.3 (–2.53 / 1.53)	2.36 / 16.7 (–2.51 / 1.51)
D$_{Ph}$-PdPDM-A	2.59 / 8.43 (–3.51 / 2.51)	2.58 / 8.92 (–3.53 / 2.53)	2.74 / 9.23 (–3.68 / 2.68)	2.79 / 10.8 (–3.61 / 2.61)	2.91 / 11.1 (–3.69 / 2.69)

[a] after excitation at the maximum absorption of the respective CMC (see **Figure 84**).

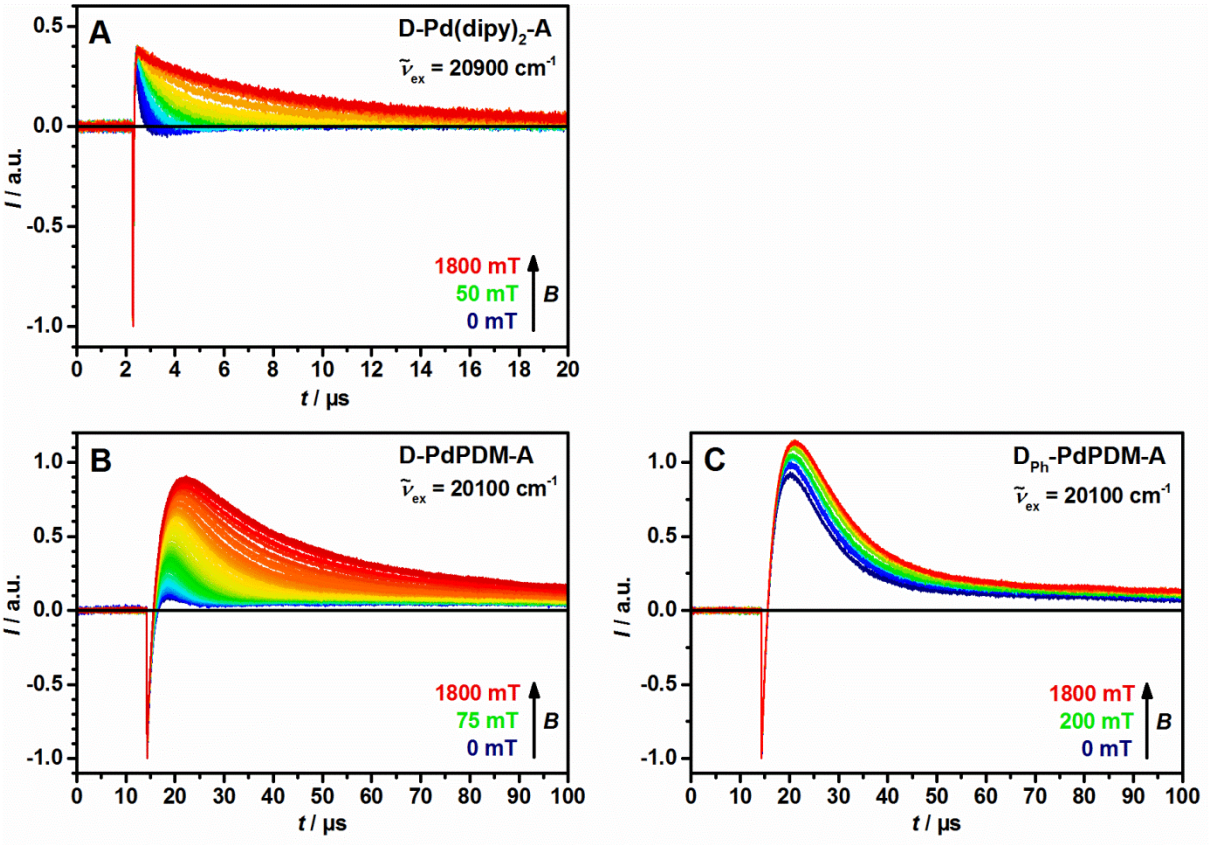

Figure 84: Magnetic field dependence of the decay traces recorded at 21100 cm^{-1} for **D-Pd(dipy)$_2$-A** (A), **D-PdPDM-A** (B) and **D$_{Ph}$-Pd(dipy)$_2$-A** (C) in MeCN at various magnetic fields after excitation at the given wavelengths.

Furthermore, with higher magnetic field strengths, the signal associated with the reduced NDI at 21100 cm^{-1} becomes more pronounced in all triads. This is not due to a possible increase of the quantum yield of charge separation, but to the modification of the ratio τ_{GSB}/τ_{CSS}. While the CS is independent of the magnetic field, the CR is slowed down with increasing field strengths, resulting in a higher maximal concentration of CSS, since less already formed CSSs recombine to the ground state during the time it takes for the complete deactivation of the triplet states by charge separation.With an increase of the signal maximum by a factor of 18, this effect is by far the strongest for **D-PdPDM-A** since here τ_{GSB}/τ_{CSS} at zero magnetic field is significantly higher than for the other two triads. A similar effect has been observed by *Miura et al*[81]*.* on a TAA-NDI dyad similar to those of *Schäfer et al*.[61-62] but with an attached Pt(II)-complex which elongates the CS-time considerably while simultaneously changing the initial population of the spins from an almost pure singlet to an almost pure triplet configuration.

To further investigate the MFE on the spin chemistry of the CSSs, the magnetic field dependent kinetic traces have to be related to a kinetic model as described in chapter 3.4. Due to the bad signal to noise ratio observed for **D-Pd(dipy)$_2$-A** and the weak MFE observed for **D$_{Ph}$-PdPDM-A**, this was only done for **D-PdPDM-A**.

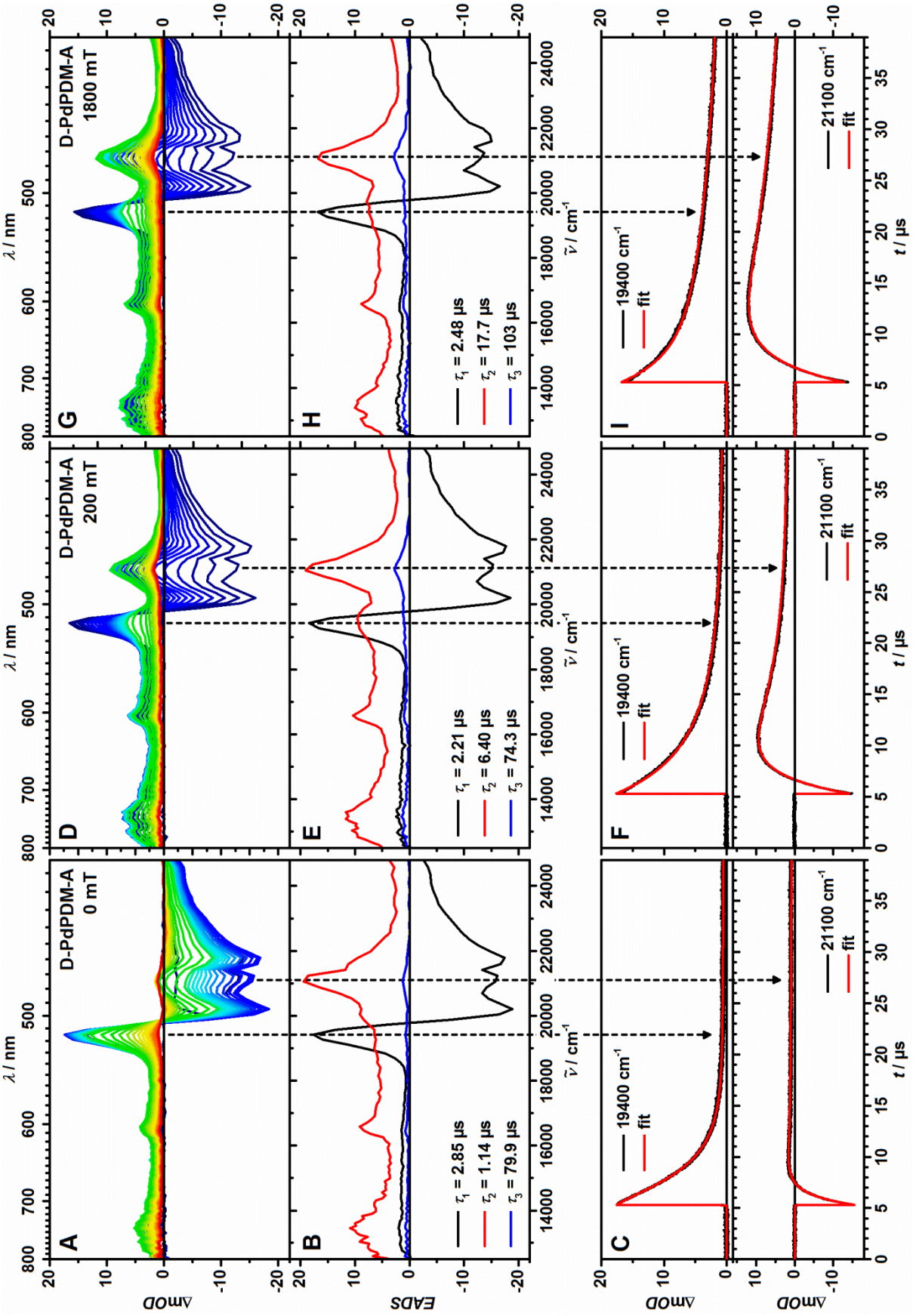

Figure 85: ns-TA spectra of **D-PdPDM-A** in MeCN at 0 mT (A), 200 mT (D) and 1800 mT (G) after excitation at 20100 cm^{-1} as well as EADS obtained from a global fit (B, E, H) and time traces at selected wavenumbers with fit (C, F, I).

Since the off-set at long times seems to be magnetic field dependent, additional transient maps were recorded at 200 mT and 1800 mT. These were analyzed globally using a sequential model and the GLOTARAN software (v. 1.2)[195] to ensure that the compound does not show any unexpected behavior at high magnetic fields prior to the spin chemical fitting procedure using MatLab. These transient maps as well as the resulting evolution associated difference spectra (EADS) and their respective lifetimes are shown in **Figure 85**. It turns out that at all tested magnetic fields, three EADS are obtained. The first EADS is associated with the ^{3}LC state of the central chromophore and thus its amplitudes and lifetime τ_{GSB} are virtually independent from the magnetic field. The second EADS is associated with CSS_2 and exhibits the expected elongation of its lifetime τ_1 towards higher fields. The final EADS has a small amplitude at 0 mT and becomes more intense towards higher magnetic fields, while its lifetime τ_2 shows no particular trend. At 200 mT and especially 1800 mT it becomes obvious that it shows all peaks characteristic for a CSS with a reduced NDI and an oxidized TAA. As mentioned before, a biexponential decay with comparable lifetimes of τ_1 = 17 µs and τ_2 = 72 µs for CSS_2 was observed in **$D_2Ir_{Ph}A$**, a cyclometalated Ir(III)-complex with the same biphenyl spacer between NDI and CMC as in **D-PdPDM-A**. The associated literature argued that to result in the observed biexponential decay kinetics, the interconversion between two possible conformations of CSS_2 would have to occur slower than 2000 s^{-1} and thus can most likely not be associated with the isomerization around the biphenyl axis which is expected to occur much faster.[59, 70, 180, 182, 186-187, 198]

On the other hand, a bimolecular mechanism was excluded by concentration- and excitation intensity-dependent measurements for the present investigations on **D-PdPDM-A**, as well as the previous work on **$D_2Ir_{Ph}A$**. However, due to the very small contribution of the second much longer lifetime to the overall decay kinetics, and the low signal intensities observed for CSS_2 in **D-PdPDM-A** at low fields, a very weak concentration dependence may have been overlooked in the present work.

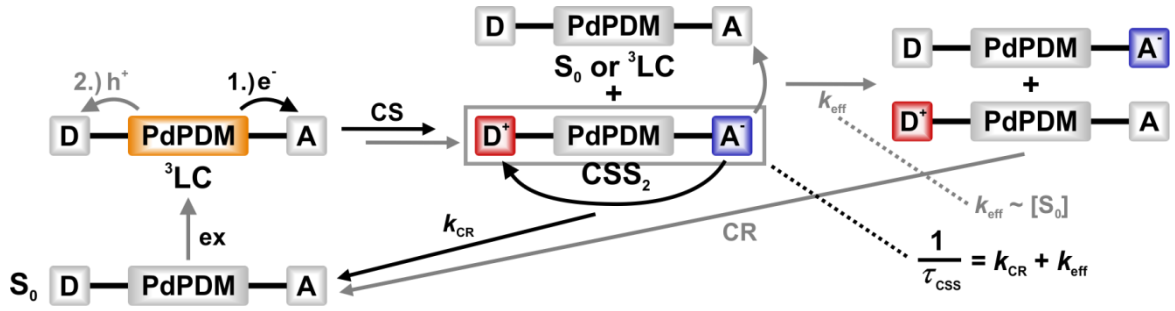

Figure 86: Possible photophysical processes in **D-PdPDM-A**.. After excitation of the CMC. CR from CSS_2 is in concurrence to the reaction of CSS_2 with residual molecules in the ground state. This reaction could result in the formation of a bimolecular CSS with the rate k_{eff} which is dependent on the concentrations of S_0 and ^{3}LC ($[S_0]$). Since the lifetime τ_{CSS} of CSS_2 is dependent on k_{eff} and k_{CR}, the contribution of a bimolecular deactivation to the overall deactivation of CSS_2 can be estimated as described in the main text.

A bimolecular deactivation pathway as depicted in **Figure 86** could possibly explain some of the observations made in **Figure 85**. In polar solvents such as MeCN, the initial geminate radical ion pair, formed by the reaction of CSS_2 with S_0 or ^3LC with k_{eff}, can separate, resulting in a solvent separated loose radical ion pair. The reaction from CSS_2 to a bimolecular, loose radical ion pair is not observable in the TA spectroscopy, since the sum of the ESA and GSB associated with the involved species stays constant. However, CR from the loose radical ion pair is significantly slower than the one from CSS_2 since it depends on the reaction of the individual radicals with a second molecule which can take the respective charge, restoring the neutral NDI or TAA. This process can take very long at low concentrations in oxygen free polar solvents such as MeCN resulting in the observed virtually time independent offset. Since the lifetime of CSS_2 is dependent on the magnetic field, more loose radical ion pairs could be formed at high magnetic fields, explaining the increased relative contribution of the offset at long times observed in **Figure 85**. Since the lifetime of the bimolecular CSS is very long already at zero field, the bimolecular CR is not strongly dependent on the external magnetic field because the charge recombination is the rate-determining step at all fields.[25-26, 59, 98, 193, 219-220, 268-272]

To further evaluate the possible contribution of a bimolecular deactivation mechanism, the reaction scheme shown in **Figure 86** was fitted numerically using the chemical kinetics program Tenua.[273] The performed calculations and computations are explained in more detail on pages 295ff in the appendix. As it turns out, the decay kinetics of the signal at 21100 cm^{-1} can be reproduced very well using the bimolecular mechanism depicted in **Figure 86**. Therefore, a bimolecular reaction mechanism cannot be excluded based on the performed numerical treatment. However, since the ratio between the long and short components of the biexponential decay kinetics are concentration independent as stated before, a bimolecular decay mechanism seems relatively unlikely nonetheless.

On the other hand, the described biexponential decay kinetics at zero field are observed exclusively for compounds comprising a biphenyl spacer between the CMC and the NDI, that is **$D_2Ir_{Ph}A$**, **D-PdPDM-A** and **D_{Ph}-PdPDM-A**. Hence, it seems reasonable that the biphenyl axis is directly responsible for the longer deactivation component. While the isomerization around the biphenyl axis of an unsubstituted biphenyl may be too fast to result in the second decay component, the isomerization could easily be slowed down by the bulky substituents on both phenyl rings of the biphenyl axis. A similar effect has been observed at various points in this thesis, where molecular rearrangements were proposed to be slowed down by bulky substituents. Such an elongation of isomerization times by bulky substituents is reasonable since the reorganization of the bulky substituents increases the interaction with the solvent molecules due to inner friction, as described in chapter 3.4.3. To confirm this hypothesis, the influence of the solvent viscosity on the lifetime and contribution of the long and short decay components could be investigated, for example by ns-TA measurements in pTHF.

Global Analysis of D-PdPDM-A

Although no final conclusion of the identity of the species associated with the offset could be reached, its decay kinetics are so slow that the observed offset is virtually time-independent. Furthermore, the decay off the offset is only affected by very high magnetic fields, if at all. Therefore, the offset was judged to be negligible compared to the massive increase in intensity and lifetime observed for CSS_2, and thus was accounted for in the data-preparation as described in chapter 3.4.

To account for the extremely slow population of CSS_2 from the ^{3}LC-precursor, as well as the width of the laser pulse and the finite response time of the instrument, all experimental decay traces were extrapolated back to the signal onset. This was achieved as described for **DPtA** in **Figure 43**, by deconvolution of the traces with a constant IRF, the lifetime of the ^{3}LC precursor τ_{GSB} as well as a variable offset at very long times and one variable decay time τ_{CSS}. For this, the amplitudes associated with τ_{GSB} and τ_{CSS} were initially determined at different fields between 200 – 1800 mT and then tested at the low magnetic fields. As can be seen from **Table 22**, this was essential for the correct back extrapolation because the values of the amplitudes a_{GSB} and a_{CSS} of the biexponential fit become very inconsistent below 100 mT due to the small intensity of the signals associated with CSS_2. Representative fits at various magnetic fields are shown in **Figure 87** (A). After deconvolution of all kinetic traces with the determined constant value for a_{GSB}, the signal onset was defined as the new time zero, and the residual of the fit was added to the isolated contribution of the decay of CSS to the kinetic traces. Finally, all back extrapolated theoretical decay curves were normalized to one. The resulting data set is shown in **Figure 87** (B).

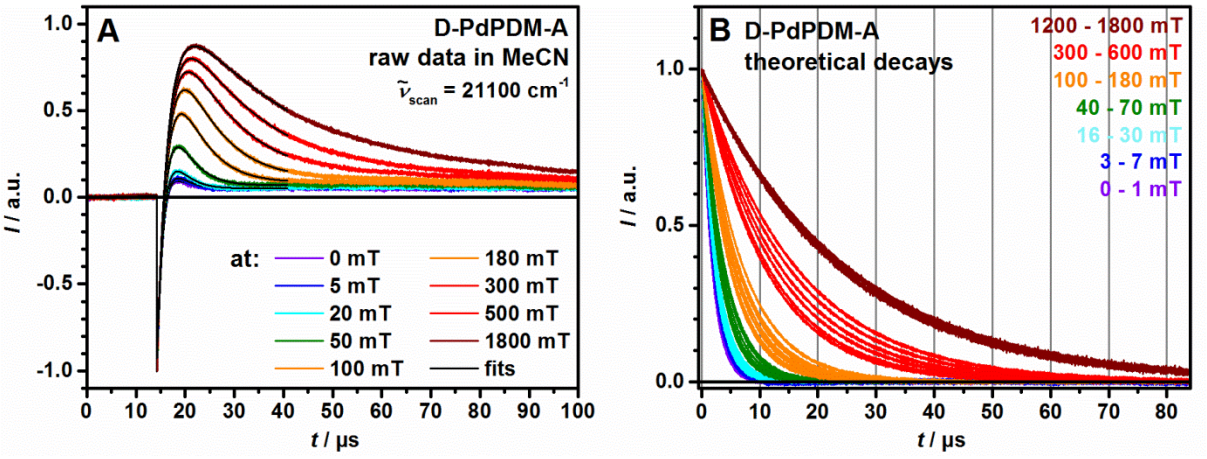

Figure 87: Kinetic traces recorded at 21100 cm^{-1} for **D-PdPDM-A** in MeCN at selected magnetic fields after excitation at 20100 cm^{-1} with the respective fits (A). The theoretical decay traces (B) were obtained as described in the main text. The vertical grey lines indicate time-steps of 10 µs to facilitate a comparison of the decay traces to those obtained for the cyclometalated complexes depicted in **Figure 44** in chapter 3.4.1.

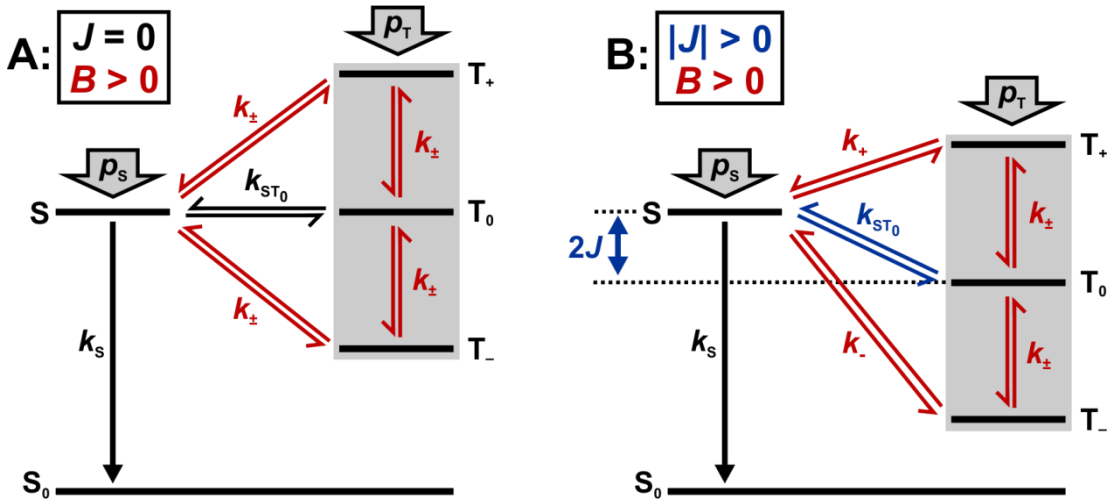

Figure 88: Spin chemical model for the charge-recombination of radical pairs with degenerate (A) and non-degenerate (B) inner Zeeman levels S and T_0. Magnetic field dependent processes are depicted in red, while blue indicates processes solely influenced by the exchange interaction *J*.

In contrast to the results obtained for the cyclometalated complexes, the obtained theoretical decay kinetics of **D-PdPDM-A** are strictly monoexponential over the whole magnetic field range. As described in chapter 3.4.2, the biexponential decay of the cyclometalated complexes at high magnetic fields can be explained based on the reaction scheme derived by *Hayashi* and *Nagakura et al.* shown in **Figure 88** (A). The virtually constant shorter lifetime was associated with the relatively fast decay of the degenerate inner *Zeeman* levels S and T_0 which is limited by the deactivation to the ground state with the rate k_S and thus independent from an external magnetic field. The longer lifetime was associated with the slow decay of the outer *Zeeman* levels T_+ and T_-. which is limited by the transition between the outer and the inner *Zeeman* levels associated with the rate $k_\pm$ and thus becomes slower with increasing magnetic field strengths.[24-25, 33, 39, 59]

A possible reason for the monoexponential behavior of **D-PdPDM-A** is the slow population of CSS_2. Since the short component in an assumed biexponential decay kinetic at higher magnetic fields corresponds to the CR of $^1CSS_2$ to the ground state with the rate k_S, the short component is at least as short as the observed charge recombination at zero field. Hence, in the time it takes for the completion of the charge separation, almost all of the inner *Zeeman* levels could already have deactivated to the ground state. Thus, the decay of S and T_0 may not be noticeable in ns-TA measurements due to a superposition with the slow charge separation. Naturally, the back extrapolation cannot reproduce exponentials which are not observed in the raw data and thus is monoexponential since it only describes the deactivation of the outer *Zeeman* levels at higher fields. This assumption is strongly supported by the observations made during the global fit of the theoretical decay curves to the mathematical description of the reaction scheme depicted in **Figure 88** (A) as given by the differential rate equations (13).[24-25, 33, 39]

$$\begin{aligned}
\frac{d[S]}{dt} &= -\left(k_S+k_+ +k_- +k_{ST_0}\right)[S]+k_{ST_0}[T_0]+k_+([T_+]+k_-[T_-]) \\
\frac{d[T_0]}{dt} &= k_{ST_0}[S]-\left(k_T+k_+ +k_- +k_{ST_0}\right)[T_0]+k_+([T_+]+k_-[T_-]) \\
\frac{d[T_+]}{dt} &= k_+[S]+k_+[T_0]-(k_T+2k_+)[T_+] \\
\frac{d[T_-]}{dt} &= k_-[S]+k_-[T_0]-(k_T+2k_-)[T_-]
\end{aligned} \tag{13}$$

The fitting was performed according to the routine described in chapter 3.4.2 but only results in somewhat satisfying fits if low values for the population of both inner Zeeman levels S and T_0 at time zero (p_S and p_{T0}) are assumed. While a low p_S indicates an initial population of CSS_2 in the triplet state and is in line with the observed CS from the ^{3}LC-state, the low value for p_{T0} is unexpected. Usually, the population of the different triplet sublevels is purely stochastic and should result in equal values for the population of the outer *Zeeman* levels T_+ and T_- ($p_{T\pm}$)and the inner Zeeman level T_0 at time zero. Therefore, a lower value of p_{T0} most likely indicates systematic errors in the data preparation such as the back extrapolation of the data being based only on the decay of the outer Zeeman levels as supposed above.[24-25, 33, 35, 59, 61-62, 79]

The back extrapolated data-set resembles a theoretical description for the magnetic field dependent deactivation of CSS starting from a pure triplet population (p_S = 0) in a system with a non-negligible exchange interaction *J* reported by *Schäfer et al.* Therefore, a variation of k_{ST0} which is dependent of *J*, was also tested. To be precise, the data would have to be fitted to a spin chemical model with non-degenerate inner *Zeeman* levels such as the one shown in **Figure 88** (B). However, in a first rough approximation, this case was treated under the assumption of equal rate constants k_+, k_- and $k_\pm$, which should be viable for magnetic fields higher than *J*, but with lower values for k_{ST0} than the value of $k_{ST0} = 4\cdot10^7$ s^{-1} expected for degenerate inner *Zeeman* levels.[33, 40, 54-56, 59, 62, 204] Representative examples of the various tested global parameters are summarized in **Table 23**, while the resulting dependence of $k_\pm$ and the associated root mean square deviations (rmsd) are depicted in **Figure 89**.

Table 23: Representative global parameters for the fit of the theoretical decay kinetics to equation (13) with k_T = 0 and the arithmetic mean over the rmsd-values ($\overline{rmsd}$) of the resulting fits.

example	p_S	p_{T0}	$p_{T\pm}$	k_S /s^{-1}10^7	k_{ST0} /10^{7}s^{-1}	$\overline{rmsd}$ /10^{-2}
A	0.03	0.17	0.40	0.22	4.00	18.8
B	0.00	0.00	0.50	0.22	4.00	8.70
C	**0.01**	**0.07**	**0.46**	**0.22**	**4.00**	**3.58**
D	0.01	0.07	0.46	0.24	0.80	3.72
E	0.01	0.07	0.46	0.34	0.16	3.81

As can be seen at first glance from the arithmetic mean over all residuals ($\overline{rmsd}$) for examples A-C, varying the starting populations of the different *Zeeman* states has a huge effect on the quality of the resulting fit. A closer look at the individual residuals depicted in **Figure 89** (B) reveals a magnetic field dependence of the fit-quality. At magnetic fields up to about 5 mT, all values for $p_{T\pm}$ result in equally good fits with rmsd-values between 0.006 and 0.02. At higher magnetic fields however, the quality of the fits decreases significantly for all tested global parameters. While for example A ($p_{T\pm}$ = 0.4) the fit is very good at around 100 mT and acceptable up to around 300 mT, it becomes very bad at higher fields. Higher values of $p_{T\pm}$ shift the optimal magnetic field range towards higher fields, and lead to an overall decrease of the residuals and thus a more optimal fit. However, for a pure population of the outer *Zeeman* levels at time zero as in example B, the quality of the fit decreases. Concerning the resulting magnetic field dependence of the transition interconversion rate between the outer and inner *Zeeman* levels $k_{\pm}$, no big differences between examples A-C can be observed as can be seen in **Figure 89** (A). This is not the case for a variation of k_{ST0} for equal values of p_S, p_{T0} and $p_{\pm}$ as done in examples C-D. Here, lower values of k_{ST0} have to be compensated with higher values of k_S to ensure similar values of k_{ST0} and $k_{\pm}$ at zero magnetic field. This is done to fulfill the condition that, since T_0 and $T_{\pm}$ are degenerate at zero field, the interconversion between S and T_0 has to be equal to the interconversion between S and $T_{\pm}$. This results in lower values of $k_{\pm}$ at low fields for example D and E, but at the same time decreases the quality of the fit. At higher magnetic fields however, the results of examples C-E converge towards the same values indicating an independence of the system from k_S and k_{ST0} as has been shown before in chapter 3.4.2 and the literature.[79]

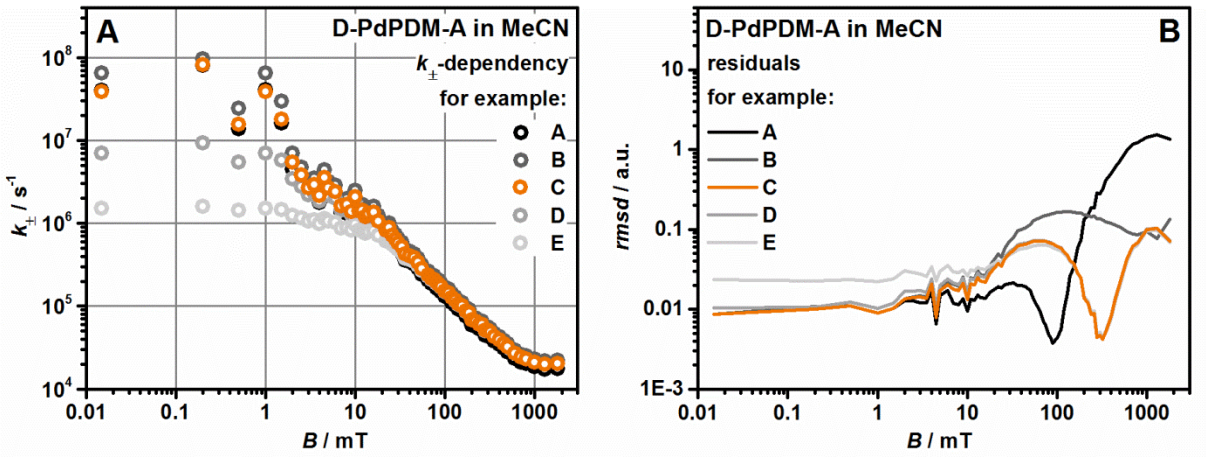

Figure 89: Influence of the global fitting parameter summarized in **Table 23** on the behavior of $k_{\pm}$ (A) and the quality of the fit of equation (13) to the decay curves as indicated by the residuals (B). While the behavior of $k_{\pm}$ is almost independent from a variation of the population of the inner *Zeeman* levels (darker grey), the quality of the fit at higher magnetic fields increases for lower values of p_S and p_{T0}. At lower magnetic field strengths on the other hand, the fit is more sensitive towards a variation of k_{ST0} and k_S (lighter grey) which have nearly no influence at fields above 100 mT. The overall best fit is achieved for example C (orange).

These observations are in line with the proposed systematic error in the data-preparation. At low magnetic fields, the deactivation of the radical pair is expected to be monoexponential, and thus no error was introduced during the back extrapolation of the data. Accordingly, at low magnetic fields, the data can be fitted equally well with all tested populations of the triplet sublevels, ranging from an equal population with $p_{T0} = p_{\pm}$ (not shown) to a population favoring $p_{\pm}$ (examples A, C) to a pure population of $T_{\pm}$ (example B). With increasing field strength, the decay of the spin correlated radical pair has a more and more biexponential character since the decay of the outer *Zeeman* levels is limited by $k_{\pm}$. Here, the back extrapolation disregards the short component since it is superimposed on the process of charge separation, and thus corrupts the data. Thus, at high magnetic fields the variation of $p_{\pm}$ has a huge increase on the quality of the fit. Since $k_{\pm}$ and therefore the deactivation of $T_{\pm}$ slows down towards higher fields, the back extrapolated data is more and more biased towards a population $T_{\pm}$ and the optimal fitting range is shifted towards higher magnetic fields with an increasing value of $p_{\pm}$.

On the other hand, the magnetic field dependent rate $k_{\pm}$ is only associated with transitions of the outer *Zeeman* levels and could thus theoretically be determined solely from the decay of $T_{\pm}$ which is treated correctly by the erroneous back extrapolation even at high fields. This results in almost identical values for $k_{\pm}$ throughout all examples and field strengths.[32, 35, 59, 70, 79]

Although the variation of k_{ST0} and k_S was treated with a wrong mathematical description of the assumed reaction sequence, it has been shown before that the performed analysis based on degenerate S and T_0 states can give first insights on the spin chemistry of linked radical ion pairs, and yields results very similar to those obtained by a more sophisticated classical approach and even quantum mechanical simulations.[61-62, 204] Thus, the decreased quality of the fit for lower values of k_{ST0} indicates that the electronic coupling and thus the exchange interaction between donor and acceptor in **D-PdPDM-A** is negligible and the associated value of $k_{ST0} = 4 \cdot 10^7\ s^{-1}$ as used in examples A-C is correct. This is in line with the observed long lifetime of CSS_2 which is even longer than for the well decoupled cyclometalated complexes described in chapter 3. Furthermore, the fit of the decays with $k_{ST0} = 4 \cdot 10^7\ s^{-1}$ results in an optimal value of $k_S = 0.22 \cdot 10^7\ s^{-1}$, which fits well to the correlation between the CSS_2-lifetime τ_{CSS} and the associated values of k_S-values observed for the cyclometalated compounds. For **DPtA** in different solvents, the pairs of values are $\tau_{CSS} = 0.39$ µs / $k_S = 1.05 \cdot 10^7\ s^{-1}$ in THF, $\tau_{CSS} = 0.66$ µs / $k_S = 0.67 \cdot 10^7\ s^{-1}$ in pTHF and $\tau_{CSS} = 1.68$ µs / $k_S = 0.24 \cdot 10^7\ s^{-1}$ in MeCN, which fits very well to the values obtained for **D-PdPDM-A** in MeCN of $\tau_{CSS} = 1.14$ µs / $k_S = 0.22 \cdot 10^7\ s^{-1}$. Thus, although the fit is still of mediocre quality, the spin chemistry of CSS_2 in **D-PdPDM-A** is best described by a fit using the global values of example C. Exemplary fits for decay kinetics at 16 characteristic magnetic fields are shown in **Figure A11** in the appendix. The resulting behavior of $k_{\pm}$ is depicted in more detail in **Figure 90**.

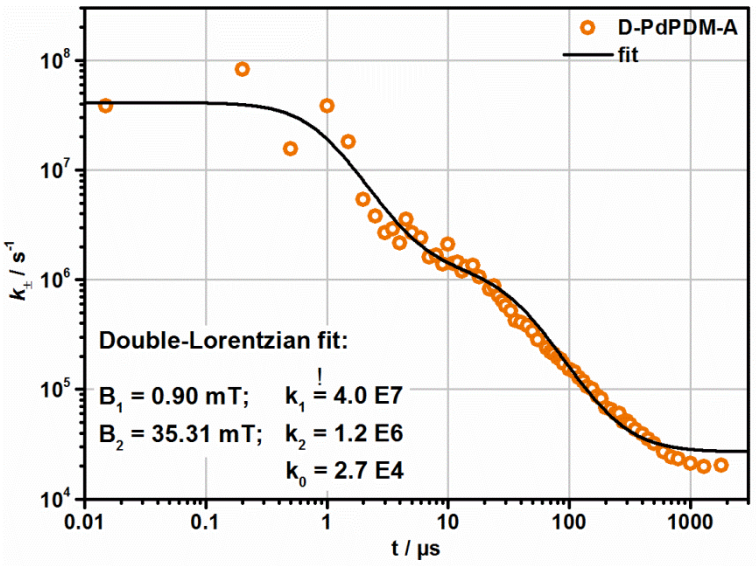

Figure 90: Magnetic field dependence of $k_{\pm}$ as obtained for the global parameters shown in **Table 23** for example C and double *Lorentzian* fit according to equation (15) resulting in the given parameters for **D-PdPDM-A** in MeCN.

Spin Chemical Interpretation

The obtained magnetic field dependence of $k_{\pm}$ shows the known two step behavior which indicates a good separation of the coherent and incoherent contributions to the overall spin interconversion. As described in chapter 3.4.2, this behavior can be described by the double *Lorentzian* equation (15).[79]

$$k_{\pm}(B) = \frac{k_1}{1+(B/B_1)^2} + \frac{k_2}{1+(B/B_2)^2} + k_0 \qquad (15)$$

The performed fit for $k_1 = k_{ST0} = 4 \cdot 10^7\ s^{-1}$ is shown in **Figure 90** and results in the values B_1 = 0.90 mT and B_2 = 35.3 mT and $k_2 = 1.2 \cdot 10^6\ s^{-1}$ for the first and second *Lorentzian*, respectively as well as the high field limit $k_0 = 2.7 \cdot 10^4\ s^{-1}$.

As described in chapter 3.4.3, the first term is associated with the coherent spin interconversion due to isotropic hyperfine coupling (ihfc). The ihfc can be characterized by the magnetic half field value $B_{1/2,hfc}$ which can be estimated using equation (16) from the hyperfine coupling constants of the nuclei involved in the radical centers.[33, 54, 56]

$$B_{1/2,\,hfc} = \sqrt{3 \sum_i \sum_k a_k^2 I_k (I_k+1)} \qquad (16)$$

With values for a_N and a_H as taken from the literature for $TAA^{\cdot+}$[224] and $NDI^{\cdot-}$[225], $B_{1/2,\,hfc}$ is estimated to 2.5 mT, which is significantly higher than the observed half field value of B_1 = 0.90 mT. This

discrepancy is caused by the different methodologies used for the determination of the respective half field value. While B_1 refers to $k_\pm$ which appears only indirectly as a parameter of an assumed reaction mechanism, $B_{1/2}$ by definition refers to directly observable reaction parameters, such as the signal intensity at certain times.[24, 32-33, 50, 54, 56, 59, 79] For the reaction mechanism assumed in this case, the signal intensity can be addressed mathematically with the observed effective decay rate k_{eff}. As shown in chapter 3.4.3, in the investigated field range, k_{eff} can be described reasonably well as a function of $k_\pm$ and thus as a function of the magnetic field using equation (20).[79]

$$k_{eff} = \frac{2k_S k_\pm}{k_S + 8k_\pm} \tag{20}$$

The characteristic magnetic field $B_{eff,\,1/2}$ at which the spin interconversion by ihfc is reduced to half its maximum rate can be derived from the arithmetic mean of extremes of k_{eff} in the field range where the spin interconversion is dominated by coherent processes. For **D-PdPDM-A** in MeCN this is estimated to be the case up to about 8 mT from the behavior of $k_\pm$ depicted in **Figure 90**. In this field range the extremes of k_{eff} are $5.46\cdot10^5$ s^{-1} at 0mT and $4.71\cdot10^5$ s^{-1} at 8,0 mT which gives an arithmetic mean of $5.09\cdot10^5$ s^{-1}. This value of k_{eff} is found at a magnetic field of $B_{eff,\,1/2}$ = 3.69 mT, which is much higher than the half field value of B_1 = 0.93 mT derived from the behavior of $k_\pm$. Furthermore, $B_{eff,\,1/2}$ can be determined purely phenomenologically by optically assessing the middle of the decay signals between 0 and 8.0 mT, which results in the very similar value of $B_{eff,\,½}$ = 3.5 mT.[56, 60, 79]

Although both the mathematical and the phenomenological approach for the determination of $B_{eff,\,½}$ are susceptible to systematic intrinsic errors, they yield very similar values. The determined values are similar to those obtained for the cyclometalated compounds and agree better with the theoretical half field value $B_{1/2,\,hfc}$ = 2.5 mT, than the value determined for B_1 = 0.90 mT from the behavior of $k_\pm$. Thus up to 8 mT the observed field dependence of $k_\pm$ is in line with the theoretical expectation for spin interconversion solely due to ihfc.

The second term of equation (15) is associated with the contribution of incoherent mechanisms to the overall spin interconversion. As discussed in chapter 3.4.3, the incoherent spin interconversion is can be described using equation (21) assuming an axial orientation of the dominating hyperfine coupling tensor.[59, 226]

$$k_{rel} = \frac{2}{27}\Delta A^2 \frac{\tau_c}{1+\omega_0^2\tau_c^2} \tag{21}$$

Here, the rate k_{rel} describes the spin relaxation of the radical pair due to the rotational modulation of the ahfc while the hyperfine coupling anisotropy ΔA is given in angular frequency units. Substituting k_{rel} and B_{rel} with the values determined for k_2 and B_2 from the behavior of $k_\pm$ one can determine the rotational correlation time τ_C and the hyperfine coupling anisotropy of **D-PdPDM-A** in MeCN.

The obtained values of τ_C = 0.16 ns and ΔA = 1.81 mT match very well with the values determined for the cyclometalated compounds (τ_C = 0.15 – 0.20 ns and ΔA = 1.68 – 1.76 mT) in solvents of low viscosity. This further confirms the validity of the applied method of data-preparation and global analysis assuming a population favoring the outer *Zeeman* levels and the resulting data.

To further evaluate the quality of the obtained rotational correlation time τ_C, the correlation time of **D-PdPDM-A** was also estimated based on the solvent viscosity η and the hydrodynamic radius r_{hydro} using the *Stokes-Einstein-Debye* (SED)-equation (25) [227-228]

$$\tau_{c,\,ED} = \frac{4\pi r_{hydro}^3}{3k_B T}\eta \tag{25}$$

With values of r_{hydro} = 9.36 Å[l] and η = 0.34 mPa·s, this results in a rotational correlation time $\tau_{C.\,SED}$ = 0.29 ns, which agrees reasonably well with the rotational correlation time of τ_C = 0.16 ns as determined from spin chemical considerations. The slight deviations can be taken into consideration using a modified version of the SED-equation (26), which takes into account the friction between the solvent molecules and the solute, as well as the shape of the solute molecules.[235, 238]

$$\tau_c = \frac{\lambda}{6}\frac{4\pi r_{hydro}^3}{3k_B T}\eta + \tau_o \tag{26}$$

For high friction between the solute and the surrounding solvent molecules a prefactor of λ = 6 is expected for a perfectly spherical solute-molecule leading to the standard SED-equation if τ_0 is neglected. However, for τ_C = 0.16 ns and r_{hydro} = 9.36 Å, a value of λ = 3.14 is obtained, indicating a non-spherical shape of the molecule which is also suggested by DFT-calculations on **D-PdPDM-A**. Similar results were also obtained for the non-spherical cyclometalated complexes.[228, 235, 238]

Finally, at high fields a considerable deviation of the double *Lorentzian* fit according to equation (15) from the determined magnetic field dependence of $k_{\pm}$ can be observed in **Figure 90**. Although this deviation cannot be explained conclusively at this point, it is most likely related to the incorrect treatment of the decay curves of CSS_2 during the data-preparation which as explained above could not reproduce the short component of the expected biexponential decay. Another possibility would be a slight influence of a magnetic field dependence on the observed off-set at very long times, which was ignored during the data-preparation since it is very long lived compared to CSS_2.

[l]The hydrodynamic radius was determined by a back calculation of the molecular surface as estimated with the Connolly Molecular Area tool of the ChemBioDraw Ultra 12.0 software to the radius of an ideal sphere. The molecular structure was obtained from DFT-calculations performed by Dr. Marco Holzapfel using *Gaussian09* with the *PBE1PBE* functional, a 6-31G* basis set and pseudo potentials for the Pd(II) central ion.

Quantum yield of D-PdPDM-A

Additionally to the investigation of the spin chemistry, the MFE on the decay kinetics of the CSS in **D-PdPDM-A** could be utilized to facilitate the determination of the quantum yield of charge separation This is possible since the CR is significantly slower at higher field strengths which increases the intermediate concentration of CSS_2 significantly, and thus enables an exact back extrapolation of the kinetic traces to the theoretical maximal concentration of CSS_2 after an instant charge separation as explained above. While no quantum yield could be determined at zero magnetic field due to massive fluctuations of the determined amplitudes of CSS_2 at time zero, a quantum yield of Φ_{CSS} = 0.66 was determined at 1800 mT. To exclude an effect of the magnetic field on the quantum yield of CSS_2, the elongated triad **D_{Ph}-PdPDM-A** for which a quantum yield Φ_{CSS} = 0.74 was determined at 0 mT was also examined at 1800 mT and yields Φ_{CSS} = 0.77. Thus, the value of Φ_{CSS} = 0.66 determined for **D-PdPDM-A** is assumed to be also valid at low magnetic fields. The relatively good agreement of the quantum yields of CSS_2 in **D_{Ph}-PdPDM-A** and **D-PdPDM-A** is in line with the proposed mechanism of charge separation which assumes the initial formation of CSS_1 as the rate determining step for both triads. The determined very good quantum yields are in line with the observed signal to noise ratios which, under the same conditions, are better than those observed in the cyclometalated complexes **DPtA** and **DPdA** which show quantum yields of CSS_2 around 0.3, but worse than in **DIrA**, which has a quantum yield of CSS_2 near unity.

Conclusion

A dependence of the decay kinetics of the respective charge separated state from an external magnetic field was observed in all investigated triads. This magnetic field effect increases the effective lifetime of the CSSs because it decreases the spin interconversion rate between the outer and inner *Zeeman* states. Since the decay of CSS_2 in **D_{Ph}-PdPDM-A** is dominated by the inherently slow charge recombination from the singlet ^{1}CSS to the ground state, the MFE is only weakly pronounced. In contrast, a strong MFE is observed for the relatively short lived CSSs in **D-Pd(dipy)$_2$-A** with a 30 fold increase of the lifetime of CSS_{1+2} and **D-PdPDM-A** with a 15-fold increase of the lifetime of CSS_2 towards higher fields. Furthermore, for **D-PdPDM-A** the increase in CSS_2-lifetime results in higher intermediate concentrations of CSS_2 towards higher fields because the charge separation is slower than the charge separation at zero field but is not affected by the magnetic field. The deactivation of CSS_2 in **D-PdPDM-A** and **D_{Ph}-PdPDM-A** shows a small contribution of a second, much longer lifetime. While the contribution of this slower component becomes stronger with increasing magnetic field, the associated lifetime stays virtually constant which is in line with published results for a cyclometalated Ir(III)-complex which also comprises a biphenyl bridge between the NDI and the CMC. Although a concentration independence of the kinetics was ensured

by ns-TA measurements at different concentrations and excitation intensities, the slow component is probably associated with the decay of a small percentage of formed loose radical ion pair. Since the lifetime of the slower component is nearly infinite on the investigated timescale, this was only treated as a constant off-set for the further discussion of the MFE.[26, 59, 220]

For **D-PdPDM-A** the MFE was described quantitatively using the classical kinetic model introduced by *Hayashi* and *Nagakura et al.* Although many simplifications and assumptions were made during the back-extrapolation of the kinetic traces, and the fitting routine, the global analysis yields results similar to those obtained for the cyclometalated complexes. A double *Lorentzian* behavior was found for the spin interconversion rate $k_{\pm}$ between the outer *Zeeman* levels T_+ and T_- and the inner *Zeeman* levels S and T_0. This indicates a clear separation of the contribution of coherent and incoherent mechanisms to the overall spin interconversion. The first *Lorentzian* is associated with the coherent spin interconversion due to isotropic hyperfine coupling and agrees well with theoretical estimations of the magnetic half field value. With increasing magnetic field strength, the energy difference between the outer and inner Zeeman levels increases and the spin interconversion rate due to ihfc decreases rapidly. Thus, incoherent spin interconversion processes which are described by the second *Lorentzian* become the dominating factor at higher fields. A spin chemical interpretation of the characteristic parameters associated with the second *Lorentzian* yield values for the hyperfine coupling anisotropy ΔA and rotational correlation times τ_c which match very well with results obtained for the cyclometalated complexes as well as literature values and hydrodynamic predictions of the rotational motion, respectively. The incoherent spin interconversion is thus confirmed to be mainly due to rotational modulation of the anisotropic hyperfine coupling tensor.[25, 32-33, 54, 59, 79, 231]

At very high fields, $k_{\pm}$ approaches its high field limit and the MFE saturates. In this region deviations of the observed behavior of $k_{\pm}$ from the double *Lorentzian* fit are observed. Since the nature of the spin interconversion mechanism associated with the high field limit could not be clarified, a conclusive interpretation of the deviation is not possible at this moment although an influence of unavoidable systematic errors during the data-preparation is likely.

Although the spin chemistry of the bisdipyrrinato triads is not as well understood as for the cyclometalated compounds, the MFE could still be utilized to gain further insights on the photophysics of the triads. The obtained results further supported the identification of the CSS in **D-Pd(dipy)$_2$-A** as a mixed CSS_{1+2}, and enabled the determination of the quantum yield of CSS_2 in **D-PdPDM-A**, which was not possible at zero magnetic field due to the low intensity of the signals associated with CSS_2. This gave a nice example of the usefulness of magnetic field dependent measurements for a variety of applications beside the obvious investigation of spin chemistry.

4.4 Conclusion and Future Outlook

In this chapter, a series of bridged and non-bridged bisdipyrrinato chromophores was tested towards their suitability as potential photosensitizers in donor acceptor substituted triads for the investigation of charge separation (CS) and charge recombination (CR) processes. Therefore, their photophysics were investigated using various steady state, transient and computational methods. All investigated compounds exhibit the desired high absorption coefficients over a relatively wide spectral range and are stable under light excitation, making them interesting chromophores for various applications. Unfortunately, **CuPDM** and **NiPDM** are completely non-emissive and have excited state lifetimes which are significantly shorter than 5 ns and where thus deemed unsuitable as photosensitizers. In contrast, the bridged Pd(II)-complex **PdPDM** exhibits a relatively intense emission in the near infrared, which has a maximum at around 12800 cm^{-1}, a quantum yield of 1-2 % and a lifetime of around 80 µs. Based on DFT-calculations, the large *Stokes*-shift and the solvent independence, this emission was associated with phosphorescence from a ligand centered triplet state ^{3}LC. Surprisingly, for the non-bridged **Pd(dipy)$_2$**, only a weak fluorescence and a significantly lower excited state lifetime of about 50 ns is observed in fluid solution at rt. This observation could be rationalized based on results from further fs-TA and fluorescence upconversion measurements as well as DFT calculations. Upon excitation of the square planar ground state of **Pd(dipy)$_2$**, a conformational rearrangement is induced which results in the lowest excited state with a disphenoidal complex geometry rarely observed for Pd(II). Because the disphenoidal state is a metal centered triplet state, it deactivates to the ground state rapidly and non-emissive. This conformational rearrangement can be prevented by a rigidification of the complex geometry as achieved in a glassy matrix at 77 K or by the dimethylmethylene bridges between the dipyrrin-subunits in **PdPDM**, resulting in an intense phosphorescence as outlined in **Figure 91**.

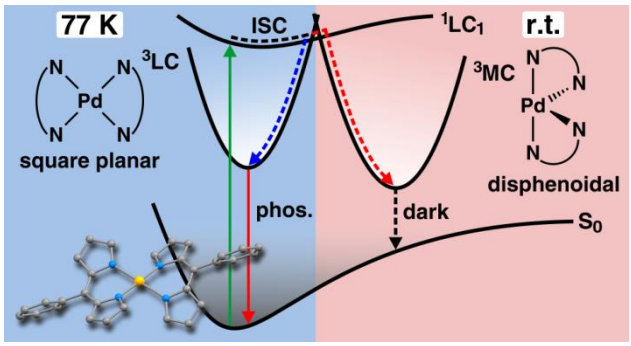

Figure 91: In fluid solution at rt a conformational rearrangement of Pd(dipy)$_2$ results in a non-emissive ^{3}MC-state with a disphenoidal complex geometry. This is prevented in the rigid glassy matrix at 77 K which leads to the observation of a strong phosphorescence. Reproduced with permission of the ACS from[274] https://pubs.acs.org/doi/10.1021/acs.inorgchem.8b00974

Finally, low emission intensities were found for **PDM** and **ZnPDM**. While **PDM** exhibits an excited state lifetime below 5 ns, **ZnPDM** has a very high excited state lifetime of about 900 µs and thus would be an ideal photosensitizer.

Nevertheless, a functionalization of the central chromophore with donor and acceptor moieties was only achieved for **Pd(dipy)$_2$**, **PDM** and **PdPDM** resulting in the novel triads **D-Pd(dipy)$_2$-A**, **D-PDM-A**, **D-PdPDM-A** and it's elongated derivative **D$_{Ph}$-PdPDM-A** as well as the respective reference dyads. All compounds were investigated by steady state experiments to gain first hints on the occurrence of charge separation and insight on the electronic coupling between the different subunits. The UV/Vis-absorption of the central chromophores is influenced by the substitution with the donor and acceptor moieties indicating a non-negligible electronic coupling between the subunits. For the compounds based on **Pd(dipy)$_2$**, this is further supported by the determined redox-potentials, which reveal a strong superposition of the first oxidation of the central metal complex (CMC) and the TAA-donor. Furthermore, the energy of potential charge separated states (CSS) can be estimated by the *Weller*-approach from the redox-potential. In the polar solvents THF and MeCN both CSS_1 and CSS_2 are lower in energy than the lowest excited triplet state of the central chromophores theoretically enabling charge separation. In the non-polar solvents toluene however, no charge separation should be possible after excitation of the central chromophore, since the lowest excited state is significantly more stable than the CSSs. Indeed, a significant quenching of the emission was observed for the dyad **PdPDM-A** as well as the triads **D-PdPDM-A** and **D$_{Ph}$-PdPDM-A** in MeCN and THF. Using ns-TA spectroscopy, the population of charge separated state was proved for all triads, as well as **PDM-A**, and was strongly suggested for **Pd(dipy)$_2$-A**. In **D-Pd(dipy)$_2$-A** the quantum yield of charge separation is very low because the relatively slow charge separation is in concurrence to the fast deactivation of the ^{3}MC state of the **Pd(dipy)$_2$**-core. For **D-PdPDM-A** a similar situation is expected. In contrast, the very long lifetime of the ^{3}LC-state of **PdPDM** results in quantum yields of CSS_2 around 0.7 despite the slow rate of the charge separation which occurs on the timescale of 1 – 2 µs. Although it could not be proved conclusively, the similar charge-separation rates of **D-PdPDM-A** and **D$_{Ph}$-PdPDM-A** strongly suggest a stepwise charge separation in which initially CSS_1 is formed by slow electron transfer from the central chromophore to the NDI and a subsequent hole transfer from the oxidized central chromophore to the TAA quickly forms CSS_2. The final CSSs show lifetimes around 0.2 µs in **D-Pd(dipy)$_2$-A**, 0.4 µs in **D-PDM-A**, 1.1 µs in **D-PdPDM-A** and 7.7 µs in **D$_{Ph}$-PdPDM-A**. The observed trend suggests a rise of the electronic decoupling of the donor and acceptor moieties in the same order, which is caused by the additional phenyl ring between the NDI and the central chromophore in **D-PDM-A**, **D-PdPDM-A** and **D$_{Ph}$-PdPDM-A** and the additional phenyl ring between the TAA and the central chromophore in **D$_{Ph}$-PdPDM-A**. Furthermore, the central moiety influences the electronic

coupling directly. From those results, **PdPDM** can be confirmed as a suitable photosensitizer, while **PDM** and **Pd(dipy)$_2$** are less ideal central chromophores.

Last but not least, for the triads based on Pd(II)-complexes the recombination of the CSSs was examined at different magnetic fields. All complexes show the expected increase of the CSS lifetimes towards higher fields. This magnetic field effect (MFE) is strongest for **D-Pd(dipy)$_2$-A** and only very small in **D$_{Ph}$-PdPDM-A**. For **D-PdPDM-A** the MFE also results in a significant rise of the observed excited state absorption intensity since the intermediate concentration of CSS_2 is increased. Furthermore, for **D-PdPDM-A** the MFE was rationalized using a classical kinetic analysis. The rate $k_{\pm}$ for the spin interconversion between the outer and inner *Zeeman* levels shows the double *Lorentzian* behavior already observed for the cyclometalated complexes. A spin chemical interpretation of the parameters associated with the two *Lorentzians* yields a magnetic half field for the coherent spin flip as well as a rotational correlation time and hyperfine coupling anisotropy for the incoherent spin interconversion. The determined values are in line with established theories for the spin interconversion, and again very similar to those observed for the cyclometalated complexes, further indicating the independence of the spin chemistry from the central chromophore.

Due to the slow charge separation a few assumptions had to be made during the back-extrapolation of the data set. To increase the charge separation rate, the biphenyl bridge between the central chromophore and the NDI-acceptor could be substituted with a single phenyl ring as outlined in **Scheme 30**, resulting in the shortened analogue of **D-PdPDM-A**. Since the synthesis of the Zn(II)-based triad was only tested using one approach, further efforts towards its synthesis in future projects could be successful, yielding another interesting triad with a less heavy central ion which could influence the spin chemistry of an eventual CSS dramatically.

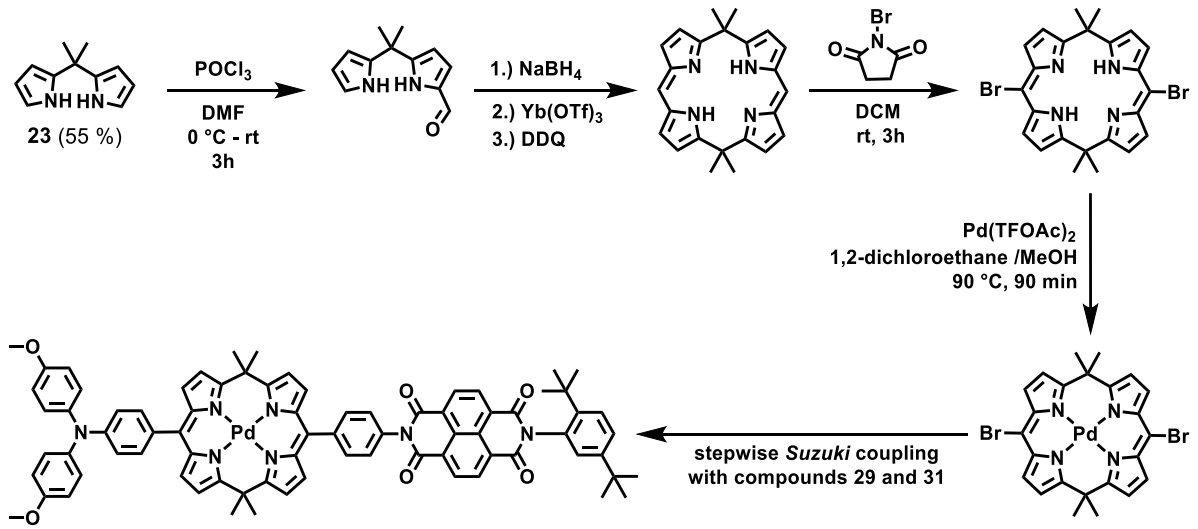

Scheme 30: Proposed reaction sequence for the synthesis of a shorter triad with only one phenyl ring between the NDI-acceptor and the central Pd(II)-porphodimethenato complex.

5 Summary

In this thesis, the photophysics and spin chemistry of donor-photosensitizer-acceptor triads were investigated. While all investigated triads comprised a TAA as an electron donor and a NDI as an electron acceptor, the central photosensitizers (PS) were different chromophores based on the dipyrrin-motif. The purity and identity of all target compounds could be confirmed by NMR spectroscopy, mass spectrometry and elemental analysis.

The first part of the work dealt with dipyrrinato-complexes of cyclometalated heavy transition metals. The successful synthesis of novel triads based on Ir(III), Pt(II) and Pd(II) was presented. The optical and electrochemical properties indicated charge separation (CS), which was confirmed by transient absorption (TA) spectroscopy. TA-spectroscopy also revealed that the process of CS is significantly slower and less efficient for the triads based on Pt(II) and Pd(II) than for the analogous Ir(III) triads. This is mostly due to a much more convoluted reaction pathway, comprising several intermediate states before the formation of the final charge separated state (CSS_2). On the other hand, CSS_2 exhibits long lifetimes which are dependent on the central metal ion. While the Ir(III) triads show lifetimes of about 0.5 µs in MeCN, the Pt(II) and Pd(II) analogues show lifetimes of 1.5 µs. The magnetic field effect on the charge recombination (CR) kinetics of CSS_2 was investigated by magnetic field dependent ns-TA spectroscopy and could be rationalized based on a classical kinetic scheme comprising only one magnetic field dependent rate constant $k_{\pm}$. The behavior of $k_{\pm}$ shows a clear separation of the coherent and incoherent spin interconversion mechanisms. While the coherent spin evolution is due to the isotropic hyperfine coupling with the magnetic nuclei of the radical centers, the incoherent spin relaxation is due to a rotational modulation of the anisotropic hyperfine coupling tensor and is strongly dependent on the viscosity of the solvent. This dependence could be used to measure the nanoviscosity of the oligomeric solvent pTHF, which was found to be distinctly different from its macroviscosity.

The second part of the work dealt with bisdipyrrinato complexes and their bridged porphodimethenato (PDM) analogues. Initially, the suitability of the different chromophores for the use as PS in donor-acceptor substituted triads was tested by a systematic investigation of their steady state and transient properties. While the PDM-complex of Zn(II) and Pd(II) exhibited promising characteristics such as a high exited state lifetime and relatively intense emission, the purely organic parent PDM and the non-bridged bisdipyrrinato-Pd(II) complex were less suitable. The difference between the two Pd(II) complexes could be explained by a structural rearrangement of the non-bridged complex which results in a non-emissive metal centered triplet state with disphenoidal geometry. This rearrangement is prevented by the dimethylmethylene-bridges in the bridged analogue resulting in higher phosphorescence quantum yields and excited state lifetimes.

With the exception of the Zn(II)PDM-complex, the synthesis of novel donor acceptor substituted triads could be realized for all desired central chromophores. They were investigated equivalently to the cyclometalated triads described in the first part. The steady state properties indicate a stronger electronic coupling between the subunits due to the lack of unsaturated bridges between the donor and the central chromophore. Photoinduced CS occurs in all investigated triads. Due to the low exited state lifetimes of the central chromophores, CSS is formed less efficiently for the triads based on the unbridged Pd(II)-complex as well as the purely organic PDM. In the triad based on the bridged Pd(II) complex, the CR of CSS_2 is faster than its formation resulting in low intermediate concentrations. For its elongated analogue, this is not the case and CSS_2 can be observed clearly. Although the spin-chemistry of the triads based on bisdipyrrinato-Pd(II) and porphodimethenato-Pd(II) is less well understood, first interpretations of the magnetic field dependent decay kinetics gave results approximately equivalent to those obtained for the cyclometalated triads. Furthermore, the MFE was shown to be useful for the investigation of the quantum yield of CS and the identity of the observed CSSs.

In both parts of this work, the influence of the central photosensitizer on the photophysics and the spin chemistry of the triads could be shown. While the process of CS is directly dependent on the PS, the PS usually is not directly involved in the final CSSs. None the less, it can still indirectly affect the CR and spin chemistry of the CSS since it influences the electronic coupling between donor and acceptor, as well as the geometry of the triads.

6 Experimental Section

6.1 Analytical Methods

6.1.1 Steady-State Absorption Spectroscopy

- JASCO V-670 UV/Vis/NIR spectrometer (software SpectraManager v. 2.08.04)
- Agilent Technologies Cary 5000 UV-Vis-NIR spectrophotometer (software Agilent Cary WinUV Analysis and Bio v.4.2)

All solvents were of spectroscopic grade and were used without further purification, only THF was destilled prior to use. Absorption spectra were recorded in 1 cm quartz cuvettes from Starna (Pfungstadt, Germany) at rt. Aggregation of the samples could be excluded by a concentration independent behaviour (10^{-6}–10^{-5} M).
Singlet energies of the reference complexes were determined by fitting a tangent on the inflexion point of the low energy side of the low energy absorption band and the x-axis.

6.1.2 Steady-State Emission Spectroscopy

- Edinburgh Instruments FLS980 fluorescence lifetime spectrometer including a 450 W xenon lamp (software F980 version 1.2.2)
- single photon counting photomultiplier (R928P), working range 200-850 nm
- nitrogen-cooled photomultiplier (Hamamatsu R5509-42), working range 600-1400 nm

Steady state emission spectra at room temperature were recorded in 1 cm quartz cells from Starna (Pfungstadt, Germany). All solvents were of spectroscopic grade and were used without further purification, only THF was destilled prior to use. The concentration was ca. 10^{-6}–10^{-5} M and oxygen was removed by sparging with Argon for at least 30 min before each measurement.
The luminescence quantum yields were determined by a calibrated integrating sphere incorporated into the FLS 980 using equation (29).

$$\Phi_{\text{eff}} = \frac{\int E_{\text{sample}}}{\int \Delta T_{\text{ex}}} \tag{29}$$

where Φ_{em} is the emission quantum yield, E_{sample} is the emission spectrum of the sample and ΔT_{ex} is the difference between the transmission of the excitation light passing the sample and the pure solvent. If the *Stokes* shift between the absorption and emission band of the sample is large enough, no further correction for self-absorption is necessary, which was the case for all measured

complexes. Emission spectra at 77 K in a 2-MeTHF glassy matrix were measured in EPR quart tubes (5 mm diameter) and were cooled to 77 K in an EPR *Dewar* vessel with liquid nitrogen.

6.1.3 Electrochemistry

Electrochemical measurements were performed in DCM with tetrabutylammonium hexafluorophosphate (TBAHFP, 0.2 M) as supporting electrolyte. DCM was dried over calcium chloride, distilled from calcium hydride and stored over activated molecular sieve (3Å) prior to use. TBAHFP was synthesised according to literature[275], recrystallized from ethanol/water and dried under high vacuum.

Cyclic Voltammetry (CV)

- Gamry Instruments Reference 600 Potentiostat/Galvanostat/ZRA (v. 6.2.2, Warminster, PA, USA)

Cyclic voltammograms were measured under an argon atmosphere at concentrations of about 3-6 mM. A conventional three electrode set-up consisting of a Platinum disc working electrode (Ø = 1 mm), a Ag/AgCl 'LEAK FREE' reference electrode (Warner Instruments, Hamden, CT, USA) and a Platinum wire counter electrode was used. The measurement cell was dried in an oven and flushed with argon before use. The measurements were performed at a scan rate of 250 mV s^{-1}. Chemical and electrochemical reversability of the redox processes were checked by multi thin layer experiments and measurements at different scan rates (from 10–1000 mV s^{-1}), respectively. All meassurments were referenced against the ferrocene/ferrocenium (Fc/Fc^{+}) redox couple.

Spectroelectrochemistry (SEC)

- Agilent Technologies Cary 5000 UV-Vis-NIR spectrophotometer (software Agilent Cary WinUV Analysis and Bio v.4.2)
- Princeton Applied Research Model 283 potentiostat

UV/Vis/NIR-spectroelectrochemistry was performed at rt in a custom built three electrode PTFE sample compartment with a sapphire window implemented in an Agilent Technologies Cary 5000 spectrometer. The cell consists of a Platinum disc working electrode (Ø = 6 mm), a Platinum plate (Ø = 1 mm) as counter electrode and an Ag/AgCl pseudo-reference electrode. All experiments were measured in reflexion with a path length of 100 µm. The concentrations of the solutes were 10^{-4}–10^{-3} M.

6.1.4 fs-Spectroscopy

- Newport-Spectra-Physics Solstice one box amplified ultrafast Ti:Sapphir laser system (CPA) with a fundamental wavenumber of 12 500 cm^{-1} (800 nm), a pulse length of 100 fs and a repetition rate of 1 kHz
- Newport-Spectra-Physics TOPAS-optical parametric amplifier as the source for the pump pulses with a pulse length shorter than 150 fs
- Ultrafast Systems Helios transient absorption spectrometer with a CMOS sensor (1.5 nm intrinsic resolution, 200–1000 nm sensitivity range)

All experiments were performed in quartz cuvettes from Spectrocell (Oreland, PA) with an optical path length of 2 mm equipped with a micro-stirrer to allow stirring during the measurement. All samples were dissolved in freshly distilled THF or spectroscopic grade MeCN, filtered and degassed for at least 15 min before each measurement. The stability of the samples was verified by recording the steady-state absorption spectra before and after the time-resolved measurements.

fs-Transient absorption spectroscopy

The output of the CPA was split into two parts. One part was used to seed an optical parametric amplifier (Newport-Spectra-Physics, TOPAS) to generate the pump pulse with an pump energy of 100–250 nJ, at the wavenumber of excitation and a pulse length shorter than 150 fs. The second part was used to generate the horizontally polarized probe beam by focusing onto a moving calcium fluoride-plate to produce a white light continuum (wlc) between 29 400 cm^{-1} (340 nm) and 11 800 cm^{-1} (850 nm). The measurements were carried out under magic angle conditions and the pump and probe beam met under an angle of 6°. The pump beam was collimated to a spot, which was at least two times larger than the diameter of the spatially overlapping probe pulse. The temporal delay of the probe pulse relative to the pump pulse was varied over a maximum range of 8 ns using a motorized, computer-controlled linear stage. The first 4 ps had a delay interval between two consecutive data points of 20 fs and the interval was increased in logarithmic steps up to 200 ps for very large delay times. After passing the sample, the probe pulses were detected by a CMOS with 4 nm resolution in a range of 350–700 nm or 400–800 nm. A typically instrument response function (IRF) was in the range of 150–250 fs depending on the used solvent and the pump wavelength and was determined by fitting of the coherent artefact. Part of the probe light pulse was used to correct for intensity fluctuations of the wlc. A mechanical chopper, working at 500 Hz, blocked every second pulse, in order to measure I and I_0. The photo induced change in optical density can directly be recorded by comparing the transmitted spectral intensity of consecutive pulses [$I(\lambda, \tau)$, $I_0(\lambda)$]:

$$\Delta OD = -\log\left[\frac{I(\lambda,\tau)}{I_0(\lambda)}\right] \quad (30)$$

For the dual probe alignment (sample/reference), each pair of laser pulses was normalized to the linear absorption spectra, after acquiring a certain number of transient spectra:

$$\Delta A = \log\left[\left(\frac{I_{ex}(\text{sample})}{I_0(\text{sample})}\right)\left(\frac{I_{ex}(\text{reference})}{I_0(\text{reference})}\right)\right] \quad (31)$$

I_{ex} (sample): intensity of the probe light after the sample when the excitation light was incident

I_{ex} (reference): intensity of light in the reference channel when the excitation light was incident

I_0 (sample): intensity of probe light after the sample when the excitation light was blocked

I_0 (reference): intensity of light in the reference channel when the excitation light was blocked

The time resolved spectra were analyzed by global fitting with GLOTARAN (v. 1.2).[195] For this purpose a sequential (i. e. unbranched unidirectional model) or a target model was applied to model the Gaussian type IRF, the coherent artefact at time zero, and to yield the evolution associated difference spectra (EADS) or the species associated difference spectra (SADS). In the case of a target model efficiencies of the different energy or electron transfer events were an additional input parameter. The white light dispersion (chirp) was corrected by fitting a third order polynomial to the cross phase modulation signal of the pure solvent under otherwise identical experimental conditions.

fs-Fluorescence upconversion (FUC)

- Commercial fluorescence upconversion setup (Halcyone from Ultrafast Systems)

The output of the Ti:Sapphire oscillator (Mai Tai) at 12500 cm^{-1} (800 nm) with a pulse length of 65 fs and a repetition rate of 80 MHz was used for the generation of the excitation pulse and the delayed gate-pulse. Therefore, the output was split into two parts. One part was frequency doubled by a BBO type I crystal to 25000 cm^{-1} (400 nm) to serve as the excitation pulse. The other part was used as the gate pulse (12500 cm^{-1}, 800 nm) and was delayed over in 20 fs steps from 0 fs to 4 ps and in steadily increasing steps from 4 ps to 100 ps with a maximum step size of 5 ps with a computer-controlled linear stage. The pump pulse was focused onto the cuvette and the fluorescence light was collected and focused on a 0.5 mm BBO type II crystal using off-axis mirrors for frequency upconversion with the gate beam. The upconverted light was focused on the entrance slit of a double monochromator and measured by a PMT detector.

6.1.5 ns-Transient absorption spectroscopy

- Edinburgh LP 920 laser flash spectrometer with a 450 W ozone-free Xe arc lamp including a photomultiplier (Hamamatsu R955), digital storage oscilloscope (Tektronix TD3012B) and software (L900 v. 7.3.5)
- Continuum Minilite II Nd:YAG laser operating at 10 Hz, 3-5 ns pulse duration, pulse energy 8 mJ at 28 200 cm^{-1} (355 nm)
- H_2-*Raman* shifter (∼50 bar)
- EKS-PLA NT 342A Nd:YAG laser operating at 10 Hz, 3-5 ns pulse duration, pulse energy 59 mJ at 28 200 cm^{-1} (355 nm)
- OPO BBO II optical parametric oscillator for generating photon energies between 28200 cm^{-1} (355 nm) and 14 300 cm^{-1} (700 nm)

All measurements were carried out in a 1 cm quartz cell (Starna, Pfungstadt, Germany). All solvents were of spectroscopic grade and were used without further purification, only THF was distilled prior to use. All solvents were degassed by freeze pump thaw cycles and stored in a glovebox under nitrogen atmosphere with an oxygen-amount of < 1 ppm in which the sample preparation was done. The samples were excited with ca. 5 ns laser pulses from a Continuum Minilite II Nd:YAG at 28 200 cm^{-1} (355 nm) or 24 000 cm^{-1} (416 nm) after shifting the third harmonic generation of the fundamental at 9400 cm^{-1} (1024 nm) to lower energy with a Raman-shifter charged with hydrogen (∼50 bar) and selecting the desired energy with a Pellni-Broca prism. Alternatively, the samples were excited with ca. 5 ns laser pulses from the 28200 cm^{-1} output of an EKS-PLA NT 342A Nd:YAG shifted to the desired wavenumber by an OPO BBO II optical parametric oscillator. The probe pulse was provided by a pulsed Xe flash lamp for measurements on timescales shorter than 100 µs. For longer timescales, the Xe flash lamp had to be used in continuous wave (cw) mode to provide a a stable light intensity. All measurements were carried out with activated fluorescence correction implemented in the L900 software and the time range was chosen such that the decay profile was completely back to zero or at least parallel to the abscissa. Measurements were performed at different concentrations (10^{-6}–10^{-5} M) and pulse energies (0.2–1.2 mJ) to exclude the presence of bimolecular deactivation processes. For all measurements a long pass (LP) filter (> 400 nm) was placed in front of the detector slit to avoid signals of higher order. The instrument response (ca. 7 ns) of the set-up was determined by measuring the scattered light using a LUDOX AS-30 colloidal silica suspension in water.

Zero-field (B=0)

Transient maps were obtained by measuring temporal decay profiles in 4 nm steps between 12500 – 25000 cm^{-1} and were at least averaged 64 times (4 × 16 shots). For selected wavelengths the signals were averaged 160–320 times depending on the signal-to-noise ratio. Using the corresponding

spectrometer software function decay curves with a lifetime shorter than 100 ns were deconvoluted with the IRF while longer decays were only tail-fitted. Residuals and autocorrelation function (without any significant structure) served as the main criteria in the evaluation of the fit. The quantum yield of CS state formation was estimated by actinometry at 28 200 cm^{-1} (355 nm) vs. benzophenone[207] (in benzene) and at 24 000 cm^{-1} (416 nm) vs. $Ru(bpy)_3Cl_2$[208] (in H_2O) using equation (32).

$$\Phi_{CSS} = \Phi_{ref} \frac{\Delta OD_{CSS}\varepsilon_{ref}}{\Delta OD_{ref}\varepsilon_{CSS}} \frac{OD_{ref}(@\lambda_{ex})}{OD_{sam}(@\lambda_{ex})} \quad (32)$$

The value of 7220 L mol^{-1} cm^{-1} [207] was used for ε_{ref} of the benzophenone transient absorption signal at 18 900 cm^{-1} (530 nm) and 11 300 L mol^{-1} cm^{-1} [208] for the $Ru(bpy)_3Cl_2$ transient signal at 22 300 cm^{-1} (448 nm). According to literature[276-278] Φ_{ref} = 1 for both references. The ε_{CSS} values for the CSS were extracted from spectroelectrochemistry measurements of the compounds or similar complexes with equivalent donor and acceptor moieties.[59, 70, 115] The OD of the reference (OD_{ref}) and the sample (OD_{sam}) at the excitation wavelength were determined by UV/Vis-spectroscopy. The ΔOD_{CSS} and ΔOD_{ref} values were determined by an average of four different measurements at four different laser intensities to ensure a linear dependence of the ΔOD with the laser intensity.

Non-zero Field (B>0)

- GMW Associates C-frame electromagnet 5403 (pole diameter = 76 mm, pole face = 38 mm, axial hole in poles 6.35 mm, pole gap = 12 mm), Sorensen (DLM40-75E) power supply
- Hall-Sensor (Single-Axis Magnetic Field Transductor YM12-2-5-5T, SENIS GmbH)

For the field-dependent measurements the aforementioned laser pump-probe set-up was equipped with an electromagnet. The pump and probe beams were perpendicular to each other, with the pump beam being focused through the poles and the probe white light being directed through the open faces of the C-frame. The magnetic field strength was controlled by a Hall-sensor which was placed at the side of the pole face. The field difference between the position of the Hall sensor at the pole face and the position where pump and flashlight met within the cuvette was corrected by a previously determined calibrating curve. Around 90 different fields between 0 – 1800 mT were applied for one single measurement. The step size between two consecutive was increased from 0.1 mT (from 0 – 2 mT) to 0.2 – 0.3 mT (from 2 – 4 mT), 0.5 mT (from 4 – 10 mT), 1 mT (from 10 – 20 mT), 2 mT (from 20 – 30 mT), 5 mT (from 30 – 100 mT), 10 mT (from 100 – 200 mT), 50 mT (from 200 – 400 mT), 100 mT (from 400 – 1000 mT) to 300 mT and 500 mT for the last two steps. The error of determining the magnetic field was assigned to ±0.02 mT (between 0 – 400 mT) and ±1 mT (between 400 – 1800 mT). Since traces of O_2 in the solution reduce the MFE drastically the transient signals at

selected magnetic fields, e.g. at 0, 5, 50, 100, 500 and 1800 mT were tested repeatedly to prove gas-tight conditions.

6.1.6 NMR Spectroscopy

- Bruker Avance III HD 400 FT-Spectrometer (^{1}H: 400.13 MHz, ^{13}C: 100.61 MHz) with a Bruker Ultrashield magnet
- Bruker Avance III HD 400 FT-Spectrometer (^{1}H: 400.03 MHz, ^{13}C: 100.59 MHz) with a Bruker Ascend magnet
- Bruker Avance III HD 600 FT-Spectrometer (^{1}H: 600.13 MHz, ^{13}C: 150.90 MHz) with an Oxford Instruments magnet (with cryoprobe unit, CPDCH 13C)
- Bruker Avance III HD 600 FT-Spectrometer (^{1}H: 600.43 MHz, ^{13}C: 150.98 MHz) with a Bruker Ascend magnet

^{1}H and ^{13}C NMR spectra were measured in deuterated solvents as indicated (e. g. acetone-d_6, chloroform-*d* ($CDCl_3$) and dichloromethane-d_2 (CD_2Cl_2). Samples were filtered and placed in frequency-matched 5 mm glass sample tubes. Chemical shifts are given in ppm relative to the respective residual nondeuterated solvent signal (in ppm: ^{1}H: $CHCl_3$: δ 7.26, acetone: δ 2.05, CH_2Cl_2: 5.32,; ^{13}C: CH_2Cl_2: 53.84).[279] Deuterated solvents were used as received. For acid sensitive compounds CD_2Cl_2 and $CDCl_3$ were rinsed over basic alumina prior to use.

The abbreviations used to assign the spin multiplicities are: s = singlet, bs = broad singlet, d = doublet, dd = doublet of doublet, ddd = doublet of doublet of doublet, t = triplet, m = multiplet and AA' / BB'. Multiplet signals or overlapping signals in proton NMR spectra that could not be assigned to first order couplings are given as (-). The order of declaration for proton spectra is: chemical shift (spin multiplicity, coupling constant, number of protons).

C-atom types are abbreviated as: CH_3 = primary, CH_2 = secondary, CH = tertiary, C = quaternary.

6.1.7 Mass Spectrometry

Mass spectra were recorded with a Bruker Daltonics autoflex II (MALDI) in positive mode (POS) using a DCTB (trans-2-[3-(4-tert-butylphenyl)-2-methyl-2-propenyl-idene]malononitrile) matrix or with a Bruker Daltonic microTOF focus (ESI). All mass spectrometry peaks are reported as m/z. For calculation of the respective mass values of the isotopic distribution, the software module "Bruker Daltonics IsotopePattern" from the software Compass 1.1 from Bruker Daltonics GmbH, Bremen was used. Calculated (calc.) and measured (found) peak values correspond to the most intense peak of the isotopic distribution.

6.1.8 Microanalysis (CHN)

Elemental analyses were either performed with a vario MICRO cube CHNS instrument for non-halogenated compounds or with Euro EA for halogenated compounds at the Institut für Anorganische Chemie, Universität Würzburg. $KMnO_4$, or V_2O_5 was added to some samples to enhance the combustion process.

6.1.9 X-ray structure analysis

Single crystals of complexes **Pt**, **Pd**, **Pd(dipy)$_2$** and **PdPDM** were obtained by slow diffusion of hexane into a concentrated solution of the respective compound in DCM. The crystallographic analysis was performed at the Center for Nanosystems Chemistry at the Universität Würzburg. Single-crystal X-ray diffraction data were collected at 100 K on a Bruker D8 Quest Kappa diffractometer with a Photon100 CMOS or CMOS PhotonII detector and multi-layered mirror monochromated CuKα radiation. The structure was solved using direct methods, expanded with Fourier techniques and refined with the Shelx software package.[280] All non-hydrogen atoms were refined anisotropically. Hydrogen atoms were included in the structure factor calculation on geometrically idealized positions. The atomic coordinates of the determined structures can be found in the appendix.

Crystal data for **Pt**($C_{24}H_{18}N_4Pt$):
*M*r = 557.51, crystal size: 0.20x0.11x0.06 mm^3, monoclinic space group P2(1)/c, *a* = 28.1541(9) Å, α = 90°, *b* = 7.8910 (3) Å, β = 106.2110(10)°, *c* = 17.6912(6) Å, γ = 90°, *V* = 3774.1(2) Å^3, *Z* = 8, ρ(*calcd)* = 1.962 g·cm^{-3}, μ = 14.046 mm^{-1}, $F_{()}$ = 2144, *GooF*(F^2) = 1.203, R_1 = 0.0474, wR^2 = 0.0982 for I>2σ(I), R_1 = 0.0525, wR^2 = 0.1005 for all data, 7444 unique reflections [θ = 67.679°] with a completeness of 100 % and 523 parameters, 0 restraints.
The large residual electron density found as a B-level error in the checkcif-file is located in close proximity to the heavy atom Platinum and might arise from insufficient absorption correction.

Crystal data for **Pd**($C_{24}H_{18}N_4Pd*C_2Cl_2$):
*M*r = 553.75, crystal size: 0.92x0.38x0.14 mm^3, monoclinic space group P2(1)/c, *a* = 12.6868(4) Å, α = 90°, *b* = 18.9392 (6) Å, β = 108.9400(10)°, *c* = 9.8058(3) Å, γ = 90°, *V* = 2228.55(12) Å^3, *Z* = 4, ρ(*calcd)* = 1.650 g·cm^{-3}, μ = 9.088 mm^{-1}, $F_{()}$ = 1112, *GooF*(F^2) = 1.117, R_1 = 0.0345, wR^2 = 0.0932 for I>2σ(I), R_1 = 0.0348, wR^2 = 0.0935 for all data, 4402 unique reflections [θ = 67.679°] with a completeness of 100 % and 289 parameters, 0 restraints.

Crystal data for **Pd(dipy)$_2$** ($C_{30}H_{22}N_4Pd$) [CCDC no.: 1835934]:
*M*r = 544.91, crystal size: 0.28x0.18x0.08 mm^3, triclinic space group P-1, *a* = 9.7375(4) Å, α = 71.8690°, *b* = 10.7168(4) Å, β = 69.7130° *c* = 12.7682(5) Å, γ = 71.5660°, *V* = 1154.83(8) Å^3, *Z* = 2, ρ(*calcd)* = 1.567 g·cm^{-3}, μ = 6.686 mm^{-1}, $F_{()}$ = 552, *GooF*(F^2) = 1.077, R_1 = 0.0225, wR^2 = 0.0576 for I>2σ(I), R_1 = 0.0240, wR^2 = 0.0586 for all data, 4515 unique reflections [θ = 67.679°] with a completeness of 99.4 % and 319 parameters, 0 restraints.

Crystal data for **PdPDM** ($C_{36}H_{30}N_4Pd$) [CCDC no.: 1835935]:
*M*r = 625.04, crystal size: 0.17x0.17x0.07 mm^3, orthorhombic space group Pna2(1), *a* = 14.7539(6) Å, α = 90°, *b* = 18.8004(8) Å, β = 90° *c* = 10.2206(4) Å, γ = 90°, *V* = 2835.0(2) Å^3, *Z* = 4, ρ(*calcd)* = 1.464 g·cm^{-3}, μ = 5.524 mm^{-1}, $F_{()}$ = 1280, *GooF*(F^2) = 1.062, R_1 = 0.0197, wR^2 = 0.0497 for I>2σ(I), R_1 = 0.0199, wR^2 = 0.0498 for all data, 5342 unique reflections [θ = 67.679°] with a completeness of 100 % and 375 parameters, 1 restraint.

6.1.10 Microwave Oven

- *μCHEMIST microPREP Microwave Digestion System ATC-FO 300* from MLS (Leutkirch, Germany)

Microwave reactions were performed in a microwave oven with a fibre optical thermometer sensor (ATC-FO, 0–270 °C), which controls the reaction temperature by regulation of the output power (0–1200 W) of the microwave oven. The reaction mixture was placed in a pressure quartz vessel (max. 12 bar) with an adapter for the fibre optical thermometer.

6.1.11 Recycling Gel Permeation Chromatography (GPC)

- JASCO Gel Permeation Chromatography System: interface box (LC-NetII ADC), intelligent HPLC pump (PU-2080 plus), inline degasser (DG-2080-53), solvent selection valve unit (LV-2080-03), multi wavelength UV/Vis detector 195–700 nm (UV-2077), software Chrompass (v. 6.1)

Gel permeation chromatography (GPC) was done using two preparative GPC columns (styrene-divinylbenzene-copolymer, 50 and 500 Å, 600 x 20.8 mm) from PSS (Mainz, Germany), and a four channel UV/Vis-detector (195–700 nm). The flow rate was 4 mL·min^{-1} and the used solvent was HPLC grade THF.

6.1.12 DFT-Calculations

(U)DFT- and (U)TD-DFT-calculations were performed by Dr. Marco Holzapfel using *Gaussian09* at a (U)PBE1PBE level of theory and a 6-31G* basis set for C, H, N and O and pseudo potentials (SDD) for the Pt and Pd atoms.[194] Frequency analyses were done to check whether the optimized structures are minima.

6.2 Synthesis

All reactions were carried out under an atmosphere of nitrogen (dried with Sicapent from Merck, oxygen was removed with a cupric oxide catalyst R3-11 from BASF) using standard Schlenk-techniques.[281] Solvent for oxygen and/or moisture sensitive reactions were freshly distilled under nitrogen from the appropriate dehydrating agent (sodium/benzophenone "ketyl blue" for THF and dioxane, sodium for toluene, CaH_2 for DMF, CH_2Cl_2, pyridine, MeCN and 1,2-dichloroethane and Mg/I_2 for EtOH and MeOH) and degassed with dry nitrogen before use. Solvents for chromatography and work-up procedures were of technical grade and distilled prior to use. Flash chromatography[282] was performed on silica gel (Macherey-Nagel "Silica 60 M", 40–63 µm) wet-packed in glass columns.

6.2.1 Reagents

$Ir(III)Cl_3 \cdot nH_2O$ was received from Heraeus (Hanau, Germany). Benzophenone and $Ru(bpy)_3Cl_2$ were purified twice by sublimation prior to use. All other chemicals were obtained commercially and were used without further purification. Compounds **1**[174], **2**[173], **3**[70], **4**[70], **7**[178], **14**[115], **15**[115], **24**[255], **25**[255], **26**[162], **PDM**[162] and **DIrA**[70] were synthesized as described in the given literature. Compounds **16**[246], **17**[246] and **20**[247] were synthesized as described in the given literature and further purified by recrystallization from a mixture of EtOH and water (approx. 4/1 by volume).

6.2.2 General Procedures

General procedure for the synthesis of dipyrromethanes according to literature[177] (GP I).

The appropriate carbonyle (1.0 eq.) and 1*H*-pyrrole (filtered over a small plug of alumina act. I directly prior to use) (25 eq.) were added to a dry round-bottom Schlenk-flask and degassed with a stream of nitrogen for 15 min. TFA (0.1 eq) was added under nitrogen and the reaction mixture was stirred at rt for 10 min before it was quenched with TEA (10 ml). The reaction mixture was then distilled under reduced pressure at low temperature to yield a yellow to brown oil. The crude product was purified by flash column chromatography on silica.

General procedure for the synthesis of asymmetric naphthalene diimides (NDIs) according to literature[115, 179] (GP II).

Naphthalene-1,4,5,8-tetracarboxylic dianhydride (1.0 eq) and the appropriate amines (1.0 eq and 1.0 eq) were dissolved in dry pyridine in a quartz microwave tube and heated in a microwave oven (300 W) at 140 °C for 2.5 h. The solvent was removed under reduced pressure and the resulting solid

was purified by flash column chromatography on silica gel. The crude product was then further purified by precipitation from DCM into hexane.

General procedure for the synthesis of cyclometalated dipyrrinato-metal complexes according to literature[136, 138] (GP III).

Under nitrogen the appropriate dipyrromethane (1.0 eq) was dissolved in dry THF and DDQ (1.1 eq) was added before the mixture was stirred at rt for 2 h. Then, finely powdered K_2CO_3 (10 eq) was added and the mixture was stirred for 15 min before the appropriate binuclear cyclometalated μ-bridged metal-dimer (0.5 eq) and TEA (2 ml) were added. The reaction was then stirred at rt or 80 °C for 18 h and cooled down to rt before DCM (20 ml) and celite (aprox. 10 g) were added. The resulting mixture was filtered through a small plug of celite which was rinsed with DCM until the eluent was colorless. The solvents were removed under reduced pressure and the crude product was purified by flash column chromatography on silica and if necessary with preparative recycling GPC (THF, 4 ml/min). Finally, the product was precipitated from DCM into MeOH. The obtained solid was again precipitated from DCM into n-pentane. The obtained desired compounds were analytically pure after drying under high vacuum (approx., 10^{-5} mbar) for 24 h.

General procedure for the *Miyaura* borylation of halogenated compounds according to literature[248] (GP IV).

Under nitrogen atmosphere the appropriate halogenated compound (1.0 eq), bis(pinacolato)diboron (1.1 eq) and KOAc (1.3 eq) were placed in a Schlenk-flask. After the flask was evacuated and flushed with nitrogen three times, dry and degassed 1,4-dioxane was added. After the addition of $Pd(PhCN)_2Cl_2$ (0.02 eq) and 1,1'-bis(diphenylphosphino)ferrocene (DPPF) (0.02 eq) the solution was further degassed with a stream of nitrogen for 10 min before it was heated to reflux for 18 h. The solvent was removed under reduced pressure and the residue was purified by flash column chromatography on silica. If necessary, the crude product was further purified by recrystallization or precipitation.

General procedure for the *Suzuki* coupling of borylated and halogenated compounds according to literature[249-250] (GP V).

Under nitrogen atmosphere the appropriate borylated compound (1.0 eq) and halogenated compound (1.0 eq) were placed in a Schlenk-flask. After the flask was evacuated and flushed with nitrogen three times, a degassed mixture of an aqueous solution of Na_2CO_3 (1 M) and an organic solvent were added. After the addition of $Pd(PPh_3)_4$ (0.03 – 0.05 eq) the mixture was further degassed with a stream of nitrogen for 10 min before it was heated to refluxed for 24 - 72 h. After

the reaction cooled down to rt, DCM (200 ml) was added and the mixture was washed with water (3 x 100 ml). The organic layer was dried over Na_2SO_4 and the solvent was removed under reduced pressure. The residue was purified by flash chromatography on silica. The crude product was further purified by recrystallization or precipitation.

General procedure for the synthesis of bis-dipyrrinato-metal complexes according to literature[142, 144, 160, 251] (GP VI)

Under nitrogen the appropriate dipyrromethanes (1.0 eq and 1.0 eq) were dissolved in dry THF and DDQ (2.2 eq) was added before the mixture was stirred at rt for 2 h. Then, finely powdered K_2CO_3 (25 eq) was added and the mixture was stirred for 15 min before the appropriate metal-source (1 - 10 eq) was added together with a supporting base (TEA or $NH_{3(aq)}$, 1ml). The reaction mixture was then degassed with a stream of nitrogen for 15 min and stirred at rt – 60 °C for 3 - 72 h. After the reaction cooled down to rt DCM (20 ml) and celite (approx. 10 g) were added. The resulting mixture was filtered through a small plug of celite which was rinsed with DCM until the eluent was colorless. The solvents were removed under reduced pressure and the crude product was purified by flash column chromatography on silica and if necessary with preparative recycling GPC (THF, 4 ml/min). Finally the product was precipitated by dropping a concentrated DCM-solution of the desired complex into MeOH. The obtained desired compounds were analytically pure after drying under high vacuum (approx., 10^{-5} mbar) for 24 h.

General procedure for the synthesis of PDM-metal complexes according to literature[132, 162, 167] (GP VII).

Under nitrogen the appropriate porphodimethene (1.0 eq) was dissolved in a polar organic solvent (either $CHCl_3$, THF or 1,2-dichloroethane) before a solution of the appropriate metal-source (1.5 - 5 eq) in MeOH was added together with TEA (1ml). The reaction mixture was then degassed with a stream of nitrogen for 15 min and stirred at rt – 90 °C for 5 min - 48 h. After the reaction cooled down water (50 ml) was added and the precipitate was collected by filtration. The resulting solid was dissolved in DCM and extracted with water (3 x 30 ml). The organic phase was dried over Na_2SO_4, the solvent removed under reduced pressure and the crude product was purified by flash column chromatography on silica. Finally the product was precipitated by dropping a concentrated DCM-solution of the desired complex into MeOH. The obtained desired compounds were analytically pure after drying under high vacuum (approx., 10^{-5} mbar) for 24 h.

6.2.3 Cyclometalated complexes and precursors

6.2.3.1 Precursors

5-Phenyldipyrromethane (5)

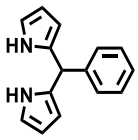

CA: [107798-98-1]

Synthesis following GP I:

Benzaldehyde (2.62 g, 2.50 ml, 24.7 mmol), 1*H*-pyrrole (41.5 g, 42.9 ml, 618 mmol), TFA (282 mg, 190 µl, 2.47 mmol); flash column chromatography (eluent: PE/DCM/EA = 8/1/1).

Yield: 3.82 mg (17.2 mmol, 70 %) of a greyish solid.

$C_{15}H_{14}N_2$ [222.29]

^{1}H-NMR (400 MHz, acetone-d_6):

δ [ppm] = 9.68 (bs, 2H), 7.30–7.15 (-, 5H), 6.67 (ddd, $^3J_{HH}$ = 4.3 Hz, $^3J_{HH}$ = 2.7 Hz, $^4J_{HH}$ = 1.6 Hz, 2H), 5.97 (dd, $^3J_{HH}$ = 3.1 Hz, $^3J_{HH}$ = 2.7 Hz, $^4J_{HH}$ = 2.7 Hz, 2H), 5.95-5.91 (m, 2H), 5.48 (s, 1H).

5-(4-Nitrophenyl)dipyrromethane (6)

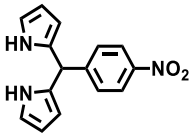

CA: [143859-77-2]

Synthesis following GP I:

4-Nitrobenzaldehyde (9.00 g, 59.6 mmol), 1*H*-pyrrole (99.6 g, 103 mL, 1.48 mol), TFA (680 mg, 440 µl, 5.96 mmol); flash column chromatography (eluent: PE/EA = 3: 1) and recrystallization from DCM/cyclohexane = 1/2.

Yield: 8.25 g (30.9 mmol, 52 %) of a green crystalline solid.

$C_{15}H_{13}N_3O_2$ [267.28]

^{1}H-NMR (400 MHz, acetone-d_6):

δ [ppm] = 9.82 (bs, 2H), 8.16 (AA', 2H), 7.46 (BB', 2H), 6.72 (ddd, $^3J_{HH}$ = 2.7 Hz, $^3J_{HH}$ = 2.7 Hz, $^4J_{HH}$ = 1.6 Hz, 2H), 6.01 (ddd, $^3J_{HH}$ = 2.8 Hz, $^3J_{HH}$ = 2.7 Hz, $^4J_{HH}$ = 2.7 Hz, 2H), 5.78-5.74 (m, 2H), 5.65 (s, 1H).

_N_-(2,5-Di-_tert_-butylphenyl)-_N'_-(4-(dipyrrolylmethyl)phenyl)-naphthalene-1,4,5,8-tetracarboxylic diimide (8)

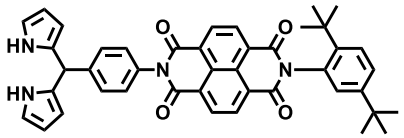

CA: [1463527-67-4]

Synthesis following GP II:

Naphthalene-1,4,5,8-tetracarboxylic dianhydride (1.70 g, 6.34 mmol), 2,5-di-*tert*-butylaniline (1.30 g, 6.33 mmol), **7** (1.50 g, 6.32 mmol), pyridine (30 ml); flash column chromatography (eluent: PE/EA = 3/1 → 1/2).

Yield: 1.32 g (1.96 mmol, 31 %) of a yellowish tan solid.

$C_{43}H_{38}N_4O_4$ [674.79]

^{1}H-NMR (400 MHz, $CDCl_3$):

δ [ppm] = 8.87–8.82 (-, 4H), 8.08 (bs, 2H), 7.61 (d, $^3J_{HH}$ = 8.6 Hz, 1H), 7.50 (dd, $^3J_{HH}$ = 8.6 Hz, $^4J_{HH}$ = 2.2 Hz, 1H), 7.40 (AA', 2H), 7.26 (BB', 2H), 7.02 (d, $^4J_{HH}$ = 2.2 Hz, 1H), 6.72 (ddd, $^3J_{HH}$ = 2.6 Hz, $^3J_{HH}$ = 2.6 Hz, $^4J_{HH}$ = 1.6 Hz, 2H), 6.19 (ddd, $^3J_{HH}$ = 3.2 Hz, $^3J_{HH}$ = 2.7 Hz, $^4J_{HH}$ = 2.7 Hz, 2H), 6.03-5.98 (m, 2H), 5.60 (s, 1H), 1.33 (s, 9H), 1.28 (s, 9H).

_N_-(2-Ethylhexyl)-_N'_-(4-(dipyrrolylmethyl)phenyl)-naphthalene-1,4,5,8-tetracarboxylic diimide (9)

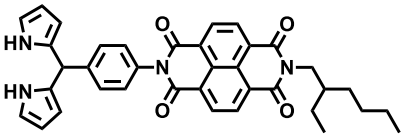

CA: [–]

Synthesis following GP II:

Naphthalene-1,4,5,8-tetracarboxylic dianhydride (1.13 g, 4.21 mmol), 2-ethylhexyl-1-amine (560 mg, 690 µl, 4.33 mmol), **7** (1.00 g, 4.21 mmol), pyridine (20 ml); flash column chromatography (eluent: DCM/EA = 50/1).

Yield: 610 mg (1.02 mmol, 24 %) of a slightly tan solid.

$C_{37}H_{34}N_4O_4$ [598.69]

^{1}H-NMR (400 MHz, $CDCl_3$):

δ [ppm] = 8.80 (s, 4H), 8.02 (bs, 2H), 7.41 (AA', 2H), 7.27 (BB', 2H), 6.75 (ddd, $^3J_{HH}$ = 2.6 Hz, $^3J_{HH}$ = 2.6 Hz, $^4J_{HH}$ = 1.6 Hz, 2H), 6.19 (ddd, $^3J_{HH}$ = 3.2 Hz, $^3J_{HH}$ = 2.7 Hz, $^4J_{HH}$ = 2.7 Hz, 2H), 6.02-5.98 (m, 2H), 5.61 (s, 1H), 4.23-4.10 (m, 2H), 2.02-1.89 (m, 1H), 1.46-1.24 (-, 8H), 0.95 (t, $^3J_{HH}$ = 7.4 Hz, 3H), 0.89 (t, $^3J_{HH}$ = 7.1 Hz, 3H).

^{13}C-NMR (100 MHz, $CDCl_3$):

δ [ppm] = 163.3 (C), 163.2 (C), 143.2 (C), 133.4 (C), 132.0 (C), 131.6 (CH), 131.3 (CH), 129.7 (CH), 128.8 (CH), 127.2 (C), 127.1 (C), 127.0 (C), 126.8 (C), 117.7 (CH), 108.6 (CH), 107.7 (CH), 44.8 (CH_2), 43.8 (CH), 38.1 (CH), 30.8 (CH_2), 28.8 (CH_2), 24.2 (CH_2), 23.2 (CH_2), 14.2 (CH_3), 10.7 (CH_3).

MALDI-MS (pos.): $[M^{+\bullet}]$ = $C_{37}H_{34}N_4O_4$; calc.: 598.257, found 598.271

***Bis*(1-phenylpyrazolyl)(*µ*-dichloro)diPlatinum(II) (10)**

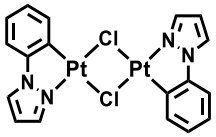

CA: [59161-16-9]

Synthesis according to lit.[171-172]

Under nitrogen, K_2PtCl_4 (1.00 g, 2.41 mmol) and 1-phenylpyrazole (350 mg, 320 µl, 2.41 mmol) were added to a degassed mixture of 2-ethoxyethanole and deionized water (30 ml, 3/1 by volume). The reaction mixture was stirred at 80 °C for 18 h. After the suspension cooled down to rt, distilled water (40 ml) was added and the precipitate was filtered of with a sintered glass funnel (P4) and washed with water (3 x 10 ml). The crude product was then dried under reduced pressure and was used without further purification.

Yield: 620 g (830 µmol, 69 %) of a slightly grey solid.

$C_{18}H_{14}Cl_2N_4Pt_2$ [747.41]

***Bis*(1-phenylpyrazolyl)(*μ*-diacetato)dipaladium(II) (11)**

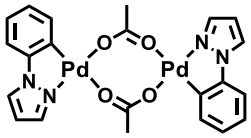

CA: [1263103-50-9]

Synthesis according to lit.[170]

Under nitrogen, $Pd(OAc)_2$ (500 mg, 2.23 mmol) was added to a degassed solution of 1-phenylpyrazole (320 mg, 290 µl, 2.22 mmol) in dry DCM (20 ml). After stirring for at rt for 3h, the orange solution was concentrated nearly to dryness under reduced pressure and the residue is triturated with Et_2O (30 ml). The precipitate was then filtered off with a sintered glass funnel (P4) and washed with Et_2O (3 x 10 ml). The crude product was then dried under reduced pressure and was used without further purification.

Yield: 640 mg (1.04 mmol, 94 %) of a yellow solid.

$C_{22}H_{20}N_4O_4Pd_2$ [617.25]

(12)

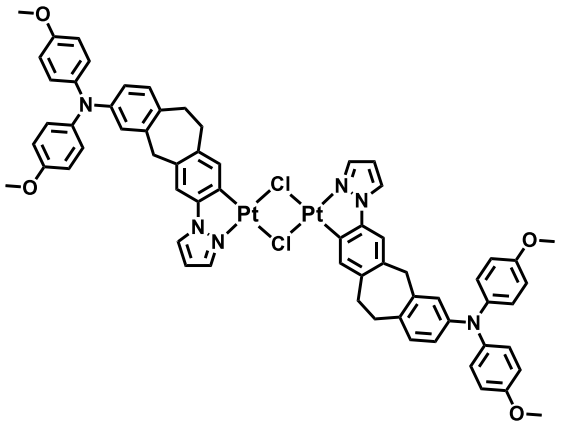

CA: [–]

Synthesis according to lit.[171-172]

Under nitrogen, K_2PtCl_4 (170 mg, 410 µmol) and **4** (200 mg, 410 µmol) were added to a degassed mixture of 2-ethoxyethanole and deionized water (10 ml, 3/1 by volume). The reaction mixture was stirred at 80 °C for 18 h. After the suspension cooled down to rt, distilled water (40 ml) was added and the precipitate was filtered off with a sintered glass funnel (P4) and washed with water (3 x 10

ml). The crude product was then dried under reduced pressure and was used without further purification.

Yield: 270 mg (190 µmol, 92 %) of a grey solid.

$C_{64}H_{65}Cl_2N_6O_4Pt_2$ [1434.26]

(13)

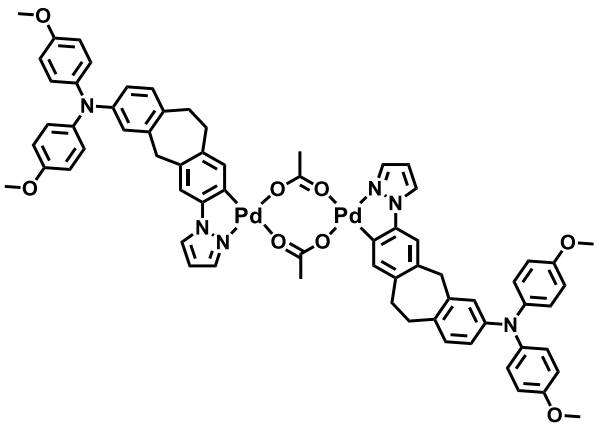

CA: [–]

Synthesis according to lit.[170]

Under nitrogen, $Pd(OAc)_2$ (200 mg, 890 µmol) was added to a degassed solution of **4** (430 mg, 882 µmol) in dry DCM (20 ml). After stirring for at rt for 3h, the orange solution was concentrated nearly to dryness under reduced pressure and the residue was triturated with Et_2O (30 ml). The precipitate was then filtered off with a sintered glass funnel (P4) and washed with Et_2O (3 x 10 ml). The crude product was then dried under reduced pressure and was used without further purification.

Yield: 550 mg (422 µmol, 96 %) of a dark yellow solid.

$C_{68}H_{62}N_6O_8Pd_2$ [1304.09]

6.2.3.2 Cyclometalated metal-dipyrrinato complexes

Pt

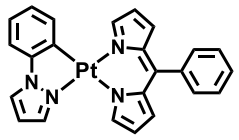

CA: [–]

Synthesis following GP III:

5 (89.0 mg, 402 µmol), DDQ (100 mg, 442 µmol), potassium carbonate (560 mg, 4.02 mmol), **10** (150 mg, 201 µmol) in THF (10 ml), rt, 18 h; flash column chromatography (eluent: DCM/PE = 1/3 → 1/1).

Yield: 45.0 mg (80.0 µmol, 20 %) of a red solid.

$C_{24}H_{18}N_4Pt$ [557.52]

^{1}H-NMR (400 MHz, CD_2Cl_2):

δ [ppm]= 8.12-8.11 (m, 1H), 8.10 (dd, $^3J_{H,H}$ = 2.9 Hz, $^4J_{H,H}$ = 0.6 Hz, 1H), 8.03-8.02 (m, 1H), 7.92 (d, $^3J_{H,H}$ = 2.4 Hz, 1H), 7.53-7.44 (-, 5H), 7.35-7.33 (m, 1H), 7.29-7.27 (m, 1H,), 7.18-7.10 (-, 2H), 6.86 (dd, $^3J_{H,H}$ = 4.3 Hz, $^3J_{H,H}$ = 1.2 Hz, 1H), 6.63-6.61 (-, 2H), 6.57 (dd, $^3J_{H,H}$ = 4.3 Hz, $^4J_{H,H}$ = 1.5 Hz, 1H), 6.47 (dd, $^3J_{H,H}$ = 4.4 Hz, $^3J_{H,H}$ = 1.7 Hz, 1H).

^{13}C-NMR (100 MHz, CD_2Cl_2):

δ [ppm] = 152.3 (CH), 150.9 (CH), 148.5 (C), 145.4 (C), 140.2 (CH), 138.1 (C), 137.3 (C), 136.4 (C), 135.7 (CH), 131.8 (CH), 131.4 (CH), 131.3 (C), 130.9 (CH), 128.9 (CH), 127.7 (CH), 126.9 (CH), 125.6 (CH), 124.2 (CH), 117.5 (CH), 117.1 (CH), 111.0 (CH), 107.3 (CH).

Microanalysis (CHN): calc. for $C_{24}H_{18}N_4Pt$ C-%: 51.70, H-%: 3.25, N-%: 10.05
found for $C_{24}H_{18}N_4Pt$ C-%: 51.67, H-%: 3.45, N-%: 10.07.

ESI-MS (pos., high res.): $[M^{+\bullet}]$ = $C_{24}H_{18}N_4Pt$; calc.: 557.11757, found: 557.11712
Δ = 0.81 ppm

DPt

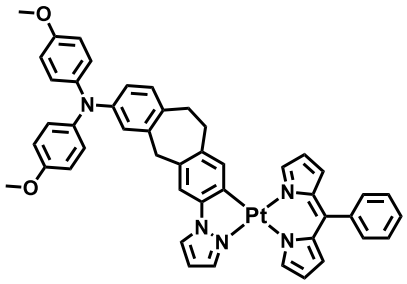

CA: [–]

Synthesis following GP III:

5 (46.0 mg, 207 µmol), DDQ (52.0 mg, 229 µmol), potassium carbonate (290 mg, 2.10 mmol), **12** (150 mg, 105 µmol) in THF (15 ml), rt, 18 h; flash column chromatography (eluent: DCM).

Yield: 51.0 mg (56.6 µmol, 27 %) of a red solid.

$C_{47}H_{39}N_5O_2Pt$ [900.92]

^{1}H-NMR (400 MHz, CD_2Cl_2):

δ [ppm]= 8.11-8.10 (m, 1H), 8.03-8.01 (-, 2H), 7.87 (d, $^3J_{H,H}$ = 2.4 Hz, 1H), 7.52-7.43 (-, 5H), 7.06-7.04 (-, 2H), 6.97 (AA‘, 4H), 6.93 (d, $^3J_{H,H}$ = 8.2 Hz, 1H), 6.85 (dd, $^3J_{H,H}$ = 4.3 Hz, $^3J_{H,H}$ = 1.2 Hz, 1H), 6.81-6.97 (-, 5H), 6.69 (dd, $^3J_{H,H}$ = 8.2 Hz, $^4J_{H,H}$ = 2.4 Hz, 1H), 6.62 (dd, $^3J_{H,H}$ = 4.4 Hz, $^4J_{H,H}$ = 1.4 Hz, 1H), 6.58 (dd, $^3J_{H,H}$ = 2.7 Hz, $^3J_{H,H}$ = 2.5 Hz, 1H), 6.56 (dd, $^3J_{H,H}$ = 4.4 Hz, $^4J_{H,H}$ = 1.5 Hz, 1H), 6.47 (dd, $^3J_{H,H}$ = 4.4 Hz, $^3J_{H,H}$ = 1.7 Hz, 1H), 3.95 (s, 2H), 3.76 (s, 6H), 3.18-3.07 (-, 4H).

^{13}C-NMR (100 MHz, CD_2Cl_2):

δ [ppm] = 155.9 (C), 152.2 (CH), 150.9 (CH), 148.5 (C), 147.1 (C), 143.5 (C), 141.8 (C), 140.3 (C), 139.9 (CH), 138.2 (C), 137.3 (C), 136.9 (C), 136.7 (CH), 136.3 (C), 135.2 (C), 132.4 (C), 131.8 (CH), 131.4 (C), 131.2 (CH), 130.9 (CH), 130.8 (CH), 129.0 (CH), 127.7 (CH), 126.5 (CH), 126.4 (CH), 122.2 (CH), 120.2 (CH), 117.6 (CH), 117.1 (CH), 114.9 (CH), 111.4 (CH), 107.1 (CH), 55.8 (CH_3), 41.0 (CH_2), 33.0 (CH_2), 32.4 (CH_2).

Microanalysis (CHN): calc. for $C_{47}H_{39}N_5O_2Pt$ C-%: 62.66, H-%: 4.36, N-%: 7.77
found for $C_{47}H_{39}N_5O_2Pt$ C-%: 62.52, H-%: 4.51, N-%: 7.50.

ESI-MS (pos., high res.): $[M^{+\bullet}]$ = $C_{47}H_{39}N_5O_2Pt$; calc.: 900.27496, found: 900.27389
Δ = 1.19 ppm

PtA

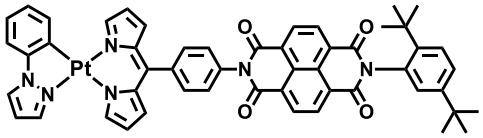

CA: [–]

Synthesis following GP III:

8 (271 mg, 401 µmol), DDQ (100 mg, 441 µmol), potassium carbonate (560 mg, 4.05 mmol), **10** (150 mg, 201 µmol) in THF (15 ml), rt, 18 h; flash column chromatography (eluent: DCM → DCM/MeOH = 99/1) and GPC.

Yield: 172 mg (170 µmol, 42 %) of a red solid.

$C_{52}H_{42}N_6O_4Pt$ [1010.01]

^{1}H-NMR (400 MHz, CD_2Cl_2):

δ [ppm]= 8.88-8.84 (-, 4H), 8.18-8.17 (m, 1H), 8.12 (dd, $^3J_{H,H}$ = 2.6 Hz, $^4J_{H,H}$ = 0.5 Hz, 1H), 8.08-8.07 (m, 1H), 7.95 (d, $^3J_{H,H}$ = 2.3 Hz, 1H), 7.75 (AA‘, 2H), 7.62 (d, $^3J_{H,H}$ = 8.6 Hz 1H), 7.52 (dd, $^3J_{H,H}$ = 8.6 Hz, $^4J_{H,H}$ = 2.2 Hz, 1H), 7.47 (BB‘, 2H), 7.38-7.35 (m, 1H), 7.31-7.29 (m, 1H), 7.20-7.12 (-, 2H), 7.05 (d, $^3J_{H,H}$ = 2.2 Hz, 1H), 7.02 (dd, $^3J_{H,H}$ = 4.3 Hz, $^3J_{H,H}$ = 1.1 Hz, 1H), 6.77 (dd, $^3J_{H,H}$ = 4.4 Hz, $^4J_{H,H}$ = 1.3 Hz, 1H), 6.66-6.64 (-, 2H), 6.54 (dd, $^3J_{H,H}$ = 4.4 Hz, $^3J_{H,H}$ = 1.7 Hz, 1H), 1.33 (s, 9H), 1.26 (s, 9H).

^{13}C-NMR (100 MHz, CD_2Cl_2):

δ [ppm] = 164.3 (C), 163.4 (C), 152.7 (CH), 151.3 (CH), 151.0 (C), 147.9 (C), 147.1 (C), 145.4 (C), 144.6 (C), 140.2 (CH), 138.9 (C), 137.1 (C), 136.3 (C), 135.75 (C), 135.69 (CH), 133.0 (C), 131.9 (CH), 131.7 (CH), 131.5 (CH), 131.2 (CH), 130.9 (CH), 129.5 (CH), 128.2 (CH), 128.0 (CH), 127.8 (C), 127.7 (C), 127.6 (C), 127.5 (C), 126.91 (CH), 126.87 (CH), 125.6 (CH), 124.2 (CH), 117.9 (CH), 117.4 (CH), 111.1 (CH), 107.4 (CH), 35.9 (C), 34.6 (C), 31.8 (CH_3), 31.3 (CH_3).

Microanalysis (CHN): calc. for $C_{52}H_{42}N_6O_4Pt$ C-%: 61.84, H-%: 4.19, N-%: 8.32

found for $C_{24}H_{18}N_4Pt$ C-%: 61.58, H-%: 4.29, N-%: 8.11.

ESI-MS (pos., high res.): $[M^{+\bullet}]$ = $C_{52}H_{42}N_6O_4Pt$; calc.: 1009.29136, found: 1009.29022

Δ = 1.13 ppm

DPtA

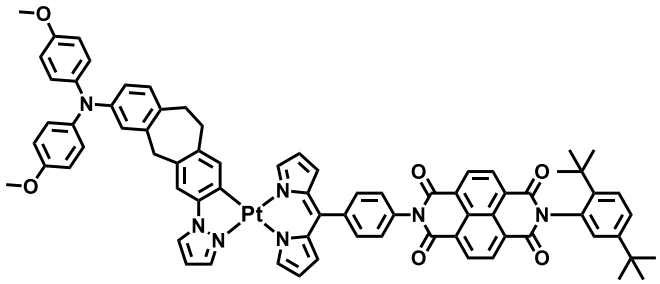

CA: [–]

Synthesis following GP III:

8 (250 mg, 418 µmol), DDQ (104 mg, 460 µmol), potassium carbonate (580 mg, 4.18 mmol), **12** (300 mg, 209 µmol) in THF (30 ml), rt, 18 h; flash column chromatography 1 (eluent: DCM → DCM/MeOH = 100/0.2), flash column chromatography 2 (eluent: DCM/PE/THF = 60/40/1), and GPC.

Yield: 52.0 mg (38.0 µmol, 9 %) of a red solid.

$C_{75}H_{63}N_7O_6Pt$ [1353.46]

^{1}H-NMR (400 MHz, CD_2Cl_2):

δ [ppm]= 8.88-8.84 (-, 4H), 8.16-8.15 (m,1H), 8.07-8.04 (-, 2H), 7.91 (d, $^3J_{H,H}$ = 2.3 Hz, 1H), 7.75 (AA‘, 2H), 7.63 (d, $^3J_{H,H}$ = 8.6 Hz, 1H), 7.52 (dd, $^3J_{H,H}$ = 8.6 Hz, $^4J_{H,H}$ = 2.2 Hz, 1H), 7.46 (BB‘, 2H), 7.09-7.04 (-, 3H), 7.01-6.96 (-, 5H), 6.94 (d, $^3J_{H,H}$ = 8.3 Hz, 1H) 6.82-6.76 (-, 6H), 6.70 (dd, $^3J_{H,H}$ = 8.2 Hz, $^4J_{H,H}$ = 2.4 Hz, 1H), 6.63 (dd, $^3J_{H,H}$ = 4.4 Hz, $^4J_{H,H}$ = 1.4 Hz, 1H), 6.61 (dd, $^3J_{H,H}$ = 2.7 Hz, $^3J_{H,H}$ = 2.5 Hz, 1H), 6.55 (dd, $^3J_{H,H}$ = 4.5 Hz, $^3J_{H,H}$ = 1.6 Hz, 1H), 3.96 (s, 2H), 3.76 (s, 6H), 3.20-3.09 (-, 4H), 1.33 (s, 9H), 1.26 (s, 9H).

^{13}C-NMR (100 MHz, CD_2Cl_2):

δ [ppm] = 164.3 (C), 163.3 (C), 155.9 (C), 152.6 (CH), 151.3 (CH), 151.0 (C), 147.09 (C), 147.06 (C), 144.6 (C), 143.6 (C), 141.8 (C), 139.90 (CH), 139.86 (C), 138.9 (C), 137.1 (C), 137.0 (CH), 136.7 (CH),136.2 (C), 136.1 (C), 135.7 (C), 135.3 (C), 133.0 (C), 132.4 (C),131.9 (CH), 131.7 (CH), 131.4 (CH), 130.8 (CH), 129.5 (CH), 129.3 (CH), 128.6 (C), 128.2 (CH), 128.1 (CH), 127.8 (C), 127.7 (C), 127.6 (C), 127.5 (C), 126.9 (CH), 126.6 (CH), 126.4 (CH), 122.2 (CH), 120.3 (CH), 117.9 (CH), 117.4 (CH), 114.9 (CH), 111.4 (CH), 107.2 (CH), 55.8 (CH_3), 41.0 (CH_2), 35.9 (C), 34.6 (C), 33.0 (CH_2), 32.4 (CH_2), 31.8 (CH_3), 31.3 (CH_3).

Microanalysis (CHN):	calc. for $C_{75}H_{63}N_7O_6Pt$	C-%: 66.56,	H-%: 4.69,	N-%: 7.24
	found for $C_{75}H_{63}N_7O_6Pt$	C-%: 66.18,	H-%: 4.67,	N-%: 7.09.

ESI-MS (pos., high res.): $[M^{+\bullet}]$ = $C_{75}H_{63}N_7O_6Pt$; calc.: 1353.45042, found: 1353.45117

Δ = 0.55 ppm

Pd

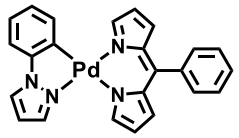

CA: [–]

Synthesis following GP III:

5 (58.0 mg, 261 µmol), DDQ (65.0 mg, 286 µmol), potassium carbonate (360 mg, 2.60 mmol), **11** (80.0 mg, 130 µmol) in THF (10 ml), rt, 18 h; flash column chromatography (eluent: Et_2O/PE/TEA = 30/20/1).

Yield: 83.0 mg (177 µmol, 68 %) of a orange solid.

$C_{24}H_{18}N_4Pd$ [468.84]

^{1}H-NMR (400 MHz, CD_2Cl_2):

δ [ppm]= 8.10 (dd, $^3J_{H,H}$ = 2.8 Hz, $^4J_{H,H}$ = 0.6 Hz, 1H), 7.98-7.95 (-, 2H), 7.85 (dd, $^3J_{H,H}$ = 1.3, $^3J_{H,H}$ = 1.3 Hz, 1H), 7.53-7.42 (-, 5H), 7.32-7.29 (m, 1H), 7.23 (dd, $^3J_{H,H}$ = 7.8 Hz, $^4J_{H,H}$ = 1.5 Hz, 1H), 7.20-7.15 (m, 1H), 7.08 (ddd, $^3J_{H,H}$ = 7.6 Hz, $^3J_{H,H}$ = 7.1 Hz, $^4J_{H,H}$ = 1.5 Hz, 1H), 6.78 (dd, $^3J_{H,H}$ = 4.3 Hz, $^4J_{H,H}$ = 1.2 Hz, 1H), 6.59 (dd, $^3J_{H,H}$ = 2.7 Hz, $^3J_{H,H}$ = 2.4 Hz, 1H), 6.55 (dd, $^3J_{H,H}$ = 2.4 Hz, $^4J_{H,H}$ = 1.4 Hz, 1H), 6.51 (dd, $^3J_{H,H}$ = 4.3 Hz, $^4J_{H,H}$ = 1.4 Hz, 1H), 6.46 (dd, $^3J_{H,H}$ = 4.3 Hz, $^4J_{H,H}$ = 1.6 Hz,1H).

^{13}C-NMR (100 MHz, CD_2Cl_2):

δ [ppm] = 152.6 (CH), 151.2 (CH), 148.5 (C), 144.6 (C), 141.0 (CH), 140.6 (C), 138.9 (C), 138.5 (C), 137.9 (C), 137.2 (CH), 132.1 (CH), 131.6 (CH), 131.1 (CH), 128.9 (CH), 127.6 (CH), 126.2 (CH), 125.7 (CH), 125.2 (CH), 117.8 (CH), 117.3 (CH), 111.5 (CH), 107.4 (CH).

Microanalysis (CHN): calc. for $C_{24}H_{18}N_4Pd$ C-%: 61.48, H-%: 3.87, N-%: 11.95

found for $C_{24}H_{18}N_4Pd$ C-%: 61.71, H-%: 3.65, N-%: 11.81.

ESI-MS (pos., high res.): $[M^{+\bullet}]$ = $C_{24}H_{18}N_4Pd$; calc.: 468.05701, found: 468.05671

Δ = 0.64 ppm

DPd

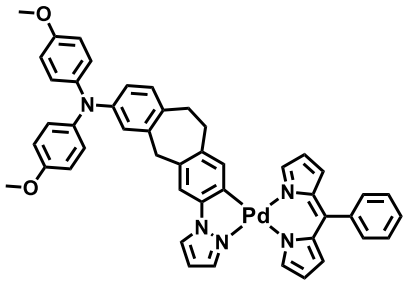

CA: [–]

Synthesis following GP III:

5 (27.3 mg, 123 µmol), DDQ (30.6 mg, 135 µmol), potassium carbonate (170 mg, 1.23 mmol), **13** (80.0 mg, 61.3 µmol) in THF (10 ml), rt, 18 h; flash column chromatography (eluent: Et_2O/TEA = 50/1).

Yield: 42.0 mg (51.7 µmol, 42 %) of a red solid.

$C_{47}H_{39}N_5O_2Pd$ [812.26]

^{1}H-NMR (400 MHz, CD_2Cl_2):

δ [ppm]= 8.02 (dd, $^3J_{H,H}$ = 2.8 Hz, $^4J_{H,H}$ = 0.6 Hz, 1H), 7.96-7.94 (m, 1H), 7.92 (d, $^3J_{H,H}$ = 2.3 Hz, 1H), 7.82-7.84 (m, 1H), 7.52-7.41 (-, 5H), 7.04-6.95 (-, 6H), 6.93 (d, $^3J_{H,H}$ = 8.4 Hz, 1H), 6.82-6.77 (-, 5H), 6.76 (dd, $^3J_{H,H}$ = 4.2 Hz, $^3J_{H,H}$ = 1.2 Hz, 1H), 6.69 (dd, $^3J_{H,H}$ = 8.2 Hz, $^4J_{H,H}$ = 2.4 Hz, 1H), 6.56-6.53 (-, 2H), 6.50 (dd, $^3J_{H,H}$ = 4.3 Hz, $^4J_{H,H}$ = 1.4 Hz, 1H), 6.46 (dd, $^3J_{H,H}$ = 4.3 Hz, $^4J_{H,H}$ = 1.6 Hz, 1H), 3.96 (s, 2H), 3.76 (s, 6H), 3.17-3.05 (-, 4H).

^{13}C-NMR (100 MHz, CD_2Cl_2):

δ [ppm] = 156.0 (C), 152.6 (CH), 151.2 (CH), 148.4 (C), 147.1 (C), 142.6 (C), 141.8 (2x C), 140.7 (CH), 139.8 (C), 139.0 (C), 138.5 (C), 138.1 (CH), 137.9 (C), 137.1 (C), 136.3 (C), 132.3 (C), 132.1 (CH), 131.5 (CH), 131.1 (CH), 130.7 (CH), 128.9 (CH), 127.6 (CH), 126.4 (CH), 125.9 (CH), 122.1 (CH), 120.2 (CH), 117.8 (CH), 117.3 (CH), 114.9 (CH), 111.9 (CH), 107.2 (CH), 55.8 (CH_3), 40.9 (CH_2), 33.0 (CH_2), 32.3 (CH_2).

Microanalysis (CHN): calc. for $C_{47}H_{39}N_5O_2Pd$ C-%: 69.50, H-%: 4.84, N-%: 8.62
found for $C_{47}H_{39}N_5O_2Pd$ C-%: 69.21, H-%: 4.53, N-%: 8.28.

ESI-MS (pos., high res.): $[M^{+\bullet}]$ = $C_{47}H_{39}N_5O_2Pd$; calc.: 811.21496, found: 811.21263
Δ = 2.87 ppm

PdA

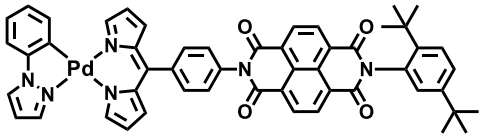

CA: [–]

Synthesis following GP III:

8 (219 mg, 325 µmol), DDQ (81.0 mg, 357 µmol), potassium carbonate (450 mg, 3.26 mmol), **11** (100 mg, 162 µmol) in THF (15 ml), rt, 18 h; flash column chromatography (eluent: Et_2O/PE/TEA = 30/20/1 → Et_2O/MeOH/TEA = 50/1/1) and GPC.

Yield: 98.0 mg (106 µmol, 33 %) of a red solid.

$C_{52}H_{42}N_6O_4Pd$ [921.35]

^{1}H-NMR (400 MHz, CD_2Cl_2):

δ [ppm]= 8.89-8.81 (-, 4H), 8.11 (dd, $^3J_{H,H}$ = 2.8 Hz, $^4J_{H,H}$ = 0.5 Hz, 1H), 8.03-8.00 (m, 1H), 7.98 (d, $^3J_{H,H}$ = 2.2 Hz, 1H), 7.90 (m, 1H), 7.74 (AA', 2H), 7.63 (d, $^3J_{H,H}$ = 8.6 Hz 1H), 7.52 (dd, $^3J_{H,H}$ = 8.6 Hz, $^4J_{H,H}$ = 2.2 Hz, 1H), 7.44 (BB', 2H), 7.33 (dd, $^3J_{H,H}$ = 7.6 Hz, $^4J_{H,H}$ = 1.1 Hz, 1H), 7.24 (dd, $^3J_{H,H}$ = 7.9 Hz, $^4J_{H,H}$ = 1.4 Hz, 1H), 7.19 (ddd, $^3J_{H,H}$ = 7.2 Hz, $^3J_{H,H}$ = 7.0 Hz, $^4J_{H,H}$ = 1.3 Hz, 1H), 7.10 (ddd, $^3J_{H,H}$ = 7.6 Hz, $^3J_{H,H}$ = 7.2 Hz, $^4J_{H,H}$ = 1.5 Hz, 1H), 7.05 (d, $^3J_{H,H}$ = 2.2 Hz, 1H), 6.93 (dd, $^3J_{H,H}$ = 4.3 Hz, $^4J_{H,H}$ = 1.1 Hz, 1H), 6.70 (dd, $^3J_{H,H}$ = 4.3 Hz, $^4J_{H,H}$ = 1.3 Hz, 1H), 6.60 (dd, $^3J_{H,H}$ = 2.6 Hz, $^3J_{H,H}$ = 2.4 Hz, 1H), 6.58 (dd, $^3J_{H,H}$ = 4.3 Hz, $^4J_{H,H}$ = 1.4 Hz, 1H), 6.53 (dd, $^3J_{H,H}$ = 4.4 Hz, $^4J_{H,H}$ = 1.6 Hz, 1H), 1.33 (s, 9H), 1.26 (s, 9H).

^{13}C-NMR (100 MHz, CD_2Cl_2):

δ [ppm] = 164.3 (C), 163.4 (C), 153.0 (CH), 151.6 (CH), 151.0 (C), 147.1 (C), 144.6 (C), 144.5 (C), 141.0 (CH), 140.5 (C), 139.6 (C), 138.4 (C), 137.8 (C), 137.2 (CH), 135.7 (C), 133.0 (C), 132.2 (CH), 132.1 (CH), 131.8 (CH), 131.7 (2 x CH), 129.4 (CH), 128.1 (CH), 128.0 (CH), 127.74 (C), 127.69 (C), 127.6 (C), 127.5 (C), 126.9 (CH), 126.3 (CH), 125.8 (CH), 125.3 (CH), 118.1 (CH), 117.6 (CH), 111.7 (CH), 107.5 (CH), 35.9 (C), 34.6 (C), 31.8 (CH_3), 31.3 (CH_3).

Microanalysis (CHN): calc. for $C_{52}H_{42}N_6O_4Pd$ C-%: 67.79, H-%: 4.59, N-%: 9.12
found for $C_{52}H_{42}N_6O_4Pd$ C-%: 67.43, H-%: 4.27, N-%: 8.96.

ESI-MS (pos., high res.): $[M^{+\bullet}]$ = $C_{52}H_{42}N_6O_4Pd$; calc.: 920.23148, found: 920.23026
Δ = 1.33 ppm

DPdA

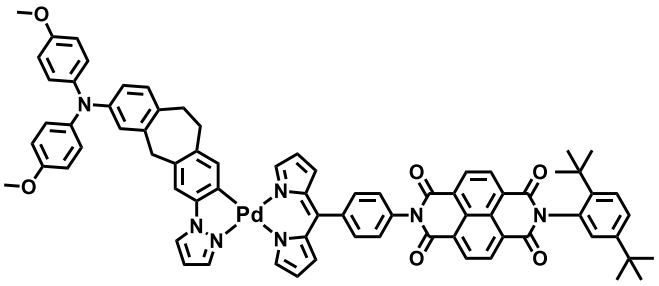

CA: [–]

Synthesis following GP III:

8 (155 mg, 230 µmol), DDQ (57.4 mg, 253 µmol), potassium carbonate (320 mg, 2.32 mmol), **13** (150 mg, 115 µmol) in THF (30 ml), rt, 18 h; flash column chromatography 1 (eluent: DCM → DCM/MeOH = 100/0.2), flash column chromatography 2 (eluent: Et_2O/PE/TEA = 30/20/1 → Et_2O/MeOH/TEA = 50/1/1) and GPC.

Yield: 46.0 mg (36.4 µmol, 16 %) of a brownish red solid.

$C_{75}H_{63}N_7O_6Pd$ [1264.76]

^{1}H-NMR (400 MHz, CD_2Cl_2):

δ [ppm]= 8.89-8.83 (-, 4H), 8.04 (dd, $^3J_{H,H}$ = 2.8 Hz, $^4J_{H,H}$ = 0.5 Hz, 1H), 8.02-8.02 (m, 1H), 7.95 (d, $^3J_{H,H}$ = 2.3 Hz, 1H), 7.89-7.88 (m, 1H), 7.74 (AA‘, 2H), 7.63 (d, $^3J_{H,H}$ = 8.6 Hz, 1H), 7.52 (dd, $^3J_{H,H}$ = 8.6 Hz, $^4J_{H,H}$ = 2.3 Hz, 1H), 7.45 (BB‘, 2H), 7.07-7.04 (-, 2H), 7.01-6.95 (-, 5H), 6.94 (d, $^3J_{H,H}$ = 8.3 Hz, 1H), 6.92 (dd, $^3J_{H,H}$ = 4.3 Hz, $^4J_{H,H}$ = 1.1 Hz, 1H), 6.83-6.77 (-, 5H), 6.72-6.68 (-, 2H), 6.58-6.55 (-, 2H), 6.53 (dd, $^3J_{H,H}$ = 4.3 Hz, $^3J_{H,H}$ = 1.6 Hz, 1H), 3.97 (s, 2H), 3.76 (s, 6H), 3.19-3.05 (-, 4H), 1.33 (s, 9H), 1.26 (s, 9H).

^{13}C-NMR (100 MHz, CD_2Cl_2):

δ [ppm] = 164.3 (C), 163.4 (C), 156.0 (C), 153.0 (CH), 151.6 (CH), 151.0 (C), 147.1 (C), 147.0 (C), 144.6 (C), 142.6 (C), 141.8 (C), 140.8 (CH), 139.8 (C), 139.7 (C), 138.4 (C), 138.1 (CH), 137.8 (C), 137.7 (C), 136.4 (C), 135.7 (C), 133.0 (C), 132.3 (C), 132.2 (CH), 132.1 (CH), 131.73 (CH), 131.71 (CH), 131.67 (CH), 130.8 (CH), 129.5 (CH), 128.08 (CH), 128.05 (CH), 127.8 (C), 127.7 (C), 127.6 (C), 127.5 (C), 126.9 (CH), 126.4 (CH), 126.0 (CH), 122.1 (CH), 120.2 (CH), 118.1 (CH), 117.6 (CH), 114.9 (CH), 111.9 (CH), 107.2 (CH), 55.8 (CH_3), 41.0 (CH_2), 35.9 (C), 34.6 (C), 33.1 (CH_2), 32.3 (CH_2), 31.8 (CH_3), 31.3 (CH_3).

Microanalysis (CHN): calc. for $C_{75}H_{63}N_7O_6Pd$ C-%: 71.22, H-%: 5.02, N-%: 7.75
found for $C_{75}H_{63}N_7O_6Pd$ C-%: 70.94, H-%: 4.87, N-%: 7.59.

ESI-MS (pos., high res.): $[M^{+\bullet}]$ = $C_{75}H_{63}N_7O_6Pd$; calc.: 1263.38928, found 1263.38613
Δ = 2.50 ppm

D_2IrA'

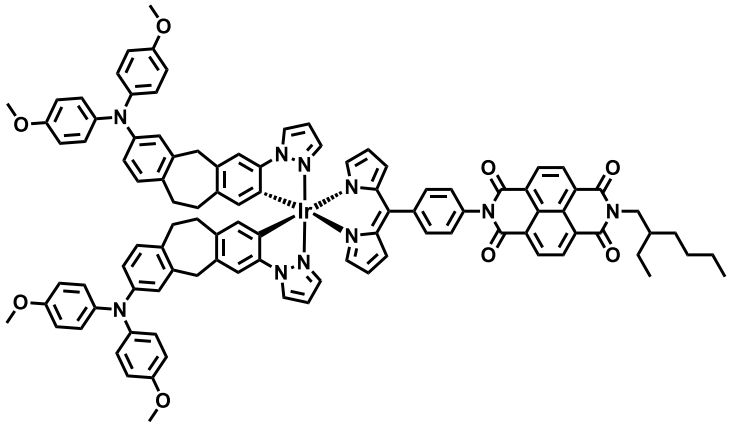

CA: [–]

Synthesis following GP III:

9 (100 mg, 167 µmol), DDQ (41.8 mg, 184 µmol), potassium carbonate (230 mg, 1.66 mmol), **14** (201 mg, 83.7 µmol) in THF (20 ml), 80 °C, 18 h; flash column chromatography (eluent: DCM → DCM/MeOH = 99/1) and GPC.

Yield: 62.0 mg (35.2 µmol, 21 %) of a red solid.

$C_{101}H_{87}IrN_{10}O_8$ [1761.05]

^{1}H-NMR (400 MHz, CD_2Cl_2):

δ [ppm]= 8.83-8.75 (-, 4H), 7.99 (d, $^3J_{HH}$ = 2.4 Hz, 2H), 7.65 (AA', 2H), 7.39 (BB', 2H), 7.06-7.00 (-, 6H), 6.97 (AA', 8H), 6.88 (d, $^3J_{HH}$ = 8.3 Hz, 2H), 6.83-6.72 (-, 10H), 6.67 (dd, $^3J_{HH}$ = 8.3 Hz, $^4J_{HH}$ = 2.4 Hz, 2H), 6.59 (dd, $^3J_{HH}$ = 4.3 Hz, $^4J_{HH}$ = 1.3 Hz, 2H), 6.48 (dd, $^3J_{HH}$ = 2.7 Hz, $^3J_{HH}$ = 2.3 Hz, 2H), 6.26 (dd, $^3J_{HH}$ = 4.3 Hz, $^4J_{HH}$ = 1.4 Hz, 2H), 6.11 (s, 2H), 4.22-4.07 (m, 2H), 3.87 (s, 4H), 3.74 (s, 12H), 3.07–2.84 (-, 8H), 2.01-1.88 (m, 1H), 1.47-1.24 (-, 8H), 0.95 (t, $^3J_{HH}$ = 7.3 Hz, 3H), 0.95 (t, $^3J_{HH}$ = 7.0 Hz, 3H).

^{13}C-NMR (100 MHz, CD_2Cl_2):

δ [ppm] = 163.5 (C), 163.4 (C), 155.9 (C), 152.7 (CH), 147.4 (C), 147.0 (C), 142.5 (C), 141.8 (2 x C), 140.6 (C), 140.3 (C), 137.8 (CH), 137.4 (C), 135.2 (CH), 135.13 (C), 135.11 (C), 132.63 (C), 132.56 (C), 131.8 (CH), 131.5 (CH), 131.3 (2x CH), 130.6 (CH), 127.8 (CH), 127.46 (C), 127.44 (C), 127.3 (C), 127.1 (C), 126.4 (CH), 125.6 (CH), 122.2 (CH), 120.1 (CH), 117.2 (CH), 114.9 (CH), 111.7 (CH), 107.3 (CH), 55.8 (CH_3), 44.8 (CH_2), 41.2 (CH_2), 38.4 (CH), 32.8 (CH_2), 32.4 (CH_2), 31.1 (CH_2), 29.0 (CH_2), 24.4 (CH_2), 23.5 (CH_2), 14.3 (CH_3), 10.8 (CH_3).

Microanalysis (CHN): calc. for $C_{101}H_{87}IrN_{10}O_8$ C-%: 68.88, H-%: 4.98, N-%: 7.95
found for $C_{101}H_{87}IrN_{10}O_8$ C-%: 68.52, H-%: 4.62, N-%: 7.59.

ESI-MS (pos., high res.): $[M^{+\bullet}]$ = $C_{101}H_{87}IrN_{10}O_8$; calc.: 1760.63433, found: 1760.63187

Δ = 1.40 ppm

6.2.4 Bis-dipyrrinato- and PDM-compounds and precursors

6.2.4.1 Precursors

5-(*N*,*N*-Bis(4-methoxyphenyl)aminophenyl)dipyrromethane (18)

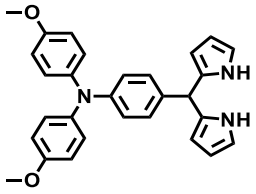

CA: [1372788-08-3]

Synthesis following GP I:

17 (1.00 g, 3.00 mmol), 1*H*-pyrrole (5.03 g, 5.20 ml, 75.0 mmol), TFA (3.42 mg, 2.31 µl, 30.0 µmol); flash column chromatography (eluent: PE/EA = 8/1→ 3/1) and column filtration over alumina act III (eluent: DCM).

Yield: 690 µg (1.53 mmol, 51 %) of an orange solid which is stored at -40 °C.

$C_{29}H_{27}N_3O_2$ [449.55]

^{1}H-NMR (400 MHz, acetone-d_6):

δ [ppm] = 9.64 (bs, 2H), 7.05 (AA', 2H), 6.99 (AA', 4H), 6.87 (BB', 4H), 6.79 (BB', 2H), 6.66 (ddd, $^3J_{HH}$ = 2.6 Hz, $^3J_{HH}$ = 2.6 Hz, $^4J_{HH}$ = 1.6 Hz, 2H), 5.96 (ddd, $^3J_{HH}$ = 3.2 Hz, $^3J_{HH}$ = 2.6 Hz, $^4J_{HH}$ = 2.6 Hz, 2H), 5.76-5.72 (m, 2H), 5.35 (s, 1H), 3.77 (s, 6H).

4-(4,4,5,5-tetramethyl-1,3,2-dioxaborolan-2-yl)benzaldehyde (19)

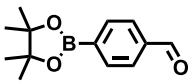

CA: [68716-49-4]

Synthesis following GP IV:

4-Bromobenzaldehyde (5.00 g, 27.0 mmol), bis(pinacolato)diboron (7.55 g, 29.7 mmol), KOAc (3.45 g, 35.2 mmol), $Pd(PhCN)_2Cl_2$ (310 mg, 808 µmol), 1,1'-bis(diphenylphosphino)ferrocene (450 mg, 812 µmol); flash column chromatography (eluent: PE/EA = 8/1→ 4/1)

$C_{13}H_{17}BO_3$ [232.08]

Yield: 6.11 g (26.3 mmol, 97 %) of a colorless solid.

^{1}H-NMR (400 MHz, $CDCl_3$):

δ [ppm] = 10.05 (s, 1H), 7.96 (AA', 2H), 7.86 (BB', 2H), 1.36 (s, 12H).

4-(*N*,*N*-Bis(4-methoxyphenyl)aminophenyl)benzaldehyde (21)

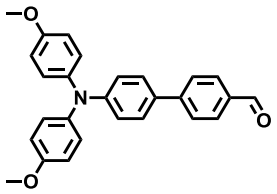

CA: [1447273-67-7]

Synthesis following GP V:

20 (1.34 g, 3.49 mmol), **19** (810 mg, 3.49 mmol), $Pd(PPh_3)_4$ (140 mg, 121 µmol), 1M $Na_2CO_{3(aq)}$/tol = 1/3 (40 ml), 110 °C, 72 h; flash chromatography (eluent: PE/EA = 9/1→ 4/1).

Yield: 1.23 g (3.00 mmol, 86 %) of a slightly tan solid.

$C_{27}H_{23}NO_3$ [409.48]

^{1}H-NMR (400 MHz, $CDCl_3$):

δ [ppm] = 10.01 (s, 1H), 7.90 (AA', 2H), 7.70 (BB', 2H), 7.47 (AA', 2H), 7.11 (AA', 4H), 6.98 (BB', 2H), 6.86 (BB', 4H), 3.81 (s, 6H).

5-(*N*,*N*-Bis(4-methoxyphenyl)aminophenyl)dipyrromethane (22)

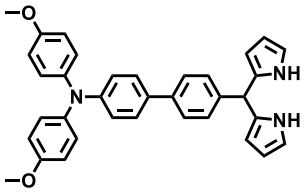

CA: [–]

Synthesis following GP I:

21 (500 mg, 1.22 mmol), 1*H*-pyrrole (2.05 g, 2.12 ml, 30.6 mmol), TFA (1.39 mg, 0.91 µl, 12.2 µmol); flash column chromatography (eluent: PE/EA = 8/1 → 4/1) and column filtration over alumina act III (eluent: DCM).

Yield: 370 mg (704 µmol, 58 %) of an orange solid which is stored at -40 °C.

$C_{35}H_{31}N_3O_2$ [525.64]

^{1}H-NMR (400 MHz, $CDCl_3$):

δ [ppm] = 7.96 (bs, 2H), 7.49 (AA', 2H), 7.39 (AA', 2H), 7.24 (BB', 2H), 7.09 (AA', 4H), 6.97 (BB', 2H), 6.84 (BB', 4H), 6.71 (ddd, $^3J_{HH}$ = 2.7 Hz, $^4J_{HH}$ = 2.7 Hz, $^4J_{HH}$ = 1.6 Hz, 2H), 6.17 (ddd, $^3J_{HH}$ = 3.2 Hz, $^3J_{HH}$ = 2.7 Hz, $^4J_{HH}$ = 2.7 Hz, 2H), 5.98-5.94 (m, 2H), 5.50 (s, 1H), 3.80 (s, 6H).

5,5-Dimethyldipyrromethane (23)

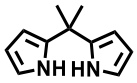

CA: [99840-54-7]

Synthesis following GP I:

Acetone (3.35 g, 4.24 ml, 57.7 mmol), 1*H*-pyrrole (97.0 g, 100 ml, 1.44 mol), TFA (660 mg, 440 µl, 5.77 mmol); flash column chromatography (eluent: PE/DCM = 2/1→ 1/1).

Yield: 5.57 g (32.0 mmol, 55 %) of a slightly tan solid.

$C_{11}H_{14}N_2$ [174.25]

^{1}H-NMR (400 MHz, $CDCl_3$):

δ [ppm] = 7.77 (bs, 2H), 6.63 (ddd, $^3J_{HH}$ = 2.6 Hz, $^3J_{HH}$ = 2.6 Hz, $^4J_{HH}$ = 1.6 Hz, 2H), 6.13 (ddd, $^3J_{HH}$ = 3.4 Hz, $^4J_{HH}$ = 2.7 Hz, $^4J_{HH}$ = 2.7 Hz, 2H), 6.10 - 6.08 (m, 2H), 1.65 (s, 6H).

1-(4-Bromobenzoyl)-5,5-dimethyldipyrromethane (27)

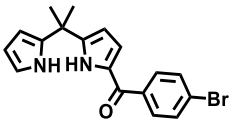

CA: [–]

Synthesis according to lit.[162, 254]

Under nitrogen, a solution of **23** (3.00 g, 17.2 mmol) in dry THF (20 ml) was added to a freshly prepared solution of EtMgBr (45.0 mmol, 45.0 ml, 1 M in THF) in a 3-neck round bottom flask. The resulting mixture was stirred for 10 min at rt before it was cooled to -78 °C. A solution of **25** (5.06 g, 17.2 mmol) in dry THF (40 ml) was added to the cooled reaction over the course of 5 min. The reaction was stirred at -78°C for 10 min before the cooling bath was removed. The reaction mixture was stirred until TLC-analysis showed a completed reaction (approx. 30 min). The still cool reaction

was quenched with saturated NH_4Cl, warmed to rt, and extracted with DCM. The combined organic extracts were washed with water, dried over Na_2SO_4 and the solvent was removed under reduced pressure. The residue was purified by flash-column-chromatography on silica (eluent: PE/EA = 9/1 → 4/1) and recrystallization from acetone/water = 2/1 to remove the side product as the precipitate and acetone/water = 1/1 to precipitate the desired compound.

Yield: 4.48 g (12.5 mmol, 73 %) of a yellowish crystalline solid.

$C_{18}H_{17}BrN_2O$ [357.24]

^{1}H-NMR (400 MHz, $CDCl_3$):

δ [ppm] = 9.07 (s, 1H), 7.91 (s, 1H), 7.71 (AA', 2H), 7.60 (BB', 2H), 6.76 (dd, $^3J_{HH}$ = 3.9 Hz, $^3J_{HH}$ = 2.5 Hz, 1H), 6.69 (ddd, , $^3J_{HH}$ = 2.6 Hz, $^3J_{HH}$ = 2.6 Hz, $^4J_{HH}$ = 1.5 Hz, 1H), 6.20-6.12 (- , 3H), 1.71 (s, 6H).

^{13}C-NMR (100 MHz, CD_2Cl_2):

δ [ppm] = 183.6 (C), 149.3 (C), 137.7 (C), 137.6 (C), 131.9 (CH), 130.8 (CH), 130.4 (C), 126.7 (C), 121.4 (CH), 117.8 (CH), 108.3 (CH), 108.0 (CH), 104.6 (CH), 36.0 (C), 28.7 (CH_3).

5,5,15,15-Tetramethyl-10,20-di(4-bromophenyl)porphodimethene (28)

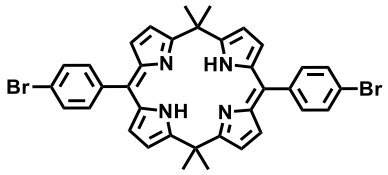

CA: [–]

Synthesis according to lit.[162]

Under nitrogen, $NaBH_4$ (10.7 g, 284 mmol) was added in small portions to a solution of **27** (3.38 g, 9.46 mmol) in dry THF/MeOH = 3/1 (200 ml). After complete addition the reaction was stirred at rt until TLC-analysis (silica, eluent: PE/EA = 9/1) showed a complete consumption of the starting material (approx. 45 min). The mixture was then poured into a stirred mixture of saturated aqueous NH_4Cl and DCM (approx. 1/1 by volume), the organic phase was separated, the aqueous phase extracted with DCM (3 x 50 ml), the combined organic phases washed again with water (3 x 100 ml), dried over Na_2SO_4 and the solvent removed under reduced pressure. The resulting yellow solid was dissolved in DCM (200 ml) and then dropped over the course of 6 h into a suspension of $Yb(OTf)_3$ (530 mg, 854 µmol) in DCM (1.60 l). The mixture was then stirred over night at rt before DDQ (2.63 g, 11.6 mmol) was added. After 2 h the reaction was quenched with TEA (10 ml), concentrated under

vacuum to about 300 ml and filtered through a pack of alumina (act. I, eluted with DCM until the eluent was only slightly yellow). The solvent was removed under reduced pressure and the crude product was purified by flash-column-chromatography on silica (eluent: PE/DCM = 3/1 → 1/1) and subsequent precipitation from DCM into MeOH.

Yield: 790 mg (1.16 mmol, 25 %) of a purple, microcrystalline solid.

$C_{36}H_{30}Br_2N_4$ [678.46]

^{1}H-NMR (400 MHz, CD_2Cl_2):

δ [ppm] = 14.15 (s, 2H), 7.54 (AA', 4H), 7.30 (BB', 4H), 6.31-6.25 (-, 8H), 1.92 (s, 12H).

^{13}C-NMR (100 MHz, CD_2Cl_2):

δ [ppm] = 166.1 (C), 140.4 (C), 139.2 (C), 136.3 (C), 132.7 (CH), 131.2 (CH), 128.4 (CH), 123.3 (C), 115.0 (CH), 38.7 (C), 28.9 (CH_3).

[5,5,15,15-Tetramethyl-10,20-di(4-bromophenyl)porphodimethenato]palladium(II) (Pd-28)

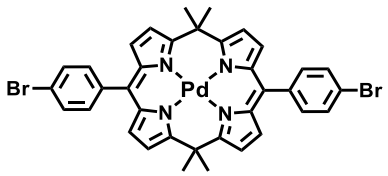

CA: [–]

Synthesis following GP VII:

28 (590 mg, 870 µmol), $Pd(CF_3CO_2)_2$ (440 mg, 1.32 mmol), 50 ml 1,2-dichloroethane/MeOH = 4/1, 90 °C, 1h; flash column chromatography (eluent: PE/DCM = 6/1→ 2/1) and precipitation from DCM into MeOH.

Yield: 370 mg (473 µmol, 54 %) of a red solid.

$C_{36}H_{28}Br_2N_4Pd$ [782.86]

^{1}H-NMR (400 MHz, CD_2Cl_2):

δ [ppm] = 7.56 (AA', 4H), 7.30 (BB', 4H), 6.45 (d, $^3J_{HH}$ = 4.4 Hz, 4H), 6.40 (d, $^3J_{HH}$ = 4.4 Hz, 4H), 1.90 (s, 12H).

^{13}C-NMR (100 MHz, CD_2Cl_2):

δ [ppm] = 164.8 (C), 144.1 (C), 136.8 (C), 135.0 (C), 132.5 (CH), 131.4 (CH), 131.0 (CH), 123.1 (C), 114.8 (CH), 40.9 (C), 31.0 (CH_3).

***N*,*N*-Bis(4-methoxyphenyl)aminophenyl-4-(4,4,5,5-tetramethyl-1,3,2-dioxaborolan-2-yl)aniline (29)**

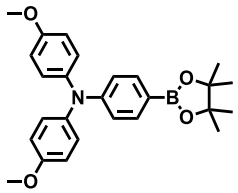

CA: [875667-84-8]

Synthesis following GP IV:

20 (3.00 g, 7.81 mmol), bis(pinacolato)diboron (2.18 g, 8.58 mmol), KOAc (1.00 g, 10.2 mmol), $Pd(PhCN)_2Cl_2$ (60.0 mg, 156 µmol), 1,1'-bis(diphenylphosphino)ferrocene (88.7 mg, 160 µmol); flash column chromatography (eluent: PE/EA = 6/1 → 4/1) and recrystallization from EtOH/water =4/1.

Yield: 2.94 g (6.82 mmol, 87 %) of a colorless, crystalline solid.

$C_{26}H_{30}BNO_4$ [431.33]

^{1}H-NMR (400 MHz, acetone-d_6):

δ [ppm] = 7.53 (AA', 2H), 7.08 (AA', 4H), 6.93 (BB', 4H), 6.77 (BB', 2H), 3.80 (s, 6H), 1.30 (s, 12H).

***N*-(2,5-Di-*tert*-butylphenyl)-*N'*-(4-bromophenyl)-naphthalene-1,4,5,8-tetracarboxylic diimide (30)**

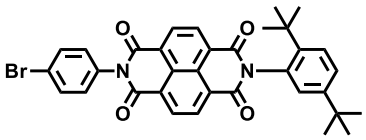

CA: [1163177-10-3]

Synthesis following GP II:

Naphthalene-1,4,5,8-tetracarboxylic dianhydride (1.50 g, 5.59 mmol), 2,5-di-*tert*-butylaniline (1.15 g, 5.60 mmol), 4-bromoaniline (960 mg, 5.58 mmol), pyridine (20 ml); flash column chromatography (eluent: PE/EA = 4/1 → 2/1).

Yield: 1.02 g (1.67 mmol, 30 %) of a yellowish solid.

$C_{34}H_{29}BrN_2O_4$ [609.51]

^{1}H-NMR (400 MHz, $CDCl_3$):

δ [ppm] = 8.89–8.83 (-, 4H), 7.72 (AA', 2H), 7.61 (d, $^3J_{HH}$ = 8.7 Hz, 1H), 7.50 (dd, $^3J_{HH}$ = 8.7 Hz, $^4J_{HH}$ = 2.2 Hz, 1H), 7.22 (BB', 2H), 7.01 (d, $^4J_{HH}$ = 2.1 Hz, 1H), 1.33 (s, 9H), 1.28 (s, 9H).

_N_-(2,5-Di-_tert_-butylphenyl)-_N'_-(4,4,5,5-tetramethyl-1,3,2-dioxaborolan-2-ylphenyl)-naphthalene-1,4,5,8-tetracarboxylic diimide (31)

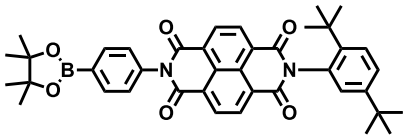

CA: [–]

Synthesis following GP IV:

30 (1.00 g, 1.64 mmol), bis(pinacolato)diboron (460 mg, 1.81 mmol), KOAc (210 mg, 2.14 mmol), $Pd(PhCN)_2Cl_2$ (13.0 mg, 33.9 µmol), 1,1'-bis(diphenylphosphino)ferrocene (18.0 mg, 32.5 µmol); flash column chromatography (eluent: PE/EA = 6/1→ 4/1) and precipitation from DCM into MeOH.

Yield: 770 mg (1.17 mmol, 71 %) of a yellowish white solid.

$C_{40}H_{41}BN_2O_6$ [656.58]

^{1}H-NMR (400 MHz, $CDCl_3$):

δ [ppm] = 8.87–8.85 (-, 4H), 8.04 (AA', 2H), 7.61 (d, $^3J_{HH}$ = 8.6 Hz, 1H), 7.50 (dd, $^3J_{HH}$ = 8.5 Hz, $^4J_{HH}$ = 2.2 Hz, 1H), 7.35 (BB', 2H), 7.01 (d, $^4J_{HH}$ = 2.1 Hz, 1H), 1.38 (s, 12H), 1.33 (s, 9H), 1.28 (s, 9H).

^{13}C-NMR (100 MHz, CD_2Cl_2):

δ [ppm] = 164.3 (C), 163.3 (C), 151.0 (C), 144.5 (C), 136.1 (CH), 133.0 (C), 131.7 (CH), 131.6 (CH), 129.4 (CH), 128.4 (CH), 128.0 (CH), 127.7 (C), 127.6 (C), 127.5 (C), 126.9 (CH), 84.5 (C), 35.9 (C), 34.6 (C), 31.8 (CH_3), 31.3 (CH_3), 25.1 (CH_3).

32

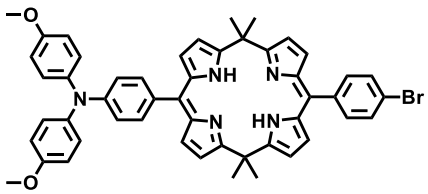

CA: [–]

Synthesis according to lit.[173, 257]

A Schlenk-flask under nitrogen was charged with **28** (300 mg, 442 µmol), bis(4-methoxyphenyl)amine (120 mg, 523 µmol), NaO^{t}Bu (110 mg, 1.14 mmol) and Pd_2dba_3 x $CHCl_3$ (22.9 mg, 22.1 µmol). The flask was then evacuated and flushed with nitrogen three times before dry and degassed toluene (10

ml) was added. The mixture was further degassed with a stream of nitrogen for 10 min before a dry and degassed solution of P^tBu_3 (39.8 µl, 39.8 µmol, 1M in toluene) was added. The resulting suspension was heated at 100 °C until TLC analysis showed a complete consumption of the bis(4-methoxyphenyl)amine (approx. 1d). The reaction was cooled to rt and diluted with DCM (100 ml) and water (100 ml). The aqueous phase was washed with DCM (3 x 50 ml), and the combined organic extracts were washed with water (2 x 50 ml) and saturated aqueous NaCl (50 ml), dried over $MgSO_4$ and the solvent was removed under reduced pressure. The resulting crude dark oil was purified by flash column chromatography on silica (eluent: PE/DCM = 9:1 → 3/2). The resulting red solid was further purified by precipitation from DCM into hexane.

Yield: 108 mg (131 µmol, 30 %) of a red solid, containing impurities of the debrominated species.

$C_{50}H_{44}BrN_5O_2$ [826.82]

^{1}H-NMR (400 MHz, CD_2Cl_2):

δ [ppm] = 14.20 (bs, 2H), 7.53 (AA', 2H), 7.30 (BB', 2H), 7.22 (AA', 2H), 7.12 (AA', 4H), 6.86 (BB', 4H), 6.84 (BB', 2H), 6.47 (dd, $^3J_{H,H}$ = 4.1 Hz, $^4J_{H,H}$ = 1.0 Hz, 2H), 6.31-6.23 (-, 6H), 3.78 (s, 6H), 1.92 (s, 12H).

No ^{13}C-NMR and high resolution mass spectra were recorded because the compound was contaminated with debrominated side product which could not be separated.

Pd-32, D-PdPDM

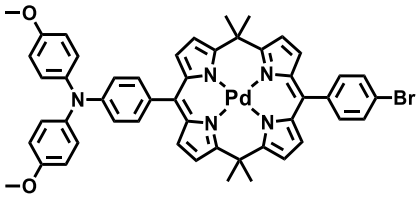

Pd-32

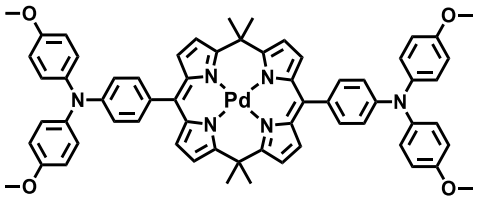

D-PdPDM

CA: [–]

Synthesis according to lit.[173, 257]

A Schlenk-flask under nitrogen was charged with **Pd-28** (200 mg, 255 µmol), bis(4-methoxyphenyl)amine (58.6 mg, 256 µmol), NaO^tBu (61.4 mg, 639 µmol) and Pd_2dba_3 x $CHCl_3$ (13.3

mg, 12.8 µmol). The flask was then evacuated and flushed with nitrogen three times before dry and degassed toluene (10 ml) was added. The mixture was further degassed with a stream of nitrogen for 10 min before a dry and degassed solution of P^tBu_3 (38.0 µl, 38.0 µmol, 1M in toluene) was added. The resulting suspension was heated at 100 °C until TLC analysis showed a complete consumption of the bis(4-methoxyphenyl)amine (approx. 1d) before it was cooled to rt and diluted with DCM (100 ml) and Water (100 ml). The aqueous phase was washed with DCM (3 x 50 ml), and the combined organic extracts were washed with water (2 x 50 ml) and saturated aqueous NaCl (50 ml), dried over $MgSO_4$ and the solvent was removed under reduced pressure. The resulting crude dark oil was purified by flash column chromatography on silica (eluent: PE/DCM = 9:1 → 3/2). The resulting red solids were further purified by precipitation from DCM into hexane.

Yields: **Pd-32**: 81.8 mg (87.8 µmol, 34 %) of a red solid, containing impurities of the debrominated species.

D-PdPDM: 27.1 mg (25.1 µmol, 10 %) of a red solid

Pd-32: $C_{50}H_{42}BrN_5O_2Pd$ [931.24]

^{1}H-NMR (400 MHz, CD_2Cl_2):

δ [ppm] = 7.55 (AA', 2H), 7.30 (BB', 2H), 7.22 (AA', 2H), 7.13 (AA', 4H), 6.90-6.83 (-, 6H), 6.65 (d, $^3J_{H,H}$ = 4.3 Hz, 2H), 6.44 (d, $^3J_{H,H}$ = 4.4 Hz, 2H), 6.40 (d, $^3J_{H,H}$ = 4.3 Hz, 2H), 6.38 (d, $^3J_{H,H}$ = 4.4 Hz, 2H), 3.78 (s, 6H), 1.91 (s, 12H).

No ^{13}C-NMR and high resolution mass spectra were recorded because the compound was contaminated with debrominated side product which could not be separated.

D-PdPDM: $C_{64}H_{56}N_6O_4Pd$ [1079.59]

^{1}H-NMR (400 MHz, CD_2Cl_2):

δ [ppm] = 7.21 (AA', 4H), 7.12 (AA'', 8H), 6.89-6.83 (-, 12H), 6.63 (d, $^3J_{H,H}$ = 4.4 Hz, 4H) 6.39 (d, $^3J_{H,H}$ = 4.3 Hz, 4H), 3.78 (s, 12H), 1.91 (s, 12H).

^{13}C-NMR (100 MHz, CD_2Cl_2):

δ [ppm] = 163.9 (C),156.9 (C), 149.8 (C), 146.4 (C), 140.7 (C), 135.4 (C), 132.0 (CH), 131.4 (CH), 129.1 (C), 127.6 (CH), 118.0 (CH), 115.1 (CH), 114.0 (CH), 55.8 (CH_3), 40.7 (C).

The missing CH_3-signal corresponds to the primary C-atom at the 5- and 15- position of the PDM-unit. The C-atom could be confirmed by measurement of a HSQC – ETGP spectrum of **D-PdPDM-A**, which showed a clear coupling of the CH_3-H-atoms to the seemingly missing peak of the primary C-atom in the region around 31.8 ppm. For reasons of time and economy these measurements were not

performed for this compound but are assumed to be transferable because the CH_3-group in question is confirmed by ^{1}H-NMR- spectroscopy and mass spectrometry.

Microanalysis (CHN): calc. for $C_{64}H_{56}N_6O_4Pd$ C-%: 71.20, H-%: 5.23, N-%: 7.78

found for $C_{64}H_{56}N_6O_4Pd$ C-%: 70.83, H-%: 5.42, N-%: 7.65.

ESI-MS (pos., high res.): $[M^{+\bullet}]$ = $C_{64}H_{56}N_6O_4Pd$; calc.: 1078.34134, found: 1078.34346

Δ = 1.97 ppm

33

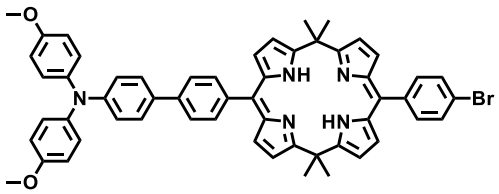

CA: [–]

Synthesis following GP V:

29 (127 mg, 295 µmol), **28** (200 mg, 295 µmol), $Pd(PPh_3)_4$ (11.9 mg, 10.3 µmol), 1M $Na_2CO_{3(aq)}$/tol = 1/10 (10 ml), 110 °C, 48 h; flash chromatography (eluent: PE/DCM/TEA = 80/20/1 → 60/40/1, precipitation from DCM into hexane.

Yield: 73.0 mg (80.8 µmol, 27 %) of a red solid.

$C_{56}H_{48}BrN_5O_2$ [902.92]

^{1}H-NMR (400 MHz, CD_2Cl_2):

δ [ppm] = 14.68-14.25 (-, 2H), 7.59 (AA', 2H), 7.54 (AA', 2H), 7.49-7.43 (-, 4H), 7.31 (BB', 2H), 7.08 (AA', 4H), 6.95 (BB', 2H), 6.85 (BB', 4H), 6.40 (dd, $^3J_{H,H}$ = 4.2 Hz, $^4J_{H,H}$ = 0.9 Hz, 2H), 6.31-6.25 (-, 6H), 3.78 (s, 6H), 1.93 (s, 12H).

No ^{13}C-NMR and high resolution mass spectra were recorded because the compound was contaminated with debrominated side product which could not be separated.

Pd-33

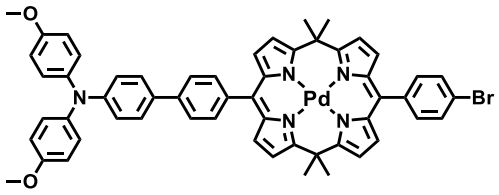

CA: [–]

Synthesis following GP V:

29 (83.0 mg, 192 µmol), **28-Pd** (150 mg, 192 µmol), $Pd(PPh_3)_4$ (11.0 mg, 9.52 µmol), 1M $Na_2CO_{3(aq)}$/tol = 1/10 (10 ml), 110 °C, 48 h; flash chromatography (eluent: PE/DCM/TEA = 80/20/1 → 60/40/1, precipitation from DCM into hexane.

Yield: 56.0 mg (55.6 µmol, 29 %) of a red solid.

$C_{56}H_{46}BrN_5O_2Pd$ [1007.34]

^{1}H-NMR (400 MHz, CD_2Cl_2):

δ [ppm] = 7.60 (AA', 2H), 7.56 (AA', 2H), 7.48 (AA', 2H), 7.45 (BB', 2H), 7.31 (BB', 2H), 7.08 (AA', 4H), 6.96 (BB', 2H), 6.85 (BB', 4H), 6.56 (d, $^3J_{H,H}$ = 4.4 Hz, 2H), 6.45 (d, $^3J_{H,H}$ = 4.4 Hz, 2H), 6.43-638 (-, 4H), 3.78 (s, 6H), 2.11 (s, 12H).

No ^{13}C-NMR and high resolution mass spectra were recorded because the compound was contaminated with debrominated side product which could not be separated.

6.2.4.2 Discussed bis-dipyrrinato- and PDM-compounds

$Pd(dipy)_2$

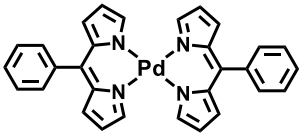

CA: [–]

Synthesis following GP VI:

5 (99.0 mg, 450 µmol), DDQ (111 mg, 490 µmol), K_2CO_3 (770 mg, 220 µmol), $Pd(OAc)_2$ (50.0 g, 220 µmol), rt, 18 h; flash column chromatography (eluent: Et_2O/TEA = 50/1).

Yield: 65.0 mg (120 µmol, 54 %) of a red, microcrystalline solid.

$C_{30}H_{22}N_4Pd$ [544.95]

^{1}H-NMR (400 MHz, CD_2Cl_2):

δ [ppm] = 7.60-7.45 (-, 10H), 7.38 (dd, $^{3}J_{H,H}$ = 1.5 Hz, $^{3}J_{H,H}$ = 1.5 Hz, 4H), 6.70 (dd, $^{4}J_{H,H}$ = 4.3 Hz, $^{3}J_{H,H}$ = 1.4 Hz, 4H), 6.37 (dd, $^{4}J_{H,H}$ = 4.3 Hz, $^{3}J_{H,H}$ = 1.6 Hz, 4H).

^{13}C-NMR (100 MHz, CD_2Cl_2):

δ [ppm] = 152.0 (CH), 148.2 (C), 137.8 (C), 137.5 (C), 131.6 (CH), 130.8 (CH), 129.1 (CH), 127.9 (CH), 117.3 (CH).

Microanalysis (CHN): calc. for $C_{30}H_{22}N_4Pd$ C-%: 66.12, H-%: 4.07, N-%: 10.28
found for $C_{30}H_{22}N_4Pd$ C-%: 65.94, H-%: 3.92, N-%: 9.95.

ESI-MS (pos., high res.): $[M^{+\bullet}]$ = $C_{30}H_{22}N_4Pd$; calc.: 544.08851, found: 544.08766
Δ = 1.56 ppm

Zn(dipy)$_2$

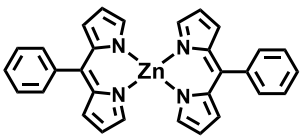

CA: [286464-42-4]

Synthesis following GP VI:

5 (111 mg, 499 µmol), DDQ (135 mg, 595 µmol), K_2CO_3 (1.73 g, 12.5 mmol), $Zn(OAc)_2$ x $2H_2O$ (274 mg, 1.25 mmol), 60 °C, 72 h; flash column chromatography (eluent: DCM/MeOH = 99/1), sonication in MeOH.

Yield: 52.0 mg (103 µmol, 41 %) of an orange solid.

$C_{30}H_{22}N_4Zn$ [503.92]

^{1}H-NMR (400 MHz, CD_2Cl_2):

δ [ppm] = 7.59-7.54 (-, 8H), 7.52-7.43 (-, 6H), 6.71 (dd, $^{4}J_{H,H}$ = 4.2 Hz, $^{3}J_{H,H}$ = 1.1 Hz, 4H), 6.41 (dd, $^{4}J_{H,H}$ = 4.1 Hz, $^{3}J_{H,H}$ = 1.4 Hz, 4H).

Cu(dipy)$_2$

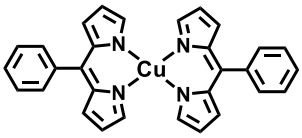

CA: [1139796-64-7]

Synthesis following GP VI:

5 (300 mg, 1.35 mmol), DDQ (337 mg, 1.48 mmol), K_2CO_3 (2.33 g, 16.9 mmol), $Cu(OAc)_2$ x H_2O (1.35 g, 6.76 mmol) in 10 ml MeOH, 3 h, rt; flash column chromatography (eluent: PE/DCM/acetone = 7/2/1).

Yield: 280 mg (558 µmol, 83 %) of a green, crystalline solid.

$C_{30}H_{22}N_4Cu$ [502.07]

^{1}H-NMR:

No measurement possible due to the paramagnetic character of the Cu(II) central metal ion.

Microanalysis (CHN):	calc. for $C_{30}H_{22}N_4Cu$	C-%: 71.77,	H-%: 4.42,	N-%: 11.16
	found for $C_{30}H_{22}N_4Cu$	C-%: 71.67,	H-%: 4.49,	N-%: 11.26.

Pd(dipy)$_2$-A, D-Pd(dipy)$_2$-A, D-Pd(dipy)$_2$

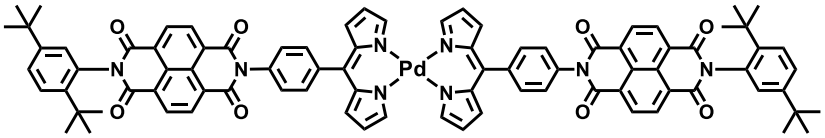

Pd(dipy)$_2$-A

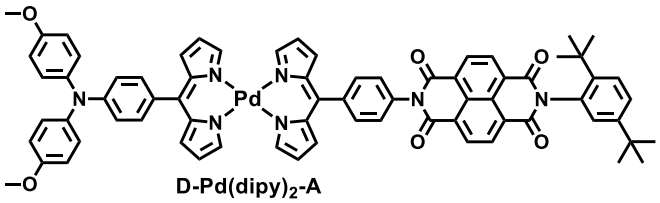

D-Pd(dipy)$_2$-A

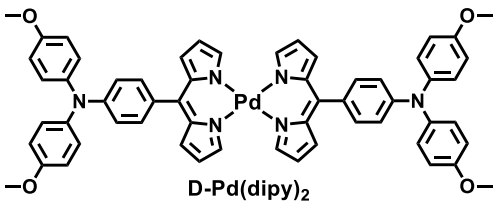

D-Pd(dipy)$_2$

CA: [–]

Synthesis following GP VI:

8 (150 mg, 222 µmol), **18** (100 mg, 222 µmol), DDQ (111 mg, 489 µmol), K_2CO_3 (770 mg, 5.57 mmol), $Pd(OAc)_2$ (50.0 g, 223 µmol); flash column chromatography (eluent: Et_2O/cyclohexane/TEA = 10/40/1 → 50/0/1) and GPC.

Yields: **Pd(dipy)$_2$-A:** 39.0 mg (26.9 µmol, 12 %) of a brownish red solid,

D-Pd(dipy)$_2$-A: 91.0 mg (74.3 µmol, 33 %) of a brownish red solid,

D-Pd(dipy)$_2$: 36.0 mg (36.0 µmol, 16 %) of a brownish red solid.

Pd(dipy)$_2$-A: $C_{86}H_{70}N_8O_8Pd$ [1449.94]

^{1}H-NMR (400 MHz, CD_2Cl_2):

δ [ppm] = 8.91-8.84 (-, 8H), 7.82 (AA', 4H), 7.64 (d, $^3J_{H,H}$ = 8.6 Hz, 2H), 7.55-7.49 (-, 6H), 7.48 (dd, $^3J_{H,H}$ = 1.4 Hz, $^3J_{H,H}$ = 1.4 Hz, 4H), 7.05 (d, $^4J_{H,H}$ = 2.2 Hz, 2H), 6.87 (dd, $^4J_{H,H}$ = 4.3 Hz, $^3J_{H,H}$ = 1.2 Hz, 4H), 6.47 (dd, $^4J_{H,H}$ = 4.4 Hz, $^3J_{H,H}$ = 1.6 Hz, 4H), 1.34 (s, 18H), 1.27 (s, 18H).

^{13}C-NMR (100 MHz, CD_2Cl_2):

δ [ppm] = 164.3 (C), 163.4 (C), 152.4 (CH), 151.0 (C), 146.9 (C), 144.5 (C), 138.5 (C), 137.3 (C), 135.9 (C), 133.0 (C), 131.8 (CH), 131.74 (3 x CH), 131.72 (CH), 129.5 (CH), 128.4 (CH), 128.0 (CH), 127.8 (C), 127.7 (C), 127.6 (C), 127.5 (C), 126.9 (CH), 117.7 (CH), 35.9 (C), 34.6 (C), 31.9 (CH_3), 31.3 (CH_3).

Microanalysis (CHN): calc. for $C_{86}H_{70}N_8O_8Pd$ C-%: 71.24, H-%: 4.87, N-%: 7.73
found for $C_{86}H_{70}N_8O_8Pd$ C-%: 71.01, H-%: 5.02, N-%: 7.39.

ESI-MS (pos., high res.): $[M^{+\bullet}]$ = $C_{86}H_{70}N_8O_8Pd$; calc.: 1448.43719, found: 1448.43308
Δ = 2.84 ppm

D-Pd(dipy)$_2$-A: $C_{72}H_{59}N_7O_6Pd$ [1224.70]

^{1}H-NMR (400 MHz, CD_2Cl_2):

δ [ppm] = 8.90-8.83 (-, 4H), 7.79 (AA', 2H), 7.63 (d, $^3J_{H,H}$ = 8.6 Hz, 1H), 7.52 (dd, $^3J_{H,H}$ = 8.6 Hz, $^4J_{H,H}$ = 2.3 Hz, 4H), 7.49 (BB', 2H), 7.45-7.35 (-, 6H), 7.17 (AA''', 4H), 7.05 (d, $^4J_{H,H}$ = 2.2 Hz, 1H), 6.95 (BB'', 2H), 6.93-6.87 (-, 6H), 6.83 (dd, $^4J_{H,H}$ = 4.3 Hz, $^3J_{H,H}$ = 1.2 Hz, 2H), 6.43 (dd, $^4J_{H,H}$ = 4.3 Hz, $^3J_{H,H}$ = 1.6 Hz, 2H), 6.40 (dd, $^4J_{H,H}$ = 4.3 Hz, $^3J_{H,H}$ = 1.6 Hz, 2H), 3.80 (s, 6H), 1.33 (s, 9H), 1.27 (s, 9H).

^{13}C-NMR (100 MHz, CD_2Cl_2):

δ [ppm] = 164.3 (C),163.4 (C), 157.0 (C), 152.4 (CH), 151.4 (CH), 151.0 (C), 150.2 (C), 149.0 (C), 146.8 (C), 144.5 (C), 140.6 (C), 138.6 (C), 137.6 (C), 137.3 (C), 135.8 (C), 133.0 (C), 132.0 (CH), 131.8 (CH), 131.7 (2 x CH), 131.6 (CH), 131.4 (CH), 129.5 (CH), 128.9 (C), 128.4 (CH), 128.0 (CH), 127.77 (CH), 127.74 (C), 127.70 (C), 127.6 (C), 127.4 (C), 126.9

(CH), 118.0 (CH), 117.6 (CH), 117.0 (CH), 115.2 (CH), 55.8 (CH_3), 35.9 (C), 34.6 (C), 31.9 (CH_3), 31.3 (CH_3).

Microanalysis (CHN): calc. for $C_{72}H_{59}N_7O_6Pd$ C-%: 70.61, H-%: 4.86, N-%: 8.01
found for $C_{72}H_{59}N_7O_6Pd$ C-%: 79.56, H-%: 4.98, N-%: 7.86.

ESI-MS (pos., high res.): $[M^{+\bullet}]$ = $C_{72}H_{59}N_7O_6Pd$; calc.: 1223.35791, found: 1223.36068
Δ = 2.26 ppm

D-Pd(dipy)$_2$: $C_{58}H_{48}N_6O_4Pd$ [999.46]

^{1}H-NMR (400 MHz, CD_2Cl_2):

δ [ppm] = 7.37 (AA', 4H), 7.34 (dd, $^3J_{H,H}$ = 1.5 Hz, $^3J_{H,H}$ = 1.5 Hz, 4H), 7.16 (AA', 8H), 6.93 (BB', 4H), 6.89 (BB', 8H), 6.86 (dd, $^4J_{H,H}$ = 4.3 Hz, $^3J_{H,H}$ = 1.3 Hz, 4H), 6.37 (dd, $^4J_{H,H}$ = 4.4 Hz, $^3J_{H,H}$ = 1.7 Hz, 4H), 3.80 (s, 12H).

^{13}C-NMR (100 MHz, CD_2Cl_2):

δ [ppm] = 157.0 (C), 151.4 (CH), 150.1 (C), 148.9 (C), 140.6 (C), 137.6 (C), 132.1 (CH), 131.3 (CH), 129.0 (C), 127.8 (CH), 118.0 (CH), 116.9 (CH), 115.2 (CH), 55.8 (CH_3).

Microanalysis (CHN): calc. for $C_{58}H_{48}N_6O_4Pd$ C-%: 69.70, H-%: 4.84, N-%: 8.41
found for $C_{58}H_{48}N_6O_4Pd$ C-%: 69.82, H-%: 5.07, N-%: 8.15.

ESI-MS (pos., high res.): $[M^{+\bullet}]$ = $C_{58}H_{48}N_6O_4Pd$; calc.: 998.27859, found: 998.27693
Δ = 1.66 ppm

PdPDM

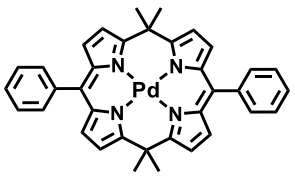

CA: [852244-75-8]

Synthesis following GP VII:

PDM (100 mg, 190 µmol), $Pd(CF_3CO_2)_2$ (96.0 mg, 290 µmol), 10 ml 1,2-dichloroethane/MeOH = 4/1, 90 °C, 1h; flash column chromatography (eluent: PE/DCM = 3/1) and precipitation from DCM into MeOH.

Yield: 52.0 mg (83.0 µmol, 43 %) of a red solid.

$C_{36}H_{30}N_4Pd$ [625.08]

^{1}H-NMR (400 MHz, $CDCl_3$):

δ [ppm] = 7.47-7.37 (-, 10H), 6.49 (d, $^3J_{HH}$ = 4.4 Hz, 4H), 6.38 (d, $^3J_{HH}$ = 4.4 Hz, 4H), 2.00 (s, 12H).

Microanalysis (CHN): calc. for $C_{36}H_{30}N_4Pd$ C-%: 69.17, H-%: 4.84, N-%: 8.96
found for $C_{36}H_{30}N_4Pd$ C-%: 68.92, H-%: 4.66, N-%: 8.74.

ESI-MS (pos., high res.): $[M^{+\bullet}]$ = $C_{36}H_{30}N_4Pd$; calc.: 624.15131, found: 624.15043
Δ = 1.41 ppm

ZnPDM

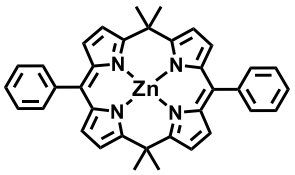

CA: [925430-46-2]

Synthesis following GP VII:

PDM (100 mg, 192 µmol), $Zn(OAc)_2$ x $2H_2O$ (210 mg, 957 µmol), 30 ml $CHCl_3$/MeOH = 1/2, 60 °C, 3d; flash column chromatography (eluent: PE/DCM = 1/1) and precipitation from DCM into MeOH.

Yield: 54.0 mg (92.5 µmol, 48 %) of a red microcrystalline solid.

$C_{36}H_{30}N_4Zn$ [584.05]

^{1}H-NMR (400 MHz, $CDCl_3$):

δ [ppm] = 7.68-7.47 (-, 10H), 6.46 (d, $^3J_{HH}$ = 4.1 Hz, 4H), 6.40 (d, $^3J_{HH}$ = 4.1 Hz, 4H), 1.84 (s, 12H).

^{13}C-NMR (100 MHz, $CDCl_3$):

δ [ppm] = 170.1 (C), 145.9 (C), 142.1 (C), 139.1 (C),132.6 (CH), 131.1 (CH), 128.6 (CH), 127.5 (CH), 114.6 (CH), 38.9 (C), 31.8 (CH_3).

Microanalysis (CHN): calc. for $C_{36}H_{30}N_4Zn$ C-%: 74.03, H-%: 5.18, N-%: 9.59
found for $C_{36}H_{30}N_4Zn$ C-%: 72.80, H-%: 5.38, N-%: 9.62.

During the sample preparation a rise of the mass of the sample was observed, indicating a hygroscopic behaviour of the compound. Thus no accurate microanalysis could be achieved.

ESI-MS (pos., high res.): $[M^{+\bullet}]$ = $C_{36}H_{30}N_4Pd$; calc.: 582.17565, found: 582.17453
Δ = 1.92 ppm

CuPDM

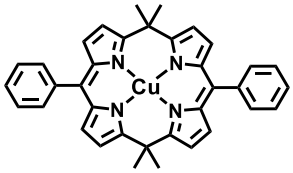

CA: [–]

Synthesis following GP VII:

PDM (100 mg, 192 µmol), $Cu(OAc)_2$ x H_2O (190 mg, 1.05 mmol), 30 ml $CHCl_3$/MeOH = 1/2, rt, 5 min; flash column chromatography (eluent: PE/DCM = 1/1) and precipitation from DCM into MeOH.

Yield: 109 mg (187 µmol, 97 %) of a dark purple, crystalline solid.

$C_{36}H_{30}N_4Cu$ [582.20]

^{1}H-NMR:

No measurement possible due to the paramagnetic character of the Cu(II) central metal ion.

Microanalysis (CHN): calc. for $C_{36}H_{30}N_4Cu$ C-%: 74.27, H-%: 5.19, N-%: 9.62

found for $C_{36}H_{30}N_4Cu$ C-%: 74.02, H-%: 5.41, N-%: 9.66.

ESI-MS (pos., high res.): $[M^{+\bullet}]$ = $C_{36}H_{30}N_4Cu$; calc.: 581.17610, found: 581.17455

Δ = 2.67 ppm

NiPDM

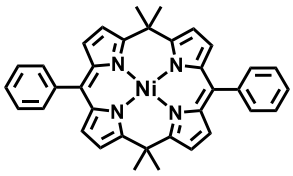

CA: [–]

Synthesis following GP VII:

PDM (100 mg, 192 µmol), $Ni(OAc)_2$*$2H_2O$ (239 mg, 960 µmol), 25 ml THF/MeOH = 4/1, 110 °C, 3d; flash column chromatography (eluent: PE/DCM = 1/1) and precipitation from DCM into MeOH.

Yield: 30.0 mg (52.0 µmol, 27 %) of a dark purple, crystalline solid.

$C_{36}H_{30}N_4Ni$ [577.35]

^{1}H-NMR (400 MHz, CD_2Cl_2):

δ [ppm] = 7.68-7.24 (-, 10H), 6.37 (d, $^3J_{HH}$ = 4.3 Hz, 4H), 6.16 (d, $^3J_{HH}$ = 4.3 Hz, 4H), 2.72 (s, 6H), 1.62 (s, 6H).

Microanalysis (CHN): calc. for $C_{36}H_{30}N_4Ni$ C-%: 74.89, H-%: 5.24, N-%: 10.17
found for $C_{36}H_{30}N_4Ni$ C-%: 73.07, H-%: 5.36, N-%: 9.81.

During the sample preparation a rise of the mass of the sample was observed, indicating a hygroscopic behaviour of the compound. Thus no accurate microanalysis could be achieved.

ESI-MS (pos., high res.): $[M^{+\bullet}]$ = $C_{36}H_{30}N_4Ni$; calc.: 576.18185, found: 576.18113
Δ = 1.25 ppm

D-PDM-A

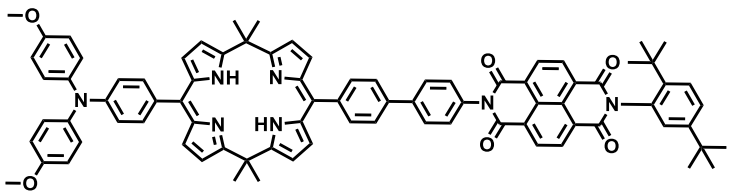

CA: [–]

Synthesis following GP V:

31 (50.0 mg, 76.2 µmol), **32** (63.0 mg, 76.2 µmol), $Pd(PPh_3)_4$ (3.52 mg, 3.05 µmol), 1M $Na_2CO_{3(aq)}$ / THF = 1/10 (5 ml), 110 °C, 72 h; flash chromatography (eluent: PE/DCM/TEA = 80/20/1 → 60/40/1, GPC and precipitation from DCM into MeOH and again from DCM into hexane.

Yield: 40.0 mg (31.3 µmol, 41 %) of a red solid.

$C_{84}H_{73}N_7O_6$ [1276.53]

^{1}H-NMR (400 MHz, CD_2Cl_2):

δ [ppm] = 14.30 (s, 1H), 14.26 (s, 1H), 8.88-8.81 (-, 4H), 7.87 (AA', 2H), 7.74 (AA', 2H), 7.63 (d, $^3J_{H,H}$ = 8.6 Hz, 1H), 7.57 (BB', 2H), 7.52 (dd, $^3J_{H,H}$ = 8.6 Hz, $^4J_{H,H}$ = 2.3 Hz, 1H), 7.45 (BB', 2H), 7.25 (AA', 2H), 7.13 (AA', 4H), 7.04 (d, $^4J_{H,H}$ = 2.2 Hz, 1H), 6.90-6.83 (- , 6H), 6.50 (dd, $^3J_{H,H}$ = 4.2 Hz, $^4J_{H,H}$ = 0.6 Hz, 2H), 6.43 (dd, $^3J_{H,H}$ = 4.1 Hz, $^4J_{H,H}$ = 0.6 Hz, 2H), 6.32-6.27 (-, 4H), 3.78 (s, 6H), 1.95 (s, 12H), 1.33 (s, 9H), 1.26 (s, 9H).

^{13}C-NMR (100 MHz, CD_2Cl_2):

δ [ppm] = 166.0 (C), 164.9 (C), 164.3 (C), 163.5 (C), 157.0 (C), 151.0 (C), 150.2 (C), 144.5 (C), 141.7 (C), 141.4 (C), 140.9 (C), 140.62 (C), 140.60 (C), 140.5 (C), 140.2 (C), 136.9 (C), 134.8 (C), 133.0 (C), 132.5 (CH), 131.8 (CH), 131.71 (CH), 131.70 (CH), 129.5 (CH), 129.4 (CH), 128.5 (2 x CH), 128.4 (C), 128.0 (CH), 127.8 (2 x CH), 127.75 (C), 127.72

(C), 127.6 (C), 127.5 (C), 126.90 (CH), 126.87 (CH), 118.0 (CH), 115.2 (CH), 114.7 (CH), 114.3 (CH), 55.8 (CH_3), 38.6 (C), 35.9 (C), 34.6 (C), 31.8 (CH_3), 31.3 (CH_3).

The missing CH_3-signal corresponds to the primary C-atom at the 5- and 15- position of the PDM-unit. The C-atom could be confirmed by measurement of a HSQC – ETGP spectrum of **D-PdPDM-A**, which shows a clear coupling of the CH_3-H-atoms to the seemingly missing peak of the primary C-atom in the region around 31.8 ppm. For reasons of time and economy these measurements were not performed for this compound but are assumed to be transferable because the CH_3-group in question is confirmed by ^{1}H-NMR- spectroscopy and mass spectrometry.

ESI-MS (pos., high res.): $[M^{+\bullet}]$ = $C_{84}H_{73}N_7O_6$; calc.: 1275.56169, found: 1275.56076
Δ = 0.73 ppm

D-PdPDM-A

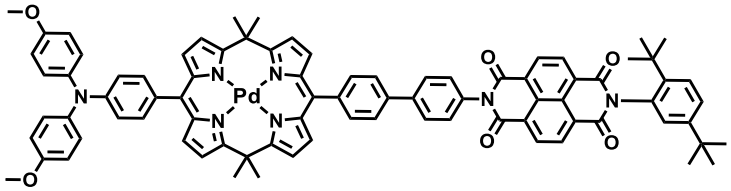

CA: [–]

Synthesis following GP V:

31 (50.0 mg, 76.0 µmol), **Pd-32** (63.0 mg, 76.0 µmol), $Pd(PPh_3)_4$ (3.52 mg, 3.05 µmol), 1M $Na_2CO_{3(aq)}$ / THF = 1/10 (5 ml), 110°C, 72 h; flash chromatography (eluent: PE/DCM/TEA = 80/20/1 → 60/40/1, GPC and precipitation from DCM into MeOH and again from DCM into hexane.

Yield: 24.0 mg (17.0 µmol, 54 %) of a red solid.

$C_{84}H_{71}N_7O_6Pd$ [1380.96]

^{1}H-NMR (600 MHz, CD_2Cl_2):

δ [ppm] = 8.87-8.82 (-, 4H), 7.88 (AA', 2H), 7.75 (AA', 2H), 7.63 (d, $^3J_{H,H}$ = 8.4 Hz, 1H), 7.56 (BB', 2H), 7.52 (dd, $^3J_{H,H}$ = 8.6 Hz, $^4J_{H,H}$ = 2.3 Hz, 1H), 7.46 (BB', 2H), 7.23 (AA', 2H), 7.13 (AA', 4H), 7.04 (d, $^4J_{H,H}$ = 2.2 Hz, 1H), 6.90-6.85 (- , 6H), 6.67 (d, $^3J_{H,H}$ = 4.3 Hz, 2H), 6.59 (d, $^3J_{H,H}$ = 4.3 Hz, 2H), 6.45-6.40 (-, 4H), 3.78 (s, 6H), 1.94 (s, 12H), 1.33 (s, 9H), 1.26 (s, 9H).

^{13}C-NMR (150 MHz, CPDCH 13C, CD_2Cl_2):

δ [ppm] = 164.7 (C), 164.3 (C), 163.8 (C), 163.5 (C), 156.9 (C), 151.0 (C), 149.9 (C), 146.5 (C), 145.2 (C), 144.6 (C), 141.8 (C), 140.70 (C), 140.66 (C), 137.5 (C), 135.4 (C), 135.2 (C),

134.8 (C), 133.0 (C), 132.1 (CH), 131.72 (CH), 131.70 (CH), 131.55 (CH), 131.48 (CH), 131.45 (CH), 129.5 (CH), 129.4 (CH), 129.1 (C), 128.6 (CH), 128.0 (CH), 127.8 (C), 127.72 (C), 127.67 (CH), 127.6 (C), 127.5 (C), 126.9 (CH), 126.7 (CH), 118.0 (CH), 115.1 (CH), 114.5 (CH), 114.1 (CH), 55.8 (CH_3), 40.8 (C), 35.9 (C), 34.6 (C), 31.8 (CH_3), 31.3 (CH_3).

The missing CH_3-signal corresponds to the primary C-atom at the 5- and 15- position of the PDM-unit. The signal is assumed to be very broad and to overlap with the primary signals at 31.8 ppm. This assumption could be confirmed by measurement of a HSQC – ETGP spectrum, which shows a clear coupling-signal of the CH_3-H-atoms to the seemingly missing peak of the primary C-atom in the aforementioned region.

Microanalysis (CHN): calc. for $C_{84}H_{71}N_7O_6Pd$ C-%: 73.06, H-%: 5.18, N-%: 7.10
found for $C_{84}H_{71}N_7O_6Pd$ C-%: 72.87, H-%: 5.32, N-%: 7.23.

ESI-MS (pos., high res.): $[M^{+\bullet}]$ = $C_{84}H_{71}N_7O_6Pd$; calc.: 1379.45208, found: 1379.44983
Δ = 1.63 ppm

PdPDM-A

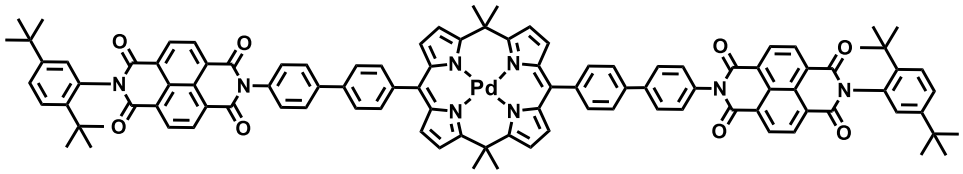

CA: [–]

Synthesis following GP V:

31 (88.0 mg, 134 µmol), **Pd-28** (50.0 mg, 63.9 µmol), $Pd(PPh_3)_4$ (2.95 mg, 2.55 µmol), 1M $Na_2CO_{3(aq)}$ / THF = 1/10 (10 ml), 95 °C, 72 h; flash chromatography (eluent: DCM → DCM/MeOH = 100/1, GPC and precipitation from DCM into MeOH and again from DCM into hexane.

Yield: 26.8 mg (15.9 µmol, 26 %) of a red solid.

$C_{104}H_{86}N_8O_8Pd$ [1682.26]

^{1}H-NMR (400 MHz, CD_2Cl_2):

δ [ppm] = 8.90-8.80 (-, 8H), 7.90 (AA', 4H), 7.78 (AA', 4H), 7.63 (d, $^3J_{H,H}$ = 8.6 Hz, 2H), 7.59 (BB', 4H), 7.52 (dd, $^3J_{H,H}$ = 8.6 Hz, $^4J_{H,H}$ = 2.2 Hz, 2H), 7.47 (BB', 4H), 7.05 (d, $^4J_{H,H}$ = 2.2 Hz, 2H), 6.62 (d, $^3J_{H,H}$ = 4.4 Hz, 4H), 6.46 (d, $^3J_{H,H}$ = 4.4 Hz, 4H), 1.97 (s, 12H), 1.33 (s, 18H), 1.26 (s, 18H).

^{13}C-NMR (100 MHz, CD_2Cl_2):

δ [ppm] = 164.6 (C), 164.3 (C), 163.5 (C), 151.0 (C), 145.3 (C), 144.6 (C), 141.8 (C), 140.7 (C), 137.4 (C), 135.2 (C), 134.9 (C), 133.0 (C), 131.73 (CH), 131.71 (CH) 131.6 (2 x CH), 129.53 (CH), 129.45 (CH), 128.6 (CH), 128.0 (CH), 127.8 (C), 127.7 (C), 127.6 (C), 127.5 (C), 126.9 (CH), 126.7 (CH), 114.6 (CH), 40.9 (C), 35.9 (C), 34.6 (C), 31.9 (CH_3), 31.3 (CH_3).

The missing CH_3-signal corresponds to the primary C-atom at the 5- and 15- position of the PDM-unit. The C-atom could be confirmed by measurement of a HSQC – ETGP spectrum of **D-PdPDM-A**, which showed a clear coupling of the CH_3-H-atoms to the seemingly missing peak of the primary C-atom in the region around 31.8 ppm. For reasons of time and economy these measurements were not performed for this compound but are assumed to be transferable because the CH_3-group in question is confirmed by ^{1}H-NMR- spectroscopy and mass spectrometry.

Microanalysis (CHN): calc. for $C_{104}H_{86}N_8O_8Pd$ C-%: 74.25, H-%: 5.15, N-%: 6.66
found for $C_{104}H_{86}N_8O_8Pd$ C-%: 74.34, H-%: 5.36, N-%: 6.41.

ESI-MS (pos., high res.): $[M^{+\bullet}]$ $C_{104}H_{86}N_8O_8Pd$; calc.: 1680.56275, found: 1680.55893
Δ = 2.27 ppm

D_{Ph}-PDM-A

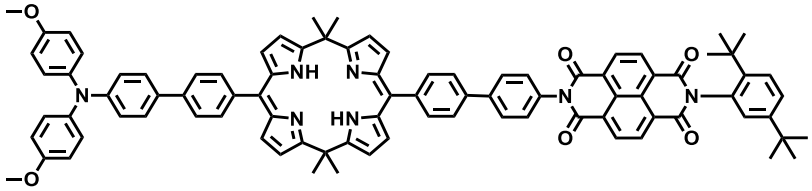

CA: [–]

Synthesis following GP V:

31 (50.0 mg, 76.2 µmol), **33** (57.3 mg, 63.5 µmol), $Pd(PPh_3)_4$ (3.67 mg, 3.18 µmol), 1M $Na_2CO_{3(aq)}$ / THF = 1/10 (10 ml), 110 °C, 72 h; flash chromatography (eluent: PE/DCM/TEA = 80/20/1 → 40/60/1, GPC and precipitation from DCM into MeOH and again from DCM into hexane.

Yield: 33.0 mg (24.4 µmol, 38 %) of a red solid.

$C_{90}H_{77}N_7O_6$ [1352.62]

^{1}H-NMR (400 MHz, CD_2Cl_2):

δ [ppm] = 14.28 (s, 2H), 8.88-8.81 (-, 4H), 7.87 (AA', 2H), 7.75 (AA', 2H), 7.63 (d, $^3J_{H,H}$ = 8.6 Hz, 1H), 7.61-7.55 (-, 4H), 7.52 (dd, $^3J_{H,H}$ = 8.6 Hz, $^4J_{H,H}$ = 2.2 Hz, 1H), 7.50-7.43 (-, 6H), 7.08

(AA', 4H), 7.04 (d, $^4J_{H,H}$ = 2.2 Hz, 1H), 6.96 (BB', 2H), 6.85 (BB', 4H), 6.46-6.40 (-, 4H), 6.34-6.27 (-, 4H), 3.78 (s, 6H), 1.97 (s, 12H), 1.33 (s, 9H), 1.26 (s, 9H).

^{13}C-NMR (100 MHz, CD_2Cl_2):

δ [ppm] = 164.6 (C), 164.4 (C), 164.3 (C), 163.5 (C), 156.6 (C), 151.0 (C), 149.0 (C), 145.8 (C), 145.3 (C), 144.6 (C), 141.8 (C), 141.4 (C), 141.0 (C), 140.7 (C), 137.4 (C), 136.0 (C), 135.3 (C), 135.2 (C), 134.8 (C), 133.0 (C), 132.2 (C), 131.72 (CH), 131.71 (CH), 131.6 (2 x CH), 131.5 (CH), 129.52 (CH), 129.46 (CH), 128.6 (CH), 128.0 (CH), 127.82 (CH), 127.75 (C), 127.7 (C), 127.6 (C), 127.5 (C), 127.2 (2 x CH), 126.9 (CH), 126.7 (CH), 125.5 (CH), 120.6 (CH), 115.1 (CH), 114.6 (CH), 114.5 (CH), 55.8 (CH_3), 40.9 (C), 35.9 (C), 34.6 (C), 31.9 (CH_3), 31.3 (CH_3).

The missing CH_3-signal corresponds to the primary C-atom at the 5- and 15- position of the PDM-unit. The C-atom could be confirmed by measurement of a HSQC – ETGP spectrum of **D-PdPDM-A**, which showed a clear coupling of the CH_3-H-atoms to the seemingly missing peak of the primary C-atom in the region around 31.8 ppm. For reasons of time and economy these measurements were not performed for this compound but are assumed to be transferable because the CH_3-group in question is confirmed by ^{1}H-NMR- spectroscopy and mass spectrometry.

ESI-MS (pos., high res.): $[M^{+\bullet}]$ = $C_{90}H_{77}N_7O_6$; calc.: 1352.596201, found 1352.59428

Δ = 1.42 ppm

D_{Ph}-PdPDM-A

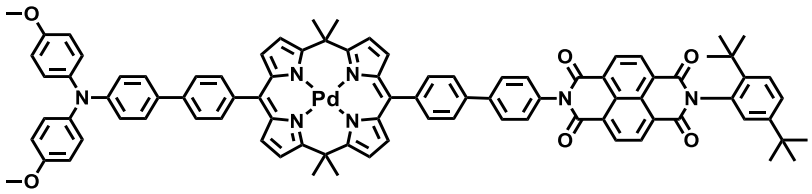

CA: [–]

Synthesis following GP V:

31 (39.1 mg, 59.6 µmol), **Pd-33** (49.6 mg, 50.0 µmol), $Pd(PPh_3)_4$ (4.59 mg, 3.97 µmol), 1M $Na_2CO_{3(aq)}$ / THF = 1/10 (5 ml), 95 °C, 72 h; flash chromatography (eluent: PE/DCM/TEA = 80/20/1 → 60/40/1, GPC and precipitation from DCM into MeOH and again from DCM into hexane.

Yield: 24.0 mg (16.5 µmol, 33 %) of a red solid.

$C_{90}H_{75}N_7O_6Pd$ [1457.02]

^{1}H-NMR (400 MHz, CD_2Cl_2):

δ [ppm] = 8.88-8.82 (-, 4H), 7.89 (AA', 2H), 7.76 (AA', 2H), 7.63 (d, $^{3}J_{H,H}$ = 8.6 Hz, 1H), 7.61 (AA', 2H), 7.58 (BB', 2H), 7.52 (dd, $^{3}J_{H,H}$ = 8.6 Hz, $^{4}J_{H,H}$ = 2.2 Hz, 1H), 7.51-7.44 (-, 6H), 7.09 (AA', 4H), 7.04 (d, $^{4}J_{H,H}$ = 2.2 Hz, 1H), 6.97 (BB', 2H), 6.86 (BB' , 4H), 6.60 (d, $^{3}J_{H,H}$ = 4.4 Hz, 2H), 6.58 (d, $^{3}J_{H,H}$ = 4.4 Hz, 2H), 6.44 (d, $^{3}J_{H,H}$ = 4.4 Hz, 2H), 6.43 (d, $^{3}J_{H,H}$ = 4.4 Hz, 2H), 3.79 (s, 6H), 1.95 (s, 12H), 1.33 (s, 9H), 1.26 (s, 9H).

^{13}C-NMR (100 MHz, CD_2Cl_2):

δ [ppm] = 164.6 (C), 164.4 (C), 164.3 (C), 163.5 (C), 156.6 (C), 151.0 (C), 149.0 (C), 145.8 (C), 145.3 (C), 144.6 (C), 141.8 (C), 141.4 (C), 141.0 (C), 140.7 (C), 137.4 (C), 136.0 (C), 135.3 (C), 135.2 (C), 134.8 (C), 133.0 (C), 132.2 (C), 131.72 (CH), 131.71 (CH), 131.6 (CH), 131.56 (CH), 131.55 (CH), 131.54 (CH), 129.51 (CH), 129.45 (CH), 128.6 (CH), 128.0 (CH), 127.8 (CH), 127.75 (C), 127.72 (C), 127.6 (C), 127.5 (C), 127.2 (CH), 126.9 (CH), 126.7 (CH), 125.5 (CH), 120.6 (CH), 115.1 (CH), 114.6 (CH), 114.5 (CH), 55.8 (CH_3), 40.9 (C), 35.9 (C), 34.6 (C), 31.9 (CH_3), 31.3 (CH_3).

The missing CH_3-signal corresponds to the primary C-atom at the 5- and 15- position of the PDM-unit. The C-atom could be confirmed by measurement of a HSQC – ETGP spectrum of **D-PdPDM-A**, which showed a clear coupling of the CH_3-H-atoms to the seemingly missing peak of the primary C-atom in the region around 31.8 ppm. For reasons of time and economy these measurements were not performed for this compound but are assumed to be transferable because the CH_3-group in question is confirmed by ^{1}H-NMR- spectroscopy and mass spectrometry.

Microanalysis (CHN): calc. for $C_{90}H_{75}N_7O_6Pd$ C-%: 74.19, H-%: 5.19, N-%: 6.73
found for $C_{90}H_{75}N_7O_6Pd$ C-%: 73.98, H-%: 5.06, N-%: 6.84.

ESI-MS (pos., high res.): $[M^{+\bullet}]$ = $C_{90}H_{75}N_7O_6Pd$; calc.: 1455.48350, found: 1455.48773
Δ = 2.91 ppm

7 Literature

[1] W. Wiltschko, F. W. Merkel, *Verh. Dtsch. Zool. Ges.* **1966**, *59*, 362-367.

[2] W. Wiltschko, *Z. Tierpsychol.* **1968**, *25*, 537-558.

[3] W. Wiltschko, R. Wiltschko, *Science* **1972**, *176*, 62-64.

[4] W. Wiltschko, R. Wiltschko, *J. Exp. Biol* **1996**, *199*, 29-38.

[5] K. J. Lohmann, C. M. F. Lohmann, *Nature* **1996**, *380*, 59.

[6] M. E. Deutschlander, S. C. Borland, J. B. Phillips, *Nature* **1999**, *400*, 324.

[7] M. M. Walker, C. E. Diebel, C. V. Haugh, P. M. Pankhurst, J. C. Montgomery, C. R. Green, *Nature* **1997**, *390*, 371.

[8] J. B. Phillips, O. Sayeed, *J. Comp. Physiol. A* **1993**, *172*, 303-308.

[9] S. D. Cain, L. C. Boles, J. H. Wang, K. J. Lohmann, *Integr. Comp. Bioly* **2005**, *45*, 539-546.

[10] S. Marhold, W. Wiltschko, H. Burda, *Naturwissenschaften* **1997**, *84*, 421-423.

[11] D. Presti, J. D. Pettigrew, *Nature* **1980**, *285*, 99.

[12] J. L. Kirschvink, J. L. Gould, *Biosystems* **1981**, *13*, 181-201.

[13] T. Ritz, S. Adem, K. Schulten, *Biophys. J.* **2000**, *78*, 707-718.

[14] K. Schulten, E. Swenberg Charles, A. Weller, in *Z. Phys. Chem., Vol. 111*, **1978**, p. 1.

[15] K. Schulten, in *Festkörperprobleme 22: Plenary Lectures of the 46th Annual Meeting of the German Physical Society (DPG) and of the Divisions "Semiconductor Physics" "Metal Physics" "Low Temperature Physics" "Thermodynamics and Statistical Physics" "Thin Films" "Surface Physics" "Magnetism" Münster, March 29–April 2, 1982* (Ed.: P. Grosse Aachen), Springer Berlin Heidelberg, Berlin, Heidelberg, **1982**, pp. 61-83.

[16] S. Johnsen, K. J. Lohmann, *Nat. Rev. Neurosci.* **2005**, *6*, 703.

[17] K. Maeda, A. J. Robinson, K. B. Henbest, H. J. Hogben, T. Biskup, M. Ahmad, E. Schleicher, S. Weber, C. R. Timmel, P. J. Hore, *Proc. Natl. Acad. Sci. U.S.A.* **2012**, *109*, 4774-4779.

[18] E. W. Evans, C. A. Dodson, K. Maeda, T. Biskup, C. J. Wedge, C. R. Timmel, *Interface Focus* **2013**, *3*.

[19] K. Maeda, K. B. Henbest, F. Cintolesi, I. Kuprov, C. T. Rodgers, P. A. Liddell, D. Gust, C. R. Timmel, P. J. Hore, *Nature* **2008**, *453*, 387.

[20] C. T. Rodgers, P. J. Hore, *Proc. Natl. Acad. Sci. U.S.A.* **2009**, *106*, 353-360.

[21] R. Kaptein, L. J. Oosterhoff, *Chem. Phys. Lett.* **1969**, *4*, 214-216.

[22] P. W. Atkins, A. J. Dobbs, G. T. Evans, K. A. McLauchlan, P. W. Percival, *Mol. Phys.* **1974**, *27*, 769-777.

[23] Y. Tanimoto, M. Takashima, K. Hasegawa, M. Itoh, *Chem. Phys. Lett.* **1987**, *137*, 330-335.

[24] H. Hayashi, *Introduction to Dynamic Spin Chemistry, Vol. 8*, World Scientific Publishing, Singapore, **2004**.

[25] H. Hayashi, S. Nagakura, *Bull. Chem. Soc. Jpn.* **1984**, *57*, 322-328.

[26] J. Q. Wu, D. Baumann, U. E. Steiner, *Mol. Phys.* **1995**, *84*, 981-994.

[27] U. E. Steiner, T. Ulrich, *Chem. Rev.* **1989**, *89*, 51-147.

[28] P. P. Levin, V. A. Kuzmin, *Chem. Phys.* **1992**, *162*, 79-93.

[29] Y. Liu, R. Edge, K. Henbest, C. R. Timmel, P. J. Hore, P. Gast, *Chem. Commun.* **2005**, 174-176.

[30] W. Schlenker, T. Ulrich, U. E. Steiner, *Chem. Phys. Lett.* **1983**, *103*, 118-123.

[31] M. B. Smith, J. Michl, *Chem. Rev.* **2010**, *110*, 6891-6936.

[32] T. Klumpp, M. Linsenmann, S. L. Larson, B. R. Limoges, D. Burssner, E. B. Krissinel, C. M. Elliott, U. E. Steiner, *J. Am. Chem. Soc.* **1999**, *121*, 1076-1087.

[33] U. Werner, Y. Sakaguchi, H. Hayashi, G. Nohya, R. Yoneshima, S. Nakajima, A. Osuka, *J. Phys. Chem.* **1995**, *99*, 13930-13937.

[34] P. Gilch, F. Pollinger-Dammer, C. Musewald, M. E. Michel-Beyerle, U. E. Steiner, *Science* **1998**, *281*, 982-984.

[35] M. T. Rawls, G. Kollmannsberger, C. M. Elliott, U. E. Steiner, *J. Phys. Chem. A* **2007**, *111*, 3485-3496.

[36] E. A. Weiss, E. T. Chernick, M. R. Wasielewski, *J. Am. Chem. Soc.* **2004**, *126*, 2326-2327.

[37] M. R. Wasielewski, *J. Org. Chem.* **2006**, *71*, 5051-5066.

[38] A. M. Lewis, D. E. Manolopoulos, P. J. Hore, *J. Chem. Phys.* **2014**, *141*, 044111.

[39] M. T. Colvin, A. B. Ricks, A. M. Scott, A. L. Smeigh, R. Carmieli, T. Miura, M. R. Wasielewski, *J. Am. Chem. Soc.* **2011**, *133*, 1240-1243.

[40] E. A. Weiss, M. J. Tauber, M. A. Ratner, M. R. Wasielewski, *J. Am. Chem. Soc.* **2005**, *127*, 6052-6061.

[41] H. Hayashi, S. Nagakura, *Bull. Chem. Soc. Jpn.* **1978**, *51*, 2862-2866.

[42] P. Desai, P. Shakya, T. Kreouzis, W. P. Gillin, *J. Appl. Phys.* **2007**, *102*, 073710.

[43] Y. Goto, T. Noguchi, U. Takeuchi, K. Hatabayashi, Y. Hirose, T. Uchida, T. Sasaki, T. Hasegawa, T. Shimada, *Organic Electronics* **2010**, *11*, 1212-1216.

[44] P. J. Jadhav, A. Mohanty, J. Sussman, J. Lee, M. A. Baldo, *Nano Lett.* **2011**, *11*, 1495-1498.

[45] M. B. Smith, J. Michl, in *Annual Review of Physical Chemistry, Vol 64, Vol. 64* (Eds.: M. A. Johnson, T. J. Martinez), Annual Reviews, Palo Alto, **2013**, pp. 361-386.

[46] B. Brocklehurst, *Chem. Soc. Rev.* **2002**, *31*, 301-311.

[47] H. R. Ward, *Acc. Chem. Res.* **1972**, *5*, 18-24.

[48] J. R. Woodward, *Prog. React. Kinet. Mech.* **2002**, *27*, 165-207.

[49] K. A. McLauchlan, U. E. Steiner, *Mol. Phys.* **1991**, *73*, 241-263.

[50] J. W. Verhoeven, *J. Photochem. Photobiol., C* **2006**, *7*, 40-60.

[51] A. M. Scott, T. Miura, A. B. Ricks, Z. E. X. Dance, E. M. Giacobbe, M. T. Colvin, M. R. Wasielewski, *J. Am. Chem. Soc.* **2009**, *131*, 17655-17666.

[52] E. A. Weiss, M. J. Ahrens, L. E. Sinks, M. A. Ratner, M. R. Wasielewski, *J. Am. Chem. Soc.* **2004**, *126*, 9510-9511.

[53] A. M. Scott, A. Butler Ricks, M. T. Colvin, M. R. Wasielewski, *Angew. Chem.* **2010**, *49*, 2904-2908.

[54] K. Schulten, P. G. Wolynes, *J. Chem. Phys.* **1978**, *68*, 3292-3297.

[55] E. W. Knapp, K. Schulten, *J. Chem. Phys.* **1979**, *71*, 1878-1883.

[56] K. Schulten, *J. Chem. Phys.* **1985**, *82*, 1312-1316.

[57] K. A. McLauchlan, U. E. Steiner, *Mol. Phys.* **1991**, *73*, 241-263.

[58] B. Brocklehurst, K. A. McLauchlan, *Int. J. Radiat. Biol.* **1996**, *69*, 3-24.

[59] J. H. Klein, D. Schmidt, U. E. Steiner, C. Lambert, *J. Am. Chem. Soc.* **2015**, *137*, 11011-11021.

[60] A. Weller, F. Nolting, H. Staerk, *Chem. Phys. Lett.* **1983**, *96*, 24-27.

[61] J. Schäfer, M. Holzapfel, A. Schmiedel, U. E. Steiner, C. Lambert, *Phys. Chem. Chem. Phys.* **2018**.

[62] U. E. Steiner, J. Schäfer, N. N. Lukzen, C. Lambert, *J. Phys. Chem. C* **2018**, *122*, 11701-11708.

[63] J. R. Biller, H. Elajaili, V. Meyer, G. M. Rosen, S. S. Eaton, G. R. Eaton, *J. Magn. Reson.* **2013**, *236*, 47-56.

[64] P. J. Hore, in *Advanced EPR* (Ed.: A. J. Hoff), Elsevier, Amsterdam, **1989**, pp. 405-440.

[65] E. Terreno, D. D. Castelli, A. Viale, S. Aime, *Chem. Rev.* **2010**, *110*, 3019-3042.

[66] R. W. Darbeau, *Appl. Spectrosc. Rev.* **2006**, *41*, 401-425.

[67] K. A. Hötzer, A. Klingert, T. Klumpp, E. Krissinel, D. Bürssner, U. E. Steiner, *J. Phys. Chem. A* **2002**, *106*, 2207-2217.

[68] K. Lüders, K. M. Salikhov, *Chem. Phys.* **1987**, *117*, 113-131.

[69] L. Banci, I. Bertini, C. Luchinat, *Nuclear and electron relaxation: the magnetic nucleus-unpaired electron coupling in solution*, VCH, **1991**.

[70] J. H. Klein, PhD thesis, Julius-Maximilians-Universität Würzburg (Würzburg), **2015**.

[71] U. E. Steiner, J. Q. Wu, *Chem. Phys.* **1992**, *162*, 53-67.

[72] S. V. Isakov, N. N. Lukzen, V. A. Morozov, R. Z. Sagdeev, *Chem. Phys.* **1995**, *199*, 119-127.

[73] P. W. Atkins, D. Kivelson, *J. Chem. Phys.* **1966**, *44*, 169-174.

[74] Y. A. Serebrennikov, U. E. Steiner, *J. Chem. Phys.* **1994**, *100*, 7508-7514.

[75] U. E. Steiner, H. J. Wolff, in *Photochemistry and Photophysics, Vol. IV* (Eds.: J. F. Rabek, G. W. Scott), CRC Press, Boca Raton, FL, **1991**, pp. 1-130.

[76] U. Werner, Y. Sakaguchi, H. Hayashi, G. Nohya, R. Yoneshima, S. Nakajima, A. Osuka, *J. Phys. Chem.* **1995**, *99*, 13930-13937.

[77] G. L. Closs, *J. Am. Chem. Soc.* **1969**, *91*, 4552-4554.

[78] H. Hisaharu, I. Koichi, N. Saburo, *Bull. Chem. Soc. Jpn.* **1966**, *39*, 199-199.

[79] N. N. Lukzen, J. H. Klein, C. Lambert, U. E. Steiner, *Z. Phys. Chem.* **2017**, *231*, 197-223.

[80] S. R. T. Neil, J. Li, D. M. W. Sheppard, J. Storey, K. Maeda, K. B. Henbest, P. J. Hore, C. R. Timmel, S. R. Mackenzie, *J. Phys. Chem. B* **2014**, *118*, 4177-4184.

[81] T. Miura, D. Fujiwara, K. Akiyama, T. Horikoshi, S. Suzuki, M. Kozaki, K. Okada, T. Ikoma, *J. Phys. Chem. Lett.* **2017**, *8*, 661-665.

[82] L. Flamigni, E. Baranoff, J. P. Collin, J. P. Sauvage, *Chem.-Eur. J.* **2006**, *12*, 6592-6606.

[83] E. Baranoff, J.-P. Collin, L. Flamigni, J.-P. Sauvage, *Chem. Soc. Rev.* **2004**, *33*, 147-155.

[84] G. Kodis, P. A. Liddell, A. L. Moore, T. A. Moore, D. Gust, *J. Phys. Org. Chem.* **2004**, *17*, 724-734.

[85] R. T. Hayes, M. R. Wasielewski, D. Gosztola, *J. Am. Chem. Soc.* **2000**, *122*, 5563-5567.

[86] J. Hankache, M. Niemi, H. Lemmetyinen, O. S. Wenger, *Inorg. Chem.* **2012**, *51*, 6333-6344.

[87] S. Suzuki, R. Sugimura, M. Kozaki, K. Keyaki, K. Nozaki, N. Ikeda, K. Akiyama, K. Okada, *J. Am. Chem. Soc.* **2009**, *131*, 10374-10375.

[88] M. Kuss-Petermann, O. S. Wenger, *J. Am. Chem. Soc.* **2016**, *138*, 1349-1358.

[89] O. Yushchenko, R. V. Hangarge, S. Mosquera-Vazquez, S. V. Boshale, E. Vauthey, *J. Phys. Chem. B* **2015**, *119*, 7308-7320.

[90] J. P. Sauvage, J. P. Collin, J. C. Chambron, S. Guillerez, C. Coudret, V. Balzani, F. Barigelletti, L. Decola, L. Flamigni, *Chem. Rev.* **1994**, *94*, 993-1019.

[91] R. A. Marcus, *J. Chem. Phys.* **1956**, *24*, 966-978.

[92] R. A. Marcus, *J. Chem. Phys.* **1965**, *43*, 679-&.

[93] A. Heckmann, C. Lambert, *Angew. Chem., Int. Ed.* **2012**, *51*, 326-392.

[94] P. Chen, T. J. Meyer, *Chem. Rev.* **1998**, *98*, 1439-1478.

[95] J. Stubbe, D. G. Nocera, C. S. Yee, M. C. Y. Chang, *Chem. Rev.* **2003**, *103*, 2167-2202.

[96] B. Albinsson, J. Mårtensson, *J. Photochem. Photobiol., C* **2008**, *9*, 138-155.

[97] V. Balzani, G. Bergamini, S. Campagna, F. Puntoriero, in *Photochemistry and Photophysics of Coordination Compounds I* (Eds.: V. Balzani, S. Campagna), Springer Berlin Heidelberg, Berlin, Heidelberg, **2007**, pp. 1-36.

[98] A. Rosspeintner, E. Vauthey, *Phys. Chem. Chem. Phys.* **2014**, *16*, 25741-25754.

[99] R. Carlo Andrea, T. Filippo, T. Ivano, *J. Phys.: Condens. Matter* **2018**, *30*, 013002.

[100] J. Schäfer, M. Holzapfel, B. Mladenova, D. Kattnig, I. Krummenacher, H. Braunschweig, G. Grampp, C. Lambert, *J. Am. Chem. Soc.* **2017**, *139*, 6200-6209.

[101] C. Lambert, M. Moos, A. Schmiedel, M. Holzapfel, J. Schäfer, M. Kess, V. Engel, *Phys. Chem. Chem. Phys.* **2016**, *18*, 19405-19411.

[102] O. S. Wenger, *Coord. Chem. Rev.* **2009**, *253*, 1439-1457.

[103] J. W. Verhoeven, H. J. van Ramesdonk, M. M. Groeneveld, A. C. Benniston, A. Harriman, *ChemPhysChem* **2005**, *6*, 2251-2260.

[104] R. Carmieli, Q. Mi, A. B. Ricks, E. M. Giacobbe, S. M. Mickley, M. R. Wasielewski, *J. Am. Chem. Soc.* **2009**, *131*, 8372-8373.

[105] F. D. Lewis, T. F. Wu, Y. F. Zhang, R. L. Letsinger, S. R. Greenfield, M. R. Wasielewski, *Science* **1997**, *277*, 673-676.

[106] S. E. Miller, A. S. Lukas, E. Marsh, P. Bushard, M. R. Wasielewski, *J. Am. Chem. Soc.* **2000**, *122*, 7802-7810.

[107] M. R. Wasielewski, *Chem. Rev.* **1992**, *92*, 435-461.

[108] M. Kuss-Petermann, O. S. Wenger, *Angew. Chem.* **2015**, *55*, 815-819.

[109] L. Flamigni, E. Baranoff, J.-P. Collin, J.-P. Sauvage, B. Ventura, *ChemPhysChem* **2007**, *8*, 1943-1949.

[110] S. Campagna, F. Puntoriero, F. Nastasi, G. Bergamini, V. Balzani, in *Photochemistry and Photophysics of Coordination Compounds I, Vol. 280* (Eds.: V. Balzani, S. Campagna), Springer-Verlag Berlin, Berlin, **2007**, pp. 117-214.

[111] L. Flamigni, A. Barbieri, C. Sabatini, B. Ventura, F. Barigelletti, in *Photochemistry and Photophysics of Coordination Compounds Ii, Vol. 281* (Eds.: V. Balzani, S. Campagna), Springer-Verlag Berlin, Berlin, **2007**, pp. 143-203.

[112] H. Yersin, in *Transition Metal and Rare Earth Compounds Iii, Vol. 241*, **2004**, pp. 1-26.

[113] G. Baryshnikov, B. Minaev, H. Ågren, *Chem. Rev.* **2017**, *117*, 6500-6537.

[114] S. Lamansky, P. Djurovich, D. Murphy, F. Abdel-Razzaq, R. Kwong, I. Tsyba, M. Bortz, B. Mui, R. Bau, M. E. Thompson, *Inorg. Chem.* **2001**, *40*, 1704-1711.

[115] J. H. Klein, T. L. Sunderland, C. Kaufmann, M. Holzapfel, A. Schmiedel, C. Lambert, *Phys. Chem. Chem. Phys.* **2013**, *15*, 16024-16030.

[116] C. Lambert, R. Wagener, J. H. Klein, G. Grelaud, M. Moos, A. Schmiedel, M. Holzapfel, T. Bruhn, *Chem. Commun.* **2014**, *50*, 11350-11353.

[117] E. Pomarico, M. Silatani, F. Messina, O. Braem, A. Cannizzo, E. Barranoff, J. H. Klein, C. Lambert, M. Chergui, *J. Phys. Chem. C* **2016**, *120*, 16459-16469.

[118] A. Juris, V. Balzani, F. Barigelletti, S. Campagna, P. Belser, A. von Zelewsky, *Coord. Chem. Rev.* **1988**, *84*, 85-277.

[119] K. Kalyanasundaram, *Coord. Chem. Rev.* **1982**, *46*, 159-244.

[120] M. S. Lowry, W. R. Hudson, R. A. Pascal, S. Bernhard, *J. Am. Chem. Soc.* **2004**, *126*, 14129-14135.

[121] A. B. Tamayo, B. D. Alleyne, P. I. Djurovich, S. Lamansky, I. Tsyba, N. N. Ho, R. Bau, M. E. Thompson, *J. Am. Chem. Soc.* **2003**, *125*, 7377-7387.

[122] J. Li, P. I. Djurovich, B. D. Alleyne, M. Yousufuddin, N. N. Ho, J. C. Thomas, J. C. Peters, R. Bau, M. E. Thompson, *Inorg. Chem.* **2005**, *44*, 1713-1727.

[123] A. B. Tamayo, S. Garon, T. Sajoto, P. I. Djurovich, I. M. Tsyba, R. Bau, M. E. Thompson, *Inorg. Chem.* **2005**, *44*, 8723-8732.

[124] T. E. Wood, A. Thompson, *Chem. Rev.* **2007**, *107*, 1831-1861.

[125] A. Loudet, K. Burgess, *Chem. Rev.* **2007**, *107*, 4891-4932.

[126] J. A. van Koeveringe, J. Lugtenburg, *Recueil des Travaux Chimiques des Pays-Bas* **1977**, *96*, 55-57.

[127] R. Bonnett, *Chem. Soc. Rev.* **1995**, *24*, 19-33.

[128] G. Ulrich, R. Ziessel, A. Harriman, *Angew. Chem., Int. Ed.* **2008**, *47*, 1184-1201.

[129] N. Boens, V. Leen, W. Dehaen, *Chem. Soc. Rev.* **2012**, *41*, 1130-1172.

[130] T. L. Arbeloa, F. L. Arbeloa, I. L. Arbeloa, I. Garcia-Moreno, A. Costela, R. Sastre, F. Amat-Guerri, *Chem. Phys. Lett.* **1999**, *299*, 315-321.

[131] L.-L. Li, E. W.-G. Diau, *Chem. Soc. Rev.* **2013**, *42*, 291-304.

[132] N. Re, L. Bonomo, C. Da Silva, E. Solari, R. Scopelliti, C. Floriani, *Chem.-Eur. J.* **2001**, *7*, 2536-2546.

[133] S. A. Baudron, *Dalton Trans.* **2013**, *42*, 7498-7509.

[134] K. Kalyanasundaram, M. Neumannspallart, *J. Phys. Chem.* **1982**, *86*, 5163-5169.

[135] E. V. Antina, E. V. Rumyantsev, N. A. Dudina, Y. S. Marfin, L. A. Antina, *Russian Journal of General Chemistry* **2016**, *86*, 2209-2225.

[136] K. Hanson, A. Tamayo, V. V. Diev, M. T. Whited, P. I. Djurovich, M. E. Thompson, *Inorg. Chem.* **2010**, *49*, 6077-6084.

[137] D. Ramlot, M. Rebarz, L. Volker, M. Ovaere, D. Beljonne, W. Dehaen, L. Van Meervelt, C. Moucheron, A. Kirsch-De Mesmaeker, *Eur. J. Inorg. Chem.* **2013**, *2013*, 2031-2040.

[138] C. Bronner, S. A. Baudron, M. W. Hosseini, C. A. Strassert, A. Guenet, L. De Cola, *Dalton Trans.* **2010**, *39*, 180-184.

[139] I. V. Sazanovich, C. Kirmaier, E. Hindin, L. H. Yu, D. F. Bocian, J. S. Lindsey, D. Holten, *J. Am. Chem. Soc.* **2004**, *126*, 2664-2665.

[140] F. R. Li, S. I. Yang, Y. Z. Ciringh, J. Seth, C. H. Martin, D. L. Singh, D. H. Kim, R. R. Birge, D. F. Bocian, D. Holten, J. S. Lindsey, *J. Am. Chem. Soc.* **1998**, *120*, 10001-10017.

[141] H. L. Kee, C. Kirmaier, L. H. Yu, P. Thamyongkit, W. J. Youngblood, M. E. Calder, L. Ramos, B. C. Noll, D. F. Bocian, W. R. Scheidt, R. R. Birge, J. S. Lindsey, D. Holten, *J. Phys. Chem. B* **2005**, *109*, 20433-20443.

[142] A. Beziau, S. A. Baudron, A. Fluck, M. W. Hosseini, *Inorg. Chem.* **2013**, *52*, 14439-14448.

[143] J. R. Stork, V. S. Thoi, S. M. Cohen, *Inorg. Chem.* **2007**, *46*, 11213-11223.

[144] J. D. Hall, T. M. McLean, S. J. Smalley, M. R. Waterland, S. G. Telfer, *Dalton Trans.* **2010**, *39*, 437-445.

[145] L. H. Yu, K. Muthukumaran, I. V. Sazanovich, C. Kirmaier, E. Hindin, J. R. Diers, P. D. Boyle, D. F. Bocian, D. Holten, J. S. Lindsey, *Inorg. Chem.* **2003**, *42*, 6629-6647.

[146] J. E. Fergusson, C. A. Ramsay, *J.Chem. Soc.* **1965**, 5222-+.

[147] F. C. March, D. A. Couch, K. Emerson, J. E. Fergusson, W. T. Robinson, *J. Phys. Chem. A* **1971**, 440-+.

[148] C. Bruckner, V. Karunaratne, S. J. Rettig, D. Dolphin, *Can. J. Chem.-Rev. Can. Chim.* **1996**, *74*, 2182-2193.

[149] M. R. Waterland, S. G. Telfer, T. M. McLean, *Chem. N. Z.* **2010**, *74*, 15-19.

[150] S. G. Telfer, T. M. McLean, M. R. Waterland, *Dalton Trans.* **2011**, *40*, 3097-3108.

[151] S. Wallin, J. Davidsson, J. Modin, L. Hammarstrom, *J. Phys. Chem. A* **2005**, *109*, 4697-4704.

[152] M. Kasha, *Radiat. Res.* **1963**, *20*, 55-70.

[153] E. McRae, M. Kasha, in *Physical Processes in Radiation Biology*, Academic Press, New York, **1964**.

[154] K. Servaty, E. Cauët, F. Thomas, J. Lambermont, P. Gerbaux, J. De Winter, M. Ovaere, L. Volker, N. Vaeck, L. Van Meervelt, W. Dehaen, C. Moucheron, A. Kirsch-De Mesmaeker, *Dalton Trans.* **2013**, *42*, 14188-14199.

[155] M. A. Filatov, A. Y. Lebedev, S. N. Mukhin, S. A. Vinogradov, A. V. Cheprakov, *J. Am. Chem. Soc.* **2010**, *132*, 9552-9554.

[156] T. J. A. Wolf, R. H. Myhre, J. P. Cryan, S. Coriani, R. J. Squibb, A. Battistoni, N. Berrah, C. Bostedt, P. Bucksbaum, G. Coslovich, R. Feifel, K. J. Gaffney, J. Grilj, T.

J. Martinez, S. Miyabe, S. P. Moeller, M. Mucke, A. Natan, R. Obaid, T. Osipov, O. Plekan, S. Wang, H. Koch, M. Gühr, *Nat. Commun.* **2017**, *8*, 29.

[157] C. Trinh, K. Kirlikovali, S. Das, M. E. Ener, H. B. Gray, P. Djurovich, S. E. Bradforth, M. E. Thompson, *J. Phys. Chem. C* **2014**, *118*, 21834-21845.

[158] S. Kusaka, R. Sakamoto, H. Nishihara, *Inorg. Chem.* **2014**, *53*, 3275-3277.

[159] R. Sakamoto, T. Iwashima, M. Tsuchiya, R. Toyoda, R. Matsuoka, J. F. Kogel, S. Kusaka, K. Hoshiko, T. Yagi, T. Nagayama, H. Nishihara, *J. Mater. Chem. A* **2015**, *3*, 15357-15371.

[160] R. Sakamoto, T. Iwashima, J. F. Kogel, S. Kusaka, M. Tsuchiya, Y. Kitagawa, H. Nishihara, *J. Am. Chem. Soc.* **2016**, *138*, 5666-5677.

[161] J. W. Buchler, L. Puppe, *Liebigs Ann. Chem.* **1970**, *740*, 142-163.

[162] D. S. Sharada, A. Z. Muresan, K. Muthukumaran, J. S. Lindsey, *J. Org. Chem.* **2005**, *70*, 3500-3510.

[163] M. G. D. Holaday, G. Tarafdar, A. Kumar, M. L. P. Reddy, A. Srinivasan, *Dalton Trans.* **2014**, *43*, 7699-7703.

[164] V. Král, J. L. Sessler, R. S. Zimmerman, D. Seidel, V. Lynch, B. Andrioletti, *Angew. Chem.* **2000**, *39*, 1055-1058.

[165] M. W. Renner, J. W. Buchler, *J. Phys. Chem.* **1995**, *99*, 8045-8049.

[166] C. Da Silva, L. Bonomo, E. Solari, R. Scopelliti, C. Floriani, N. Re, *Chem.-Eur. J.* **2000**, *6*, 4518-4531.

[167] K. Muthukumaran, S. H. H. Zaidi, L. H. Yu, P. Thamyongkit, M. E. Calder, D. S. Sharada, J. S. Lindsey, *J. Porphyrins Phthalocyanines* **2005**, *9*, 745-759.

[168] B. Dolenský, J. Kroulík, V. Král, J. L. Sessler, H. Dvořáková, P. Bouř, M. Bernátková, C. Bucher, V. Lynch, *J. Am. Chem. Soc.* **2004**, *126*, 13714-13722.

[169] M. Nonoyama, *Bull. Chem. Soc. Jpn.* **1974**, *47*, 767-768.

[170] E. C. Constable, A. Thompson, T. A. Leese, D. G. F. Reese, D. A. Tocher, *Inorg. Chim. Acta* **1991**, *182*, 93-100.

[171] J. Brooks, Y. Babayan, S. Lamansky, P. I. Djurovich, I. Tsyba, R. Bau, M. E. Thompson, *Inorg. Chem.* **2002**, *41*, 3055-3066.

[172] C. O'Brien, M. Y. Wong, D. B. Cordes, A. M. Z. Slawin, E. Zysman-Colman, *Organometallics* **2015**, *34*, 13-22.

[173] M. Holzapfel, C. Lambert, *J. Phys. Chem. C* **2008**, *112*, 1227-1243.

[174] I. Cepanec, G. Karminski-Zamola, M. Litvic, Z. Mikotic-Mihun, in *PCT Int. Appl.*, Google Patents, **1999**.

[175] H. J. Cristau, P. P. Cellier, J. F. Spindler, M. Taillefer, *Eur. J. Org. Chem.* **2004**, 695-709.

[176] B. Geiss, C. Lambert, *Chem. Commun.* **2009**, 1670-1672.

[177] B. J. Littler, M. A. Miller, C. H. Hung, R. W. Wagner, D. F. O'Shea, P. D. Boyle, J. S. Lindsey, *J. Org. Chem.* **1999**, *64*, 1391-1396.

[178] N. Malatesti, R. Hudson, K. Smith, H. Savoie, K. Rix, K. Welham, R. W. Boyle, *Photochem. Photobiol.* **2006**, *82*, 746-749.

[179] F. Zieschang, M. H. Schreck, A. Schmiedel, M. Holzapfel, J. H. Klein, C. Walter, B. Engels, C. Lambert, *J. Phys. Chem. C* **2014**, *118*, 27698-27714.

[180] T. C. Barros, S. Brochsztain, V. G. Toscano, P. Berci, M. J. Politi, *J. Photochem. Photobiol., A* **1997**, *111*, 97-104.

[181] S. V. Bhosale, C. H. Jani, S. J. Langford, *Chem. Soc. Rev.* **2008**, *37*, 331-342.

[182] S. Amthor, B. Noller, C. Lambert, *Chem. Phys.* **2005**, *316*, 141-152.

[183] C. Bronner, M. Veiga, A. Guenet, L. De Cola, M. W. Hosseini, C. A. Strassert, S. A. Baudron, *Chem.-Eur. J.* **2012**, *18*, 4041-4050.

[184] H. Miyasaka, H. Masuhara, N. Mataga, *J. Phys. Chem.* **1985**, *89*, 1631-1636.

[185] S.-L. Suraru, F. Würthner, *Angew. Chem.* **2014**, *53*, 7428-7448.

[186] C. Kaiser, A. Schmiedel, M. Holzapfel, C. Lambert, *J. Phys. Chem. C* **2012**, *116*, 15265-15280.

[187] S. Pluczyk, P. Zassowski, R. Rybakiewicz, R. Wielgosz, M. Zagorska, M. Lapkowski, A. Pron, *RSC Advances* **2015**, *5*, 7401-7412.

[188] S. Suzuki, R. Sugimura, M. Kozaki, K. Keyaki, K. Nozaki, N. Ikeda, K. Akiyama, K. Okada, *J. Am. Chem. Soc.* **2009**, *131*, 10374-+.

[189] L. Flamigni, B. Ventura, E. Baranoff, J. P. Collin, J. P. Sauvage, *Eur. J. Inorg. Chem.* **2007**, 5189-5198.

[190] D. Ramlot, M. Rebarz, L. Volker, M. Ovaere, D. Beljonne, W. Dehaen, L. Van Meervelt, C. Moucheron, A. Kirsch-De Mesmaeker, *Eur. J. Inorg. Chem.* **2013**, 2031-2040.

[191] J. Kaminski, Bachelor thesis, Heinrich-Heine-Universität (Düsseldorf), **2018**.

[192] J. Metz, Bachelor thesis, Heinrich-Heine-Universität (Düsseldorf), **2018**.

[193] A. Weller, *Z. Phys. Chem.* **1982**, *133*, 93-98.

[194] M. J. Frisch, G. W. Trucks, H. B. Schlegel, G. E. Scuseria, M. A. Robb, J. R. Cheeseman, G. Scalmani, V. Barone, B. Mennucci, G. A. Petersson, H. Nakatsuji, M. Caricato, X. Li, H. P. Hratchian, A. F. Izmaylov, J. Bloino, G. Zheng, J. L. Sonnenberg, M. Hada, M. Ehara, K. Toyota, R. Fukuda, J. Hasegawa, M. Ishida, T. Nakajima, Y. Honda, O. Kitao, H. Nakai, T. Vreven, J. A. Montgomery Jr., J. E. Peralta, F. Ogliaro, M. J. Bearpark, J. J. Heyd, E. N. Brothers, K. N. Kudin, V. N. Staroverov, T. A. Keith, R. Kobayashi, J. Normand, K. Raghavachari, A. P. Rendell, J. C. Burant, S. S. Iyengar, J. Tomasi, M. Cossi, N. Rega, J. M. Millam, M. Klene, J. E. Knox, J. B. Cross, V. Bakken, C. Adamo, J. Jaramillo, R. Gomperts, R. E.

Stratmann, O. Yazyev, A. J. Austin, R. Cammi, C. Pomelli, J. W. Ochterski, R. L. Martin, K. Morokuma, V. G. Zakrzewski, G. A. Voth, P. Salvador, J. J. Dannenberg, S. Dapprich, A. D. Daniels, O. Farkas, J. B. Foresman, J. V. Ortiz, J. Cioslowski, D. J. Fox, Gaussian Inc., Wallingford CT, **2013**.

[195] I. H. M. van Stokkum, D. S. Larsen, R. van Grondelle, *Biochim. Biophys. Acta, Bioenerg.* **2004**, *1657*, 82-104.

[196] M. A. Baldo, S. Lamansky, P. E. Burrows, M. E. Thompson, S. R. Forrest, *Appl. Phys. Lett.* **1999**, *75*, 4-6.

[197] M. Montalti, A. Credi, L. Prodi, M. T. Gandolfi, *Handbook of Photochemistry*, III ed. ed., CRC/Taylor & Francis, Boca Raton, **2006**.

[198] P. Ganesan, J. Baggerman, H. Zhang, E. J. R. Sudholter, H. Zuilhof, *J. Phys. Chem. A* **2007**, *111*, 6151-6156.

[199] B. Albinsson, M. P. Eng, K. Pettersson, M. U. Winters, *Phys. Chem. Chem. Phys.* **2007**, *9*, 5847-5864.

[200] *POLYMER DATA HANDBOOK*, Oxford University Press Inc., **1999**.

[201] P. J. Rossky, J. D. Simon, *Nature* **1994**, *370*, 263.

[202] M. R. Harris, D. J. Davis, B. Durham, F. Millett, *Biochim. Biophys. Acta, Bioenerg.* **1997**, *1319*, 147-154.

[203] C. Feng, R. V. Kedia, J. T. Hazzard, J. K. Hurley, G. Tollin, J. H. Enemark, *Biochemistry* **2002**, *41*, 5816-5821.

[204] J. Schäfer, PhD thesis, Julius-Maximilians-Universität Würzburg (Würzburg), **2017**.

[205] J. E. Rogers, L. A. Kelly, *J. Am. Chem. Soc.* **1999**, *121*, 3854-3861.

[206] H. Yersin, D. Donges, in *Transition Metal and Rare Earth Compounds: Excited States, Transitions, Interactions Ii, Vol. 214*, **2001**, pp. 81-186.

[207] J. K. Hurley, N. Sinai, H. Linschitz, *Photochem. Photobiol.* **1983**, *38*, 9-14.

[208] P. Muller, K. Brettel, *Photochem. Photobiol. Sci.* **2012**, *11*, 632-636.

[209] G. J. Hedley, A. Ruseckas, I. D. W. Samuel, *Chem. Phys. Lett.* **2008**, *450*, 292-296.

[210] M. Maroncelli, *J. Mol. Liq.* **1993**, *57*, 1-37.

[211] V. S. Thoi, J. R. Stork, D. Magde, S. M. Cohen, *Inorg. Chem.* **2006**, *45*, 10688-10697.

[212] A. Pigliucci, G. Duvanel, L. M. L. Daku, E. Vauthey, *J. Phys. Chem. A* **2007**, *111*, 6135-6145.

[213] J. Petersson, M. Eklund, J. Davidsson, L. Hammarström, *J. Phys. Chem. B* **2010**, *114*, 14329-14338.

[214] T. Elsaesser, W. Kaiser, *Annu. Rev. Phys. Chem.* **1991**, *42*, 83-107.

[215] U. Noomnarm, R. M. Clegg, *Photosynth. Res.* **2009**, *101*, 181-194.

[216] J. S. L. Yeo, J. J. Vittal, T. S. A. Hor, *Chem. Commun.* **1999**, 1477-1478.

[217] C. M. Frech, L. J. W. Shimon, D. Milstein, *Angew. Chem., Int. Ed.* **2005**, *44*, 1709-1711.

[218] C. Tsay, N. P. Mankad, J. C. Peters, *J. Am. Chem. Soc.* **2010**, *132*, 13975-13977.

[219] I. R. Gould, D. Ege, J. E. Moser, S. Farid, *J. Am. Chem. Soc.* **1990**, *112*, 4290-4301.

[220] I. R. Gould, R. H. Young, R. E. Moody, S. Farid, *J. Phys. Chem.* **1991**, *95*, 2068-2080.

[221] U. E. Steiner, P. Gilch, *High Magnetic Fields in Chemistry, Vol. 2*, World Scientific Publishing Co. Pte. Ltd, Singapore, **2003**.

[222] R. Bakova, M. Chergui, C. Daniel, A. Vlcek, S. Zalis, *Coord. Chem. Rev.* **2011**, *255*, 975-989.

[223] A. F. Rausch, U. V. Monkowius, M. Zabel, H. Yersin, *Inorg. Chem.* **2010**, *49*, 7818-7825.

[224] D. R. Kattnig, B. Mladenova, G. Grampp, C. Kaiser, A. Heckmann, C. Lambert, *J. Phys. Chem. C* **2009**, *113*, 2983-2995.

[225] K. J. Reszka, M. Takayama, R. H. Sik, C. F. Chignell, I. Saito, *Photochem. Photobiol.* **2005**, *81*, 573-580.

[226] C. Mailer, R. D. Nielsen, B. H. Robinson, *J. Phys. Chem. A* **2005**, *109*, 4049-4061.

[227] S. A. Rice, G. A. Kenney-Wallace, *Chem. Phys.* **1980**, *47*, 161-170.

[228] G. R. Alms, D. R. Bauer, J. I. Brauman, R. Pecora, *J. Chem. Phys.* **1973**, *58*, 5570-5578.

[229] M. Kaupp, S. Guckel, M. Renz, S. Klawohn, K. Theilacker, M. Parthey, C. Lambert, *J. Comput. Chem.* **2016**, *37*, 93-102.

[230] A. A. Carrington, A. D. McLachlan, *INtroduction to magnetic resonance*, Harper and Row, New York, **1967**.

[231] M. T. Rawls, I. Kuprov, C. M. Elliott, U. E. Steiner, *Carbon-Centered Free Radicals and Radical Cations*, John Wiley & Sons, New Jersey, **2010**.

[232] P. H. Fries, E. Belorizky, *J. Chem. Phys.* **2007**, *126*, 13.

[233] B. NIkolas-Ploutarch, D. Yurij, *EPR of Free Radicals in Solids I*, 2 ed., Springer, **2012**.

[234] F. B. Wyart, P. G. d. Gennes, *Eur. Phys. J. E* **2000**, *1*, 93-97.

[235] M. M. Somoza, M. I. Sluch, M. A. Berg, *Macromolecules* **2003**, *36*, 2721-2732.

[236] R. Holyst, A. Bielejewska, J. Szymański, A. Wilk, A. Patkowski, J. Gapiński, A. Żywociński, T. Kalwarczyk, E. Kalwarczyk, M. Tabaka, N. Ziębacz, S. A. Wieczorek, *Phys. Chem. Chem. Phys.* **2009**, *11*, 9025-9032.

[237] M. Dorfschmid, K. Müllen, A. Zumbusch, D. Wöll, *Macromolecules* **2010**, *43*, 6174-6179.

[238] D. A. Turton, K. Wynne, *J. Phys. Chem. B* **2014**, *118*, 4600-4604.

[239] L. Yong, J. Harbridge, R. W. Quine, G. A. Rinard, S. S. Eaton, G. R. Eaton, C. Mailer, E. Barth, H. J. Halpern, *J. Magn. Reson.* **2001**, *152*, 156-161.

[240] V. Meyer, S. S. Eaton, G. R. Eaton, *Appl. Magn. Reson.* **2014**, *45*, 993-1007.

[241] A. A. Kuzhelev, D. V. Trukhin, O. A. Krumkacheva, R. K. Strizhakov, O. Y. Rogozhnikova, T. I. Troitskaya, M. V. Fedin, V. M. Tormyshev, E. G. Bagryanskaya, *J. Phys. Chem. B* **2015**, *119*, 13630-13640.

[242] F. Frei, A. Rondi, D. Espa, M. L. Mercuri, L. Pilia, A. Serpe, A. Odeh, F. Van Mourik, M. Chergui, T. Feurer, P. Deplano, A. Vlcek, A. Cannizzo, *Dalton Trans.* **2014**, *43*, 17666-17676.

[243] S. Kusaka, R. Sakamoto, Y. Kitagawa, M. Okumura, H. Nishihara, *Chem.-Asian J.* **2012**, *7*, 907-910.

[244] Q. Miao, J.-Y. Shin, B. O. Patrick, D. Dolphin, *Chem. Commun.* **2009**, 2541-2543.

[245] H. B. Goodbrand, N. X. Hu, *J. Org. Chem.* **1999**, *64*, 670-674.

[246] D. Shi, Y. M. Cao, N. Pootrakulchote, Z. H. Yi, M. F. Xu, S. M. Zakeeruddin, M. Graetzel, P. Wang, *J. Phys. Chem. C* **2008**, *112*, 17478-17485.

[247] A. K. C. Mengel, B. He, O. S. Wenger, *J. Org. Chem.* **2012**, *77*, 6545-6552.

[248] T. Ishiyama, M. Murata, N. Miyaura, *J. Org. Chem.* **1995**, *60*, 7508-7510.

[249] M. Beinhoff, W. Weigel, M. Jurczok, W. Rettig, C. Modrakowski, I. Brudgam, H. Hartl, A. D. Schluter, *Eur. J. Org. Chem.* **2001**, 3819-3829.

[250] H. C. Schmidt, M. Spulber, M. Neuburger, C. G. Palivan, M. Meuwly, O. S. Wenger, *J. Org. Chem.* **2016**, *81*, 595-602.

[251] I. V. Sazanovich, A. Balakumar, K. Muthukumaran, E. Hindin, C. Kirmaier, J. R. Diers, J. S. Lindsey, D. F. Bocian, D. Holten, *Inorg. Chem.* **2003**, *42*, 6616-6628.

[252] M. Bernátková, B. Andrioletti, V. Král, E. Rose, J. Vaissermann, *J. Org. Chem.* **2004**, *69*, 8140-8143.

[253] C. Bucher, D. Seidel, V. Lynch, V. Král, J. L. Sessler, *Org. Lett.* **2000**, *2*, 3103-3106.

[254] P. D. Rao, B. J. Littler, G. R. Geier, J. S. Lindsey, *J. Org. Chem.* **2000**, *65*, 1084-1092.

[255] S. H. H. Zaidi, K. Muthukumaran, S. Tamaru, J. S. Lindsey, *J. Org. Chem.* **2004**, *69*, 8356-8365.

[256] S. Amthor, C. Lambert, *J. Phys. Chem. A* **2006**, *110*, 1177-1189.

[257] Y. Wei, C. T. Chen, *J. Am. Chem. Soc.* **2007**, *129*, 7478-+.

[258] J. Horníček, H. Dvořáková, P. Bouř, *J. Phys. Chem. A* **2010**, *114*, 3649-3654.

[259] H. Falk, O. Hofer, *Mon. Chem.* **1975**, *106*, 97-113.

[260] H. Falk, O. Hofer, *Mon. Chem.* **1975**, *106*, 115-120.

[261] M. Huix-Rotllant, H. Tamura, I. Burghardt, *J. Phys. Chem. Lett.* **2015**, *6*, 1702-1708.

[262] H. Imahori, K. Tamaki, D. M. Guldi, C. Luo, M. Fujitsuka, O. Ito, Y. Sakata, S. Fukuzumi, *J. Am. Chem. Soc.* **2001**, *123*, 2607-2617.

[263] C. Brückner, B. Engels, *Chem. Phys.* **2017**, *482*, 319-338.

[264] P.-K. Chow, G. Cheng, G. S. M. Tong, C. Ma, W.-M. Kwok, W.-H. Ang, C. Y.-S. Chung, C. Yang, F. Wang, C.-M. Che, *Chem. Sci.* **2016**, *7*, 6083-6098.

[265] M. Schulze, A. Steffen, F. Würthner, *Angew. Chem., Int. Ed.* **2015**, *54*, 1570-1573.

[266] H. Xiang, J. Cheng, X. Ma, X. Zhou, J. J. Chruma, *Chem. Soc. Rev.* **2013**, *42*, 6128-6185.

[267] C. Lambert, G. Nöll, *J. Am. Chem. Soc.* **1999**, *121*, 8434-8442.

[268] H. M. Hoang, T. B. V. Pham, G. Grampp, D. R. Kattnig, *J. Phys. Chem. Lett.* **2014**, *5*, 3188-3194.

[269] I. R. Gould, D. Noukakis, L. Gomez-Jahn, R. H. Young, J. L. Goodman, S. Farid, *Chem. Phys.* **1993**, *176*, 439-456.

[270] S. van de Linde, I. Krstić, T. Prisner, S. Doose, M. Heilemann, M. Sauer, *Photochem. Photobiol. Sci.* **2011**, *10*, 499-506.

[271] P. C. Beaumont, D. G. Johnson, B. J. Parsons, *J. Photochem. Photobiol., A* **1997**, *107*, 175-183.

[272] H. Görner, *Photochem. Photobiol. Sci.* **2008**, *7*, 371-376.

[273] D. H. Wachsstock, **2007**.

[274] S. Riese, M. Holzapfel, A. Schmiedel, I. Gert, D. Schmidt, F. Würthner, C. Lambert, *Inorg. Chem.* **2018**, *57*, 12480-12488.

[275] E. E. S. Dümmling, S. Schneider, B. Speiser, M. Würde, *Curr. Sep. Drug Dev.* **1996**, 53-56.

[276] I. Carmichael, G. L. Hug, *J. Phys. Chem. Ref. Data* **1986**, *15*, 1-250.

[277] J. N. Demas, G. A. Crosby, *J. Am. Chem. Soc.* **1970**, *92*, 7262-7270.

[278] A. N. Tarnovsky, W. Gawelda, M. Johnson, C. Bressler, M. Chergui, *J. Phys. Chem. B* **2006**, *110*, 26497-26505.

[279] G. R. Fulmer, A. J. M. Miller, N. H. Sherden, H. E. Gottlieb, A. Nudelman, B. M. Stoltz, J. E. Bercaw, K. I. Goldberg, *Organometallics* **2010**, *29*, 2176-2179.

[280] G. M. Sheldrick, *Acta Crystallogr. Sect. A* **2008**, *64*, 112-122.

[281] D. F. Shriver, Drezdon M. A., *The manipulation of air-sensitive compounds*, John Wiley & Sons, New York, **1986**.

[282] W. C. Still, M. Kahn, A. Mitra, *J. Org. Chem.* **1978**, *43*, 2923-2925.

[283] S. F. Völker, A. Schmiedel, M. Holzapfel, K. Renziehausen, V. Engel, C. Lambert, *J. Phys. Chem. C* **2014**, *118*, 17467-17482.

[284] N. V. Tkachenko, *Optical Spectroscopy*, Elsevier, Amsterdam, **2006**.

8 Table of Formulas

Cyclometalated compounds – ligands and precursors

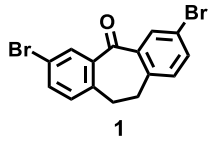

1

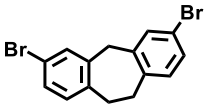

2

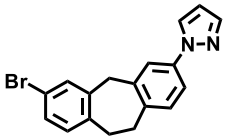

3

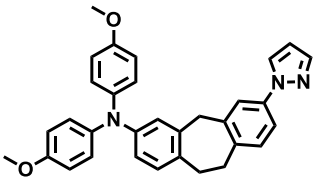

4

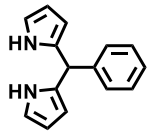

5

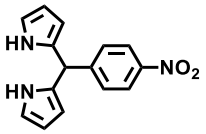

6

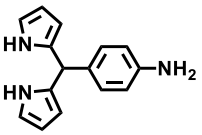

7

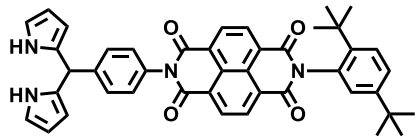

8

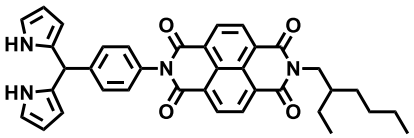

9

Cyclometalated compounds – binuclear precursor-complexes

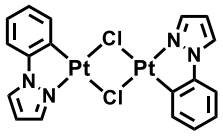

10

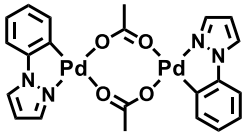

11

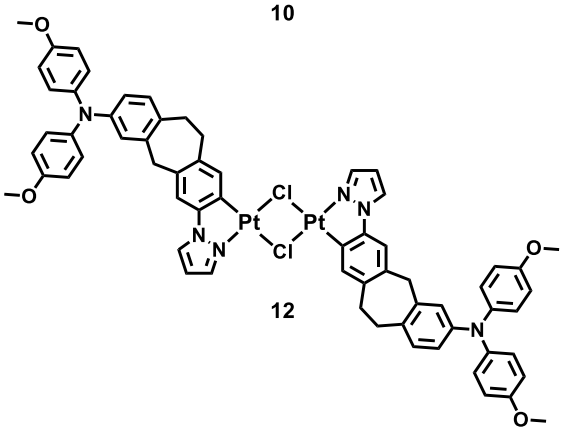

12

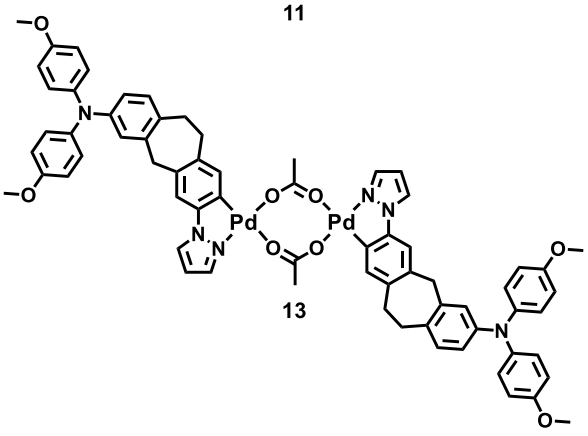

13

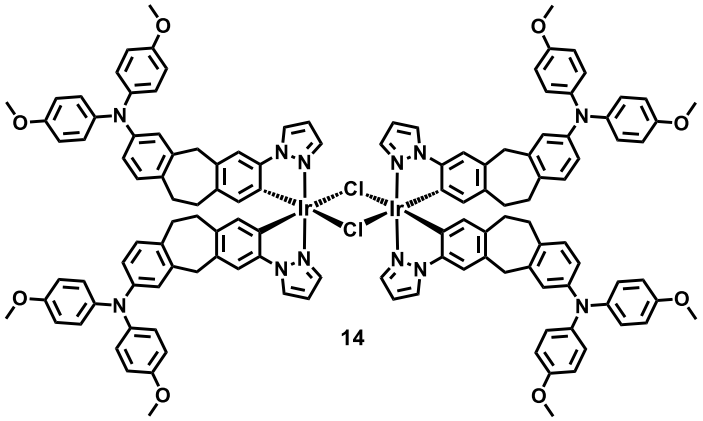

14

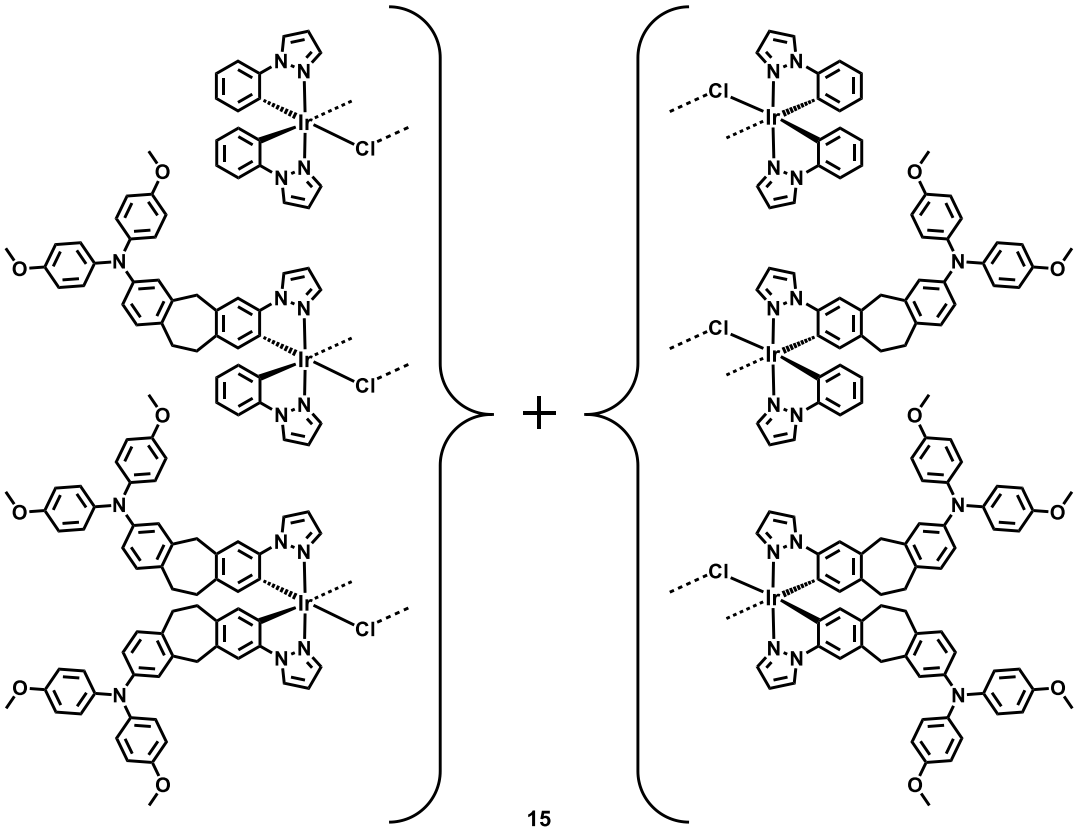

15

Cyclometalated metal-dipyrrinato complexes

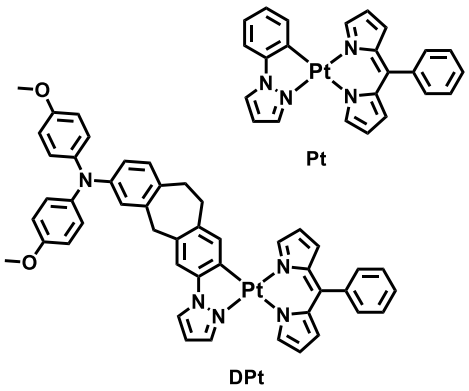

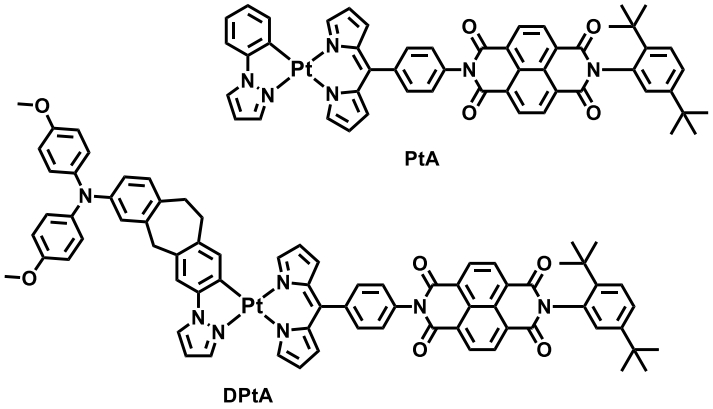

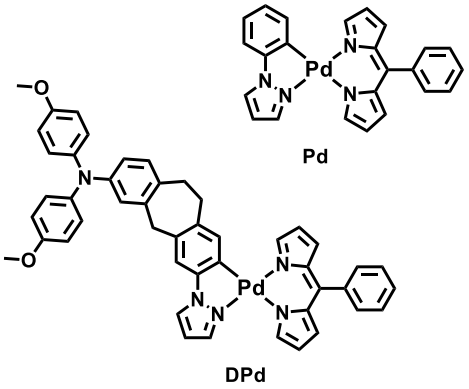

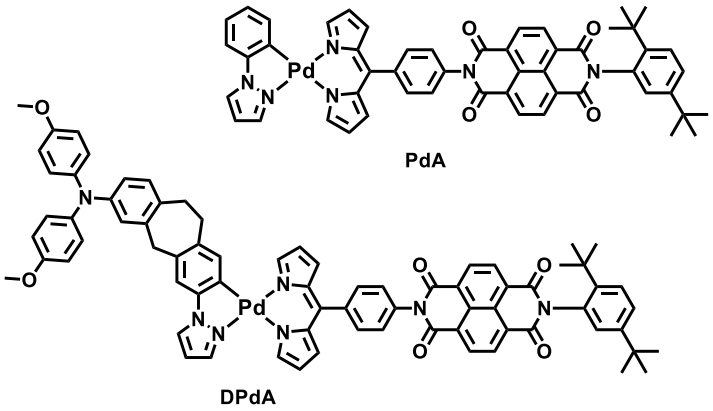

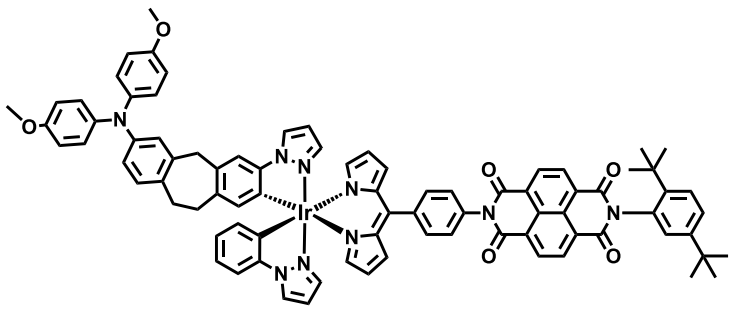

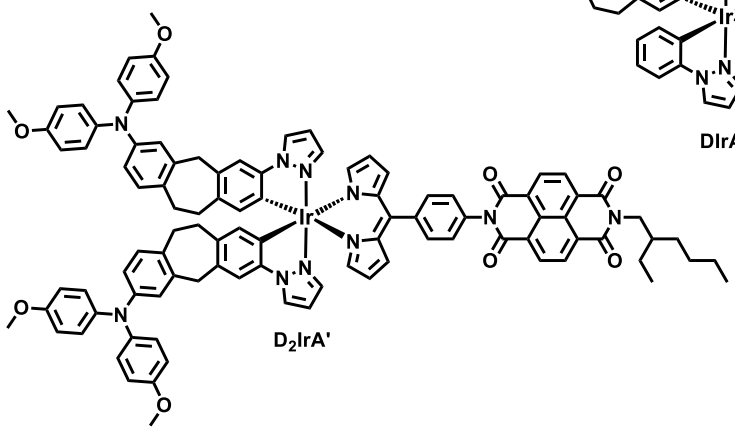

Bis-dipyrrinato- and PDM-compounds – precursors

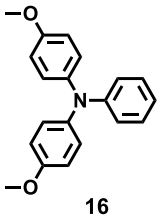
16

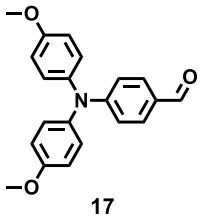
17

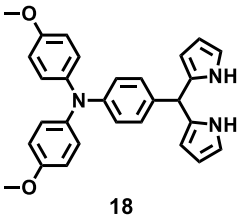
18

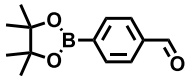
19

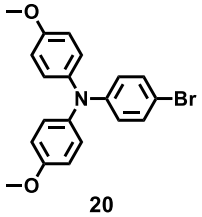
20

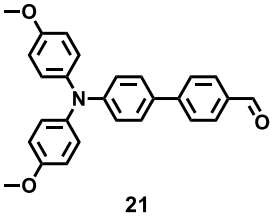
21

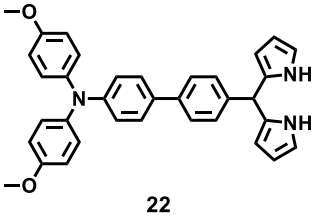
22

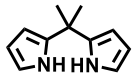
23

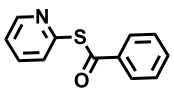
24

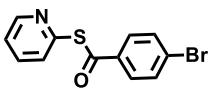
25

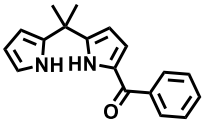
26

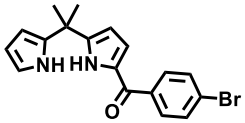
27

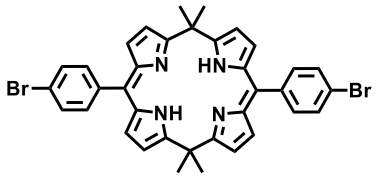
28

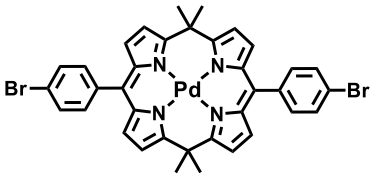
Pd-28

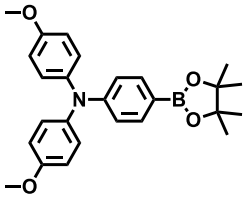
29

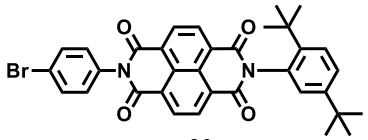
30

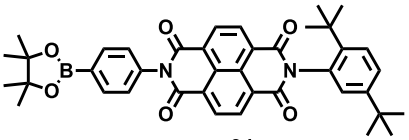
31

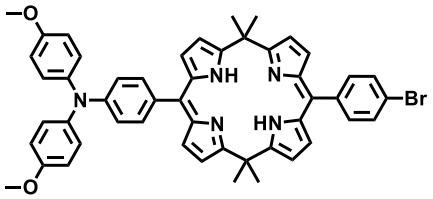
32

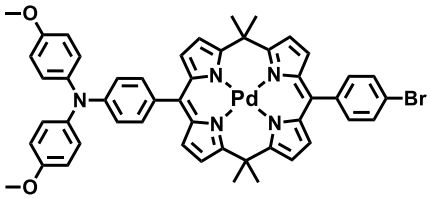
Pd-32

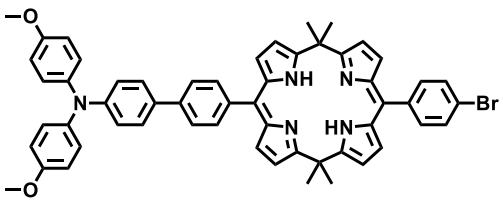
33

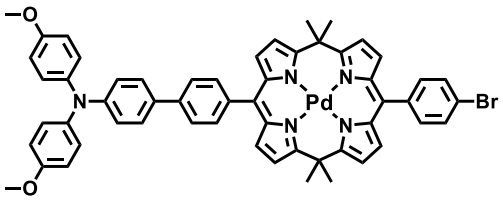
Pd-33

Bis-dipyrrinato- and PDM-compounds

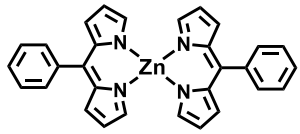

$Zn(dipy)_2$

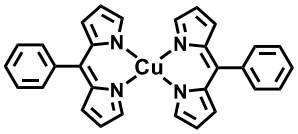

$Cu(dipy)_2$

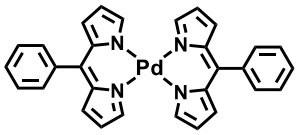

$Pd(dipy)_2$

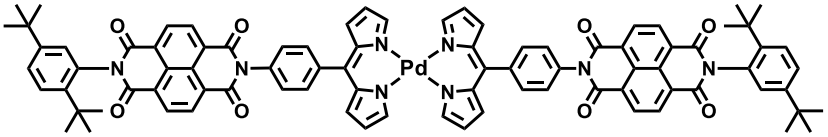

$Pd(dipy)_2$-A

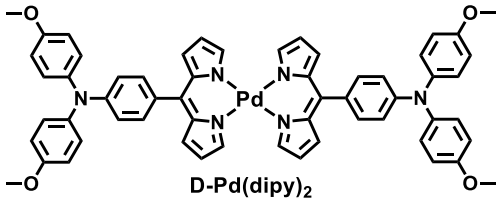

D-$Pd(dipy)_2$

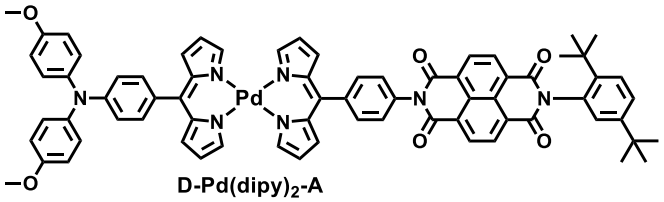

D-$Pd(dipy)_2$-A

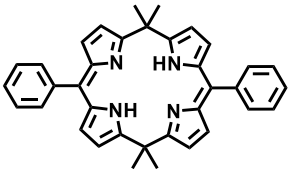

PDM

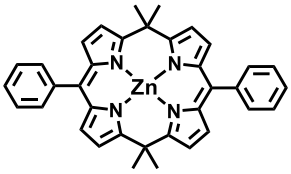

ZnPDM

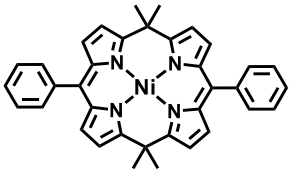

NiPDM

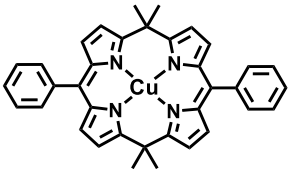

CuPDM

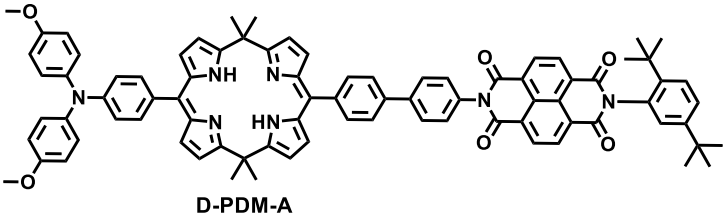

D-PDM-A

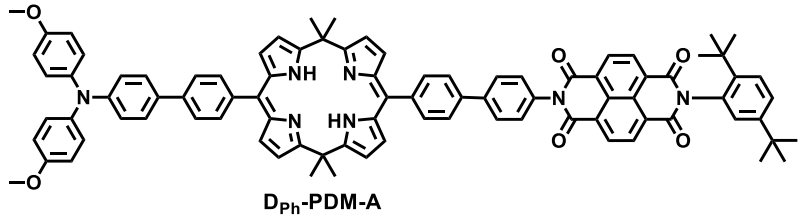

D_{Ph}-PDM-A

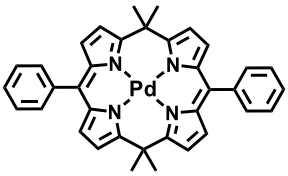

PdPDM

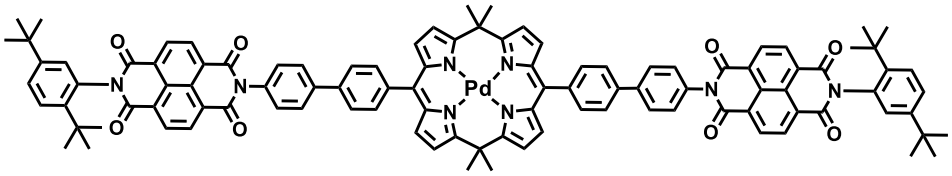

PdPDM-A

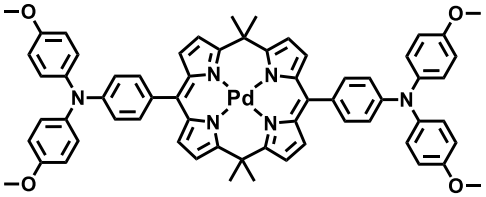

D-PdPDM

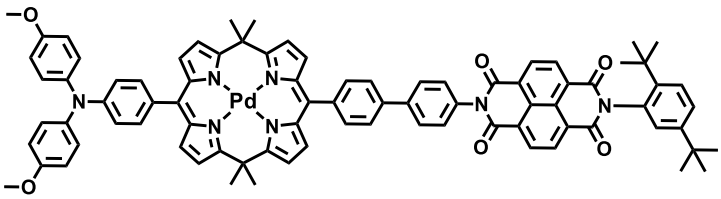

D-PdPDM-A

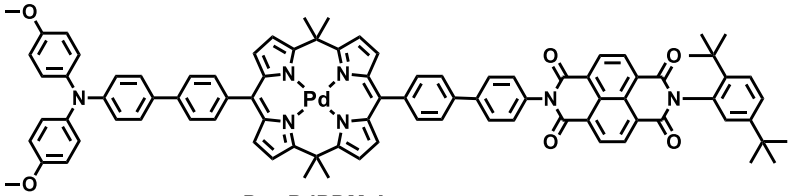

D_{Ph}-PdPDM-A

9 Zusammenfassung

In der vorliegenden Arbeit wurden die Photophysik und Spinchemie von Donor-Photosensibilisator-Akzeptor-Triaden untersucht. In allen untersuchten Triaden wurden Triarylamin (TAA) bzw. Naphthalindiimid (NDI) als Elektronen-Donor bzw. -Akzeptor verwendet. Der zentrale Photosensibilisator (PS) hingegen wurde variiert, behielt allerdings das Dipyrrin-Chromophor als gemeinsames Strukturmotiv bei. Alle Zielverbindungen wurden mittels NMR-Spektroskopie, Massenspektrometrie und Elementaranalyse auf Identität und Reinheit geprüft.

Der erste Abschnitt der Arbeit beschäftigte sich mit cyclometallierten Dipyrrinato-Komplexen schwererer Übergangsmetalle. Die erfolgreiche Synthese von neuartigen Triaden mit Ir(III)-, Pt(II)- und Pd(II)- Zentralionen wurde beschrieben. Die optischen und elektrochemischen Eigenschaften der Verbindungen deuteten auf das Auftreten von Ladungstrennung hin was mit Hilfe transienter Absorptionsspektroskopie (TA) bewiesen werden konnte. Weiterhin ergab die Untersuchung der Stoffe, dass die Ladungstrennung in den Triaden mit Pd(II) und Pt(II) als Zentralion wesentlich langsamer und weniger effizient abläuft als in den analogen Verbindungen mit Ir(III) als Zentralion. Dieser Umstand ist weitestgehend auf einen wesentlich komplizierter ablaufenden Reaktionsmechanismus zurückzuführen, welcher mehrere Zwischenstufen beinhaltet. Der resultierende ladungsgetrennte Zustand (CSS_2) weist eine hohe Lebenszeit auf, welche vom Zentralatom abhängt. Für Ir(III) beträgt diese ungefähr 0.5 µs, während sie für Pt(II) und Pd(II) auf ca. 1.5 µs ansteigt. Der Einfluss eines externen Magnetfeldes auf die Kinetik der Ladungsrekombination (CR) wurde mittels magnetfeldabhängiger ns-TA-Spektroskopie untersucht. Der auftretende Magnetfeldeffekt (MFE) konnte mit Hilfe eines klassischen Modells auf eine einzige magnetfeldabhängige Geschwindigkeitskonstante $k_{\pm}$ zurückgeführt werden. Der Verlauf von $k_{\pm}$ zeigt eine deutliche Trennung der kohärenten und inkohärenten Spin-Flip-Mechanismen. Während die kohärente Spin-Umwandlung auf die isotrope Hyperfeinkopplung mit den magnetischen Nuklei der Radikalzentren zurückgeht, wird die inkohärente Spin Relaxation durch die Rotationsmodulation des anisotropen Hyperfeinkopplung-Tensors hervorgerufen und ist daher stark abhängig von der Viskosität des Lösungsmittels. Dieser Umstand wurde dazu genutzt die Nanoviskosität des polymeren Lösungsmittels pTHF zu messen, welche stark von der angegebenen Makroviskosität abweicht.

Im zweiten Teil dieser Arbeit wurden zunächst mehrere Bisdipyrrinato-Metall-Komplexe sowie ihre verbrückten Porphodimethenato (PDM)-Analoga hinsichtlich ihrer Eignung als PS in Donor-Akzeptor-substituierten Triaden getestet. Während die verbrückten Zn(II)- und Pd(II)-Komplexe vielversprechende Eigenschaften wie langlebige angeregte Zustände und relativ intensive Emission aufweisen, erscheinen der unverbrückte Pd(II)-Komplex sowie der nicht komplexierte PDM-Ligand

weniger geeignet. Der große Unterschied zwischen den beiden augenscheinlich ähnlichen Pd(II)-Komplexen ist auf eine strukturelle Reorganisation der Geometrie des unverbrückten Komplexes zurück zu führen. Diese resultiert in einem Metall-zentrierten Triplet-Zustand mit bisphenoidaler Geometrie, welcher schnell und strahlungslos in den Grundzustand übergeht. Im verbrückten Komplex hingegen verhindern die Dimethylmethylen-Brücken zwischen den beiden Dipyrrin-Chromophoren die strukturelle Umordnung und erhöhen daher die Lebenszeit und Quantenausbeute der Phosphoreszenz.

Mit Ausnahme des Zn(II)-PDM-Komplexes konnten für alle geeigneten PS die entsprechenden Donor-Akzeptor substituierten Triaden synthetisiert werden. Diese wurden mit den bereits für die cyclometallierten Triaden beschriebenen Methoden untersucht. Da keine ungesättigte Verbindung zwischen Donor und PS vorhanden ist, sind die elektronischen Wechselwirkungen zwischen den einzelnen Untereinheiten nicht vernachlässigbar. In allen untersuchten Triaden konnte photo-induzierte Ladungstrennung (CS) nachgewiesen werden. Diese ist weniger effizient für Photosensibilisatoren in welchen der angeregte Zustand eine kurze Lebenszeit aufweist. Während für die Triade mit dem verbrückten Pd(II)-PDM-Komplex als PS, die CR von CSS_2 schneller ist als seine Bildung, ist die Lebensdauer von CSS_2 im verlängerten Anlog deutlich höher und CSS_2 kann klar nachgewiesen werden. Obwohl die Spin-Chemie der Bisdipyrrinato- und Porphodimethenato-Triaden weniger gut untersucht wurden, ergab die Analyse der durchgeführten Magnetfeld-abhängigen Messung der CR-Kinetik Ergebnisse, die gut mit den Befunden für die cyclometallierten Triaden übereinstimmen. Weiterhin konnte der MFE genutzt werden um die Quantenausbeute der Ladungstrennung und die Identität der CSSs eingehender zu untersuchen.

In beiden Teilen dieser Arbeit konnte der Einfluss des Photosensibilisators auf die Photophysik und Spin-Chemie der Triaden gezeigt werden. Während die CS direkt vom PS abhängt, ist dieser normalerweise nicht direkt am finalen CSS beteiligt. Dennoch kann der PS die CR und Spin-Chemie des ladungsgetrennten Zustandes indirekt beeinflussen, da er die elektronische Wechselwirkung zwischen Donor und Akzeptor sowie die Struktur der Triaden bestimmt.

10 Appendix

List of Publications and conference contributions

1. "Photoinduced Dynamics of Bis-dipyrrinato-palladium(II) and Porphodimethenato-palladium(II) Complexes: Governing Near Infrared Phosphorescence by Structural Restriction"

Stefan Riese, M. Holzapfel, A. Schmiedel, I. Gert, D. Schmidt, F. Würthner, C. Lambert

Inorg. Chem., **2018***, 57,* 12480-12488.

2. "Nanoviscosity Effect on the Spin Chemistry of an Electron Donor/Pt-Complex /Electron Acceptor Triad - Classical and Quantum Kinetics Interpretation"

Stefan Riese, L. Mungenast, A. Schmiedel, M. Holzapfel, N. Lukzen, U. Steiner, C. Lambert

Mol. Phys., **2018**, *116*, DOI: 10.1080/00268976.2018.1511867

3. "Facile Synthesis and Photophysics of Graphene Quantum Dots"

A. Ojha, B. Ahmed, S. Kumar, F Hirsch, S. Riese, I. Fischer

J. Photochem. Photobiol. A, **2018**, *634*, 671-678

Conference Contributions:

1. Oral presentations:

1.1 Conjugated Oligomers and Polymers, September **2015**, Würzburg, Germany.

1.2 XXVI IUPAC Symposium on Photochemistry, April **2016**, Osaka, Japan, **JPC Student Oral Presentation Award winner**.

1.3 GRK 2112 – Molecular biradicals: Structure, Properties and Reactivity, March **2018**, Würzburg, Germany

2. Posters:

2.1 XXV IUPAC Symposium on Photochemistry, July **2014**, Bordeaux, France.

2.2 Solar Technologies Go Hybrid Workshop, March **2015**, Kloster Banz, Germany.

2.3 21th International Symposium on the Photochemistry and Photophysics of Coordination Compounds (ISPPCC), July **2015**, Kraków, Poland.

2.4 GDCh 25. Lecture Conference on Photochemistry, September **2016**, Jena, Germany.

2.5 15th International Symposium on Spin and Magnetic Field Effects in Chemistry and Related Phenomena, October **2017**, Schluchsee, Germany.

MatLab-Script

```
function [x,resnorm,residual,exitflag,output] = Difg(xo,Mx,My)
options     =     optimset('Display',     'iter','TolFun',2E-30,'TolX',2E-
30,'Algorithm',{'levenberg-
marquardt',.001},'MaxIter',1000,'MaxFunEvals',10000);
[x,resnorm,residual,exitflag,output]=
lsqcurvefit(@nestedfun1,xo,Mx,My,[],[],options);
    function output = nestedfun1(x,Mx)

        x(1:16,2)=4e7;
        x(1:16,3)= x(1,3);
        x(1:16,4)=0;

        k=x;

        o=length(Mx(1,:));

        for b=1:o
            l(b) = find(Mx(:,b)>0,1,'last');
        end

        function dy = ode1(t,y)
        dy =zeros(4,1);
dy(1)=-k(1,3)*y(1)-k(1,1)*y(1)+k(1,1)*y(4)+k(1,1)*y(3)-k(1,1)*y(1)-
k(1,2)*y(1)+k(1,2)*y(2);
dy(2)=-k(1,4)*y(2)-k(1,1)*y(2)-k(1,1)*y(2)+k(1,1)*y(3)+k(1,1)*y(4)-
k(1,2)*y(2)+k(1,2)*y(1);
dy(3)=-k(1,4)*y(3)-k(1,1)*y(3)-k(1,1)*y(3)+k(1,1)*y(2)+k(1,1)*y(1);
dy(4)=-k(1,4)*y(4)-k(1,1)*y(4)-k(1,1)*y(4)+k(1,1)*y(2)+k(1,1)*y(1);
        end
        function dy = ode2(t,y)
            dy =zeros(4,1);
dy(1)=-k(2,3)*y(1)-k(2,1)*y(1)+k(2,1)*y(4)+k(2,1)*y(3)-k(2,1)*y(1)-
k(2,2)*y(1)+k(2,2)*y(2);
dy(2)=-k(2,4)*y(2)-k(2,1)*y(2)-k(2,1)*y(2)+k(2,1)*y(3)+k(2,1)*y(4)-
k(2,2)*y(2)+k(2,2)*y(1);
dy(3)=-k(2,4)*y(3)-k(2,1)*y(3)-k(2,1)*y(3)+k(2,1)*y(2)+k(2,1)*y(1);
dy(4)=-k(2,4)*y(4)-k(2,1)*y(4)-k(2,1)*y(4)+k(2,1)*y(2)+k(2,1)*y(1);
        end
        function dy = ode3(t,y)
            dy =zeros(4,1);
dy(1)=-k(3,3)*y(1)-k(3,1)*y(1)+k(3,1)*y(4)+k(3,1)*y(3)-k(3,1)*y(1)-
k(3,2)*y(1)+k(3,2)*y(2);
dy(2)=-k(3,4)*y(2)-k(3,1)*y(2)-k(3,1)*y(2)+k(3,1)*y(3)+k(3,1)*y(4)-
k(3,2)*y(2)+k(3,2)*y(1);
dy(3)=-k(3,4)*y(3)-k(3,1)*y(3)-k(3,1)*y(3)+k(3,1)*y(2)+k(3,1)*y(1);
dy(4)=-k(3,4)*y(4)-k(3,1)*y(4)-k(3,1)*y(4)+k(3,1)*y(2)+k(3,1)*y(1);
        end
        function dy = ode4(t,y)
            dy =zeros(4,1);
dy(1)=-k(4,3)*y(1)-k(4,1)*y(1)+k(4,1)*y(4)+k(4,1)*y(3)-k(4,1)*y(1)-
k(4,2)*y(1)+k(4,2)*y(2);
dy(2)=-k(4,4)*y(2)-k(4,1)*y(2)-k(4,1)*y(2)+k(4,1)*y(3)+k(4,1)*y(4)-
k(4,2)*y(2)+k(4,2)*y(1);
dy(3)=-k(4,4)*y(3)-k(4,1)*y(3)-k(4,1)*y(3)+k(4,1)*y(2)+k(4,1)*y(1);
dy(4)=-k(4,4)*y(4)-k(4,1)*y(4)-k(4,1)*y(4)+k(4,1)*y(2)+k(4,1)*y(1);
        end
        function dy = ode5(t,y)
            dy =zeros(4,1);
```

```
dy(1)=-k(5,3)*y(1)-k(5,1)*y(1)+k(5,1)*y(4)+k(5,1)*y(3)-k(5,1)*y(1)-
k(5,2)*y(1)+k(5,2)*y(2);
dy(2)=-k(5,4)*y(2)-k(5,1)*y(2)-k(5,1)*y(2)+k(5,1)*y(3)+k(5,1)*y(4)-
k(5,2)*y(2)+k(5,2)*y(1);
dy(3)=-k(5,4)*y(3)-k(5,1)*y(3)-k(5,1)*y(3)+k(5,1)*y(2)+k(5,1)*y(1);
dy(4)=-k(5,4)*y(4)-k(5,1)*y(4)-k(5,1)*y(4)+k(5,1)*y(2)+k(5,1)*y(1);
        end
        function dy = ode6(t,y)
            dy =zeros(4,1);
dy(1)=-k(6,3)*y(1)-k(6,1)*y(1)+k(6,1)*y(4)+k(6,1)*y(3)-k(6,1)*y(1)-
k(6,2)*y(1)+k(6,2)*y(2);
dy(2)=-k(6,4)*y(2)-k(5,1)*y(2)-k(6,1)*y(2)+k(6,1)*y(3)+k(6,1)*y(4)-
k(6,2)*y(2)+k(6,2)*y(1);
dy(3)=-k(6,4)*y(3)-k(6,1)*y(3)-k(6,1)*y(3)+k(6,1)*y(2)+k(6,1)*y(1);
dy(4)=-k(6,4)*y(4)-k(6,1)*y(4)-k(6,1)*y(4)+k(6,1)*y(2)+k(6,1)*y(1);
        end
        function dy = ode7(t,y)
            dy =zeros(4,1);
dy(1)=-k(7,3)*y(1)-k(7,1)*y(1)+k(7,1)*y(4)+k(7,1)*y(3)-k(7,1)*y(1)-
k(7,2)*y(1)+k(7,2)*y(2);
dy(2)=-k(7,4)*y(2)-k(7,1)*y(2)-k(7,1)*y(2)+k(7,1)*y(3)+k(7,1)*y(4)-
k(7,2)*y(2)+k(7,2)*y(1);
dy(3)=-k(7,4)*y(3)-k(7,1)*y(3)-k(7,1)*y(3)+k(7,1)*y(2)+k(7,1)*y(1);
dy(4)=-k(7,4)*y(4)-k(7,1)*y(4)-k(7,1)*y(4)+k(7,1)*y(2)+k(7,1)*y(1);
        end
        function dy = ode8(t,y)
            dy =zeros(4,1);
dy(1)=-k(8,3)*y(1)-k(8,1)*y(1)+k(8,1)*y(4)+k(8,1)*y(3)-k(8,1)*y(1)-
k(8,2)*y(1)+k(8,2)*y(2);
dy(2)=-k(8,4)*y(2)-k(8,1)*y(2)-k(8,1)*y(2)+k(8,1)*y(3)+k(8,1)*y(4)-
k(8,2)*y(2)+k(8,2)*y(1);
dy(3)=-k(8,4)*y(3)-k(8,1)*y(3)-k(8,1)*y(3)+k(8,1)*y(2)+k(8,1)*y(1);
dy(4)=-k(8,4)*y(4)-k(8,1)*y(4)-k(8,1)*y(4)+k(8,1)*y(2)+k(8,1)*y(1);
        end
        function dy = ode9(t,y)
            dy =zeros(4,1);
dy(1)=-k(9,3)*y(1)-k(9,1)*y(1)+k(9,1)*y(4)+k(9,1)*y(3)-k(9,1)*y(1)-
k(9,2)*y(1)+k(9,2)*y(2);
dy(2)=-k(9,4)*y(2)-k(9,1)*y(2)-k(9,1)*y(2)+k(9,1)*y(3)+k(9,1)*y(4)-
k(9,2)*y(2)+k(9,2)*y(1);
dy(3)=-k(9,4)*y(3)-k(9,1)*y(3)-k(9,1)*y(3)+k(9,1)*y(2)+k(9,1)*y(1);
dy(4)=-k(9,4)*y(4)-k(9,1)*y(4)-k(9,1)*y(4)+k(9,1)*y(2)+k(9,1)*y(1);
        end
        function dy = ode10(t,y)
            dy =zeros(4,1);
dy(1)=-k(10,3)*y(1)-k(10,1)*y(1)+k(10,1)*y(4)+k(10,1)*y(3)-k(10,1)*y(1)-
k(10,2)*y(1)+k(10,2)*y(2);
dy(2)=-k(10,4)*y(2)-k(10,1)*y(2)-k(10,1)*y(2)+k(10,1)*y(3)+k(10,1)*y(4)-
k(10,2)*y(2)+k(10,2)*y(1);
dy(3)=-k(10,4)*y(3)-k(10,1)*y(3)-k(10,1)*y(3)+k(10,1)*y(2)+k(10,1)*y(1);
dy(4)=-k(10,4)*y(4)-k(10,1)*y(4)-k(10,1)*y(4)+k(10,1)*y(2)+k(10,1)*y(1);
        end
        function dy = ode11(t,y)
            dy =zeros(4,1);
dy(1)=-k(11,3)*y(1)-k(11,1)*y(1)+k(11,1)*y(4)+k(11,1)*y(3)-k(11,1)*y(1)-
k(11,2)*y(1)+k(11,2)*y(2);
dy(2)=-k(11,4)*y(2)-k(11,1)*y(2)-k(11,1)*y(2)+k(11,1)*y(3)+k(11,1)*y(4)-
k(11,2)*y(2)+k(11,2)*y(1);
dy(3)=-k(11,4)*y(3)-k(11,1)*y(3)-k(11,1)*y(3)+k(11,1)*y(2)+k(11,1)*y(1);
dy(4)=-k(11,4)*y(4)-k(11,1)*y(4)-k(11,1)*y(4)+k(11,1)*y(2)+k(11,1)*y(1);
        end
        function dy = ode12(t,y)
```

```
            dy =zeros(4,1);
dy(1)=-k(12,3)*y(1)-k(12,1)*y(1)+k(12,1)*y(4)+k(12,1)*y(3)-k(12,1)*y(1)-
k(12,2)*y(1)+k(12,2)*y(2);
dy(2)=-k(12,4)*y(2)-k(12,1)*y(2)-k(12,1)*y(2)+k(12,1)*y(3)+k(12,1)*y(4)-
k(12,2)*y(2)+k(12,2)*y(1);
dy(3)=-k(12,4)*y(3)-k(12,1)*y(3)-k(12,1)*y(3)+k(12,1)*y(2)+k(12,1)*y(1);
dy(4)=-k(12,4)*y(4)-k(12,1)*y(4)-k(12,1)*y(4)+k(12,1)*y(2)+k(12,1)*y(1);
        end
        function dy = ode13(t,y)
            dy =zeros(4,1);
dy(1)=-k(13,3)*y(1)-k(13,1)*y(1)+k(13,1)*y(4)+k(13,1)*y(3)-k(13,1)*y(1)-
k(13,2)*y(1)+k(13,2)*y(2);
dy(2)=-k(13,4)*y(2)-k(13,1)*y(2)-k(13,1)*y(2)+k(13,1)*y(3)+k(13,1)*y(4)-
k(13,2)*y(2)+k(13,2)*y(1);
dy(3)=-k(13,4)*y(3)-k(13,1)*y(3)-k(13,1)*y(3)+k(13,1)*y(2)+k(13,1)*y(1);
dy(4)=-k(13,4)*y(4)-k(13,1)*y(4)-k(13,1)*y(4)+k(13,1)*y(2)+k(13,1)*y(1);
        end
              function dy = ode14(t,y)
            dy =zeros(4,1);
dy(1)=-k(14,3)*y(1)-k(14,1)*y(1)+k(14,1)*y(4)+k(14,1)*y(3)-k(14,1)*y(1)-
k(14,2)*y(1)+k(14,2)*y(2);
dy(2)=-k(14,4)*y(2)-k(14,1)*y(2)-k(14,1)*y(2)+k(14,1)*y(3)+k(14,1)*y(4)-
k(14,2)*y(2)+k(14,2)*y(1);
dy(3)=-k(14,4)*y(3)-k(14,1)*y(3)-k(14,1)*y(3)+k(14,1)*y(2)+k(14,1)*y(1);
dy(4)=-k(14,4)*y(4)-k(14,1)*y(4)-k(14,1)*y(4)+k(14,1)*y(2)+k(14,1)*y(1);
        end
        function dy = ode15(t,y)
            dy =zeros(4,1);
dy(1)=-k(15,3)*y(1)-k(15,1)*y(1)+k(15,1)*y(4)+k(15,1)*y(3)-k(15,1)*y(1)-
k(15,2)*y(1)+k(15,2)*y(2);
dy(2)=-k(15,4)*y(2)-k(15,1)*y(2)-k(15,1)*y(2)+k(15,1)*y(3)+k(15,1)*y(4)-
k(15,2)*y(2)+k(15,2)*y(1);
dy(3)=-k(15,4)*y(3)-k(15,1)*y(3)-k(15,1)*y(3)+k(15,1)*y(2)+k(15,1)*y(1);
dy(4)=-k(15,4)*y(4)-k(15,1)*y(4)-k(15,1)*y(4)+k(15,1)*y(2)+k(15,1)*y(1);
        end
        function dy = ode16(t,y)
            dy =zeros(4,1);
dy(1)=-k(16,3)*y(1)-k(16,1)*y(1)+k(16,1)*y(4)+k(16,1)*y(3)-k(16,1)*y(1)-
k(16,2)*y(1)+k(16,2)*y(2);
dy(2)=-k(16,4)*y(2)-k(16,1)*y(2)-k(16,1)*y(2)+k(16,1)*y(3)+k(16,1)*y(4)-
k(16,2)*y(2)+k(16,2)*y(1);
dy(3)=-k(16,4)*y(3)-k(16,1)*y(3)-k(16,1)*y(3)+k(16,1)*y(2)+k(16,1)*y(1);
dy(4)=-k(16,4)*y(4)-k(16,1)*y(4)-k(16,1)*y(4)+k(16,1)*y(2)+k(16,1)*y(1);
        end


        ode_options = odeset('OutputFcn',@odeplot,'Stats', 'on');
        odes = {@ode1, @ode2, @ode3, @ode4, @ode5, @ode6, @ode7, @ode8,
@ode9, @ode10, @ode11, @ode12, @ode13, @ode14, @ode15, @ode16};
        output = zeros(size(Mx));
        parfor a = 1:length(odes)
            [t,y] = ode23(odes {a},Mx(:,a),[0.25 0.25 0.25 0.25]);
            output(:,a) = sum(y, 2);
        end

    end

Eo=nestedfun1(x,Mx);
for q=1:16
p(q)=length(Eo(:,q));
end
display(p)
```

```
display(l)

figure
cmap=colormap(jet(o))
for w=1:16
plot(Mx(:,w),My(:,w),'color',cmap(w,:),'LineStyle','.');
hold on
plot(Mx(:,w),Eo(:,w),'color',cmap(w,:),'LineWidth',1);

end
xlabel('t/s')
ylabel('intensity a.u.')
axis([0 1E-5 0 1])
hold off


for u=1:16
    AusgabeD(:,u*2-1)=Mx(:,u);
    AusgabeD(:,u*2)=My(:,u);
end

for u=1:16
    AusgabeF(:,u*2-1)=Mx(:,u);
    AusgabeF(:,u*2)=Eo(:,u);
end


dlmwrite('xo.txt',x,',')
dlmwrite('Datensatz.txt',AusgabeD,',')
dlmwrite('Fit.txt',AusgabeF,',')

display(resnorm)
display(output)



end
```

Single-Crystal structure coordinates

Table A1: Atomic coordinates ($\cdot 10^4$) and equivalent isotropic displacement parameters ($Å^2 \cdot 10^3$) for **Pt**. Ueq is defined as 1/3 of the trace of the orthogonalised Uij tensor.

atom	x	y	z	U_{eq}
Pt(1)	1946(1)	7906(1)	4328(1)	17(1)
Pt(2)	3114(1)	3136(1)	5588(1)	20(1)
C(1)	1699(3)	5628(10)	2905(4)	22(2)
C(2)	1367(3)	5408(10)	2161(5)	25(2)
C(3)	1033(3)	6742(10)	2054(4)	23(2)
C(4)	1159(3)	7723(10)	2753(4)	21(2)
C(5)	855(3)	8900(10)	2974(4)	22(2)
C(6)	887(2)	9367(9)	3759(4)	17(1)
C(7)	524(3)	10215(10)	4045(4)	22(2)
C(8)	658(3)	10013(11)	4852(4)	23(2)
C(9)	1110(3)	9070(10)	5039(4)	20(1)
C(10)	439(3)	9570(10)	2327(4)	22(2)
C(11)	545(3)	10467(10)	1722(4)	25(2)
C(12)	162(3)	11055(11)	1083(4)	29(2)
C(13)	-323(3)	10721(11)	1057(4)	28(2)
C(14)	-436(3)	9824(11)	1663(4)	26(2)
C(15)	-52(3)	9251(10)	2299(4)	23(2)
C(16)	2282(3)	9560(10)	6010(4)	25(2)
C(17)	2721(3)	9519(12)	6637(5)	29(2)
C(18)	3052(3)	8608(10)	6363(5)	26(2)
C(19)	2987(3)	7375(10)	5002(5)	25(2)
C(20)	3485(3)	6913(10)	5134(5)	26(2)
C(21)	3633(3)	6357(11)	4500(6)	33(2)
C(22)	3298(3)	6316(11)	3761(5)	29(2)
C(23)	2803(3)	6794(11)	3655(5)	25(2)
C(24)	2632(3)	7281(10)	4282(5)	22(2)
C(31)	3342(3)	4302(11)	7279(4)	26(2)
C(32)	3698(3)	5205(11)	7860(5)	27(2)
C(33)	4095(3)	5413(10)	7584(4)	24(2)
C(34)	3997(3)	4574(10)	6836(4)	21(2)
C(35)	4336(3)	4103(10)	6431(4)	20(1)
C(36)	4239(3)	2945(10)	5813(4)	22(2)
C(37)	4598(3)	2023(11)	5545(4)	26(2)
C(38)	4348(3)	751(11)	5053(5)	30(2)
C(39)	3849(3)	925(10)	5031(4)	25(2)
C(40)	4855(3)	4719(10)	6731(4)	20(2)
C(41)	5135(3)	4350(10)	7502(4)	23(2)
C(42)	5623(3)	4922(10)	7767(4)	25(2)
C(43)	5833(3)	5805(10)	7272(5)	27(2)
C(44)	5565(3)	6150(10)	6503(5)	25(2)
C(45)	5073(3)	5596(10)	6232(4)	22(2)

C(46)	2777(3)	1880(10)	3842(4)	24(2)
C(47)	2334(3)	1477(10)	3283(4)	25(2)
C(48)	1974(3)	1794(12)	3650(6)	37(2)
C(49)	2051(3)	3184(11)	5020(5)	33(2)
C(50)	1556(3)	3314(13)	4939(6)	37(2)
C(51)	1425(4)	4244(13)	5495(5)	40(2)
C(52)	1771(3)	5082(11)	6077(5)	27(2)
C(53)	2272(3)	4896(10)	6153(5)	26(2)
C(54)	2435(3)	3869(11)	5644(5)	26(2)
N(1)	1582(2)	6991(8)	3267(3)	19(1)
N(2)	1252(2)	8705(8)	4403(3)	17(1)
N(3)	2347(2)	8692(9)	5404(4)	22(1)
N(4)	2821(2)	8114(9)	5611(4)	24(1)
N(5)	3509(2)	3973(8)	6665(4)	21(1)
N(6)	3780(2)	2226(9)	5467(4)	23(1)
N(7)	2708(2)	2378(9)	4511(4)	27(2)
N(8)	2207(2)	2372(9)	4419(4)	30(2)

Table A2: Atomic coordinates ($\cdot 10^4$) and equivalent isotropic displacement parameters ($Å^2 \cdot 10^3$) for **Pd**. Ueq is defined as 1/3 of the trace of the orthogonalised Uij tensor.

atom	x	y	z	U_{eq}
Pd(1)	3672(1)	4114(1)	3126(1)	8(1)
Cl(1)	7959(1)	3125(1)	3630(1)	49(1)
Cl(2)	7728(1)	1604(1)	3258(1)	38(1)
N(1)	3741(2)	3274(1)	4548(2)	10(1)
N(2)	2030(2)	3923(1)	2358(3)	10(1)
N(3)	5304(2)	4393(1)	3842(3)	14(1)
N(4)	5545(2)	4969(1)	3163(3)	14(1)
C(1)	4494(2)	3110(2)	5811(3)	13(1)
C(2)	4421(2)	2392(2)	6185(3)	14(1)
C(3)	3588(2)	2097(2)	5066(3)	11(1)
C(4)	3134(2)	2653(1)	4048(3)	9(1)
C(5)	2142(2)	2643(1)	2903(3)	8(1)
C(6)	1572(2)	3252(1)	2203(3)	8(1)
C(7)	403(2)	3312(2)	1502(3)	11(1)
C(8)	162(2)	4022(2)	1285(3)	13(1)
C(9)	1186(2)	4380(2)	1815(3)	11(1)
C(10)	1551(2)	1960(1)	2428(3)	10(1)
C(11)	1114(2)	1561(2)	3309(3)	13(1)
C(12)	534(3)	944(2)	2797(3)	15(1)
C(13)	387(2)	712(2)	1404(3)	14(1)
C(14)	821(3)	1106(2)	510(3)	16(1)
C(15)	1386(2)	1728(2)	1019(3)	13(1)
C(16)	3672(2)	4839(1)	1641(3)	10(1)
C(17)	2857(2)	5000(2)	331(3)	14(1)
C(18)	3020(3)	5519(2)	-594(3)	18(1)
C(19)	4014(3)	5894(2)	-217(4)	19(1)
C(20)	4861(3)	5736(2)	1049(4)	18(1)
C(21)	4679(2)	5208(2)	1927(3)	13(1)
C(22)	6637(2)	5136(2)	3726(3)	19(1)
C(23)	7114(3)	4666(2)	4812(4)	22(1)
C(24)	6257(3)	4209(2)	4848(4)	19(1)
C(25)	8288(4)	2382(2)	2786(5)	37(1)

Table A3: Atomic coordinates ($\cdot 10^4$) and equivalent isotropic displacement parameters ($Å^2 \cdot 10^3$) for **Pd(dipy)$_2$**. Ueq is defined as 1/3 of the trace of the orthogonalised Uij tensor.

atom	x	y	z	U_{eq}
Pd(1)	5000	5000	10000	8(1)
Pd(2)	5000	5000	5000	7(1)
N(1)	2934(2)	5774(2)	10922(1)	10(1)
N(2)	3935(2)	4586(2)	9093(1)	11(1)
N(3)	3655(2)	4065(2)	4780(1)	10(1)
N(4)	6518(2)	3205(2)	5031(1)	11(1)
C(1)	2465(2)	5835(2)	12025(2)	12(1)
C(2)	980(2)	6618(2)	12298(2)	15(1)
C(3)	532(2)	7058(2)	11305(2)	14(1)
C(4)	1745(2)	6504(2)	10447(2)	11(1)
C(5)	1654(2)	6418(2)	9396(2)	11(1)
C(6)	2651(2)	5454(2)	8786(2)	11(1)
C(7)	2454(2)	5022(2)	7911(2)	13(1)
C(8)	3561(2)	3873(2)	7741(2)	15(1)
C(9)	4449(2)	3642(2)	8481(2)	13(1)
C(10)	324(2)	7323(2)	9002(2)	12(1)
C(11)	108(2)	8723(2)	8804(2)	14(1)
C(12)	-1127(2)	9595(2)	8443(2)	20(1)
C(13)	-2168(2)	9077(2)	8290(2)	23(1)
C(14)	-1980(2)	7691(2)	8510(2)	21(1)
C(15)	-738(2)	6814(2)	8858(2)	16(1)
C(16)	2148(2)	4299(2)	5133(2)	12(1)
C(17)	1633(2)	3513(2)	4716(2)	13(1)
C(18)	2890(2)	2758(2)	4082(2)	11(1)
C(19)	4165(2)	3084(2)	4141(2)	9(1)
C(20)	5671(2)	2348(2)	3845(2)	10(1)
C(21)	6781(2)	2386(2)	4283(2)	10(1)
C(22)	8227(2)	1484(2)	4244(2)	14(1)
C(23)	8766(2)	1708(2)	5017(2)	18(1)
C(24)	7679(2)	2770(2)	5480(2)	14(1)
C(25)	6014(2)	1369(2)	3125(2)	9(1)
C(26)	6591(2)	-10(2)	3507(2)	13(1)
C(27)	6899(2)	-904(2)	2821(2)	16(1)
C(28)	6640(2)	-435(2)	1745(2)	15(1)
C(29)	6051(2)	932(2)	1363(2)	13(1)
C(30)	5726(2)	1827(2)	2051(2)	11(1)

Table A4: Atomic coordinates ($\cdot 10^4$) and equivalent isotropic displacement parameters ($Å^2 \cdot 10^3$) for **PdPDM**. Ueq is defined as 1/3 of the trace of the orthogonalised Uij tensor.

atom	x	y	z	U_{eq}
Pd(1)	2876(1)	3582(1)	3558(1)	14(1)
N(1)	4085(2)	3267(1)	2856(2)	17(1)
N(2)	3227(2)	4597(1)	3246(2)	18(1)
N(3)	1704(2)	3910(1)	4344(2)	16(1)
N(4)	2577(2)	2574(1)	4049(2)	17(1)
C(1)	4870(2)	3682(2)	2879(3)	19(1)
C(2)	4882(2)	4415(2)	3097(3)	19(1)
C(3)	4115(2)	4844(2)	3246(2)	19(1)
C(4)	4089(2)	5600(2)	3305(3)	21(1)
C(5)	3194(2)	5797(1)	3340(3)	21(1)
C(6)	2676(2)	5162(2)	3294(2)	18(1)
C(7)	1657(2)	5089(2)	3220(3)	19(1)
C(8)	1323(2)	4553(2)	4208(3)	18(1)
C(9)	555(2)	4611(2)	5023(3)	22(1)
C(10)	476(2)	3976(2)	5681(3)	23(1)
C(11)	1194(2)	3532(2)	5253(3)	19(1)
C(12)	1339(2)	2819(2)	5597(3)	20(1)
C(13)	1981(2)	2372(2)	5036(3)	19(1)
C(14)	2079(2)	1628(2)	5239(3)	22(1)
C(15)	2717(2)	1390(2)	4369(3)	21(1)
C(16)	3013(2)	1991(1)	3637(4)	18(1)
C(17)	3641(2)	2003(1)	2471(3)	19(1)
C(18)	4330(2)	2596(2)	2600(3)	18(1)
C(19)	5285(2)	2552(2)	2451(3)	21(1)
C(20)	5621(2)	3225(2)	2634(3)	21(1)
C(21)	1206(2)	5817(1)	3443(4)	23(1)
C(22)	1392(2)	4814(2)	1846(3)	22(1)
C(23)	3057(2)	2141(2)	1233(3)	21(1)
C(24)	4124(2)	1284(2)	2320(3)	24(1)
C(31)	5779(2)	4788(2)	3160(3)	20(1)
C(32)	6337(2)	4836(2)	2064(3)	25(1)
C(33)	7156(2)	5211(2)	2148(4)	33(1)
C(34)	7411(2)	5528(2)	3309(4)	32(1)
C(35)	6857(2)	5483(2)	4402(4)	30(1)
C(36)	6041(2)	5113(2)	4324(3)	24(1)
C(41)	676(2)	2521(2)	6567(3)	23(1)
C(42)	793(3)	2618(2)	7894(3)	31(1)
C(43)	127(3)	2390(2)	8776(3)	39(1)
C(44)	-650(2)	2074(2)	8319(4)	36(1)
C(45)	-767(2)	1969(2)	7002(4)	36(1)
C(46)	-110(2)	2190(2)	6120(3)	31(1)

Table A5: Dihedral angles between characteristic planes (see **Figure 47**) and bond lengths **of Pd(dipy)$_2$** and **PdPDM** from X-Ray Crystal Analysis and DFT Calculation (PBE1PBE functional and SDD-6-31G* Basis Set).[a]

	Pd(dipy)$_2$		**PdPDM**			**Pd(dipy)$_2$**		**PdPDM**	
dihedral angles /° between planes	**X-ray**	**DFT**	**X-ray**	**DFT**	**distances /Å**	**X-ray**	**DFT**	**X-ray**	**DFT**
1,2	145.9	148.2	171.0	167.8	Pd-N1	2.008	2.022	2.013	2.017
1,4	160.2	161.8	176.8	176.1	Pd-N2	2.015	2.029	2.002	2.009
3,4	148.4	149.0	158.0	160.2	Pd-N3			2.004	
3,6			177.1	175.4	Pd-N4			2.009	
4,5	173.1	174.9	177.3	177.8	N1-C1	1.338	1.335	1.337	1.337
6,7			167	165.0	N1-C4	1.393	1.387	1.396	1.387
7,8			139.3	140.2	C1-C2	1.408	1.411	1.421	1.418
					C2-C3	1.379	1.380	1.371	1.379
					C3-C4	1.418	1.424	1.424	1.422
					C4-C5	1.406	1.404	1.396	1.403
3,3’	180	180	173.6	173.5	C5-C6	1.399	1.403	1.399	1.403
4,9(=4’)	180	180	134.4	133.9	C6-C7	1.423	1.424	1.423	1.422
6,6’	180	180	173.6	173.5	C6-N2	1.399	1.390	1.390	1.386
8,8’	180	180	101.3	101.7	C7-C8	1.375	1.381	1.372	1.378
					C8-C9	1.409	1.411	1.417	1.418
					C9-N2	1.335	1.335	1.340	1.336
1’,2’			166.3		N3-C11			1.339	
1’,9(=4’)			172.8		N3-C14			1.391	
3’,9(=4’)			162.5		C11-C12			1.411	
3’,6’			177.0		C12-C13			1.376	
9(=4’),5’			178.2		C13-C14			1.418	
6’,7’			168.2		C14-C15			1.403	
7’,8’			138.1		C15-C16			1.389	
					C16-C17			1.421	
					C16-N4			1.392	
					C17-C18			1.369	
					C18-C19			1.424	
					C19-N4			1.340	

[a] The numbering refers to **Figure 54** in the main text.

Global analysis of fs-TA spectroscopic results

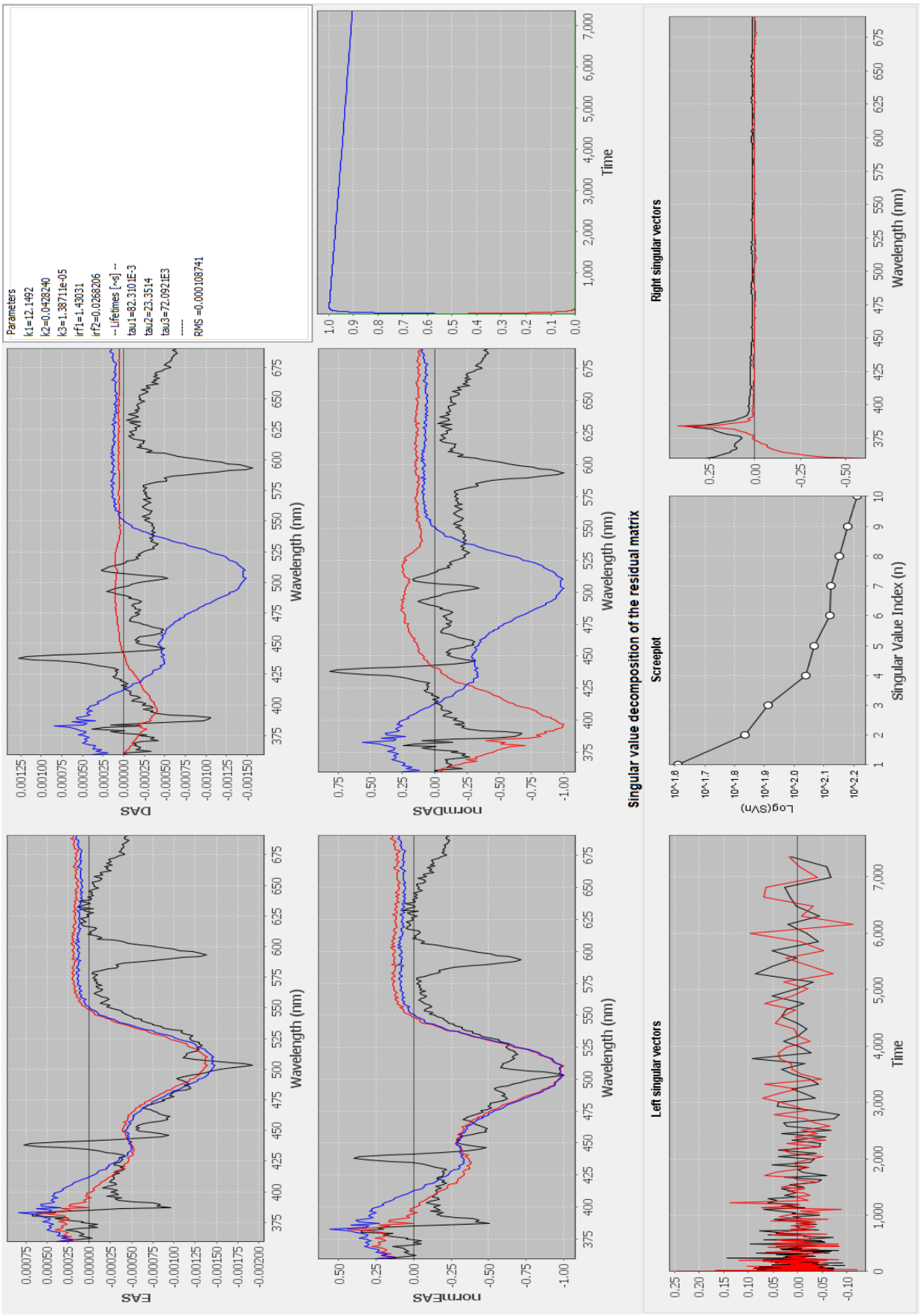

Figure A1: Global analysis of the fs-TA spectroscopy on **Pt** in THF after excitation at 19800 cm^{-1}.

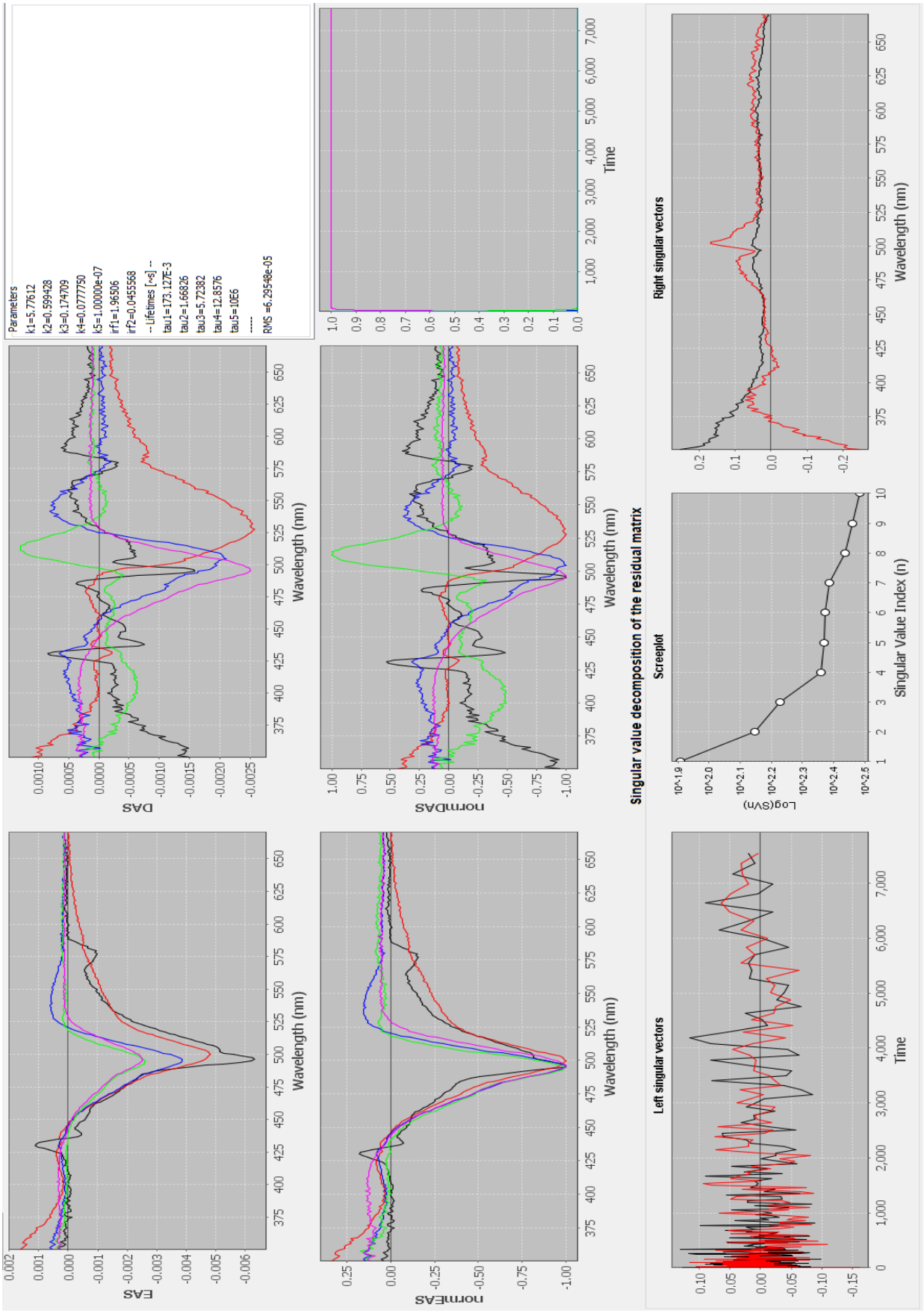

Figure A2: Global analysis of the fs-TA spectroscopy on **Pd** in THF after excitation at 20200 cm^{-1}.

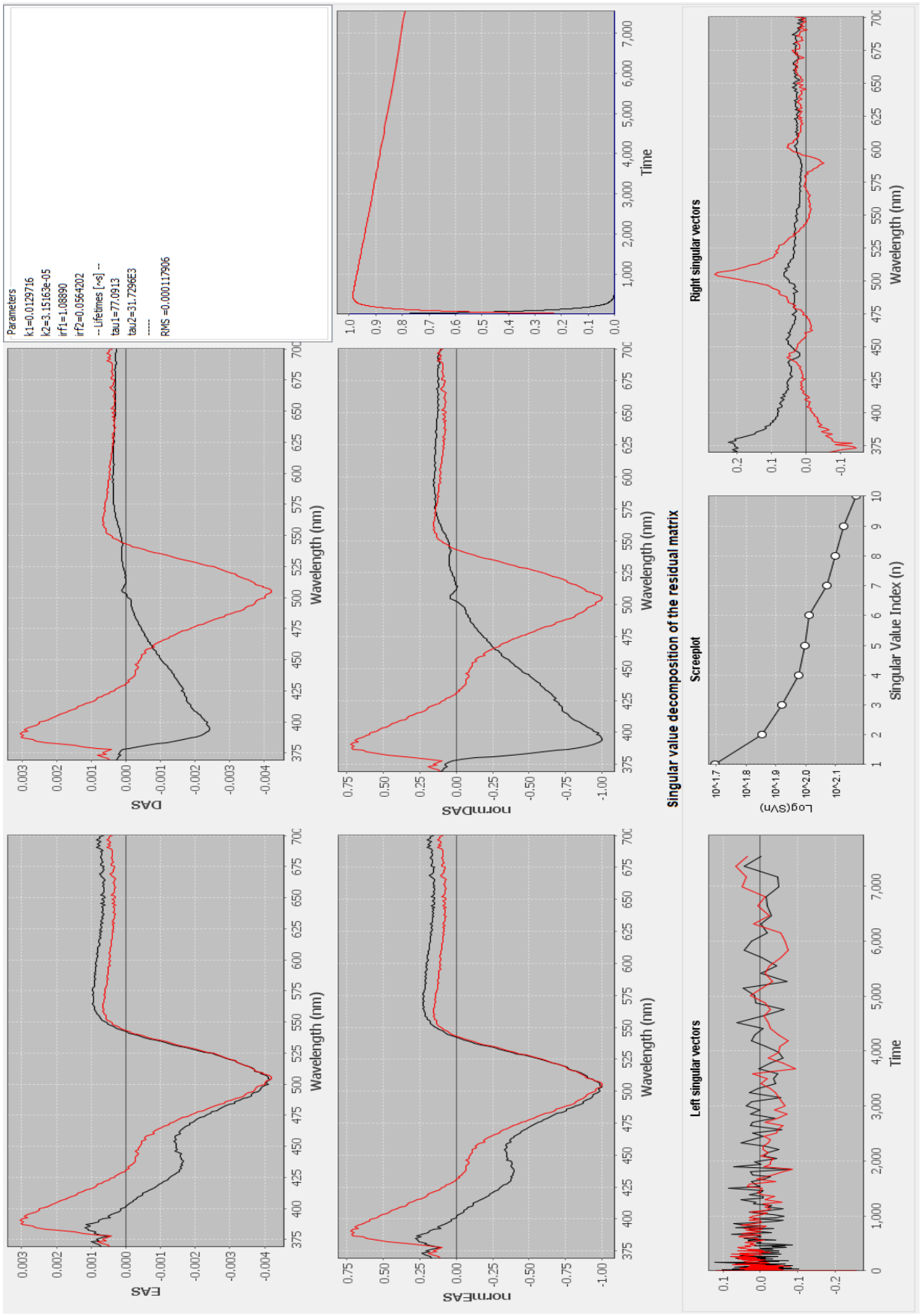

Figure A3: Global analysis of the fs-TA spectroscopy on **PtA** in THF after excitation at 19800 cm^{-1}.

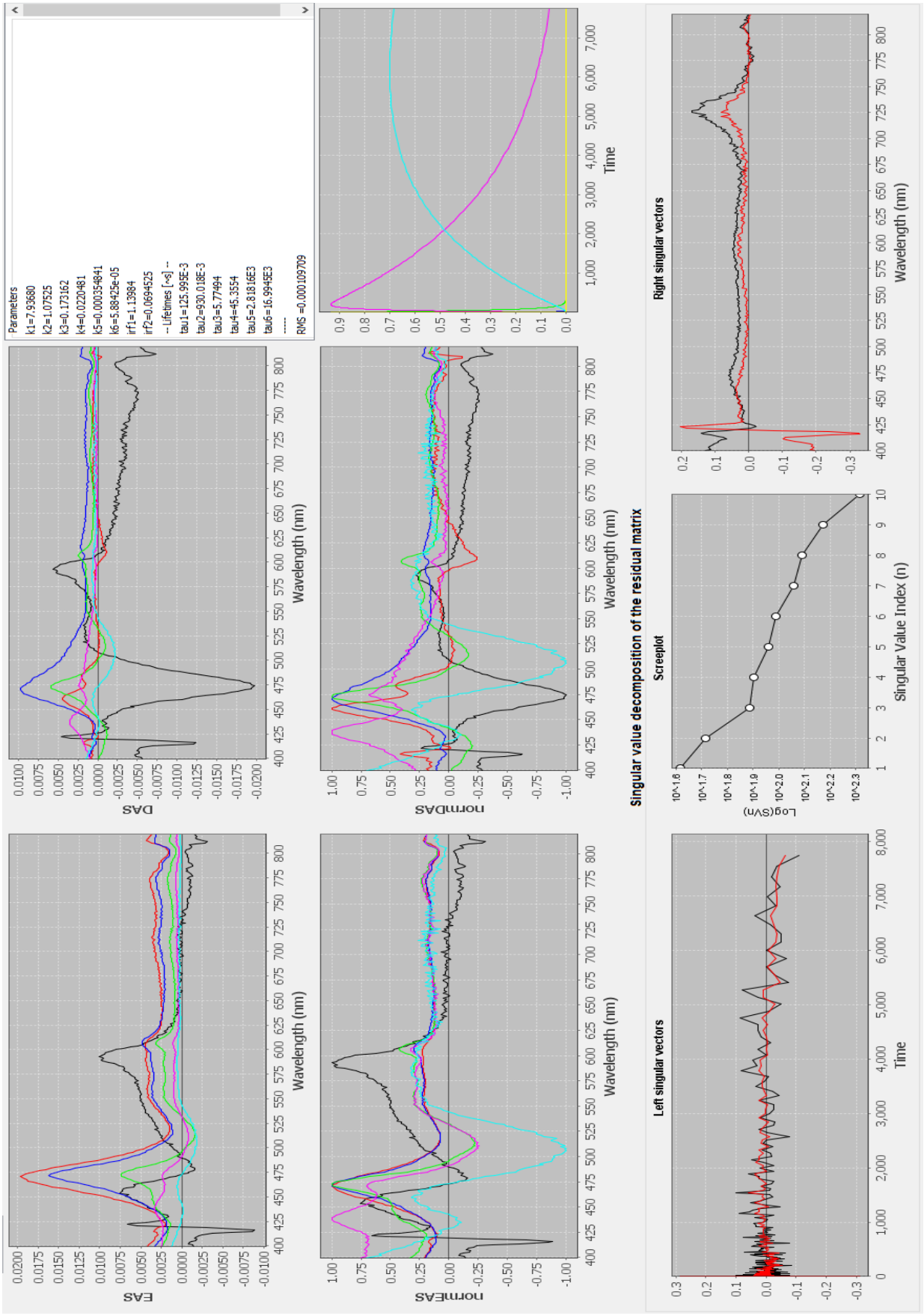

Figure A4: Global analysis of the fs-TA spectroscopy on **PtA** in THF after excitation at 26400 cm^{-1}.

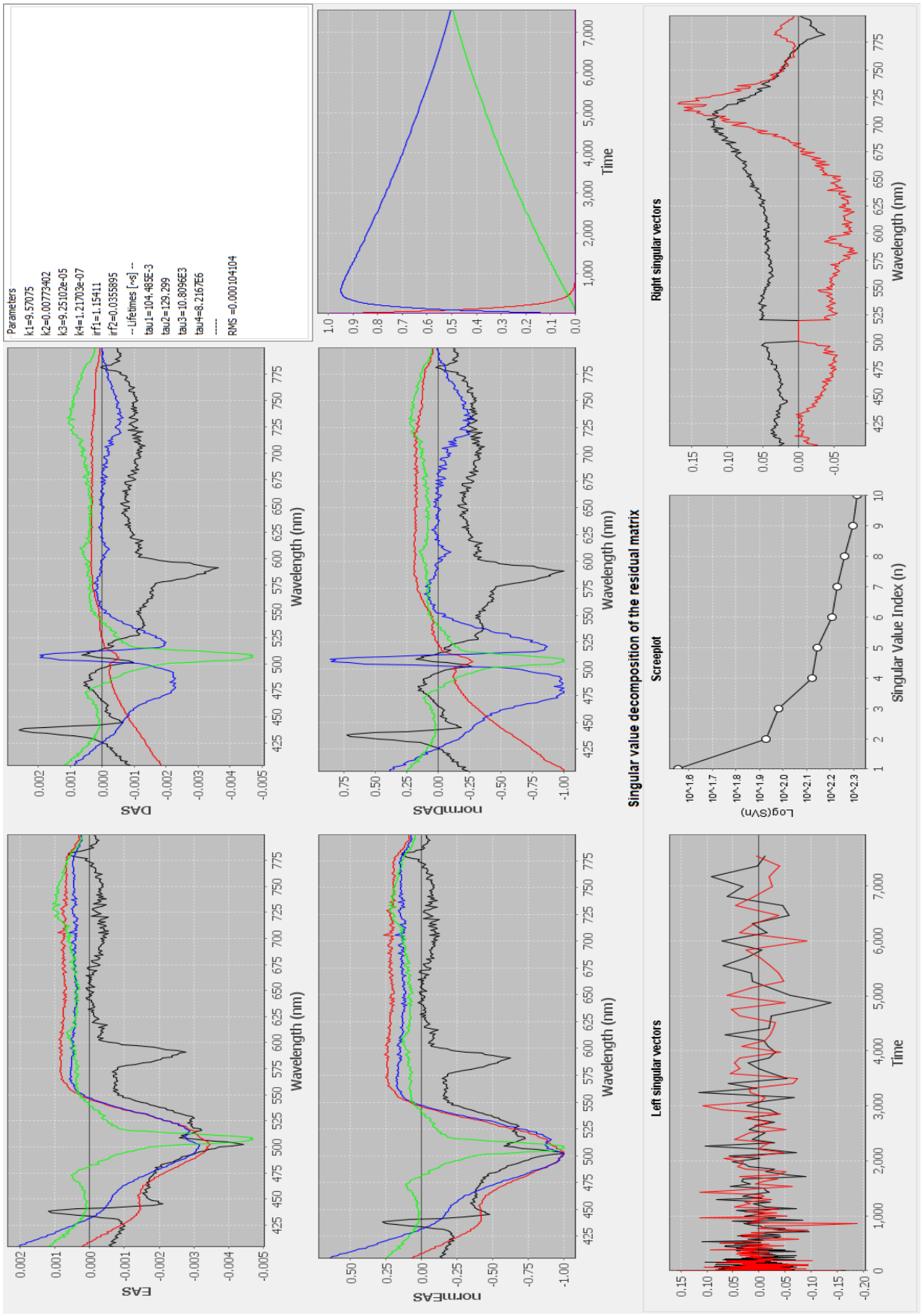

Figure A5: Global analysis of the fs-TA spectroscopy on **DPtA** in THF after excitation at 19800 cm^{-1}.

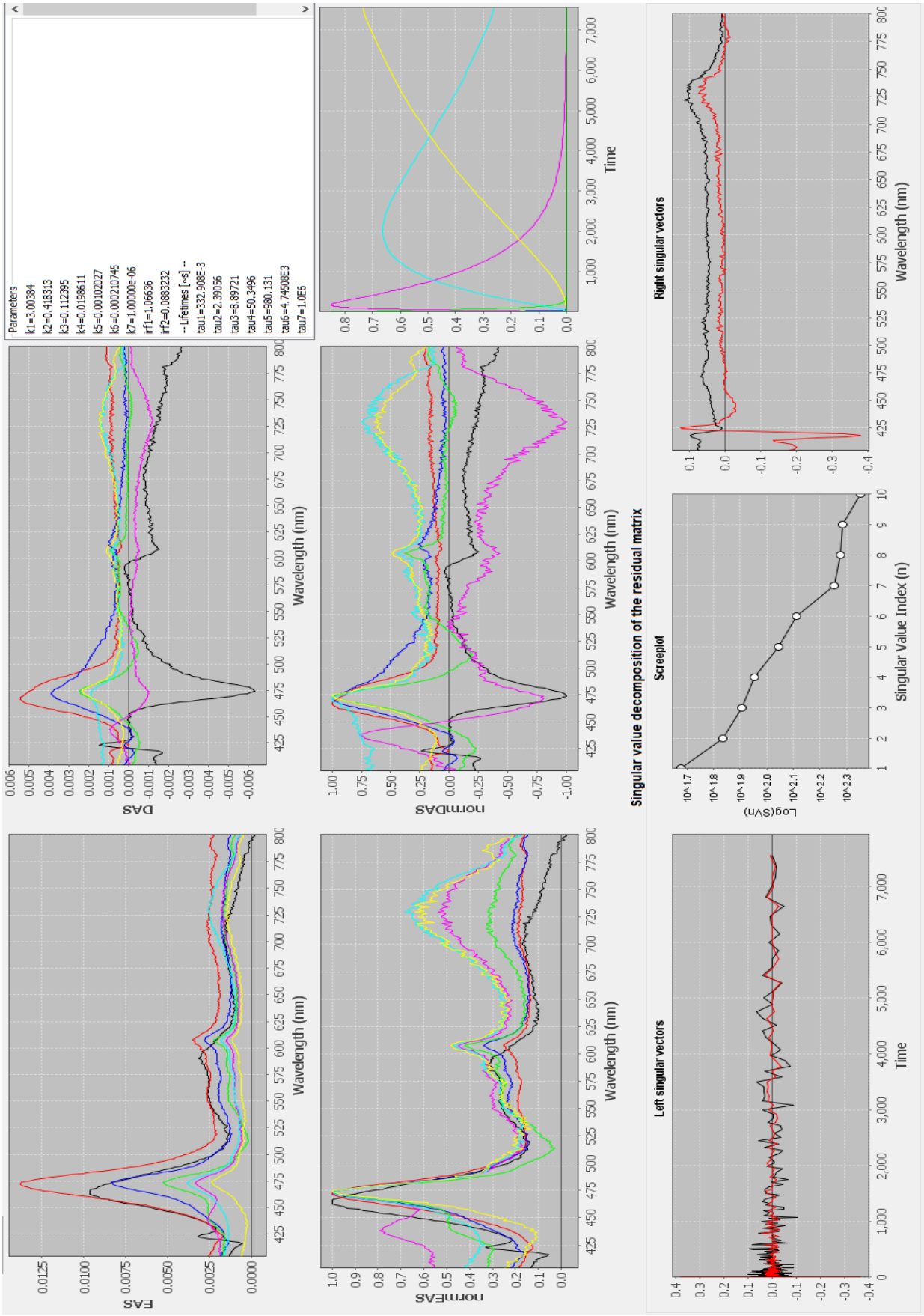

Figure A6: Global analysis of the fs-TA spectroscopy on **DPtA** in THF after excitation at 26400 cm^{-1}.

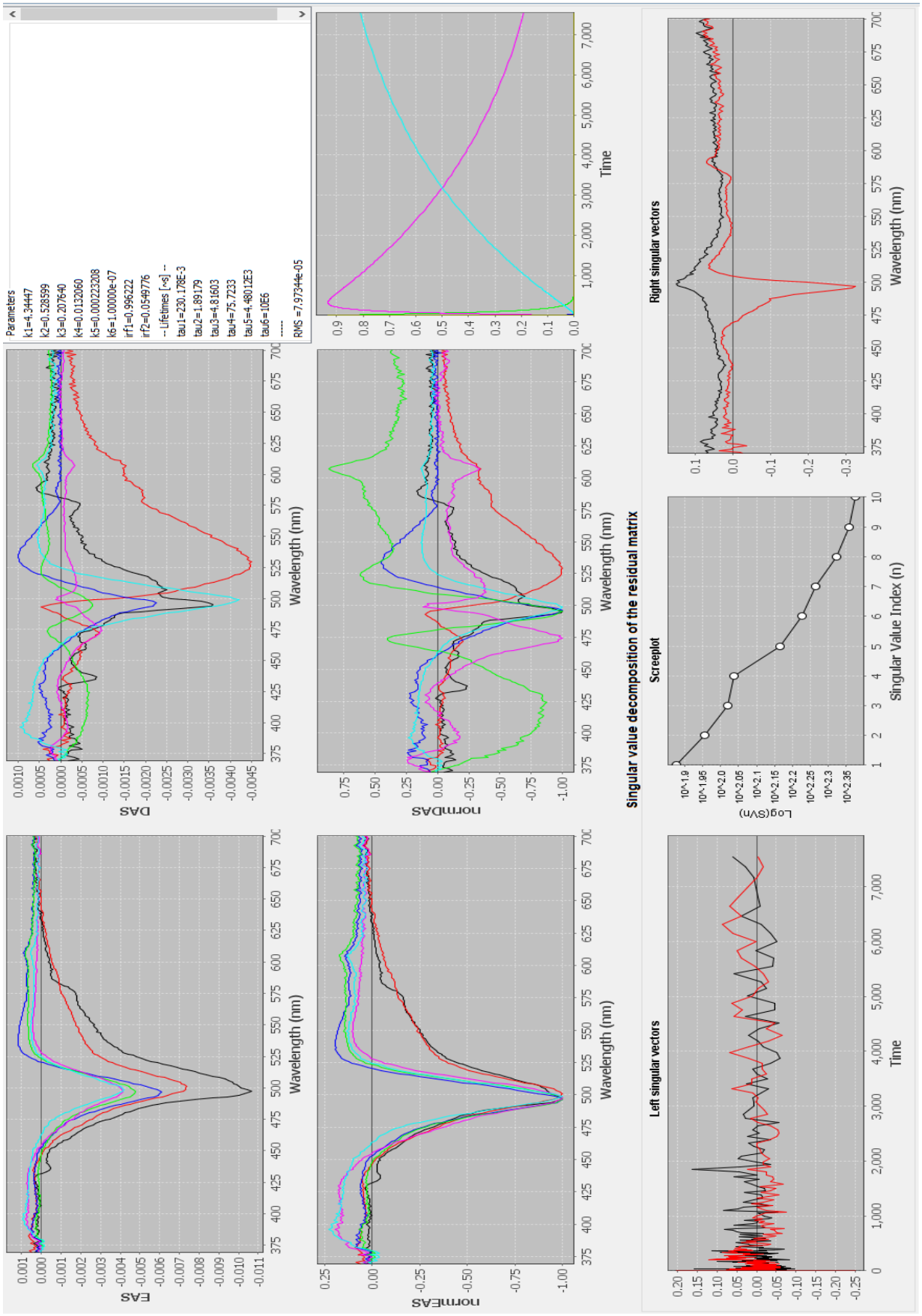

Figure A7: Global analysis of the fs-TA spectroscopy on **PdA** in THF after excitation at 20100 cm^{-1}.

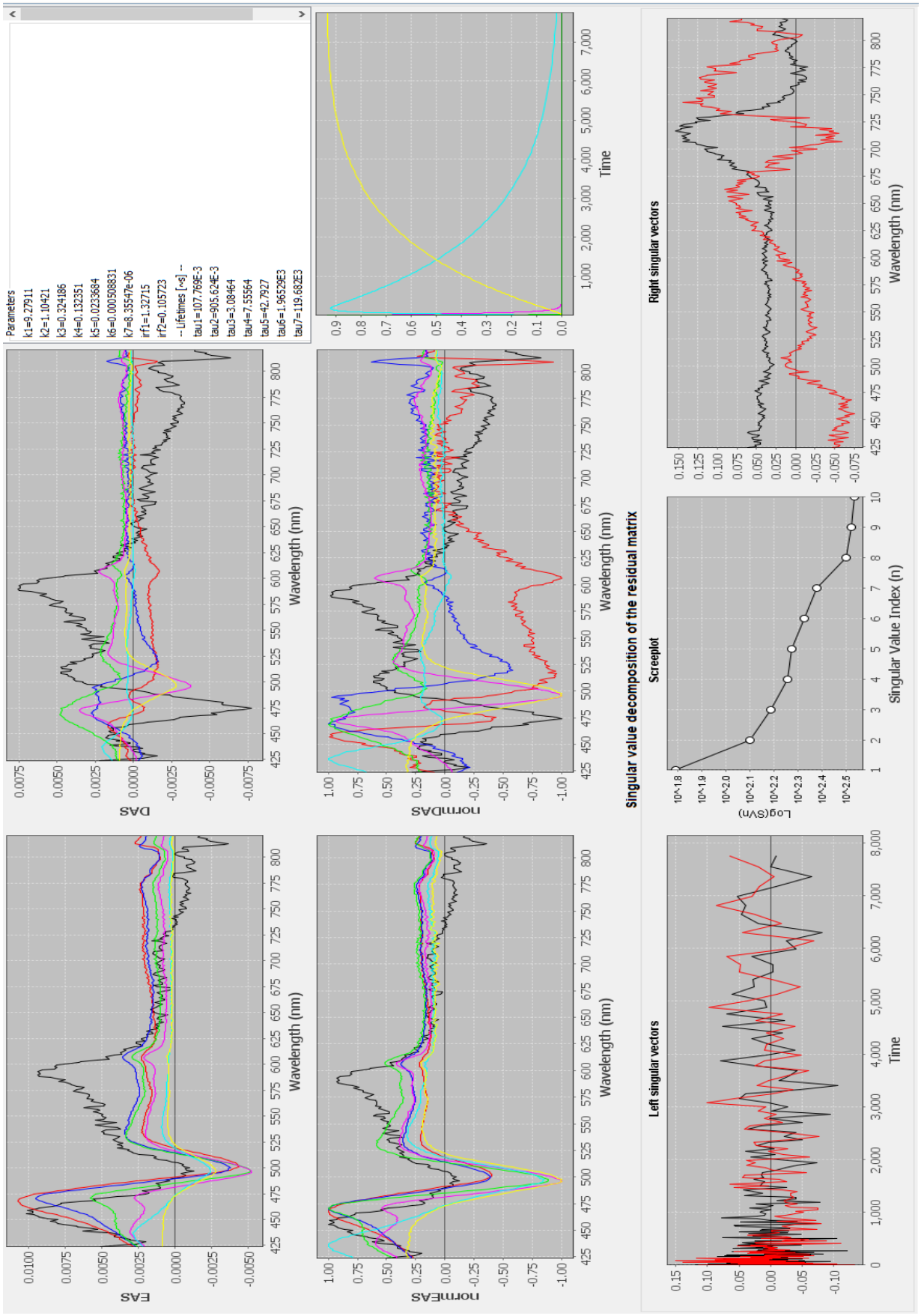

Figure A8: Global analysis of the fs-TA spectroscopy on **PdA** in THF after excitation at 26400 cm^{-1}.

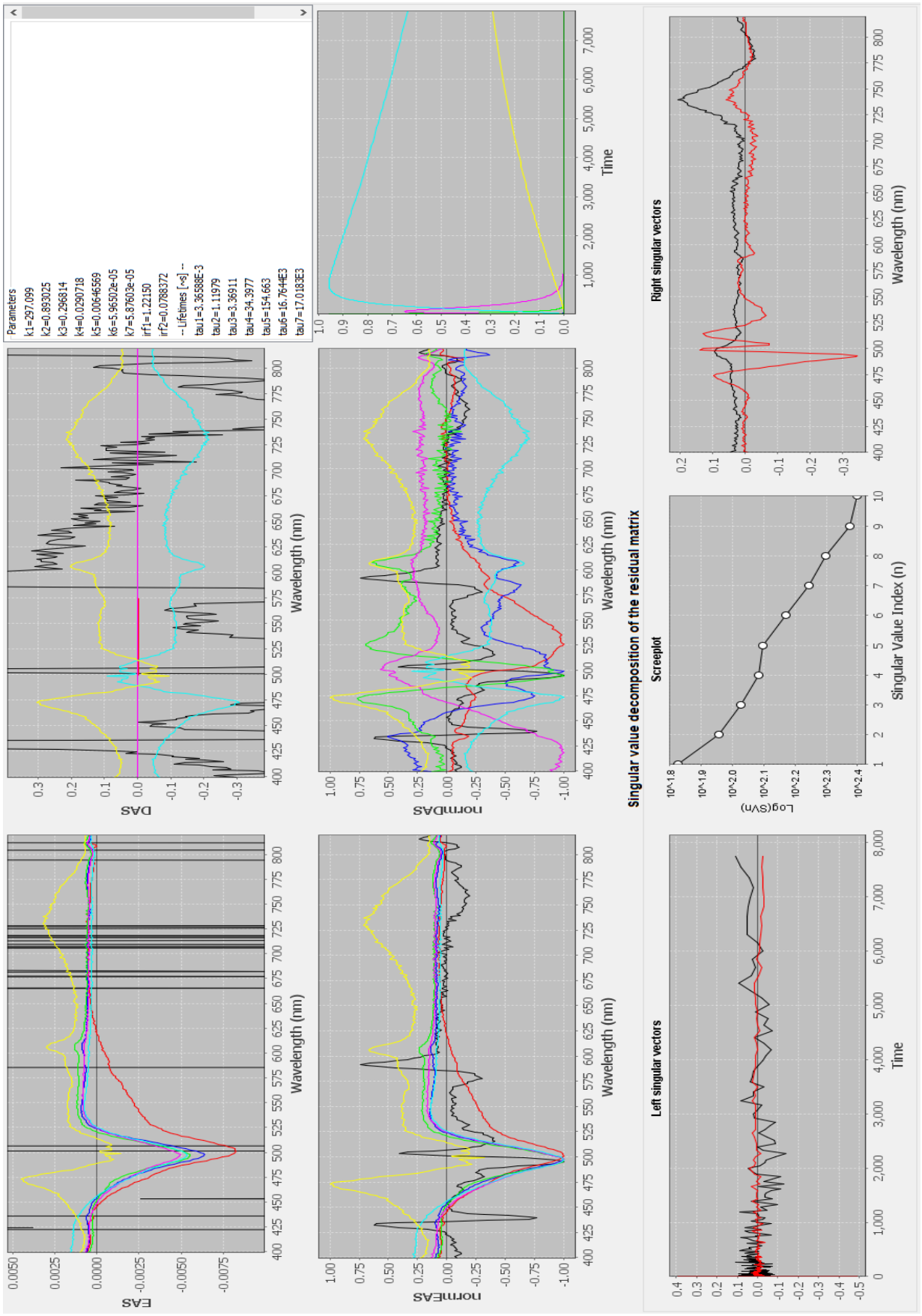

Figure A9: Global analysis of the fs-TA spectroscopy on **DPdA** in THF after excitation at 20100 cm^{-1}.

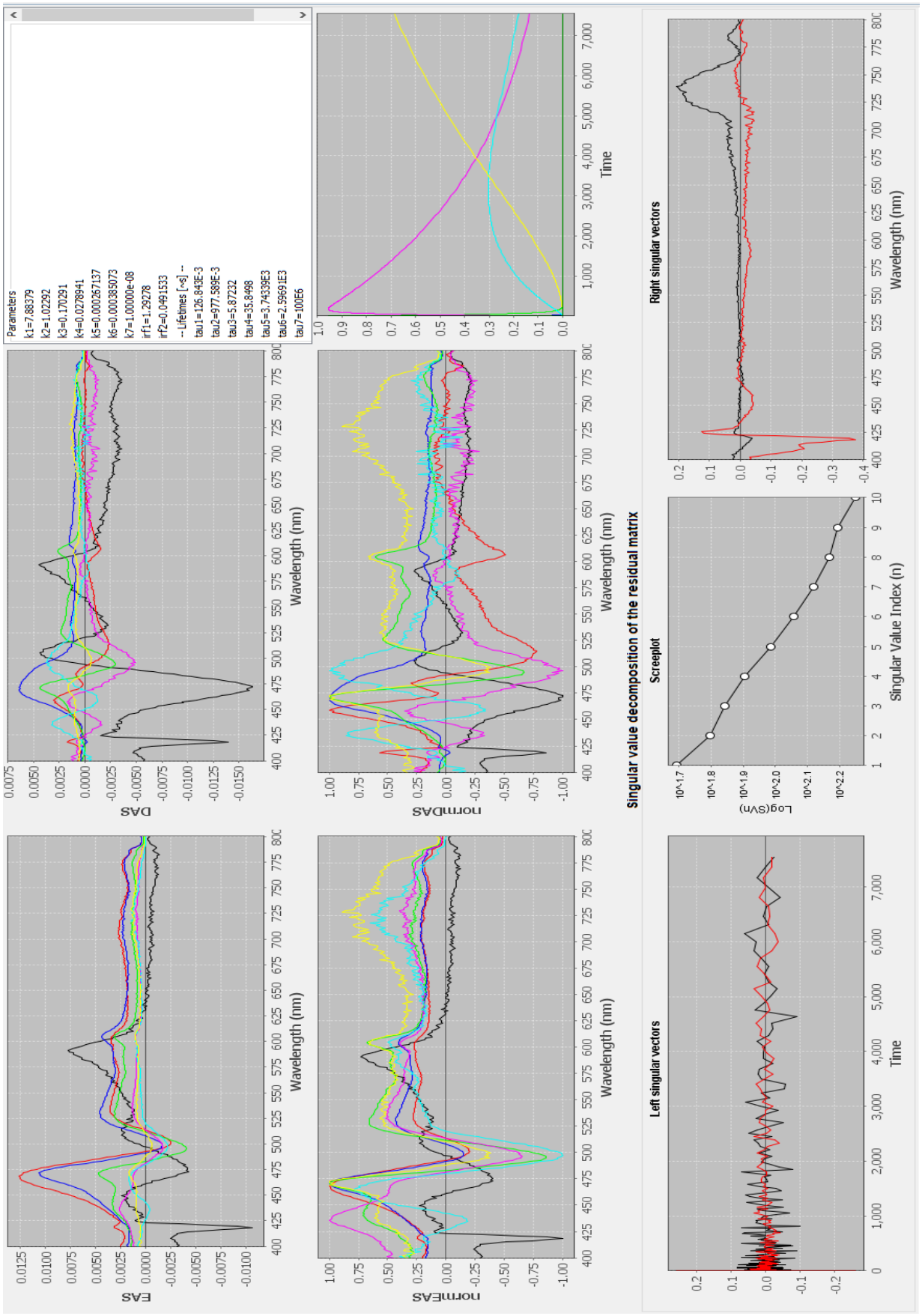

Figure A10: Global analysis of the fs-TA spectroscopy on **DPdA** in THF after excitation at 26400 cm^{-1}.

Mat-Lab-Analysis

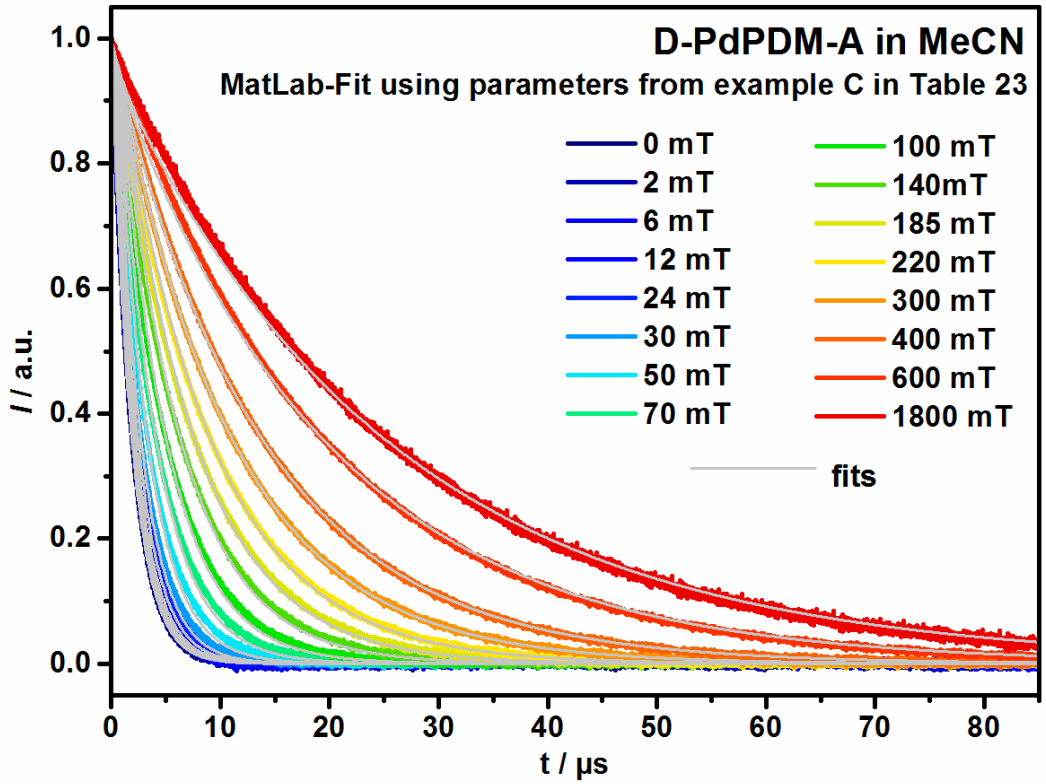

Figure A11: Theoretical decay traces of **D-PdPDM-A** in MeCN after excitation at 20100 cm^{-1} at 16 different magnetic fields and the respective analysis of the data according to equation (13). The fits were performed using script 2 given in the Appendix using the parameters given for example C in **Table 23** (chapter 4.3.3) in the main text.

Theoretical Investigation of a bimolecular deactivation of D-PdPDM-A

The possible contribution of a bimolecular reaction to the overall decay of CSS_2 was estimated as follows. As shown in **Figure 86**, the effective rate k_{eff} for the formation of a bimolecular CSS is dependent on the concentration of CSS_2 ($[CSS_2]$ and the molecules in which the charge is not separated ($[S_0]$ and $[^3LC]$). Both $[^3LC]$ and $[S_0]$ directly after excitation can be estimated from the sample concentration ($1.45 \cdot 10^{-5}$ M) and the probability of excitation (P_{ex}) using equation (33).[268-272, 283-284]

$$P_{ex} = 1 - \exp\left[-\left(\frac{E}{hc\tilde{\nu}\pi r^2}\right)\left(\frac{2302.6\varepsilon}{N_{Av}}\right)\right] \quad (33)$$

Here, h is Planck's constant ($6.63 \cdot 10^{-34}$ Js), c is the speed of light ($3.0 \cdot 10^8$ ms^{-1}) and N_{Av} is Avogadro's constant ($6.02 \cdot 10^{23}$ mol^{-1}). With the excitation energy $\tilde{\nu}$ = 2010000 m^{-1}, the extinction coefficient of the molecule at the excitation energy ε = 36800 $M^{-1}cm^{-1}$ as taken from the UV/vis absorption measurements, the radius of the excitation beam r = 0.1 cm and the energy per excitation pulse E = 1.2 mJ, a value of $P_{ex} \approx 1.0$ is obtained. Hence, nearly all molecules are excited by the excitation pulse.

In the following computations based on the kinetic scheme depicted in **Figure A12** using the free software Tenua, this was considered in the starting concentration of ^3LC (labeled $[DA^*]_0$) and the starting concentration of S_0 (labeled $[DA]_0$), which were set to $1.45 \cdot 10^{-5}$ M and $1.45 \cdot 10^{-7}$ M, respectively. Furthermore, rate constants for the charge separation from DA* to CSS_2 (k_{CS}), the deactivation of DA* to the ground state DA (k_{nr}) and the charge recombination from CSS_2 to DA (k_{CR}) were derived from the lifetimes of the involved species as estimated by the global analysis depicted in **Figure 85** and the quantum yield of charge separation of 0.66 using equations (27) and (28) introduced in chapter 4.3.2.

$$k_{CS} = \frac{1}{\tau_{GSB}} - k_{nr} \quad (27)$$

$$\Phi_{CS} = \frac{k_{CS}}{[\tau_{GSB}]^{-1}} \quad (28)$$

For an average GSB-lifetime of τ_2 = 2.5 µs, values of $k_{CS} = 2.64 \cdot 10^5$ s^{-1} and $k_{nr} = 1.36 \cdot 10^5$ s^{-1} are obtained, while k_{CR} is magnetic field dependent and is estimated to values of $k_{CR} = 8.77 \cdot 10^5$ s^{-1} at 0 mT, $k_{CR} = 1.56 \cdot 10^5$ s^{-1} at 200 mT and $k_{CR} = 5.58 \cdot 10^4$ s^{-1} at 1800 mT from τ_2 as given in **Figure 85**.

The rate constant k_{CSB} for the formation of the bimolecular CSS between D (D^+-A) and A (D-A^-) and k_{CRB} for the recombination of said bimolecular CSS to the ground state are estimated in a rough

approximation to be diffusion controlled. Therefore, k_{CSB} was chosen as $k_{CSB} \leq 1.9 \cdot 10^{10}$ s^{-1}, the diffusion controlled limit in the used solvent MeCN, while for k_{CRB} values bigger than $1.9 \cdot 10^{10}$ s^{-1} were accepted to account for the possible recombination of the bimolecular CSS from the geminate ion pair. The applied Tenua script shown below describes the reaction scheme depicted in **Figure A12**.

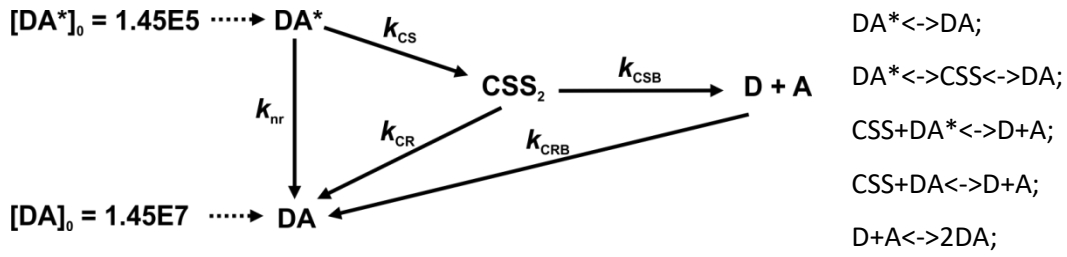

Figure A 12: Assumed reaction scheme (right) for the bimolecular deactivation of CSS_2 in **D-PdPDM-A** and theoretical description with an appropriate Tenua-script (left).

This script results in the decay kinetics depicted in **Figure A13** when considering the absorbance of the ESA associated with CSS_2 and the GSB associated with DA* at 21100 cm^{-1} as estimated from the target fits shown in **Figure 85**. All estimated values and the resulting reaction rates associated with the different fits are listed in **Table A6**.

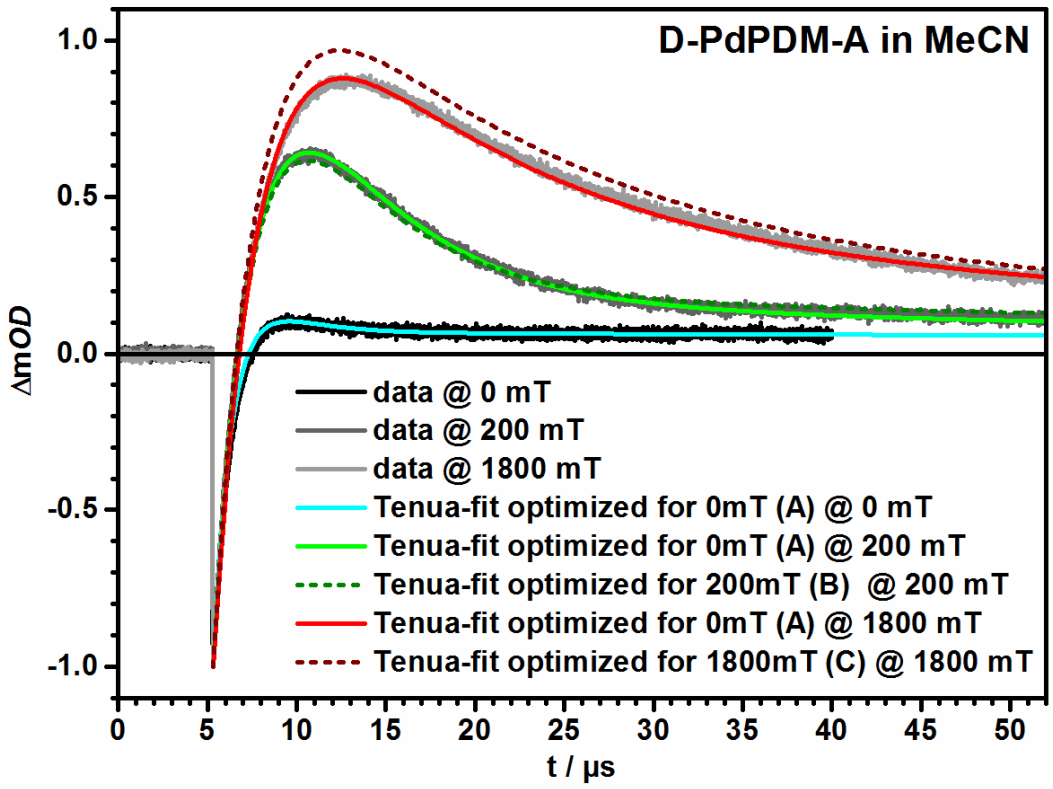

Figure A13: Observed signal intensity kinetics at 21100 cm^{-1} at 0 mT, 200 mT and 1800 mT (black to gray) and theoretical kinetics estimated using the Tenua script shown above, with the values listed in **Table A6**. Solid lines correspond to fitting conditions (A) optimized at 0 mT, while dotted lines indicate fitting conditions (B) and (C), optimized at 200 mT and 1800 mT, respectively.

Table A6: Kinetic rates associated with the simulations using the Tenua-script shown in **Figure A12** using starting concentrations of $1.45 \cdot 10^{-5}$ M for DA* and $1.45 \cdot 10^{-7}$ M for DA. Multiplication of the resulting concentration dependence of DA*, CSS and A with the absorbance of the species at 21100 cm^{-1} as estimated from the global analysis using Glotaran[a] and normalization to negative one results in the kinetic traces shown in **Figure A13**.

	B / mT	k_{nr} / s^{-1}	k_{CS} / s^{-1}	k_{CR} / s^{-1}	k_{CSB} / s^{-1}	k_{CRB} / s^{-1}
	0			$8.68 \cdot 10^5$		
(A)	200	$1.34 \cdot 10^5$	$2.66 \cdot 10^5$	$1.54 \cdot 10^5$	$2.5 \cdot 10^9$	$1 \cdot 10^{10}$
	1800			$0.56 \cdot 10^5$		
(B)	200	$1.31 \cdot 10^5$	$2.59 \cdot 10^5$	$1.62 \cdot 10^5$	$2.5 \cdot 10^9$	$1 \cdot 10^{10}$
(C)	1800	$1.22 \cdot 10^5$	$2.40 \cdot 10^5$	$0.67 \cdot 10^5$	$3 \cdot 10^9$	$1 \cdot 10^{10}$

[a] ΔmOD(DA*) = -0.013, ΔmOD(CSS+A) = 0.037

As can be seen from Figure A13 and the associated values listed in Table A6, the kinetic traces obtained by ns-TA spectroscopy can be described reasonably well with a bimolecular reaction mechanism. The reaction rates for Tenua fit (A) were optimized at 0 mT, and yield a good agreement with the ns-TA data for values very close to those estimated above from the results of a global analysis of the data using Glotaran. Transferring the optimized rates to 200 mT and changing only the magnetic field dependent rate k_{CR} decreases the quality of the fit only slightly. If the same is done for 1800 mT, the theoretical description overestimates the concentration of charge separated state but still describes the decay of the signal reasonably well. Slight variation of the reaction rates result in alternative values optimized for 200 mT (B) and 1800 mT (C) which simulate the observed kinetics very well. For all simulations, values for $k_{CSB} \approx 3 \cdot 10^9$ s^{-1} and $k_{CRB} = 1 \cdot 10^{10}$ s^{-1} give the best fit with the ns-TA data. While these values are very high, they are still lower than the theoretical maximum rates for a purely diffusion controlled reaction in MeCN.

Hence, the contribution of a bimolecular deactivation pathway to the overall decay kinetics of CSS_2 cannot be excluded based on the performed measurements and calculations.

Danksagung

First I would like to thank Prof Dr. Todd Marder for the welcoming atmosphere I experienced when asking him to be my secondary supervisor. Thank you Todd for your friendly and laid-back attitude, your uncomplicated style of managing things and your interest in my work.

Weiterhin gilt mein besonderer Dank Prof. Dr. Ulrich Steiner der mir die scheinbar unüberschaubare Welt der Spin-Chemie etwas näher gebracht hat. Herzlichen Dank für Ihren unermüdlichen Einsatz noch aus dem Ruhestand heraus, viele wertvolle Anregungen, Ihre Hilfe bei der Interpretation diverser MFE die mir einiges an Zeit und Kopfschmerzen erspart hat, Ihre unkomplizierte Art und manch gutes Gespräch abseits der Chemie.

Außerdem gilt mein ausdrücklicher Dank allen Mitarbeitern der Universität Würzburg die mir (so wie jedem anderen Doktoranden) den Arbeitsalltag beträchtlich vereinfacht haben. Dr. Alfons Ledermann, Matthias Fromm, Dr. Christian Stadler und Anette Krug für viel bürokratische und infrastrukturelle Unterstützung. Dr. Matthias Grüne, Patricia Altenberger und Elfi Ruckdeschel für das Aufsetzen einiger NMR-Spektren und die fantastische Betreuung und Instandhaltung der Messgeräte. Liselotte Michels und Sabine Timmroth für das präzise Verbrennen mehrere mg meiner Produkte und die Elementar-Analysen die dadurch entstanden sind. Dr. David Schmidt und Ana-Maria Krause für mehrere Röntgenstrukturanalysen die zum Teil einiges an Aufwand gekostet haben, die Arbeit mit euch war sehr angenehm, unkompliziert und produktiv.

Dr. Michael Büchner und Antje Heckmann für die meist schnelle Durchführung der Massenspektrometrie. Michael Ramold und Frank Förtsch, die sich vorzüglich um den Zustand aller Vakuum-Pumpen, Wasserleitungen und Elektro-Geräte kümmern.

Bernd Brunner, der meinen PC mehrmals aus dem Scheintod ins Leben zurück geholt hat, einmal davon wie sollte es anders sein 2 Wochen vor meiner Erst-Abgabe.

Markus Braun, für seine extrem hilfsbereite Art, viele unkomplizierte und erfolgreiche Problemlösungen und sein unglaubliches Gedächtnis welches Thermopapier schonmal an wen ausgeliehen wurde. Dein unermüdlicher Einsatz und die Bereitschaft einen extra Meter weiter zu gehen um anderen Menschen das Leben leichter zu machen ist bewundernswert! Danke außerdem für mehrere Kilo Trockeneis für „Kühlbäder“.

Jo Landeck, den besten Glasbläser den man sich für eine Universität wünschen kann. Danke für die (mehrmalige) Maßanfertigung einiger Spezial-Geräte und Apparaturen ohne die meine Arbeit wesentlich komplizierter geworden wäre. Außerdem hast du dir deinen suboptimalen Arbeitsplatz mit einer angenehmen Mischung aus Metal und Reggea doch recht gemütlich gemacht und Ausflüge zu dir wurden deshalb und wegen deiner gesprächigen Art immer länger als für das eigentlich geschäftliche nötig.